

9–13 ОКТЯБРЯ 2017  
ИНСТИТУТ КОСМИЧЕСКИХ ИССЛЕДОВАНИЙ РАН  
МОСКВА

9–13 OCTOBER 2017  
SPACE RESEARCH INSTITUTE  
MOSCOW

ВОСЬМОЙ  
МОСКОВСКИЙ  
СИМПОЗИУМ  
ПО СОЛНЕЧНОЙ  
СИСТЕМЕ

THE EIGHT  
MOSCOW  
SOLAR SYSTEM  
SYMPOSIUM

ISBN 978-5-00015-029-0

© Федеральное государственное бюджетное учреждение науки  
Институт космических исследований Российской академии наук (ИКИ РАН), 2017

# TABLE OF CONTENT

**INTRODUCTION**  
**PROGRAM COMMITTEE**

**PROGRAM**  
overview PROGRAM  
scientific PROGRAM

**ABSTRACTS**

**INFORMATION**  
ADDRESS  
METRO MAP  
REGISTRATION AND INFORMATION DESK  
SCIENTIFIC SESSIONS  
POSTER SESSIONS  
SOCIAL PROGRAM  
INTERNET ACCESS AND WiFi  
LUNCH POINTS

**NOTEBOOK**

# THE EIGHTH MOSCOW SOLAR SYSTEM SYMPOSIUM 8M-S<sup>3</sup>

**SPACE RESEARCH INSTITUTE**

**MOSCOW, RUSSIA**

**october 9-13, 2017**

Starting from 2010, the Space Research Institute holds annual international symposia on Solar system exploration. Main topics of these symposia include wide range of problems related to formation and evolution of Solar system, planetary systems of other stars; exploration of Solar system planets, their moons, small bodies; interplanetary environment, astrobiology problems. Experimental planetary studies, science instruments and preparation for space missions are also considered at these symposia.

The Eight Moscow international Solar System Symposium (8M-S3) will be held from October 9 till 13, 2017. This year is marked by the 60th anniversary of the First satellite launch and the starting of Space era.

Subject matter of this symposium will cover many problems of the Solar system science with the central topic "Moon, Mars and Venus research". This topic relates to scientific problems of several missions: "Mars Express", "Venus Express", the missions under development in Russia: "Luna-Glob", "Luna-Resource", "ExoMars 2016" (Roscosmos-ESA), which was launched on March 14, 2016, and "ExoMars 2020" (Roscosmos-ESA).

## **THE FOLLOWING SESSIONS WILL BE HELD DURING THE SYMPOSIUM:**

- session: PLANETARY ATMOSPHERES  
The session dedicated to the memory of Tobias Owen
- session: LUNAR AND PLANETARY GEOLOGY
- session: GIANT PLANETS
- session: ASTROBIOLOGY, METHODS AND INSTRUMENTS  
FOR SEARCH OF EXTRATERRESTRIAL LIFE
- session: EXOPLANETS
- session: DUST AND DUSTY PLASMA IN SPACE
- session: SMALL BODIES
- session: SOLAR WIND INTERACTIONS WITH PLANETS  
AND SMALL BODIES
- session: INSTRUMENTS, MISSIONS, EXPLORATION

Space Research Institute holds this symposium with participation of the following organizations:

- RUSSIAN FOUNDATION FOR BASIC RESEARCH
- VERNADSKY INSTITUTE OF GEOCHEMISTRY AND ANALYTICAL CHEMISTRY, RUSSIA
- BROWN UNIVERSITY, USA
- EARTH PHYSICS INSTITUTE, RUSSIA
- KELDYSH INSTITUTE OF APPLIED MATHEMATICS, RUSSIA
- RADIO ELECTRONICS INSTITUTE, RUSSIA
- STERNBERG ASTRONOMICAL INSTITUTE, MOSCOW STATE UNIVERSITY, RUSSIA

symposium website: <http://ms2017.cosmos.ru>

contact email address: [ms2017@cosmos.ru](mailto:ms2017@cosmos.ru)

*Мероприятие проводится при финансовой поддержке Российской академии наук и Российского фонда фундаментальных исследований, Проект № 17-02-20551*

# PROGRAM COMMITTEE

**chair:**

acad. **ZELENYI L.M.** IKI RAS

**members:**

**BAZILEVSKIY A.T.** GEOHI RAS

**BIBRING J.-P.** IAS,CNRS, France

**BOLTON S.J.** Southwest Research Institute, USA

**BOROVIN G.K.** Keldysh AMI RAS

**CHICARRO A.** ESTEC, ESA

**DUXBURY T.** George Mason University, USA

**HEAD III J.** Brown University, USA

**KORABLEV O.I.** IKI RAS

**KOSTITSYN Y.A.** GEOHI RAS

**MAROV M.Ya.** GEOHI RAS

**MITROFANOV I.G.** IKI RAS

**RODIN A.V.** IKI RAS

**SHEVCHENKO V.V.** GAISH MSU

**SMIRNOV V.M.** IRE RAS

**SVEDHEM H.** ESTEC, ESA

**VAISBERG O.L.** IKI RAS

**VOROBYOVA E.A.** MSU

**WITASSE O.** ESTEC, ESA

**WU Ji** National Space Science Center, China

**ZHARKOV V.N.** IFZ RAS

**ZAKHAROV A.V.** IKI RAS

**ZASOVA L.V.** IKI RAS

**secretary:**

**ROSTE O.** IKI RAS, [ms3@iki.rssi.ru](mailto:ms3@iki.rssi.ru)

# overview 8M-S<sup>3</sup> program

## THE EIGHTH MOSCOW SOLAR SYSTEM SYMPOSIUM (8M-S<sup>3</sup>)

IKI RAS, 9-13 OCTOBER 2017

	9 october	10 october	11 october	12 october	13 october				
10.00	opening								
10.20									
10.40									
11.00									
11.20									
11.40	Session 1. PLANETARY ATMOSPHERES	Session 2. LUNAR AND PLANETARY GEOLOGY	session 3. GIANT PLANETS	session 6. DUST AND DUSTY PLASMA	session 9. INSTRUMENTS, MISSIONS, EXPLORATION				
12.00						coffee	coffee	coffee	coffee
12.20						lunch	lunch	lunch	lunch
12.40									
13.00						coffee	coffee	coffee	coffee
14.00									
14.20									
14.40			coffee	coffee		coffee	coffee		
15.00									
15.20									
15.40	Session 4. ASTROBIOLOGY		session 5. EXOPLANETS	session 7. SMALL BODIES					
16.00						coffee	coffee	coffee	coffee
16.20						coffee	coffee	coffee	coffee
16.40									
17.00									
17.20	coffee	coffee	coffee	coffee					
17.40									
18.00									
18.20	POSTER SESSION WELCOME PARTY	SOCIAL EVENTS IN MOSCOW	POSTER SESSION	CONCERT	SOCIAL EVENTS IN MOSCOW				
18.40			SOCIAL EVENTS IN MOSCOW	RECEPTION					
19.00									
19.20									
19.40									
20.00									

# 8M-S<sup>3</sup> SCIENTIFIC PROGRAM

monday, 9 october 2017

Lev ZELENYI opening remarks 10.00-10.40

**session 1. PLANETARY ATMOSPHERES.  
THE SESSION DEDICATED  
TO THE MEMORY OF TOBIAS  
OWEN** **10.40-18.00**

**conveners: Ludmila ZASOVA, Scott BOLTON,  
Oleg KORABLEV**

8MS3-PA-01 **Mikhail MAROV  
and  
Sergei IPATOV** Heterogeneous accretion:  
some results of the  
computer modeling 10.40-11.00

8MS3-PA-02 **Jonathan LUNINE  
and  
Scott BOLTON** The origin of Titan's  
atmosphere revealed  
in isotopic and molecular  
composition: from Toby  
Owen's pioneering work  
to the end of Cassini 11.00-11.20

8MS3-PA-03 **Jack WAITE  
et al** CASSINI In Situ  
Observations of Saturn's  
Equatorial Atmosphere  
and Ionosphere 11.20-11.40

**coffee-break** **11.40-12.00**

8MS3-PA-04 **Helmut LAMMER  
et al** Element fractionation  
by hydrodynamic escape  
at early Venus: constraining  
the planet's evolution 12.00-12.20

8MS3-PA-05 **Mikhail  
GERASIMOV** On the Origin  
of Atmospheres  
of Terrestrial Planets 12.20-12.40

8MS3-PA-06 **Yeon Joo LEE  
et al** Venus' glory observed  
by the UV Imager on board  
Akatsuki 12.40-13.00

**lunch** **13.00-14.00**

8MS3-PA-07 **Vladimir  
KRASNOPOLSKY** Disulfur dioxide and its  
NUV absorption in the  
photochemical model  
of Venus atmosphere 14.00-14.20

8MS3-PA-08 **Vladimir  
KRASNOPOLSKY  
and  
Denis BELYAEV** Search for HBr and bromine  
photochemistry on Venus 14.20-14.40

8MS3-PA-09 **Mikhail LUGININ  
et al** Study of scale heights  
and detached haze layers  
at high latitudes in the upper  
haze of Venus from SPICAV  
IR data 14.40-15.00

8MS3-PA-10 **Jose Luis  
VAZQUEZ  
POLETTI  
et al** Optimal Cloud Computing  
Infrastructure for Planetary  
Image Processing: A Tale  
of Two Planets (Mars and  
Venus) 15.00-15.20

8MS3-PA-11 **Anatoliy PAVLOV  
et al** Evolution of Martian  
atmosphere in modern era,  
its isotopic imprints and  
connection with Martian  
subsurface environments 15.20-15.40

8MS3-PA-12 **Ashley PALUMBO  
et al** Late Noachian icy highlands  
climate model: Exploring  
the possibility of transient  
melting and fluvial/  
lacustrine activity through  
peak annual/seasonal  
temperatures 15.40-16.00

**coffee-break** **16.00-16.20**

8MS3-PA-13	<b>Anna FEDOROVA et al</b>	Long-term observations of water vapor in the middle atmosphere of Mars by SPICAM/MEX	16.20-16.40
8MS3-PA-14	<b>Vladimir KRASNOPOLSKY</b>	Annual mean mixing ratios of N <sub>2</sub> , Ar, O <sub>2</sub> , and CO in the martian atmosphere	16.40-17.00
8MS3-PA-15	<b>Maxim LITVAK</b>	Inter-annual variations of Martian seasonal caps from neutron spectroscopy observations onboard Mars Odyssey	17.00-17.20
8MS3-PA-16	<b>Salvador JIMÉNEZ et al</b>	Magnetic field at Mars ionosphere from MARSIS data. Models and simulations	17.20-17.40
8MS3-PA-17	<b>Valery SHEMATOVICH</b>	Neutral escape at Mars induced by the high-energy H/H <sup>+</sup> of solar wind origin	17.40-18.00
<b>POSTER SESSION (all sessions)</b>			<b>18.00-19.00</b>

tuesday, 10 october 2017

**session 2. LUNAR AND PLANETARY  
GEOLOGY**

**10.00-18.00**

**conveners: Igor MITROFANOV, Maxim LITVAK**

8MS3-PG-01	<b>Maxim LITVAK et al</b>	Crater age and hydrogen content in lunar regolith from LEND neutron data	10.00-10.20
8MS3-PG-02	<b>Alexander BAZILEVSKY et al</b>	Recent tectonic deformation in the South pole area of the Moon	10.20-10.40
8MS3-PG-03	<b>Andrew DMITROVSKY et al</b>	Preliminary data on the age interval of the Mons Rumker volcanic province formation	10.40-11.00
8MS3-PG-04	<b>Arne GRUMPE et al</b>	Daytime-dependent variations of the lunar surficial OH/H <sub>2</sub> O content	11.00-11.20
8MS3-PG-05	<b>Daniela ROMMEL et al</b>	South Pole-Aitken Basin: Anorthosite rich material as indicator for a complex layering of the basin crust structure	11.20-11.40

**coffee-break**

**11.40-12.00**

8MS3-PG-06	<b>Mariya BUCHENKOVA et al</b>	Wave phenomena in the Moon environment	12.00-12.20
8MS3-PG-07	<b>Audrey VORBURGER et al</b>	The Moon observed in Energetic Neutral Atoms: Review of the Scientific Findings from SARA/CENA on board Chandrayaan-1	12.20-12.40
8MS3-PG-08	<b>Anton SANIN et al</b>	Potentially interesting landing sites around the South pole of the Moon	12.40-13.00

**lunch**

**13.00-14.00**

8MS3-PG-09	<b>Carle PIETERS et al</b>	Diversity of materials at Luna 24 site from Moon Mineralogy Mapper (M3)	14.00-14.20
8MS3-PG-10	<b>Anastasia ZHARKOVA et al</b>	Craters features of the Moon and Mercury Southern polar regions	14.20-14.40
8MS3-PG-11	<b>Ariel DEUTSCH et al</b>	New evidence for surface ice in micro-cold traps and in three large craters at the North polar region on Mercury: implications for lunar exploration	14.40-15.00
8MS3-PG-12	<b>Ekaterina FEOKTISTOVA et al</b>	Thermal and illumination conditions in the radar features host craters in the Mercury's South pole region	15.00-15.20
8MS3-PG-13	<b>Svetlana PUGACHEVA et al</b>	Morphological features of Mercury South pole relief	15.20-15.40
8MS3-PG-14	<b>James HEAD et al</b>	Deciphering the Noachian geological and climate history of Mars: Part 2- A Noachian stratigraphic view of major geologic processes and their climatic consequences	15.40-16.00

**coffee-break**

**16.00-16.20**

8MS3-PG-15	<b>Denis LISOV et al</b>	Water and Chlorine abundance in the Gale crater according to DAN data	16.20-16.40
8MS3-PG-16	<b>Benjamin BOATWRIGHT and James HEAD</b>	MARSSIM Landform Evolution Model: Hydrologic Constraints on the Noachian Early Dry Period	16.40-17.00



8MS3-PG-17	<b>James HEAD</b>	Venus Geological History: Current Perspectives, Unknowns, and Opportunities for the Modeling Community	17.00-17.20
8MS3-PG-18	<b>Evgeniya GUSEVA</b>	Rift zones of Venus: Possible terrestrial analogues	17.20-17.40
8MS3-PG-19	<b>Piero D'INCECCO and L.S. GLAZE</b>	Imdr Regio as the landing site of the Venera-D mission: a geologic perspective	17.40-18.00

wednesday, 11 october 2017

**session 3. GIANT PLANETS**

**10.00-14.40**

**convener: Valery SHEMATOVICH,  
Scott BOLTON**

8MS3-GP-01	<b>Scott BOLTON et al</b>	The Juno Mission	10.00-10.20
8MS3-GP-02	<b>John CONNERNEY et al</b>	Jupiter's Magnetic Field and Magnetosphere: Juno's First Eight Orbits	10.20-10.40
8MS3-GP-03	<b>John JOERGENSEN et al</b>	Profiling the Jovian high energy particle flux at Juno's trajectories	10.40-11.00
8MS3-GP-04	<b>Victor KRONROD</b>	Fragmentation of planetesimals and capture of material by the circumplanetary disks of Jupiter and Saturn	11.00-11.20
8MS3-GP-05	<b>Igor ALEXEEV et al</b>	Equatorial Current Disk Dynamics in the Jovian Magnetosphere	11.20-11.40

**coffee-break**

**11.40-12.00**

8MS3-GP-06	<b>Peter WURZ et al</b>	Interaction of Jupiter's Plasma with the Galilean Moons	12.00-12.20
8MS3-GP-07	<b>Yaroslav ILYUSHIN and Paul HARTOGH</b>	The Prospects for Active and Passive Radar Probing of Ganymede	12.20-12.40
8MS3-GP-08	<b>Valery SHEMATOVICH</b>	Gas Envelopes of the Icy Moons with Oceans	12.40-13.00

**lunch**

**13.00-14.00**

8MS3-GP-09	<b>Jonathan LUNINE and Scott BOLTON</b>	Using Volatiles to Determine Planetary Formation Processes	14.00-14.20
8MS3-GP-10	<b>Alexander HAYES et al</b>	The Bathymetry and Composition of Titan's Lakes and Seas: A Post-Cassini View	14.20-14.40

**session 4. ASTROBIOLOGY, METHODS  
AND INSTRUMENTS FOR SEARCH  
OF EXTRATERRESTRIAL LIFE**

**14.40-16.00**

**convener: Elena VOROBYOVA**

8MS3-AB-01	<b>Georgi MANAGADZE</b>	Emergence of life in the meteorite impact plasma in the process of the formation and mass accumulation by the Earth	14.40-15.00
8MS3-AB-02	<b>Maxim ZAITSEV and Mikhail GERASIMOV</b>	Formation of Amino Acids from Components of a Nitrogen-Methane Atmosphere during Hypervelocity Impacts	15.00-15.15
8MS3-AB-03	<b>Leonid KSANFOMALITY</b>	Moving Living Objects on Venus: New Evidence	15.15-15.30
8MS3-AB-04	<b>Dmitrij SKLADNEV and V.V. SOROKIN</b>	Observation of biogenic nanoparticles generation for comparison of microbial communities and for detection of extraterrestrial life	15.30-15.45
8MS3-AB-05	<b>Oleg KOTSYURBENKO</b>	Astrobiology in Russia: Integration to the Worldwide Astrobiology	15.45-16.00

**coffee-break**

**16.00-16.20**

<b>session 5. EXOPLANETS</b>			<b>16.20-18.00</b>
<b>convener: Alexander TAVROV</b>			
8MS3-EP-01	<b>Jean-Loup BERTAUX</b>	A Road Map to the New Frontier: finding Extra Terrestrial Intelligenc	16.20-16.40
8MS3-EP-02	<b>Ildar SHAIKHISLAMOV et al</b>	Modeling Transit Observations of HD209458B	16.40-17.00
8MS3-EP-03	<b>Jean-Loup BERTAUX et al</b>	Retrieving the true mass distribution of exoplanets detected with the Radial velocity method: method and first results	17.00-17.15
8MS3-EP-04	<b>Vladislava ANANJEVA et al</b>	Retrieving the true mass distribution of exoplanets detected with the Radial velocity method: removing the effect of observing selection	17.15-17.30
8MS3-EP-05	<b>Seyed Javad JAFARZADEH et al</b>	The effect of unknown parameters of exoplanets on their habitability	17.30-17.45
8MS3-EP-06	<b>Alexander TAVROV et al</b>	Stellar imaging coronagraph and exoplanet coronal spectrometer – instruments for exoplanet exploration onboard the WSO-UV	17.45-18.00
<b>POSTER SESSION (all sessions)</b>			<b>18.00-19.00</b>

thursday, 12 october 2017

**session 6. DUST AND DUSTY PLASMA  
IN SPACE**

**10.00-11.40**

**convener: Alexander ZAKHAROV**

8MS3-DP-01	<b>Maria Pilar VELASCO et al</b>	Atmospheric dust dynamics: fractional models, numerical methods and computational simulations	10.00-10.20
8MS3-DP-02	<b>Dariia BETSIS et al</b>	Martian dust cycle via solar infrared occultation observations by SPICAM IR for 27–34 MY	10.20-10.40
8MS3-DP-03	<b>Evgenij ZUBKO et al</b>	Reflectance of lunar dust: Concept of experiment aboard a lunar lander	10.40-11.00
8MS3-DP-04	<b>Sergey POPEL et al</b>	Dusty plasma cloud in the lunar exosphere and impacts of meteoroids	11.00-11.20
8MS3-DP-05	<b>Andrey DUBINSKY and Sergey POPEL</b>	Hydrogen formation in lunar regolith and its possible influence on dusty plasma at the Moon	11.20-11.40

**coffee-break**

**11.40-12.00**

**session 7. SMALL BODIES**

**12.00-16.00**

**convener: Alexander BASILEVSKY**

8MS3-SB-01	<b>Olga POPOVA et al</b>	Infrasound registration of Romanian superbolide	12.00-12.15
8MS3-SB-02	<b>Anna KARTASHOVA et al</b>	The investigation of meteor events by multi technique observations	12.15-12.30
8MS3-SB-03	<b>Rob LANDIS et al</b>	The Recovery of 2012 TC4 and the International Asteroid Warning Network (IAWN)	12.30-12.45
8MS3-SB-04	<b>Ilan ROTH</b>	Anomalous Mg-26 composition in the early solar system chondrites	12.45-13.00
<b>lunch</b>			<b>13.00-14.00</b>
8MS3-SB-05	<b>Boris KONDRATYEV et al</b>	Dynamics and evolution of rings around Centaurs Chariklo and Chiron	14.00-14.15
8MS3-SB-06	<b>Sergey VOROPAEV</b>	The surface tension of small bodies under self-gravity, rotation and tidal forces	14.15-14.30
8MS3-SB-07	<b>Anastasiia DUBOVITSKAIA et al</b>	Update of shape parameters and libration amplitude for Saturnian satellites Dione and Rhea	14.30-14.45
8MS3-SB-08	<b>Rosine LALLEMENT and Jean-Loup BERTAUX</b>	Diffuse Interstellar Bands carriers and cometary organic material	14.45-15.00
8MS3-SB-09	<b>Olena SHUBINA et al</b>	Color-slope interpretation of comet C/2013 UQ4 (Catalina) using the model of agglomerated debris particles	15.00-15.15
8MS3-SB-10	<b>Vacheslav EMEL'YANENKO</b>	Nongravitational effects in the motion of near-Sun comets	15.15-15.30
8MS3-SB-11	<b>Yuri SKOROV</b>	The models of cometary gas production: Analysis for 67P/Churyumov-Gerasimenko	15.30-15.45

8MS3-SB-12	<b>Leonid KSANFOMALITY</b>	Comets 1P/Halley and 67P/ Churyumov-Gerasimenko: comparison of some their properties	15.45-16.00
<b>coffee-break</b>			<b>16.00-16.20</b>
<b>Session 8. SOLAR WIND INTERACTIONS WITH PLANETS AND SMALL BODIES</b>			
<b>convener: Oleg VAISBERG</b>			16.20-18.00
8MS3-SW-01	<b>Mingyuan WANG et al</b>	Exploring obvious lunar ionosphere based on the service module of circumlunar return and reentry spacecraft	16.20-16.30
8MS3-SW-02	<b>Alexey BEREZHNOY and G.V. BELOV</b>	Behavior of hydrogen during impact events on the Moon	16.30-16.40
8MS3-SW-03	<b>Sergey SHUVALOV et al</b>	Analysis of solar wind- Mars interaction region and pick-up ions from MAVEN measurements	16.40-16.50
8MS3-SW-04	<b>Oleg VAISBERG et al</b>	Dayside magnetosphere of Mars	16.50-17.00
8MS3-SW-05	<b>Vladimir ERMAKOV et al</b>	Initial analysis of ion fluxes in magnetotail of Mars based on simultaneous measurements on Mars Express and MAVEN	17.00-17.10
8MS3-SW-06	<b>Eduard DUBININ et al</b>	How to describe the martian space environment and how solar wind and EUV control ion escape. MAVEN observations	17.10-17.20
8MS3-SW-07	<b>Petra ODERT et al</b>	Escape of volatiles from Mars-sized planetary embryos	17.20-17.30
8MS3-SW-08	<b>Mikhail VERIGIN and Galina KOTOVA</b>	Who twists venusian magnetotail?	17.30-17.40
8MS3-SW-09	<b>Oleg VAISBERG et al</b>	Radio-occultation and in-situ measurements of plasma density in Halley's comet plasma	17.40-17.50
	discussion		17.50-18.00

friday, 13 october 2017

**session 9. INSTRUMENTS, MISSIONS,  
EXPLORATION**

**10.00-18.40**

**convener: Oleg KORABLEV**

8MS3-IM-01	<b>Thomas DUXBURY et al</b>	Restoration of the 1969 Mariner Mars Images: Phase I Results	10.00-10.20
8MS3-IM-02	<b>Thomas DUXBURY et al</b>	The International Phobos / Deimos Surface Characterization and Site Selection Working Group	10.20-10.40
8MS3-IM-03	<b>Jürgen OBERST et al</b>	DEPHINE – the Deimos and Phobos Interior Explorer – a Mission Proposal to ESA'S Cosmic Vision Program/ <b>invited talk/</b>	10.40-11.00
8MS3-IM-04	<b>Dmitrij TITOV et al</b>	Mars Express science highlights and future plans <b>/invited talk/</b>	11.00-11.20
8MS3-IM-05	<b>Sergei NIKIFOROV et al</b>	Water content in the Martian subsurface along the NASA/MSL "Curiosity» Rover traverse: data of the DAN instrument in Passive mode	11.20-11.40

**coffee-break**

**11.40-12.00**

8MS3-IM-06	<b>Jordanka SEMKOVA et al</b>	Charged particles radiation quantities onboard Exomars Trace Gas Orbiter during the transit and in high elliptic Mars orbit	12.00-12.20
8MS3-IM-07	<b>Alexey MALAKHOV et al</b>	Fine Resolution Neutron Detector (FRIEND) Instrument onboard Exomars 2016 TGO Orbiter. First Results	12.20-12.40
8MS3-IM-08	<b>Andrey VOSTRUKHIN</b>	Neutron component of radiation environment for interplanetary missions	12.40-13.00

**lunch**

**13.00-14.00**

8MS3-IM-09	<b>Ludmila ZASOVA et al</b>	VENERA-D - Concept Mission to Venus: Scientific Goals and Architecture <b>/invited talk/</b>	14.00-14.20
8MS3-IM-10	<b>Maxim LITVAK et al</b>	Active gamma ray spectrometer proposed for future Venus surface missions	14.20-14.40
8MS3-IM-11	<b>Daniel RODIONOV et al</b>	ExoMars 2020 Surface platform Payload/ <b>invited talk/</b>	14.40-15.00
8MS3-IM-12	<b>Francesca ESPOSITO et al</b>	Characterisation of Dust Suspended in the Atmosphere of Mars: the Dust Suite - Micromed Sensor for the Exomars 2020 Mission	15.00-15.20
8MS3-IM-13	<b>Diego Rodríguez DÍAZ et al</b>	AMR instrument for stationary magnetic measurements on Mars	15.20-15.40
8MS3-IM-14	<b>Marina DÍAZ- MICHELENA et al</b>	NEWTON Project: New opportunities for magnetic surveys in the planetary exploration	15.40-16.00

**coffee-break**

**16.00-16.20**

8MS3-IM-15	<b>Jinsong PING</b>	Low frequency radio astronomical missions on the farside space of the Moon	16.20-16.40
8MS3-IM-16	<b>Mariia ZAKHAROVA</b>	Compiling the navigational 3D model for prospective lunar base area	16.40-17.00
8MS3-IM-17	<b>Alexander KOSOV et al</b>	Radioscience Experiments for Martian and Lunar Missions	17.00-17.20
8MS3-IM-18	<b>Dmitry MOISEENKO et al</b>	Functional tests of ARIES-L instrument	17.20-17.40
8MS3-IM-19	<b>Victor APESTIGUE et al</b>	Mars 2020 Radiation and Dust Sensor Technical Overview	17.40-18.00
8MS3-IM-20	<b>Ryan CHAU and A.A. MARDON</b>	Lunar Caving: Usage and Exploration	18.00-18.20
8MS3-IM-21	<b>Konstantin LUCHNIKOV et al</b>	Method and Laser Ablation Mass-Spectrometer for the Search of Evidence of Life From the Europa Lander	18.20-18.40

# POSTER SESSION

9 october 18.00-19.00

11 october 18.00-19.00

## PLANETARY ATMOSPHERES

8MS3-PS-01	<b>Sanjay S. LIMAYE et al</b>	Mesoscale vortex circulations on Venus observed in AKATSUKI IR2 images
8MS3-PS-02	<b>Daria EVDOKIMOVA et al</b>	Venus cloud parameters modulating the 1.28- $\mu\text{m}$ nightside window emission observed by SPICAV IR/VEX
8MS3-PS-03	<b>Elena PETROVA</b>	Glory on the upper cloud deck of Venus and identification of the unknown UV absorber
8MS3-PS-04	<b>Vladimir GUBENKO et al</b>	Radio occultation retrievals of zonal wind speed at the high-latitude atmosphere of the Venus
8MS3-PS-05	<b>A. PAVELYEV et al</b>	Space bistatic radio-holography as applied to study atmosphere and surface of Venus and Earth
8MS3-PS-06	<b>Ashley PALUMBO and James HEAD</b>	The mineralogic alteration history of early Mars: The role of large craters and basins in transient regional high-temperature alteration
8MS3-PS-07	<b>Anton SANIN et al</b>	Impact of the Martian atmosphere properties on the spatial resolution of the FREN/D/TGO
8MS3-PS-08	<b>Herbert LICHTENEGGER et al</b>	Influence of Suprathermal Atoms on the Escape and Evolution of the Martian' CO <sub>2</sub> Atmosphere

## LUNAR AND PLANETARY GEOLOGY

8MS3-PS-09	<b>James HEAD and H. QUINTAL</b>	McMurdo Dry Valleys: Exploring Antarctica As A Mars Analog
8MS3-PS-10	<b>Adeene DENTON and James HEAD</b>	The fretted terrain, Mars: Implications of missing volume for hypotheses of origin
8MS3-PS-11	<b>James CASSANELLI and James HEAD</b>	Outflow Channels on Mars: Testing the Origin of Reull Vallis in Hesperia Planum by Large-Scale Lava-Ice Interactions and Top-Down Melting
8MS3-PS-12	<b>Erica JAWIN et al</b>	The Prinz-Harbinger Shield Volcano: A Transition in Lunar Volcanic Eruption Style
8MS3-PS-13	<b>Boris IVANOV</b>	Small lunar crater degradation: time scale and mechanisms
8MS3-PS-14	<b>Natalia KOZLOVA et al</b>	Morphometric catalogue of lunar craters 1-10 km in diameter
8MS3-PS-15	<b>Dijun GUO et al</b>	Oriente Secondary Craters: Insights Into Oriente Impact Parameters and the Largest Secondary Crater Size of the South Pole-Aitken Basin Event
8MS3-PS-16	<b>Gennady KOCHEMASOV</b>	Global Degassing Producing Formation In Crust of Hydrocarbon Concentrations, Kimberlites, and Alkaline Rocks
8MS3-PS-17	<b>Gennady KOCHEMASOV</b>	Orbital Energy As a Main Source for Shaping and Structuring Cosmic Bodies
8MS3-PS-18	<b>Tamara GUDKOVA et al</b>	On attenuation of torsional oscillations on Mars
8MS3-PS-19	<b>Vladimir ZHARKOV et al</b>	On the estimate of the dissipative factor of martian interiors
8MS3-PS-20	<b>Alexey BATOV et al</b>	Model stresses in martian interiors for two-level loading
8MS3-PS-21	<b>Evgeny SLYUTA</b>	The Scientific Tasks of the LUNA-GRUNT Project (LUNA-28)
8MS3-PS-22	<b>Sergey KRASILNIKOV et al</b>	Estimation of probability of dangerous slopes in the landing sites of LUNA-GLOB spacecraft through analysis of shadow area on the LROC NAC images



8MS3-PS-23	<b>Alexey MALAKHOV et al</b>	SAP "Luna" system for automated scientific planning of future lunar missions
8MS3-PS-24	<b>Mikhail IVANOV et al</b>	Sources of materials at the three high-priority landing sites of the LUNA-GLOB mission
8MS3-PS-25	<b>Maya DJACHKOVA et al</b>	LUNA-25 landing sites candidates: detailed analysis
8MS3-PS-26	<b>Mikhail IVANOV et al</b>	Contribution of the lunar basin ejecta to materials within the LUNA-GLOB landing zone
8MS3-PS-27	<b>Yuqi QIAN et al</b>	Geology of the CHANG'E-5 Candidate Landing Region In Northern Procellarum
8MS3-PS-28	<b>Yangxiaoyi LU and Vladislav SHEVCHENKO</b>	Crater Von Karman:CHANG'E-4 Farside Landing Mission
8MS3-PS-29	<b>Alexander GUSEV et al</b>	Spin-orbital evolution and interior of the Moon: past, modern, future
8MS3-PS-30	<b>Ekaterina KRONROD et al</b>	Lunar internal structure models consistent with seismic and selenodetic (GRAIL and LLR) data and thermodynamic constraints
8MS3-PS-31	<b>Azary BARENBAUM and Michael SHPEKIN</b>	Problem of mascons origin
8MS3-PS-32	<b>Andrey KHARITONOV</b>	The analysis of magnetic and gravity field of the Moon from satellite data for the geological analysis of lunar rocks
8MS3-PS-33	<b>Nadezhda CHUJKOVA et al</b>	A spherical harmonic and statistical analysis of the surface topography of the Moon and the connection of the relief with gravitational field
8MS3-PS-34	<b>Arthur ZAGIDULLIN et al</b>	Results of modeling the rotation of the Moon on the basis of modern theories of its physical libration
8MS3-PS-35	<b>Alexey ANDREEV</b>	Analysis of planetophysical parameters on the basis of harmonic and fractal methods and space missions data
8MS3-PS-36	<b>Sergei IPATOV</b>	Formation and growth of embryos of the Earth-Moon system
8MS3-PS-37	<b>Nikita DEMIDOV and Mikhail IVANOV</b>	Validation of Diviner rock abundance data with direct rock counting on LROC images
8MS3-PS-38	<b>Anastasia ZHARKOVA</b>	Mercury topographic roughness: calculation, analysis, mapping

#### GIANT PLANETS

8MS3-PS-39	<b>Anna DUNAEVA et al</b>	Main constraints on the hydrous silicates content for the models of partially differentiated Titan
8MS3-PS-40	<b>Sergei KULIKOV and Alexander SKALSKY</b>	Magnetic field measurements around Ganymede and at its surface
8MS3-PS-41	<b>Victor TEJFEL et al</b>	Zonal-time variations of the ammonia absorption on Jupiter in 2005-2015
8MS3-PS-42	<b>Ivan PENSIONEROV et al</b>	Is Saturn's magnetosphere open to the interplanetary magnetic field?

#### ASTROBIOLOGY, METHODS AND INSTRUMENTS FOR SEARCH OF EXTRATERRESTRIAL LIFE

8MS3-PS-43	<b>Georgi MANAGADZE et al</b>	Probability of nucleotide synthesis in the meteorite-impact plasma torch
------------	-------------------------------	--

8MS3-PS-44	<b>A. CHUMIKOV et al</b>	Elemental composition measurement as a powerful approach to searching and characterizing samples containing microorganisms
8MS3-PS-45	<b>Tatiana BORISOVA et al</b>	Inorganic martian dust simulant enriched by carbon component possess modulating effects on glutamate- and gaba-ergic neurotransmission
8MS3-PS-46	<b>Ahya REZAEI</b>	Plants growths in space, effective methods and techniques
8MS3-PS-47	<b>Mohammad Sadegh GHEIBZADEH</b>	Study of the bacterial life on similar conditions of the Europa, in the laboratory.
8MS3-PS-48	<b>Vladimir CHEPTSOV et al</b>	Putative martian microbial complexes could be viable cryopreserved in regolith during tens of millions years
8MS3-PS-49	<b>Ilya DIGEL and M. KUHLIN</b>	Temperature dependence of autofluorescence: detection limits for ubiquitous life-specific compounds
8MS3-PS-50	<b>Andrey BELOV et al</b>	High resistance of bacteria from extreme habitats to abiotic and biotic factors
8MS3-PS-51	<b>Tatyana ALEKHOVA et al</b>	Monitoring of internal environment on the board of space station
8MS3-PS-52	<b>Konstantin KLEMENTIEV et al</b>	Influence of space flight and ionizing radiation on the photosynthetic apparatus of cyanobacteria

#### EXOPLANETS

8MS3-PS-53	<b>Artem BEREZUTSKIY et al</b>	Two different regimes of interaction of planetary and stellar winds of the Glise 436 b and transit absorption in Lya line
------------	--------------------------------	---

#### DUST AND DUSTY PLASMA IN SPACE

8MS3-PS-54	<b>Iliia KUZNETSOV et al</b>	Numerical SPIS-Dust Modelling of Plasma - "Luna-Glob" Lander Interactions
8MS3-PS-55	<b>Andrey KHARITONOV</b>	The specific features of interplanetary magnetic field and dusty plasma from "ACE" satellite data
8MS3-PS-56	<b>Yulia IZVEKOVA et al</b>	Dusty plasma turbulence in the regions where the Moon crosses the Earth's magnetotail
8MS3-PS-57	<b>Tatiana SALNIKOVA and S. STEPANOV</b>	Effect of electromagnetic field on Kordylewski clouds formation

#### SMALL BODIES

8MS3-PS-58	<b>Mikhail KRESLAVSKY</b>	Gas of Dust Particles: A Possible Mechanism of Aeolian Processes on Small Bodies
8MS3-PS-59	<b>Vladimir BUSAREV et al</b>	Confirmation of sublimation and dust activity on 779 Nina and 704 Interamnia
8MS3-PS-60	<b>Marina SHCHERBINA et al</b>	Asteroid reflectance spectra modeling with laboratory databases of analog samples
8MS3-PS-61	<b>Dmitry GLAZACHEV et al</b>	Impact effect calculator. Radiation assessment from atmospheric impacts of cosmic bodies
8MS3-PS-62	<b>Atila PORO</b>	Pole of rotation and spin rate of different asteroids
8MS3-PS-63	<b>Zeinab Sadat LESANI</b>	A study on occultation and timing methods
8MS3-PS-64	<b>Gennady KOCHEMASOV</b>	Essence of the Wave Planetology Revealed in Shape of Asteroid 2014J025 and Some Other Small Celestial Bodies
8MS3-PS-65	<b>Dmitry SHESTOPALOV and L.F. GOLUBEVA</b>	Interlink between Photometric and Polarimetric Properties of Asteroids

## INSTRUMENTS, MISSIONS, EXPLORATION

8MS3-PS-66	<b>Imant VINOGRADOV et al</b>	A multichannel diode laser spectrometer experiment on board of the ExoMars-2020 mission landing platform for in situ study of atmosphere near the martian surface
8MS3-PS-67	<b>Anatoly MANUKIN et al</b>	A uniaxial seismometer is an element of a triaxial seismometer for measurements on the surface of Mars (the ExoMars program).
8MS3-PS-68	<b>Rositza KOLEVA et al</b>	Galactic cosmic rays modulation by solar wind disturbances as observed on board of ExoMars TGO
8MS3-PS-69	<b>Pauli LAINE</b>	Accessing Icy Moon's Ocean with Thermonuclear Reactor
8MS3-PS-70	<b>Yuri OZOROVICH et al</b>	Geophysical survey of the surface and subsurface planetary geo-electrical markers of the subsurface ocean on the Jupiter's and Saturn's ice moons: possibilities to adapt space technology for risk assessment and geophysical practice
8MS3-PS-71	<b>Helen POPOVA</b>	Theory of stability of nanocraft equipped with a sail accelerated by a intense laser beam
8MS3-PS-72	<b>Dmitry MOISEENKO et al</b>	Complex of low-weight miniature instruments for solar wind monitoring
8MS3-PS-73	<b>Rico FAUSCH et al</b>	Neutral gas mass spectrometry in the context of the Luna-Resurs mission
8MS3-PS-74	<b>Aleksey STAROVEROV and Oleg KHAVROSHKIN</b>	Space guns for the Moon and on the Moon
8MS3-PS-75	<b>Andrey LYASH et al</b>	Development of the Experimental Set-up for Lunar Dust Particles Investigation and Instruments calibrations
8MS3-PS-76	<b>Austin MARDON and Victoria THROCKMORTON</b>	Lunar lava tubes and pressurized tents as a suitable alternative for human habitation
8MS3-PS-77	<b>Ryan CHAU and Austin MARDON</b>	Using Meteor Burst Communications on inhabited planets
8MS3-PS-78	<b>Boris EPISHIN and Michael SHPEKIN</b>	Analysis of apparent motion of Sun, Earth and stars on lunar sky

# HETEROGENEOUS ACCRETION: SOME RESULTS OF THE COMPUTER MODELING

(Dedicated to the memory of Tobias Owen)

**M.Ya. Marov, S.I. Ipatov**

*Vernadsky Institute of Geochemistry and Analytical Chemistry, Kosygin st.,  
19, Moscow 119991, Russia, marovmail@yandex.ru*

## **KEYWORDS:**

heterogeneous accretion, migration, planetesimals, matter delivery, water, volatiles, terrestrial planets

## **INTRODUCTION:**

Toby Owen contributed in many important fields of planetary sciences involving both theoretical research and experimental results returned by space missions. It was a great privilege to discuss with him the most challenging ideas concerning the structure and composition of atmospheres of inner and outer planets, specifically isotopic ratios of noble gases on Mars and Venus aiming to reveal origin and evolution of these planets.

Here we address one of these pioneering ideas discussed by Toby Owen in the paper co-authored by F. Anders and published in Science magazine as early as in 1977 [1]. Authors attempted to explain lacking of water and other volatiles on Earth after its accumulation invoking a postulated migration process of volatile-rich bodies from periphery of the solar system at the later phase of its evolution, mainly in the course of Late Heavy Bombardment (LHB) dated around 4 billion years ago. Delivery such a matter and its layered sedimentation (late veneer) on the inner planets' surface the authors called the mechanism of heterogeneous accretion.

The idea drew attention and took further development including computer modeling to ensure its more rigorous support. Results of the study can be found in the numerous publications showing the great advancement in the field (see, e.g., [2, 3] and references therein). The study was mostly focused on the numerical models of comets, asteroids and dust transport from Kuiper belt and outer giant planets region inward through the migration mechanism involving different orbital perturbations. Based on this scenario quantitative estimates of water/volatiles that could be potentially delivered to Earth, Venus and Mars were made. Concurrently, it was attempted to evaluate bulk of water stored in the planet interior in due course of its accumulation from primordial matter in the framework of chondrite model and released later on the surface. The idea was most recently supported by the lab analysis of olivine in the archaean komatiites-basaltic associations (ultramafic lavas) resulted from melting under extreme conditions of the Earth's mantle, which argue for deep-mantle water reservoir [4]. Anyway, nowadays it is difficult to find a rationale and distinguish between exogenic or endogenic sources of water abundance that inner planets could acquire and the problem remains not unambiguous.

Our interest to the problem goes back to the time of Anders/Owen paper appearance while computer modeling aimed to volatiles amount delivery assessment began since the 1990s. Results of the original study can be found elsewhere (see, e.g., [2, 5-9]). In this paper we present a summary of how this research is in progress addressing several scenarios of migration in the course of planetary system evolution.

## **COMPUTER SIMULATIONS OF INWARD MIGRATION OF PLANETESIMALS FROM THE FEEDING ZONE OF JUPITER AND SATURN:**

Recently we [5] made computer simulations of migration of  $10^4$  planetesimals from the feeding zone of Jupiter and Saturn to forming terrestrial planets experienced gravitational influence of the planets. In series JN, all planets were assumed as having their present orbits and masses. In series JS, Uranus and Neptune were excluded. Initial eccentricities and inclinations of planetesimals were assumed to be 0.3 and 0.15 rad, respectively, while the initial semi-major axes of planetesimals were taken between 4.5 and 12 AU. We further

assumed masses of planets moving in orbits of the currently existed terrestrial planets to be equal their present masses in JS and JN series, while they were assumed to be smaller by a factor of 10 in the JS<sub>01</sub> and JN<sub>01</sub> series. These runs allowed us to model accumulation of embryos of the terrestrial planets. Based on an accepted set of orbital elements during evolution, the probabilities of collisions of migrating bodies with planets during their dynamical lifetimes were estimated. Also, calculations were carried out for a case when giant planets of present mass were initially located closer to each other compared to their present position. In such a scenario at least one of giant planets (not Jupiter) was ejected into a hyperbolic orbit in the process of evolution. For these runs probability  $p_E$  of planetesimal collision with Earth turned out not smaller than the values of  $p_E$  for series JS, JN, JS<sub>01</sub> and JN<sub>01</sub>.

## COMPUTER SIMULATIONS OF INWARD MIGRATION OF JUPITER-CROSSING OBJECTS:

The orbital evolution of more than 30,000 bodies having initial orbits close to those of Jupiter-family comets (JFCs), Halley-type comets, long-period comets, and asteroids in the resonances 3/1 and 5/2 with Jupiter was integrated until these bodies either reached radial distance 2000 AU or collided with the Sun [2, 6-9]. In such runs all planets moved in the present orbits and had their present masses. The symplectic or Bulirsh-Stoer codes were utilized. The probability  $p_E$  of collision with Earth of JFCs under consideration exceeded  $4 \times 10^{-6}$ .

## DELIVERY OF WATER AND VOLATILES TO THE TERRESTRIAL PLANETS:

Water and volatiles caused by exogenic source could be delivered to the terrestrial planets from different radial distances from the Sun. The main goal was to reconcile the D/H ratio in the cometary and Earth's oceans water. Alternatively to comets, bodies from the asteroid belt [3] were suggested as such a source. However arguments were brought [10] against this idea because oxygen isotopic composition in the primitive upper mantle better matches that of anhydrous ordinary chondrites rather than hydrous carbonaceous chondrites. Because the deep mantle water has a low D/H ratio there was assumed that it could be acquired due to water adsorption on fractal grains during the Earth's accretion [11]. As a compromise one may admit the ocean water (and respectively its D/H ratio) resulted from mixing of several sources.

The results of our computer modeling showed that ratio of the fraction of planetesimals collided with the Earth's embryo was about  $2 \times 10^{-6}$  and  $4 \times 10^{-7}$  for the Earth's mass embryos  $m_E$  and to  $0.1m_E$ , respectively. We derived that during the growth of Earth's embryo up to  $0.5m_E$  the amount of water delivered from the feeding zone of Jupiter and Saturn could be about 30% of the overall mass of water that Earth obtained from this feeding zone. In turn, mass of water delivered to Earth from the feeding zone of the giant planets and beyond turned out comparable with the total mass of the Earth's oceans (about  $2.25 \times 10^{-4}m_E$ ). Assuming the total mass of planetesimals (composed half of water) in the feeding zone of Jupiter and Saturn equal to  $100m_E$  and their collision probability with Earth  $p_E = 2 \times 10^{-6}$  this source gives rise a half of the Earth's ocean water, another a half coming from more distant regions. It should be emphasize that bulk of water delivered from these regions to the Earth's embryo came when its mass exceeded  $\sim 0.5m_E$ .

The mass of water delivered to other terrestrial planets turned out proportional to the ration of their masses to that of Earth. In the series JS it was smaller by a factor of 2, 1.25, and 1.3 for Mars, Venus and Mercury, respectively while for the series JN of 3.4, 0.7 и 0.8, respectively. For the Earth's embryo of mass  $m$  growing due to accretion of planetesimals coming from the feeding zone of Jupiter and Saturn, the increase of its mass turned out proportional to  $m^{0.74}$ .

In our calculations of the migration of objects which initially moved in cometary-type Jupiter-crossing orbits, the fraction  $p_E$  of the objects collided with the Earth exceeded  $4 \times 10^{-6}$  [7-9]. This value was greater than the above mentioned values of  $p_E$  for planetesimals because initial eccentricities of the planetesimals were smaller than those of cometary objects. Besides, not all planetesimals reached Jupiter's orbit during their lifetimes. Taking into account the mutual gravitational influence of planetesimals would increase their eccentricities during the evolution resulting in greater values of  $p_E$  as compared the model where such effect is neglected. Study of migration of the Jupiter-crossing objects and planetesimals showed that the ratio of mass of water delivered

by such bodies to the bulk mass of a planet was not smaller for Mars, Venus, and Mercury, than that for Earth. Interestingly, this larger mass fraction would result in relatively large ancient oceans on Mars and Venus.

Let us note that orbits of Earth-crossing objects migrating from outside Jupiter's orbit are typically highly eccentric. For such eccentric orbits, an amount of the material, including water, delivered from outside Jupiter's orbit is approximately proportional to effective radii of Earth and the Moon and therefore could be only by an order of magnitude smaller for the Moon than for Earth.

## CONCLUSIONS:

Anders/Owen publication in the middle of 1970s on heterogeneous accretion stimulated our advanced study of the problem through the modern computer modeling. We studied migration of bodies and dust to the terrestrial planets from the regions beyond the snow line, specifically inward migration of planetesimals from the feeding zone of Jupiter and Saturn, and estimated delivery of water and volatiles to these planets. It was found that during the growth of Earth's embryo up to a half of its present mass, the mass of water received by the embryo from the feeding zone of Jupiter and Saturn could amount to about 30% of the total mass of water delivered to the Earth from this feeding zone. Bulk of water delivered from the regions beyond Jupiter's orbit by planetesimals to the Earth's embryo came when its mass exceeded  $\sim 0.5m_{\oplus}$ . The mass of water delivered to Venus and Mercury turned out proportional to the ratio of their masses to that of Earth. Mars acquired more water per unit of mass of a planet than Earth.

## ACKNOWLEDGEMENTS:

The work was supported in part by the grant of Russian Science Foundation N 17-17-01279 and by the Program of Fundamental Studies of RAS № 22.

## REFERENCES:

- [1] Anders F., Owen T. Origin and abundance of volatiles // *Science*. 1977. V. 198. P. 453-465.
- [2] Marov M.Ya., Ipatov S.I. Volatile inventory and early evolution of planetary atmospheres // *Collisional processes in the solar system*, eds. M. Ya. Marov and H. Rickman, *Astrophysics and space science library*. V. 261. Dordrecht: Kluwer Academic Publishers. 2001. P. 223-247.
- [3] Petit J.-M., Morbidelli A., Chambers J. The primordial excitation and clearing of the asteroid belt // *Icarus*. 2001. V. 153. N 2. P. 338-347.
- [4] Sobolev A.V., Asafov E.V., Gurenko A.A., Ardnt N.T., Batanova V.G., Pottnyagin M.V., Schonberg D.G., Krashennnikov S.P. Komatiites reveal a hydrous Archaean deep mantle reservoir // *Nature*. 2016. V. 531. No. 7596. P. 628-632.
- [5] Ipatov S.I., Marov M.Ya. Migration of planetesimals to forming terrestrial planets from the feeding zone of Jupiter and Saturn // *Abstracts of 47th Lunar and Planetary Science Conference*. 2016. # 1458.
- [6] Marov M.Ya., Ipatov S.I. Migration of dust particles and volatiles delivery to the terrestrial planets // *Solar System Research*. 2005. V. 39. P. 374-380.
- [7] Ipatov S.I., Mather J.C. Migration of small bodies and dust to near-Earth space // *Adv. Space Res.* 2006. V. 37. P. 126-137. <http://arXiv.org/format/astro-ph/0411004>.
- [8] Ipatov S.I., Mather J.C. Migration of comets to the terrestrial planets // *Proc. IAU Symp.* No. 236 "Near-Earth Objects, Our Celestial Neighbors: Opportunity and Risk". Cambridge: Cambridge Univ. Press. 2007. P. 55-64. <http://arXiv.org/format/astro-ph/0609721>.
- [9] Ipatov S.I. Collision probabilities of migrating small bodies and dust particles with planets // *Proc. IAU Symposium S263*. V. 5, "Icy bodies in the Solar System". Cambridge: Cambridge Univ. Press. 2010. P. 41-44. <http://arxiv.org/abs/0910.3017>.
- [10] Drake M., Campins H. Origin of water on the terrestrial planets // *Proc. IAU Symp.* 229 "Asteroids, Comets, & Meteors". 2006. P. 381-394.
- [11] Hallis L.J., Huss G.R., Nagashima K., et al. Evidence for primordial water in Earth's deep mantle // *Science*. 2015. V. 350. P. 795-797.

# THE ORIGIN OF TITAN'S ATMOSPHERE REVEALED IN ISOTOPIC AND MOLECULAR COMPOSITION: FROM TOBY OWEN'S PIONEERING WORK TO THE END OF CASSINI

J.I. Lunine<sup>1</sup>, S. J. Bolton<sup>2</sup>

<sup>1</sup>*Cornell Center for Astrophysics and Planetary Science, Cornell University, Ithaca NY 14853 USA, jlunine@astro.cornell.edu ;*

<sup>2</sup>*Southwest Research Institute, 6220 Culebra Road, San Antonio TX 78238 USA, sbolton@swri.edu*

## KEYWORDS:

Titan; Saturn; nitrogen; argon

## INTRODUCTION:

Titan's dense atmosphere of molecular nitrogen and methane was first revealed by the Voyager 1 spacecraft during its close flyby in 1980. Scientists immediately recognized this as one of the most important discoveries in planetary science because other than Earth, Titan was the only known body in the solar system with a fully developed atmosphere dominated by nitrogen. This led immediately to the question of the molecule's origin—was it molecular nitrogen or ammonia? The answer would directly constrain theories on the origin of Titan's and its atmosphere. The rich organic chemistry in Titan's atmosphere, along with Voyager's inability to see the surface, were important motivators of what would become the Cassini-Huygens mission.

## OWEN'S NITROGEN TEST

In a classic paper published in 1982 (*Planet. Space Sci.*, 30, 833–838), Toby Owen proposed a test of the origin of nitrogen that required measuring the ratio of argon to nitrogen in Titan's atmosphere. Because argon is the noble gas closest in volatility to that of molecular nitrogen, it would tend to incorporate in ices (as clathrate, adsorbate, or direct condensate) similarly as the latter. Therefore, if the nitrogen in Titan's atmosphere were primordial—that is, trapped in planetesimals as molecular nitrogen—then the argon-to-nitrogen ratio should be approximately solar in value (or within a factor of ten). Because all plausible alternative parent species for nitrogen are less volatile—ammonia being the outstanding example—the argon-to-nitrogen ratio will be orders of magnitude less than solar for other putative parent species. This test was implemented successfully with the Cassini and Huygens mass spectrometers, pointing strongly to ammonia as the parent species of nitrogen in Titan's atmosphere. Further, isotopic data supported this conclusion.

## ISOTOPES, MOLECULES AND CASSINI

Toby Owen was an early and enduring proponent of the collection and use of isotopic data for understanding the relationships between bodies in the inner and outer solar systems, their origins and evolution. A classic paper on this subject was by Owen and Encrenaz (*Space Science Reviews*, 106, 121-138 (2003)). He was a pioneer in Earth-based observations of D/H on Mars, and their interpretation in terms of the history of atmospheric escape from that planet. His influence was keenly felt in many missions from Viking to Voyager to Galileo to Rosetta to Juno, and others. He was one of the three "founding fathers" of the Cassini-Huygens mission (the other two being Wing Ip and Daniel Gautier), drawing on his own research and breadth of knowledge of solar system problems to explain the potential for a mission to Saturn and Titan to revolutionize our understanding of the nature and origin of the Saturn system. Owen's legacy in science and planetary exploration is large and enduring.

# CASSINI IN SITU OBSERVATIONS OF SATURN'S EQUATORIAL ATMOSPHERE AND IONOSPHERE

J. Hunter Waite, Jr.<sup>1</sup>, Jan-Erik Wahlund<sup>2</sup>, William Kurth<sup>3</sup> and the INMS, CAPS, and RPWS Science Teams

<sup>1</sup> Space Science and Engineering Division, Southwest Research Institute, 6220 Culebra Rd., San Antonio, TX., 78238, USA, [hwaite@swri.edu](mailto:hwaite@swri.edu).

<sup>2</sup> IRF Uppsala, Swedish Institute of Physics Box 537 SE-751 21 Uppsala, Sweden, [JanErik.Wahlund@irfu.se](mailto:JanErik.Wahlund@irfu.se)

<sup>3</sup> Department of Physics and Astronomy, University of Iowa, Iowa City, Iowa 52242, USA, [William-kurth@uiowa.edu](mailto:William-kurth@uiowa.edu).

## KEYWORDS:

Atmosphere, Cassini, Saturn, Ionosphere, Rings

The Grande Finale of the Cassini-Huygens Mission took the spacecraft between the D ring and the upper atmosphere of Saturn over twenty times during the summer of 2017 (see Figure 1). The final plunge into Saturn's atmosphere took place on September 15<sup>th</sup> of 2017. During this time period the Ion Neutral Mass Spectrometer made numerous measurements of the atmosphere and ionosphere of Saturn and its chemical and dynamical coupling to Saturn's rings. Simultaneous measurements of the electron density were carried out by the Radio Plasma Wave Science investigation. The measurements show a surprisingly complex chemical and dynamical coupling of the D ring to the ionosphere and upper atmosphere of Saturn. We report our preliminary understanding of the processes involved.

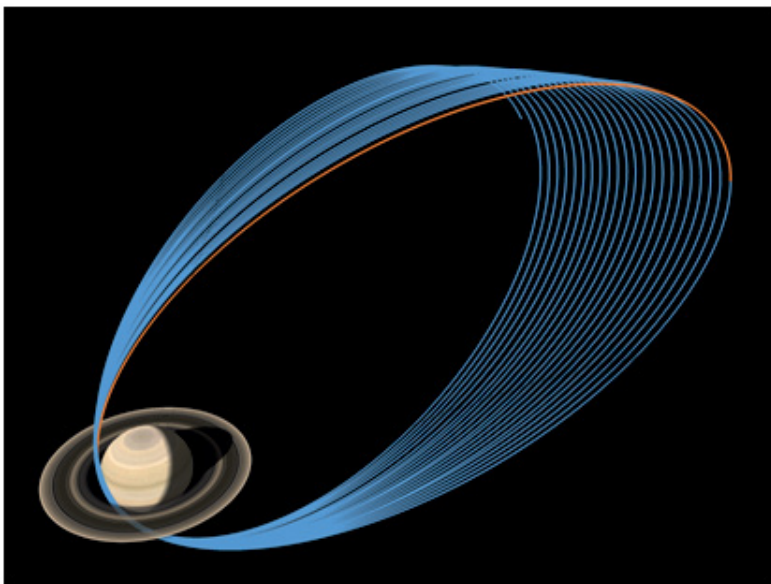


Fig. 1. Orbits from Cassini's Grand Finale mission phase.



# ELEMENT FRACTIONATION BY HYDRODYNAMIC ESCAPE AT EARLY VENUS: CONSTRAINING THE PLANET'S EVOLUTION

H. Lammer<sup>1</sup>, M. Leitzinger<sup>2</sup>, P. Odert<sup>1</sup>, M. Scherf<sup>1</sup>, C. Burger<sup>3</sup>, T. Maindl<sup>3</sup>, C. P. Johnstone<sup>3</sup>, N. V. Erkaev<sup>4,5</sup>, K. G. Kislyakova<sup>3,1</sup>, M. Güdel<sup>3</sup>, R. Dvorak<sup>3</sup>, E. A. Dorfi<sup>3</sup>

<sup>1</sup>Austrian Academy of Sciences (ÖAW), Space Research Institute (IWF), Schmiedlstr. 6, 8042 Graz, Austria, [helmut.lammer@oeaw.ac.at](mailto:helmut.lammer@oeaw.ac.at);

<sup>2</sup>Institute of Physics, Department for Geophysics, Astrophysics, and Meteorology, Univ. of Graz, Universitätsplatz 5, 8010 Graz, Austria;

<sup>3</sup>Department of Astrophysics, Univ. of Vienna, Türkenschanzstr. 17, A-1180 Vienna, Austria;

<sup>4</sup>Institute of Computational Modelling SB RAS, Krasnoyarsk 660036, Russian Federation;

<sup>5</sup>Siberian Federal University, Krasnoyarsk 660041, Russian Federation

## KEYWORDS:

protoatmospheres, hydrodynamic escape, early Venus, young Sun, element fractionation, noble gases, geochemistry

## INTRODUCTION:

The compositions of the Sun, meteorites and planets provide important information on the origin of the Solar System, and the most efficient fractionation processes involved in the evolution of planets. The bulk composition of the silicate part of the terrestrial planets is linked to chondritic meteorites, which are thought to represent their building blocks. Recent findings indicate that carbonaceous-chondrite-like objects were most likely scattered into the inner Solar System early in Earth's accretion [1]. It is unknown how fast both terrestrial planets Venus and Earth accreted to their final masses. Their growth time determines if the planets originated after the nebular gas evaporated, or if they grew to larger masses while embedded in the nebula so that hydrogen could accumulate before the gas disk disappeared. There are arguments that point to the fact that noble gases have been trapped from the nebula and left in solar composition in the planetary interiors. Via magma oceans that formed below the envelopes, solar-like isotopes, embedded in the nebular gas [2], entered the planetary interiors. Depending on the protoplanetary mass and the extreme ultraviolet (EUV) activity of the young Sun [3], hydrogen-envelopes can later be lost due to hydrodynamic escape. If hydrogen atoms escape efficiently, they can drag away heavier species, which may have led to the odd isotope and elemental ratios, as observed at Earth and Venus. Here we present the hydrodynamic escape of an early Venusian protoatmosphere and model evolution scenarios of escaping heavier species dragged with the outflowing hydrogen from accreting proto-Venus. We aim to understand, in a comparative way, how elements were fractionated within the first 100 Myr after the origin of the Solar System from their initial solar/chondritic values to the present atmospheric  $^{20}\text{Ne}/^{22}\text{Ne}$ ,  $^{36}\text{Ar}/^{38}\text{Ar}$ ,  $^{84}\text{Kr}/^{130}\text{Xe}$  [4], and measured K/U ratios from Venusian surface rocks by Vega 1,2 [5] and Venera 8 [6]. By reproducing the observed fractionated ratios, we constrain the core- and hydrogen-envelope masses of the accreting proto-Venus after the gas disk evaporated, as well as the EUV activity level of the young Sun. Finally, we discuss the implications of our results and similar work in progress related to the early Earth.

## REFERENCES:

- [1] Fischer-Gödde M., Kleine T. Ruthenium isotopic evidence for an inner Solar System origin of the late veneer // *Nature*. 2017. V. 541. P. 525-527.
- [2] Stökl A., Dorfi, E. A., Johnstone C. P., Lammer H., 2016. Dynamical Accretion of Primordial Atmospheres around Planets with Masses between 0.1 and  $5M_{\text{Earth}}$  in the Habitable Zone // *Astrophys. J.* 2016. V. 825, P. 86.
- [3] Tu L., Johnstone C. P., Güdel M., Lammer, H. The extreme ultraviolet and X-ray Sun in Time: High-energy evolutionary tracks of a solar-like star // *Astrophys. Astron.* 2015. V. 577. P. L3.
- [4] Halliday A. N. The origins of volatiles in the terrestrial planets // *Geochim. CosmochimicaActa*. 2013. V.105.P. 146-171.
- [5] Surkov Yu. A., Kirnozov F. F., Glazov V. N., Dunchenko A. G., Tatsy L. P. Sobornov O. P. Uranium, Thorium, and Potassium in the Venusian rocks at the landing sites of Vega 1 and 2 // *J. Geophys. Res.* 1987. V. 92. P. E537-E540.
- [6] Vinogradov A. P., Surkov Yu. A., Kirnozov F. F. The content of Uranium, Thorium, and Potassium in the rocks of Venus as measured by Venera 8 // 1973. *Icarus*.V. 20.P. 253-259.

# ON THE ORIGIN OF ATMOSPHERES OF TERRESTRIAL PLANETS

M.V.Gerasimov

Space Research Institute of the RAS, Profsoyuznaya, 84/32, Moscow, 117997, mgerasim@mx.iki.rssi.ru

## KEYWORDS:

Impact-induced degassing, noble gases, water, trapping efficiency, protocrust

## INTRODUCTION:

The source of primordial planetary atmospheres is considered to be the result of direct gas-dust accretion from the protoplanetary cloud and due to degassing of volatiles which were delivered with planetesimals during the planetary body's growth. The impact degassing during the planetary accretion is the earliest and rather powerful process of degassing of planetary solid material. Experiments on the decomposition of a serpentine and calcite during a shock wave loading showed that their rather efficient decomposition could be achieved beginning with impact velocities which corresponded to escape velocities of a relatively small (about Moon size) planetary embryo [1,2]. The decomposition of volatile bearing minerals with the release of gases into the primordial atmosphere was almost complete during further accumulation of planetary mass. There are two outermost scenarios of behavior of released volatiles: (1) the accumulation of gases in a primordial atmosphere providing their progressive enrichment, and (2) rapid sink of gas species from the atmosphere providing its thin residua. The first scenario is mostly related to accumulation of noble gases in terrestrial planets atmospheres. The profiles of noble gases in the atmospheres of terrestrial planets [3,4] and in meteorites gives strong evidence that the main source of volatiles was provided by planetesimals. The sink rate of released gases (e.g.  $H_2O$  and  $CO_2$ ) from the primordial atmosphere was evaluated mainly as: atmospheric impact erosion, thermal and EUV-driven escape from the atmosphere, hydration and carbonization of surface minerals, dissolution of gases in magma ocean, loss of water for oxidation of iron, etc. [5,6,7]. But even a small efficiency of impact degassing (the ratio of volatiles which are remained in the atmosphere after an impact to their amount delivered by a planetesimal) was calculated to produce huge  $H_2O-CO_2$  atmosphere.

During a set of impact simulation experiments we have investigated the chemistry of volatiles and their interaction behavior with condensing silicates at conditions relevant to impact vaporization [8,9]. First, the experiments showed that the formed gas mixture was not limited only by  $H_2O$  and  $CO_2$ . A wide variety of gases are formed during high-temperature vaporization of silicates including oxides ( $SO_2$ ,  $CO_2$ ,  $CO$  ( $CO/CO_2 \sim 1$ ),  $H_2O$ ) and reduced ( $H_2$ ,  $H_2S$ ,  $CS_2$ ,  $COS$ , and hydrocarbons) gas components. Second, experiments on high-temperature vaporization of mafic and ultramafic rocks and minerals in water and/or  $CO_2$  containing atmospheres have shown that condensing silicates provide intense trapping of water and/or  $CO_2$  during the hot stage of vapor cloud expansion. The amount of trapped water by formation of different hydroxides could amount up to 10 wt.% of the silicate mass. The trapping of atmospheric  $CO_2$  proceeded by formation of carbonates, carbides, hydrocarbons, and elemental carbon phases. Preliminary results indicate that nitrogen is also trapped by formation of  $-NO_x$ ,  $-H,N$ , and  $-CN$  phases. The maximum concentrations of trapped  $CO_2$  and  $N$  were measured up to 4 wt.% and 0.1 wt.%, respectively. Trapping is efficient even at low partial gas pressures.

Impact-induced trapping of atmospheric gases was not accounted by theoretical models but it seems to be an efficient process controlling the atmospheric mass. The ratio of volatiles which are added to the atmosphere after an impact to their amount delivered by a planetesimal can be not only positive, but sufficiently negative as well. The account of the trapping efficiency of gases inside the vapor plume suggests a model for the formation of primordial atmosphere with moderate density.

An important output of the impact-induced processing of siliceous material of the planet was the formation of a protocrust. The mechanism of its formation was based on the separation of elements between melt and vapor phases [10]. Volatile elements are converted into the vapor plume by secondary impacts more easily and from larger target volume than refractory portion of the mixture. Plume condensates could be concentrated in the upper plane-

tary layer to form protocrust. Concentration of volatile components in the upper planetary layer resulted in decrease of sink of atmospheric gases and water into the regolith what provided stabilization of the atmosphere and the ocean at the earliest stages of planetary evolution.

## ACKNOWLEDGEMENT

This research was supported by the Russian Academy of Science program P-7

## REFERENCES:

- [1] Boslough M.B., Vizgirda J., Ahrens T.J. Shock-release of vapor from calcite // Lunar and Planetary Science Conference XII. Lunar and Planet. Inst. (abstr.). Houston. Texas. 1981. P. 104-105.
- [2] Boslough M.B., Weldon R.J., Ahrens T.J. Impact-induced water loss from serpentine, nontronite and kernite // Proc. Lunar Sci. Conf. 11<sup>th</sup>. 1980. P.2145-2158.
- [3] Pepin R.O. Atmospheres on the terrestrial planets: Clues to origin and evolution // Earth and Planetary Science Letters. 2006. V. 252. P. 1–14.
- [4] Owen T.C. and Bar-Nun A. Contributions of icy planetesimals to the Earth's early atmosphere // Origins of Life and Evolution of the Biosphere. 2001. V 31. P. 435–458.
- [5] Lange M.A., and Ahrens, T.J. The evolution of an impact-generated atmosphere // Icarus. 1982. V. 51. P. 96-120.
- [6] Abe Y, and Matsui T. The formation of an impact-generated H<sub>2</sub>O atmosphere and its implications for the early thermal history of the Earth // Proc. Lunar Sci. Conf. 15<sup>th</sup>. 1985. P. C545-C559.
- [7] Zahnle K.J., Kasting, J. F.; Pollack, J. B. Evolution of a steam atmosphere during earth's accretion // Icarus. 1988. V.74. P. 62-97.
- [8] Gerasimov M.V., Dikov Yu.P., Yakovlev O.I., Wlotzka F.. Water-vapor trapping from the atmosphere by condensed silicate material produced during pulsed evaporation // Geochemistry International. 1994. V. 31(11). P. 135-146.
- [9] Gerasimov M.V., Dikov, Yu.P., Yakovlev, O.I., Wlotzka, F. Trapping of carbon dioxide from a hot atmosphere by condensing silicates // Lunar and Planetary Science XXV. Lunar and Planet. Inst. (abstr.). Houston. Texas. 1994. P. 415-416.
- [10] Yakovlev O.I., Dikov Yu.P., and Gerasimov M. V. Differentiation caused by impact-induced vaporization during the Earth's accretion // Geochemistry International. 2000. V. 38, No 10, P. 1027-1045.

# VENUS' GLORY OBSERVED BY THE UV IMAGER ON BOARD AKATSUKI

Y.J. Lee<sup>1</sup>, A. Yamazaki<sup>1</sup>, T. Imamura<sup>2</sup>, Y. Manabu<sup>3</sup>, S. Watanabe<sup>4</sup>,  
T.M. Sato<sup>1</sup>, K. Ogohara<sup>5</sup>, G. L. Hashimoto<sup>6</sup>, and S. Murakami<sup>1</sup>

<sup>1</sup>Institute of Space and Astronautical Science, Japan Aerospace  
Exploration Agency, 3-1-1 Yoshinodai, Chuoku, Sagamihara,  
Kanagawa 252-5210, Japan, leeyj@ac.jaxa.jp

<sup>2</sup>The University of Tokyo, 5-1-5 Kashiwanoha, Kashiwa,  
Chiba 277-8561, Japan

<sup>3</sup>Planetary Exploration Research Center, Chiba Institute  
of Technology, 2-17-1, Tsudanuma, Narashino, Chiba 275-0016, Japan

<sup>4</sup>Hokkaido Information University, 59-2 Nishinopporo, Ebetsu,  
Hokkaido 069-0832, Japan

<sup>5</sup>University of Shiga Prefecture, 2500 Hassaka, Hikone, Shiga 522-8533,  
Japan

<sup>6</sup>Department of Earth Sciences, Okayama University, 3-1-1 Tsushimanaka,  
Kita, Okayama 700-8530, Japan

## KEYWORDS:

Venus atmosphere, UV, Image analysis, Akatsuki

## INTRODUCTION:

The top altitude of the Venus cloud layer is around 70 km above the surface, at where solar radiation scattering occurs effectively. The scattering has a phase angle dependency which depends on microphysical properties of cloud aerosols. We analyze global mean albedo obtained by the UV Imager (UVI) on board Akatsuki [1,2]. The results show clear glory features at 283 and 365 nm at small phase angles, acquired in May 2016. We successfully simulate the observation using a radiative transfer model. We estimate  $r_{\text{eff}}=1.26$  and  $v_{\text{eff}}=0.076$  for mode 2 to explain the observation, consisting with a previously suggested low latitudinal aerosol property [3]. We find that SO<sub>2</sub> and the unknown UV absorber are necessary factors to explain the observed quick decreasing of albedo at phase angles larger than 10 degree. We suggest a range of possible SO<sub>2</sub> abundance at 70 km from 80 to 400 ppbv, depending on assumed atmospheric conditions. These results are recently published [4].

## REFERENCES:

- [1] Nakamura, M., Imamura, T., Ishii, N., et al. 2016, EP&S, 68, 75.
- [2] Yamazaki, A., Yamada, M., Lee, Y.J., et al. submitted, EP&S.
- [3] Petrova, E. V., Shalygina, O. S., &Markiewicz, W. J. 2015b, Icar, 260, 190.
- [4] Lee, Y.J., Yamazaki, A., Imamura, T., et al. 2017, AJ, 154:44.

# DISULFUR DIOXIDE AND ITS NUV ABSORPTION IN THE PHOTOCHEMICAL MODEL OF VENUS ATMOSPHERE

Vladimir A. Krasnopolsky

Moscow Institute of Physics and Technology (PhysTech),  
vlad.krasn@verizon.net

## KEYWORDS:

Venus, atmosphere, chemical composition, photochemistry, spectroscopy

## INTRODUCTION:

Frandsen et al. (2016) proved that  $S_2O_2$  is formed by  $SO + SO + M$  as cis- and trans-OSSO isomers that dissociate to SO and calculated their absorption spectra. Using the SO abundances of 12 ppb at 64-95 km observed by Na et al. (1994), they calculated abundances of OSSO that appear sufficient to explain the NUV absorption of Venus at 320-500 nm. We will implement the findings by Frandsen et al. (2016) into our photochemical model (Krasnopolsky 2012, Paper I), update the model using the chemical kinetic model (Krasnopolsky 2013), and test the hypothesis of OSSO as the NUV absorber.

## UPDATED PHOTOCHEMICAL MODEL:

It was assumed in Paper I that  $S_2O_2$  is formed as the lowest energy isomer  $S=SO_2$  that dissociates to  $S + SO_2$ . The formation of OSSO and its dissociation to  $SO + SO$  significantly affect the sulfur chemistry in the model that also adopts the OSSO formation and dissociation reaction rates from Frandsen et al. (2016). The model is updated using mixing ratios of  $H_2O = 26$  ppm,  $OCS = 140$  ppb, and  $H_2S = 8.5$  ppb at 47 km from the chemical kinetic model (Krasnopolsky 2013) as the lower boundary conditions. Similar to Paper I, a basic model and four versions with minor variations of eddy diffusion and  $SO_2$  at the lower boundary were calculated (Table). Here eddy diffusion is  $7300 \text{ cm}^2 \text{ s}^{-1}$  below  $h_p$  increasing to  $10^7 \text{ cm}^2 \text{ s}^{-1}$  at 100 km above  $h_p$ . The model results for the sulfur species  $SO_2$ , SO, OCS, and aerosol sulfur  $S_a$  are compared with the observations in Fig. 1. Minor variations of eddy diffusion induce variations of the species by a factor of  $\approx 30$  and do not require volcanism. Variations of  $H_2O$  in the model and observations are compared in Fig. 2. Again, there is a good agreement between the model and observations.

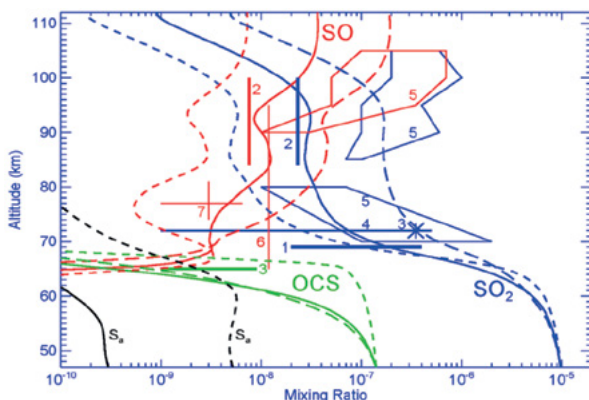


Fig. 1. Basic sulfur species: model results (solid, short and long dashes for  $h_p = 60, 57,$  and  $65$  km, respectively) and observations.  $S_a$  refers to total number of sulfur atoms in the aerosol. Observations of SO by Na et al. (1994) and Jessup et al. (2015) are (6) and (7).

## NUV ABSORPTION BY OSSO:

The calculated column photolysis rate of OSSO is  $3.9 \times 10^{13} \text{ cm}^{-2} \text{ s}^{-1}$  and peaks at 68 km in a layer of 4 km thick. The NUV absorption at 320-500 nm (Fig. 3) removes  $1.9 \times 10^{16} \text{ cm}^{-2} \text{ s}^{-1}$  solar photons and exceeds the OSSO photolysis in the model by a factor of 500. The calculated OSSO column is  $2.13 \times 10^{14} \text{ cm}^{-2}$

with the cis-to-trans isomer ratio of 0.82/0.18. The observed spectral reflectivity of Venus is compared with that of OSSO in Fig. 3. The red curve is for a thin absorbing layer above the clouds with  $\text{OSSO} = 2.8 \times 10^{16} \text{ cm}^{-2}$  exceeding the model value by a factor of 130. The green curve is for  $\text{OSSO} = 4 \times 10^{16} \text{ cm}^{-2}$  uniformly mixed in the upper cloud layer. (The cis-to-trans ratio is 0.7/0.3 in production and 0.82/0.18 in abundances because of the weaker photolysis of cis-OSSO.)

**Table.** Some data from five versions of the model

$h_e$ km	$\text{SO}_2$ 47 km	$\text{H}_2\text{O}$ 70 km	$\text{SO}_2$ 70 km	$\text{SO}$ 90 km	$\text{S}_2\text{O}_2+h\nu$ $\text{cm}^{-2} \text{ s}^{-1}$
60	9.7 ppm	3.11 ppm	128 ppb	10.1 ppb	3.91+13
57	9.7	4.38	577	43.4	5.39+13
65	9.7	2.90	57	2.44	5.99+13
60	8.7	5.36	70	6.3	2.77+13
60	10.7	1.48	342	25	5.46+13

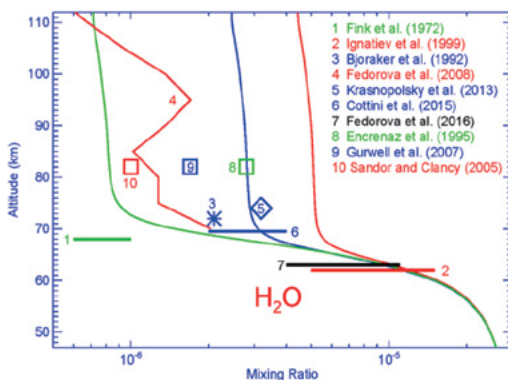


**Fig. 2.** Vertical profiles of  $\text{H}_2\text{O}$  for  $\text{SO}_2 = 8.7, 9.7,$  and  $10.7$  ppm at 47 km (red, blue, and green lines) are compared with the observations.

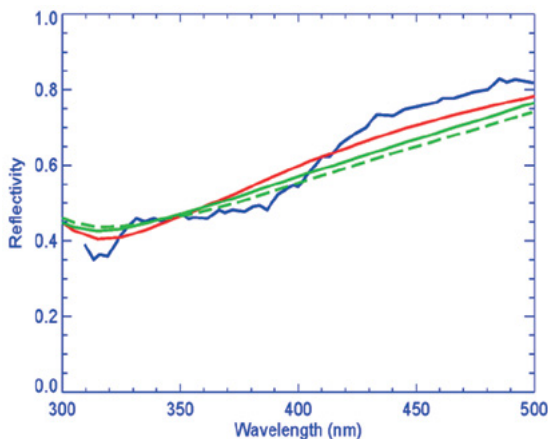


**Fig. 3.** Observed spectrum of Venus (blue, Barker et al. 1975) is compared with OSSO absorption in a thin layer (red) and for uniformly mixed absorber (green) with the isomer proportion 0.82/0.18 and 0.7/0.3 (solid and dashed curves, respectively). The OSSO abundances in the models are chosen to fit the observation at 350 nm.

This abundance exceeds the model value by a factor of 190. Frandsen et al. (2016) calculated the OSSO densities using  $\text{SO} = 12$  ppb at 64-95 km observed by Na et al. (1994). This SO exceeds the recent observations by Jessup et al. (2015, 6.5, 2, and 1 ppb at 74-81 km, Fig. 1) and the model values below 74 km. Even SO from Na et al. (1994) results in an absorption that is weaker than that observed by a factor of 3. The spectral fit by OSSO to the observed NUV absorption is not perfect as well. Even if SO from Na et al. (1994) is valid below 74 km, then OSSO contributes to but

does not completely explain the NUV absorption. Na and Esposito (1997) proposed  $S_2O$  as the NUV absorber. They calculated  $[S_2O] \approx 5 \times 10^9 \text{ cm}^{-3}$  at 64 km, close to that at 47-60 km in our model. However, absorption spectra of gaseous  $S_2O$  are lacking. Strong arguments in favour of  $FeCl_3$  diluted to  $\approx 1\%$  in the droplets of sulphuric acid in the upper cloud layer may be found in Krasnopolsky (2017). This species explains the NUV absorption, though contribution of other candidates is not ruled out.

## REFERENCES:

- [1] Barker, E.S., et al., *J. Atmos. Sci.* 32, 1205-1211, 1975.
- [2] Frandsen, B.N., Wennberg, P.O., Kjaergaard, H.G., *Geophys. Res. Lett.* 43, 11146-11155, 2016.
- [3] Jessup, K.L., et al., *Icarus* 258, 309-336, 2015.
- [4] Krasnopolsky, V.A., *Icarus* 218, 230-246, 2012.
- [5] Krasnopolsky, V.A., *Icarus* 225, 570-580, 2013.
- [6] Krasnopolsky, V.A., *Icarus* 286, 134-137, 2017.
- [7] Na, C.Y., et al., *Icarus* 112, 389-395, 1994.
- [8] Na, C.Y., Esposito, L.W., *Icarus* 364-368, 1997.

# SEARCH FOR HBR AND BROMINE PHOTOCHEMISTRY ON VENUS

Vladimir A. Krasnopolsky<sup>1</sup>, Denis A. Belyaev<sup>2</sup>

<sup>1</sup>Moscow Institute of Physics and Technology (PhysTech),  
vlad.krash@verizon.net;

<sup>2</sup>Space Research Institute, Moscow, Russia, bdenya.iki@gmail.com

## KEYWORDS:

Venus, atmosphere, chemical composition, spectroscopy, photochemistry

## INTRODUCTION:

The high temperature near the surface of Venus stimulates reactions between the rocks and atmospheric species that release HCl and HF, which looked unexpected and exotic when they were detected by Connes et al. (1967). No attempts have been made to search for HBr, and the only relevant result is an upper limit of 0.2 ppb to Br<sub>2</sub> near 15 km from the Venera 11 and 12 descent probes (Moroz et al. 1981). Search for HBr is the subject of this work.

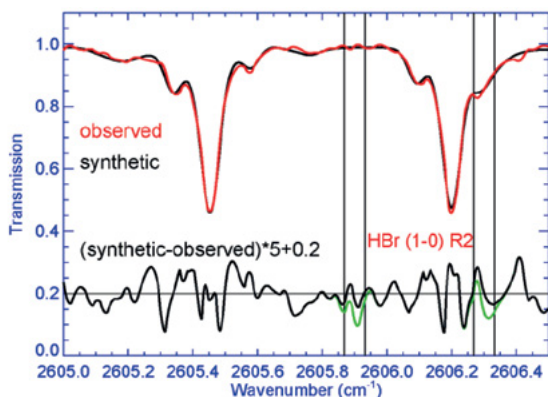


**Fig. 1.** Observed and synthetic spectra of Venus at the equator. Vertical lines show resolution elements at the expected positions of the Doppler-shifted HBr lines. The black line near the bottom shows a difference between the synthetic and observed spectra scaled by a factor of 5. The green line is for HBr = 10 ppb.

## OBSERVATIONS AND ANALYSIS:

We chose for our study the strongest line R2 of the fundamental band of HBr at 2605.8/6.2 cm<sup>-1</sup>. Though the line is strong, it is weaker than the similar HCl and HF lines by factors of 8 and 36, respectively. Venus was observed in July 2015 using NASA IRTF and a long-slit spectrograph CSHELL with resolving power of 4×10<sup>4</sup>. We used our standard tools for observations and processing

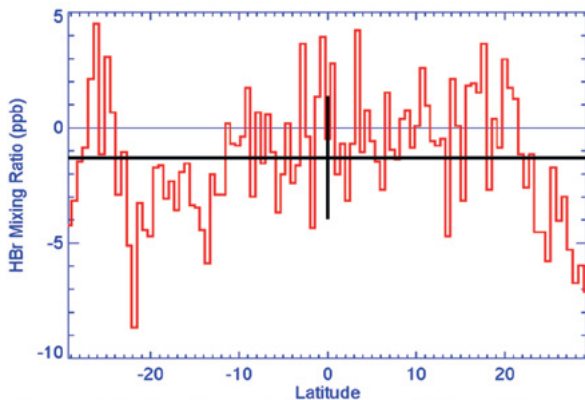


**Fig. 2.** HBr mixing ratio in the observed 101 spectra of Venus. The mean value and standard deviation are shown by black solid lines.



of the observed spectra. 101 spectra along the slit that crossed the bright crescent of Venus were analyzed and compared with best-fit synthetic spectra. A spectrum observed near the equator is shown in Fig. 1. The synthetic spectra were calculated in Fig. 1 for the best fit with HBr near zero and for HBr = 10 ppb, and the latter is close to the detection limit for an individual spectrum. Combinations of the HBr and CO<sub>2</sub> lines provide mixing ratios of HBr that refer to 78 km. Retrievals for all 101 spectra are shown in Fig. 2. The values scatter between -8 and 5 ppb with a mean value of -1.2 ppb and standard deviation of 2.5 ppb. According to the Gauss statistics, uncertainty of the mean of 101 values is smaller by a factor of 10 and equal to 0.25 ppb. Our observations result in an upper limit of 1 ppb for HBr at 78 km on Venus.

### POSSIBLE HBR PHOTOCHEMISTRY:

Quantitative assessment of the HBr chemistry on Venus is made by inclusion of ten major photochemical reactions of bromine (Table) into the photochemical model by Krasnopolsky (2012) and assuming HBr = 10 ppb below 60 km.

Table. Column rates (CR) of bromine reactions

#	Reaction	CR	CR (Cl)
1	HBr + $h\nu$ → H + Br	3.27+10	9.46+10
2	HBr + O → Br + OH	1.15+10	1.60+9
3	HBr + H → Br + H <sub>2</sub>	1.30+10	2.31+9
4	H + Br + M → HBr + M	1.47+10	-
5	Br + HO <sub>2</sub> → HBr + O <sub>2</sub>	4.12+10	6.71+10
6	Br + O <sub>3</sub> → BrO + O <sub>2</sub>	2.16+12	6.89+12
7	BrO + O → Br + O <sub>2</sub>	4.35+11	3.50+12
8	BrO + NO → Br + NO <sub>2</sub>	1.73+12	4.22+12
9	Br + Br + M → Br <sub>2</sub> + M	1.04+14	1.64+13
10	Br <sub>2</sub> + $h\nu$ → Br + Br	1.04+14	3.18+13

$3.27+10 = 3.27 \times 10^{10} \text{ cm}^{-2} \text{ s}^{-1}$ . CR (Cl) is the column rate of the similar Cl reaction in the model by Krasnopolsky (2012)

Photolysis of HBr and its reactions with O and H strongly deplete the HBr mixing ratio above 65 km (Fig. 3). The fast photolysis of Br<sub>2</sub> and the reactions of BrO with O and NO convert these species to Br, which dominates above 67 km. The most significant effect of the bromine chemistry is in the production of H<sub>2</sub> (reaction 3), which exceeds that without Br by a factor of 5, and in the production of O<sub>2</sub>, which is a third of that without Br. Our upper limit of 1 ppb at 78 km is applicable to the uniform distribution of HBr. To constrain the HBr abundance below 60 km from our observation and the model, we use the Venus albedo of 0.028 at 3.66 μm (Krasnopolsky 2010). This low value is caused by the H<sub>2</sub>SO<sub>4</sub> absorption, Single scattering approximation is reasonable for this black atmosphere in our observation at 3.84 μm. Assuming the aerosol scale height of 3 and 4 km above 70 km and a constant extinction coefficient at 60-70 km, the calculated upper limits to HBr below 60 km are 70 and 20 ppb, respectively, and  $\tau \approx 0.7$  at 70 km, in accord with Cottini et al. (2015) and Fedorova et al. (2016). The bromine chemistry may be effective on Venus even under

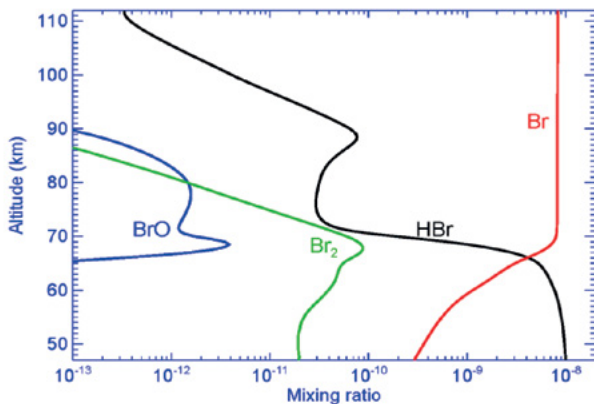


Fig. 3. Vertical profiles of bromine species in the photochemical model.

the observed upper limit. However, if a Cl/Br ratio in the Venus atmosphere is similar to that in the Solar System, then HBr  $\approx$  1 ppb in the lower atmosphere and the bromine chemistry is insignificant.

## REFERENCES:

- [1] Connes, P., et al., *Astrophys. J.* 147, 1230-1237, 1967
- [2] Cottini, V., et al., *Planet. Space Sci.* 113-114, 219-225, 2015.
- [3] Fedorova, A., et al., *Icarus* 275, 143-162, 2016.
- [4] Krasnopolsky, V.A., *Icarus* 208, 539-547, 2010.
- [5] Krasnopolsky, V.A., *Icarus* 218, 230-246, 2012.
- [6] Krasnopolsky, V.A., *Icarus* 225, 570-580, 2013.
- [7] Moroz, V.I., et al., *Cosmic Res.* 19, 599-612, 1981.

# STUDY OF SCALE HEIGHTS AND DETACHED HAZE LAYERS AT HIGH LATITUDES IN THE UPPER HAZE OF VENUS FROM SPICAV IR DATA

M.S. Luginin<sup>1</sup>, A.A. Fedorova<sup>1</sup>, D.A. Belyaev<sup>1</sup>, F. Montmessin<sup>2</sup>,  
O.I. Korablev<sup>1</sup>, J.-L. Bertaux<sup>2,1</sup>

<sup>1</sup>Space Research Institute (IKI), Moscow, Russia [mikhail.luginin@phystech.edu](mailto:mikhail.luginin@phystech.edu)

<sup>2</sup>LATMOS/IPSL, Guyancourt, France

## KEYWORDS:

Infrared observations; atmosphere of Venus; solar occultation; upper haze; detached layers.

## ABSTRACT:

Surface of Venus is totally concealed from the observations in the visible light by a thick layer of clouds, that extends from 50 to 70 km above the surface. Upper haze is located above the clouds and is located at 70-90 km. Ground based polarimetric observations showed that particles on the cloud deck level are spherical with a mean radius  $\sim 1 \mu\text{m}$  and refractive index  $n=1.44$  at  $0.55 \mu\text{m}$  [1]. These authors suggested, that the clouds consist of liquid droplets of concentrated sulfuric acid solution (75–85 %  $\text{H}_2\text{SO}_4$  by weight). Analysis of polarimetry data from Pioneer Venus orbiter [2] allowed to estimate radius size of the upper haze particles to be  $0.23 \pm 0.04 \mu\text{m}$ . The average optical thickness of the haze layer in the polar region was measured to be 0.83 at 365 nm, while at low latitudes the optical thickness of the haze was typically one order of magnitude smaller. Until recently, it was believed that the upper haze is composed of predominately submicron particles.

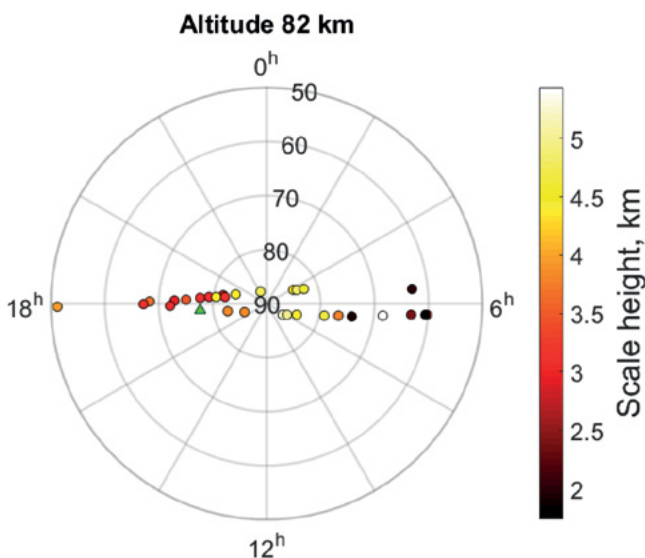


**Fig. 1.** Map of retrieved scale heights in the polar local time – latitude coordinates. It is greater in the polar region than in the high latitudes both in the morning and in the evening. The green triangle corresponds to the observation with 7.6 km scale height.

Analysis of transmission altitude profiles of the upper haze in the visible and infrared spectral ranges, acquired during solar occultation experiments performed by SPICAV IR instrument, resulted in discovery of bimodal distribution in particles size with a mean radius  $\sim 0.1 \mu\text{m}$  and  $\sim 0.8 \mu\text{m}$  and number density  $200 \text{ cm}^{-3}$  and  $0.5 \text{ cm}^{-3}$  for mode 1 and mode 2 respectively at 80 km [3]. In this work, we analyzed scale heights and detached haze layers properties in  $60^\circ\text{N}$ – $90^\circ\text{N}$  latitude region in 70–95 km altitude range. Scale heights were calculated for 43 orbits (Fig. 1), and equaled 4–5.5 km at the North Pole ( $80^\circ\text{N}$ – $90^\circ\text{N}$ ) and decreased to 2–4 km at high latitudes ( $60^\circ\text{N}$ – $80^\circ\text{N}$ ).

In some occultations, a distinct inversion layer was observed at the altitudes between 80 and 90 km in the slant optical depth, extinction coefficient, and effective radius profiles (Fig. 2). It points to the presence of a detached layer that appears from time to time in the upper atmosphere. The structures can be sometimes observed over consecutive orbits. We suggest, that this phenomenon is a result of condensation of water vapor on sulfuric acid aerosol.

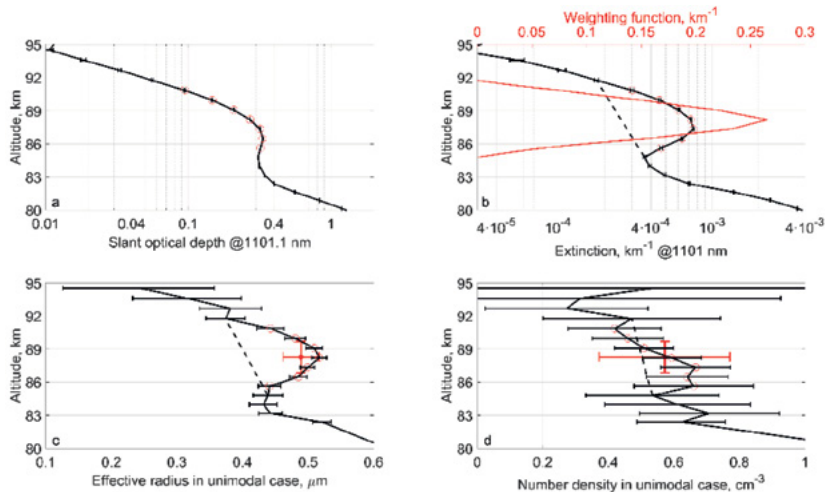


**Fig. 2.** Data processing for orbit #488 containing distinct detached layer. Red circles represent altitudes of DL. (a) Slant optical depth profile at the 1101.1 nm wavelength. (b) Bottom black axis in logarithmic scale: extinction coefficient profile at the 1101.1 nm wavelength with DL (black solid line). (c) Profile of effective radius in unimodal case. (d) Profile of number density in unimodal.

## ACKNOWLEDGEMENTS:

M.L., A.F., D.B., and O.K. acknowledge the support from the RFFI grant № 16-52-16011 in the study of the scale heights of the Venesian mesosphere. M.L. and D.B. acknowledge the support from the RFFI grant № 16-02-00633ain the study of the detached haze layers. M.L., A.F., D.B., O.K., and J.-L.B. acknowledge the support from Russian Government grant № 14.W03.31.0017.

## REFERENCES:

- [1] Hansen, J.E., Hovenier, J.W., 1974. Interpretation of the Polarization of Venus. *J. Atmos. Sci.* 31, 1137–1160.
- [2] Kawabata, K. et al., 1980. Cloud and haze properties from Pioneer Venus polarimetry. *J. Geophys. Res.* 85, 8129.
- [3] Luginin, M. et al., 2016. Aerosol properties in the upper haze of Venus from SPICAV IR data. *Icarus*, 277, 154–170. [1] Author A.B., Author C.D., Author E.F. First example of a cited article title// *First Example Journal*. 2016. V. 1. No. 1. P. 1-100.

# OPTIMAL CLOUD COMPUTING INFRASTRUCTURE FOR PLANETARY IMAGE PROCESSING: A TALE OF TWO PLANETS (MARS AND VENUS)

J.L. Vázquez-Poletti<sup>1</sup>, P.J. Pascual<sup>2</sup>, M. Ramírez-Nicolás<sup>1</sup>, S. Jiménez<sup>3</sup>, D. Usero<sup>1</sup>, O. Korablev<sup>4</sup>, M. Patsaeva<sup>4</sup>, D. Belyaev<sup>4</sup>, M.P. Velasco<sup>3</sup>, I.M. Llorente<sup>1</sup>, L. Vázquez<sup>1</sup>

<sup>1</sup>Universidad Complutense de Madrid (UCM), Spain;

<sup>2</sup>Universidad Autónoma de Madrid (UAM), Spain;

<sup>3</sup>Universidad Politécnica de Madrid (UPM), Spain;

<sup>4</sup>Space Research Institute (IKI), Russia;

jlvazquez@fdi.ucm.es

## KEYWORDS:

Image processing, Mars, Venus, cloud computing, optimization

## INTRODUCTION:

Much of the data used in planetary studies comes in the form of images or needs to be converted to this representation form in order to process it. Moreover, the computing requirements use to be prohibitive by means of time, cost or even a combination of both, preventing further advances in the research process.

In the present work we are considering two representative applications. The first one is related to the MARSIS radar instrument from ESA Mars Express mission, which data is processed as images in order to study the Martian ionosphere [1]. The second application processes images from the Venus Monitoring Camera from the ESA Venus Express mission for studying the dynamics of its atmosphere [2,3].

These two applications have different characteristics by means of input file arrival and computing requirements, preventing the use of in-house solutions (such as supercomputers) due to budget restrictions or the inexistence of dedicated environments.

With this in mind, we have relied on cloud computing, a seamless paradigm that allows a dynamic, elastic and on-demand provision of computing resources like CPU and storage [4]. In particular, we have focused in public cloud infrastructures, which follow a “pay as you go” basis. Estimating an optimal computing setup based on the offerings of these providers adds a level of complexity to the whole solution [5]. For this reason, we have fostered execution models that allow establishing the best cloud infrastructure for the considered applications.

## REFERENCES:

- [1] M. Ramírez-Nicolás, B. Sánchez-Cano, O. Witasse, P.-L. Blelly, L. Vázquez, M. Lester, The effect of the induced magnetic field on the electron density vertical profile of the Mars' ionosphere: A Mars Express MARSIS radar data analysis and interpretation, a case study, *Planetary and Space Science*, Volume 126, 2016, Pages 49-62.
- [2] I.V. Khatuntsev, M.V. Patsaeva, D.V. Titov, N.I. Ignatiev, A.V. Turin, S.S. Limaye, W.J. Markiewicz, M. Almeida, Th. Roatsch, R. Moissl, Cloud level winds from the Venus Express Monitoring Camera imaging, *Icarus*, Volume 226, Issue 1, 2013, Pages 140-158.
- [3] M.V. Patsaeva, I.V. Khatuntsev, D.V. Patsaev, D.V. Titov, N.I. Ignatiev, W.J. Markiewicz, A.V. Rodin, The relationship between mesoscale circulation and cloud morphology at the upper cloud level of Venus from VMC/Venus Express, *Planetary and Space Science*, Volume 113, 2015, Pages 100-108.
- [4] Peter M. Mell, Timothy Grance, The NIST Definition of Cloud Computing, Technical Report SP 800-145, NIST, 2011.
- [5] J.L. Vazquez-Poletti, S. Santos-Muñoz, I.M. Llorente, F. Valero, A Cloud for Clouds: Weather Research and Forecasting on a Public Cloud Infrastructure, *Cloud Computing and Services Sciences*, Volume 512, 2015, Pages 3-11.

# EVOLUTION OF MARTIAN ATMOSPHERE IN MODERN ERA, ITS ISOTOPIC IMPRINTS AND CONNECTION WITH MARTIAN SUBSURFACE ENVIRONMENTS

A.K. Pavlov<sup>1</sup>, G.I. Vasiliyev<sup>1</sup>, D.A. Tsurkov<sup>1</sup>, D.A. Frolov<sup>1</sup>, A.A. Pavlov<sup>2</sup>

<sup>1</sup>*Ioffe Institute, Saint Petersburg, Russia, 194021, Polytekhnicheskay 26, anatoli.pavlov@mail.ioffe.ru*

<sup>2</sup>*Planetary Environments Laboratory, NASA Goddard Space Flight Center, Greenbelt, MD20771, USA*

## KEYWORDS:

Mars, atmosphere, variations, cosmic rays, isotopes.

## INTRODUCTION:

We consider evolution of Martian atmosphere within last 10<sup>9</sup> years taking into account obliquity oscillation of planet, which produce global variations of climate and atmospheric pressure. We simulate cosmogenic isotopes production rates (<sup>3</sup>He, <sup>21</sup>Ne, <sup>36</sup>Ar) by galactic and solar cosmic rays in surface martian rocks for periods of "thin", "thick" and modern atmosphere. Results are compared with MSL isotope measurements in different sites. Our simulations demonstrate the observed isotopic imprints cannot be explained in scope of stable modern atmosphere hypothesis. Existence of periods with low atmospheric pressure (~0.1 mbar) in combination with high atmospheric pressure (>0.1 bar) are required to explain measured cosmogenic isotope ratios for case of cosmic rays rock irradiation on surface of planet. We also analyze other possible ways to solve the problem (covering by regolith etc). Possible subsurface CO<sub>2</sub> reservoirs for atmospheric pressure variation process are discussed using results of experimental modeling of "gas traps" formation in martian regolith. Effects of such processes on atmospheric isotopic ratios <sup>13</sup>C/<sup>12</sup>C, <sup>15</sup>N/<sup>14</sup>N, rare gases and habitability of martian soil are discussed.

# LATE NOACHIAN ICY HIGHLANDS CLIMATE MODEL: EXPLORING THE POSSIBILITY OF TRANSIENT MELTING AND FLUVIAL/LACUSTRINE ACTIVITY THROUGH PEAK ANNUAL/SEASONAL TEMPERATURES

A.M. Palumbo<sup>1</sup>, J.W. Head<sup>1</sup>, R.D. Wordsworth<sup>2</sup>

<sup>1</sup>Department of Earth, Environmental, and Planetary Sciences, Brown University, Providence, RI 02912 USA Ashley\_Palumbo@Brown.edu

<sup>2</sup>School of Engineering and Applied Sciences, Harvard University, Cambridge, MA 02138 USA

## KEYWORDS:

climate, seasonal, Noachian, cold and icy

## INTRODUCTION:

Climate models have suggested that under the influence of a younger Sun, with  $\sim 75\%$  the present luminosity [1,2], early Mars would be forced into a cold steady state with mean annual temperatures (MAT) consistently below the melting point of water [3,4]. In contrast, there is geological evidence for fluvial and lacustrine activity during the Late Noachian and Early Hesperian, including valley networks (VNs) [5] and open- and closed- basin lakes [6]. With current models unable to produce relatively continuous clement conditions (MAT  $> 273$  K) [3,4], we consider the possibility of a “cold and icy” planet (MAT  $< 273$  K) and address the question: is formation of fluvial/lacustrine features possible from shorter periods of punctuated heating and associated snowmelt and runoff?

## BACKGROUND:

General circulation models (GCMs) [3,4] show that when atmospheric pressure exceeds tens to hundreds of mbar, an altitude-dependent temperature effect is induced and H<sub>2</sub>O preferentially accumulates in the highlands, producing a “Late Noachian Icy Highlands” (LNIH) scenario [7]. The location of precipitation under a nominal “cold and icy” LNIH scenario versus a forced “warm and wet” scenario was examined by [8], who found that snow/ice accumulation under a cold climate is better correlated with the VN distribution than rainfall in a “warm and wet” climate.

The requirement remains, however, for melting of the snow/ice and runoff to incise the VNs [9,10]. There are several end member options for transient atmospheric warming on early Mars including: (1) SO<sub>2</sub>-induced warming from periods of intense volcanism [11], (2) impact cratering induced warming [12], and (3) transient melting from peak seasonal temperatures [e.g. 7]. Punctuated volcanism could lead to snowmelt and runoff from the increased SO<sub>2</sub> in the atmosphere, but rapid conversion of SO<sub>2</sub> to aerosols (cooling) would prevent heating from extending beyond decades to centuries [11]. Impact cratering induces extreme high-temperature conditions and precipitation for a short duration (centuries) [12], but may produce too much rainfall and too high rainfall rates to form the delicate and equatorially-concentrated VNs [13].

The focus of this work is to test hypothesis (3) by (1) assessing whether regions with peak annual temperatures (PAT)  $> 273$  K correlate with the predicted snow/ice distribution, producing meltwater, and (2) calculating meltwater volumes in order to place constraints on the cumulative duration required for this process to form the VNs. This work highlights the importance of considering seasonal and diurnal temperature variation in addition to MAT, and contributes an understanding of the climatic effects of modest greenhouse warming and varying eccentricity on early Mars.

## METHODS:

In this analysis, we use the Laboratoire de Meteorologie Dynamique (LMD) GCM for early Mars and focus on a range of pressures (600, 800, and 1000 mbar) for a pure CO<sub>2</sub> atmosphere [e.g. 3] and a range of obliquities (25, 35, 45, and 55°) and eccentricities (0 and 0.17) in the Late Noachian [14]. We collect model data four times per model martian day (every six hours).

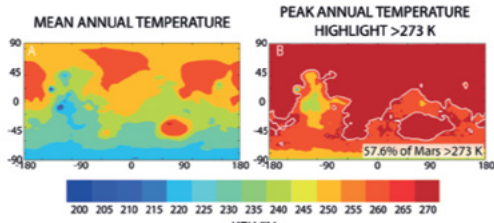


**Fig. 1.** (a) MAT and (b) PAT maps for 25° obliquity, 1000 mbar CO<sub>2</sub> atmosphere, additional greenhouse warming.

choose a relatively small absorption coefficient,  $\kappa$ , to raise MAT by  $\sim 18$  K, maintaining an overall “cold and icy” climate ( $\kappa = 2.5e-5$  kg m<sup>-2</sup>).

**MAT and PAT maps:** Is transient melting and runoff a viable mechanism for VN formation? We assess which spin-axis orbital conditions and atmospheric pressures produced PAT  $> 273$  K in the locations where VNs are abundant and snow/ice is predicted to accumulate, producing meltwater (Fig. 1).

What percentage of the year  $> 273$  K would be required to cause melting and fluvial erosion? At Lake Hoare in the Antarctic

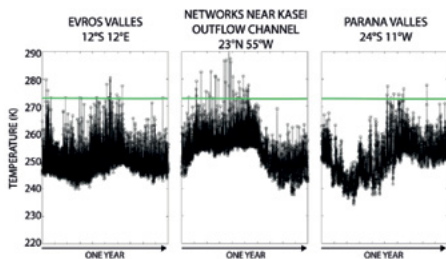


**Fig. 2.** Temperature time-series at three VNs. Green line indicates 273 K.

McMurdo Dry Valleys (MDV) (MAT  $\sim 255$  K), temperatures are  $> 273$  K for  $\sim 5-7\%$  of the year, a duration sufficient to maintain the lake through fluvial input. We hypothesize that a similar percentage of the year  $> 273$  K may be sufficient to form comparable features on early Mars. However, our analysis thus far (MAT and PAT maps) does not represent durations of conditions  $> 273$  K; each data point on the PATmap represents only the maximum annual temperature.

Based on Fig. 1, we cannot conclude whether these conditions exist for more than a few hours yearly, a duration which is likely insufficient to cause the necessary scale of melting and erosion [9]. To reconcile this, we 1) determine the annual duration of melt conditions at three VNs and compare the duration with the observed  $\sim 5-7\%$  of the year above freezing at Lake Hoare, and 2) use “positive degree day” (PDD) calculations to assess the total global amount of annual meltwater produced [9,15] and the number of years that this process must be active to produce sufficient meltwater for VN formation.

**VN study:** We examine Parana Valles, Evros Valles, and the Kasei networks, which are distributed near the edges of the predicted LNIH ice sheet at locations that require melting of ice and subsequent runoff to form in this climate. We produce temperature time-series for one martian year at each VN to determine the fraction of the year with temperatures  $> 273$  K (Fig. 2).

**PDD analysis:** We define a PDD as a day that experiences at least 6 hours  $> 273$  K, and determine number of PDD at each model grid point (lat, lon; Fig. 3). Adopting the PDD conversion factor for Mars, 1.08 mm/PDD [9], we find the thickness of ice melted at all model grid points where PDD  $\geq 1$  and LNIH snow/ice is present. Next, we integrate over the area of the LNIH ice sheet to determine the total (global) thickness/volume of ice melted in one martian year. We then compare the annual amount of meltwater produced to the total volume required to form the VNs [10] to determine the number of years that this process must operate to carve the VNs.

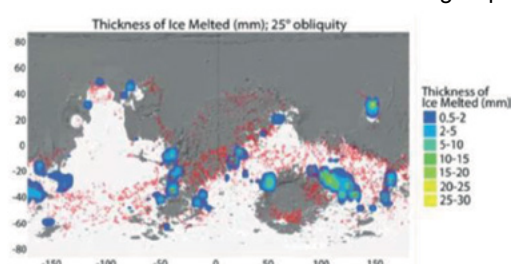


**Fig. 3.** Results of PDD calculations and VN distribution.



## RESULTS AND DISCUSSION:

We include a specific example from our study that represents optimal conditions for equatorial melting: 25° obliquity, 1000 mbar CO<sub>2</sub> atmosphere, circular orbit, and additional greenhouse warming (MAT=243 K). Lower obliquity concentrates maximum solar insolation near the equator and a thicker atmosphere increases the greenhouse effect. Thinner atmospheres prevent the studied VNs from experiencing melting conditions for day annually, a duration insufficient for VN formation. Additionally, we find that varying the eccentricity does not contribute to significant further seasonal warming.

Our models show that PAT can be >273 K in regions where both VNs are abundant and snow/ice accumulates (Fig. 1). Time-series at the three VN study sites show that each VN either approaches or exceeds 273 K for a few data points each year (Fig. 2). In this case, the VNs experience conditions above freezing for a fraction of the year comparable to the MDV, implying that these conditions might be sufficient to form the VNs if this process operates for a sufficiently long duration.

For these spin axis/orbital conditions, a volume of  $2.92 \times 10^{10} \text{ m}^3$  ( $\sim 2 \times 10^{-4} \text{ m GEL}$ ) meltwater is produced annually (Fig. 3). If 3-100 m GEL is required to form the VNs [10], this process must repeat for  $\sim 1.5 \times 10^4$  to  $\sim 5 \times 10^5$  years to produce enough meltwater. Previous analysis suggest that VN formation may have required a cumulative  $10^5$ - $10^7$  years of fluvial activity [16]. In concert with the predicted distribution of meltwater (Fig. 3), our results indicate that this mechanism could plausibly be responsible for VN formation.

Critically, runoff rates produced by this mechanism may be too low to produce the necessary erosion. At any grid point, the maximum thickness of ice melted annually is  $\sim 30 \text{ cm}$  (Fig. 3). Unless all meltwater is produced and runs off within one day, runoff rates are lower than the rates required for VN formation [mm-cm/day; 15,16]. Thus, while significant meltwater is produced in our model, slightly warmer conditions may be required to generate the necessary higher runoff rates, a subject of ongoing work.

## CONCLUSIONS:

We highlight the importance of considering seasonal/diurnal temperature variations along with MAT to assess melting in “cold and icy” early Mars climate scenarios. We find that low obliquity and high atmospheric pressure are required to produce temperatures >273 K in the equatorial regions. PAT >273 K durations are not conducive to VN formation in the nominal MAT=225 K “cold and icy” climate and we suggest that additional heating is required, such as by impact cratering [12] or volcanism [11]. Under warmer conditions (MAT=243 K), however, transient melting of ice can occur during the warmest hours of the summer season. Under these conditions, a sufficient volume of meltwater can be produced to form the VNs, although runoff rates may be too low.

## REFERENCES:

- [1] Gough D. Solar interior structure and luminosity variations. *Solar Physics*. 1981. V. 74, P. 21-24.
- [2] Sagan C. and Mullen G. Earth and Mars: Evolution of atmospheres and surface temperatures. *Science*. 1972. V. 177. No. 4043. P. 52-56.
- [3] Forget F. et al. 3D modelling of the early Martian Climate under a denser CO<sub>2</sub> atmosphere: Temperatures and CO<sub>2</sub> ice clouds. *Icarus*. 2013. V. 222. P. 81-99.
- [4] Wordsworth R. et al. Global modelling of the early martian climate under a denser CO<sub>2</sub> atmosphere: Water cycle and ice evolution. *Icarus* 2013. V. 222. P. 1-19.
- [5] Hynek B. et al. Updated global map of Martian valley networks and implications for climate and hydrologic processes. *JGR: Planets*. 2010. V. 115. No. E9. E090008.
- [6] Fassett C. and Head J. The timing of martian valley network activity: Constraints from buffered crater counting. *Icarus*. 2008. V. 195. P. 61-89.
- [7] Head J. and Marchant D. The climate history of early Mars: insights from the Antarctic McMurdo Dry Valleys hydrologic system. *Antarctic Science*. 2014. V. 26. No. 6. P. 774-800.
- [8] Wordsworth R. et al. Comparison of “warm and wet” and “cold and icy” scenarios for early Mars in a 3-D climate model. *JGR: Planets*. 2015. V. 120. P. 1201-1219.
- [9] Fastook J. and Head J. Glaciation in the Late Noachian Icy Highlands: Ice accumulation, distribution, flow rates, basal melting, and top-down melting rates and patterns. *PSS*. 2015. V. 106, P. 82-98.
- [10] Rosenberg E. and Head J. Late Noachian fluvial erosion on Mars: Cumulative water volumes required to carve the valley networks and grain size of bed-sediment. *PSS*. 2015. V. 117P. 429-35.
- [11] Halevy I. and Head J. Episodic warming of early Mars by punctuated volcanism. *Nature Geoscience Letters*. 2014. V. 7. No. 12. P. 865-868.

- [12] Segura T. et al. Environmental Effects of Large Impacts on Mars. *Science*. 2002.V. 298. P. 1997-1980.
- [13] Palumbo A. and Head J. Impact Cratering as a Cause of Climate Change and the Effects on Dating of Surfaces on Late Noachian Mars. *MAPS*. In Revision.
- [14] Laskar J. et al. Long term evolution and chaotic diffusion of the insolation quantities of Mars. *Icarus*. 2004.V. 170. No. 2.P. 343-364.
- [15] Scanlon K. et al. *GRL*. 2013.V. 40. P. 4182-4187. [16] Hoke M. et al. Formation timescales of large Martian valley networks. *EPSL*. 2011.V. 312, P. 1-12.

# LONG-TERM OBSERVATIONS OF WATER VAPOR IN THE MIDDLE ATMOSPHERE OF MARS BY SPICAM/MEX

A.A. Fedorova<sup>1</sup>, D.S. Betsis D.<sup>1</sup>, J.-L. Bertaux<sup>2,1</sup>, F. Montmessin<sup>2</sup>, O.I. Korablev<sup>1</sup>

<sup>1</sup>Space Research Institute of RAS, 84/32, Profsoyuznaya str., Moscow, 117997, Russia (fedorova@iki.rssi.ru);

<sup>2</sup>LATMOS-UVSQ, 11 Bd d'Alembert, F-78280 Guyancourt, France.

## KEYWORDS:

Mars, Atmosphere, Solar occultations, water vapour.

## INTRODUCTION:

While the H<sub>2</sub>O column density in the Martian atmosphere is well known now and has been monitored by different missions for last decades [1, 2, 3], the behavior of water in the middle atmosphere, its interannual and seasonal variability, is still opened question due to a few amount of observational material.

It is well known that the Martian atmospheric water vapor is trapped close to the surface of Mars by condensation and its vertical distribution is variable with season and location. In the aphelion season when the atmosphere is colder, water is located near the surface and blocked in the Northern hemisphere by the aphelion cloud belt [4]. The hygropause (condensation level) altitude is as low as 10-15 km. During warmer perihelion season this altitude could reach 40-50 km [2].

Several recent findings in water vapor vertical distribution were related to changes of Martian climate and evolution of the atmosphere. The discovery of the water supersaturation and access of water to altitude higher 30 km in the aphelion season [5] is directly affecting long-term representation of water transport, chemistry and accumulation on Mars on a global scale. Recent observations of the Martian hydrogen corona reported a rapid change of the hydrogen escape rate on the seasonal scale [6-8] that can relate to water access at 80 km, providing an additional source of hydrogen for the upper atmosphere [9]. That was supported by SPICAM observations of high altitude water during the MY28 global dust storm [10].

In this work we present long-term observations of the H<sub>2</sub>O vertical distribution in the Martian atmosphere by SPICAM on Mars-Express for a period of several Martian years and study the seasonal and spatial variations of the H<sub>2</sub>O density and mixing ratio at different altitudes as well as interannual variations.

## OBSERVATIONS:

Since 2004 the SPICAM IR spectrometer on Mars-Express [11] carries out measurements of the vertical distribution of water vapor in the 1.38  $\mu\text{m}$  band, the CO<sub>2</sub> density in the 1.43  $\mu\text{m}$  band and aerosol properties in the middle atmosphere of Mars by means of solar occultations. The observations cover now more than 7 Martian Years from MY27 to MY34 with 2 occultation campaigns for a year.

## INTERANNUAL VARIATIONS:

Despite the solar occultation campaigns are not completely repeatable in spatial distribution and time, the interannual comparison and a seasonal trend can be obtained. Figure 1 shows a comparison of the H<sub>2</sub>O density at 70 km for MY 28-33 for the second half of year.

In the Northern hemisphere observations don't show a prominent increase of the water content as it was during the MY28 global dust storm. This difference can not be related to the difference in latitudinal coverage. The increase of the water density above 60 km in the Northern hemisphere looks like special case of the global storm on Mars. In the Southern hemisphere MY28, 29, 32 show the increase of the density with higher values for MY28. MY33 at Ls=199-230° didn't show the prominent increase of the density.

In case of vertical distribution of H<sub>2</sub>O mixing ratio, the observations show a high value of H<sub>2</sub>O >100 ppm in the Southern hemisphere during the South summer at altitude of 50-80 km for all years than should give a seasonal feedback to the hydrogen corona escape.

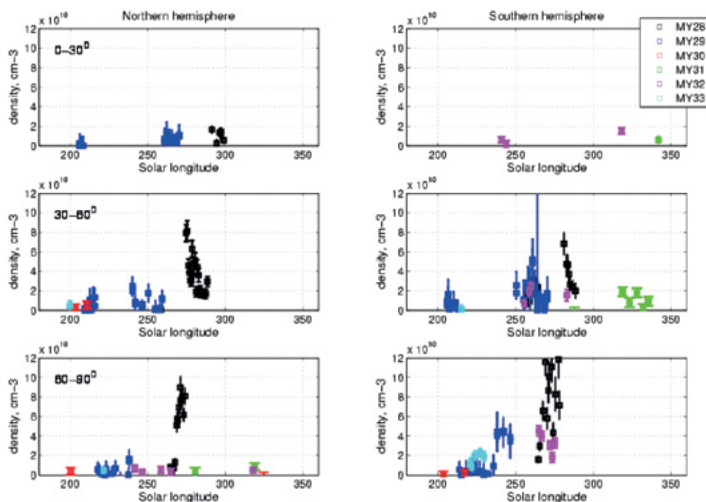


Fig. 1.  $H_2O$  density for MY28-33 (6 years) at 70 km.

## ACKNOWLEDGEMENTS:

A.A. Fedorova, D.S. Betsis D., J.-L. Bertaux and O.I. Korablev acknowledge support from the Ministry of Education and Science of Russian Federation grant 14.W03.31.0017.

## REFERENCES:

- [1] Smith, M.D. Interannual variability in TES atmospheric observations of Mars during 1999-2003 // *Icarus*, 2005. V.167. P. 148-165
- [2] Trokhimovskiy A.Yu. et al. Mars' water vapor mapping by the SPICAM IR spectrometer: Five martian years of observations // *Icarus*, 2015. V.251. P.50-64.
- [3] Maltagliati, L. et al. Annual survey of water vapor behavior from the OMEGA mapping spectrometer onboard Mars Express // *Icarus*, 2011. V.213 (2), P.480-495. [4]
- [4] Clancy R.T. et al. Water Vapor Saturation at Low Altitudes around Mars Aphelion: A Key to Mars Climate? // *Icarus*. 1996. V. 122. P.36-62.
- [5] Maltagliati L. et al. Evidence of Water Vapor in Excess of Saturation in the Atmosphere of Mars // *Science* 2011. V. 333, P.1868-.
- [6] Clarke, J. T., et al. A rapid decrease of the hydrogen corona of Mars // *Geophys. Res. Lett.* 2014. V. 41, 8013–8020.
- [7] Chaffin, M. S. et al. Unexpected variability of Martian hydrogen escape // *Geophys. Res. Lett.* 2014. V. 41, 314–320.
- [8] Bhattacharyya, D. et al., A strong seasonal dependence in the Martian hydrogen exosphere // *Geophys. Res. Lett.* 2015. V. 42, 8678–8685.
- [9] Chaffin, M. S., et al. Elevated atmospheric escape of atomic hydrogen from Mars induced by high-altitude water // *Nature Geosci.* 2017. V10(3): 174-178.
- [10] Fedorova A. et al. Water vapor in the middle atmosphere of Mars during the 2007 global dust storm // *Icarus* 2017 submitted
- [11] Korablev, O. et al.. SPICAM IR acousto-optic spectrometer experiment on Mars Express // *J. Geophys. Res.* 2006. V. 111, E09S03.

# ANNUAL MEAN MIXING RATIOS OF $N_2$ , AR, $O_2$ , AND CO IN THE MARTIAN ATMOSPHERE

Vladimir A. Krasnopolsky

Moscow Institute of Physics and Technology (PhysTech),  
vlad.krasn@verizon.net

## KEYWORDS:

Mars, atmosphere, chemical composition, variations, Curiosity rover

## INTRODUCTION:

The high-precision measurements of mixing ratios of  $N_2$ , Ar,  $O_2$ , and CO were made using the quadrupole mass spectrometer as a part of Mars Science Laboratory at the Curiosity rover (Mahaffy et al. 2013, Franz et al. 2015). These measurements must be corrected for the seasonal variations of the atmospheric pressure to reproduce annual mean mixing ratios on Mars.

## LIFETIMES OF $CO$ , $O_2$ , $N_2$ , AND AR ON MARS:

Lifetimes of long-living species are ratios of their column abundances to their column production or loss rates. The calculation is simple for  $CO$ , whose production is just the photon flux at  $\lambda < 200$  nm times the disk-to-sphere area ratio of 1/4, with the lifetime of six Earth's years.  $O_2$  recycles in some reactions, and only two processes,  $O + O + M \rightarrow O_2 + M$  and  $OH + O \rightarrow O_2 + H$ , result in formation of the  $O = O$  bonds and the  $O_2$  lifetime of 60 years.  $N_2$  is affected by outgassing from the interior and is lost by photochemical escape and sputtering (Jakosky et al. 1994). Its current lifetime is  $\approx 1$  Byr. Evolution of radiogenic  $^{40}Ar$  was considered by Krasnopolsky and Gladstone (1996, 2005), and its current lifetime relative to sputtering is very long, 19 Byr. Here we confirm the conclusion by Mahaffy et al. (2013) that the differences between the Viking and MSL data on  $N_2$  and Ar cannot be explained by their variations.

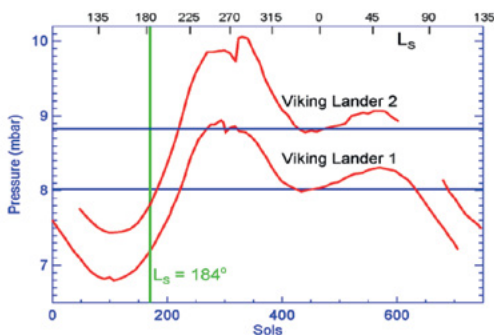


**Fig.1.** Variations of pressure for the first martian year (669 sols) of Viking Landers. Horizontal lines are calculated annual mean pressures  $p_o$ . Vertical line marks the season of the MSL measurements.

## SEASONAL CORRECTIONS TO MSL MIXING RATIOS:

Long-living species on Mars have two components of variations: (1) seasonal-latitudinal variations induced by condensation/sublimation of  $CO_2$  on the polar caps and (2) the component related to seasonal variations of the total  $CO_2$  amount in the atmosphere. The first component is significant at high latitudes exceeding  $60^\circ$  and negligible in the MSL observations at  $5^\circ S$ . The second component may be considered as independent of latitude, though it may be affected by weather. To correct the MSL mixing ratios for this component and get annual-mean mixing ratios, the MSL values should be scaled by  $p_m/p_o$ . Here  $p_m$  is the atmospheric pressure at the season of the MSL measurements ( $L_s \approx 184^\circ$ ) and  $p_o$  is the annual mean pressure. Both values should be measured at the same conditions anywhere at low latitudes on Mars. The most detailed data of this type were published for the Viking Landers (Hess et al. 1980), and we will use them (Fig. 1).

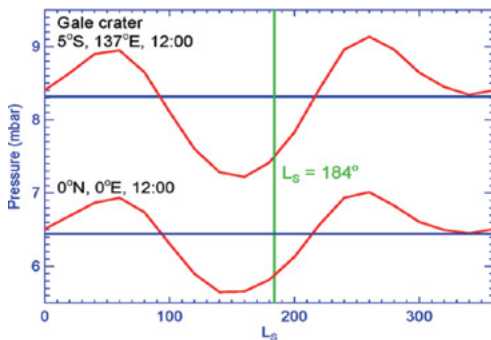


Fig. 2. Same as in Fig. 1 for two points from MCD.

The peak-to-peak variation of pressure is a factor of 1.3, the Viking Landers were at the opposite longitudes and different latitudes ( $22^{\circ}\text{N}$  and  $48^{\circ}\text{N}$ ), and the calculated  $p_m/p_o = 0.897$  and  $0.886$  are rather similar. These calculations were also made for two points using the Mars Climate Database (Fig. 2). Figure 2 is in the more convenient format ( $L_s$  instead of sols) but requires corrections for variable angular velocity of Mars. The calculated  $p_m/p_o = 0.902$  and  $0.911$  with a mean of the four values of  $0.899 \pm 0.006$ . Annual mean mixing ratios can be obtained by scaling the MSL mixing ratios from Franz et al. (2015) by this factor (Table).

Species	Franz et al. (2015)	Annual mean
$\text{N}_2$	$(2.03 \pm 0.03)\%$	$(1.83 \pm 0.03)\%$
Ar	$(2.07 \pm 0.02)\%$	$(1.86 \pm 0.02)\%$
$\text{O}_2$	$(1.73 \pm 0.06) \times 10^{-3}$	$(1.56 \pm 0.06) \times 10^{-3}$
CO	$749 \pm 2.6$ ppm	$673 \pm 2.6$ ppm

## COMPARISON WITH OTHER OBSERVATIONS OF $\text{O}_2$ AND CO:

The seasonally corrected Herschel observation (Hartogh et al. 2010)  $\text{O}_2 = (1.45 \pm 0.12) \times 10^{-3}$  agrees with MSL. The mean of three ground-based observations is  $(1.2 \pm 0.2) \times 10^{-3}$  (Nair et al. 1994). Corrected by a factor of 1.3 for dust extinction, this agrees with MSL as well. The MRO/CRISM observations of CO (Smith et al. 2009) showed the seasonally and globally averaged mixing ratio of 700 ppm. This value was 667, 693, and 684 ppm in the observations by Krasnopolsky (2015) at  $L_s = 60, 89, \text{ and } 110^{\circ}$ .

## REFERENCES:

- [1] Franz, H.B., et al., Planet. Space Sci. 109-110, 154-158, 2015.
- [2] Hartogh, P., et al., Astron. Astrophys. 521, L49, 2010.
- [3] Hess, S.L., et al., Geophys. Res. Lett. 7, 197-200, 1980.
- [4] Jakosky, B.M., et al., Icarus 111, 271-288, 1994.
- [5] Krasnopolsky, V.A., Icarus 207, 638-647, 2010.
- [6] Krasnopolsky, V.A., Icarus 253, 149-155, 2015.
- [7] Krasnopolsky, V.A., Gladstone, G.R., JGR 101A, 15,765-15,772, 1996.
- [8] Krasnopolsky, V.A., Gladstone, G.R., Icarus 176, 395-407, 2005.
- [9] Mahaffy, P.R., et al., Science 341, 263-266, 2013.
- [10] Nair, H., et al., Icarus 111, 124-150, 1994.
- [11] Smith, M.D., et al., JGR 114, E00D03, 2009.

# INTER-ANNUAL VARIATIONS OF MARTIAN SEASONAL CAPS FROM NEUTRON SPECTROSCOPY OBSERVATIONS ONBOARD MARS ODYSSEY

M.L. Litvak<sup>1</sup>

<sup>1</sup>Space Research Institute, Russia, Moscow, 117997, Profsovnaya street, 84/32, litvak@mx.iki.rssi.ru

## KEYWORDS:

Mars, Mars Odyssey, HEND, seasonal caps, neutron spectroscopy.

## INTRODUCTION:

Starting from 2002 Mars Odyssey continues orbital observations of Mars surface accumulating unique science data gathered by different instrumentation including Russian neutron spectrometer HEND (as part of Mars Odyssey Gamma Ray Spectrometer suite). The neutron spectroscopy data were often used to develop global maps of martian neutron flux and subsurface water ice distribution [1-3, 5]. Taking into account long period of observation, HEND data were also analyzed to study local and global variations of martian seasonal caps with time [4-8]. The growing and sublimation of martian snow caps significantly influence on seasonal variations of neutron flux. It provides possibility to use neutron data as a sensitive method to monitor behavior of seasonal caps (variations of column density and mass) and search for their inter annual variations. We used all available HEND/Odyssey data (8 martian years) to study seasonal variations of atmospheric CO<sub>2</sub> both within one seasonal cycle, and among successive seasonal cycles (see example on Figure 1).

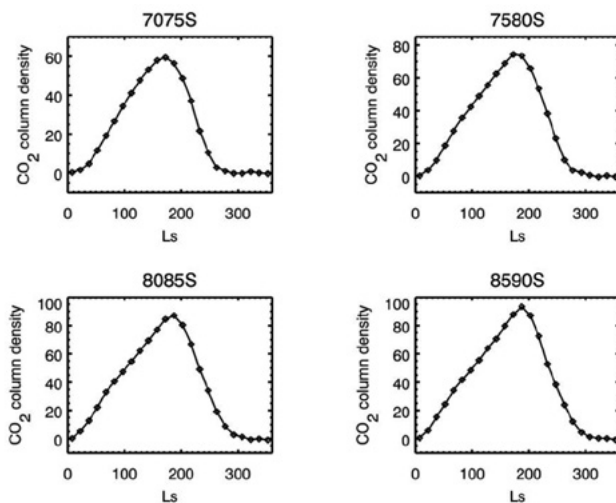


**Fig. 1.** The example of seasonal variations of condensed CO<sub>2</sub> deposit (column density in g/cm<sup>2</sup>) at different latitude belts in southern hemisphere.

## REFERENCES:

- [1] Feldman W.C. et al., (2002), *Science*, 297, 5578, 75-78.
- [2] Mitrofanov I.G et al. (2002), 297, 5578, P. 78-81.
- [3] Boynton W.V. et al., (2002) *Science*, 297, 5578, P. 81-85.
- [4] Mitrofanov I.G. et al., (2003) *Science*, 300, P. 2081-2084.
- [5] Litvak M.L. et al. (2006) *ICARUS*, 180, 1, P. 23-37.
- [6] Kelly N. J. et al (2006) *J. Geophys. Res.*, E03S07.
- [7] Litvak M.L. et al., (2007) *J. Geophys. Res.*, E03S13.
- [8] Prettyman T. H. et al., (2009) *J. Geophys. Res.*, 114, CitelID E08005.

# MAGNETIC FIELD AT MARS IONOSPHERE FROM MARSIS DATA. MODELS AND SIMULATIONS

S. Jiménez<sup>1</sup>, M. Ramírez-Nicolás<sup>2</sup>, D. Usero<sup>2</sup>, P.J. Pascual<sup>3</sup>, M.P. Velasco<sup>1</sup>, L. Vázquez<sup>2</sup>

<sup>1</sup>Universidad Politécnica de Madrid, Spain,

<sup>2</sup>Universidad Complutense de Madrid, Spain,

<sup>3</sup>Universidad Autónoma de Madrid Spain.

s.jimenez@upm.es

## KEYWORDS:

Mars, Magnetic Field, Ionosphere, Solar Radiation.

## INTRODUCTION:

Evidence of an induced magnetic field in the ionosphere of Mars was measured indirectly through its effects on the electron density behaviour, based on the observations by the Mars Advanced Radar for Subsurface and Ionospheric Sounding (MARSIS) onboard Mars Express [1].

This, which was done for a limited number of orbits on June 2006, can now be extended systematically, analysing the data for all orbits as measured by MARSIS during its ongoing mission.

The measures are in the form of ionograms representing the time delay of the echo of the signal as a function of the emitted frequency. From the inversion procedure of the ionospheric echos [2] it is possible to obtain the vertical electronic density and, from there and the cyclotronic frequencies of the electrons, to deduce the modulus of the magnetic field at the spacecraft height.

That magnetic field can be due to cortical remanent magnetic fields on the planet and to the induced effect of the charged particles of the solar wind.

We simulate the motion of charged particles in the magnetic using specific conservative techniques, considering the symmetry reduction of the Störmer model [3] as well as the general case [4,5]. The system is open to exhibit chaotic behaviour [6] that can be relevant to the confinement of particles trapped in the field.

## REFERENCES:

- [1] M. Ramírez-Nicolás, B. Sánchez-Cano, O. Witasse, P.-L. Blelly, L. Vázquez. The effect of the induced magnetic field on the electron density vertical profile of the Mars' ionosphere: A Mars Express MARSIS radar data analysis and interpretation, a case study // Planetary and Space Science 126 (2016) 49–62.
- [2] Sánchez-Cano, B., Witasse, O., Herraiz, M., Radicella, S.M., Bauer, J., Blelly, P.-L., Rodríguez-Caderot, G. Retrieval of ionospheric profiles from the Mars Express MARSIS experiment data and comparison with radio occultation data // Geoscientific Instrumentation, Methods and Data System 1, 1, 77-84, 2012.
- [3] Vázquez, L., and Jiménez, S. Motion of a charge in a magnetic dipole field I. Painlevé, Analysis and a conservative numerical scheme, Applied Mathematics and Computation 25, 207-217, 1988.
- [4] María Ramírez-Nicolás, David Usero, Luis Vázquez, Numerical studies of charged particles in a magnetic field: Mars application // Central European Journal of Physics, 12(8), 521-531, 2014.
- [5] M. Ramírez-Nicolás, D. Usero, M.P. Velasco, L. Vázquez, Numerical study of a charged particle in a general magnetic field // International Journal of Pure and Applied Mathematics, Volume 106 No.2, 401-414, 2016.
- [6] Rui Dilao and Rui Alves-Pires, Chaos in the Störmer Problem. // Progress in Nonlinear Differential Equations and Their Applications, Vol. 75, 175–194, 2007.



# NEUTRAL ESCAPE AT MARS INDUCED BY THE HIGH-ENERGY H/H<sup>+</sup> OF SOLAR WIND ORIGIN

V.I. Shematovich

*Institute of Astronomy of the Russian Academy of Sciences, Moscow, Russia;*  
shematov@inasan.ru

## KEYWORDS:

Mars, solar wind, hot corona, neutral atmosphere loss, high-energy proton and hydrogen atom precipitation, kinetic Monte Carlo model.

## INTRODUCTION:

One of the first surprises of the NASA MAVEN mission was the observation by the SWIA instrument of a tenuous population of protons with solar wind energies traveling anti-sunward near periapsis, at altitudes of ~150-250 km [1]. While the penetration of solar wind protons to low altitude is not completely unexpected given previous Mars Express results, this population maintains exactly the same velocity as the solar wind observed. From previous studies it was known that some fraction of the solar wind can interact with the extended corona of Mars. By charge exchange with the neutral particles in this corona, some fraction of the incoming solar wind protons can gain an electron and become an energetic neutral hydrogen atom. Once neutral, these particles penetrate through the Martian induced magnetosphere with ease, with free access to the collisional atmosphere/ionosphere.

The origin, kinetics and transport of the suprathermal O atoms in the transition region (from thermosphere to exosphere) of the Martian upper atmosphere due to the precipitation of the high-energy protons and hydrogen atoms is discussed. Kinetic energy distribution functions of suprathermal and superthermal (ENA) oxygen atoms formed in the Martian upper atmosphere were calculated using the kinetic Monte Carlo model [2,3] of the high-energy proton and hydrogen atom precipitation into the atmosphere. These functions allowed us: (a) to estimate the non-thermal escape rates of neutral oxygen from the Martian upper atmosphere due to the extreme solar events, and (b) to compare with available MAVEN measurements of the extended oxygen corona. Escape of hot oxygen atoms induced by precipitation of the solar wind plasma may become one of the dominant loss processes under conditions of extreme solar events - solar flares and coronal mass ejections, - as it was shown by recent observations of the NASA MAVEN spacecraft [4].

This work is supported by the RFBR project and by the Basic Research Program of the Presidium of the Russian Academy of Sciences (Program 1.7).

## REFERENCES:

- [1] Halekas C., et al. // *Geophys. Res. Lett.* 2015. V. 42. doi:10.1002/2015GL064781.
- [2] Shematovich V.I. et al. // *J. Geophys. Res.* 2011. V.116. P. A11320.
- [3] Shematovich V.I. // *Solar System Res.* 2017. V.51. P. 285-294.
- [4] Jakosky B. et al. // *Science.* 2015. V. 350. Issue 6261. P. aad0210:1-7.

# CRATER AGE AND HYDROGEN CONTENT IN LUNAR REGOLITH FROM LEND NEUTRON DATA

M.L. Litvak<sup>1</sup>, Richard D. Starr<sup>2</sup>, I.G. Mitrofanov, A.B. Sanin<sup>1</sup> and Noah E. Petro<sup>3</sup>

<sup>1</sup>*Space Research Institute, Russia, Moscow, 117997, Profsovnaya street, 84/32, litvak@mx.iki.rssi.ru*

<sup>2</sup>*Physics Department, The Catholic University of America, Washington, DC 20064,*

<sup>3</sup>*Planetary Geology, Geophysics, and Geochemistry Laboratory, NASA Goddard Space Flight Center, Greenbelt, MD 20771, USA*

## KEYWORDS:

LEND/LRO, Moon, hydrogen.

## INTRODUCTION:

Analysis of Lunar Exploration Neutron Detector (LEND) neutron count rates for a large set of mid-latitude craters provides evidence for lower hydrogen content in the crater interiors compared to typical highland values. Epithermal neutron count rates for crater interiors measured by the LEND Sensor for Epithermal Neutrons (SETN) were compared to crater exteriors for 301 craters and displayed an increase in mean count rate at the  $\sim 9\text{-}\sigma$  confidence level, consistent with a lower hydrogen content. This difference is greatest for a small subset of craters that appear to be dominated by very young (Copernican) craters and their ejecta, where both neutron count rates and optical maturity display a significant offset from background.

The weak correlation between neutron count rates and optical maturity found for the full set of crater interiors suggest that hydrogen abundances may not be simply related to exposure time and solar wind implantation. Other weathering processes must play a role. Finally, while neutron measurements do not provide a very fine discriminator of crater ages, they do appear to isolate Copernican craters from other older craters and therefore provide some measure of bulk regolith maturity.

# RECENT TECTONIC DEFORMATION IN THE SOUTH POLE AREA OF THE MOON

A.T. Basilevsky<sup>1</sup>, M.A. Ivanov<sup>1</sup>, S.S. Krasilnikov<sup>1</sup>, M.A. Zakharova<sup>1</sup>, J.W. Head<sup>2</sup>, A. Deutsch<sup>2</sup>

<sup>1</sup>Vernadsky Institute, Kosygin str., 19, 119991, Moscow, Russia, atbas@geokhi.ru;

<sup>2</sup>Brown University, 02912, Providence, Rhode Island, USA

## KEYWORDS:

The Moon, lunar, south, pole, thrust fault, H<sub>2</sub>O equivalent, moonquake

## INTRODUCTION:

An imaging survey of the Moon with a resolution ~0.5 m by the LROC NAC cameras onboard the Lunar Reconnaissance Orbiter [1] allowed us to identify ~3200 scarps in the lunar highlands probably formed by young (<50-100 Ma) thrust faults [2-4]; these discoveries have significantly changed our understanding of the post-mare geological history of the Moon. Here we describe several such thrust faults in the South Pole area of the Moon, which is of special interest as a location where Russian missions Luna-Glob (Luna-25) and Luna-Resource (Luna-27) will land in the near future [e.g., 5-8]. In the more distant future there are plans to build a habitable lunar base [e.g., 9].

## POLAR SCARPS AND GENERAL GEOLOGY:

Several scarps interpreted to have been formed by young thrust faults identified by [2] in South pole area are shown in Figures 1 and 2.

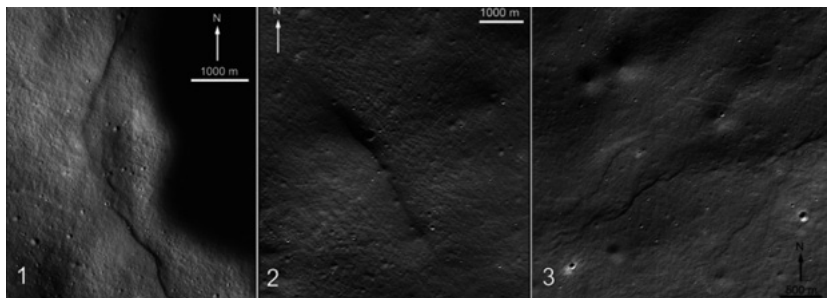


**Fig. 1.** Scarps of possible thrust faults in the South pole area: 1, 2, 3 – near craters Cabeus, Shoemaker and Simpelius, respectively; parts of images M1154412657LR, M108891721LR, M106807247LR, NASA/ASU.

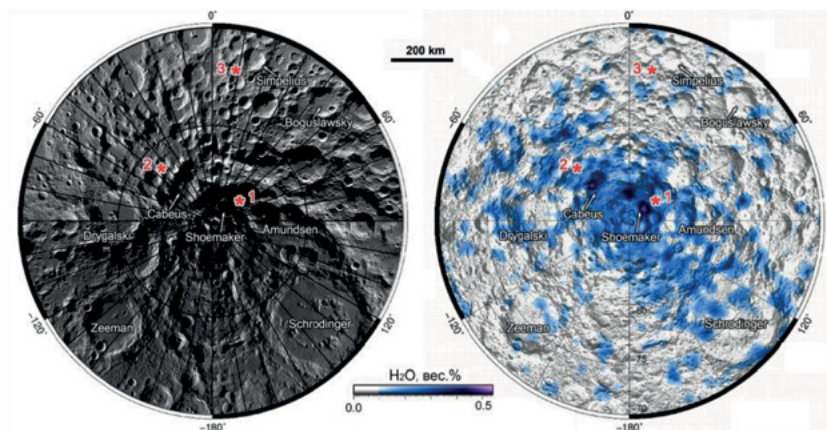


**Fig. 2.** South Pole area of the Moon. Left – mosaic of LROC WAC images, NASA/ASU. Right – distribution of H<sub>2</sub>O equivalent in the upper 1 m of the surface layer ([10], modified), 1, 2, 3 - locations of scarps shown in Fig. 1.

As measured by [11] the scarps shown in Fig. 1 are 4-5 to 10-15 km long, 30 to 100 m high and their slopes are 5-10 to 15-20 degrees steep, simi-

lar to the measurements of [11]. As discussed by [3, 4], formation/movement of these scarps should be accompanied by moonquakes related to 28 near-surface moonquakes registered in 1969-1977 by the Apollo seismic network and having magnitudes (M) from 1.6 to 4.2 on the Richter scale [12-13]. Additional consideration of these results led [4] to the determination of the locations of 25 of those moonquakes. For our analysis, it is important that one of these moonquakes, with  $M \sim 4$ , is located in the South Pole area.

The area shown in Fig. 2 represents part of the southern segment of the largest basin on the Moon, the South Pole-Aitken basin with a diameter of  $\sim 2500$  km [14-19]. It is one of the most ancient impact basins on the Moon (4.2-4.3 Ga [20]) and information on its materials, which should be sampled by the Luna-Glob and Luna-Resource missions, is very important for understanding the earliest part of the geologic history of the Moon.

## H<sub>2</sub>O IN THE STUDY AREA:

On the basis of the LEND measurements [21] the distribution of the H<sub>2</sub>O equivalent in the South Pole area is shown in Fig. 2 (right) with variations from  $\sim 0.05$  to  $\sim 0.5$  mass % [10]. The lateral resolution of this parameter is  $\sim 10$  km and it characterizes  $\sim 1$  m thickness of the upper layer of regolith, which includes the "dry" uppermost part of indeterminate thickness [21]. It is shown in [10] that if the thickness of the uppermost "dry" layer is 90-100 cm the H<sub>2</sub>O (ice) content in the underlying material may be 4 to 10 mass %; this agrees with LCROSS experiment results ( $\sim 6\%$  [22]). These values, if presented as volume percents, suggest that 20-30% of H<sub>2</sub>O ice forms a significant portion of the regolith pore space. This is a high enough content of ice such that it should increase the regolith material mechanical strength and in the case of moonquakes could influence the seismic response [23, 24]; if the quake is rather strong the material might become heated along the fault and loose H<sub>2</sub>O and other volatiles.

It is seen in Figure 2-right that two of three localities of the thrust faults considered (Shoemaker and Cabeus) are within the areas with high H<sub>2</sub>O equivalent contents and one locality (Simpelius) is outside the H<sub>2</sub>O equivalent anomalies.

## TERRESTRIAL ANALOG:

The Meckering thrust fault in Western Australia formed by the 6.9 Richter magnitude earthquake on November 14, 1968 [25] (Fig. 3), can be considered as a terrestrial analog for the lunar thrust fault scarps.



**Fig. 3.** Left: Photo of the Meckering thrust fault scarp (Source: <http://www.aees.org.au/gallery/1968-meckering>) Right: One of the tension fractures in the vicinity of the Meckering epicenter, its width is  $\sim 1$  m (Source: <http://www.ydcm.com.au/2008/September/MGapA.jpg>.)

The Meckering scarp (Fig. 3 left) height is up to 3 m, and the total length (with branches) is  $\sim 37$  km. Analysis of the appropriate seismograms showed that the thrust fault started at the depth of 1.5 km and extended to the depth of 6 km. As part of that event there was formation of tension fractures (Figure 3 right) which may be compared with small graben associated with some lunar thrust fault scarps [3]. The Meckering quake (and other earthquakes as well) also led to seismic fluidization of dry near-surface sand [26]. Similar phenomenon may also be caused by lunar quakes.

## DESTRUCTIONS CAUSED BY THE MECKERING AND OTHER EARTHQUAKES:

The town of Meckering (population 240) was essentially destroyed (Figure 4 left). Even the rails were locally buckled (Figure 4 right).



**Fig. 4.** Left: Building destroyed by the Meckering quake (Source <http://www.ournauke-ustralia.com.au/tag/meckering/>) Right: Buckled rails (Source:<http://www.mingor.net/images-large/meckering-eq-buckled-rail-2011/>)

Consideration of the Meckering event shows that seismic quakes on the Moon should be studied and taken into account as risk factor of in lunar base design and construction. Of course, the Meckering 1968 quake with  $M = 6.9$  was much stronger than the moonquakes registered to date ( $M = 1.6-4.2$ ). However, 1) there is no guarantee that moonquakes can not be higher in magnitude than these, and 2) moonquakes with known magnitudes ( $M = 1.6-4.2$ ) can lead to noticeable destruction (Fig. 5).



**Fig. 5.** Destruction caused by earthquakes with  $M = 4.2$ . Left – Veliko Tarnovo, Bulgaria. Right – Norcia, Umbria, Italy; Sources: <https://pronedra.ru/uploads/d/cP/OC/cPOC-mQu3.orig.jpg> and <http://www.tvc.ru/news/show/id/99704#&gid=1&pid=2>.

## CONCLUSIONS:

We conclude that the South Pole area of the Moon shows the presence of geologically young thrust-fault scarps. The South Pole region is of special interest as a place where Russian missions Luna-Glob and Luna-Resource are planned to land in near future and in more distant future a lunar base may be built. The young thrust-fault scarp formation was accompanied by moonquakes which, in turn, could lead to seismic fluidization of surface materials as well as to mobilization and loss of volatiles from cold traps. Moonquakes also represent a factor of risk in the design, building and exploitation of a lunar base and thus should be studied and carefully taken into consideration. This study should include development of landed seismic experiments (such as the SEISMO experiment on Luna 25 and 27 [27]) and networks, and long duration observations.

## ACKNOWLEDGEMENTS:

The work is supported by the Russian Science Foundation grant № 17-17-01149: «Reconstruction of geologic history of polar areas of the Moon using new high-accuracy data to understand sources, distribution and accumulation of volatiles (water) on the Moon. The authors are grateful to B.A. Ivanov for helpful consultations.

## REFERENCES:

- [1] Robinson M. et al. Lunar Reconnaissance Orbiter Camera (LROC) instrument overview // *Space Science Reviews*. 2010. V. 150, P. 81-124.
- [2] Watters T. et al. Evidence of recent thrust faulting on the Moon revealed by the Lunar Reconnaissance Orbiter Camera // *Science*. 2010. V. 329. P. 936-940.
- [3] Watters T. et al. Global thrust faulting on the Moon and the influence of tidal stresses // *Geology*. 2015. V. 43. No. 10. P. 851–854.
- [4] Watters T. Shallow lunar seismic activity and the current stress state of the Moon // *Lunar and Planetary Science XLVIII*. 2017. abs 2569.
- [5] Ivanov M. et al. Geological Context of Potential Landing Site of the Luna-Glob Mission // *Solar System Research*. 2014. V. 48 P. 391-402.
- [6] Marov M. et al. Selection and characterization of landing sites for the upcoming Russian robotic missions to the Moon // *The 40th COSPAR Scientific Assembly*. 2014. Moscow. Abstract B0.1-33-14.
- [7] Ivanov M. et al. Landing site selection for Luna-Glob mission in crater Boguslawsky // *Planetary and Space Science*. 2015. V. 117. P. 45–63.
- [8] Djachkiva M. et al. Selection of *Luna-25* Landing Sites in the South Polar Region of the Moon // *Solar System Research*, 2017, Vol. 51, No. 3, pp. 185–195.
- [9] Zelenyi L. Milestones of the Russian space science program for the decade 2016-2025 // *The Seventh Moscow Solar System Symposium 7m-s3, 2016*, abstract 7MS3-OS-01.
- [10] Sanin A. et al. Hydrogen distribution in the lunar polar regions // *Icarus*. 2017. V. 283. P. 20-30.
- [11] Basilevsky A. et al. Young tectonic deformations in the South pole area of the Moon // *Solar System Research*. 2017. in press.
- [12] Nakamura Y. et al. Shallow moonquakes—Depth, distribution and implications as to the present state of the lunar interior // *Proceedings, 10th LPSC*. 1979. Pergamon Press, P. 2299–2309.
- [13] Nakamura Y. Shallow moonquakes: How they compare with earthquakes // *Proceedings, 11th LPSC*. 1980. Pergamon Press, P. 1847–1853.
- [14] Stuart-Alexander, D. Geological Map of the Central Far Side of the Moon // *US Geological Survey Map I-1047*, 1978. United States.
- [15] Wilhelms et al. Geologic Map of the South Side of the Moon // *US Geological Survey Map I-1192*, 1979. United States.
- [16] Spudis P. Ancient multiring basins on the Moon revealed by Clementine laser altimetry // *Science*. 1994. V. 266. P. 1848–1851.
- [17] Hiesinger H, Head J. Lunar South Pole–Aitken impact basin: topography and mineralogy // *The 34<sup>th</sup> LPSC*. 2004. Abstract 1164.
- [18] Shevchenko et al. Structure of the South Pole–Aitken lunar basin // *Solar System Research*. 2007. V. 41. P. 447–462.
- [19] Garrick-Bethell I., Zuber M. Elliptical structure of the lunar South Pole–Aitken basin // *Icarus*. 2009. V. 204, P. 399–408.
- [20] Hiesinger H. et al. New crater size-frequency distribution measurements of the South Pole–Aitken basin // *The 43<sup>rd</sup> LPSC*. 2012. Abstract 2863.
- [21] Mitrofanov I. et al. Hydrogen mapping of the lunar south pole using the LRO neutron detector experiment LEND // *Science*. 2010. V. 330(6003) P. 483–486.
- [22] Colaprete A. et al. Detection of water in the LCROSS ejecta plume // *Science*. 2010. V. 330, No 463. 463-468.
- [23] Che A. et al. Stability of pile foundations base on warming effects on the permafrost under earthquake motions // *Soils and Foundations*. 2014. V. 54(4). P. 639–647.
- [24] Dadfar B. et al. Experimental and analytical study of seismic site response of discontinuous permafrost // *Canadian Geotechnical Journal*. 2016. V. 53(9). P. 1363-1375.
- [25] Everingham I.B. Preliminary report on the 14 October 1968 earthquake at Meckering, Western Australia // *Bureau of Mineral Resources, Geology and Geophysics, Commonwealth of Australia*. 1968. Record No 1968 / 142. 93 p.
- [26] Collins C. et al., Paleoliquefaction studies in Australia to constrain earthquake hazard estimates // *Proceedings of 2004 NZSEE Conference, Rotorua, 19-24 March 2004*, 2004. Paper 50.
- [27] Zelenyi L.M., Khartov V., Mitrofanov I.G., Skalsky A., 2010. “LUNA-GLOB” AND “LUNA-RESOURCE” MISSIONS. The 1<sup>st</sup> Moscow Solar System Symposium. Abstract1MS3-3-9

# PRELIMINARY DATA ON THE AGE INTERVAL OF THE MONS RUMKER VOLCANIC PROVINCE FORMATION

A.A. Dmitrovsky, M.A. Zacharova and E.N. Slyuta, Vernadsky Institute of Geochemistry and Analytical Chemistry of the Russian Academy of Sciences, Moscow, Kosygina str., 19, andredmitrovsky@gmail.com

## KEYWORDS:

Mons Rumker, lunar magmatism, Oceanus Procellarum, craters size-frequency distribution (cSFD).

## INTRODUCTION:

Mons Rumker are known as volcanic dome midst the Oceanus Procellarum. It is exceptionally attractive place because of spatial superposition of unexplored volcanic features and marine materials of wide spectrum of ages (from Lower Imbrian Series to Copernican System) in the nearest neighborhood around it [1]. That is why this region is supposed for being primary target for russian heavy rover "Lunar Robot-Geologist" [2, 3]. In order to prepare for the mission, the study of morphology, history and matter of the volcanic province has been begun.

The dome's relative elevation is about 1 km and about 70 km in diameter [4]. It has asymmetric slopes, the eastern is gentler. The rise consists of at least ten individual volcanoes, as they are understood. Some of them have calderas at the top.

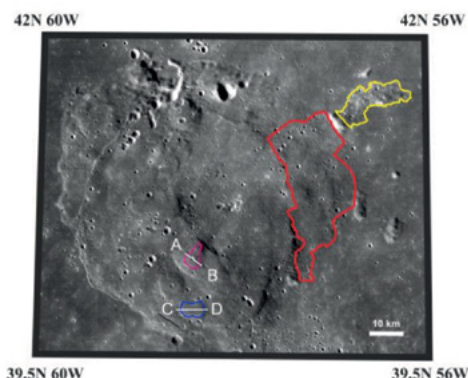


Fig.1. Mons Rumker volcanic province. Distinguished young swells outlined in blue and violet; old areas are inside red and yellow contours.

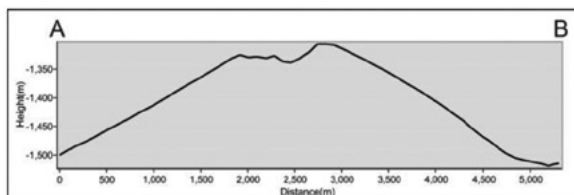


Fig. 2. Topographic section across swell along the A-B line at Fig.1

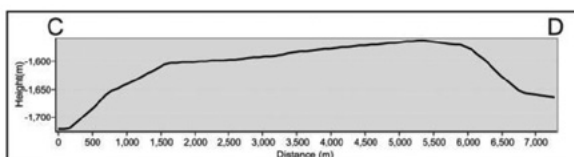
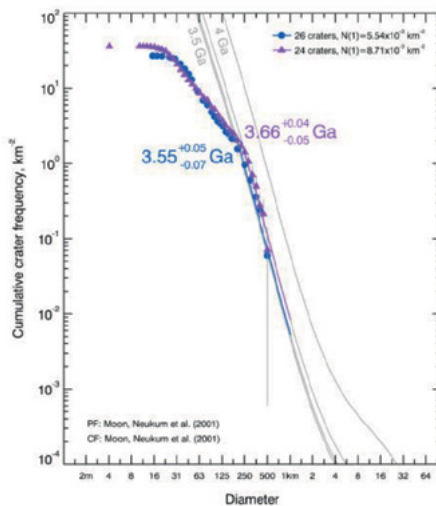
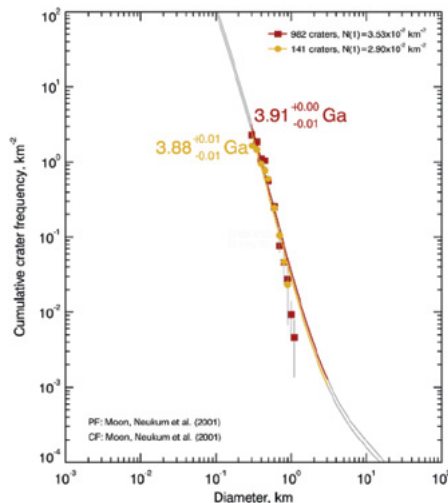


Fig. 3. Topographic section across swell along the C-D line at Fig.1



**Fig. 4.** CumulativeCSD curve for the young swells. Only craters with diameter >200m for blue and >230m were accounted for. SFD curves colours are similar to at Fig.1



**Fig. 5.** CumulativeCSD curve for the old areas. Only craters with diameter >300m were accounted for. SFD curves colours are similar to at Fig.1

In this work we study the ages of the probable oldest and the possible youngest areas of the province to understand time of active magmatic processes in the Mons Rumker.

## METHODOLOGY:

The whole research is based upon the LRO WAC images mosaic with mean resolution 100 m/pixel, and the LRO NAC image M1169891715RE with resolution 1.35m/pixel and incidence angle 75°. The crater counting was performed using CraterTools for ArcGIS. The crater statistics was performed using Craterstats.

Distinguishing of the relative age of different areas is based on geomorphological analysis of the province: we suggest the youngest areas, which do not overlaid by any visible magmatic flux. Magmatic fluxes covered by others are proposed to be the oldest parts of the studied territory. In this way, we demarked two young swells (Fig.2,3) in the south-western part and two old areas in the north-eastern part of the province (Fig.1). Then ages of these areas were estimated with craters size-frequency distribution (SFD) [5, 6], which was counted for young swells with NAC image and with WAC mosaic for old areas.



Craters density was calculated with ArcGIS instrument (Fig.3).

## RESULTS:

Calculated ages for two young swells are 3.55G.a. and 3.66G.a., while for old areas there is a little disparity between both estimation with 3.88 G.a. and 3.91 G.a.. According to [1], the interval correspond to Upper Imbrian (3.20G.a.– 3.80G.a.) – Lower Imbrian - Nectarian (3.85 G.a.- 3.95 G.a.) epoch. According to [8] the mean age of the whole province is 3.79 G.a., that well correlate with derived results.

## REFERENCES:

- [1] Wilhelms D. E. (1987) USGS Prof. paper 1348
- [2] Slyuta E. N., Galimov E. M., Marov M. Ya. (2014) Fundamental space research. V. 2. Solar System. 103-128.
- [3] Slyuta E. N. (2016) 7MS3 Abst. # PS-18.
- [4] Zakharova M. A. and Slyuta E.N. (2016) 7MS3 Abst. MN-15.
- [5] Trask N. J. (1966) NASA Technical Report.
- [6] Neukum G. et al. (2001) Chronology and Evolution of Mars. 96, 55–86.
- [7] Zhao J. et al. (2016) LPS XLVII Abst. #1758.
- [8] Dmitrovsky A.A. et al. (2017)LPS XLVIII Abst. #1629.
- [9] Zhao J. et al. (2017) doi: 10.1002/2016JE005247.

# DAYTIME DEPENDENT VARIATIONS OF THE LUNAR SURFICIAL OH/H<sub>2</sub>O CONTENT

A. Grumpe<sup>1</sup>, C. Wöhler<sup>1</sup>, A. A. Berezhnoy<sup>2</sup>, V. V. Shevchenko<sup>2</sup>

<sup>1</sup>Image Analysis Group, TU Dortmund University, Otto-Hahn-Str. 4, 44227 Dortmund, Germany;

<sup>2</sup>Sternberg Astronomical Institute, Universitetskij pr., 13, Moscow State University, 119234 Moscow, Russia

## KEYWORDS:

Moon; volatiles; hydroxyl; water; modeling; solar wind.

## INTRODUCTION:

The occurrence of surficial hydroxyl (OH) and/or water (H<sub>2</sub>O) has been revealed by the analysis of near-infrared hyperspectral imagery in the wavelength range of the absorption band near 3 μm using data of Deep Impact mission [1] and the Moon Mineralogy Mapper (M<sup>3</sup>) instrument [2, 3] on the Chandrayaan-1 spacecraft. Variations with local daytime and selenographic latitude have been found in [1], and the presence of lunar surficial OH/H<sub>2</sub>O has been found to be restricted to high selenographic latitudes in [2, 3]. The strength of the OH/H<sub>2</sub>O absorption band has been found to be strongly correlated with the illumination conditions in [4]. Using a physically motivated method for removal of the thermal emission component that also takes into account the surface roughness [6], it is observed in [5] based on M<sup>3</sup> data that the OH/H<sub>2</sub>O absorption band is also present at equatorial latitudes and largely illumination-independent. For the highland crater Boguslavsky located at high southern latitudes, it has been observed in [7], using an extension of the thermal equilibrium based method of [8] for surface temperature estimation, that the OH/H<sub>2</sub>O absorption band is strong in the local morning and decreases towards a lower but non-zero value at midday.

In this work we provide preliminary results of a M<sup>3</sup>-based analysis of the dependence of the OH/H<sub>2</sub>O absorption band depth on local daytime for 18 lunar highland regions, which are located at different latitudes and have been observed under 4-8 different illumination conditions [9]. The observations are compared with modeling results.

## DATA AND METHOD:

Maps of the spectral reflectance were constructed for the set of 18 highland regions based on the M<sup>3</sup> level-1B spectral radiance data published on the PDS ([pds.imaging.jpl.nasa.gov/volumes/m3.html](https://pds.imaging.jpl.nasa.gov/volumes/m3.html)). For derivation of bidirectional spectral reflectance, the M<sup>3</sup> data processing framework of [7] has been used. The surface temperature estimation approach of [10] used for constructing the M<sup>3</sup> level-2 spectral reflectance data set on the PDS [11] is meanwhile considered to be inaccurate (e.g. [12]). Hence, we estimated the surface temperature and the spectral emissivity, quantities required to remove the thermal emission component that strongly affects the wavelength range of the OH/H<sub>2</sub>O absorption band, using the method of [7]. This technique extends the thermal equilibrium based approach of [8] by performing an iterative adjustment of the surface temperature, spectral reflectance and spectral emissivity, and by including a correction for surface roughness similar to [13].

Based on the spectral reflectance data corrected for thermal emission and local topography and normalized to uniform observation and illumination geometry, a map of the relative OH band depth integrated over M<sup>3</sup> channels 78-84 between 2697 and 2936 nm (here termed OHIBD) was constructed for each region for all local daytimes with available M<sup>3</sup> data.

## RESULTS AND DISCUSSION:

In highland regions located at moderate to high latitudes beyond 45°, the OHIBD is maximal in the morning around 08:00 local time. It decreases within the next few lunar hours and reaches its minimum in the early afternoon around 14:00. The minimal OHIBD value is typically lower by about one third than the morning value, and slight OHIBD increase occurs in the late afternoon. At low latitudes of <20°, a significant OHIBD level comparable with

the midday OHIBD level at high latitudes is found, which changes only insignificantly during the lunar day. Results are shown in Fig. 1 for a high-latitude region at (172.5° E, 73° N) and a low-latitude region at (125.5° E, 18° N). This observation is in contrast to [3] but in consistency with [12, 5].

A commonly accepted mechanism for the formation of surficial OH/H<sub>2</sub>O on regolith surfaces is the adsorption of solar wind protons reacting with O atoms bound in the surface material (e.g. [14, 4]). The physical processes responsible for the behavior of H and OH on regolith surfaces as well as the relevant physical parameters are discussed in [14]. The behavior of H was analyzed using Monte Carlo methods in [15] and based on a continuity equation based treatment in [16].

In this work we provide a comparison between our daytime-dependent OHIBD observations and an extension of the continuity equation based approach suggested in [15, 16] towards the interaction between H and OH [17]. Our model considers the competing source and sink processes of solar proton adsorption [14], delivery of OH by micrometeorites [18], reaction of H with O from the surface material to form OH [14, 15], surface temperature dependent diffusion/evaporation [15] and solar flux dependent photolysis of OH [19]. The surface temperature depending on the reflectance spectrum and the illumination conditions was estimated according to [7]. In order to explain the non-zero OHIBD level at midday, we assume the presence of an "offset" OH component that is more strongly bound to the surface material than the component formed by adsorption and is thus stable against diffusion/evaporation and photolysis and adds up spectrally with the adsorbed, daytime-dependent component. This model results in two coupled ordinary differential equations describing the H and OH column densities [17]. The boundary condition that the difference between the OH column densities at sunrise and sunset corresponds to the amount of micrometeoroid-delivered OH during the lunar night is imposed, under the presupposition that no evaporation, photolysis or condensation occurs at night. The model is adapted to the OHIBD observations of all 18 regions,

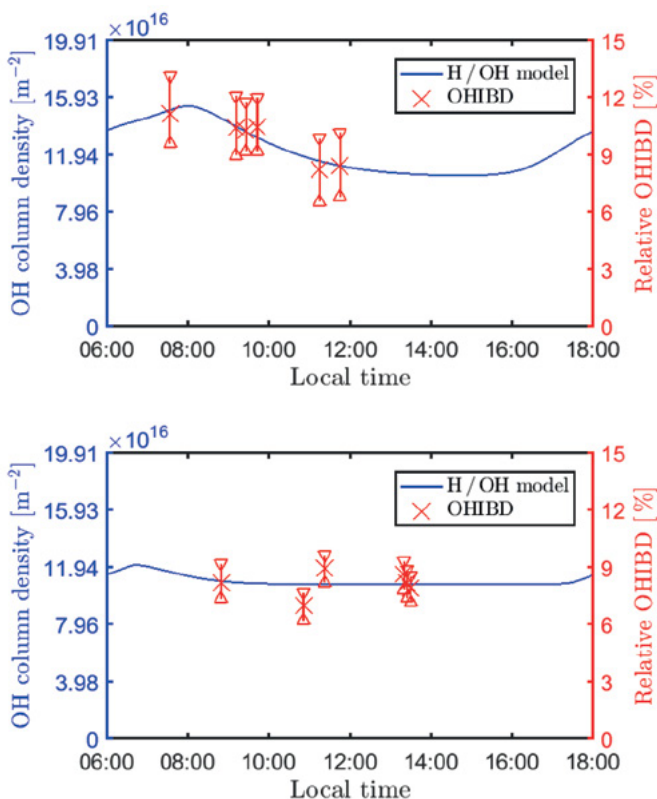


**Fig. 1.** Observed daytime-dependent OHIBD values and modeled OH column densities for two highland regions located at (172.5° E, 73° N) (top) and (125.5° E, 18° N) (bottom), respectively.

where a uniform activation energy of diffusion and a region-specific offset component are assumed. The OH activation energy was set to 0.8 eV, corresponding to the activation temperature of 9200 K of OH in SiO<sub>2</sub> stated in [14]. The model was simultaneously fitted to the 18 regions with uniform H activation energy but region-specific offset component. The other physical parameters were chosen as in [17]. The best-fit value of the H activation energy corresponds to 0.56 eV. Modeling results are shown in comparison with observational data in Fig. 1.

## SUMMARY AND CONCLUSION:

We have examined the daytime dependence of the lunar OH/H<sub>2</sub>O absorption band depth for a set of 18 lunar highland regions with available M<sup>3</sup> data acquired under 4-8 different illumination conditions. We have provided a comparison with the results of a continuity equation based model of the sources and sinks of lunar H and OH.

## ACKNOWLEDGEMENTS:

A. G. and C. W. were supported by RFBR-DFG grant WO 1800/7-1. A. A. B. and V. V. S. were supported by RFBR-DFG grant 15-52-12369.

## REFERENCES:

- [1] Sunshine, J. et al. (2009) *Science* 326, 565-568.
- [2] Pieters, C. M. et al. (2009) *Current Science* 96(4), 500-505.
- [3] Pieters, C. M. et al. (2009) *Science* 326, 568-572.
- [4] McCord, T. B. et al. (2011) *JGR* 116 (E6), E00G05, doi:10.1029/2010JE003711.
- [5] Bandfield, J. L. et al. (2017) *LPSC XLVIII*, abstract #2083.
- [6] Bandfield, J. L. et al. (2015) *Icarus* 248, 357-372.
- [7] Wöhler, C. et al. (2017) *Icarus* 285, 118-136.
- [8] Shkuratov, Y. G. et al. (2011) *PSS* 59, 1326-1371.
- [9] Grumpe, A. et al. (2017) *NVM2 Europe*, abstract #6018.
- [10] Clark, R. N. et al. (2011) *JGR* 116, E00G16, doi: 10.1029/2010JE003751.
- [11] Isaacson, P. et al. (2011) *M<sup>3</sup> Data Tutorial*, [http://pds-imaging.jpl.nasa.gov/documentation/Isaacson\\_M3\\_Workshop\\_Final.pdf](http://pds-imaging.jpl.nasa.gov/documentation/Isaacson_M3_Workshop_Final.pdf)
- [12] Bandfield, J. L. et al. (2016) *LPSC XXXVII*, abstract #1594.
- [13] Davidsson, B. J. R. et al. (2015) *Icarus* 252, 1-21.
- [14] Starukhina, L. (2001) *JGR* 106(E7), 14701-14710.
- [15] Farrell, W. M. et al. (2015) *Icarus* 255, 116-126.
- [16] Farrell, W. M. et al. (2017) *JGR* 122(1), 269-289 (2017).
- [17] Wöhler, C. et al. (2017) *Europ. Lunar Symp.* [18] Berezhnoy, A. A. et al. (2012) *ASR* 50, 1638-1646.
- [19] Mitchell, E. H. et al. (2013) *PSS* 89, 42-46.

# SOUTH POLE-AITKEN BASIN: ANORTHOSITE RICH MATERIAL AS INDICATOR FOR A COMPLEX LAYERING OF THE BASIN CRUST STRUCTURE

D. Rommel<sup>1</sup>, C. Wöhler<sup>1</sup>, A. Grumpe<sup>1</sup>, H. Hiesinger<sup>2</sup>

<sup>1</sup>Image Analysis Group, TU Dortmund, Otto-Hahn-Str. 4, D-44227 Dortmund, Germany ([daniela.rommel@tu-dortmund.de](mailto:daniela.rommel@tu-dortmund.de))

<sup>2</sup>Institut fuer Planetologie, Westfaelische Wilhelms-Universitaet Muenster, D-48149 Muenster, Germany

## KEYWORDS:

Alder, Anorthosite, Antoniadi, Dryden, Poincaré X, South Pole-Aitken Basin

## INTRODUCTION:

The South Pole-Aitken basin (SPA) with its diameter of about 2500 km [1, 2] was formed during the pre-Nectarian period [1]. Due to its early formation and large size, the basin has been subject to further impacts, and on the basis of the ejected material conclusions can be drawn about the internal composition of the lunar crust. In this study, we used petrological maps of the four craters Alder, Antoniadi, Dryden and Poincaré X located inside SPA, for the discussion of the interior structure of the SPA. They revealing exposed anorthosite rich material inside their crater rims or crests. The main investigation of our study explored a correlation between: (a) crater, which indicate anorthosite rich material inside of the crater rim/crest to abutting craters (Antoniadi), (b) crater, which indicate anorthosite rich material inside of the crater rim/crest, lying inside of the floor of a large crater (Dryden and Poincaré X) and (c) craters, which indicate anorthosite rich material inside of the crater rim/crest, without neighbouring craters of similar size (Alder). We try to reconstruct the layering of the crust of the SPA under using of existing crater profiles [3, 4]

## METHODS AND DATASET:

The used hyperspectral imagery of the near-global Moon Mineralogy Mapper (M<sup>3</sup>) [5] mosaic can divided into the steps of accurate georeferencing, thermal emission removal, topographic and photometric correction performed using the framework described in [6]. Elemental abundance maps and petrological maps were constructed by applying the techniques of [7]. In the petrographic maps, the red, green and blue channel corresponds to basalt, Mg-rich rock and ferroan anorthosite, respectively.

## RESULTS AND DISCUSSION:

The craters Alder and Antoniadi are located at about 400 km distance from the SPA centre, i.e. approximately on the rim of the SPA transient cavity with its radius of 410 km as given in [8]. Hence, our observations indicate anorthositic subsurface deposits also relatively close to the SPA centre, indicating a complex layering of the crust. This finding is unexpected, given the model of [8].

The crater Alder (82 km diameter, centred at 49° S, 178° W) is located near the centre of the SPA. It exhibits a large ferroan anorthosite patch in its southern part. This structure looks like a large debris flow of about 20 km extent and appears to superpose the inner and outer sides of the crater rim. A possible source of the anorthositic material is an outcrop on top of the crater rim, and there is evidence that material has been excavated from an anorthosite rich layer at great depth in the crust (float structure). The central peak and the eastern part of the crater rim show a high Mg-rich rock content. The crater floor and the surrounding regions mainly show a basaltic signature.

The large crater Antoniadi (138 km diameter, centred at 69°S, 173°W) is situated in the southern part of SPA. It has a flat floor covered by basaltic lava (see e.g. [9]). A high Mg-rich rock content is apparent for the central peak and the inner peak ring. In the western part, the rim of Antoniadi intersects the rim of Minnaert and the crater walls on both sides display patches of ferroan anorthosite material, which appears to have slid down the crater wall onto the floor. Our investigation suggests that the crater Minnaert may already have lifted up anorthosite-rich to shallow depth below the surface, and the impact of Antoniadi excavated parts of this layer. In the eastern part of Antoniadi, a similar

overlap with the crater Numerov can be observed, where the relatively deep crater rim exhibits small deposits anorthositic material. Both occurrences on the crater rim indicate that consecutive impacts may have lifted up anorthositic material.

The crater Dryden (54 km diameter, centred at 33 S, 156°W) is located in the eastern part of SPA at about 700 km distance from the basin centre between the Apollo basin rim and peak ring. Its central peak and crater rim show a significant Mg-rich rock content. The floor is partially covered by basaltic material but still shows a signature of Mg-rich rock. Due to the fact that the crater rim of Dryden intersects the peak-ring structure of the Apollo basin [10], parts of the northeastern crater wall reveal a deposit with an anorthosite signature, like the surrounding material of the peak ring structure of the Apollo basin. The deposit appears to superpose the inner side of the rim of Dryden onto its floor like a flow, and looks like well-defined continuous Apollo-peak-ring material.

The crater Poincaré X (21 km diameter, centred at 53°S, 161°E) and an unnamed crater are located in the western part of the SPA at about 1000 km distance from the basin centre between the inner ring and the rim of the Poincaré basin. The floor is for the most part covered by a signature of Mg-rich rock material but still in the southwestern part of the crater wall reveals a deposit with an anorthosite signature, which looks like a flow from the southern unnamed crater into the crater floor of Poincaré X. The striking distance to the South Pole-Aitken basin rim and the surrounding highland material may have led to the excavation of an anorthosite subsurface deposit that probably resulted from crustal overturn and mixture with the highland material as a consequence of the Poincaré peak-ring basin impact.

## SUMMARY AND CONCLUSION:

We have performed a petrological mapping of the craters Alder, Antoniadi, Dryden and Poincaré X located inside SPA, revealing anorthosite-rich deposits associated with them. Petrologic mapping of the craters Antoniadi and Alder indicates that even at distances of less than 400 km to the SPA centre anorthositic material can be found. A possible mechanism to explain these occurrences is the uplift by subsequent impacts of anorthositic crustal material previously buried during formation of the the SPA basin. The anorthositic material at the northwestern rim of the crater Dryden is probably due to mass-wasting of material from the western peak ring of the Apollo basin, which contains a significant fraction of anorthosite, into the crater after its formation. This anorthositic material was presumably excavated from shallow depth due to the proximity of the Apollo basin to the northeastern SPA rim. Similarly, the anorthositic material extending from the southwestern rim of the crater Poincaré X has probably been excavated from shallow depth, due to the location of the Poincaré basin close to the western SPA rim, and flowed down the southwestern rim of Poincaré X as indicated by the presence of elongated flow structures. All in all, our observations indicate a highly complex layering of the crust at the examined crater locations.

## REFERENCES:

- [1] Petro, N.E. and Pieters, M. C. Surviving the heavy bombardment: Ancient material at the surface of South Pole-Aitken Basin // *JGR*. 2004. V. 109. No. E6. P. E06004.
- [2] Kim, K.J. et al. The South Pole-Aitken basin region, Moon: GIS-based geologic investigation using Kaguya elemental information // *ASR*. 2012. No. 50. P. 1629-1637.
- [3] Morgan et al., The formation of peak rings in large impact craters // *Science*. 2016. V. 354. P. 878-882.
- [4] Melosh and Ivanov, Impact crater collapse // *Ann. Rev. Earth Planet. Sci.*. 1999. V. 27. P. 385-415.
- [5] Pieters, C.M. et al., The Moon Mineralogy Mapper (M3) on Chandrayaan-1 // *Current Science*. 2009. V. 96. No. 4. P. 500-505.
- [6] Wöhler et al., Temperature Regime and Water/Hydroxyl Behavior in the Crater Boguslawsky on the Moon // *Icarus*. 2017. V. 285. P. 118-136
- [7] Wöhler, C. et al. Integrated topographic, photometric and spectral analysis of the lunar surface: Application to impact melt flows and ponds // *Icarus*. 2014. V. 235. P. 86-122.
- [8] Hurwitz, D. M. and Kring, D. A. Differentiation of the South Pole-Aitken basin impact melt sheet: Implications for lunar exploration // *JGR*. 2014. V. 119. P. 1110-1133.
- [9] Sruthi, U. and Senthil Kumar, P. Volcanism on farside of the Moon: New evidence from Antoniadi in South Pole Aitken basin // *Icarus*. 2014. V. 242. P. 249-268.
- [10] Baker et al., The transition from complex craters to multi-ring basins on the Moon: Quantitative geometric properties from Lunar Reconnaissance Orbiter Lunar Orbiter Laser Altimeter (LOLA) data // *JGR*. 2012. V. 117. P. E00H16.

# WAVE PHENOMENA IN THE MOON ENVIRONMENT

M. Buchenkova<sup>1,2</sup>, A. Skalsky<sup>1</sup>, A. Sadovski<sup>1</sup>

<sup>1</sup>Space Research Institute of the Russian Academy of Sciences,  
Profsoyuznaya Str 84/32, Moscow, 117997, Russian Federation,  
mariya.buchenkova@phystech.edu.

<sup>2</sup>Moscow Institute of Physics and Technology (State University),  
9 Institutskiy per., Dolgoprudny, Moscow Region, 141701, Russian  
Federation.

## KEYWORDS:

Electrostatic solitary waves, ULF waves, magnetic anomalies, Moon.

The paper is aimed to review actual observations and different mechanisms of wave and magnetic disturbances generation in plasma environment around the Moon: in solar wind closely to the Moon, over the magnetic field anomalies at its surface, in the lunar wake and around its boundaries. The generating mechanisms, propagation and other characteristics of waves are presented.

Particular attention is pointed on Electrostatic Solitary Waves (ESWs), monochromatic whistlers, large-amplitude monochromatic ULF waves and non-monochromatic whistler waves.

## REFERENCES:

- [1] J. S. Halekas, D. A. Brain, D. L. Mitchell, R. P. Lin, and L. Harrison, "On the occurrence of magnetic enhancements caused by solar wind interaction with lunar crustal fields", *Geophysical research letters*, 2006.
- [2] K. Shin, H. Kojima, H. Matsumoto, and T. Mukai, "Characteristics of electrostatic solitary waves in the Earth's foreshock region: Geotail observations", *Journal of geophysical research*, 2008.
- [3] X.H. Deng, R.X. Tang, H. Matsumoto, J.S. Pickett, A.N. Fazakerley, H. Kojima, W. Baumjohann, A. Coates, R. Nakamura, D.A. Gurnett, Z.X. Liu, "Observations of electrostatic solitary waves associated with reconnection by Geotail and Cluster", *Advances in space research*, 2006.

# THE MOON OBSERVED IN ENERGETIC NEUTRAL ATOMS: REVIEW OF THE SCIENTIFIC FINDINGS FROM SARA/CENA ON BOARD CHANDRAYAAN-1

A. Vorburger<sup>1</sup>, P. Wurz<sup>1</sup>, S. Barabash<sup>2</sup>, M. Wieser<sup>2</sup>, Y. Futaana<sup>2</sup>, A. Bhardwaj<sup>3</sup>, M. B. Dhanya<sup>3</sup>, K. Asamura<sup>4</sup>

<sup>1</sup>University of Bern, Space Research and Planetary Sciences, Bern, Switzerland (vorburger@space.unibe.ch);

<sup>2</sup>Swedish Institute of Space Physics, Kiruna, Sweden

<sup>3</sup>Space physics Laboratory, Vikram Sarabhai Space Center, Trivandrum, India

<sup>4</sup>Institute of Space and Astronautical Science, Sagamihara, Japan

## KEYWORDS:

Moon, energetic neutral atoms, solarwind – moon interaction, backscattering, sputtering, Chandrayaan-1, SARA/CENA

## INTRODUCTION:

The Moon, not being protected by a global magnetic field or an atmosphere, is under constant bombardment by solar wind ions. Until a few years ago, it was commonly assumed that the impinging solar wind ions are almost completely absorbed by the lunar surface (< 1% reflection; see for example [1, 2]). Recent observations by IBEX and the Sub-keV Atom Reflecting Analyzer (SARA) onboard Chandrayaan-1 invalidated this assumption, though, showing that lunar surface very efficiently reflects impinging solar wind protons as Energetic Neutral Atoms (ENAs), with reflection ratios typically between 10% and 20% (e.g. [3, 4]). With such high ENA fluxes coming from the lunar surface, ENA monitoring offers a powerful method for investigating the solar wind interaction with the lunar surface. Herein we present a review of all scientific findings from SARA's ENA sensor.

## INSTRUMENTATION:

We report here on scientific measurements based on measurements conducted by the Chandrayaan-1 Energetic Neutrals Analyzer (CENA) [5], which is a part of the SARA instrument [6] onboard Chandrayaan-1 [7]. CENA measured ENAs originating from the lunar surface within the energy range 10 eV to 3.3 keV and an energy resolution of  $\Delta E/E \sim 50\%$ . CENA was capable of mass discrimination, being able to distinguish H and O from heavier elements. CENA's field of view consisted of seven angular sectors (five of which were purely surface pointing), with surface-projected footprints of approximately 100 – 400 km  $\times$  10 – 20 km, depending on the sector number and spacecraft altitude.

## RESULTS & DISCUSSION:

Figure 1 presents an overview of the most significant scientific findings based on measurements conducted by CENA. Panel a) shows that there is a substantial flux of reflected, neutralized hydrogen coming from the lunar surface. The plot shows a clear cosine-correlation with solar zenith angle, as is expected for pure geometrical reasons. A global analysis showed that on average 16% of the impinging solar wind protons are reflected as neutral hydrogen atoms, with a standard deviation of 5%. The ENA reflection ratio is rather featureless over the lunar surface, showing only strong variations at local crustal magnetic fields due to the interaction of the plasma with so-called mini-magnetospheres. An example of such a mini-magnetosphere ENA image is shown in Panel b): There is a clear void of ENAs coming from the centre of the magnetic anomaly, where the surface is shielded from the impinging solar wind ions, whereas there is an enhanced ring surrounding the void, denoting the region where the ions have been deflected to.

CENA measurements were also used to identify a large, positive electric potential associated with the magnetic anomaly. This electric potential was expected based on charge separation in the impinging plasma, where ions can penetrate further into the mini-magnetosphere region than electrons, which are deflected by the magnetic field. The charge separation produces an outward-facing electric field. The ENA energy spectrum in general resembles a Maxwell Boltz-



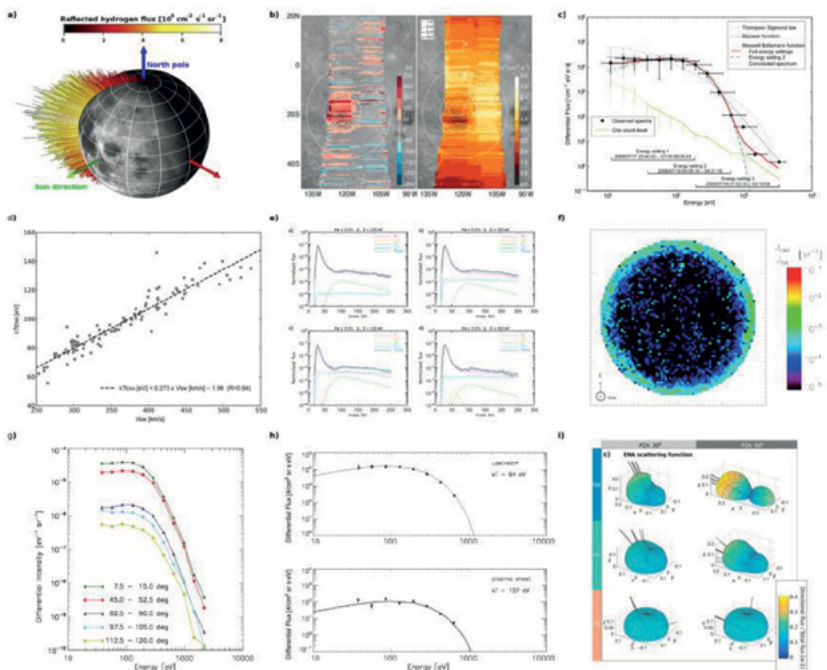


**Fig. 1.** Scientific results based on measurements conducted by CENA. Panel a): Reflected neutral hydrogen flux measured during one orbit of Chandrayaan-1. Panel b): Electric potential and reflection ratio imaging of a mini-magnetosphere above a lunar magnetic anomaly. Panel c): Energy spectrum of measured ENAs and best fitting Maxwell Boltzmann Function. Panel d): Correlation between ENA characteristic energy and solar wind velocity. Panel e): Mass spectra recorded during flight containing neutral hydrogen, oxygen, and helium. Panel f): Lunar nightside energy spectrum exhibiting a  $\sim 20^\circ$  broad ring parallel to the terminator. Panel g): Energy spectrum of dayside and nightside ENAs showing the similarity of the two. Panel h): Energy spectrum of ENAs measured in the solar wind and in the terrestrial plasma sheet. Panel i): Scattering function of ENAs measured upstream, in the magnetosheath, and in the terrestrial plasma sheet.

mann distribution (see Panel c), a fact still not completely understood, because the energy loss observed does not agree with the ENAs having been thermalized. An additional mystery is the correlation between the characteristic energy and the solar wind velocity, and not the solar wind energy, a fact hinting at the backscattering processes at the surface being controlled by the momentum of the impinging particle velocity rather than its energy (see Panel d).

Whereas all these findings were based on energetic neutral hydrogen measurements, other mass groups were also observable by CENA. CENA presented first direct measurements of sputtered lunar oxygen, with surface densities of  $\sim 1.3 \cdot 10^7 \text{ m}^{-3}$  and column densities of  $\sim 1.6 \cdot 10^{13} \text{ m}^{-2}$ . In addition, backscattered helium was detected in the CENA data set (see Panel e), but due to uncertainties in the instrument's geometric factor, no surface or column densities could be derived.

Nightside ENA measurements showed that a significant fraction of the solar wind plasma is able to reach much further into the lunar nightside wake than the proton temperature would allow: CENA measured a  $30^\circ$  broad ENA ring parallel to the terminator, with a flux of  $\sim 1.5\%$  of the dayside flux (see Panel f). Energy analysis showed, that whereas the nightside ENAs' energy spectrum clearly resembles the dayside backscattered ENAs' energy spectrum, their characteristic energy is slightly lower (by about 4 eV), hinting at the plasma having been decelerated in the lunar wake (see Panel g).

CENA measurements in the terrestrial plasma sheet (Panel h) revealed that the characteristic energy and the backscatter ratio in Earth's plasma sheet is similar to the upstream solar wind case. In contrast to the upstream observations, though, no ENA void was observed over large and strong magnetized lunar surface regions. Analyses suggest that the magnetic shielding of the lunar surface in the plasma sheet is less effective in the terrestrial plasma

sheet than in the solar wind, probably due to the broad velocity distributions of the plasma sheet ions.

A final analysis included lunar ENAs recorded when the Moon was located inside the terrestrial magnetosheath (see Panel i). As in the upstream solar wind and in the terrestrial plasma sheet case, on average 10% to 20% of the impinging protons are reflected back as neutral hydrogen atoms in Earth's magnetosheath. Similar to the upstream solar wind case, and contrary to the terrestrial plasma sheet case, clear signatures of plasma shielding by magnetic anomalies were observed. Overall, the scattering process seems unchanged in the Earth's magnetosheath, with the only exception being that in the terrestrial magnetosheath the energy spectrum becomes broader and less peaked, probably due to the increase in plasma temperature.

Overall, CENA was exceptionally successful. The instrument not only achieved all its set science goals but also revealed several hitherto unknown and unexpected properties of the solar wind interaction with the lunar surface.

## REFERENCES:

- [1] Crider D. H., Vondrak R. R. Hydrogen Migration to the Lunar Poles by Solar Wind Bombardment of the Moon // *Advance Space Research*. 2002. V. 30. No. 8. P. 1869-1874.
- [2] Feldman W. C., Lawrence D. J., Elphic R. C., Barraclough B. L., Maurice S., Genety I., Binder A. B. Polar Hydrogen Deposits on the Moon // *Journal of Geophysical Research*. 2000. V. 105. No. E2. P. 4175-4195.
- [3] McComas D. J., Allegrini F., Bochsler P., Frisch P., Funsten H. O., Gruntman M., Janzen P. H., Kucharek H., Möbius E., Reisenfeld D. B., Schwadron N. A. Lunar Backscatter and Neutralization of the Solar Wind: First Observations of Neutral Atoms from the Moon // *Geophysical Research Letters*. 2009. V. 36. No. L12104.
- [4] Wieser M., Barabash S., Futaana Y., Holmström M., Bhardwaj A., Sridharan R., Dhanya M. B., Wurz P., Schaufelberger A., Asamura K. Extremely High Reflection of Solar Wind Protons as Neutral Hydrogen Atoms from Regolith in Space // *Planetary and Space Science*. 2009. V. 57. P. 2132-2134.
- [5] Kazama Y., Barabash S., Wieser M., Asamura K., Wurz P. Development of an LENA Instrument for Planetary Missions by Numerical Simulations // *Planetary and Space Science*. 2007. V. 55. P. 1518-1529.
- [6] Bhardwaj A., Barabash S., Futaana Y., Kazama Y., Asamura K., McCann D., Sridharan R., Holmström M., Wurz P., Lundin R. Low Energy Neutral Atom Imaging on the Moon with the SARA instrument aboard Chandrayaan-1 Mission // *Journal of Earth System Science*. 2005. V. 114. No. 6. P. 749-760.
- [7] Goswami J. N., Annadurai M. Chandrayaan-1: India's First Planetary Science Mission to the Moon // *Current Science*. 2009. V. 96. No. 8. P. 486-491.

# POTENTIALLY INTERESTING LANDING SITES AROUND THE SOUTH POLE OF THE MOON

**A.B. Sanin<sup>1</sup>, I.G. Mitrofanov<sup>1</sup>, M.V. Djachkova<sup>1</sup>**

*<sup>1</sup>Space Research Institute of the Russian Academy of Sciences (IKI), 84/32 Profsoyuznaya Str, Moscow, Russia, 117997*

## **KEYWORDS:**

Moon, Luna-25, landing site.

## **INTRODUCTION:**

The landing site selection method primarily developed by our team for Luna-25 mission allowed us to identify several scientifically interesting and safe for landing locations in the South Polar Region of the Moon. These locations can be considered as possible landing sites for future lunar missions. Here we present three most promising sites and discuss their properties.

# DIVERSITY OF MATERIALS AT LUNA 24 SITE FROM MOON MINERALOGY MAPPER (M<sup>3</sup>)

C.M. Pieters<sup>1</sup>, A.T. Basilevsky<sup>2</sup>, D. Dhingra<sup>3</sup>, J.W. Head<sup>1</sup>

<sup>1</sup>Dept. Earth, Environmental, & Planetary Sciences, Brown Univ. Providence, RI (Carle\_Pieters@brown.edu);

<sup>2</sup>Vernadsky Institute, Russian Academy of Sciences, Moscow 119991, Russia;

<sup>3</sup>Dept. Earth Sciences, Indian Institute of Tech. Kanpur (IIT-K), Kalyanpur, Kanpur, India 208016

## KEYWORDS:

Luna 24, Moon Mineralogy Mapper, M<sup>3</sup>, lunar basalts,

## INTRODUCTION:

Imaging spectrometer data acquired with the Moon Mineralogy Mapper (M<sup>3</sup>) onboard the Chandrayaan-1 spacecraft enables the mineralogy of the lunar surface to be evaluated in geologic context [1]. One of the few M<sup>3</sup> scenes of data acquired at optimal full resolution (Target) [2] includes the Luna 24 site in Mare Crisium shown in Figure 1. We have evaluated these high-resolution data in order to identify the principal types of basalt in the region and possible effects of secondary craters from Giordano Bruno [3].

## SUMMARY:

All Mare Crisium lunar basalts exhibit two diagnostic absorption bands centered near 1  $\mu\text{m}$  and 2  $\mu\text{m}$  in the near-infrared due to Fe,Ca-pyroxene. As shown in Figure 2, the properties of these absorptions can be evaluated by estimating and removing a sloped but featureless continuum. A measure of the relative strength of these absorptions is captured by integrating across the absorption band after continuum removal. Well-developed, weathered soils have weak absorptions and basalts freshly exposed by a crater have strong absorptions as shown in Fig. 2.

The M<sup>3</sup> color composite of Figure 1 captures three key properties displayed as RGB in a spatial context: the integrated strength of the pyroxene absorption at 1  $\mu\text{m}$ , the integrated strength of the pyroxene absorption at 2  $\mu\text{m}$ , and the overall reflectance (brightness) of surface materials. Well-developed basalt soils appear dark and colorless in this figure. In contrast, basalts exposed by craters appear bright and often colored, depending on the relative strength of the pyroxene absorptions at that location.

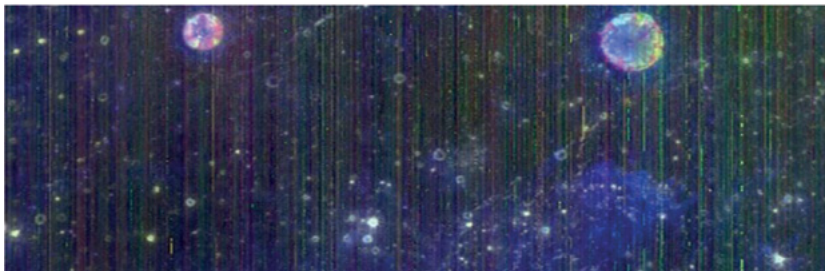
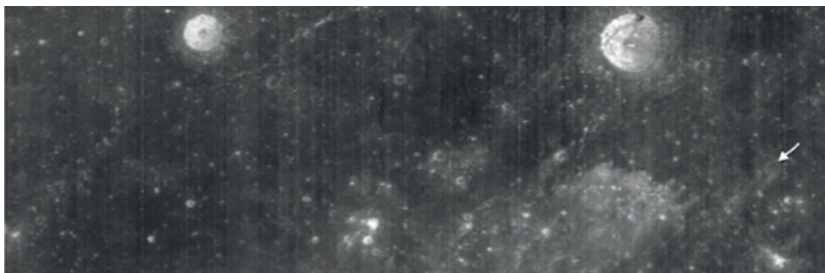


**Fig. 1.** M<sup>3</sup> images of the Mare Crisium region that includes the Luna 24 area (arrow). The two large craters near the image top are Picard Y (left; 4 km) and Fahrenheit (right; 6 km). **Top:** Reflectance at 1600 nm; **Bottom:** Color composite [R=integrated 1  $\mu\text{m}$  a bsorption; G=integrated 2  $\mu\text{m}$  absorption; B=Reflectance]

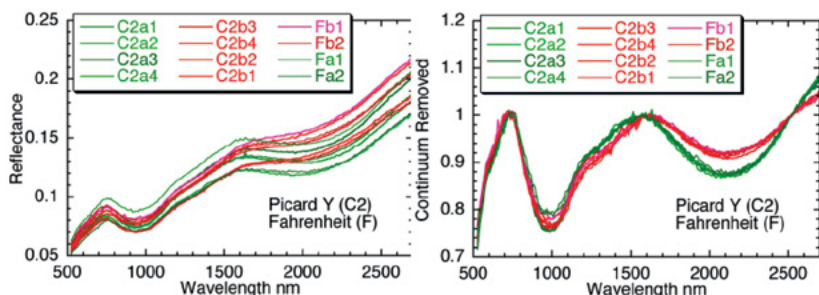


**Fig. 2.**  $M^3$  reflectance spectra for several small areas (3x3 pixel average) within craters Picard Y and Fahrenheit, illustrating two different types of basalt (a, b) exposed by these craters. Shown on the right are the same spectra after continuum removal. All spectra exhibit the 1 and 2  $\mu\text{m}$  absorption bands diagnostic of Fe,Ca-pyroxene. Spectra drawn in red (and appear red in the  $M^3$  color composite) exhibit relatively weak 2  $\mu\text{m}$  absorption bands but strong and broad 1  $\mu\text{m}$  absorptions. Since the diagnostic properties of olivine include a broad multicomponent 1  $\mu\text{m}$  absorption with no 2  $\mu\text{m}$  absorption, these combined properties suggest olivine has a higher abundance in this basalt lithology (b, red).

Two principal results from  $M^3$  are relevant to evaluating Luna 24 samples:

- 1) The combined results from Figures 1 and 2 indicate that two distinct basalt types occur in this part of Mare Crisium, one of which is relatively olivine-rich (red in Figs 1&2). Although this basalt type does not dominate at Fahrenheit, outcrops do exist and components might be expected in the Luna 24 core.
- 2) The abundant Giordano Bruno secondary craters [3] have excavated local basalts and exhibit freshly exposed pyroxene absorptions. However, these craters are often embedded in a diffuse field of relatively bright soils (dark blue in Fig. 2 color composite) and exhibit no enhanced pyroxene absorption. We interpret this to be a small bright and featureless foreign component that contaminates the well-developed local basaltic soil without significantly stirring the regolith. This is similar to Copernicus 'compositional' rays [4], and likely represents minor fine grained feldspathic debris from Giordano Bruno.

## REFERENCES:

- [1] Pieters, C. M. et al., *Current Science* 96, NO. 4, 2009.
- [2] Boardman, J.W. et al. *JGR* 116, 2011. doi:10.1029/2010JE003730
- [3] Basilevsky, A. T. and J. W. Head, *Planet. & Sp. Sci.*, 2012. 302-309.
- [4] Pieters et al., *JGR* 90, 1985. 12393-12413; Hawke et al., *Icarus* 170, 2004. 1-16.

# CRATERS FEATURES OF THE MOON AND MERCURY SOUTHERN POLAR REGIONS

A.Yu. Zharkova<sup>1,2</sup>, N.A. Kozlova<sup>2</sup>, Zh.F. Rodionova<sup>1</sup>, E.A. Feoktistova<sup>1</sup>, V.V. Shevchenko<sup>1</sup>

<sup>1</sup>Lomonosov Moscow State University Sternberg Astronomical Institute  
Universitetskiiy pr.13, Moscow, Russia, 11923. jeanna@sai.msu.ru

<sup>2</sup>MExLab, Moscow State University of Geodesy and Cartography,  
Gorokhovskiy per.4, Moscow, Russia, 105064.  
a\_zharkova@miigaik.ru; n\_kozlova@miigaik.ru

## KEYWORDS:

Planetary science, Mercury, the Moon, craters, morphometric analysis.

## INTRODUCTION:

In this study, we explored about 1130 Lunar craters and 835 craters of Mercury; they are located in latitude range from 60° to 90° S and their diameters are larger than 10 km. We used craters' profiles to perform the comparative morphometric analysis of the southern subpolar regions.

## MAIN STUDY:

The profiles for observed craters were drawn with the special ArcGIS tool [1]. Four profiles were automatically created on the each crater. The length of profiles deliberately exceeded the diameters of craters. The profiles covered external rims; profiles' length allowed us to take possible inaccuracies in the determination of craters initial diameter into account, and avoid them (Fig.1).

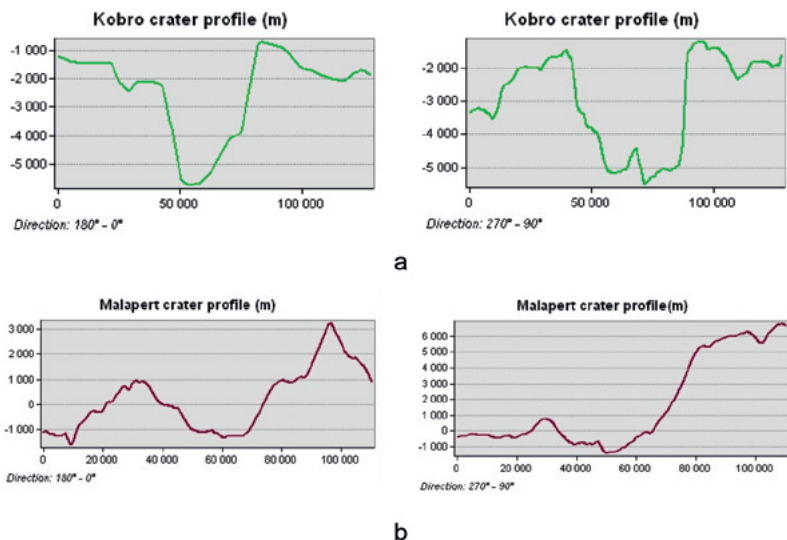


**Fig. 1** ab. a) Kobro crater profiles, diameter: 54 km, center latitude: -82.16°, center longitude: 278.78°; b) Malapert crater profiles, diameter: 72 km, center latitude: -85.00°, center longitude: 11.40°

In order to create the profiles we used several DEMs to acquire the data about heights on the Moon and Mercury:

1. Global Mercury DEM with the resolution 665 m/pixel, obtained with the photogrammetric processing of the MESSENGER data [2].
2. Global DEM of the Moon with the resolution 118 m/pixel, obtained with the LRO data (WAC\_GLD100\_P900S0000\_256P.IMG) [3].

Also we used various craters catalogs. For Mercury:

1. The vector catalog provided by the Brown University (USA) [4], which attributive table contains the coordinates for the central points of each object, diameter, craters area, and the objects names in English.

2. The morphological catalog of Mercury craters compiled by the SAI [5]. This catalog contains craters' coordinates and diameters, like the previous one; but also, it provides the information about the craters' preservation degree covers different features, as terraces, peaks, ridges, fissures, secondary craters chains, and ray systems.

Besides, we applied the SAI morphological catalog of the Moon craters to explore their features as well. [6]. This catalog provides us with the coordinates which were refined by the modern global mosaics of the Lunar Reconnaissance Orbiter (LRO).

The new data including higher resolution images of the celestial bodies allows us to update the morphological catalogs and use the most recent data for further studies. The referred papers [7,8] revealed: the depths of the Mercury's impact craters (their diameters are ranging from 1 to 100 km) agreed with the depth measures from the previous studies in almost all explored cases. The exception was discovered while measuring the large complex craters depth. In that particular diameter, they appeared to be shallower than the Mariner 10 data have showed.

## CONCLUSION:

We investigated the craters with diameters larger than 10 km in the Moon and Mercury southern subpolar regions. It's occurred that Mercury has less first-class craters (the newest ones) than the Moon: Comparing to 19 percent of such craters that was observed on the Moon, on Mercury surface we discovered as little as 2 percent of their kind (Table 1).

**Table 1.** Percentage of craters by classes of preservation degree

Class of preservation degree	For Mercury (%)	For The Moon (%)
1	2	19
2	18	24,1
3	44	27,1
4	30	23,7
5	6	6,1

## REFERENCES:

- [1] Kokhanov A.A., Bystrov A.Y., Kreslavsky M.A., Matveev E.V., Karachevtseva I.P. Automation of morphometric measurements for planetary surface analysis and cartography // In Int. Arch. Photogramm. Remote Sens. Spatial Inf. Sci., XLI-B4, 2016. P.431-433, doi: 10.5194/isprs-archives-XLI-B4-431-2016.
- [2] [https://pdsimage2.wr.usgs.gov/data/mess-h-mdis-5-dem-elevation-v1.0/MESSDEM\\_1001/DEM/](https://pdsimage2.wr.usgs.gov/data/mess-h-mdis-5-dem-elevation-v1.0/MESSDEM_1001/DEM/)
- [3] [http://wms.lroc.asu.edu/lroc/view\\_rdr/WAC\\_GLD100](http://wms.lroc.asu.edu/lroc/view_rdr/WAC_GLD100)
- [4] [http://www.planetary.brown.edu/html\\_pages/mercury\\_craters.htm](http://www.planetary.brown.edu/html_pages/mercury_craters.htm)
- [5] Kozlova E.A., Sitnikov B.D., Rodionova J.F., Shevchenko V.V. Analysis of Mercurian craters by means of cartographic methods. [http://icaci.org/files/documents/ICC\\_proceedings/ICC2005/html/pdf/oral/TEMA23/Session%202/EKATERINA%20KOZLOVA.pdf](http://icaci.org/files/documents/ICC_proceedings/ICC2005/html/pdf/oral/TEMA23/Session%202/EKATERINA%20KOZLOVA.pdf)
- [6] Rodionova Zh.F., Karlov A.A., Skobeleva T.P. et al. Ed. by Shevchenko. Morphological catalogue of the craters of the Moon. Issued by Moscow State University., 1987. 174 p.
- [7] Susorney H.C.M., Barnouin O.S., Ernst C.M., Johnson C.L. Morphometry of impact craters on Mercury from MESSENGER altimetry and imaging // *Icarus* 271, 2016. P. 180–193.
- [8] Pike R.J. Geomorphology of impact craters on Mercury. In: Vilas, F., Chapman, C.R., Matthews, M.S. (Eds.) *Mercury*. University of Arizona Press, Tucson, Ariz, 1988. P. 165–273.

# NEW EVIDENCE FOR SURFACE ICE IN MICRO-COLD TRAPS AND IN THREE LARGE CRATERS AT THE NORTH POLAR REGION OF MERCURY: IMPLICATIONS FOR LUNAR EXPLORATION

Ariel N. Deutsch<sup>1</sup>, James W. Head<sup>1</sup>, Gregory A. Neumann<sup>2</sup>

<sup>1</sup>Department of Earth, Environmental and Planetary Sciences, Brown University, Providence RI 02912, USA (ariel\_deutsch@brown.edu);

<sup>2</sup>NASA Goddard Space Flight Center, Greenbelt, MD 20771, USA

## KEYWORDS:

Water ice; surface reflectance; radar; Mercury; Moon.

## INTRODUCTION:

Both Earth-based and spacecraft observations provide evidence that Mercury hosts waterice within its permanently shadowed regions (PSRs) near the poles. Earth-based radar images of Mercury first revealed highly reflective materials that are consistent with water ice [1–6]. These “radar-bright” materials collocate with PSRs derived from images and topography [7–9]. Thermal models derived from topography indicate that PSRs are stable environments for near-surface and sometimes surface water ice on geologic timescales [10]. Furthermore, enhanced concentrations of hydrogen have been detected in the north polar region [11].

## OBJECTIVES AND METHODS:

The Mercury Laser Altimeter (MLA) measured surface reflectance,  $r_s$ , at 1064 nm [12]. On Mercury, most water-ice deposits have anomalously low  $r_s$  values indicative of an insulating layer beneath which ice is buried [12]. Previous detections of surface water ice (without an insulating layer) were limited to seven craters [12]. Here we map  $r_s$  and density of energy returns in Chesterton, Tolkien, and Trygvdóttir craters. These three permanently shadowed craters host extensive radar-bright deposits indicative of water ice [6]. However, MESSENGER only acquired limited off-nadir observations of these craters due to their proximity to the pole, and they were never identified as hosting water-ice deposits. The nominally calibrated  $r_s$  measurements of these craters did not show distinctive regions of  $r_s > 0.3$ . The greater density of returns observed within the PSRs prompted a reexamination of the calibration to account for a downward bias due to highly oblique geometry [13]. Utilizing the complete orbital dataset and empirically re-calibrated data, we calculate the mean  $r_s$  within the craters and outside the craters, and discuss the implications for surface water-ice deposits hosted by permanently shadowed craters close to the north pole of Mercury.

Additionally, we investigate the presence of possible micro-cold traps, or small-scale exposures of ice. Given that surface reflectance increases northward of  $\sim 85^\circ\text{N}$  [13] and that micro-cold traps may be ubiquitous at latitudes northward of  $\sim 75^\circ\text{N}$  [14], we are interested in the detection of exposures of water-ice deposits present at the surface of Mercury at these small spatial scales at the footprint of MESSENGER instruments. Following the Earth-based identification of high radar-backscatter deposits in polar craters, the only detections of exposed water ice have been in large, permanently shadowed craters: Prokofiev crater, as well as limited off-nadir MLA measurements of A, C, D2, Kandinsky, i5, and Y craters [12] (For craters that do not have formal IAU names, we adopt informal nomenclature from published maps). Here we investigate the presence of specific micro-cold traps by searching for clustered MLA-measured  $r_s$  enhancements at 1064-nm wavelength that can be observed at the resolution of MLA footprints. We compare the distribution of  $r_s$  enhancements to that of Earth-based radar data [6], areas of permanent shadow [9], and biannual maximum surface temperatures,  $T_{\text{max}} < 100\text{ K}$  [10] to discuss the implications for reservoirs of long-lived water ice exposed at the surface of Mercury inside micro-cold traps.

## RESULTS:

There is a bimodal distribution of surface reflectance on Mercury in which anomalously low-reflectance deposits correlate with lag deposits insulating water ice and anomalously high-reflectance deposits correlate with exposed water ice. The overall surface reflectance is observed to sharply increase from



$\sim 85^\circ\text{N}$  to the pole, even when the presence of large, permanently shadowed craters are removed, suggesting that micro-cold traps may harbor substantial water ice on the surface of Mercury [13]. Here we investigated the possibility that micro-cold traps could be resolved at the spatial scale of the MLA footprint by searching for clusters of  $r_s$  enhancements. We identified four micro-cold traps that are between 2 and 5 km in diameter (in craters n5, o7, i7, and to the north of e5) on the basis of  $r_s$  values  $> 0.3$  (**Fig. 1**). These clusters collocated with PSRs and  $T_{\text{max}} < 100$  K.

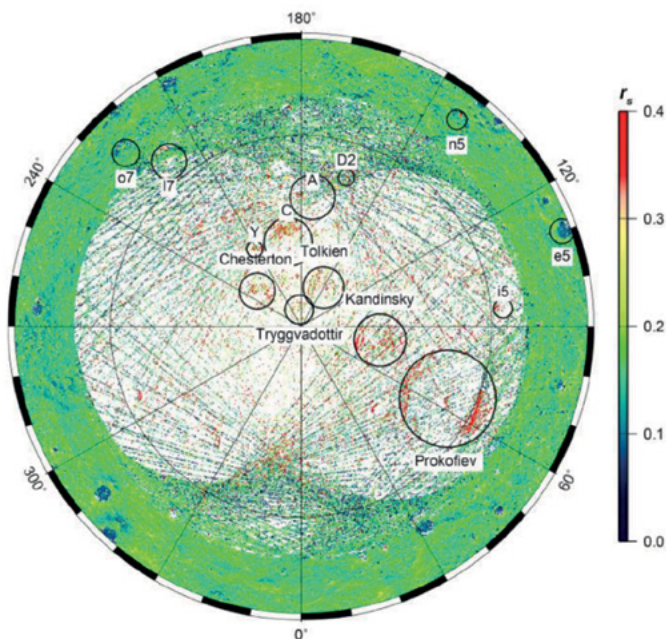


**Fig. 1.** MLA-derived surface reflectance,  $r_s$ , at 1064 nm from  $82.5^\circ\text{N}$  to  $90^\circ\text{N}$ , modified from [13]. Large craters (Prokofiev, Chesterton, Tolkien, Tryggvadóttir, Kandinsky, and C) that are identified as hosting exposed water ice are labeled. Micro-cold traps (n5, o7, e5, and i7) that are identified as hosting exposed water ice are labeled. Polar stereographic projection.

We also mapped  $r_s$  values for Chesterton, Tolkien, and Tryggvadóttir (**Fig. 1**). Each crater has high radar cross sections indicative of water-ice deposits [6], and the derived  $r_s$  value for each crater exceeds 0.3, suggesting that water ice is exposed at the surface. The proximity of these three craters to the pole creates a hyper-stable thermal environment dominated by temperatures  $< 100$  K in which insufficient sublimation occurs to produce an insulating lag deposit. Thus we identify three new large craters on the surface of Mercury that host extensive water-ice deposits exposed at their surfaces.

## IMPLICATIONS FOR LUNAR EXPLORATION:

Thermal models [14, 15] indicate that micro-cold traps may be ubiquitous on the surfaces of Mercury and the Moon. Recent models suggest that surfaces with slope RMS  $\sim 15^\circ$  near the poles of the Moon have  $\sim 10\%$  exposed cold-trap area fraction [15]. The diffusion barrier created by overlying regolith increases this area fraction to  $\sim 40\%$  [15]. It is possible that surface and subsurface ice in rough surfaces [15] may be more accessible than ice in large PSR craters.

## CONCLUSIONS:

Previously, the extent of water-ice deposits was thought to be confined to the extent of large permanently shadowed impact craters and some permanently shadowed rough terrain. However, this conclusion was heavily influenced by the footprint size of the Earth-based observations of the radar-bright material [6] and the MESSENGER-derived PSRs [7–9]. We suggest that large craters are not the only hosts of substantial water-ice deposits on the surface of Mercury, which is consistent with thermal modeling [14] and reflectance mapping [13] results that indicate that micro-cold traps are capable of hosting substantial quantities of water-ice deposits. Here we identify four deposits within MES-

SENGER footprint resolutions, and suggest that many other deposits exist below the detection limit, within rough patches and inter-crater terrain. We expect that the BepiColombo Laser Altimeter [16] will be able to resolve additional high reflectance deposits indicative of surface water ice in mapping the south polar region of Mercury.

## REFERENCES:

- [1] Slade, M. A., B. J. Butler, and D. O. Muhleman (1992), Mercury Radar Imaging: Evidence for Polar Ice // *Science*, 258(5082), 635–640.
- [2] Harmon, J. K., and M. A. Slade (1992), Radar Mapping of Mercury: Full-Disk Images and Polar Anomalies // *Science*, 258(5082), 640–643.
- [3] Butler, B. J., D. O. Muhleman, and M. A. Slade (1993), Mercury: full-disk radar images and the detection and stability of ice at the North Pole // *J. Geophys. Res.*, 98(E8), 15003–15023.
- [4] Harmon, J. K., M. A. Slade, R. A. Vélez, A. Crespo, M. J. Dryer, and J. M. Johnson (1994), Radar mapping of Mercury's polar anomalies // *Nature*, 369(6477), 213–215.
- [5] Harmon, J. K., P. J. Perillat, and M. A. Slade (2001), High-Resolution Radar Imaging of Mercury's North Pole // *Icarus*, 149(1), 1–15.
- [6] Harmon, J. K., M. A. Slade, and M. S. Rice (2011), Radar imagery of Mercury's putative polar ice: 1999–2005 Arecibo results // *Icarus*, 211(1), 37–50.
- [7] Chabot, N. L., C. M. Ernst, B. W. Denevi, J. K. Harmon, S. L. Murchie, D. T. Blewett, S. C. Solomon, and E. D. Zhong (2012), Areas of permanent shadow in Mercury's south polar region ascertained by MESSENGER orbital imaging // *Geophysical Research Letters*, 39(9), L09204.
- [8] Chabot, N. L., C. M. Ernst, J. K. Harmon, S. L. Murchie, S. C. Solomon, D. T. Blewett, and B. W. Denevi (2013), Craters hosting radar-bright deposits in Mercury's north polar region: Areas of persistent shadow determined from MESSENGER images, *J. Geophys. Res. Planets*, 118(1), 26–36.
- [9] Deutsch, A. N., N. L. Chabot, E. Mazarico, C. M. Ernst, J. W. Head, G. A. Neumann, and S. C. Solomon (2016), Comparison of areas in shadow from imaging and altimetry in the north polar region of Mercury and implications for polar ice deposits // *Icarus*, 280, 158–171.
- [10] Paige, D. A., et al. (2013), Thermal Stability of Volatiles in the North Polar Region of Mercury // *Science*, 339(6117), 300–303.
- [11] Lawrence, D. J., et al. (2013), Evidence for Water Ice Near Mercury's North Pole from MESSENGER Neutron Spectrometer Measurements // *Science*, 339(6117), 292–296.
- [12] Neumann, G. A., et al. (2013), Bright and Dark Polar Deposits on Mercury: Evidence for Surface Volatiles // *Science*, 339(6117), 296–300.
- [13] Neumann, G. A., A. Sun, E. Mazarico, A. N. Deutsch, J. W. Head, D. A. Paige, L. Rubanenko, and H. C. M. Susorney (2017), Latitudinal variation in Mercury's reflectance from the Mercury Laser Altimeter // *Lunar Planet. Sci.*, 48, abstract 2660.
- [14] Rubanenko, L., E. Mazarico, G. A. Neumann, and D. A. Paige (2017), Evidence for surface and subsurface ice inside micro cold-traps on Mercury's north pole // *Lunar Planet. Sci.*, 48, abstract 1461.
- [15] Rubanenko, L., O. Aharonson (2017), Stability of ice on the Moon with rough topography // *Icarus*, 296, 99–109. [16] Thomas, N., T. et al. (2007), The BepiColombo Laser Altimeter (BELA): Concept and baseline design // *Planetary and Space Science*, 55(10).

# THERMAL AND ILLUMINATION CONDITIONS IN THE RADAR FEATURES HOST CRATERS IN THE MERCURY'S SOUTH POLE REGION

V.V. Shevchenko<sup>1</sup>, E. A. Feoktistova<sup>2</sup>, A.Yu. Zharkova<sup>1,2</sup>

<sup>1</sup>*Sternberg Astronomical Institute, Moscow University, Universitetski pr., 13, 119992, Moscow, Russia, Hrulis@yandex.ru;*

<sup>2</sup>*Moscow State University of Geodesy and Cartography (MIIGAiK), Gorokhovskypereulok 105064, Moscow, Russia, a\_zharkova@migaik.ru*

## KEYWORDS:

Mercury, impact crater, volatiles.

## INTRODUCTION:

The illumination and thermal conditions, and stability of volatiles deposits in the South Pole region of Mercury are calculated on the basis of a LAMP.

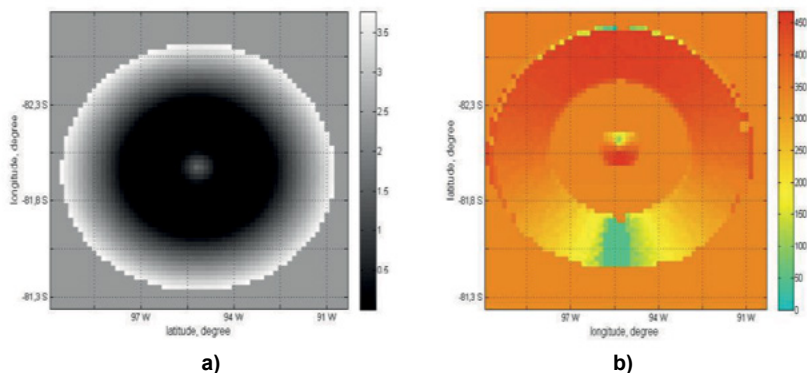
Radar-bright regions were revealed by earth-based radar observations at both poles of Mercury [1, 2]. Further studies have shown the correlation of these features with locations of high-latitude impact craters. It was suggested that these features are formed by volatiles deposits (including water ice) and located in permanently shaded areas in host craters. These suggestions also have been confirmed by the data from neutron spectrometer of the MESSENGER probe [3].

We investigated the possibility existence and stability of volatiles deposits in several craters at South Pole region of Mercury, which contain radar-bright features. To do this we used data from [4]. We take into account four altitude profiles for each crater, thus the crater was divided into 8 sectors. Unfortunately, for some host crater, such as Chao Meng-Fu, Lovecraft and some other, were was no correct data because of the global Mercury DEM [4] defects on South Pole region. Currently, this DEM (with resolution 665 m/pixel) obtained by photogrammetric methods, is the only DEM available for these latitudes.

Because of this we simulated the inner structure of these craters, using the relationship for morphologic characteristics of impact craters from [5] and crater's images from [6].

Thermal regime of a surface area is determined by solution of the one-dimension heat conductivity equation. In upper boundary condition the flux of direct solar radiation incident on a given surface element, the fluxes of reflected and infrared radiation from all adjacent illuminated surface elements visible from a given element, and the heat flux from the Mercury's interior were taken into account. We simulated the subsurface layer using a two-layer soil model similarly to that described in the study [7]. The combined effect of the orbital motion of Mercury around the Sun and its axial rotation is that the duration of a solar day on the planet is equal to three sidereal Mercurial days or two Mercurial years. Because of Mercury's slow rotation, the distance to the Sun and the angular size of the solar disk have a large effect on the magnitude of the solar radiation. To investigate the diurnal variation of solar flux and illumination conditions for surface area we have computed the distance from the Sun, Mercury's orbital velocity and part of the solar disk above the horizon for each moment of time. For each elements of surface the position of the Sun has been determined by its coordinates in the horizontal system: zenith distance ( $z$ ) and azimuth ( $A$ ). The time increment has corresponded to the Sun's azimuth displacement by  $1^\circ$ .

We considered the possibility existence deposits of volatile compounds on the surface and under insulation layer of regolith in host craters. Paige et al. (2012) [8] suggested that part of radar-bright deposits can contain of some carbonaceous material, which observed on the surface of comets and asteroids. For this reason four models of structure of volatiles deposit were used in our calculations: 1) pure water ice on the surface; 2) pure water ice under the layer of regolith; 3) mixture of water ice and other volatiles compounds on the surface and 4) under the layer of regolith. For each crater the thickness of a layer of regolith, that necessary to protect the deposits of volatiles from thermal evaporation was calculated.



a)

b)

**Fig. 1.** Simulated morphometry of crater hosting the radar-bright feature B4 (a) and diurnal maximum surface temperatures in this crater (b). In the northern part of the crater there is an area that corresponds to radar-bright deposit. The maximum temperatures in this area do not exceed 100 K.

## REFERENCES:

- [1] Harmon J.K., Slade M.A. Radar mapping of Mercury: Full-disk images and polar-anomalies // *Science*. 1992. V. 258. P. 640-643.
- [2] Harmon J.K., Slade M.A., Rice M.S. Radar imagery of Mercury's putative polar ice: 1999-2005 Arecibo results // *Icarus*. 2011. V. 211. P. 37-50.
- [3] Lawrence D.J., Feldman W.C., Goldsten J.O. et al. Evidence for water ice near Mercury's North Pole from MESSENGER neutron spectrometer measurements// *Science*. 2013. V. 339. P. 292-296.
- [4].[https://pdsimage2.wr.usgs.gov/data/mess-h-mdis-5-dem-elevation-v1.0/MESS-DEM\\_1001/DEM/GLOBAL/JPEG2000/](https://pdsimage2.wr.usgs.gov/data/mess-h-mdis-5-dem-elevation-v1.0/MESS-DEM_1001/DEM/GLOBAL/JPEG2000/)
- [5] Pike J.R. *Geomorphology of impact craters on Mercury* // Mercury / Eds Vilas F., Chapman C.R., Matthews M.S. Tucson: Univ. Arizona Press. 1988. P. 165-273.
- [6] <https://planetarynames.wr.usgs.gov/Page/mercuryQuadMap>
- [7] Vasavada A.R., Paige D.A., Wood S.E. Near-Surface Temperatures on Mercury and the Moon and the Stability of Polar Ice Deposits // *Icarus*. 1999. V. 141. P. 179-193.
- [8] Paige D.A., Siegler M.A., Harmon J.K. et al., Thermal stability of Volatiles in the North Polar Region of Mercury// *Science*. 2013. V. 339. P. 2300-303.

# MORPHOLOGICAL FEATURES OF MERCURY SOUTH POLE RELIEF

S.G. Pugacheva, E.A. Feoktistova, V.V. Shevchenko  
*Sternberg Astronomical Institute, Moscow State, Russia,*  
 sve-pugacheva@yandex.ru

## KEYWORDS:

South Pole of Mercury, photometry methods, relative brightness, color-coded photo mosaic, main types of relief

## INTRODUCTION

The paper reveals results of Mercury South pole surface relief research by photometry methods. The photometry method searches out the intensity of reflectivity of planet's surface and provides studying of ground fine texture [4]. Main materials of the research are photographic images of Mercury surface transferred by "Messenger" interplanetary station during its passing near Mercury. For Mercury surface relief structure evaluation the images of Mercury Southern hemisphere have been used. The photographic images of Mercury surface transferred by "Messenger" have high spatial resolution of 2 km/pixel, while the accuracy of Southern hemisphere altitudes evaluation makes at average 1,5 m.

## FEATURES OF MERCURY SURFACE RELIEF

According to its photometric features Mercury resembles the Moon, however the planet has its unique physical characteristics. Surface of Mercury is the combination of craters, worn-down plains, saw-edged cliffs (escarpments) and ray patterns. The relief of Mercury surface differs with numerous escarpments hundreds kilometers long, formation of which is linked with compression processes in crust taken place during cooling of mantle and partial consolidation of planet's core. There

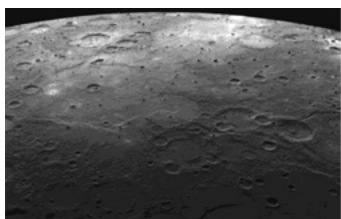


**Fig.1.** The mosaic of craters on the South pole of Mercury. The mosaic includes numerous craters with lava streams and great spaces of even volcanic plains, which by their structure resemble volcanic deposits on the Moon [3]

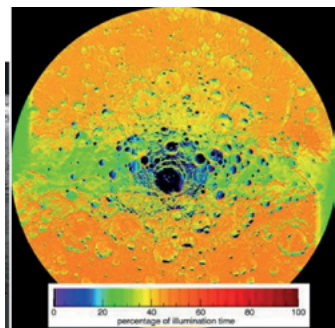


**Fig.2.** The illumination of surface on the South pole of Mercury. The craters painted dark blue are located in permanent shadow. In such areas there are probably deposits of water ice, presence of which had been predicted by scientists on the assumption of Mercury surface albedo observations performed by means of radio telescope.

are more ray craters on Mercury than on the Moon – probably, the impact force here is strengthened by bigger planet's mass and its vicinity to the Sun. On photographic images of Mercury there are also spots of some dark substance that is much darker than general background, which are probably the traces of meteorite hits. Composition of the dark formations remains unknown, however by its look the material resembles ferrous titanate [1, 2]. During the second passing "Messenger" had monitored changes of Mercurian relief. Evaluation of altitudes had revealed the surface of Western hemisphere and equator's localities are 30% more even in comparison to opposite hemisphere. In history of Mercury and the Moon there was a period when streams of lava exposed to surface. The significant part of plains of Mercury Western hemisphere is covered with lava. In addition, lava beds occur inside and around huge Caloris basin, as well as at the bottom of other big basins. Probably, the plains of Mercury had been formed by huge flows of molten material expelled to the surface after basin-forming hits. The lava-covered areas look brighter than other ones.

## PHOTOMETRIC EVALUATION OF MERCURY SURFACE RELIEF.

Two main types of Mercury surface are: cratered terrain and intercrater plains that had demolished craters with low diameter. At the bottom of big basins, including areas around and inside huge Caloris basin, there are even plains formed by molten materials. The cratered terrain has approximately the same mean albedo the Moon continents have, how-

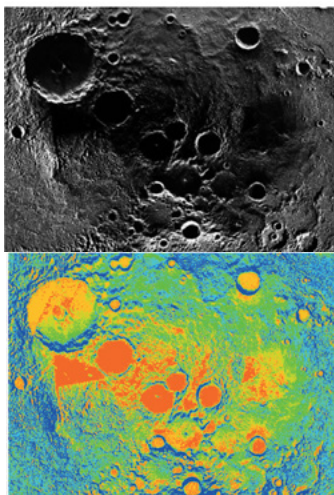


**Fig.3.** This new color-coded photo mosaic of Mercury's south polar region, Severnyiy-polyus Mekuriya1 (-85S, -10W). This new color-coded photo mosaic of Mercury's south polar region shows these "freezer" areas as dark blotches.

ever, Mercurian even plains are much darker than ones on the Moon. Each image has reference data and a calibration scale for translating the image density into relative brightness values. Photometric processing of space photographs made by Mariner-10 and "Messenger" space vehicles allowed us to evaluate various type of Mercury surface reflectivity and define its soil structure [4]. In general the surface of Mercury is being more homogeneous and monotonous by its photometric parameters. Radar researches of circumpolar areas reveal presence of ice in shadow points of craters in polar areas of Mercury. The minimum temperature of surface in polar craters reduces to 90 K, while maximum temperature within Caloris Planitia reaches 700 K.

The temperature differentials on the surface of Mercury are related with different intensity of surface's insolation during planet's orbital movement. The relief of the Southern pole of Mercury is characterized with bigger crater density. On the photographs of surface there are flows of molten material at the bottom of craters and lava streams on their top. We have selected several photographs of Mercury Southern hemisphere made by "Messenger". The photographs have been processed by pixel scanning system for definition of surfaces with equal brightness [5, 6]. At the same time, using MultiSpecWin32 system we have defined areas with different reflectivity [3]. Thus, we have evaluated surface roughness and relative number of impact craters on it. As a result, three main morphological units have been obtained: the surface with low reflection coefficient characterized by high roughness and high density of impact craters; the surface of linear form characterized by extra low reflection coefficient; and even surface characterized by less density of craters and median reflectivity, which is typical for relatively recent formations.

Conclusion. "Messenger" space vehicle is an American automatic interplanetary station designed for research of Mercury. The vehicle had been launched on August 3, 2004 with help of carrier booster "Delta 7925H-9.5". "Messenger" entered the orbit of Mercury on March 18, 2011 at 01:10 (UTC). Photographic prints transferred to Earth helped to determine that in the past on Mercury quite intense tectonic activity had place. Its traces can be found in the Eastern and Western hemispheres of the planet in the form of large even plains. "Messenger" discovered new earlier unknown craters within the area of Mercury South pole. During its passing near the planet "Messenger" made a number of shots of unexplored areas (6% of the whole planet's surface), carried out research of Mercurian atmosphere and revealed traces of recent volcanic eruptions. Thus, as of today about 98% of Mercury surface is explored. The rest 2% are polar areas that are supposed to be explored in future. At the present time European Space Agency (ESA) together with Japanese Aerospace Exploration Agency (JAXA) develop BepiColombo mission that implies use of two space vehicles - Planetary Orbiter (MPO) and Magnetospheric Orbiter (MMO). The European MPO will explore surface of Mercury and its depths, while Japanese MMO will perform observations of magnetic field and magnetosphere of the planet.

Conclusion. "Messenger" space vehicle is an American automatic interplanetary station designed for research of Mercury. The vehicle had been launched on August 3, 2004 with help of carrier booster "Delta 7925H-9.5". "Messenger" entered the orbit of Mercury on March 18, 2011 at 01:10 (UTC). Photographic prints transferred to Earth helped to determine that in the past on Mercury quite intense tectonic activity had place. Its traces can be found in the Eastern and Western hemispheres of the planet in the form of large even plains. "Messenger" discovered new earlier unknown craters within the area of Mercury South pole. During its passing near the planet "Messenger" made a number of shots of unexplored areas (6% of the whole planet's surface), carried out research of Mercurian atmosphere and revealed traces of recent volcanic eruptions. Thus, as of today about 98% of Mercury surface is explored. The rest 2% are polar areas that are supposed to be explored in future. At the present time European Space Agency (ESA) together with Japanese Aerospace Exploration Agency (JAXA) develop BepiColombo mission that implies use of two space vehicles - Planetary Orbiter (MPO) and Magnetospheric Orbiter (MMO). The European MPO will explore surface of Mercury and its depths, while Japanese MMO will perform observations of magnetic field and magnetosphere of the planet.

## REFERENCES:

- Head J, Murchie S., Prockter L., et al. Volcanism on Mercury: Evidence from the Messenger flyby // *Science*. 2008. V. 321. P. 69-72.
- Neumann G.A., Cavanaugh J.F., Sun X., Mazarico E., et al. Dark Material at the Surface of Polar Crater Deposits on Mercury // 2012. 43rd Lunar and Planetary Science Conference. № 1659.
- Robinson M.S., Murchie S.L., Blewett D.T., et al. Reflectance and Color Variations on Mercury: Regolith Processes and Compositional Heterogeneity. *Science*. 2008. V. 321. P. 66-69.
- Shevchenko V.V. Remote estimation of the structure of the surface layer of Mercury // *Advances in Space Research* (a COSPAR Publication). 2004. P. 2147-2151.
- Шевченко В.В. Структура реголита Меркурия по фотометрическим данным // *Астрономический Вестник*. 2004. Том 38. № 6. С. 504-512.
- Shevchenko V.V. Mercury: local photometric relief as roughness index // *Advances in Space Research* (a COSPAR Publication). 2006. P. 590-593.

# DECIPHERING THE NOACHIAN GEOLOGICAL AND CLIMATE HISTORY OF MARS: PART 2 - A NOACHIAN STRATIGRAPHIC VIEW OF MAJOR GEOLOGIC PROCESSES AND THEIR CLIMATIC CONSEQUENCES

J. Head<sup>1</sup>, R. Wordsworth<sup>2</sup>, F. Forget<sup>3</sup>, and M. Turbet<sup>3</sup>

<sup>1</sup>Brown Univ., Providence, RI 02912 USA ([james\\_head@brown.edu](mailto:james_head@brown.edu)),

<sup>2</sup>Harvard University, Cambridge MA 02138 USA, <sup>3</sup>Lab. de Météorologie Dynamique du CNRS, Université Paris 6, Paris, France.

## KEYWORDS:

Mars, Noachian, Climate, Fluvial, Icy Highlands, Warm and Wet, Cold and Icy, Fluvial

## INTRODUCTION

We apply a stratigraphic approach to the major Noachian geological processes and observation, knowns and unknowns [1-3] to provide insight into potential changes as a function of time, and to assess their climatic consequences.

## EARLY NOACHIAN

This is the era of large impact basins, with Hellas Basin defining the base of the Noachian, followed by formation of Isidis and Argyre. Impacts are known to have size-dependent effects in terms of ejecta and influence on the atmosphere, ranging from blowing off a significant part of the atmosphere, through global distribution of silicate vapor that results in precipitation of silicate vapor cloud condensate, and significant but short-lived very hot rainfall [4-6]. Recent research has underlined the size-dependent effects, finding that large basins could form global effects while those below ~50 km would have only local effects [7]. Could the global effects form a global stratigraphic marker horizon for the major Noachian basin analogous to the Imbrium basin on the Moon?

## THE NOACHIAN MINERALOGICAL ALTERATION PARADOX

Ever since OMEGA [8] documented the dominance of phyllosilicates (clays) in the Noachian, a solution has been sought to provide the three necessary ingredients to account for their formation: 1) abundant liquid water, 2) temperatures >273K, and 3) prolonged exposure [9], while at the same time accounting for other observed minerals (e.g., olivine) that are unstable under these conditions. A "warm and wet" climate has often been cited as the solution [10], but the phyllosilicates do not clearly coincide in time or space with the Late Noachian VN/ CBL/OBL assemblage [3], leading many to consider that at least some of the phyllosilicates formed deeper in the crust under hydrothermal conditions [11]. A solution to this paradox might be found in the formation of impact basins earlier in the Noachian: In an update [6] of the global effects of impact basin formation [4-5], the immediate aftermath of the vapor cloud condensation is shown to be characterized by the global precipitation of sustained hot rains (considerably above 273K), and lasting for several centuries. This mechanism (Fig. 1) [6] provides widespread, extremely hot water interacting with the surface and near-surface substrate for centuries, a duration sufficient to provide leaching of decameters of substrate. Support for this hypothesis [6] comes from extensive the association of many of the phyllosilicates with the Noachian basins Hellas, Isidis and Argyre [9,12-13] and other extensive deposits dated to this period [14]. These deposits may provide stratigraphic time- markers for the specific impact basins [6, 15].

This is the post-Argyre basin period; impact cratering at the sub-large basin scale continues with declining flux. In the "warm and wet/arid" climate scenario [10], the dominant process of crater degradation (loss of small craters; erosion of larger crater rim/ejecta, infilling of crater interior) is rainfall-related diffusional processes that are intermittent and at sufficiently low rates that water infiltration dominates over surface runoff and VN systems do not form. In this scenario, although the climate is arid, MAT is required to be >273 K [10], implying a vertically integrated hydrologic system in the equatorial/mid latitudes. This

ambient “warm and arid” climate is envisioned to persist for several hundred million years [10] (Fig. 1). The Late Noachian dominance of the VN-CBL-OBL geomorphic assemblage is envisioned as representing a “climatic optimum” [16], producing “warm and wet” conditions characterized by sufficient rainfall precipitation to overcome infiltration, and cause widespread fluvial and lacustrine activity. Here we separate out the “crater loss/ degradation” component of the “warm and arid/wet geomorphic assemblage” and treat separately the remaining “pluvial/fluvial/lacustrine” component (VN/CBL/OBL).

### “CRATER LOSS/DEGRADATION” COMPONENT

Are there alternatives to the “warm and arid crater loss/degradation” [10] scenario? Could the formation of the earlier Noachian impact basins have played a role? Following [4-5], [6] have proposed that global deluge-scale rainfall phases that immediately follow basin formation could obliterate small craters and cause extensive planation and infilling of pre-existing distal craters. Furthermore, [7] have shown that smaller basins and large craters may also produce regional erosion and degradation effects. Detailed stratigraphic analyses are required to assess this option further [6]. A second alternative, involving the “cold and icy” climate scenario [17-19]; [20] explores the effects of a regional ice sheet predicted by this model in masking the sub-ice surface from smaller impacts, and facilitating the observed rim degradation and infilling of Noachian craters. Neither of these two options requires MAT in the  $>273$  K range. We conclude that the “crater loss/degradation” component of the “warm and arid/wet geomorphic assemblage” may also be consistent with other climate scenarios.

### VOLCANISM AND VOLCANIC RESURFACING

The beginning of the LN-EH volcanism phase; resurfacing of Arabia Terra and other Noachian plains formation, potential explosive volcanism, and peak eruptive phases could potentially cause decades to centuries of warming [22].

### LATE NOACHIAN “CLIMATE OPTIMUM”

This is the known period of dominance of the VN-CBL-OBL geomorphic assemblage envisioned as representing a “climatic optimum” [16] (Fig. 1), transitioning from “warm and arid” to produce “warm and wet” conditions characterized by sufficient rainfall precipitation to overcome infiltration, and cause widespread fluvial and lacustrine activity. Because of the alternative explanations for the “crater loss/degradation” component [6, 20], not involving MAT in the 273 K range, here we focus only on the “pluvial/fluvial/lacustrine” component (VN/CBL/OBL) of the “warm and arid/wet geomorphic assemblage” and assess the climate implications (Fig. 1). Key questions are: Nature of ambient climate [10, 18], source of water [21], volume of water [21], continuous or discontinuous conditions [21], intermittency [23], total duration [23], and presence of oceans [24]?

### THE LATE NOACHIAN CLIMATE PARADOX (LNCP)

The Late Noachian climate paradox [1] can be stated as follows: 1) Robust LN Mars climate and general circulation models [17-18] predict MAT  $\sim 225$  K, and an altitude-dependent stability of snow and ice, such that the surface water inventory is deposited preferentially above an ELA of  $\sim +1$  km (southern uplands and south circumpolar regions), the “icy highlands” model [18-19]. In this ambient atmosphere, no combination of spin-axis/orbital parameters can produce significant melting of this snow and ice anywhere on the planet [25]. 2) The well-documented, “pluvial/fluvial/lacustrine (VN/CBL/OBL)” component of the “warm and wet geomorphic assemblage” [10, 16], in contrast, shows unequivocally that liquid water flowed extensively across the surface, ponded, and overflowed, creating fluvial networks systems as long as 1000 km [3]. Clearly, these two aspects are incompatible and represent a paradox. On the one hand, climate modelers find great difficulty in achieving MAT  $>273$  K (no combination of sustained greenhouse gas sources have been able to achieve MAT  $>273$  K for the duration of M-L Noachian), and geologists have not found an alternate explanation to widespread flowing liquid water for the VN/CBL/OBL fluvial assemblage.

### A CANDIDATE SOLUTION TO THE LATE NOACHIAN CLIMATE PARADOX

We propose that a solution to the LNCP lies in a “cold and icy” ambient background climate (MAT  $\sim 225$  K) [17-19] that undergoes multiple episodic/periodic regional to global warming perturbations, that either individually or collectively are sufficient to account for the observed “warm and wet geomorphic fluvial



assemblage". Among the candidates for such perturbations are: 1) periods of abbreviated greenhouse gas release sufficient to raise MAT 10-15 K so that peak seasonal (PST) seasonal or peak daytime melting (PDT) can melt snow-pack to form the observed VN/CBL/OBL [19,25]; 2) Effusive/explosive volcanic eruptions at high enough fluxes that SO<sub>2</sub> release causes equatorial/mid-latitude atmospheric heating for decades to centuries to form the VN before global cooling [22]; 3) Post-Argyre large crater/small basin formation sufficient to perturb the atmosphere regionally to form the VN [7].

## CONCLUSIONS

A stratigraphic approach to understanding the climate of Noachian Mars [1-3] indicates that: 1) The Early Noachian is dominated by the formation of Hellas, Isidis and Argyre basins; associated with each basin is the collapse of a global vapor plume, condensation of silicate vapor and a hundreds of year long phase of torrential hot rains, potentially accounting for significant alteration of surface materials to phyllosilicates [15]. The formation of each basin emplaced a global meters-thick isochronous silicate condensate time marker accompanied by significant associated alteration to phyllosilicates [15]. The Early Noachian ambient background climate was profoundly perturbed by each impact event, with exact recovery pathways and times uncertain [7]. On the basis of the difficulty of sustaining a "warm and wet/arid" climate [10] for several hundred million years (Fig. 1), we adopt the "cold and icy" post-basin period (MN-LN) climate to be the ambient background climate. The LN "climatic optimum", during which the VN/CBL/OBL systems formed, is interpreted to be due to one or more climatic perturbations operating to perturb MAT, PST, and/or PDT on the "icy highlands" climate model. These ideas can be tested with further analyses of the critical stages as described above. The transition from the Late Noachian to Early Hesperian sulfate formation is interpreted to be related to EH basaltic flood volcanism resurfacing at least 30% of the planet [26]; the subsequent waning global volcanic flux [21], together with losses to space [27], transitioned the global atmosphere toward decreased atmospheric pressure [28], an end to the "icy highlands", the reduction of south polar cap (DAF) area/volume [29], the beginning of a bipolar Mars, and reduction to even lower weathering/erosion rates.

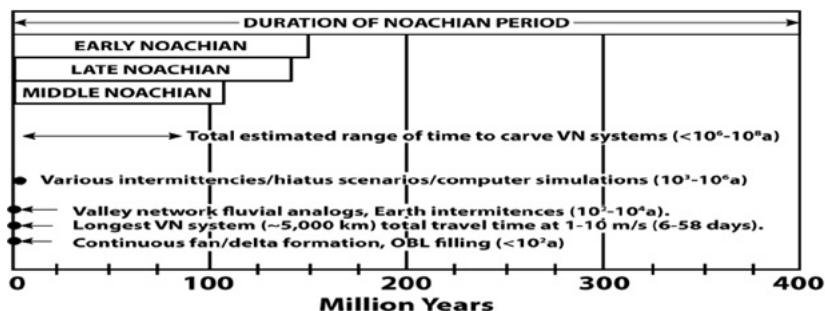


Fig. 1. Estimates for VN formation duration (from [23]).

## REFERENCES:

- [1] Head et al., 2017, 4th EMC;
- [2] Head et al., 2015, LPSC46, #2176;
- [3] Fassett & Head, 2011, Icarus 211, 1204;
- [4] Segura et al., 2008, JGR, 113, E11;
- [5] Toon et al., 2010, AREPS 38, 303;
- [6] Palumbo et al., 2017, 6th MAMO;
- [7] Turbet et al., 2017, 6th MAMO;
- [8] Bibring et al., 2006, Science 312, 400;
- [9] Bishop et al., 2017, LPSC 48 1804;
- [10] Craddock & Howard, 2002, JGR 107, 5111;
- [11] Ehlmann et al., 2011, HNature 479.53;
- [12] Murchie et al., 2009, JGR 114;
- [13] Mustard et al., 2006, JGR 112;
- [14] Bishop & Rampe, 2016, EPSL 448, 42;
- [15] Palumbo & Head, 2017, 8th Moscow S3;
- [16] Irwin et al., 2005, JGR110, E12515;
- [17] Forget et al. 2013, Icarus 222, 5111;

- [18] Wordsworth et al., 2013, *Icarus* 222, 1;
- [19] Head & Marchant, 2014, *Ant. Sci.* 26,774;
- [20] Weiss and Head, 2015, *Planet. Space Sci.* 117, 401;
- [21] Carr & Head, 2015, *GRL* 42, 1;
- [22] Halevy & Head, 2014, *Nat. Geosci.* 1-4;
- [23] Buhler et al., 2014, *Icarus* 241, 130;
- [24] Clifford & Parker, 2001, *Icarus* 154, 40;
- [25] Palumbo et al, 2017, *LPSC 48* 2107;
- [26] Head et al., 2002, *JGR* 107, E1;
- [27] Jakosky et al., 2017, *LPSC 45* 1114;
- [28] Halevy & Head 2017, *LPSC 48* 2519;
- [29] Scanlon et al., 2016, *LPSC47* 1315.

# WATER AND CHLORINE ABUNDANCE IN THE GALE CRATER ACCORDING TO DAN DATA

D.I. Lisov<sup>1</sup>, A.S. Kozyrev<sup>1</sup>, M.L. Litvak<sup>1</sup>, I.G. Mitrofanov<sup>1</sup>, A.B. Sanin<sup>1</sup>

<sup>1</sup>*Space Research Institute of the Russian Academy of Sciences (IKI), 84/32  
Profsoyuznaya Str, Moscow, Russia, 117997*

## KEYWORDS:

Mars, MSL, Curiosity, neutrons, water, hydrogen, chlorine

## INTRODUCTION:

The Dynamic Albedo of Neutrons (DAN) active neutron spectrometer[1] has been operating onboard the Curiosity rover in the Gale crater since the MSL landing in 2012. Here we present the equivalent water and chlorine abundances measured in DAN active mode over the five years of operation and more than 17 kilometers of Curiosity traverse.

## REFERENCES:

[1] Mitrofanov I.G., Litvak M.L., Varenikov A.B., et al. Dynamic Albedo of Neutrons (DAN) experiment onboard NASA's Mars science laboratory. // Space science reviews. 2012. V. 170. No. 1-4 P. 559-582.

# MARSSIM LANDFORM EVOLUTION MODEL: HYDROLOGIC CONSTRAINTS ON THE NOACHIAN EARLY DRY PERIOD

B.D. Boatwright, J.W. Head

*Brown University, Providence, RI USA, benjamin\_boatwright@brown.edu*

## KEYWORDS:

Mars, valley networks, landform evolution, morphology, hydrology, climate

## INTRODUCTION:

The formation of valley networks, open- and closed-basin lakes, deltas and alluvial fans in the Noachian highlands of Mars has been constrained to a brief but intense episode of fluvial activity, known as the "terminal epoch," around the Noachian-Hesperian boundary [1]. Surveys of the valley networks have shown that they likely formed through the action of liquid water flowing at the surface [2-4]. However, climate modeling studies have failed to raise mean annual average temperatures (MAAT) above 273 K with an H<sub>2</sub>O+CO<sub>2</sub> atmosphere at variable pressures [5-7]. This "cold and dry" model maintains a subfreezing, hyperarid environment during the Noachian with a global cryosphere more typical of present-day Mars [8]. Liquid water would have existed on the surface only during transient warming events caused by volcanism [9] or impact heating [10-11]. This is seemingly in contradiction to the geologic evidence, which suggests that the Noachian was instead "warm and wet," with a robust hydrologic cycle dominated by precipitation and surface runoff [12-14]. Recent work on an "icy highlands" model has attempted to reconcile some of these differences by allowing limited runoff from glaciers while maintaining MAAT below freezing [15-16].

Morphometric studies have shown that valley network profiles closely follow regional slopes and incise into previously reworked intercrater plains material [13-14, 17]. This earlier, more extended period of highland degradation, herein referred to as the "early dry period," is significantly less well characterized than the terminal epoch. Discharges were too low to effectively transport sediment, drainage integration was localized, and valley networks, where they existed, generally did not form incised channels [17]. This led to a weathering- and infiltration-dominated regime that gradually filled crater floors and alluvial plains with hundreds of meters of permeable, loosely consolidated sediment [18-20]. The total volume of sediment removed during the early dry period was much greater than the amount eroded by the valley networks, but average erosion rates were comparable (Tables 1-2). This implies that the early dry period lasted many times longer than the terminal epoch, perhaps on the order of several tens to hundreds of millions of years, encompassing most of the Middle and Late Noachian.

Beyond a qualitative idea of the climatic conditions that prevailed in the early dry period, little is known of the exact rates, amounts, and transport mechanisms that might have created the substrate that existed in the highlands before the valley networks formed. We propose a variety of tests using a landform evolution model [21] that can simulate fluvial and slope processes under accurate Martian conditions. In particular, we attempt to constrain hydrologic parameters to match the transport-limited regime of the early dry period.

## ESTIMATES OF EROSION RATES AND SEDIMENT VOLUMES:

A handful of studies in the 1990s and early 2000s [18-20] attempted to estimate how much material had been reworked by fluvial processes in the Noachian, mostly by comparing populations of degraded craters to modeled production functions. [19] and [20] used craters in and around Arabia Terra for their estimates, while [18] made a more comprehensive survey of all highland craters between 30 degrees north and south latitude. However, [18] also extended their age range to the end of the Hesperian, which given more recent evidence of the abrupt cessation of intense erosion shortly after the Noachian-Hesperian transition [1], is probably not accurate. Instead, each erosion estimate can be recalculated to fall within either the Middle-Late Noachian or strictly the Late Noachian, providing two alternative constraints on how long the early dry period may have lasted. In such a scenario, erosion rates are on the order of 10<sup>-4</sup> to 10<sup>-2</sup> mm/yr (Table 1).

**Table 1.** Estimated erosion rates during the early dry period.

Normalized sediment volume /10 <sup>6</sup> km <sup>2</sup> (km <sup>3</sup> )	Erosion rate (mm/yr)	
	Middle-Late Noachian 230-410 Myr [23-24]	Late Noachian 120-300 Myr [23-24]
2.9x10 <sup>5</sup> (min) [18] 2.3x10 <sup>6</sup> (max) [18]	0.0007-0.001 0.006-0.01	0.001-0.002 0.008-0.02
2.2x10 <sup>5</sup> [19]	0.0005-0.001	0.0007-0.002
1.0x10 <sup>6</sup> [20]	0.002-0.004	0.003-0.008

Erosion rates can also be estimated for the terminal epoch, which occurred primarily in the channelized flows of valley networks [13]. [22] calculated a total sediment volume of 1.5x10<sup>5</sup> km<sup>3</sup> based on cavity volumes and sediment porosity from [25]. Table 2 normalizes this volume based on Noachian drainage densities and compares erosion rates for a likely range of valley network formation timescales. If we assume that valley incision was occurring constantly throughout this time, then erosion rates would have been on the order of 10<sup>-4</sup> to 10<sup>-1</sup> mm/yr. If incision was episodic, however, then actual rates during periods of incision would be higher. For example, if the valleys formed over 10<sup>3</sup> years or less, as suggested for a “deluge”-style flow [27], erosion rates could easily surpass those of the early dry period and approach 2-10 mm/yr.

**Table 2.** Estimated erosion rates during the terminal epoch.

Sediment volume (km <sup>3</sup> )	Drainage area (km <sup>2</sup> )	Normalized sediment volume/10 <sup>6</sup> km <sup>2</sup> (km <sup>3</sup> )	Erosion rate (mm/yr)	
			10 <sup>7</sup> yr [26-27]	10 <sup>5</sup> yr [26-27]
1.5x10 <sup>5</sup> [22]	6.2x10 <sup>7</sup> [2]	2.4x10 <sup>3</sup>	0.00024	0.024
	1.3x10 <sup>7</sup> [3]	1.1x10 <sup>4</sup>	0.0011	0.11
	6.8x10 <sup>7</sup> [4]	2.1x10 <sup>3</sup>	0.00021	0.021

## PROPOSED LANDFORM EVOLUTION MODELING:

We use the MARSSIM landform evolution model first described by [21] and further explored in [27-33]. The model is written primarily with simulation of physical processes in mind, and therefore requires a fairly robust understanding of the underlying hydrologic and geologic conditions to produce accurate results. We propose to test several different parameters in order

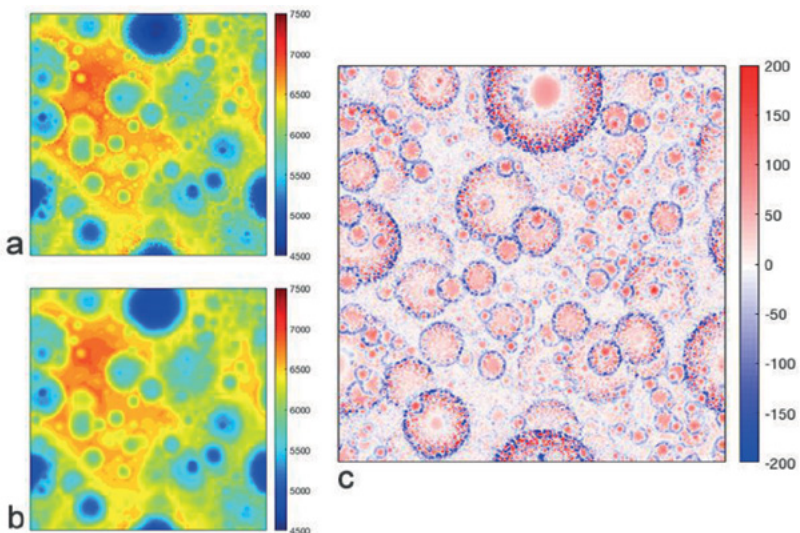


**Fig. 1.** Topographic maps for a 10 million-year simulation (this study) using a 256x256 pixel DEM from the MARSSIM source code [37], scaled to 400 m/pixel with doubly periodic boundary conditions. Groundwater sapping and mass wasting were modeled over a pre-cratered surface. a) input elevation; b) output elevation; c) elevation change, all in meters. Note the infilling of crater floors and lowering of crater rims.

to constrain 1) the conditions under which the model produces transport-limited flow, as observed in the early dry period; 2) the erosion rates and sediment volumes typical of such a regime, and how they compare to previous estimates; and 3) how long the early dry period lasted.

The model has the ability to output both text and image files for individual runs during the simulation; these can then be analyzed further using geospatial mapping tools such as ArcGIS. Previous studies have relied on an inverse method by taking the largest “missing” crater diameter in an expected size distribution as a baseline for the amount of degradation that occurred [18]. Instead, MARSSIM implements a crater geometry model [34-36] that can be used to quantify degradation with known initial conditions. By measuring elevation changes on crater floors between the input and output DEMs, the exact amount of infilling can be determined (Figure 1).

## REFERENCES:

- [1] Fassett C.I., Head J.W. (2008) *Icarus* 195, 61-89.
- [2] Carr M.H. (1995) *JGR* 100, 7479-7507.
- [3] Luo W., Stepinski T.F. (2009) *JGR* 114, E11010.
- [4] Hynek B.M. et al. (2010) *JGR* 115, E09008.
- [5] Kasting J.F. (1991) *Icarus* 94, 1-13.
- [6] Wordsworth R. et al. (2013) *Icarus* 222, 1-19.
- [7] Forget F. et al. (2013) *Icarus* 222, 81-99.
- [8] Clifford S.M., Parker T.J. (2001) *Icarus* 154, 40-79.
- [9] Halevy I., Head J.W. (2014) *Nature Geosci.*
- [10] Segura T.L. et al. (2008) *JGR* 113, E11007.
- [11] Toon O.B. et al. (2010) *Annu. Rev. EPS* 38, 303-322.
- [12] Craddock R.A., Howard A.D. (2002) *JGR* 107, E11, 5111.
- [13] Howard A.D. et al. (2005) *JGR* 110, E12S14.
- [14] Irwin R. P. et al. (2005) *JGR* 110, E12S15.
- [15] Head J.W., Marchant D.R. (2014) *Antarctic Sci.* 26, 774-800.
- [16] Fastook J.L., Head J.W. (2014) *Plan. Space Sci.* 106, 82-98.
- [17] Irwin R.P. et al. (2011) *JGR* 116, E02005.
- [18] Craddock R.P., Maxwell T.A. (1993) *JGR* 98, 3453-3468.
- [19] Craddock R.P. et al. (1997) *JGR* 102, 13321-13340.
- [20] Hynek B.M., Phillips R.J. (2001) *Geology* 29, 407-410.
- [21] Howard A.D. (1994) *Water Resources Res.* 30, 2261-2285.
- [22] Rosenberg E.N. et al. (in prep).
- [23] Hartmann W.K., Neukum G. (2001) *Mars Space Sci. Rev.* 96, 165-194.
- [24] Hartmann W.K. (2005) *Icarus* 174, 294-320.
- [25] Luo W. et al. (2017) *Nature Comms.*
- [26] Hoke M.R. et al. (2011) *EPSL* 312, 1-12.
- [27] Barnhart C.J. et al. (2009) *JGR* 114, E01003.
- [28] Forsberg-Taylor N.K. et al. (2004) *JGR* 109, E05002.
- [29] Howard A.D. (2007) *Geomorph.* 91, 332-363.
- [30] Luo W., Howard A.D. (2008) *JGR* 113, E05002.
- [31] Matsubara Y. et al. (2011) *JGR* 116, E04001.
- [32] Matsubara Y. et al. (2013) *JGR* 118, 1365-1387.
- [33] Boatwright B.D., Fassett C.I. (2014) *LPSC* 45, 2478.
- [34] Garvin J.B. et al. (2000) *Icarus* 144, 329-352.
- [35] Garvin J.B. et al. (2002) *LPSC* 33, 1255.
- [36] Garvin J.B. et al. (2003) *Intl. Conf. on Mars* 6, 3277.
- [37] Howard A.D. (2009) MARSSIM Release 3.0, <http://erode.evsc.virginia.edu>.

# VENUS GEOLOGICAL HISTORY: CURRENT PERSPECTIVES, UNKNOWN, AND OPPORTUNITIES FOR THE MODELING COMMUNITY

James W. Head<sup>1</sup>

<sup>1</sup>*Department of Earth, Environmental and Planetary Sciences,  
Brown University, Providence, RI 02912 USA, james\_head@brown.edu*

## KEYWORDS

Venus, Atmosphere, surface, interior, Magellan, modeling

## INTRODUCTION

Acquisition of Earth-based radar image observations, followed by regional image coverage (Venera 15/16) and finally global image coverage by Magellan, together with global altimetry, have provided the data necessary to analyze stratigraphic relationships and produce a global geological map of Venus [1]. The resulting stratigraphic column provides an outline of the major themes in the geological evolution of Venus in terms of fundamental processes such as tectonism [2] and volcanism [3]. The paucity of superposed and embayed impact craters and the impression that they are randomly distributed precluded the traditional counting of superposed craters on individual geological units to derive an impact crater size frequency distribution-based absolute chronology. The recent utilization of techniques of buffered crater counting and related methods has recently provided a basis for linking the sequence of events in the geology/stratigraphy to an absolute chronology [4]. We now have an interpretative framework for the geologic history of Venus that can be used as a basis for identifying outstanding questions and applying a wide range of modeling techniques to address these questions.

The geological history of Venus can be characterized by three basic consecutive phases (Fig. 1): **Phase I** represents the period prior to the formation age of the geo-morphological/geological units on the surface (the pre-Fortunian Period) and occupies the majority of the history of Venus. Although some rocks comprising the oldest observed preserved unit, the tessera, could date from this era, the observed geologic record starts with Phase II. Phase II is comprised of two regimes, an initial global tectonic regime which begins with the intense tectonic deformation (the Fortunian Period) interpreted to have formed the globally distributed tesserae highlands of thickened crust that comprise about 7.3% of the planet, followed by many tectonic structures in the surrounding highly deformed plains, including ridge belts, groove belts and coronae. The second regime in **Phase 2**, the global volcanic regime, starts with the emplacement of volcanic plains dotted with thousands of small shield volcanoes, and is immediately followed by regional plains interpreted to have been emplaced as flood basalts in lows between the tesserae highlands, and then de-formed by wrinkle ridges. The shield and regional plains comprise 61.3% of the surface of Venus. Thus, the vast majority of the observed surface geologic units on Venus (80.7%) formed over a relatively short period of time (the Fortunian and Guineverian Periods), estimated to have lasted less than several hundreds of millions of years. **Phase III** represents a distinctive change in style, an extended period of global network rifting (the Atlian Period), with rift zones often radiating from topographic rises; volcanism continues (perhaps to today [5]), but is primarily characterized by lobate lava flows associated with the rifts (the network rifting-volcanism regime). In summary, the geological record consists of the majority of history that leaves no geological/geomorphological record (Phase I), followed by Phase II, a period of intense global tectonic deformation followed immediately by global shield plains and regional plains volcanically resurfacing over 60% of the planet, followed by Phase III, relative quiescence and development of a global rifting system linking several broad rises. The last two phases occurred in less than the last ~15-20% of the history of Venus.

This scenario presents multiple major challenges to various modeling communities: internal structure and evolution, mantle convection, thermal evolution, geodynamic, geochemical, petrogenetic, atmospheric origin-dynamics-geochemistry-evolution, ionosphere, solar system formation and evolution. We outline these here.

## PLANETARY PERSPECTIVES:

What phases of typical terrestrial planet evolution (e.g., accretion, satellite acquisition and loss, core formation, crustal segregation/growth/aftermath, magnetic field evolution, volatile acquisition and degassing to form atmosphere/oceans, impact flux and basin formation, mantle and lithospheric evolution, ionospheric structure and evolution, influence of solar and interplanetary environment) can be established, modulated or ruled out from our knowledge of Venus? If Venus transitioned from an Earth-like planet to its current state, when, over what time period, and how did this take place? What is the cause of Venus' slow retrograde rotation? Could Venus have undergone true polar wander? What is the explanation for the lack of a detectable magnetic field? What can evolutionary models say about the presence and fate of a moon(s)? What do solar system evolution models tell us about the initial position and residence time of Venus relative to its current position in the Solar System? What do spin-axis, orbital parameter (e.g., obliquity, eccentricity) evolution models tell us about the evolution of Venus? How can Venus' geologic history models inform us about how plate tectonics might have initiated Earth? How do Venus and Earth fit into the context of new models of exoplanetary system formation and evolution?

## INTERIOR EVOLUTION, MANTLE CONVECTION AND GEODYNAMICS

Venus appears to have undergone a relatively recent distinctive global tectonic phase, followed by a near global volcanic phase, a significant reduction in volcanic flux, followed by an extended rift-dominated phase of tectonism and volcanism. What is the relative role of Pratt, Airy and flexural isostasy in accounting for the current topography of Venus? What are the more detailed, testable predictions of models of the transition from mobile lithospheric lid to stagnant lid regimes? Can geodynamic models explain the observed near-global flood basalt phase following tessera formation? What geodynamic and petrogenetic models can account for the near-global distribution of small shield volcanoes? What coupled geodynamic/petrogenetic models can account for the apparently very viscous magma represented by the steep-sided domes and festoons? How can mantle convection and geodynamic models account for both global small shield volcanoes (<~20 km) and global large shields (>~200 km)? What temperature-dependent crust-mantle viscosity structure seems most consistent with the geological features and evolution? How can geodynamic models distinguish between episodic global resurfacing and a one-time mobile-lid to stagnant lid transition? What does the global and temporal distribution of coronae and large shield volcanoes tell us about mantle convection patterns and the thermal evolution of the lithosphere? Is Venus currently volcanically active? Where and why? Can the current cratering record reveal information about changes in the evolution of CO<sub>2</sub> atmospheric pressure? How can impact flux modeling and observations improve the chronology of Venus' recent geologic history? What does the configuration of the late stage global rift systems tell us about recent mantle convection patterns?

Surface Evolution and Relation to Atmosphere and Interior: What was the nature of the global event that produced the tessera terrain? Was it truly global and what was the duration of this event? What do models of atmospheric evolution and climate change predict about the influence of the thermal structure of the crust and lithosphere how changes could be reflected and recognized in the style of tectonic deformation? What explains the common correlation of coronae and rift zones? Are coronae causing rifting, or is rifting inducing upwelling? On the basis of comparative planetology modeling, what is the most plausible scenario for the nature and fate of water and oceans in earlier Venus history? How can impact cratering hydrocode models increase our understanding of crustal and mantle structure and evolution? How can impact cratering hydrocode models inform us about the influence of major impact events on the atmosphere? How can physical volcanology models explain the apparent dearth of pyroclastic deposits? How can volcanic eruption and impact crater ejecta modeling link Venera lander panoramas to global processes?

## IONOSPHERE, ATMOSPHERE, CLIMATE AND HYDROSPHERE

What are the most plausible current models for the history and evolution of the climate of Venus? What was the nature of the evolutionary transition to the current atmosphere? Was it gradual, or did the apparently short-term global





# RIFT ZONES OF VENUS: POSSIBLE TERRESTRIAL ANALOGUES

E.N. Guseva

*Vernadsky Institute of Geochemistry and Analytical Chemistry of RAS, Moscow, Russia. Contact: guseva-evgeniya@ya.ru*

## INTRODUCTION:

The terrestrial plate tectonics likely does not work on Venus [1]. Because of this, rift zones within the stable platforms on Earth may represent as a possible analog of the Venusian rift zones. The similarities of the rifts of Venus with the intracontinental rifts on Earth were noted earlier [2-4].

## THE GOAL OF THE STUDY

was to compare the results of the investigation of the rift zones of Venus (Atla and Beta regions) with the rift zones in the East African Rift System. This comparison can provide new information for a better understanding of the mechanism of rift formation on Venus.

## THE EAST AFRICAN RIFT SYSTEM (EARS)

is formed in a stable platform region [5; 6]. This is the largest system of classical continental rifts of the Earth, which extends for more than 6000 km and consists of Western and Eastern branches [7; 8]. The Western branch has no spatial association with the dome-like rises and is characterized by a narrow, 40-100 km wide and deep (~ 3 km) rift valley [7; 9; 10], which is accompanied by weak volcanic activity [11]. The Eastern branch occurs in association with the dome-like rises and is characterized by a slightly wider (~ 50-150 km) and less deep (~2 km) rift valley [7]. Fissure-related lava fields and volcanoes of a central type commonly occur in association with Eastern branch [7; 11].

The NW-SE extension dominates within the EARS and determines the direction of opening of the rift valleys in both branches [8]. The EARS began to form and developed in the Cenozoic due to influence of a mantle diapir on the thick (~100 km) continental lithosphere [12; 13].

## THE RIFTS ZONES OF VENUS

extend for thousands of kilometers and represent wide (hundreds of km) zones of deformation [14; 15]. Topographically, they are deep (up to several kilometers) canyons and are associated with the dome-shaped rises of the Beta-Atla-Themis region [16]. These rises are classified as rifts-associated ones [17] and are interpreted as areas elevated by the action of mantle diapirs [e.g., 3]. The rift valleys usually propagate from the top of the rises [18]. The rift valleys in Atla Regio have a width from 170 to 385 km and a depth of 1.5-2.5 km [15]. These valleys are spatially associated with lava

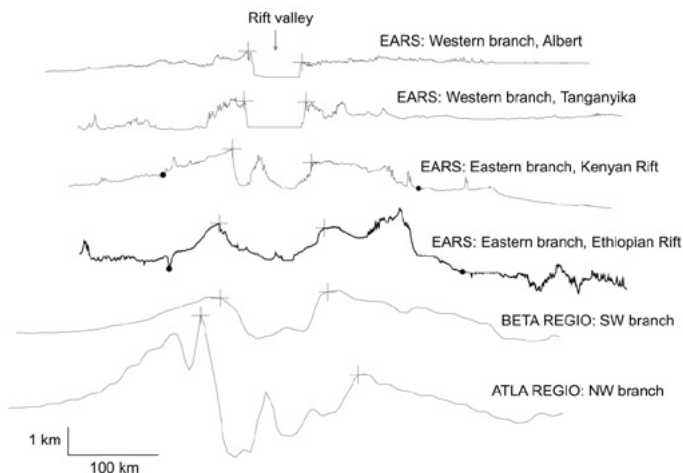


Fig. 1. (left). The rift valleys of Venus and Earth in cross-section of the middle part of rifts.

fields a few hundred kilometers across [19] and with large volcanoes of Maat and Ozza Mons [17]. The rift valleys of Beta region are about 180-235 km wide and about 1.5-2 km deep [15]. They are spatially associated with extensive lava plains [19] and a large volcano of Theia Mons [17; 20].

## DISCUSSION AND CONCLUSIONS:

The rifts of Atla and Beta regions and the Eastern branch of EARS are spatially associated with the dome-shaped rises [21; 22]. The Venusian domes, however, are much larger than their terrestrial counterparts. The largest dome is observed in Beta Regio, it is about 2000-2500 km across [23; 17; 20] and ~ 5 km high [23]. The dome of Atla Regio is slightly smaller, it is about 1600 km across and about 2.5 km high [17]. These characteristics significantly exceed those of the terrestrial rises. The Kenyan and the Ethiopian domes are about 1000 km across [24; 25] and reach 1.5-2 km in height [7]. The rift zones of Atla and Beta were formed on top of the Venusian domes as a result of cracking and extension of the lithosphere [26; 21].

The length of individual rift branches of Venus varies from 1300 to 3300 km, while the length of the Eastern branch of the EARS is ~ 1200 km, and the Western branch is ~ 1500 km long. The rift zones of the studied regions of Venus and Earth are expressed in relief by linear graben with pronounced flanks (Fig. 1). The rift valleys of Atla and Beta regions are about twice as wide as the rift valleys of Eastern Africa. The width of the rift valleys in Atla Regio is ~ 270 km, and in Beta region it is ~ 200 km, on the average. The width of the rift valleys of EARS: in the Western branch it is ~ 90 km and in the Eastern branch it is ~ 140 km, on the average. At the same time, the visible depths of the Venusian rift valleys are similar to the depths of the terrestrial valleys in the Eastern branch and are smaller than the valleys in the Western branch. On the average, the depth of the rifts in Atla Regio is ~ 2 km, in Beta region it is ~ 1.8 km, for the EARS Eastern branch it is ~ 2 km [7], and for the Western branch it is ~ 3 km [7; 10].

The rift-bearing domes of Atla and Beta are about twice as large as their terrestrial analogues and the Venusian rift valleys are about two times longer and wider than the terrestrial counterparts. However, estimates of the horizontal extension of the rift zones of Venus are noticeably smaller than the total extension of the continental rifts of EARS. The estimates of horizontal extension for the rift zones in Atla are about 2% and are ~ 3% for Beta, whereas these estimates for the African rifts are ~ 8% for the Western branch [8; 9] and ~10% for the Eastern branch of the EARS [27].

The general similarities in the shape, association with the dome-like rises and abundant volcanism suggest that the mechanisms of rifting in Atla and Beta, and in the Eastern branch of the EARS are similar. The differences in the morphometric characteristics of the studied rifts are probably due to different thicknesses of the pre-rifting lithosphere. The rift zones of Venus were probably formed on a thicker lithosphere than that in the EARS (Fig. 2).

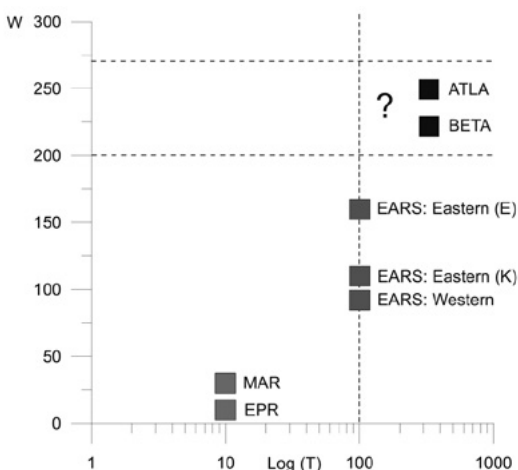


**Fig. 2.** (right). Correlation of thickness pre-rifting lithosphere (T) with a width of rift valley (W): EPR – East Pacific Rise; MAR – Mid-Atlantic Ridge; EARS – East African Rift System, Western branch; Eastern branch: (K) Kenyan Rift and (E) Ethiopian Rift; Atla and Beta – rift region's of Venus.

**REFERENCES:**

- [1] Solomon et al. JGR. 1992. V.97. P.13199-13256;  
 [2] Malin and Saunders. SCI. V.196. 1977. P.987-990;  
 [3] McGill et al. GRL. V.8. No.7. 1981. P.737-740;  
 [4] Foster and Nimmo. EPSL. V.143. 1996. P.183-195;  
 [5] Milanovsky, Tectonophys. V 15(65). 1972;  
 [6] Burke//in Ramberg and Neumann, eds. Tectonics and Geophysics of Continental rifts, p. 1-9.1978;  
 [7] Белоусов и др. Восточно-Африканская рифтовая система. т.2. 1974. С. 131-200;  
 [8] Rosendahl. EPS. V.15. 1987. P.445-503;  
 [9] Ebinger. Geol. Soc. Am. Bull.101. 1989. P.885-903;  
 [10] Upcott et al. JGR. V.101. 1996. P. 3247-3268;  
 [11] Логачев, Вулканогенные и осадочные формации рифтовых зон Восточной Африки.1977;  
 [12] Ebinger et al. JGR. V.98. 1993. P.17,821-17,836;  
 [13] Лобковский и др. Современные проблемы геотектоники и геодинамики. 2004. С.107-175;  
 [14] Basilevsky and Head. JGR. V.105. 2000a. P.24.583-24.611;  
 [15] Guseva. SSR. V.50. № 3. 2016. P.184-196;  
 [16] Masursky et al. JGR. V.85. 1980. P.8232-8260;  
 [17] Stofan et al. JGR. V.100. 1995. P.23.317-23.327;  
 [18] Ivanov et al., SSR. V. 49. P.1-11. 2015;  
 [19] Head et al. JGR. V.97. 1992. P.13.153-13.197;  
 [20] Basilevsky and Head. ICR. V.192. 2007. P.167-186;  
 [21] Smrekar et al.//in Venus II, eds. Bougher et al. Univ. of Arizona Press. 1997. P. 845-878;  
 [22] Милановский. Рифтовые зоны континентов. М.: Недра, 1976. 279 С;  
 [23] Campbell et al. SCI. V.226. 1984. P.167-170;  
 [24] Chorowicz. J.AES. V.43. 2005. P. 379-410;  
 [25] Baker and Wohlenberg. NAT. V.229. 1971. P.538-542;  
 [26] Kiefer and Hager. GJR. V.96. 1991. P.20,497-20,966;  
 [27] Bosworth, GEOL. V.15. 1987. P.397-400.

# IMDR REGIO AS THE LANDING SITE OF THE VENERA-D MISSION: A GEOLOGIC PERSPECTIVE

P. D'Incecco<sup>1</sup>, L.S. Glaze<sup>2</sup>

<sup>1</sup>*piero.dincecco@dlr.de*

<sup>2</sup>*Goddard Space Flight Center, Greenbelt, Maryland, US,  
lori.s.glaze@nasa.gov*

## KEYWORDS:

Venera-D, Magellan, Venus Express, Imdr Regio, Idunn Mons, Age determination, Volcanism, Resurfacing, Geologic mapping, Chemistry

## INTRODUCTION:

During the last decades, the geologic history of Venus has been characterized by a major debate on whether the planet underwent a catastrophic or equilibrium resurfacing. While the random global distribution of impact craters indicates that a global rejuvenation of the crust took place about 300-600 Myr ago [1,2] and supports a catastrophic resurfacing [3], the number and non-random distribution of volcanoes on Venus is in contrast with this hypothesis [1], favoring instead a steadier (equilibrium) resurfacing.

Preliminary observations based on the NASA Magellan and on the ESA Venus Express datasets suggest a possibly young geologic age of formation for Imdr Regio, a volcano-dominated large topographic rise of Venus. However, this area still remains poorly studied.

Nonetheless, Imdr Regio offers a great opportunity to improve our understanding of the present style of resurfacing on Venus. Finding evidences that geologically recent volcanic activity occurred over a localized area would point toward a steadier resurfacing, with important implications for the rheological structure of the interior of Venus. For these reasons, we propose Imdr Regio as a potential landing site for the future Venera-D mission [4].

In preparation for consideration of Imdr Regio as a landing site, we are currently planning an extensive geologic study of Imdr Regio. As part of this effort, candidate landing regions within Imdr Regio will be identified.

During the Venera-D mission, we would use remote observations from orbit as well as in-situ measurements of the surface chemical composition and volatile content provided by the Venera-D lander to answer key questions about Imdr's volcanic history.

## BACKGROUND STUDIES ON IMDR REGIO:

Previous studies of this area provided hints pointing toward its relatively young geologic age. Compared to the other volcanic rises of Venus, Imdr Regio exhibits the smallest amount of associated volcanic deposits, with an approximate volume of  $48 \times 10^6 \text{ km}^3$  [5]. Wrinkle ridge patterns predate the formation of the topographic swell and have been uplifted by about 200 m [5]. The density of wrinkle ridges at Imdr is relatively small compared with the neighboring areas [6]. One possible interpretation is that the wrinkle ridges within Imdr Regio have been partially covered by subsequent volcanic eruptions.

More recently, the VIRTIS instrument of the Venus Express mission observed high 1 micron emissivity anomalies which indicate the presence of chemically unweathered lavas on the top and eastern flank of Idunn Mons [7,8], the major volcanic structure (200 km diameter) of Imdr Regio. The emissivity anomalies observed by VIRTIS are possibly due to the occurrence of geologically recent volcanic activity [7,8]. The smaller volume of volcanic deposits, the lower density of wrinkle ridges and the 1 micron emissivity anomalies observed by the VIRTIS instrument on Idunn Mons all suggest that the topographic rise of Imdr Regio might currently be in an early stage of evolution with ongoing volcanic activity.

## GEOLOGIC MAPPING OF THE V-51 QUADRANGLE

We are currently working on a proposal to the NASA Solar System Workings (SSW) Program Element, for assignment of the geologic mapping of the V-51 (Imdr Regio) quadrangle of Venus, that is currently unassigned (<https://planetarymapping.wr.usgs.gov/Target/project/2>). If successful, we will proceed with the mapping following the guidelines provided by previous works [9,10]. We

will divide geologic mapping of the V-51 quadrangle into the three main layers which respectively include: a) all visible tectonic features (i.e., wrinkle ridges, grabens), b) the geomorphologic units, c) impact craters. This geologic mapping is crucial for identifying preferred landing regions for the Venera-D lander. On this regard, we will give priority to relatively unweathered and geologically young volcanic deposits.

## ANALYSIS AND INTERPRETATION OF THE VENERA-D DATASETS

This phase will be focused on the analysis and interpretation of the datasets provided by the Venera-D mission. Looking at Imdr Regio, and in particular at Idunn Mons, we plan to use the dielectric permittivity derived by the higher resolution radar dataset to determine the approximate bulk composition of the surface deposits (assuming the orbiter payload includes radar instrumentation). These results will then be compared to the surface chemistry of the young volcanic deposits retrieved by the Venera-D lander.

The cross-correlation between morphometry, chemical composition and volatile content of young volcanic deposits of Imdr Regio may provide better constraints on the style and rate of currently active volcanism on Venus.

## REFERENCES:

- [1] Strom, R. G., Schaber, G. G., Dawson, D. D., 1994. The global resurfacing of Venus. *J. Geophys. Res.*, 99(E5), 10899–10926, doi:10.1029/94JE00388.
- [2] Nimmo, F., Mckenzie, D., 1998. Volcanism and tectonics on Venus. *Annu. Rev. Earth Planet. Sci.*, 26, 23-51, doi: 10.1146/annurev.earth.26.1.23.
- [3] Turcotte, D. L., Morein, G., Roberts, D., Malamud, B. D., 1999. Catastrophic Resurfacing and Episodic Subduction on Venus. *Icarus*, 139, 1, 49-54, ISSN 0019-1035, <http://dx.doi.org/10.1006/icar.1999.6084>.
- [4] Zasova, L.V., Ignatiev, N.I., Gerasimov, M.V., 2014. Future Venus exploration: mission Venera-D. Venus Exploration Targets Workshop, #6037.
- [5] Smrekar, S.E., Kiefer, W.S., Stofan E.R., 1997. Large volcanic rises on Venus, in Bougher, S.W., et al., eds., *Venus II: Geology, geophysics, atmosphere and solar wind environment*: Tucson, Univ. of Ariz. Press, p. 845-878.
- [6] Bilotti, F., Suppe, J., 1999. The Global Distribution of Wrinkle Ridges on Venus, *Icarus*, Volume 139, Issue 1, 137-157, ISSN 0019-1035, <http://dx.doi.org/10.1006/icar.1999.6092>.
- [7] Smrekar, S. E., et al., 2010. Recent hot-spot volcanism from VIRTIS Emissivity data. *Science*, 328, 5978, 605-608.
- [8] D’Incecco, P., Mueller, N., Helbert, J., D’Amore, M., 2016b. Idunn Mons on Venus: location and extent of recently active lava flows. *Planetary and Space Science journal*, available online 21 December 2016, ISSN 0032-0633, <http://dx.doi.org/10.1016/j.pss.2016.12.002>.
- [9] Tanaka, Kenneth L.; Schaber, G. G.; Chapman, M. G.; Stofan, E. R.; Campbell, D. B.; Davis, P. A.; Guest, J. E.; McGill, G. E.; Rogers, P. G.; Saunders, R. S.; Zimbelman, J. R., 1993. *The Venus geologic mappers’ handbook*, USGS OFR, 93-516.
- [10] Wilhelms, D.E., 1990. Geologic mapping, in Greeley, Ronald, and Batson, R.M., *Planetary Mapping*: New York, Cambridge University Press, 208-260.

# OVERVIEW OF JUNO RESULTS

S. Bolton<sup>1</sup>, J. Connerney<sup>2</sup>, S. Levin<sup>3</sup>

<sup>1</sup>SwRI,

<sup>2</sup>NASA-GSFC,

<sup>3</sup>JPL

NASA's Juno mission to Jupiter launched in 2011 and arrived at Jupiter on July 4, 2016. Juno's scientific objectives include the study of Jupiter's interior, atmosphere and magnetosphere with the goal of understanding Jupiter's origin, formation and evolution. An extensive campaign of Earth based observations of Jupiter and the solar wind were orchestrated to complement Juno measurements during Juno's approach to Jupiter and during its orbital mission around Jupiter. This presentation provides an overview of results from the Juno measurements and the collaborative campaign during the early phases of Juno's prime mission. Scientific results include Jupiter's interior structure, magnetic field, deep atmospheric dynamics and composition, and the first in-situ exploration of Jupiter's polar magnetosphere and aurorae.

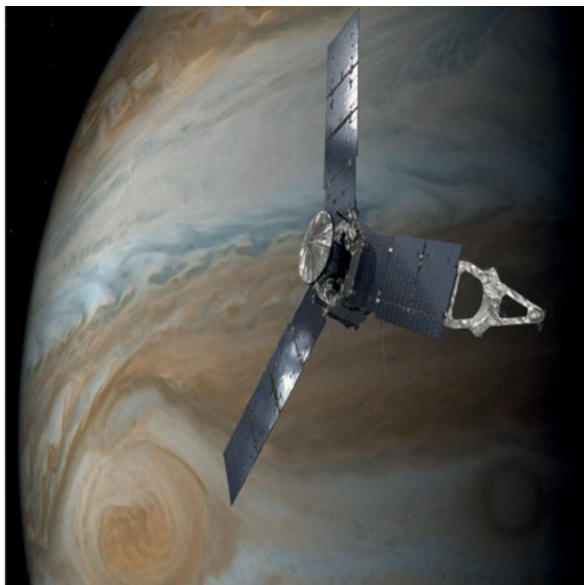


Fig. 1.

# JUPITER'S MAGNETIC FIELD AND MAGNETOSPHERE: JUNO'S FIRST EIGHT ORBITS

J. E. P. Connerney<sup>1,2</sup>, D. J. Gershman<sup>1,3</sup>, S. Kotsiaros<sup>1,3</sup>, J. L. Joergensen<sup>4</sup>, P. S. Joergensen<sup>4</sup>, J. M. G. Merayo<sup>4</sup>, J. Bloxham<sup>5</sup>, K. M. Moore<sup>5</sup>, S. J. Bolton<sup>6</sup>, S. M. Levin<sup>7</sup>

<sup>1</sup>NASA Goddard Space Flight Center, Greenbelt, MD, United States  
jack.connerney@nasa.gov

<sup>2</sup>Space Research Corporation, Annapolis, MD, United States.

<sup>3</sup>University of Maryland College Park, College Park, Maryland, United States.

<sup>4</sup>Technical University of Denmark (DTU), Lyngby, Denmark.

<sup>5</sup>Harvard University, Cambridge, MA, United States.

<sup>6</sup>Southwest Research Institute, San Antonio, TX, United States.

<sup>7</sup>Jet Propulsion Laboratory (JPL), Pasadena, CA, United States.

## KEYWORDS:

Jupiter's magnetic field; magnetosphere; magnetodisc;

## INTRODUCTION:

The Juno spacecraft entered polar orbit about Jupiter on July 4, 2016, embarking upon an ambitious mission to map Jupiter's magnetic and gravitational potential fields and probe its deep atmosphere, in search of clues to the planet's formation and evolution [1]. Juno is also instrumented to conduct the first exploration of the polar magnetosphere [2] and to acquire images and spectra of its polar auroras and atmosphere.

Juno's 53.5-day orbit trajectory carries her science instruments from pole to pole in approximately 2 hours, with a closest approach to within  $\sim 1.05 R_J$  of the center of the planet (one  $R_J = 71,492$  km, Jupiter's equatorial radius), just a few thousand km above the clouds. Repeated periapsis passes will eventually encircle the planet with a dense net of observations equally spaced in longitude ( $<12^\circ$  at the equator) and optimized for characterization of the Jovian dynamo [3]. Such close passages are sensitive to small spatial scale variations in the magnetic field and therefore many such passes are required to bring the magnetic field into focus. Nevertheless, after only 8 orbits, low-degree spherical harmonics can be extracted from a partial solution to a much more complicated representation (e.g., 20 degree/order), providing the first new information about Jupiter's internal magnetic field in decades.

Juno is equipped with two magnetometer sensor suites [3], located 10 and 12 m from the center of the spacecraft at the end of one of Juno's three solar panel wings. Each contains a very accurate (100 ppm absolute vector accuracy) fluxgate magnetometer (FGM) sensor and a pair of co-located non-magnetic star tracker camera heads, providing accurate attitude determination for the FGM sensors. The co-located star cameras monitor the attitude of the magnetometer sensors continuously (providing up to 4 quaternions/s), correcting for the slight deformation of the spacecraft solar array experienced during maneuvers and periapse passes. Such deformations, if not measured and corrected, would otherwise compromise measurement vector accuracy.

Juno's 53-day orbit trajectory also carries her fields and particles instruments to great distances in the magnetosphere ( $\sim 110 R_J$ ) at apoapse. This affords ample opportunity to sample the distant magnetodisc and source regions linked to Jovian aurora, for comparison with infrared [4] and ultraviolet [5] images of Jovian aurora. We present an overview of the magnetometer observations obtained during Juno's first year in orbit [6,7] in context with prior observations and those acquired by Juno's other science instruments [8,9].

## REFERENCES:

- [1] Bolton, S. J. and the Juno Science Team (2010). The Juno mission. *Proceedings of the International Astronomical Union Symposium*, No. 269: 92-100.
- [2] Bagenal, F., Adriani, A., Allegrini, F., et al.: Magnetospheric science objectives of the Juno mission, *Space Sci. Rev.*, doi 10.1007/s11214-014-0036-8.
- [3] Connerney, J. E. P., Benn, M., Bjarno, et al. (2017) The Juno Magnetic Field Investigation, *Space Sci. Rev.*, doi: 10.1007/s11214-017-0334-z.
- [4] Adriani, A., Filacchione, G., Di Iorio, T., et al.: JIRAM, the Jovian infrared auroral mapper, *Space Sci. Rev.*, doi 10.1007/s11214-014-0094-y.



- [5] Gladstone, G. R., Persyn, S. C., Eterno, J. S., et al.: The ultraviolet spectrograph on NASA's Juno mission, *Space Sci. Rev.*, doi: 10.1007/s11214-014-0040-z.
- [6] Bolton, S. J., Adriani, A., Adumitroaie, V., et al.: Jupiter's interior and deep atmosphere: the first pole-to-pole pass with the Juno spacecraft, *Science*, doi: 10.1126/science.aal2108, 2017.
- [7] Connerney, J. E. P., Adriani, A., Allegrini, F., et al., Jupiter's Magnetosphere and Aurorae Observed by the Juno Spacecraft During its First Polar Orbits, *Science*, 10.1126/science.aam5928, 2017.
- [8] Mauk, B. H., Haggerty, D. K., Jaskulek, S. E., et al.: The Jupiter Energetic Particle Detector Instrument (JEDI) Investigation for the Juno Mission, *Space Sci. Rev.*, doi: 10.1007/s11214-013-0025-3.
- [9] McComas, D. J., Alexander, N., Allegrini, F., et al.: The Jovian auroral distributions experiment (JADE) on the Juno mission to Jupiter, *Space Sci. Rev.*, doi:10.1007/s11214-013-9990-9.

# PROFILING THE JOVIAN HIGH ENERGY PARTICLE FLUX AT JUNO'S TRAJECTORIES

John Leif Joergensen<sup>1</sup>, Peter S. Joergensen<sup>1</sup>, Julia Sushkova<sup>1</sup>, Trolz Denver<sup>1</sup>, Ian E. P. Connerney<sup>1,4</sup>, John E. P. Connerney<sup>2,3</sup>, Scott J Bolton<sup>5</sup>, Steven M Levin<sup>6</sup>

<sup>1</sup>Technical University of Denmark (DTU), Lyngby, Denmark.

<sup>2</sup>NASA Goddard Space Flight Center, Greenbelt, MD, United States.

<sup>3</sup>Space Research Corporation, Annapolis, MD, United States.

<sup>4</sup>Virginia Polytechnic Institute & State University, VA, United States.

<sup>5</sup>Southwest Research Institute, San Antonio, TX, United States.

<sup>6</sup>Jet Propulsion Laboratory (JPL), Pasadena, CA, United States.

Juno was launched August 5th, 2011, and entered the highly-elliptical polar orbit about Jupiter on July 4th, 2016, some 5 years later. Juno's science objectives include, the mapping of Jupiter's gravity and magnetic fields and observation of the planet's deep atmosphere, aurora and polar regions [1]. The Juno MAG instrumentation is accommodated on a boom at the end of one of the solar arrays, and consists of two magnetometer sensor suites each instrumented with two star trackers for accurate attitude determination at the MAG sensors [2]. The inboard magnetometer is located 10m from the spin axis of Juno and the outboard at 12m.

This configuration ensures minimal magnetic disturbance to the magnetometers from other equipment onboard the spacecraft, but also put severe mass constraints on the allowable radiation shielding and performance envelope of the collocated, otherwise non-magnetic, star trackers. Only a modest amount of radiation shielding material protecting the star camera CCDs could be accommodated on each Magnetometer Optical Bench (MOB), and as a result the CCDs has to cope with unusually high levels of penetrating energetic particles, in spite of a Juno trajectory optimized to avoid the worst part of the fierce energetic particle flux.

By virtue of Juno's orbit, and the moderate shielding level of the star trackers, the majority of energetic particle flux penetrating to the star tracker's CCD consists of e<sup>-</sup> with energies >15MeV and, to a much lesser, extent p<sup>+</sup> with energies >80MeV. To reliably fulfill the star tracker's attitude determination requirements, even within regions characterized by high radiation fluxes, a special morphological filter has been developed whereby ionization signatures are removed from CCD images. This allows the ensuing matching of star centroids against the onboard star catalog to proceed with limited interference from penetrating radiation. This system tolerates more than 10,000 penetrating particles per integration time (0.25 s) of the CCD. This filter has proven to operate extremely well, and the star tracker's attitude determination requirements have been met thus far in all environments encountered in orbit around Jupiter.

The star tracker hotspot filter detects and removes the signatures from passing energetic particles, as when doing so, stores information about the particle signatures removed. One of the metrics recorded tracks the number of objects removed by the hotspot filter. By telemetering this "particle count number" to ground, this functionality is repurposed as a very precise high-energy particle detector. Since the magnetometer star trackers operate at a cadence of up to 4Hz (typically near periapsis), the high energy electron flux experienced by Juno is measured at a rate of up to 4 times per second. In the more distant magnetosphere, the sample rate falls to 1 per s or 1 per several seconds, depending on telemetry allocation constraints.

Juno's elliptical trajectory carries the spacecraft from 110R<sub>J</sub> to 1.05R<sub>J</sub>, where 1 R<sub>J</sub> = 71,492 km, throughout which the energetic particle flux is measured continuously: from deep space, through the magneto-disk and the radiation horns at low mid-latitudes, and through periapsis just over the Jovian cloud tops [3,4] near the equator. Enroute Juno often passes field lines connecting to the Jovigraphic equator at radial distances mapping to Jovian satellites.

We present the radiation environment encountered in the first 8 science orbits of Juno, and discuss the fluxes of penetrating radiation measured and the main radiation belt features.

**REFERENCES:**

- [1] Bolton, S. J. and the Juno Science Team (2010). The Juno mission. *Proceedings of the International Astronomical Union Symposium*, No. 269: 92-100.
- [2] Connerney, J. E. P., Benn, M., Bjarno, et al. (2017) The Juno Magnetic Field Investigation, *Space Sci. Rev.*, doi: 10.1007/s11214-017-0334-z.
- [3] Bolton, S. J., Adriani, A., Adumitroaie, V., et al.: Jupiter's interior and deep atmosphere: the first pole-to-pole pass with the Juno spacecraft, *Science*, doi: 10.1126/science.aal2108, 2017.
- [4] Connerney, J. E. P., Adriani, A., Allegrini, F., et al., Jupiter's Magnetosphere and Aurorae Observed by the Juno Spacecraft During its First Polar Orbits, *Science*, 10.1126/science.aam5928, 2017.

# FRAGMENTATION OF PLANETESIMALS AND CAPTURE OF MATERIAL BY THE CIRCUMPLANETARY DISKS OF JUPITER AND SATURN

V.A. Kronrod<sup>1</sup>, A.B. Makalkin<sup>2</sup>

<sup>1</sup>V.I. Vernadsky Institute of Geochemistry and Analytical Chemistry RAS, Moscow, va\_kronrod@mail.ru;

<sup>2</sup>O.Y. Schmidt Institute of Physics of the Earth RAS, Moscow

## KEYWORDS:

Jupiter, Saturn, Ganymede, Callisto, Titan, circumplanetary disk, planetesimals, aerodynamic braking, ablation, fragmentation

We simulated planetesimals passing through the circumplanetary disks of Jupiter and Saturn and capture of their material into the disks with consideration of combined processes of aerodynamic braking, fragmentation, and ablation of planetesimals in the disk's gas medium. Described below are the results of simulation for the comet material of the planetesimals. We estimated maximum planetesimal size which the body should have at the entrance to the disk in order to stay in the disk after losing mass and velocity due to gas drag and ablation. We have obtained limitations on planetesimal at which the body is fragmented and its mass remains in the protosatellite disk. The conditions for disk capture of the entire mass of planetesimals are different for satellites. For material strength  $2 \cdot 10^4 \text{ Pa} < \sigma < 2 \cdot 10^5 \text{ Pa}$  (scale factor  $\lambda=0.2$ ) a significant difference in the total masses of planetesimals with radii from 0 to 10 km capturing by the circumplanetary disks in the feeding area of Ganymede, Callisto and Titan is possible and could lead to a low differentiation of Callisto and Titan compared to Ganymede.

## INTRODUCTION

Here we consider the problem of interaction of the circumplanetary disk and solid bodies (planetesimals) falling onto the disk. We suppose that solution of the problem will allow estimation of the masses and composition of bodies that fell on the growing icy moons. This would provide explanation of the differences in the mean density and internal structure of icy moons of Jupiter and Saturn [1]. The multiparameter problem of gas drag, fragmentation and ablation of planetesimals in the gas medium of the circumplanetary disk is solved by a modified approach of the meteor physics [2-4]. The formulation of the problem and the solution method are described in [5]. In the present work, the processes of fragmentation of planetesimals during the passage of the gas medium of the disk and their influence on the mass captured by the disk are discussed.

## THE MOTION AND LOSS OF MASS OF THE BODIES IN THE DISK

We simulated passing planetesimals through the circumplanetary disks of Jupiter and Saturn and capture of their material into the disks with consideration of combined processes of aerodynamic braking and ablation of planetesimals in the disk's gas medium. We estimated maximum planetesimal size (radius  $R_{1,max}$ ) which the body should have at the entrance to the disk in order to stay in the disk after mass and velocity loss due to gas drag and ablation. The maximum radius of captured planetesimal  $R_{1,max}$  is obtained as a function of distances from the central planet. For the planetesimals with radii  $R > R_{1,max}$  which were able to escape the disk, the velocities at the exit after crossing the disk should be higher than the escape velocity from the Hill (gravitational) sphere of the planet.

## FRAGMENTATION OF THE BODIES

We assume the start of mechanical fragmentation process at the moment when the magnitude of the dynamical pressure  $\rho_g V^2$  becomes of the order of the body strength  $\sigma$ . The value of  $\sigma$  depends on body size, according to the statistical theory of strength [6]:  $\sigma = \sigma^*(m^*/M)^\lambda$ , where  $\sigma^*$  и  $m^*$  are the strength and mass of the tested specimen,  $\sigma$  is an effective strength of the body

of the same material, but with mass  $M$ . Planetesimals of a larger size have less effective strength and can be destroyed by the action of the gas stream, while smaller planetesimals remain intact under similar conditions. The smallest radius of planetesimals of not subjected to fragmentation ( $R_{f, \min}$ ). We use the scale factor  $\lambda=0.2$  adopted for material of the comet [7]. In case of the destruction of planetesimals in the body with radii  $R_{f, \min} < R_{f, \max}$ , all the total mass of the fragments remain in the disk. For sufficiently large bodies, the forces of self-gravitation of planetesimals become of the same order as the forces of dynamic pressure. In this case, the body cannot be broken into large fragments. Estimates of the minimum body size ( $R_{f, \min}$ ), not fragmented as a result of self-gravitation, are given in [8]:  $\approx 10$  km for ice bodies and  $\approx 20$  km for stone bodies. We assume that the planetesimals consist of a substance identical to the comet,  $R_{f, \min} \approx 10$  km. All planetesimals with radii from  $R_{f, \min} < R_{f, \max}$  will be destroyed to fragments with dimensions  $R < R_{f, \min}$ . It can be assumed that when the condition  $R_{f, \min} < R_{f, \max}$ , the entire mass of planetesimals in the satellite feed zone in the range of sizes  $0 < R < R_{f, \min}$  remains in the disk.

## COMET STRENGTH:

The strength of the substance of comets in tension, shear and compression has been investigated many times by several independent methods. There is no consensus about the strength of cometary material, primarily because of the scale factor. According to estimates [9], the strength at the scale of a comet is estimated to be  $\sigma^* \sim 100$  Pa. Based on the average size of comets of 5-10 km and their average density of 0.5-0.6 g/cm<sup>3</sup>, for a sample with mass  $m^* = 1 \cdot 10^3$  g, we obtain strength estimates  $\sigma^* = (4-12)$  kPa. Estimates of the strength of the comet at scales of 10 m - 1 km were carried out for comet 67P [10]. The tensile strength of 3-15 Pa (upper limit of 150 Pa) was obtained, the shear strength was determined to be 4-30 Pa.

## RESULTS:

Simulation of joint processes of aerodynamic braking, fragmentation, and ablation (a comet substance) in the gas environment of the accretion disks of Jupiter and Saturn was carried out. The values of the maximum capture radius  $R_{f, \max}$  and the radii of fragmentation of planetesimals  $R_{f, \min}$  are determined, depending on the scale factor and strength of the substance at distances of the regular satellites of Jupiter and Saturn (Fig. 1, Fig. 2). The strengths of weak (IIIB) and strong (IIIA) cometary material, carbonaceous (II) and ordinary (I) chondrites according to the classification [11] are shown in the Fig. 2. It follows from Fig. 2 that the entire mass of planetesimals with radii

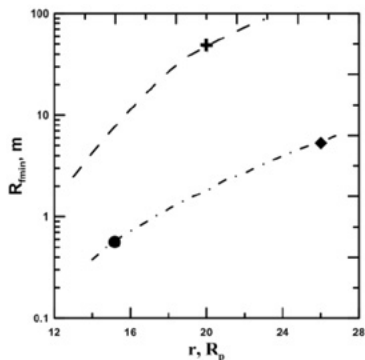


**Fig. 1** Dependence between the minimum radius of fragmentation of planetesimals  $R_{f, \min}$  in Jupiter systems (dot-dashed line) and Saturn (dashed line) and the distance to the central planet  $r$ . The circle, the rhombus, the cross -  $r$  at the distances of Ganymede, Callisto, Titan, respectively. The strength of the planetesimal substance is  $\sigma^* = 10^4$  Pa, the scale factor  $\lambda=0.2$ .

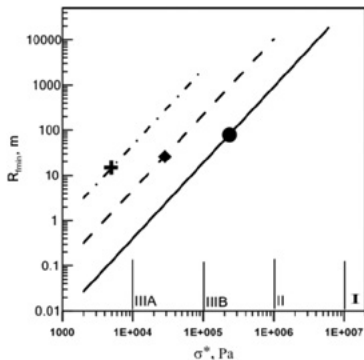


**Fig. 2** Dependence of the minimum radius of fragmentation of planetesimals  $R_{f, \min}$  on the strength of planetesimals  $\sigma^*$  at the distances of Ganymede from the central planet (solid line), Callisto (dashed line). The circle, the rhombus, the cross are the points of equality to the values of the maximum radii of capture of the planetesimal disk ( $R_{f, \min} = R_{f, \max}$ ) at the distances of Ganymede, Callisto, Titan, respectively. In the case of  $R_{f, \min} < R_{f, \max}$ , all the matter falling on the disk is captured by the disk. The scale factor is  $\lambda = 0.2$ . The abscissa axis shows the strength of meteoritic matter in accordance with the classification [11]

$R < R_{\text{crit}}$  is captured by a disk under the condition:  $\sigma < 2 \cdot 10^5$  Pa for Ganymede,  $\sigma < 2 \cdot 10^4$  Pa for Callisto and  $\sigma < 5 \cdot 10^3$  Pa for Titan. Thus, for a material strength of  $2 \cdot 10^4$  Pa  $< \sigma < 2 \cdot 10^5$  Pa, a significant difference in the amount of matter captured by the disk in the feeding region of the regular ice satellites of Ganymede, Callisto and Titan is possible. This could be one of the main reasons for the low differentiation of Callisto and Titan compared to Ganymede.

## CONCLUSION

Fragmentation of planetesimals can be the main parameter in the mechanism of capture of planetesimals by the accretion disks of giant planets. The presence of fragmentation is perhaps one of the reasons for the difference in the internal structure of Ganymede, Callisto and Titan.

## ACKNOWLEDGMENTS

This research was supported by the RFBR grant 15-05-0257 and 15-05-01161.

## REFERENCES:

- [1] Kuskov O.L., Dorofeeva V.A., Kronrod V.A. Makalkin, A.B. Jupiter and Saturn Systems: Formation, Composition, and Internal Structure of Large Satellites, Moscow: Izd. LKI. 2009.
- [2] Bronshten V.A. Physics of Meteoric Phenomena. D. Reidel Publishing Company, Dordrecht. 1983.
- [3] Stulov V.P., Mirskii V.N., Vislyi A.I. Aerodinamika bolidov. Nauka, Moscow (in Russian). 1995.
- [4] Gritsevich, M., and Koschny, D., Constraining the luminous efficiency of meteors // Icarus, 2011. V. 212. № 2. P. 877-884.
- [5] V. A. Kronrod, A. B., Makalkin. Capture of bodies into the circumplanetary disks of young Jupiter and Saturn // Lunar and Planetary Science XLVIII. 2007. 1096.pdf.
- [6] Weibull W. A statistical theory of the strength of material // Proc. Roy. Swedish Inst. Engn. Res. 1939. V.151. P. 1-45.
- [7] Petrovic J.J. Review Mechanical properties of ice and snow // Journal of materials science. 2003. V. 38. P.1– 6.
- [8] D'Angelo G., Podolak M. Capture and evolution of planetesimals in circumjovian disks // The Astrophysical Journal. 2015. V. 806. P. 203 (29pp).
- [9] Bar-Nun A., Pat-El I., Laufer D. Comparison between the findings of Deep Impact and our experimental results on large samples of gas-laden amorphous ice // Icarus. 2007. V. 187, Issue 1, P. 321-325.
- [10] Groussin O., L. Jorda, A. T. Auger. et al. Gravitational slopes, geomorphology, and material strengths of the nucleus of comet 67P/Churyumov-Gerasimenko from OSIRIS Observations // A&A 583, A32 (2015). DOI: 10.1051/0004-6361/201526379.
- [11] Revelle D. O. Recent advances in bolide entry modeling: a bolide potpourri // Earth, Moon, and Planets. 2005. V. 97. P. 1–35. DOI 10.1007/s11038-005-2876-4

# EQUATORIAL CURRENT DISK DYNAMICS IN THE JOVIAN MAGNETOSPHERE

I.I. Alexeev, E.S. Belenkaya, V.V. Kalegaev, S.Yu. Bobrovnikov, A.S. Lavruchin, D.A. Parunakian, I.A. Pensionerov  
*Federal State Budget Educational Institution of Higher Education M.V. Lomonosov Moscow State University, Skobeltsyn Institute of Nuclear Physics, Moscow, Russia*

## KEYWORDS:

Jupiter, Juno, magnetosphere, equatorial plasma disk, solar wind

## INTRODUCTION:

After one year of orbiter phase of the Juno's mission in Jupiter's environment a new information about the equatorial magnetodisk response to the solar wind and interplanetary magnetic field dynamics could be received [2].

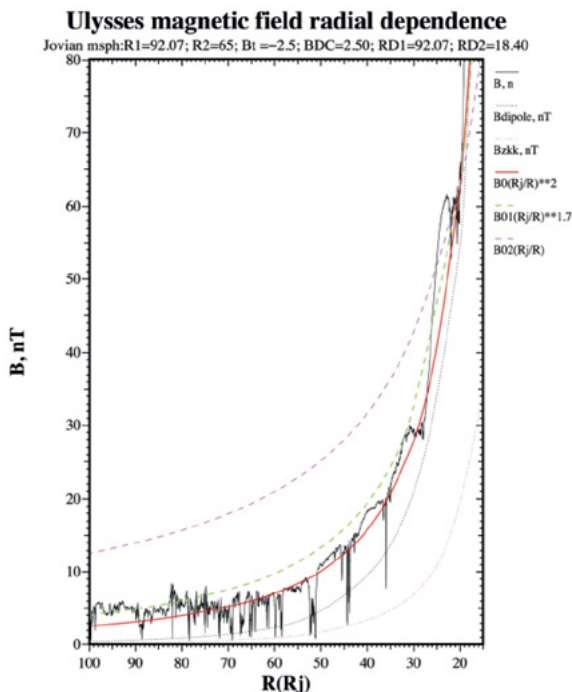


Fig. 1.

Measured by Ulysses the Jovian magnetospheric magnetic field dependent on the radial distance  $r$  is marked by a solid curve [3]. For comparison power law curves with different indexes are also shown. The power law curves were normalized on the measured field strength at  $20 R_j$ : 62.2 nT. Data (PIA. Balogh, Imperial College, London, UK) have been received by using COHOWEB system, NSSDC, NASA/GSFC, USA.

## THE EQUATORIAL MAGNETODISK:

The equatorial plasma disk radial size is determined by the magnetosphere size (subsolar magnetopause distance). The square of the outer disk radius is proportional to the magnetic moment of the disk. The inner planetary dipole and the thin current disk are the main contributors to the magnetospheric magnetic field. The bow shock crossing occurred once at the distance of  $128 R_j$  in the course of Juno JOI orbit on July-Aug 2016. The magnetopause was crossed several times at average distance of  $94 R_j$  (from  $74 R_j$  up to  $114 R_j$ ). Using the paraboloid of revolution approaches for both surfaces (the bow shock and magnetopause) the subsolar distances have been calculated for Juno JOI solar wind conditions. It is known that as a result of plasma disk

formation the Jupiter's magnetospheric size is about twice as large compared to a purely planetary dipole case [1]. But sometimes the Jovian magnetosphere is becoming compressed, as it happened during the Pioneer 10 flyby, when the magnetopause crossing was first observed at  $98 R_J$  and then at  $55 R_J$  and  $48 R_J$ , demonstrating its large variability. In this sense the dependence of the equatorial disk total current on the solar wind conditions is a critical point for Jupiter's outer magnetosphere dynamics.

## REFERENCES:

- [1] Alexeev I.I., and Belenkaya E. S., Modeling of the Jovian Magnetosphere // *Ann. Geophys.*, 2005, V. 23, P. 809-826, <https://doi.org/10.5194/angeo-23-809-2005>.
- [2] Gladstone, G. R., et al., Juno-UVS Approach Observations of Jupiter's Auroras, // *Geophys. Res. Lett.*, 2017, 44, doi:10.1002/2017GL073377
- [3] Cowley, S. W. H., et al., Plasma flow in the Jovian magnetosphere and related magnetic effects: Ulysses observations // *J. Geophys. Res.*, 1996, 101, A7, 15 197–15 210.



# INTERACTION OF JUPITER'S PLASMA WITH THE GALILEAN MOONS

P. Wurz<sup>1</sup>, A. Galli<sup>1</sup>, and A. Vorburger<sup>1</sup>,

<sup>1</sup>Physics Institute, University of Bern, Sidlerstrasse 5, 3012 Bern, Switzerland; peter.wurz@space.unibe.ch

## KEYWORDS:

Jupiter's icy moons, plasma-surface interaction, ice sputtering, icy moons exospheres, JUICE

## INTRODUCTION

The Galilean moons are immersed in the plasma and particle environment of Jupiter's magnetosphere. The interaction of these particles with the surface of the moons results in the release of material from the surface into the exosphere. The JUICE (JUpiter ICy moons Explorer) mission of ESA will visit the three icy Galilean moons, Europa, Ganymede, and Callisto, to perform detailed measurements. Since these moons all have a water ice surface we studied the interaction of these plasma particles with water ice in laboratory experiments and modelled the resulting exospheres.

## MAGNETOSPHERIC PLASMA

There are two particle populations in Jupiter's magnetosphere, which are of concern for this study. The first particle population is the thermal plasma, also called cold plasma, that is more or less co-rotating with Jupiter's rotation [1,2]. The ions are mainly composed of oxygen, sulphur and hydrogen, with relative abundances of  $H^+:O^{n+}:S^{n+} = 1:3:1.7$ . The electron density is slightly higher than the ion density, with averaged values of 200 electrons  $cm^{-3}$  versus 130 ions  $cm^{-3}$ . The second population is the energetic particle populations, also called hot plasma population, with their energy spectra reaching beyond 100 MeV particle energy [3,4,5]. The temperatures of the electrons and ions of the hot plasma population are quite high, with values of 1 keV for electrons and tens of keV for ions. The energy spectrum of the hot ions is generally modelled by a kappa distribution with characteristic energies of a few tens to hundreds keV, and a power-law tail modelling the ions forming Jupiter's radiation belt. The energy spectra for the ions and electrons of the cold and the hot plasma are shown in Figure 1 for the energy range of interest.

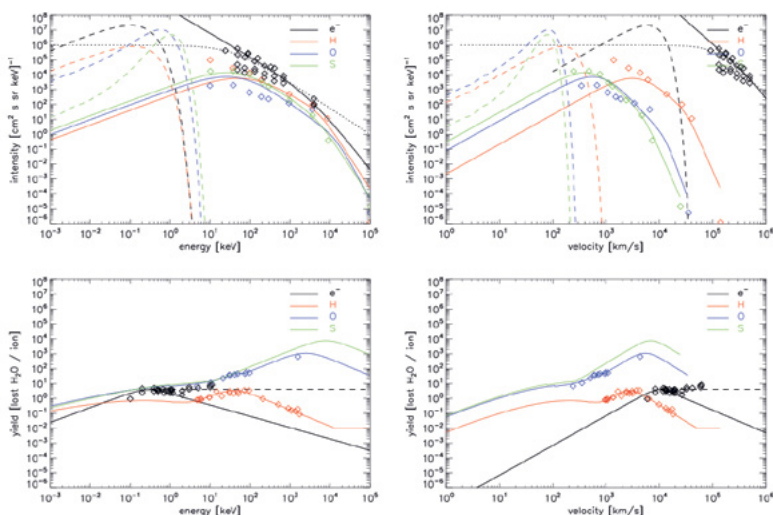


**Fig. 1.** Input data for exospheric modelling from [10]. Top row: Energy spectra for H, O, S ions, and  $e^-$  of the two plasma populations at Europa where points represent measurements and lines give modelled spectra. Bottom row: Sputter yields for water for H, O, S ions, and  $e^-$  for the energy (velocity) range of interest.

## MAGNETOSPHERE-SURFACE INTERACTION

All these plasma populations cause sputtering of surface materials to populate the exospheres of the Galilean moons to various degrees. The neutral exosphere and the thermal plasma interact via charge exchange and electron ionisation, resulting in induced currents in the ionosphere (if existing), in mass loading of the plasma flow (pick-up ions), and in deflection of the plasma flow around the moon [6]. Deflection of plasma ions will reduce the plasma fluxes onto the moon's surface, thereby reducing the sputtering, and in turn the exospheric densities. Thus the moons exospheres and the magnetospheric thermal plasma are intimately coupled. These plasma-surface and plasma-exosphere interaction processes will all occur near the moon, at lengths scales commensurate with the scale height of the dominant exospheric species, thermal  $O_2$ . Some atoms and molecules escape from the moons atmospheres via gravitational escape and ionisation. In case of Europa these loss processes are significant, forming the Europa torus of neutral and ionised particles. Over time, these particles will become part of the plasma of Jupiter's magnetosphere.

## EXPERIMENTAL STUDIES:

There are only a few studies reported in the literature related to sputtering of ice at temperatures relevant to the surfaces of Jupiter's icy moons. These studies were performed on thin layers of ice. However, on the icy moons an ice regolith surface is expected. Therefore, we set up a laboratory experiment to study the interaction of ions and electrons with ice regolith surfaces, with the ice at temperatures between 90 and 150 K to emulate the surfaces of the icy moons [7,8,9]. We studied sputtering by ions ( $H^+$ ,  $O^+$ ,  $O_2^+$ ,  $O^{2+}$ ,  $S^+$ ,  $Ar^+$ , and  $Ar^{2+}$ ) and electrons, measured the sputter yield and composition of the sputtered species, as well as surface charging and sublimation. The sputter yields for the ions (compiled from available literature) and electrons over the energy range of interest are shown in Figure 1. Ion sputter yields for water ice are much higher than for sputtering of minerals, even more so for heavier ions. Therefore, the hot plasma population, although of much lower density than the thermal plasma, contributes significantly to the total sputter yield. Also, the sputter yield of electrons is high already at low energies. Even though the electrons have a low mean energy related to their average movement with the co-rotation velocity, their temperature of about 100 eV is sufficient for a substantial sputter contribution to the exosphere [10].

## EXOSPHERE MODELLING:

We calculate the contribution to the atmospheres of Europa, Ganymede, and Callisto by sputtering (using the two plasma types) and sublimation by modelling the formation of the moons atmospheres ab initio. As inputs to calculate the sputter contribution we use available energy spectra of plasma ions and electrons and the corresponding sputter yields (see Figure 1). Based on first principles we calculate atmospheric densities, without applying any scaling to observed data [10]. For Europa the particle release into exosphere is mostly



**Fig. 2.** Sample holder for regolith ice (with Cu ring) mounted on cryogenic stage, for ion irradiation experiments.

due to sputtering in about equal amounts by the thermal and the hot plasma. Since the plasma densities thin out with distance to Jupiter, the contribution by sputtering becomes less significant, and at Callisto the exosphere is mostly due to sublimation [11].

## REFERENCES:

- [1] Kivelson, M. G., K. K. Khurana, and M. Volwerk, Europa's Interaction with the Jovian Magnetosphere, 2009, p. 545.
- [2] Bagenal, F., E. Sidrow, R. J. Wilson, T. A. Cassidy, V. Dols, F. J. Crary, A. J. Steffl, P. A. Delamere, W. S. Kurth, and W. R. Paterson, Plasma conditions at Europa's orbit, 2015, *Icarus*, 261, 1–13.
- [3] Divine, N., and H. B. Garrett, Charged particle distributions in Jupiter's magnetosphere, 1983, *J. Geophys. Res.*, 88, 6889–6903.
- [4] Cooper, J. F., R. E. Johnson, B. H. Mauk, H. B. Garrett, and N. Gehrels, Energetic Ion and Electron Irradiation of the Icy Galilean Satellites, 2001, *Icarus*, 149, 133–159.
- [5] Paranicas, C., R. W. Carlson, and R. E. Johnson, Electron bombardment of Europa, 2001, *Geophys. Res. Lett.*, 28, 673–676.
- [6] Rubin, M., X. Jia, K. Altwegg, M. Combi, L.K.S. Daldorff, T.I. Gombosi, K. Khurana, M.G. Kivelson, V.M. Tennishev, G. Tóth, B. van der Holst, and P. Wurz, Self-consistent multifluid MHD simulations of Europa's exospheric interaction with Jupiter's magnetosphere, 2015, *Jou. Geophys. Res.* 120, 1–22.
- [7] Galli, A., A. Pommerol, P. Wurz, B. Jost, J.A. Scheer, A. Vorburger, M. Tulej, N. Thomas, M. Wieser, and S. Barabash, Surface charging of thick porous water ice layers relevant for ion sputtering experiments, 2016, *Planet. Sp. Sci.* 126, 63–71.
- [8] A. Galli, A. Vorburger, P. Wurz, and M. Tulej, Sputtering of water ice films: a re-assessment with singly and doubly charged oxygen and argon ions, molecular oxygen, and electrons, *Icarus* 291 (2017a) 36–45.
- [9] A. Galli, A. Vorburger, P. Wurz, A. Pommerol, R. Cerubini, B. Jost, O. Poch, M. Tulej, and N. Thomas, 0.2 to 10 keV electrons interacting with water ice: radiolysis, sputtering, and sublimation, *Icarus* 291 (2017b), 36–45.
- [10] Vorburger, A. and P. Wurz, Monte-Carlo Simulation of Europa's Exosphere, 2017, *Icarus*, submitted.
- [11] A. Vorburger, P. Wurz, H. Lammer, S. Barabash, and O. Mousis, Monte-Carlo Simulation of Callisto's Exosphere, *Icarus* 262 (2015), 14–29.

# THE PROSPECTS FOR ACTIVE AND PASSIVE RADAR PROBING OF GANYMEDE

Y.A. Ilyushin<sup>1,2,3</sup>, P. Hartogh<sup>3</sup>

<sup>1</sup> *Moscow State University, 119992 Russia, ilyushin@phys.msu.ru*

<sup>2</sup> *Institute of Radio-engineering and Electronics of RAS, Mokhovaya 11/7, Moscow 125009 Russia*

<sup>3</sup> *Max-Planck-Institut für Sonnensystemforschung Justus-von-Liebig-Weg 3, Göttingen 37077 Germany hartogh@mps.mpg.de*

## KEYWORDS:

Jupiter, Ganymede, ground penetrating radar, passive radar, ionosphere, magnetosphere

Jovian icy moons are in a certain sense unique objects of the Solar System. Their wave scattering characteristics, e.g. albedo and polarization curves in optical and radar wave bands, notably distinguish them from other types of celestial bodies, i.e. terrestrial and giant planets, comets and asteroids. At least several of them have global liquid water layers (oceans) beneath many kilometers thick icy crusts [1]. Despite of many observational evidences of that, ice thickness and ocean depth are at present rather uncertain. Immediate instrumental assessment of the ice thickness would help to address some key question of icy moons' geology, to constrain parameters of present geological models and derive some implications for chemical composition and internal heat balance and the thermal regime of icy moons.

Electromagnetic probing is the only way to explore the internal structure remotely, e.g. with a ground penetrating radar. Instruments of this type proved to be very useful for investigations of Lunar and Martian interiors. In the vicinity of Jupiter, strong electromagnetic noise generated in the Jovian ionosphere and magnetosphere can mask weak echo signals coming from beneath the icy shell. Transmitted power of the instrument is strictly limited due to the energy budget of the spacecraft and requirements of electromagnetic compatibility with other instruments and devices on board. However, that noise can be effectively used as a signal source for the so-called passive radar. The passive radar in fact is a correlation reflectometer, probing the object with radio waves coming from an external source rather than from its own local transmitter.

Both types of radars have their specific advantages and disadvantages. The active radar is somewhat more convenient in use, since it provides wider freedom of choice in selection of operating frequencies, signal waveforms and other technical parameters, and observational strategies. The passive radar, instead, does not have a transmitter, and can have extremely low weight, size and power consumption. As an option, it can be combined with an active radar instrument and share with it some common units, e.g. the antenna system.

In this talk, we discuss and compare the capabilities of instruments of both types to probe thick and rough icy crusts of the Jovian satellites. We present results of the numerical simulations of performance of active [2] and passive [3] radars on Ganymede for typical geological units of its icy crust. We also built a working prototype of the passive radar instrument [3] and tested it in the laboratory for detection of ionospheric echoes of noise-like radio signals.

The study is partially supported by the Max-Planck-Institut für Sonnensystemforschung. One of the authors (Y.I.) is grateful to the German academic exchange service (DAAD) for the scholarship 50015739 supporting this research. Support from Russian Fundamental Research Fund with the grant 15-02-05476 "Development of new techniques and means of meteorological radar sounding of atmospheric precipitation in the millimeter wave band" and Russian National Fund with the grant 17-77-20087 is also kindly acknowledged. Y.I. thanks the administration of the Scientific Research Computing Center of the Moscow State University for granting the access to the computational resources of the parallel computing systems SKIF-GRID "Tchshebyshev" and "Lomonosov".

## REFERENCES:

- [1] Vance, S., Bouffard, M., Choukroun, M., Sotin, C., Ganymede's internal structure including thermodynamics of magnesium sulfate oceans in contact with ice. // *Planet. Space Sci.* 2014. V.96. P. 62–70.
- [2] Ilyushin Ya.A. Subsurface radar location of the putative ocean on Ganymede:

Numerical simulation of the surface terrain impact. // Planetary and Space Science 2014. V.92. P.121-126.

[3] Hartogh P., Ilyushin Ya. A. A passive low frequency instrument for radio wave sounding the subsurface oceans of the Jovian icy moons: An instrument concept. // Planetary and Space Science. 2016. V.130. P.30-39.

# GAS ENVELOPES OF THE ICY MOONS WITH OCEANS

V.I. Shematovich

*Institute of Astronomy of the Russian Academy of Sciences, Moscow, Russia;*  
*shematov@inasan.ru*

## KEYWORDS:

Giant planets, icy moons, subsurface oceans, neutral gas envelopes, atmospheric biomarkers, kinetic Monte Carlo models.

## INTRODUCTION

The outer solar system contains a diverse array of planetary bodies: Europa, with its bizarre array of surface features; tiny, geologically-active Enceladus; Titan, the only moon with a substantial atmosphere; Pluto, with its nitrogen glaciers; and many others. Over the last twenty-five years spacecraft measurements have revealed that many of these bodies are "ocean worlds", possessing large volumes of liquid water beneath insulating ice shells. Ocean worlds are important for several reasons, but the most compelling is also the simplest: they could be habitable. Life as we know it requires liquid water, in addition to energy and nutrients, and all three requirements can potentially be satisfied within some of these bodies.

There are important reasons that ocean worlds should be studied. First, they represent systems that are both more complex and less well understood than the terrestrial planets. For example, on many ocean worlds the main source of heat is energy extracted from their orbits. There is thus a strong coupling between thermal and orbital evolution that is almost entirely absent from the terrestrial planets. Second, the characteristics of these worlds provide clues to their history, and the evolution of the solar system as a whole. For instance, the fact that tiny Enceladus has managed to retain a global subsurface ocean may be telling us something profound about both its orbital history and the evolution of the Saturnian system.

We focus in particular on the following bodies - Europa, Ganymede, and Enceladus, - for which oceans are currently best established. The simulation results [1-3] of the rarefied gaseous envelopes of these moons will be presented and the relationship between the composition of atmospheres and oceans concerning the possible atmospheric biomarkers will be discussed.

The formation and dynamics of rarefied gas envelope near the icy surface of a celestial body, such as the icy moons of the giant planets, icy Kuiper belt objects, and others, are discussed in this report. In the case of massive icy moons of the giant planets, such as Ganymede and Europa, a tenuous exosphere with relatively dense near-surface layer may be formed. The main parent component of the gaseous envelope is the water vapor entering the atmosphere through the processes of thermal degassing, non-thermal radiolysis, and other active processes and phenomena on the icy surface of the moon. The numerical kinetic model [1] to study on the molecular level the formation, chemical evolution and dynamics of the H<sub>2</sub>O and O<sub>2</sub>-dominant rarefied gas envelopes around the icy celestial bodies is discussed.

Ionization processes in such rarefied gas envelopes occur as a result of exposure to solar ultraviolet (UV) radiation, the solar wind plasma and/or magnetospheric plasma of the giant planet. The chemical complexity of the gaseous envelope of icy satellite is arising due to the impact of the ultraviolet solar photons and plasma electrons onto the rarefied H<sub>2</sub>O- or O<sub>2</sub>-dominated atmosphere. Important role in the formation of chemical diversity in the gaseous envelope belongs to the ionization chemistry, including ion-molecule reactions, dissociative recombination of molecular ions and charge-exchange reactions with the magnetospheric ions. The model was used to calculate the formation and development of chemical diversity in a rarefied gas envelope near the surface of Jupiter's moons Europa [3] and Ganymede [2], and Saturn's moon Enceladus [1].

This work was supported by the Presidium of the Russian Academy of Sciences, Program no. 1.7 "Experimental and Theoretical Studies of Solar System Bodies and Stellar Planetary Systems."

**REFERENCES:**

- [1] Shematovich V.I. Gaseous envelopes of the icy moons// Mechanics, control, and informatics. 2015. V. 7. No. 3(56). P. 270-310.
- [2] Shematovich V.I. Neutral Atmosphere Near the Icy Surface of Jupiter's Moon Gany-mede// Solar System Research. 2016. V. 50. P. 262–280.
- [3] Lucchetti A., Plainaki Ch., Cremonese G., Milillo A., Cassidy T., Jia X., Shema-tovich V. Loss rates of Europa's tenuous atmosphere// Planet. Space Sci. 2016. V. 130. P. 14-23.

# USING VOLATILES TO DETERMINE PLANETARY FORMATION PROCESSES

J.I. Lunine<sup>1</sup>, S. J. Bolton<sup>2</sup>

<sup>1</sup>*Cornell Center for Astrophysics and Planetary Science, Cornell University, Ithaca NY 14853 USA, jlunine@astro.cornell.edu;*

<sup>2</sup>*Southwest Research Institute, 6220 Culebra Road, San Antonio TX 78238 USA, sbolton@swri.edu*

## KEYWORDS:

Solar nebula; protoplanetary disk; planetesimals; water; clathrate; amorphous ice; giant planets; Juno; Jupiter

## INTRODUCTION

The giant planets of our own and other planetary systems are complex self-gravitating assemblages of hydrogen, helium and other elements. How, when and where they formed in a given protoplanetary disk are essential to know as boundary conditions for eventual formation of terrestrial planets in the same system. Because Jupiter and Saturn are mostly hydrogen and helium, like the sun, we know they must have formed early before the dissipation of the proto-planetary nebula. Unlike terrestrial planets, two conceptually distinct modes of formation of giant planets--disk instability versus core accretion--have been proposed. Which of the two different formation mechanisms obtained for Jupiter may be determined by a combination of data on core mass, total abundance of elements other than hydrogen and helium in the envelope, and the abundance pattern of molecular carriers of oxygen, carbon and nitrogen along with noble gases. Juno, in orbit around Jupiter since July 2016, is designed to obtain key data in all three of these areas. Juno's data sets will provide a point of reference for studies of the formation of Saturn and of extrasolar giant planets as well. By using Jupiter as ground truth for studies of exoplanetary metallicity and stellar properties, it may be possible to assess whether two distinct species of giant planets exist in the galaxy -- those formed directly from the disk versus through the growth of a heavy element core.

## WATER IN JUPITER AND IN THE PROTOPLANETARY DISK

While the Galileo probe's measurements during its descent to 22 bars pressure in Jupiter provided tight constraints on the abundances of various heavy elements (carbon, nitrogen, etc.) it did not do so for oxygen, because water, the primary carrier of oxygen, was likely affected by the dynamics of the probe entry site (a 5 micron hot spot). A key objective of the Juno mission is to determine the global water abundance in Jupiter so as to complete the inventory of molecular carriers of the major elements for comparison with models of planetesimals in the solar nebula. Alternate models for planetesimal compositions within the protoplanetary disk include direct condensation of all volatiles, trapping of volatiles in amorphous ice, trapping within clathrate hydrate, alteration of the nebular water abundance by snowline formation, severe depletion of water such that C/O  $\gg 1$  (hence  $\gg 2x$  solar), and subsequent diffusive redistribution of condensate and gas, or enrichment by photoevaporation of either the nebular surface or the nascent Jovian envelope. This paper quantifies how Juno's measurement of water in the deep interior, coupled with previous Galileo probe data and Juno's determination of Jupiter's composition and interior structure, provide crucial information for constraining both the original planetesimal population and the formation mechanism for Jupiter.



# THE BATHYMETRY AND COMPOSITION OF TITAN'S LAKES AND SEAS: A POST-CASSINI VIEW

A.G. Hayes<sup>1</sup>, M. Mastrogiuseppe<sup>2</sup>, J.I. Lunine<sup>1</sup>, V. Poggiali<sup>1</sup>

<sup>1</sup>Department of Astronomy, Cornell University, Ithaca NY, USA

<sup>2</sup>Sapienza University of Rome, Rome, Italy, hayes@astro.cornell.edu

## KEYWORDS:

Cassini; Titan; Lakes and Seas; Bathymetry; Saturn

## EXECUTIVE SUMMARY:

Titan is the only extraterrestrial ocean world known to have a thick atmosphere and abundant surface organics. During its 13-year mission in the Saturn System the Cassini spacecraft has explored the distribution of surface organics on Titan, including a campaign to determine the bathymetry and composition of its lakes and seas. We will review the results of Cassini's exploration of Titan's hydrocarbon lakes and seas and discuss the outstanding questions that remain for future exploration.

## INTRODUCTION:

Despite pre-launch predictions that hydrocarbon liquids would be transparent to Cassini's 13.8 GHz radar [1] and that the radar's altimetry mode might be used as a sounder to probe Titan's liquids [2], experiments using liquefied natural gas by Paillou et al. [3] suggested that penetration would be significantly shallower than the altimeter's 35 m range resolution. Nevertheless, Mastrogiuseppe et al. [4] successfully detected subsurface reflections in altimetry echoes acquired over Ligeia Mare in May 2013 (Figure 1). Coherent processing of these echoes revealed the bottom reflection and allowed construction of a bathymetry profile as well as an estimation of the liquid loss tangent from the relative variation in subsurface power. Subsequent altimetry observations of Kraken and Punga Maria obtained in August 2014 and January 2015, respectively, also showed detectable subsurface echoes. During Cassini's final close flyby of Titan (T126 in April 2017), subsurface echoes were obtained over several smaller lakes. After applying these new techniques, subsurface echoes were also observed in altimetry data acquired over Ontario Lacus in 2008. In this proceeding, we will report on the latest results from the analyses of these altimetry passes.

## BATHYMETRY:

The relative variations in received subsurface power as a function of depth provided an estimate for the Ligeia Mare's loss tangent  $\tan\Delta = \epsilon_i/\epsilon_r = 4.8 \pm 1.0 \times 10^{-5}$  [5]. Initial analysis of Kraken and Punga Maria suggest liquid absorptivities that are similar to Ligeia Mare. Portions of Kraken Mare were too deep (or too absorptive) to detect the subsurface. Recent laboratory experiments reported by Mitchell et al. [6] confirmed the low absorption of methane and ethane.

Mastrogiuseppe et al. [7] applied similar processing to low altitude (~1800 km) altimetry acquired over Ontario Lacus in December 2008 and, despite significant saturation in many echoes, detected subsurface reflections and retrieved depths of up to 50 m across the observed transect. These results are consistent with the near-shore depths reported in Hayes et al [8], which extended shoreline slopes into the lake. The best-fit loss tangent for Ontario is  $\tan\Delta = 7.0 \pm 1.0 \times 10^{-5}$ . This is ~45% greater than the loss tangent reported for Ligeia Mare but an order of magnitude less than the absorptivity suggested by Hayes et al. [8] from analysis of near-shore off-axis SAR. This discrepancy could be explained by an increase in microwave absorptivity near the shore resulting from an increased concentration of solutes or suspended particles as compared to the center of the lake. This is consistent with the observation that the near-shore ethane bands, unlike central Ontario Lacus, are not saturated [9]. This suggests that photons are scattered before traveling through a path length sufficient to saturate the ethane absorption.

Prior to the work of Mastrogiuseppe et al. [4], the unknown dielectric properties of both the liquid and the seabed limited the utility of SAR backscatter as a tool for estimating the depth of Titan's lakes and seas. With the bathymetry profile and liquid loss tangent of Ligeia Mare in hand, SAR data can be calibrated and used to generate bathymetric maps. Hayes et al. [10] derived an empirical

backscatter function for the seabed using SAR backscatter in the altimetry footprints of Ligeia Mare. This empirical function was used to derive depths for all of the Mare observations that have SAR returns above the instrument noise floor, assuming uniform seabed reflectivity (Figure 2). A similar analysis was performed for Ontario Lacus, revealing that the lake reaches depths of up to 90 m. Lorenz et al. [11] calculated a liquid volume by assuming that sea-depth was linearly proportional to the distance from the nearest shoreline, calibrated such that the maximum depth scaled linearly with the square root of Mare area. Combining results from both techniques yields a lower limit of  $\sim 70,000 \text{ km}^3$  for the total volume of Titan's lakes and seas. If this liquid were spread across the surface equally it would be equivalent to a global ocean depth of  $\sim 1 \text{ m}$ . This is equivalent to 14 times the volume of Lake Michigan, 300 times the mass of Earth's proven natural gas reserves, and 35 times the mass of all terrestrial fossil fuel reserves (natural gas, crude oil, and coal). Unlike Earth, where the total water content in the atmosphere ( $1.29 \times 10^4 \text{ km}^3$ ) is only a fraction of the surficial reservoir ( $1.35 \times 10^9 \text{ km}^3$ ), the moisture content in Titan's atmosphere is approximately seven times larger than the volume found in its lakes and seas. Unless Titan had a significantly larger liquid reservoir as compared to atmospheric methane, or currently has a large subsurface reservoir hidden from remote sensing, climate feedback would be improbable since the detectable volume is unlikely to significantly impact the atmospheric composition.

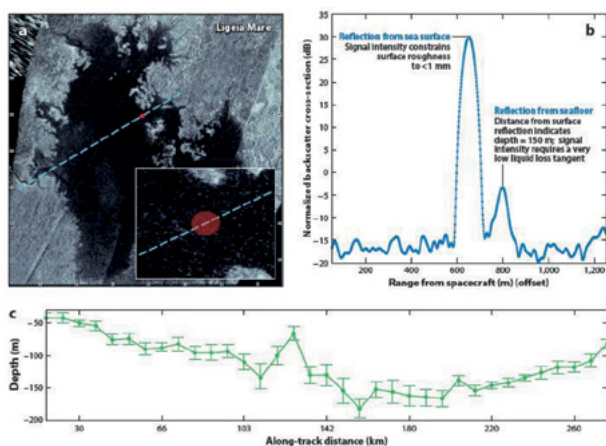


**Fig. 1.** RADAR sounding measurements over Ligeia Mare. (a) A Synthetic Aperture Radar (SAR) mosaic of Ligeia Mare with the position of the May 2013 (flyby T91) altimetry track highlighted and the location of an example altimetry echo shown on the right. (b) An example of a double-peaked waveform observed over Ligeia, with returns from the sea surface and seabed labeled. (c) The along-track bathymetry derived by Mastrogiuseppe et al. [4,5].

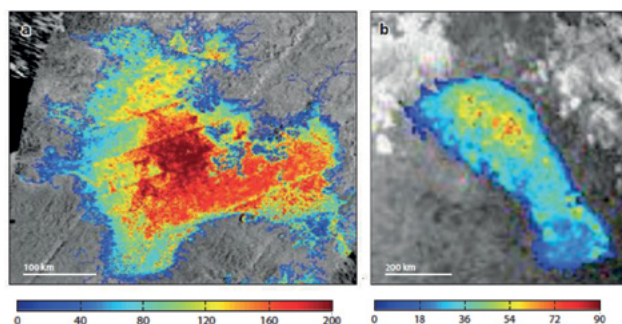


**Fig. 2.** Synthetic Aperture Radar (SAR)-based bathymetric maps of (a) Ligeia Mare and (b) Ontario Lacus generated assuming a uniformly scattering seabed using the techniques and algorithms described by Hayes et al. [10]. Ligeia Mare has an estimated volume of  $14,000 \text{ km}^3$ , equivalent to 2.8 times the volume of Lake Michigan. Ontario Lacus has an estimated volume of  $560 \text{ km}^3$ , equivalent to 1/3 the volume of Earth's Lake Ontario.

## COMPOSITION:

Thermodynamic equilibrium models by Cordier et al [12] predict ethane-rich lake compositions, while more recent work by Glein and Shock [13] and Tan et al. [14] predict methane-dominated compositions at Titan's polar latitudes. Luspay-Kuti

et al. [15] attribute the differences between these models to the use of varying underlying theories relying on experimental data which may not be relevant in Titan conditions. The most recent experimental results reflect methane-dominated compositions. Using the laboratory measurements of Mitchell et al. [6] and assuming a methane-ethane-nitrogen composition, Mastrogiuseppe et al. [5] determined that the measured loss tangent of Ligeia Mare was consistent with ~69% CH<sub>4</sub>, ~14% C<sub>2</sub>H<sub>6</sub>, and ~17% N<sub>2</sub>, similar to the equilibrium compositions predicted by Glein and Shock [13] and Tan et al. [14]. Note that if Titan's lakes are near vapor equilibrium with the atmosphere, evaporation rates would be significantly reduced despite their methane-dominated compositions.

Assuming a similar ternary composition, the increased loss tangent at Ontario Lacus is consistent with ~47% CH<sub>4</sub>, ~40% C<sub>2</sub>H<sub>6</sub>, and ~13% N<sub>2</sub> [7]. The higher loss tangent could result from an increased abundance of more involatile hydrocarbons and/or nitriles; these species could be concentrated as a consequence of orbital-driven insolation cycles that may have slowly transported volatile components (methane/ ethane) to the north over the past several tens of millennia [16].

Non-polar solutes such as acetylene (C<sub>2</sub>H<sub>2</sub>) and benzene (C<sub>6</sub>H<sub>6</sub>) may have low loss tangents similar to methane and ethane. Nitriles, like hydrogen cyanide (HCN) and acetonitrile (C<sub>2</sub>H<sub>3</sub>N), are likely quite absorptive and even minor concentrations may affect the loss tangent. Once the complex permittivities of potential hydrocarbon and nitrile solutes in Titan's lakes are measured in the lab, they can be used to place upper limits on the concentration of these species in Titan's lakes. Methane-dominated compositions are not in chemical equilibrium with photolytic processes over long timescales (which are expected to predominantly yield ethane). This suggests that the products of methane photolysis fall into a sink other than the lakes and seas, such as crustal sequestration of ethane in clathrate-hydrates [17]. Also of note is that while the transparency of Ligeia Mare allows SAR backscatter to penetrate through over 100 m of liquid, the backscatter from many of the smaller lakes are below the radar's noise floor [18]. This suggests that these smaller lakes are either extremely deep or, perhaps more likely, that they have a more absorptive composition than the seas. The latter hypothesis is consistent with dissolution-based formation scenarios for the smaller lake basins wherein liquids become saturated with soluble components from the regolith. Regardless, the lakes still can't account for the missing ethane. Recent results from the recent T126 flyby suggest that the smaller lakes are deep and methane-dominated.

## REFERENCES:

- [1] Thompson WR and Squyres SW (1990), *Icarus*, 86;
- [2] Picardi G, et al. (1992), *Nuovo Climento Physics* 15;
- [3] Paillou P, et al. (2008), *GRL*, 35;
- [4] Mastrogiuseppe, M., et al. (2014) *GRL*, 41;
- [5] Mastrogiuseppe, M., et al. (2016) *IEEE*;
- [6] Mitchell, K.L., et al. (2015) *GRL*, 42;
- [7] Mastrogiuseppe M., et al. (Sub.) *Icarus*;
- [8] Hayes, A. et al. (2010) *JGR*, 115, E09009;
- [9] Brown, R.H. et al. (2008) *Nature*;
- [10] Hayes, AG et al. (2016) *AREPS* 44;
- [11] Lorenz, R.D. (2014) *GRL*, 41;
- [12] Cordier, D et al. (2009) *ApJ* 707;
- [13] Glein, C.R and Shock, E.R. (2013) *Geochim. et Cosmochim. Acta*;
- [14] Tan, S.P., et al. (2015) *Icarus*, 250;
- [15] Luspay-Kuti A et al. (2015) *EPSL* 410;
- [16] Aharonson, O., et al. (2009) *Nat. Geo.*, 2;
- [17] Choukroun, M. & Sotin C. (2012) *GRL*, 39, L04201; [18] Hayes AG et al. (2008) *GRL*, 35

# EMERGENCE OF LIFE IN THE METEORITE IMPACT PLASMA IN THE PROCESS OF THE FORMATION AND MASS ACCUMULATION BY THE EARTH

G.G. Managadze<sup>1</sup>

<sup>1</sup>Space Research Institute, Profsoyuznaya, st.84/32, Moscow 117997, Russia;

Mankind has been pursuing the problem of the emergence of life since the antiquity. However, meaningful and purposeful studies of this problem began much later, initiated by the famous discovery by L. Pasteur who showed experimentally that molecular base of life is chiral and asymmetric in 1884.

The new vision brought about new difficulties and contradictions, and only in the mid-20<sup>th</sup> century it was shown, as a result of studies carried out by several generations of outstanding scientists, that the most primitive living organism capable of replication and possessing the simplest genetic code could appear only if a number of difficult to realize conditions were fulfilled. These conditions have to ensure spontaneous formation of some extremely complex macromolecular structures and physical environments in nonliving matter.

## THE FIRST

requirement is that molecular structures synthesized in this environment must have been homochiralic and have L or D chirality «sign» depending on their purpose. [1]

## THE SECOND

requirement is that this environment must have ensured simultaneous synthesis of L amino acids and polypeptides, D-nucleotides and their oligomers.

## THE THIRD

requirement states that for life to emerge natural processes must have ensured an enormous number of statistical trials, which within a finite time could guarantee the formation of the «right» sequence of molecular structures resulting in the «animation» of inorganic substance.

These requirements are based on experimental results obtained while studying primitive bacteria and determining the basic properties of the natural environments where they could originate, live and evolve. The most difficult task in this period was, as it often happens, to demonstrate the possibility of finding a natural environment or mechanisms ensuring the realization of the above requirements.

The stagnation that happened in the late 20<sup>th</sup> century was due to the fact that the then known natural mechanisms could not explain the emergence in non-living matter of molecular structures comparable in complexity or functional capabilities with molecular structures arising in biology. It was in this anxious time that a new, plasma concept of the origin of life was proposed at the Space Research Institute of the Russian Academy of Sciences. According to this concept, the conditions for the realization of the emergence of life – the most important event in the Earth history – arose in the plasma ejecta (or plasma torch) in the process of adiabatic fly-away of hot plasma.

The development of the plasma concept required certain extensive knowledge in several branches of science. For example, it was necessary to understand that plasma ejecta arising in a laser irradiated target are highly similar to those arising when a target is subject to particle impacts. These and many other pieces of information at our disposal made it possible to correctly interpret the results of laser experiments according to which new OCs are synthesized in laser plasma and the same process could also occur in the impact-produced plasma. Then we performed a series of laboratory experiments simulating impact via laser irradiation and direct impact experiments to show that if the power density of external exposure reaches  $W=10^9$  W/cm<sup>2</sup>, the target matter, after its complete atomization and ionization, transformed into plasma, and the process of the fly-away of the plasma torch results in the synthesis of new compounds including OCs if the target contained biogenic elements. This is a rather likely process, which is of special interest because in impact simulating experiments the medium reaches relatively high degree of self-organization with a probability of  $10^{-3}$  -  $10^{-4}$ .

It was also shown that in impact experiments protein amino acids, nucleotides, and short polypeptides form, and the breaking of the mirror symmetry of amino acids is observed under similar conditions. Hence the possibility of the fulfillment of **the first two above requirements** should be beyond any doubt. Moreover, the observed property of plasma self-organization of matter may in some very rare cases reach the highest level and show up as homochirality. For addressing the **third** requirement necessary for the emergence of life and for preparing a preliminary scenario of this event, it is important to know the «appearance» of such being – the progenitor of the biosphere. Biologists invented many such beings, but we adopted the hypothetical model of the first living being proposed by A. Altshtein [2]. It is a molecular structure called protoviroid consisting of two molecules – a polynucleotide and its coded protein (processive polymerase). The system self-replicates via unified process of replicative translation based on matrix principle similar to the present-day process, and evolves in accordance with Darwinian principle «inheritance - mutation – natural selection». The structure had a mass of 100 000 amu, or  $1.6 \times 10^{-19}$  g. It is now reliably known that the Earth formed and accumulated mass only as a result of meteorites falling onto it from outside. This process lasted 100 million years and the total energy amounted to  $10^{39}$  erg. However, the impact of each meteorite involved the participation of Earth crust matter with the total mass 125 times the mass of the meteorite itself. Note, however, that only a part of the crust matter was subject to plasma processing. Considering this, we can conclude that the total effective mass of meteorite and crust matter amounted to about 10 Earth masses or  $6 \cdot 10^{26}$  g. In this case a total of  $N = 6 \times 10^{26} / 1.6 \times 10^{-19} = 3 \times 10^{47}$  protoviroid must have been subject to plasma processing (and statistical trials) over the time of the Earth formation and hence  $N \gg 10^{35}$ . Thus in plasma processes the above number of statistical trials required for the origination of a protoviroid, is ensured by a wide margin. Furthermore, given that the formation of the Earth and origination of life occurred simultaneously within one and the same process, the energy consumption of the two processes should be comparable.

The most important experimental results presented here suggest that the plasma concept and the preliminary scenario of the origin of life are most likely, well-thought out, and most easily implementable under natural conditions. This is due to the fact that the plasma concept was from the very beginning empirical and based on experimental results whose reliability could hardly be doubted. And all the crucial conclusions presented in the plasma concept were incorporated into it after preliminary experimental validation. That is why we can believe in the plasma concept of the origin of life and in the scenario of its realization under the conditions of abiogenous nature.

## REFERENCES:

- [1] Managadze G.G., Engel M.H., Getty S., Wurz P., Brinckerhoff W.B., Shokolov A.G., Sholin G.V., Terent'ev S.A., Chumikov A.E., Skalkin A.S., Blank V.D., Prokhorov V.M., Managadze N.G., Luchnikov K.A. (2016) Excess of L-alanine in amino acids synthesized in a plasma torch generated by a hypervelocity meteorite impact reproduced in the laboratory // *Planetary and Space Science*. V. 131, P. 70–78.
- [2] Altshtein A.D. (1987) Origin of the genetic system: the progene hypothesis. // *Mol. Biol.* V. 21 (2), P. 309-322 (in Russian)

# FORMATION OF AMINO ACIDS FROM COMPONENTS OF A NITROGEN-METHANE ATMOSPHERE DURING HYPERVELOCITY IMPACTS

M.A. Zaitsev, M.V. Gerasimov

Space Research Institute of Russian Academy of Sciences (IKI RAS), 84/32 Profsoyuznaya str., 117997 Moscow, Russia, mzaitsev@iki.rssi.ru;

## KEYWORDS:

Hypervelocity impacts, nitrogen–methane atmosphere, early Earth, stony impactors, peridotite, amino acids, experimental simulation, high–temperature vaporization, pulse laser, GC/MS, extraction.

## INTRODUCTION:

As they assume in the aspect of the prebiotic evolution of organics on the early Earth, the impact-induced synthesis of organic compounds (OC) was highly competitive in efficiency with other main abiotic sources of OC, such as delivery by falling bodies, photochemical synthesis, synthesis under the action of lightning discharges, etc. [1].

We observed formation of simple amino acids from components of nitrogen-methane gas mixtures during laboratory high temperature (4000-5000 K) laser vaporization of peridotite. The simulated conditions of high temperature vapor are similar to the conditions which are formed during hypervelocity impacts as a result of vaporization of colliding bodies (at velocities of 10-15 km/s) [2].

## EXPERIMENT:

Laser vaporization of a peridotite was carried out by a Nd-glass pulse laser ( $\lambda=1.06 \mu\text{m}$ ), according to the standard technique [2]. The peridotite sample, consisting of olivine and pyroxene – the main constituents of stony meteorites [3], was a mineral analogue of stony asteroids. Nitrogen-methane gas mixtures in the chamber for laser vaporization ( $P = 1 \text{ atm}$ ,  $T = 298 \text{ K}$ ) contained 4 and 50 vol. % of methane. These mixtures were possible analogues for the early Earth atmosphere. Components of the model gas mixtures were the only sources of carbon, hydrogen, and nitrogen (which were essential for OC formation) in our experiments.

Solid condensates, formed after the laser vaporization of the peridotite sample, were subjected to triple water extraction in an ultrasonic bath. The water extracts were evaporated, dried and subjected to derivatization with N-(tert-butyl-dimethylsilyl)-N-methyltrifluoroacetamide (MTBSTFA) in the optimal conditions [4]. Then, volatile and thermally stable derivatives of initial thermally labile OC were analyzed by gas chromatography – mass spectrometry (GC/MS).

## RESULTS AND THEIR DISCUSSION:

We found in the condensates obtained in the atmosphere of 50 vol. %  $\text{CH}_4$ , such amino acids like sarcosine (the main product), alanine, glycine, serine, aspartic acid and some others at ppm level. Other detected products were: urea (the main product), some hydroxycarboxylic and dicarboxylic acids. In the condensates, obtained in the atmosphere of 4 vol. %  $\text{CH}_4$ , we found amino acids: alanine (the main product), and glycine. We also detected urea (the main product), succinic acid, and some hydroxycarboxylic acids. In the gas mixture with 50 vol. %  $\text{CH}_4$  the yield of amino acids and other OC was much more significant.

An impact-generated vapor cloud provides itself extreme conditions (high temperature and pressure, the presence of free oxygen, etc.), which are incompatible with the presence of any significant abundances of complex OC. But even in such conditions, the impact-driven formation of OC can take place due to some phenomena. The first one is heterogeneous catalytic reactions (in particular, Fischer–Tropsch type reactions), proceeding on the extremely developed surface of silicate particles, condensing in the cloud. The second one is the formation of a mantle, composed of high molecular (soot-like) organic matter and molecular carbon, on the surface of condensing silicate particles. The carbonaceous matter preserves the low-molecular OC (forming simultaneously) from oxidation and thermal destruction.

The nitrogen–methane atmosphere itself, even with low abundance of CH<sub>4</sub>, favors the impact–induced formation of biologically significant OC despite the absence in stony impactors of C, H, N and other chemical elements, essential for the formation of the OC. The combination of carbon- and nitrogen-bearing atmospheric gases as sources of C, H, and N with condensing silicate particles as a catalyst could provide efficient impact-induced synthesis of biologically significant prebiotic OC.

### CONCLUSION:

The actual composition of the early Earth atmosphere is unknown. But there are hypotheses, that it could contain significant amounts of methane [5]. In case this atmosphere also contains nitrogen, or other N-bearing gases, as the main constituents, the impact-generated organic matter could contain simple (consisted of 2-4 carbon atoms) protein and non-protein amino acids together with hydrocarbons and high-molecular weight soot-like products (which are the main components of synthesized organic matter). The atmosphere could be a significant source of C, H, N for the impact-induced formation of amino acids in the case of volatile poor stony impactors.

Important biomolecules could be synthesized even at early stages of planetary evolution due to impacting planetesimals. However, the efficiency of the organic matter accumulation on a planetary surface was determined by conditions (mainly temperature conditions), that could favor or impede its preservation in different periods.

### ACKNOWLEDGEMENTS:

This work was supported in part by P-22 Program of the RAS.

### REFERENCES:

- [1] Chyba C. and Sagan C. Endogenous production, exogenous delivery and impact-shock synthesis of organic molecules: an inventory for the origins of life // *Nature*, 1992. V. 355 No. 6356. P. 125–132.
- [2] Gerasimov M.V., Ivanov B.A., Yakovlev O.I., and Dikov Yu.P. Physics and chemistry of impacts // *Earth, Moon, Planets*. 1998. V. 80, P. 205–259.
- [3] Rubin A.E. Mineralogy of meteorite groups // *Meteor. Planet. Sci.* 1997. V. 32. P. 231–247.
- [4] MacKenzie S. L., Tenaschuk D., and Fortier G. Analysis of amino acids by gas-liquid chromatography as tert.-butyldimethylsilyl derivatives. Preparation of derivatives in a single reaction // *J. Chromatogr.* 1987. V. 387. P. 241-253.
- [5] Galimov E.M. Role of Low Solar Luminosity in the History of the Biosphere // *Geochem. International*. 2017. V. 55. No.5. P. 383-401.

# MOVING LIVING OBJECTS ON VENUS: NEW EVIDENCE

L.V. Ksanfomality

*Space Research Institute of RAS, 117997 Moscow Profsojuznaya str., 84/32*

*leksanf@gmail.com*

## KEYWORDS:

Venus, extraterrestrial life, space investigations

The Venusian flora, "stems", are vertically arranged thin knotty trunks, which are 0.3-3 cm thick and 0.2-0.5 m tall. The first detected "stem" had a large bulge at the top end, a "burgeon", with a lighter center [1]. At the base of the 'stem', there are features that resemble leaves in a quatrefoil. Each of the "leaves" has a size of approximately 5-10 cm. Both at the VENERA-13 and -14 landing sites, "stems" are placed in cracks between the stones. There are eight distinct images (duplicates) of VENERA-13, which allows for a batch processing and animation. The attention is drawn to the top of the stem, which appears as a triad of bright spots in the original high-contrast images. The position of the triad varies slightly with respect to the adjacent light-colored stones close to it. Changes arise from the swinging of the triad by the wind as seen by animation. The wind speed is low, about 0.4 m/s but the gas density is very high. When processing the image with a lowered contrast, it allowed to see the whole "flower" of a regular shape, with a white spot (pestle?) in the center and the surrounding petals. The flower is composed of six to eight light petals. Its right-hand bright part forms the triad that is repeated on all of the duplicates in Fig. 3, as part of an open flower. The flower size is approximately the same as a "quatrefoil" at the base of the stem. The VENERA-13 panorama has been organized in such a way that Fig. 3 represents only a fragment of the black-and-white image; thus, one can talk about only the bright colors of the petals, and their color in Fig. 4 is unknown.

The shape of the amisada (VENERA-14 fauna) resembles a 15-cm lizard climbing up a stone. The amisada was located in the immediate vicinity of the lander's buffer [2]. Thus TV- images of VENERA-14 makes possible to recognize fine and slow displacements of the amisada's forward parts, which made it possible to animate the motion in a sequence of six sequential positions of amisada. Movement of the fauna objects is demonstrated, too, by the established small shifts of the detected second 'snake' that seems is in a process of hunting and overcame 15 cm for 26 min. It reveals once again that the style of physical activity of the hypothetical Venus fauna is very slow, less than 1 mm/s.

## REFERENCES:

1. Ksanfomality L.V. Hypothetical flora and fauna of Venus // *Acta Astronautica*, 2014, V.105, pp. 521-533.
2. L.V.Ksanfomality. Possible Signs of Life on the Planet Venus. *International Journal of Astronomy and Astrophysics*, 2013, 3, pp.57-79.



# OBSERVATION OF BIOGENIC NANOPARTICLES GENERATION FOR COMPARISON OF MICROBIAL COMMUNITIES AND FOR DETECTION OF EXTRATERRESTRIAL LIFE

D.A. Skladnev, V.V. Sorokin, V.F. Gal'chenko  
*Winogradsky Institute of Microbiology, Research Center of Biotechnology, RAS,*

## KEYWORDS:

biogenic nanoparticles, microbial communities, presence of the microorganism or phages

Observation of biogenic nanoparticles generation method (OBNG) is a fundamentally new, simple and universal strategic approach for detection of low-concentrated biological objects and for comparison of microbial communities by registration of metal nanoparticles formed in situ in the investigated water samples. Its use is determined by the relevance of the analytical instrumentation devices, capable to register a unique optical properties (due to the phenomenon of surface plasmon resonance), highly developed surface, catalytic activity, high capacity electrical double layer, and allow to apply successfully the bass to amplify the signal of individual organic biomolecules in fluorescence spectroscopy, in Raman spectroscopy, as well as in the spectroscopy of surface-enhanced Raman scattering.

The OBNG method is based on the principle that biological objects in natural water samples generate metal nanoparticles from added sterile solution of cations in the small volume of the reaction mixture 50  $\mu$ l for 20–60 minutes even at +40C. The formation of biogenic nanoparticles is a kinetic-controlled process favored by relatively slow ions reduction, nucleation in clusters of zero-valent atoms and nanoparticles crystallization and growth. The size and shape of biogenic nanoparticles is determined by the presence of the microorganism or phages.

The investigation of formation of silver nanoparticles in the samples of natural water, which evidently differs in the composition of microbial communities, is of special interest. We compared formation of silver nanoparticles in the samples of water from different horizons of ice-covered Antarctic Lake Untersee.

Because bacteriophages can generate metal nanoparticles from salts, the OBNG method can be used for detection. The argument for searching for phage particles in outer Space is that their total number in the biosphere significantly exceeding the number of cellular life forms. Many features of phages can be certainly considered as markers in searching for extraterrestrial cellular life. Indeed, a simple chemical composition of phage particles, the quasicrystalline structure, and morphological features suggest a high probability of their finding even under conditions of outer Space.

ISSN 0026-2617, *Microbiology*, 2017, Vol. 86, No. 3, pp. 355–362.

© Pleiades Publishing, Ltd., 2017. Original Russian Text

© D.A. Skladnev, V.V. Sorokin, V.F. Gal'chenko, 2017, published in *Mikrobiologiya*, 2017, Vol. 86, No. 3, pp. 326–334.

# ASTROBIOLOGY IN RUSSIA: INTEGRATION TO THE WORLDWIDE ASTROBIOLOGY

O.R. Kotsyurbenko<sup>1,2</sup>

<sup>1</sup>Lomonosov Moscow State University, Biology Department, Leninskie Gory, 1-12, Moscow, Russian Federation, 119234, kotsor@mail.ru;

<sup>2</sup>Yugra State University (16, Chekhova str., Khanty-Mansiysk, Tyumen region, 628012, Russian Federation)

## KEYWORDS:

Astrobiology, ESA, NASA, Education, Research, Analytical Centers, Extremophiles

Astrobiology is a science that studies the origin, evolution, distribution, and future of life in the universe. It is now a discipline of a global meaning and among the scientific priorities in USA and Europe. The Russian Space Agency plans future space programs including astrobiological experiments of a great value in cooperation with ESA and NASA experts. Such scientific prospects of cooperation for the next years have been identified and included Mars mission Simulation, Mars Express, Russian Phobos Sample Return mission called 'Phobos Grunt 2', ESA's ExoMars project, several astrobiological and biomedical experiments on the Russian biosatellites: Bion & Photon.

Next to USA, EU now made a great progress in developing astrobiology. Different education and scientific programs are prepared and working groups are created within departments in European universities. Annual meetings, summer schools and internet courses in astrobiology are conducted to increase the level of the researches, bring together all the scientists involved in this problem and enhance its influence as innovative discipline on the modern society.

This is a valuable experience for Russian astrobiologists to be adopted for perspective developing this discipline in Russia. The most progressive way is to improve cooperative work in both education and research and to pay a special attention to the joint achievements of EU and Russia in the field of astrobiology. It will require groups of highly qualified experts and scientists who would have sufficient knowledge and fundamental ideas on novel technologies in astrobiology. The crucial decision is the realization of the joint international education project in this field. Now, none of Russian universities has multidisciplinary up-to-date graduate program in astrobiology and only few of them offer lectures on astrobiology as a part of the basic courses such as "Space researches" or "Biology of extreme environments". This project can be prepared in the framework of Erasmus Plus program managed by Education, Audiovisual and Culture Executive Agency (EACEA) of European Commission. A few Russian universities from Moscow, Saint-Petersburg and Novosibirsk have already initiated the preliminary discussion on the aforementioned idea with European partners.

The main outcome will be the development of curriculum for MSc&PhD in astrobiology according to EU-Modernization Agenda for European High Education Sectors. The actual requirement is to adjust educational system in Russia in the field of astrobiology to the world tendencies in its development. We plan to involve representatives from other scientific institutions, university authorities, professors and students in the realization of the project. The sustainability of the project will be also guaranteed by including experienced managers from EU partners in the project as well as by regular assessments of the modern needs in astrobiology and building strong links between courses and research projects.

One of the main research subjects of modern astrobiology is extreme terrestrial environments. These are not only analogs to putative extraterrestrial ecosystems, but also a valuable resource of unique enzymes, chemical compounds and unique microorganisms (extremophiles) having specific cell machinery to withstand aggressive environments. The gained knowledge can be used to develop new bio-based products and bioprocesses in such fields as fine chemicals, cosmetics, food industry, pharmaceuticals, medicine, bioremediation and generation of sustainable energy. Thus, astrobiology now includes perspective and practice-oriented studies in fields of biotechnology, ecology and medicine.

Astrobiology related terrestrial ecosystems are now intensively investigated all over the world. There is a lack of information about such ecosystems located in Russia. In the mean time, Russian territory is very big and extensive and

includes a huge diversity of ecosystems and climatic zones from permafrost to hot springs and hypersaline lakes. The cataloging and cooperation in research of such sites could be a good opportunity for joint perspective projects between Russian, EU and US astrobiologists.

The initiative for strengthening of interactions and creation of associations between researches in Russia, Asia and South America as regions having many unexplored ecosystems well related to astrobiology and their valuable contribution is now being discussed as well. It can be also realized in the framework of European programs by creation of national astrobiology analytical centers for strong and perspective cooperation within common education and research space.

# A ROAD MAP TO THE NEW FRONTIER: FINDING EXTRA TERRESTRIAL INTELLIGENCE

J.L. Bertaux<sup>1,2</sup>

<sup>1</sup>LATMOS/UVSQ/CNRS/INSU, 11 Boulevard d'Alembert, 78280  
Guyancourt, France, jean-loup.bertaux@latmos.ipsl.fr

<sup>2</sup>Laboratory for planetary and exo-planets atmospheres, IKI, Moscow

## KEYWORDS:

exo-planets, habitable zone, bio-signature, space telescopes, cosmonauts, astronauts, New Frontier, extra-terrestrial intelligence.

## INTRODUCTION:

An obvious New Frontier for humanity is to locate our nearest neighbours technically advanced. This quest can be made with three steps that will be sketched briefly.

1. Find the nearest (from Sun) exo-planets in the habitable zone (HZ)
2. Find bio-signatures (signs of life) in their spectra.
3. Find signs of advanced technology: techno-signatures emitted inadvertently (not on communication purpose).

## FIND THE NEAREST EXO-PLANETS IN THE HABITABLE ZONE (HZ)

The first step calls for a systematic survey of all nearest stellar systems to detect all terrestrial planets (solid) at an habitable distance from their host star, which can be done with long-term ground based measurements of the Radial Velocity of the stars. The detection of an exo-planet in the HZ suitable for life requires to monitor the same star for a long time, larger than at least 10 periods (10 years for the Earth), to extract a stable periodic signal from the noise. An ensemble of 33 telescopes+spectrometers would be able to make an exhaustive search of all exo-planets around about 3,000 stars within 100 light-years from sun.

Statistics on exoplanets are good enough to claim today that about 40% of stars host a rocky planet with a size smaller than 2.8 times the Earth's size (Petigura et al., 2014). What fraction of these planets are in the Habitable Zone is still a matter of debate, but it is safe to say that probably from 0.5 to 10 % of stars host a rocky planet in their Habitable Zone. Therefore, between 1 and 20 billion planets in our galaxy must have a planet in the Habitable Zone.

## FIND BIO-SIGNATURES (SIGNS OF LIFE) IN THEIR SPECTRA

Finding bio-signatures calls for the study of the atmospheres of habitable exo-planets. The 6.5 m JWST space telescope will be a precursor of larger telescopes (range 10-100 m diameter), which will have to be deployed in space. Search for ozone, O<sub>2</sub>, H<sub>2</sub>O, CH<sub>4</sub>, CO<sub>2</sub>, chlorophyll edge, are foreseen. The transiting planets may be observed by the absorption of their thin atmosphere on the stellar disk. But non-transiting planets are much more numerous (within the same distance to the sun) than transiting planets, and therefore they are nearer and easier to study than transiting exo-planets. Their atmospheres may be studied by the reflected star light, requiring systems decreasing the light of the star with internal or external occulting systems. NASA is considering such systems; they could be implemented in the years 2025-2050.

## FIND SIGNS OF ADVANCED TECHNOLOGY: TECHNO-SIGNATURES EMITTED INADVERTENTLY

Among possible techno-signatures in the optical domaine, one may think of lights illuminating at night the big cities. Signatures of sodium light or mercury light could be searched for. The third step may require multi-kilometer size telescopes, but with a "diluted pupil" scheme as advocated by Antoine Labeyrie. Obviously other techno-signatures in the radio domain could be searched for, possibly requiring large radio telescopes in space or on the back side of the moon, free of terrestrial interference and with the whole spectral domain available.

## **CONCLUSION: THE ROLE OF MAN IN SPACE.**

The role of man in space may be crucial for the development of steps 2 and 3. Astronauts and cosmonauts have demonstrated their capability to assemble in space large and complex mechanical structures in space, from the servicing mission of the Hubble Space Telescope to the deployment of the huge International Space Station.

It may be remarked that the signs of life on planet Earth are already existing since about two billions of years, therefore the fact that there is life on Earth is known from the whole Galaxy and beyond. We cannot conceal it. On the other hand, our techno-signatures are existing since only  $\approx 100$  years; they propagate at the speed of light, and therefore only a very small fraction of space is aware of the presence of man on Earth as a technologically advanced living species. But this sphere of knowledge is increasing in radius at the speed of light, and the number of exo-planets within this sphere is increasing as the cube of time. Since step 3 is within our each in a reasonably foreseeable future ( $\sim 100$  years), it is already done by slightly more advanced civilizations. If they can spot us, we must be able to spot them. Communication is a different issue to be debated separately.

## **REFERENCES:**

[1] Petigura E.A., et al., PNAS, vol. 110 , no. 48 | pp 19273–19278 ,2013

# MODELING TRANSIT OBSERVATIONS OF HD209458B

I.F. Shaikhislamov<sup>1</sup>, M.L. Khodachenko<sup>2,3</sup>, H. Lammer<sup>2</sup>, A.G. Berezutsky<sup>1</sup>, I.B. Miroshnichenko<sup>1</sup>

<sup>1</sup>*Institute of Laser Physics SB RAS, Novosibirsk, Russia, ildars@ngs.ru;*

<sup>2</sup>*Space Research Institute, Austrian Acad. Sci., Graz, Austria;*

<sup>3</sup>*Skobeltsyn Institute of Nuclear Physics, Moscow State University*

## KEYWORDS:

Exoplanets, exosphere, absorption, planetary wind, plasma

The interpretations of available spectral observations in Ly $\alpha$  line at transits of HD209458b remain controversial. Studies based on 1D hydrodynamic models of Hot Jupiters explain the detected absorption by natural line broadening extending over high velocity wings  $\sim 100$  km/s caused by dense warm exosphere filling the Roche lobe of the planet. Modeling by kinetic codes claims that the absorption due to thermal broadening by fast resonant atoms taking place beyond the Roche lobe is more important. In the present work we apply developed earlier 2D hydrodynamic multi-fluid model [1] which not only describes self-consistently the generation of planetary wind of Hot Jupiter due to heating by stellar XUV flux, but the spatial structure of planetary exosphere in a flow of stellar plasma, the radiation pressure acceleration and charge exchange of planetary atoms as well. The simulations of HD209458b in a wide range of intensities of stellar XUV flux and plasma wind show that at normal conditions expected for the Sun-like star the number of generated fast atoms is too small, mostly due to photo-ionization, and the observed absorption at a level of 6-8% is explained by the natural line broadening. However, at low XUV fluxes the number of atoms surviving photo-ionization and interacting with stellar wind becomes sufficiently large to increase the absorption at the blue wing of the Ly $\alpha$  line up to 10-15%. The similar asymmetric absorption can be also seen during Coronal Mass Ejection events when the stellar wind pressure is large enough to sweep planetary material and form a compact bowshock around the planet. In all cases it was found that the radiation pressure makes a negligible contribution into the absorption, either in comparison to charge exchange or natural line broadening. We also modeled the observed absorption at transits of HD209458b in lines of OI and CII which has not been so far satisfactorily explained. Our previous results [1] shown that for conditions expected at HD209458b the exosphere expands far beyond the Roche lobe and planetary wind forms two supersonic tidally accelerated streams, one directed tailward and the other towards the star. As the flow remains strongly collisional, the heavier species are captured and dragged by the streams accelerating to velocities above 50 km/s. Simulations show that oxygen atoms and carbon ions present in those streams with expected standard abundances quantitatively explain the observed absorption at a level of 6-10%.

## ACKNOWLEDGMENTS:

This work was supported by RFBR grant № 16-52-14006, RAS SB research program (project II.10 №0307-2016-0002), as well as by the projects S11606-N16 and S11607-N16 of the Austrian Science Foundation (FWF). Parallel simulations have been performed at Novosibirsk State University and SB RAS Supercomputer Centers.

## REFERENCES:

[1] Shaikhislamov et al. Two regimes of interaction of a Hot Jupiter's escaping atmosphere with the stellar wind and generation of energized atomic hydrogen corona // The Astrophysical Journal. – 2016. – T. 832. – №. 2. – C. 173.

# RETRIEVING THE TRUE MASS DISTRIBUTION OF EXOPLANETS DETECTED WITH THE RADIAL VELOCITY METHOD: METHOD AND FIRST RESULTS

Jean-Loup Bertaux<sup>1,2</sup>, Alexander Tavrov<sup>1</sup> and Vladislava Ananjeva<sup>1</sup>

<sup>1</sup>Laboratory for atmospheres of planets and exoplanets, Moscow, Russia

<sup>2</sup>LATMOS, 78280, Guyancourt, France

The use of radial velocity (RV) of stars has proven very successful at the indirect detection of planets orbiting other stars. Unfortunately the mass  $m$  of the exo-planet cannot be retrieved: only the product  $m \sin i$  is derived from the amplitude of the RV wobble, where  $i$  is the inclination of the polar axis of the orbit on the line of sight (LOS) from the observer to the star.

However, when a reasonable number of exo-planets are detected, giving an observed distribution of  $m \sin i$  it is possible to retrieve the true distribution function of planetary masses  $f(m)$  that will give the observed distribution  $f_0(m \sin i)$ . For this purpose we establish a special geometrical representation of all detected exo-planets. Then the classical onion-peeling numerical method, heavily used in atmospheric physics for the inversion of Abel's integral, is performed to retrieve the true distribution function. The method will be described, and some examples of retrievals focused on different regions of the mass distribution (Jupiter mass or Earth mass) will be shown.

# RETRIEVING THE TRUE MASS DISTRIBUTION OF EXOPLANETS DETECTED WITH THE RADIAL VELOCITY METHOD: REMOVING THE EFFECT OF OBSERVING SELECTION

V. Ananjeva<sup>1</sup>, A. Venkster<sup>1</sup>, A. Tavrov<sup>1</sup>, J-L Bertaux<sup>1,2</sup>

<sup>1</sup>Space Research Institute of the Russian Academy of Sciences (IKI), 84/32 Profsoyuznaya Str, Moscow, Russia, 117997, a-lada@yandex.ru

<sup>2</sup>Université Versailles St.-Quentin, Sorbonne Universités, UPMC Univ. Paris 06, CRNS/INSU, LATMOS-IPSL, 11 boulevard d'Alembert, 78280 Guyancourt, France

## KEYWORDS:

exoplanets, retrieving the true mass

The problem to retrieve the true mass distribution from Radial velocity (RV) measured data is not new and it was touched upon in [1, 2]. The RV measurements produce projective mass  $m_p$ , which is the true mass  $m_{\text{true}}$  times  $\sin(i)$ , where  $i$  means the angle between the line to observer and the exoplanet orbit plane. Several algorithms have been discussed here, because the inverse Abel integral transformation fails in the non-regularized, non-smooth raw data [3].

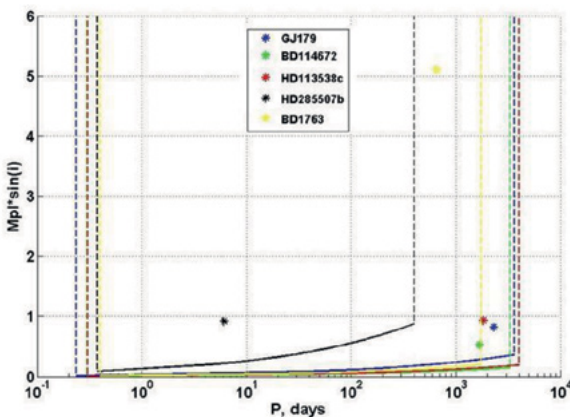


Fig. 1. Algorithm to filter the regular RV data

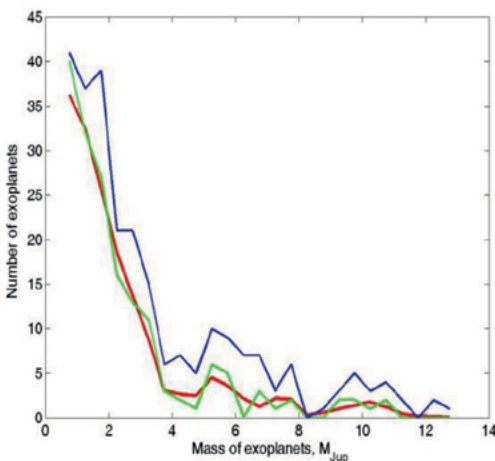


Fig. 2. Results of smoothed RV data



In fact, the raw data from RV exoplanets database are contaminated by factors of observing selection. Many RV facilities starting from 1995 have delivered data with different accuracy. Old RV facilities have been insensitive to lightweight exoplanets which have been detected in recent years with more sensitive instruments. Moreover many stars have their own stellar jitter noise limiting the RV accuracy. Therefore the whole RV exoplanetary database represents a non-regular data, which cannot be used for the retrieving the true mass distribution as row data.

We have elaborated the algorithm to filter the exoplanets which are regular and less contaminated by observing selection.

Also we found that some amount of RV exoplanets have been measured by their true masses because they have been simultaneously observed in transit configurations. Therefore we can preliminary compare the results.

## REFERENCES:

- [1]. A. Jorissen, M. Mayor, and S. Udry, The distribution of exoplanet masses, *A&A* 379, 992-998 (2001).
- [2]. S. Lopez and J. S. Jenkins, The effects of viewing angle on the mass distribution of exoplanets, *The Astrophysical Journal*, 756:177 (5PP) (2012).
- [3]. S. Chandrasekhar and G. Münch, On the integral equation governing the distribution of the true and the apparent rotational velocities of stars, *Astrophysical Journal*, vol. 111, p.142 (1950).

# THE EFFECT OF UNKNOWN PARAMETERS OF EXOPLANETS ON THEIR HABITABILITY

S.J. Jafarzadeh<sup>1</sup>, M. Bahrami Nasr<sup>1</sup>, F. Montazeri Najafabadi<sup>1</sup>

<sup>1</sup>The International Occultation Timing Association-Middle East Section (IOTA-ME), Iran, sj.jafarzade@gmail.com

## KEYWORDS:

Energy Balance Model, habitability, planetary system, exoplanet atmosphere, habitable zone.

## INTRODUCTION:

The habitable zone is usually defined as the region surrounding a star where the water upon the planet's surface could remain liquid. There are different models for assessing this zone. Among them, is the Energy Balance Model and its generalization, Latitudinal Energy Balance Model. LEBM can consider different parameters of the planet, like its obliquity, rotational velocity, eccentricity and even its atmosphere pressure [1]. In this work, we use this model to study the effect of changes in these parameters on the planet's habitability in some real cases.

## LATITUDINAL ENERGY BALANCE MODEL (LEBM)

Energy balance model relates the amount of energy received and radiates by the planet to the energy stored in it. Latitudinal or one-dimensional energy balance model treat each zone separately and so the rate of transporting of energy between different layers is also considered.

The general formalism of LEBM is:

$$C \frac{\partial T[x, t]}{\partial t} - \frac{\partial}{\partial x} \left( D(1-x^2) \frac{\partial T[x, t]}{\partial x} \right) + [T] = S(1A[T]).$$

Where  $C$  is the atmosphere heat capacity,  $x$  is the latitude,  $D$  is diffusion coefficient,  $T$  is the temperature,  $[T]$  is the outgoing long wave radiation,  $S$  is the insolation, and  $A$  represents the albedo of the layer.

## MODEL PARAMETERS

The atmosphere heat capacity depends on fraction of the planet's surface that is ocean,  $f_o$ , the fraction of land,  $f_l$ , and the fraction of the planet's surface that is ice,  $f_i$ . When we consider different level of pressure, heat capacity becomes

$$C_i = 1 \times 10^9 + C_{atm}$$

$$C_o = 210 \times 10^9 + C_{atm}$$

$$\left. \begin{array}{l} T < 263 \text{ } C_{ice} = 11.1 \times 10^9 \\ 263 < T < 273 \text{ } C_{ice} = 53.1 \times 10^9 \end{array} \right\}$$

Diffusion coefficient is

$$D = 5.394 \times 10^2 \left( \frac{\Omega}{\Omega_0} \right)^{-2} \left( \frac{P}{P_0} \right)$$

Where  $\Omega$  and  $\Omega_0$  are the rotational periods of the planet and the earth.

Albedo is defined based on the fraction of land, ocean, ice, and the fraction of cloud on water and land. Thus, we have

$$A = f_o \left\{ (1-f_i) [a_o(1-f_{cw}) + a_c f_{cw}] + f_i [a_{i,o}(1-f_{ci}) + a_c f_{ci}] \right\} + f_l \left\{ (1-f_i) [a_l(1-f_{cl}) + a_c f_{cl}] + f_i [a_{l,i}(1-f_{ci}) + a_c f_{ci}] \right\}$$

The outgoing long wave radiation is

$$I = \frac{\sigma T^4}{1 + 0.75 \tau_{IR} [T, P]}$$

The diurnal insolation is

$$S = \frac{q_0}{\pi} (H \sin \lambda \sin \delta + \cos \lambda \cos \delta \sin H)$$

Where  $F$  is the bolometric flux,  $H$  is the radian half-day length, and  $\delta$  is the solar declination.

The habitability function of each latitude is defined as

$$H[\lambda, t, \rho] = \begin{cases} 1 & 273 \leq T[\lambda, t] \leq T_{boil}(\rho_0) \\ 0 & \text{otherwise} \end{cases}$$

and the fraction of the potentially habitable surface at time  $t$  is [2]

$$f_{area} [a, t] = \frac{\int_{-\pi/2}^{\pi/2} H[\alpha, \lambda, t] \cos[\lambda] d\lambda}{2}$$

## SIMULATION PROCEDURE

Our goal is to study the impact of different unknown parameters of an exoplanet on its temperature and habitability. These parameters include pressure, the fraction of ocean and land, eccentricity, obliquity and rotational period. Usually, these parameters are set to be equal to the earth parameters. However, it is just one case among numerous cases, which have different parameters. We want to study as many as possible cases to see how the planet habitability behave with a change in those parameters.

The initial conditions like longitude of periastron, initial orbital longitude, and starting temperature were the same for all simulations.

## APPLICATION TO REAL CASES

At first, we apply our simulation for an earth-sun like system and compare it with real earth data. Then, the results of different states of the trappist-1 d planet are presented.

## COMPARISON WITH EARTH DATA

In figure1, the green line shows the average taken from the NCEP/NCAR global temperature data and the red one is our model simulation for an earth-like planet orbiting a sun-like star. It is in good match except in the South Pole [3].

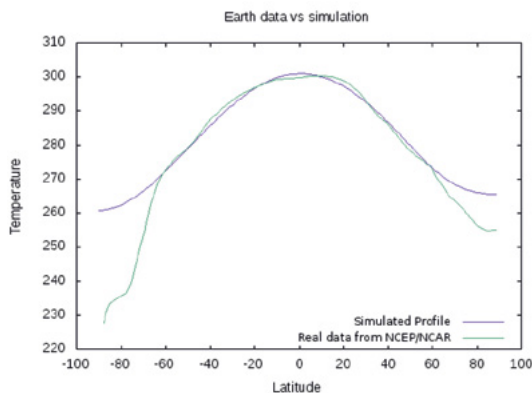


Fig. 1. Temperature versus latitude for real earth data and the LEBM data for an earth-sun like system

Figure 2 Shows temperature profile in different latitudes over a one hundred simulation run. The decreasing temperature from the equator to the poles and the effect of season changing are visible in this figure.

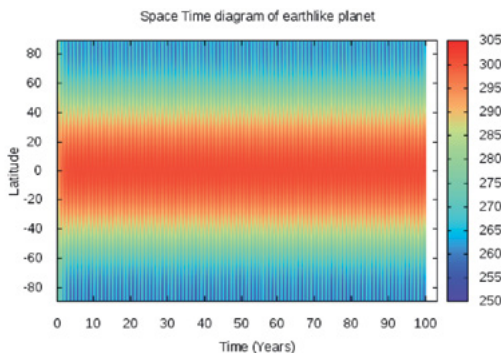


Fig. 2. Temperature profile in different latitudes over time for an Earth-like planet

## TRAPPIST-1 D

The first exoplanet, which is studied is Trappist-1d. It is orbiting an ultracool dwarf star, which is located possibly in the habitability region.

The atmosphere pressure is set to be equal to 0.3, 1 and 3 bar, the obliquity 0, 45 and 90 degrees, the rotational period 0.25, 1 and 3 days, the fraction of ocean 0, 0.5 and 1 and the eccentricity is set to be equal to 0 and 0.07.

Overall, 162 cases were simulated and the maximum, minimum and mean temperature in addition to the fraction of the potentially habitable of the exoplanet's surface were calculated.

## RESULTS

Table1 shows the classification of cases based on their temperature. Table2 shows the fraction of these cases with different habitability.

Table 1. The fraction of simulation cases with different habitability

planet condition	habitable	too warm	too cold
Percentage	45%	33%	22%

Table 2. The classification of simulations cases based on their temperature

	0	< 0.3	0.3 to 1	1
Percentage	46%	9%	21%	24%

As we can see in nearly half of the cases the planet would not be habitable. However, it is definitely worthy for more consideration in future.

Moreover, some general trend could be seen by changing the parameters like warming up the planet with increasing the pressure or a direct relation between habitability and the fraction of water, when the planet is cold.

The importance of this work is that when the number of discovered exoplanets rises dramatically, we can have an evaluation of what planets are prior to study their atmosphere. Planets that have a better chance to be habitable. Especially, if we can surmise the more probable values of unknown parameters, it is possible to calculate a probability of an exoplanet to be habitable. The result is to pick the best exoplanet candidate for studying their atmosphere in depth by telescopes like JamesWebb, which has a very limited time.

## REFERENCES:

- [1] Forgan, Duncan. "Assessing circumbinary habitable zones using latitudinal energy balance modelling." *Monthly Notices of the Royal Astronomical Society* 437.2 (2013): 1352-1361.
- [2] Vladilo, Giovanni, et al. "The habitable zone of Earth-like planets with different levels of atmospheric pressure." *The Astrophysical Journal* 767.1 (2013): 65.
- [3] Montazeri F., Bahrami M., Jafarzadeh S. J. "Habitability in different climate models." *Journal of Occultation and Eclipse* 3 (2016): 29-36.

# STELLAR IMAGING CORONAGRAPH AND EXOPLANET CORONAL SPECTROMETER – INSTRUMENTS FOR EXOPLANET EXPLORATION ONBOARD THE WSO-UV

A. Tavrov<sup>1</sup>, I. Shashkova<sup>1</sup>, I. Dzyuban<sup>1</sup>, A. Kiselev<sup>1</sup>, O. Korablev<sup>1</sup>, M. Sachkov<sup>2</sup>, J. Nishikawa<sup>3</sup>, M. Tamura<sup>3</sup>, S. Kameda<sup>4</sup>, G. Murakami<sup>5</sup>, K. Enya<sup>5</sup>, M. Ikoma<sup>6</sup>, N. Narita<sup>6</sup>

<sup>1</sup>Space Research Institute of the Russian Academy of Sciences (IKI), 84/32 Profsoyuznaya Str, Moscow, Russia, 117997, tavrov@iki.rssi.ru

<sup>2</sup>INASAN Institute of Astronomy of the Russian Academy of Sciences, Pyatnitskaya str., 48, Moscow, 119017, Russia

<sup>3</sup>NAOJ National Astronomical Observatory of Japan, 2-21-1 Osawa, Mitaka, Tokyo 181-8588, Japan

<sup>4</sup>Rikkyo University, 3-34-1 Nishi-Ikebukuro, Toshima, Tokyo, 171-8501, Japan

<sup>5</sup>JAXA Japan Aerospace Exploration Agency, 3-3-1 Yoshinodai, Chuo, Sagami-hara, Kanagawa, 229-8510, Japan

<sup>6</sup>The University of Tokyo, 7-3-1 Hongo, Bunkyo, Tokyo, 113-8654, Japan

## KEYWORDS:

space telescope, exoplanets, UV spectroscopy, coronagraphy

The WSO-UV (World Space Observatory for Ultraviolet) is the orbital optical telescope with a 1.7 m diameter of primary mirror, under development. The WSO-UV is aimed for a 110-310 nm UV spectral range observations. The two major science instruments are UV spectrographs and UV imaging field camera with filter wheels. The WSO-UV project is currently in the implementation phase, with a tentative

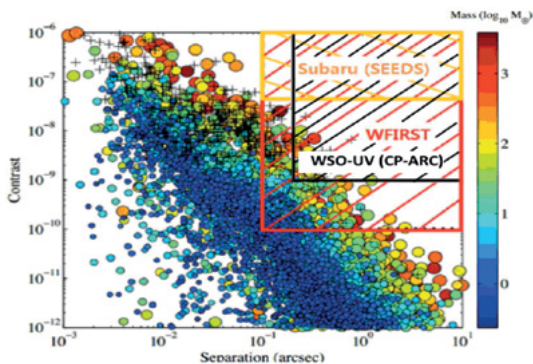


**Fig. 1.** The known exoplanets distribution, the vertical axis is the logarithmic contrast, the ratio of luminosity of the host-star to exoplanet, the horizontal axis is the apparent separation between the planet and the host star and the color shows the exoplanets mass in logarithms of  $M_{\odot}$ .

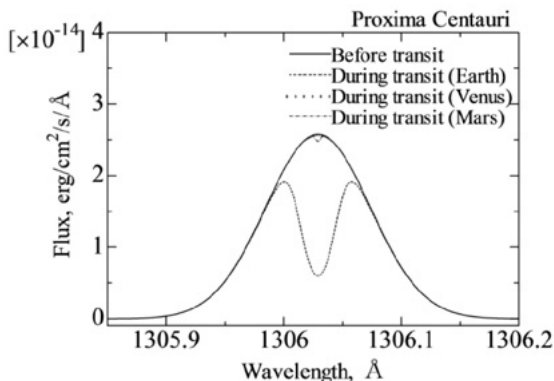


**Fig. 2.** Predicted theoretical transit photometric curves of Proxima Centauri exoplanet in oxygen OI spectral line at 130.6 nm

launch date in 2022. As designed, the telescope field of view (FoV) in the focal plane is not fully occupied by science instruments. Recently, two additional science instruments devoted to exoplanets have been proposed for *WSO-UV*.

*UVSETI*, a UV-Spectrograph for Exoplanet Transit Investigations is aimed to in depth study of transit photometric curves in the spectral range of 110-130 nm to resolve the *hot atoms* of hydrogen, oxygen and nitrogen to determine their abundances in the exospheres of telluric exoplanets.

*SCEDI*, a Stellar Coronagraph for Exoplanet Direct Imaging is aimed to directly detect the starlight reflected from exoplanets orbiting their parent stars or from the star vicinity including circumstellar discs, dust and clumps. *SCEDI* will create an achromatic, (optimized to 420-700 nm wavelength range) high-contrast stellocentric coronagraphic image of a circumstellar vicinity. Present communication outlines the science goals of the both proposed instruments and explains some of their engineering features.

## REFERENCES:

- [1]. A. A. Boyarchuk, B. M. Shustov, A. A. Moisheev, M. E. Sachkov, "“Spektr-UF” project", Solar System Research, Volume 47, Issue 7, pp.499-507 (2013).
- [2]. P. Frolov, I. Shashkova, Yu. Bezymyannikova, A. Kiselev and A. Tavrov, "Achromatic interfero-coronagraph with variable rotational shear: reducing of star leakage effect, white light nulling with lab prototype", J. Astronomical Telescopes, Instruments, and Systems, Vol. 2, Issue 1, p. 011002-1. (2016).
- [3]. S. Kameda, I. Yoshikawa, M. Taguchi, M. Sato, M. Kuwabara, "Observation of Geocorona using Lyman Alpha Imaging CAmera (LAICA) onboard the very small deep space explorer PROCYON", 40th COSPAR Scientific Assembly. Held 2-10 August 2014, in Moscow, Russia, Abstract D2.3-23-14.

# ATMOSPHERIC DUST DYNAMICS: FRACTIONAL MODELS, NUMERICAL METHODS AND COMPUTATIONAL SIMULATIONS

M.P. Velasco<sup>1</sup>, D. Usero<sup>2</sup>, S. Jiménez<sup>1</sup>, J.L. Vázquez-Poletti<sup>2</sup>, L. Vázquez<sup>2</sup>

<sup>1</sup>Universidad Politécnica de Madrid, mp.velasco@upm.es, s.jimenez@upm.es;

<sup>2</sup>Universidad Complutense de Madrid; umdavid@mat.ucm.es,

jlvarez@fdi.ucm.es, lvazquez@fdi.ucm.es

## KEYWORDS:

Dust, Solar Radiation, Fractional Calculus, Mittag-Leffler functions, Fractional Ordinary and Partial Differential Equations, Cloud Computing.

## INTRODUCTION:

The dust aerosols have an important effect on the solar radiation in the Martian atmosphere and both surface and atmospheric heating rates, which are also basic drivers of atmospheric dynamics [1]-[3].

Under different Martian atmospheric scenarios, the measure of the amount of solar radiation at the Martian surface will be useful to gain some insight into the following issues:

- a) UV irradiation levels at the bottom of the Martian atmosphere to use them as an habitability index.
- b) Incoming shortwave radiation and solar heating at the surface.
- c) Relative local index of dust in the atmosphere.

Aerosols cause an attenuation of the solar radiation traversing the atmosphere and this attenuation is modeled by the Lambert-Beer-Bouguer law, where the aerosol optical thickness plays an important role. Through Angstrom law, the aerosol optical thickness can be approximated as a second order moment and then this law allows to model attenuation of the solar radiation traversing the atmosphere by a fractional diffusion equation [4]-[7].

The analytical solution of the fractional diffusion equation is available in the case of one space dimension and three space dimensions with radial symmetry. When we extend the fractional diffusion equation to the case of two or more space variables, we need large and massive computations to approach the solutions through numerical schemes. In this case a suitable strategy is to use the cloud computing to carry out the simulations.

In this study, we discuss some questions of the model and experimental data. We present analytic solutions for this modeling problem in one and three space dimensions and numerical methods that allow us to obtain computational simulations of the solutions. Also, the fractional model provides information that can be understood in term of higher order moments and this relation establishes a meeting point and discussion regarding to the experiments. In this context, we are working in the fitting of the fractional model to dust observational data [8].

## REFERENCES:

- [1] Cachorro V.E., de Frutos A.M., Casanova J.L. Determination of the Angstrom turbidity parameters // *Applied Optics*. 1987. V. 26. No. 15. P. 3069-3076.
- [2] Córdoba C., Vázquez L. Characterization of atmospheric aerosols by an in-situ photometric technique in planetary environments // In Bearman G.H., Beauchamp P.M. (eds.). *First Jet Propulsion Laboratory In Situ Instruments Workshop*. SPIE. 2003. V. 4878.
- [3] Angstrom A. On the atmospheric transmission of sun radiation and on dust in the air // *Geografiska Annaler*. 1929. V. 11. P. 156-166.
- [4] Diethelm K. *The analysis of fractional differential equations*. Springer, 2010.
- [5] Kilbas A.A., Srivastava H.M., Trujillo J.J. *Theory and Applications of Fractional Differential Equations*. Elsevier, 2006.
- [6] Zaslavsky G.M., Baleanu D., Tenreiro J.A. *Fractional Differentiation and its Applications*. Physica Scripta, 2009.
- [7] Velasco M.P., Usero D., Jiménez S., Aguirre C., Vázquez L. *Mathematics and Mars Exploration // Pure and Applied Geophysics*. 2015. V. 172. No. 1. P. 33-47.
- [8] Adeyewa Z.D., Balogun E.D. Wavelength dependence of aerosol optical depth and the fit of the Angstrom law // *Theoretical and Applied Climatology*. 2003. V. 74. P. 105-122.

# MARTIAN DUST CYCLE VIA SOLAR INFRARED OCCULTATION OBSERVATIONS BY SPICAM IR FOR 27–34 MY

D. Betsis<sup>1</sup>, A. A. Fedorova<sup>1</sup>, O.I. Korablev<sup>1</sup>, J.-L. Bertaux<sup>2,1</sup>, F. Montmessin<sup>2</sup>

<sup>1</sup>Space Research Institute (IKI), 84/32 Profsoyuznaya, 117997 Moscow, Russia;

<sup>2</sup>CNRS LATMOS, 11 bd d'Alembert, 78280 Guyancourt, France

## KEYWORDS:

Mars; Aerosols; Atmospheres; Solar occultations; Spectroscopy.

## INTRODUCTION:

Atmospheric aerosol is an important feature of a planetary atmosphere. The Martian climate is in great part controlled by the presence of suspended particles, which include mineral dust aerosols and ice particles. They affect the atmospheric dynamics modulating the absorption and reflection of the solar radiation and their distribution is very important for climate models. The main source of dust is at the surface, from where it is lifted by different wind-driven processes. Sometimes these processes may be intensified resulting in localized (dust devils and local storms) or large scale phenomena, such as global dust storms.

We present results on solar occultations performed with the IR channel of the SPICAM instrument on board the Mars Express spacecraft. This dataset includes over 1200 occultations (January 2005 – May 2017, MY 27–34), the profiles for opacity, extinction coefficient, particle size and number density were obtained. It allows characterization of the seasonal evolution and inter-annual comparisons of aerosol particles. The 28 Mars Year (MY) global dust storm is also covered by the dataset.

The IR channel of SPICAM is an infrared spectrometer employing an Acousto-Optic Tunable Filter and can be used in various observation modes: nadir, limb and solar occultation [1]. The spectral resolution of the instrument is nearly constant in wavenumbers and amounts to 3.5–4 cm<sup>-1</sup>, the resolving power varying from 1800 at 1.6 μm to 2400 at 1.1 μm. In solar occultations, the vertical resolution depends on the spacecraft to limb distance, varying from 1000 to 13000 km. With the FOV of 4.2 arc min (1.2 mrad) the vertical resolution on the limb is typically better than 4–5 km (varies from 1 to 12 km). The direction of the IR line of sight (LOS) is known in the spacecraft bodyaxis frame with an accuracy of ~0.5 mrad (or nearly half of the FOV) or 0.4–4 km on the limb. The vertical speed at the limb varies from 0.5 to 2 km/s.

In solar occultations, a configuration of 664 spectral points has been used, including 620 points covering continuously the 1.35–1.5 μm range with the strongest CO<sub>2</sub> (1.43, 1.57 and 1.65 μm) and H<sub>2</sub>O (1.1 and 1.37 μm) bands, the remaining 45 points dedicated to measuring transmission at several wavelengths outside the gaseous absorption bands. Such points (or “reference wavelengths”) are distributed in the full range from 1 to 1.7 μm to measure the spectral dependence of extinction and to determine optical properties of the aerosol. The set of 11 reference wavelengths was chosen: 996.4, 1093.7, 1158.2, 1197.0, 1241.4, 1272.9, 1304.4, 1321.9, 1514.6, and 1552.2 nm.

## DATA RETRIEVAL:

Radiative properties of the aerosol, such as the single scattering albedo and the asymmetry parameter, may be described in Mie theory for the visible-to-infrared opacity ratio and depend on the particle size distribution [2]. For each altitude we assume lognormal size distribution specified by first two moments of this function: effective radius ( $r_{eff}$ ) and effective variance ( $v_{eff}$ ) [3]. The retrieval algorithm for solar occultations was adapted for SPICAM IR earlier [4] and now was improved.

Firstly we measured the transmission of solar radiance versus wavelengths, then we calculated the slant optical depth for each altitude layer. Retrieval of the extinction coefficient profiles was done using “onion peeling” method for all reference wavelengths. For a constraining of size particle distribution a classical Mie theory was used assuming the lognormal law. Five different fixed values of effective variance and two cases of refractive index, for the



mineral dust and water ice were considered. The minimization of  $\chi^2$  statistically weighted according to uncertainties of the measured extinction factor  $k_{\text{ext}}(\lambda)/k_{\text{ext}}(\lambda_0)$  has been routinely applied using the Levenberg–Marquardt algorithm [5]. With the retrieved particle size distribution and knowing the vertical profile of extinction coefficient we calculated the aerosol number density. Also we made a decision about water ice cloud presence for each altitude we observed based on extinction and opacity profiles and model predictions.

## EXTINCTION:

The seasonal, latitudinal and altitudinal map of extinction coefficient was plotted. We observe the increase of extinction during the dusty season in the second half of the year. Also the higher values are at low and equatorial latitudes. Some profiles exhibit detached layers, where extinction locally increases, and such layers may be considered as clouds of water ice. Usually there are altitudes between 40 and 60 km. According to technical parameters of SPICAM IR we can observe values from approximately  $0.0001 \text{ km}^{-1}$  to  $\approx 0.2 \text{ km}^{-1}$ . In different seasons and locations such values of extinction are observed on generally 20–70 km above the surface. The upper bound varies from  $\approx 40 \text{ km}$  at high southern latitudes during the southern winter to  $\approx 80 \text{ km}$  at the middle of the southern summer almost for all latitudes.

## SIZE DISTRIBUTION AND NUMBER DENSITY:

For aerosol particles we choose the log-normal size distribution following Montmessin et al. 2002:

$$n(r) = \text{Const} \cdot r^{-1} \exp\left(-\frac{(\ln r - \ln r_g)^2}{2 \ln^2 \sigma_g}\right)$$

where  $r_g$  and  $\sigma_g$  are parameters (modal radius and variance) connected with the effective radius and variance as

$$r_{\text{eff}} = r_g \exp\left(\frac{5}{2} \ln^2 \sigma_g\right)$$

$$v_{\text{eff}} = \exp(\ln^2 \sigma_g) - 1.$$

The spectral range of SPICAM IR alone allows to detect particles with sizes in the range 0.2–1.2  $\mu\text{m}$  and to put constraints on particles with  $r_{\text{eff}} > 2 \mu\text{m}$ . The retrieved effective radius ranges within 0.2–1.3  $\mu\text{m}$  for mineral dust. Smaller particles were observed at high latitudes (70–90°) in both hemispheres. Particles about 1  $\mu\text{m}$  and larger were located commonly at low and middle latitudes and they can reach altitudes above 60 km during dust storms. In the period of the MY28 global dust storm the clear increase of  $r_{\text{eff}}$  value was detected almost for all latitudes and for altitudes 40–80 km. It may be interpreted as lifting of large dust particles ( $\sim 1 \mu\text{m}$ ) up to 80 km during the  $L_s \approx 265\text{--}300^\circ$ , MY 28.

The effective variance dependence on altitude also was analyzed. The general trend is that the distribution is wider in lower layers and narrow ( $v_{\text{eff}} < 0.2$ ) higher 50 km. For the global dust storm period the average profile changes indicating the wide distributions up to 60 km ( $v_{\text{eff}} \sim 0.4$ ) which may be explained by large particles loading to high altitudes and other effects of this global phenomena. At high and polar southern latitudes during the southern winter the size distribution becomes narrow ( $v_{\text{eff}} \sim 0.1$ ) already above 15 km. At the same time in the Northern hemisphere  $v_{\text{eff}} \sim 0.3$  are observed up to 35 km. Such typical profiles were plotted for different season and location.

Typical values of number density vary from 0.5–10  $\text{cm}^{-3}$  to 0.03–0.8  $\text{cm}^{-3}$  according to technical characteristics of SPICAM IR. For some orbits the number density and effective radius behave in the opposite way: where the  $r_{\text{eff}}$  is large the number density is low, and vice versa. For example during the global dust storm  $r_{\text{eff}}$  increases at low latitudes and in the same time number density decreases from 2–5  $\text{cm}^{-1}$  to 0.3–0.5  $\text{cm}^{-1}$ .

## ACKNOWLEDGMENTS:

Mars Express is a space mission of ESA. Science operations of SPICAM are funded by CNES and Roscosmos. We thank our collaborators at LATMOS/France for the support of science operations. DSB, AAF, and OIK acknowledge RFBR grant 16-52-16011. JLB acknowledges grant of Ministry for Education and Science of Russian Federation #14.W03.31.0017.

**REFERENCES:**

- [1] Korablev, O.I. et al. SPICAM IR acousto-optic spectrometer experiment on Mars Express // *J. Geophys. Res.* 2006. V. 111. p. E09S03.
- [2] Martin, T.Z. Thermal infrared opacity of the Mars atmosphere. 1986. *Icarus*. V. 66. P. 2–21.
- [3] Hansen, J.E., Travis, L.D. Light scattering in planetary atmosphere. 1974. *Space Sci. Rev.* V. 16. P. 527–610.
- [4] Fedorova, A.A. et al. Solar infrared occultations by the SPICAM experiment on Mars Express: Simultaneous observations of H<sub>2</sub>O, CO<sub>2</sub> and aerosol vertical distribution. 2009. *Icarus*. V. 200 (1), P. 96–117.
- [5] Press, W.H. et al. Numerical Recipes in Fortran 90: The Art of Parallel Scientific Computing. 1996. Vol. 2 of Fortran Numerical Recipes, Cambridge University Press, 2 edition.

# REFLECTANCE OF LUNAR DUST: CONCEPT OF EXPERIMENT ABOARD A LUNAR LANDER

E.S. Zubko <sup>1</sup>, A.V. Zakharov <sup>2</sup>, G. Videen <sup>3,4</sup>

<sup>1</sup>*School of Natural Sciences, Far Eastern Federal University, 8 Sukhanova St., Vladivostok 690950, Russia; evgenij.s.zubko@gmail.com;*

<sup>2</sup>*Space Research Institute of Russian Academy of Sciences, 84/32 Profsoyuznaya St., Moscow, Russia; zakharov@iki.rssi.ru;*

<sup>3</sup>*Space Science Institute, 4750 Walnut St., Boulder Suite 205, CO 80301, USA; gorden.videen@gmail.com;*

<sup>4</sup>*U.S. Army Research Laboratory, 2800 Powder Mill Road, Adelphi, MD 20783, USA*

## KEYWORDS:

The Moon; exosphere; dust; reflectance; volume concentration; Umov effect.

## INTRODUCTION:

The Moon as an airless body is exposed to significant influence of solar radiation and the solar wind. The upper layer of the illuminated lunar regolith is charged positively to a potential of several volts, mainly as a result of photoelectron emission [1]. Low-energy photoelectrons above the surface and the charged surface form a near-surface (about 1 m) electric field  $\sim 10 \text{ Vm}^{-1}$  [1, 2]. It is commonly believed that submicron and micron-size dust particles of the regolith are able to lift off above the surface, forming together with the surrounding plasma, a plasma-dust exosphere near the surface of the Moon. The first indications of dust particles levitated over the lunar surface were received from the Surveyor-5, -6 and -7 lunar landers. The TV cameras mounted on these landers registered a glow near the surface extending from tens of centimeters to a meter just after the sunset [3]. It was shown that this "low altitude horizon glow" was the result of the dispersion of sunlight on 5-10  $\mu\text{m}$  dust particles above the surface. Indications of dispersion of sunlight from above the lunar surface were also received by the astrophotometer onboard Lunokhod-2 [4]. The astronauts of the Apollo-17 mission observed and made drawings of the "lunar horizon glow," appearing like streamers [5, 6]. Registration of dust particles near the lunar surface was implemented by the Lunar Ejecta and Meteorite (LEAM) instrument [7] mounted on the lunar surface by astronauts of the Apollo-17 mission. According to the modeling study [8], the characteristic size and characteristic number density of charged grains in the near-surface layer on the illuminated part of the Moon are on the order of 100 nm and  $10^3 \text{ cm}^{-3}$ , respectively. In this paper we present a concept of a simple optical experiment to measure the polarization of solar radiation scattered from dust particles levitated over the lunar surface. These data can provide information on optical reflectivity of lunar dust particles, which is a key characteristic for the experimental estimation of the volume concentration of dust particles forming an exosphere.

## THE UMOV EFFECT:

Solar radiation is initially unpolarized. When it gets scattered from dust particles, it acquires partial linear polarization that is quantified in terms of the degree of linear polarization  $P = (I_{\perp} - I_{\parallel}) / (I_{\perp} + I_{\parallel})$ . Here,  $I_{\perp}$  and  $I_{\parallel}$  stand for intensity of the scattered sunlight that is polarized perpendicular to the scattering plane and within that plane, respectively.  $P$  is dependent on the geometry of light scattering that is described with phase angle  $\alpha$ . Laboratory optical measurements of various analogs of cosmic dust (e.g., [9]) and numerical simulations of light scattering by irregularly shaped particles (e.g., [10]) reveal qualitatively the same angular profiles of  $P$ . Namely, nearly all samples show positive polarization at side scattering (i.e.,  $I_{\perp} > I_{\parallel}$ ) with maximum of polarization  $P_{\text{max}}$  being squeezed to the range  $\alpha = 70^{\circ} - 110^{\circ}$ . Furthermore, polarization slowly varies over these phase angles, so polarimetric measurement at any  $\alpha$  within that range constrains  $P_{\text{max}}$  quite well.

An important feature of  $P_{\text{max}}$  is that it appears inversely correlated with the geometric albedo  $A$  of dust particles. Note that the geometric albedo compares the backscattering reflectance of a given particle with that of a white Lambertian disk of equal projected area  $G$ :  $A = M_{11}(0^{\circ})\pi / (k^2 G)$ , where  $M_{11}(0^{\circ})$  is the corre-

sponding element of the Mueller matrix at backscattering  $\alpha = 0^\circ$  and wavenumber  $k$  (e.g., [10]). As recently shown in [10, 11],  $\log(P_{\max})$  linearly correlates with  $\log(A)$  in single-scattering, micron-sized particles. Furthermore, the interrelation between  $\log(P_{\max})$  and  $\log(A)$  in small single particles resembles very much what is long known in regolith surfaces, where this phenomenon is referred to as the *Umov effect* (e.g., [12]). In Fig. 1 we reproduce some results obtained in [10] for two types of irregular morphology, the so-called *agglomerated debris particles* and *loose clusters*. The Umov diagrams in Fig. 1 have been computed for a real part of refractive index  $\text{Re}(m) = 1.6$  and imaginary part of refractive index spanning the range from  $\text{Im}(m) = 0.0005$  up to 0.15. These refractive indices are representative of various cosmic species, including lunar dust. The light-scattering response was averaged over particle sizes with a power-law size distribution  $r^{-n}$ . Fig. 1 shows results for  $n = 2.5$  (left panel) and  $n = 3$  (right panel). We refer the reader to [10, 11] for more details on the Umov effect. It is significant that, using Fig. 1, reflectance of dust particles can be inferred from their  $P_{\max}$ .

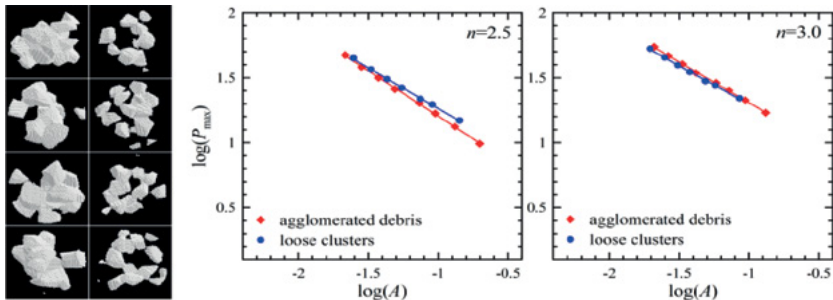


Fig. 1. Four examples of agglomerated debris particles (on left) and loose clusters (on right) and their Umov diagrams at power indices  $n = 2.5$  and 3.

## CONCEPT OF EXPERIMENT:

The maximum of linear polarization occurs at phase angle  $\alpha = 70^\circ - 110^\circ$ . It is important that the phase function of polarization only slightly changes in this range of  $\alpha$ . Therefore,  $P_{\max}$  can be well constrained by a single measurement, for instance, at  $\alpha \approx 90^\circ$ . Such geometry has an interesting feature. Indeed, when orienting a detector (radiometer equipped with a polarizer) toward zenith,  $\alpha = 90^\circ$  occurs exactly at the moment of sunset/sunrise. Shortly after sunset or before sunrise, the phase angle remains quite close  $\alpha \approx 90^\circ$ . However, measurements in twilight make it possible to discriminate the polarimetric response produced by dust particles located at different altitude. This can be accomplished in practice due to motion of the shadow boundary while the Sun moves beneath the horizon; see Fig. 2 for more details.

In twilight the exosphere is illuminated only above the shadow boundary that is

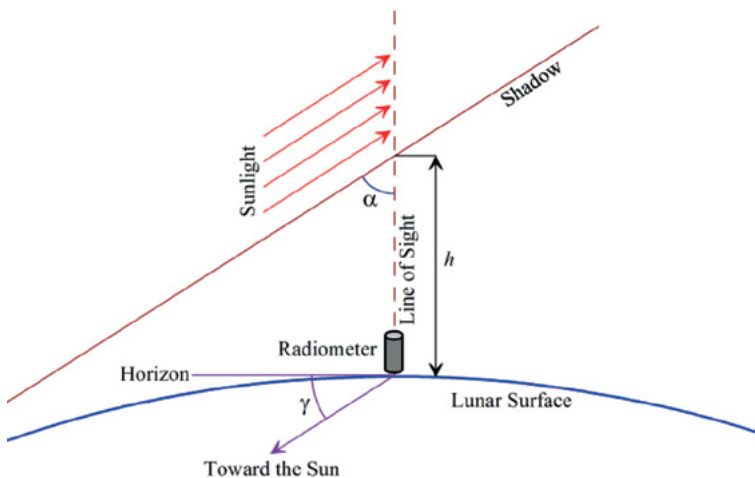


Fig. 2. Scheme illustrating circumstances of the polarimetric measurements.

characterized with the altitude  $h$ . The latter is defined by the radius of the Moon ( $R \approx 1737$  km) and by the angle  $\gamma$  (counted from the top edge of the solar disk to horizon) as follows:  $h = R(1 - \cos\gamma) / \cos\gamma$ . Note,  $\gamma$  is a complementary angle to the phase angle, i.e.,  $\alpha = \pi/2 - \gamma$ . The altitude of  $h \approx 10$  m will be achieved at  $\gamma \approx 0.1944^\circ$ ; whereas,  $h \approx 100$  m at  $\gamma \approx 0.6148^\circ$ . Such angles are quite small and, in the terrestrial circumstances, even the largest of them is achieved within  $\sim 4$  minutes after sunset or before sunrise. However, the apparent motion of the Sun on the Moon is some 29.5 times slower as compared to Earth. Therefore,  $h \approx 100$  m will be achieved in approximately 2 hours after sunset or before sunset. This provides enough time to accumulate the signal if needed and, furthermore, repeat the measurements over this time period. Thus, one can increase the altitude resolution in  $P^{\max}$  of lunar dust particles and, as a consequence, their geometric albedo  $A$ . Finally, it is important to stress that accurate measurements of  $P^{\max}$  not only provide crucial information on reflectance of dust particles but, also they put further constraints on size distribution and chemical composition of dust particles.

## REFERENCES:

- [1] Manka R.H., Plasma and potential at the lunar surface // Proceedings of the 6th ESLAB Symposium. Noordwijk. The Netherlands. 1973. P. 347–361.
- [2] Poppe A., Horányi M. Simulations of the photoelectron sheath and dust levitation on the lunar surface // J. Geophys. Res. 2010. V. 115. A08106.
- [3] Rennilson J.J., Criswell D.R. Surveyor observations of lunar horizon-glow // Moon. 1974. V. 10, P. 121–142.
- [4] Severny A.B., Terez E.I., Zvereva A.M. The measurements of sky brightness on Lunokhod-2 // Moon. 1975. V. 14. P. 123–128.
- [5] McCoy J.E., Criswell D.R. Evidence for a high latitude distribution of lunar dust // Proc. Lunar Sci. Conf., 5th. Houston. USA. 1974. P. 2991–3005.
- [6] Zook H.A., McCoy J.E. Large-scale lunar horizon glow and a high altitude lunar dust exosphere // Geophys. Res. Lett. 1991. V. 18. P. 2117–2120.
- [7] Berg O.E., Wolf H., Rhee J. Lunar soil movement registered by the Apollo 17 cosmic dust experiment // In: Interplanetary dust and zodiacal light. H. Elsasser, H. Fechtig (Eds.). Springer. New York. 1976. P. 233–237.
- [8] Popel S.I., Kopnin S.I., Golub' A.P., et al. Dusty plasma at the surface of the moon // Solar Syst. Res. 2013. V. 47. P. 419–429.
- [9] Muñoz O., Moreno F., Guirado D., et al. The Amsterdam–Granada light scattering database // J. Quant. Spectrosc. Radiat. Transfer. 2012. V. 113. P. 565–574.
- [10] Zubko E., Weinberger A.J., Zubko N., et al. Umov effect in single-scattering dust particles: Effect of irregular shape // Opt. Lett. 2017. V. 42. P. 1962–1965.
- [11] Zubko E., Videen G., Zubko N., Shkuratov Yu. Reflectance of micron-sized dust particles retrieved with the Umov law // J. Quant. Spectrosc. Radiat. Transfer. 2017. V. 190. P. 1–6.
- [12] Shkuratov Yu.G., Opanasenko N.V. Polarimetric and photometric properties of the moon: Telescope observation and laboratory simulation. II – The positive polarization // Icarus. 1992. V. 99. P. 468–484.

# DUSTY PLASMA CLOUD IN THE LUNAR EXOSPHERE AND IMPACTS OF METEOROIDS

S.I. Popel<sup>1,2,3</sup>, A.P. Golub<sup>\*1</sup>, L.M. Zelenyi<sup>1, 2, 3</sup>, M. Horányi<sup>4</sup>

<sup>1</sup>Space Research Institute of the Russian Academy of Sciences, Profsoyuznaya 84/32, Moscow 117997, Russia;

<sup>2</sup>Moscow Institute of Physics and Technology (State University), Institutskiy per. 9, Dolgoprudnyi, Moscow region 141700, Russia;

<sup>3</sup>National Research University Higher School of Economics, Myasnitskaya 20, Moscow 101000, Russia;

<sup>4</sup>University of Colorado at Boulder, Boulder, CO 80303, United States

## KEYWORDS:

Dusty plasma, meteoroids, the Moon, exosphere

## INTRODUCTION:

The possibility of the formation of a dusty plasma cloud in the exosphere of the Moon owing to impacts of meteoroids on the lunar surface is discussed. Attention is focused on dust particles at large altitudes of ~10-100 km at which measurements were performed within the NASA LADEE mission. It has been shown that a melted material ejected from the lunar surface owing to the impacts of meteoroids plays an important role in the formation of the dusty plasma cloud. Drops of the melted material acquire velocities in the range between the first and second cosmic velocities for the Moon and can undergo finite motion around it. Rising over the lunar surface, liquid drops are solidified and acquire electric charges, in particular, owing to their interaction with electrons and ions of the solar wind, as well as with solar radiation. We show that the number density of dust particles in the dusty plasma cloud present in the exosphere of the Moon is in agreement with the LADEE measurements.

## MEASUREMENT DATA:

Within the Apollo missions, dust particles with sizes ~100 nm were observed in the exosphere of the Moon up to an altitude of about 100 km. Similar conclusions can be obtained from the data of the recent US LADEE (Lunar Atmosphere and Dust Environment Explorer) mission (September 2013–April 2014) [1] according to which a cloud of submicron dust particles is continuously present around the Moon up to altitudes of at least several hundred kilometers.

The characteristics of dust were measured within the LADEE mission, in particular, by means of a LDEX impact ionization dust detector, which allows the direct detection of dust particles at the orbit of a spacecraft. The scientific aim of the experiments was to determine the altitude, size, and density distributions of dust particles over various regions of the lunar surface. The LDEX instrument made it possible to detect individual dust particles with radii larger than 0.3  $\mu\text{m}$  and to measure the cumulative charge from several smaller particles (from 0.1 to 0.3  $\mu\text{m}$ ).

The LDEX data were used to determine the average rate of collisions of dust particles with the instrument. This rate appeared to be approximately 1 and 0.1 impacts per minute for particles with charges  $q > 0.5$  fC and  $q > 5$  fC, respectively, which correspond to the particle sizes  $a > 0.3$   $\mu\text{m}$  and  $a > 0.7$   $\mu\text{m}$ , respectively. The LDEX measurements reveal the presence of stably existing rarefied cloud of small dust particles with radii from  $< 0.3$   $\mu\text{m}$  to  $> 0.7$   $\mu\text{m}$ . The number density of dust particles in the cloud observed within the LADEE mission is in the range of  $(0.4 - 4) \times 10^{-9}$   $\text{cm}^{-3}$ . The measurements did not reveal an increase in the density of dust over the terminator region owing to electrostatic processes that is expected within a dynamic fountain model for lunar dust [2]. However, a stepwise increase in the dust density in the process of interaction of some of annual meteor showers with the Moon was revealed. This effect was particularly pronounced during the Geminid meteor shower. All these circumstances indicate a correlation between processes of formation of the dust cloud and collisions of meteoroids with the lunar surface.

There are also indirect indications of the existence of the lunar dusty plasma cloud. In particular, the radio occultation data [3, 4] from the Luna-19 and Luna-22 Soviet spacecrafts on the determination of the electron number density over the lunar surface indicate [5] that the "lunar ionosphere" with the characteristic altitude scale of ~10-30 km exists over the illuminated side of the Moon.

## METEOROID IMPACTS AND DUSTY PLASMA CLOUD FORMATION:

Here, we consider a possibility [6] of the formation of a dusty plasma cloud at large altitudes of  $\sim 10$ - $100$  km over the Moon owing to impacts of meteoroids on the lunar surface. Impacts of meteoroids can result in the elevation of dust particles, in particular, to high altitudes. The number density of dust particles at these altitudes is determined by the flow of particles that appear because of impacts of meteoroids and elevate over the lunar surface. This flow is in turn related to the number of collisions of meteoroids with the lunar surface. The number of collisions of meteoroids with a unit lunar surface per unit time is about  $100 \text{ m}^{-2} \text{ day}^{-1}$ . Most of the impactors have submicron and micron sizes. The average velocity of impactors is about  $27 \text{ km/s}$ .

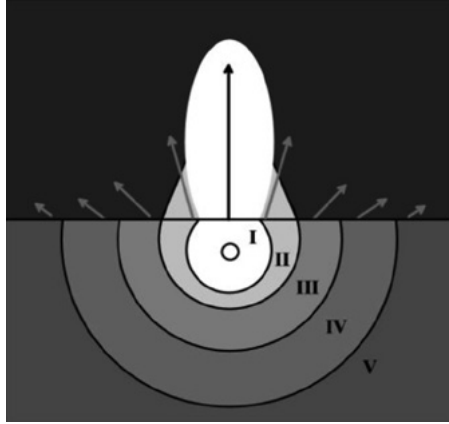


**Fig. 1.** Scheme of the formation of zones I-V around the equivalent center of the meteoroid. The circle in zone I represents an unperurbed meteoroid located at the equivalent center of a meteoroid explosion. Arrows indicate the ejection of material (in particular, dust particles) at high velocities from the lunar surface from zones I-V. The upward ejections of evaporated and melted material are shown by the same colors as the corresponding zones.

We consider the collision of a fast meteoroid with the lunar surface. The calculations are performed for the case where the incident meteoroid and target consist of continuous and porous gabbroid anorthosite, respectively. The impact of a fast meteoroid on the lunar surface leads to the formation of zones around the equivalent center of the meteoroid. These zones are (I) material evaporation zone; (II) material melting zone; (III) destruction zone of lunar regolith particles and their irreversible deformations; and (IV) zone of nonlinear elastic deformations of regolith material, where pressures in a nonlinear acoustic wave are lower than the dynamic elasticity limit (Fig. 1). In zone V of linear elastic deformations, which is formed behind zone IV, the acoustic wave can be considered as linear.

The calculations of the velocity and amount of the material rising over the lunar surface from various zones provide the following conclusions [6].

- The mass of dust particles that originate from zone V of linear elastic deformations of the regolith material and rise over the lunar surface to altitudes higher than  $10 \text{ m}$  ( $1 \text{ km}$ ) is  $80$  ( $6$ ) times larger than the mass of the material rising from other zones (I-IV).
- The mass of dust particles that originate from zones IV and V of elastic deformations and rise over the lunar surface to altitudes higher than  $10 \text{ km}$  is four times larger than the mass of the material rising from zones I-III.
- Only the material from material evaporation zone I, material melting zone II, and zone III of destruction of lunar regolith particles and their irreversible deformations can reach an altitude of  $100 \text{ km}$  or higher over the lunar surface.
- Only the material ejected by the shock wave from material evaporation zone I and material melting zone II can reach an altitude of  $700 \text{ km}$ .

Furthermore, the material melting zone II is the most important zone for the formation of the dust cloud over the lunar surface. Only drops formed in the material melting zone II have velocities in the range from the first to second cosmic velocities (for the Moon), i.e., from  $1.68$  to  $2.38 \text{ km/s}$ . Only these drops

can undergo finite motion around the Moon. The material from the material melting zone is ejected in the form of melted drops to altitudes of about 100 km and higher. We estimate the sizes and number density of these drops. We show that these drops form the dusty plasma cloud in the lunar exosphere. The cloud is characterized by the number density  $\leq 10^{-8} \text{ cm}^{-3}$  of dust particles with sizes  $300 \text{ nm} \leq a_p \leq 1 \text{ }\mu\text{m}$  in agreement with the LADEE data. Since the meteoroid flux (including micrometeoroids) on the lunar surface exists always, the dust cloud over the Moon also exists always.

### ACKNOWLEDGEMENTS:

This work was carried out as part of the Russian Academy of Sciences Presidium program no. 7 and was supported by the Russian Foundation for Basic Research (project no. 15-02-05627-a).

### REFERENCES:

- [1] Horányi M., Szalay J.R., Kempf S., et al. A permanent, asymmetric dust cloud around the Moon // *Nature*. 2015. V. 522, P. 324-326.
- [2] Stubbs T.J., Vondrak R.R., Farrell W.M. A dynamic fountain model for lunar dust // *Adv. Space Res.* 2006. V. 37, P. 59-66.
- [3] Vasil'ev M.B., Vinogradov V.A., Vyshlov A.S., et al. Radio transparency of circumlunar space using the Luna-19 station // *Kosm. Issled.* 1974. V. 12. P. 102-107.
- [4] Vyshlov A.S., Mycroft M.J. Preliminary results of circumlunar plasma research by the Luna 22 spacecraft // in *Space Research (COSPAR, Paris, 1975)*, Vol. 16, p. 945-949.
- [5] Stubbs T.J., Glenar D.A., Farrell W.M., et al. On the role of dust in the lunar ionosphere // *Planet. Space Sci.* 2011. V. 59. P. 1659-1664.
- [6] Popel S.I., Golub' A.P., Zelenyi L.M., Horányi M. Impacts of fast meteoroids and a plasma-dust cloud over the lunar surface // *JETP Lett.* 2017. V. 105. P. 635-640.



# HYDROGEN FORMATION IN LUNAR REGOLITH AND ITS POSSIBLE INFLUENCE ON DUSTY PLASMA AT THE MOON

A. Yu. Dubinsky<sup>1</sup>, S.I. Popel<sup>1,2,3</sup>

<sup>1</sup>Space Research Institute of the Russian Academy of Sciences, Profsoyuznaya 84/32, Moscow 117997, Russia;

<sup>2</sup>Moscow Institute of Physics and Technology (State University), Institutskiy per. 9, Dolgoprudnyi, Moscow region 141700, Russia;

<sup>3</sup>National Research University Higher School of Economics, Myasnitskaya 20, Moscow 101000, Russia

## KEYWORDS:

Lunar regolith, dusty plasma, hydrogen, solar wind.

Recent studies [1] based on the Lunar Reconnaissance Orbiter data and aimed at detecting the neutron fluxes that passed through the lunar surface regions in the southern hemisphere of the Moon revealed the presence of hydrogen-rich areas in the near-surface lunar region at latitudes exceeding  $70^\circ$ . The emergence of near-surface hydrogen-rich areas may be driven by the solar wind electrons and protons that impact the Moon, are absorbed by (implanted into) its surface, and form neutral atoms and molecules of hydrogen or chemical compounds that contain hydrogen, for example, in the form of hydroxyl groups [2]. This implanted hydrogen may accumulate at the lunar surface according to the following mechanism. The solar wind protons are absorbed by the lunar regolith particles at depths of up to  $10^{-5}$  cm. At the end of the proton path they are chemically bound with atoms of the lunar regolith, in particular with oxygen atoms; as a result, tens of percent of oxygen atoms in the lunar soil regions that interact with the solar wind protons get bound into the OH hydroxyl groups. This implanted hydrogen rises to the lunar surface due to diffusion. The desorption of hydrogen bound in this way progresses very slowly at temperatures lower than 400 K that are typical for the lunar surface. As a result, the surface concentration of hydrogenous materials on the Moon may reach sufficiently large values (up to  $10^{17}$  cm<sup>-2</sup>) in several thousand years [2].

However, the results obtained by Mitrofanov et al. [1] are treated often as those which point at the presence of water ice in the near-surface lunar regions. Justification of such a treatment is important from the viewpoint of future lunar missions and exploration of the Moon, especially with taking into account very low probability of the existence of free water (say, not incorporated in near-surface lunar soil) on the Moon because of strong evaporation into atmosphereless space at day time and impossibility to condense at night time. Determination of a mechanism of the formation of water molecules incorporated in the near-surface lunar soil is important for understanding the processes occurring in the lunar regolith. The purpose of this work is the description of a mechanism of formation of water incorporated in the crystal lattice of SiO<sub>2</sub>, which takes into account the presence in the lunar soil of sulfur compounds, e.g., Ag<sub>2</sub>S.

Ag<sub>2</sub>S was found (see Fig. 1) in the form of microscale particles in feldspar of lunar regolith collected by "Luna-24" [3], [4]. The presence of Ag<sub>2</sub>S in the lunar regolith can be explained by considering magmatic processes at early stage of lunar evolution. In accordance with the conception [2], the energy of the solar wind proton is enough to uncouple a molecule of SiO<sub>2</sub> in the crystal lattice of quartz. Then the proton is coupled with an oxygen atom forming hydroxyl (OH-) group. However, the hydroxyl group remains coupled with a silicon atom presenting in the crystal lattice of SiO<sub>2</sub>. Such a configuration is not related to the presence of water on the Moon. The thermal energy is not sufficient to break chemical bonds in quartz. To explain the release of oxygen atoms from the crystal lattice of SiO<sub>2</sub> we consider sulfur compounds (e.g., Ag<sub>2</sub>S) containing in the lunar regolith. Sulfur and oxygen atoms have similar structures of outer electron shell, although the size of the sulfur atom is larger than that of the oxygen one. Furthermore, the structure of the molecule Ag<sub>2</sub>S is analogous to that of H<sub>2</sub>O. This results in a possibility of substitution of oxygen atom in the crystal lattice of SiO<sub>2</sub> by sulfur atom and, correspondingly, in the release of oxygen atom in the regions of lunar near-surface soil where argen-tum sulphide contacts with silicon oxide.

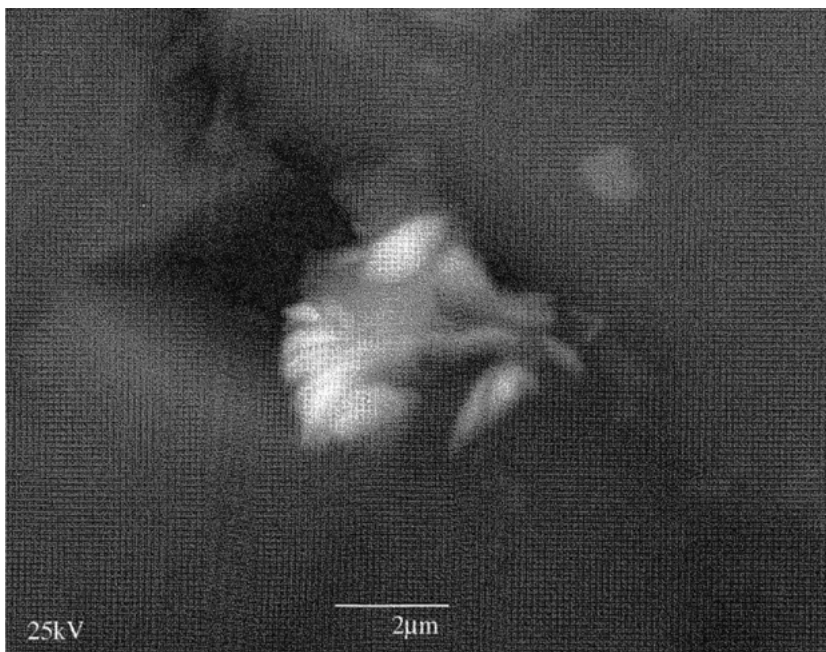
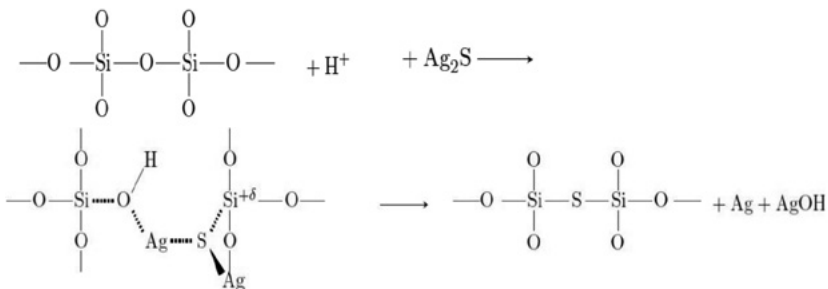


**Fig. 1.** Electron microscope image of a microscale particle containing argentum sulphide from the lunar regolith collected by "Luna-24" [4].

The exchange between sulfur and oxygen occurs in the following manner.



The above mechanism of exchange between sulfur and oxygen does not require an additional energy immediately after the first energy pulse which corresponds to binding of H and O. Seemingly, this mechanism is a realistic one from the viewpoint of formation of water molecules incorporated in the crystal lattice of  $\text{SiO}_2$ .

The rate of the process described by the above chemical reactions is limited by the following factor. Breaking of the chemical bond Si-O is possible only during the lunar day because the flux of the solar wind protons is needed for the chemical bond breaking.

The above chemical reactions occur at the illuminated part of the Moon in the layer of regolith of thickness of about  $10^{-5}$  cm. This is caused by a necessity for the solar wind protons to reach the zone of their contact with argentum sulphide (to provide breaking of the chemical bond Si-O). The estimate of the probability of exchange between sulfur and oxygen atoms gives the magnitude on the order  $10^{-5}$ .

The presence of water molecules in the near-surface lunar soil influences the photoemission properties of lunar regolith, and finally, the properties of the dusty plasma system at the Moon, which will be studied within the future space missions "Luna-25" and "Luna-27" [5]. We discuss the character of this influence on the properties of the dusty plasma system.

This work was carried out as part of the Russian Academy of Sciences Presidium program no. 7 and was supported by the Russian Foundation for Basic Research (project no. 15-02-05627-a).

**REFERENCES:**

- [1] Mitrofanov I.G., Sanin A.B., Boynton W.V., et al. Hydrogen mapping of the lunar south pole using the LRO neutron detector experiment LEND // *Science*. 2010. V. 330, P. 483-486.
- [2] Starukhina L. Water detection on atmosphereless celestial bodies: alternative explanations of the observations // *J. Geophys. Res.* 2001. V. 106, P. 14701-14710.
- [3] Bogatikov O.A., Gorshkov A.I., Mokhov A.V., et al.: High-quality gold, Cu-Zn-Au-Ag solid solution, and native Mo in the AS Luna 16 regolith // *Doklady Earth Sci.* 2002. V. 386. No. 7. P. 827-831.
- [4] Mokhov, A.V., Kartashev, P.M., Bogatikov, O.A. The Moon under microscope: new data on mineralogy of the Moon. Nauka, Moscow, 2007. 127 p. (in Russian).
- [5] Popel S.I., Kopnin S.I., Golub' A.P., et al. Dusty plasma at the surface of the Moon // *Solar System Research*. 2013. V. 47. P. 419-429.

# INFRASOUND REGISTRATION OF ROMANIAN SUPERBOLIDE

O. Popova<sup>1</sup>, Yu. Rybnov<sup>1</sup>, V. Kharlamov<sup>1</sup>, D.Ghica<sup>2</sup>, J.Borovička<sup>3</sup>,  
D. Glazachev<sup>1</sup>, E. Podobnaya<sup>1</sup>

<sup>1</sup>*Institute for Dynamics of Geospheres Russian Academy of Sciences (Leninsky prospect, 38 (bldg.1), Moscow, Russia, olga\_idg@rambler.ru*

<sup>2</sup>*National Institute for Earth Physics (Strada Călugăreni 12, Măgurele, Romania)*

<sup>3</sup>*Ondřejov observatory, Astronomical Institute Czech Academy of Sciences (Ondřejov, Czech Republic)*

## KEYWORDS:

Superbolide, infrasound and optical observation, energy estimate

## INTRODUCTION:

Superbolides, i.e. extremely bright meteors produced by entries of meter-sized bodies into terrestrial atmosphere occurs roughly 10-20 times per year over the globe, i.e. are rare events. The majority of observational data for superbolides consist of fireball detections reported from US Government sensors (USG), which provide limited information (mainly irradiated energy, altitude of maximal luminosity and entry velocity for smaller part of the events). Less than two dozen of these events were recorded by groundbased observations.

Infrasound signals of fireballs are usually recorded by professional equipment at great distances (in far zone) when waveguide propagation. Measurements of weak shock waves in the direct propagation zone is an urgent task and enable both to estimate the parameters of the cosmic body and to study the processes of generation and propagation of infrasonic signals.

## ROMANIAN SUPERBOLIDE:

Optical observational data on Romanian superbolide (January 7, 2015) include optical and radiometric records obtained by the European Fireball Network (EN), casual video records from Romania and USG data [1]. The strong infrasonic signals generated by the superbolide were detected by both the local stations of the Romanian Seismic Network (operated by NIEP) and the IPLOR array microbarometers. It is important to mention here that the main energy deposition took place almost above the area where the IPLOR station is deployed, i.e. the signal was recorded in the area of direct propagation, which is rare. The infrasound signal was also detected by three CTBTO infrasound stations in Germany (I26DE), Russia (I43RU) and Kazakhstan (I31KZ) at large distances.

Analysis of optical data allowed to determine the trajectory, the entry velocity, the deceleration curve and the light curve. The meteoroid entered the atmosphere at 27.76 km/s at an angle of 43° to the horizon. The maximum energy release (maximum luminosity) was observed at an altitude of 42.8 km, the length of the luminous trajectory was close to 70 km [1]. Analysis of infrasound data allowed to determine the location of the source of the signal (i.e. corresponding part of the trajectory), to study the generation of overpressure pulse during the flight and fragmentation of meteoroid.

Different approaches were used to estimate meteoroid energy based on available optical and infrasound data. The relation connected the amplitude of the overpressure and energy of the source was suggested. Independent estimates of meteoroid energy were compared and reasonable agreement was found.

## REFERENCES:

[1] Borovička J., Spurný P., Grigore V., Svoren J. The January 7, 2015, superbolide over Romania and structural diversity of meter-sized asteroids // Planetary and Space Science.2017.V.143, 147-158.

# THE INVESTIGATION OF METEOR EVENTS BY MULTI TECHNIQUE OBSERVATIONS

A. Kartashova<sup>1</sup>, Yu. Rybnov<sup>2</sup>, O. Popova<sup>2</sup>, D. Glazachev<sup>2</sup>, G. Bolgova<sup>1</sup>

<sup>1</sup>Institute of Astronomy Russian Academy of Sciences, Moscow, Russia, Pyatnitskaya str., 48, Moscow, Russia, akartashova@inasan.ru

<sup>2</sup>Institute for Dynamics of Geospheres Russian Academy of Sciences, Leninskiyprospect, 38, building 1, Moscow, Russia

## KEYWORDS:

Meteor observations, meteoroids, acoustic meteor observations, meteor mass.

## INTRODUCTION:

The interaction of meteoroids with the atmosphere generates an optical (meteors), and acoustic radiation. Most meteor particles do not fall on the Earth's surface and their properties (mass, size and etc.) are estimated by observational data under certain assumptions and with the help of the models of the meteor-atmosphere interaction. The multi technique meteor observations provide independent sets of observational data. The analysis of these data would allow to improve meteor parameters and models of particle interactions with the atmosphere.

Multi technique (optical and acoustical) meteor observations were organized by Institute Astronomy RAS and Institute for Dynamics of Geospheres RAS in 2014 [1] and continued in August 2016. The double - station observations are conducted on Zvenigorod observatory of INASAN (ZO INASAN) and Geophysical observatory IDG RAS Mikhnevo (GPhOMikhnevo). Simultaneously infrasound meteor observations are carried out on three stations (IDG RAS, GPhOMikhnevo, ZO INASAN) in 2016 (and present time).

The dynamic parameters (the radiant position, the geocentric velocities, the beginning and end heights, the orbital parameters) and the light curves of detected double-stations meteors were obtained. Meteoroid energies were obtained based on infrasonic detections. Meteoroids masses, which were estimated by both optical and acoustical observations, are compared and observed uncertainties are discussed.

The work was partially supported by Program № 7 of the fundamental research of the Presidium of RAS.

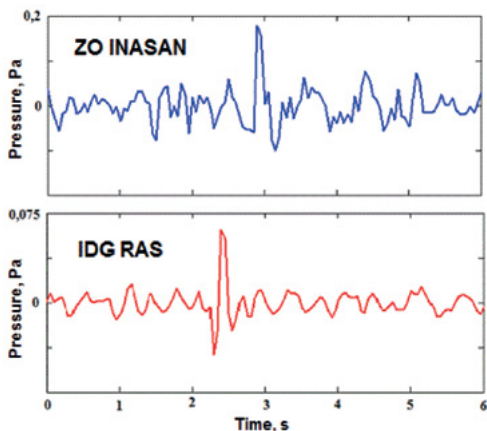


Fig.1. Acoustic signals of the meteor 10-08-2016 (18:58:27) recorded at two stations.

## REFERENCES:

[1] Kartashova A. et al. The multi technique meteor observations in 2014//Proceedings of the International Meteor Conference. 2016. P.120-122.

# THE RECOVERY OF 2012 TC<sub>4</sub> AND THE INTERNATIONAL ASTEROID WARNING NETWORK (IAWN)

R.R. Landis<sup>1</sup>, B.M. Shustov<sup>2</sup>

<sup>1</sup>NASA Headquarters, Planetary Defense Coordination Office, 300 E St. SW, Washington, DC 20546 USA, rob.r.landis@nasa.gov

<sup>2</sup>Institute of Astronomy, Russian Academy of Sciences (INASAN), Pyatnitskaya Str. 48, Moscow 119017, Russian Federation, bshustov@mail.ru

## KEYWORDS:

near-Earth asteroid, near-Earth object, NEO, IAWN, 2012 TC<sub>4</sub>, close approach

## INTRODUCTION:

The International Asteroid Warning Network (IAWN) is a United Nations-endorsed organization composed of a wide variety of experts in the field of near-Earth Objects (NEOs). In addition, the IAWN [1] includes experts in public policy, disaster relief and communication, and education. There are currently eight signatories to the Statement of Intent, including members in Russia, Europe, Asia, South and North America. The main IAWN functions include (but, not limited to):

- the conduct and coordination of the NEO search effort;
- follow-up and characterization of NEOs;
- communicating the risks and benefits of NEOs to a wide audience;
- educating the public on NEOs;
- maintaining a clearinghouse for NEO data;
- maintaining a database of potential impact consequences; and
- serving as the single trusted source for information on NEOs.

The current flyby of the near-Earth asteroid 2012 TC<sub>4</sub> is an opportunity for the IAWN to exercise a variety of interfaces to recover this inner solar system interloper. 2012 TC<sub>4</sub> makes a close approach to Earth on 12 October 2017 at a distance of ~13,600 km (~2.2 Earth radii) over Antarctica. It was discovered by Pan-STARRS (on Haleakalā, Maui, Hawaii) on 4 October 2012 [2] and is probably no larger than 27 meters across. Photometric observations [3] indicate 2012 TC<sub>4</sub> possibly as a rotational period of ~12.24 minutes. However, 2012 TC<sub>4</sub> has an orbit condition code<sup>1</sup> of 5, meaning the longitude uncertainty [in its orbit] 28.2 arc-minutes or less. The current apparition of 2012 TC<sub>4</sub> provides an opportunity to exercise the interfaces of IAWN to better coordinate the recovery and crucial follow-up observations of this Apollo asteroid by observatories around the world, representative of the critical first step in planetary defense.

## REFERENCES:

- [1] Spahr, T., Landis, R.R., "The International Asteroid Warning Network: History, Background, and Current Status," Planetary Defense Conference, Tokyo, Japan (2017).
- [2] MPEC 2012-T18: 2012 TC<sub>4</sub>, <http://www.minorplanetcenter.net/mpec/K12/K12T18.html> (7 October 2012).
- [3] Polishook, D., "Fast Rotation of the NEA 2012 TC<sub>4</sub> Indicates a Monolithic Structure," *Minor Planet Bulletin* **40**, 42-43 (2013).

---

<sup>1</sup> The orbit condition code is also known as the "U uncertainty parameter." It is an integer between 0 and 9 indicating how well an object's orbit is known on a logarithmic scale, where 0 indicates a well-determined orbit. Orbit condition codes are significant when computing spacecraft transfer trajectories. Small bodies with higher orbit condition codes imply inherently greater uncertainties in the existence and Dv values associated with trajectories to those bodies. Orbit condition codes can be reduced as more optical or radar observations become available.

# ANOMALOUS MG-26 COMPOSITION IN THE EARLY SOLAR SYSTEM CHONDRITES

I. Roth,

Space Sciences, University of California, Berkeley, CA 94720, USA; ilan@ssl.berkeley.edu

## KEYWORDS:

Meteorites, chondrites, Ca-Al inclusions, anomalous compositions, early sun, solar flares.

## INTRODUCTION:

Meteorites are the raw materials for planetary formation, believed to contain dust and grain particles that accreted to form primitive asteroids in the early solar system. Most of the meteorites that reach Earth are chondrites, stony matrix material of the oldest rocks in solar system that have not been modified due to melting or differentiation. They provide an important clue to the understanding of the processes that transformed a disk of gas and dust into planets, moons, asteroids, and comets. An important constrain for understanding the first chondrites of the early solar system is embedded in the (a) calcium-aluminum rich inclusions (CAIs) - mm-to-cm calcium-and aluminum rich refractory inclusions found in carbonaceous chondrites produced by flash heat, then accreted onto their parent asteroids, and (b) observations of fossil short-lived (half-lives of <Myr) products of radio-nuclides (such as  $^{26}\text{Al}$ ) in meteorites at abundances inconsistent with galactic nucleosynthesis. Of particular interest are the observations of CAI inclusions with enhanced abundance of  $^{26}\text{Mg}$ , which is a daughter product of  $^{26}\text{Al}$  decaying into  $^{26}\text{Mg}$  while emitting 1.809 MeV photons, with a lifetime of  $1.1 \times 10^6$  years. The galactic ratio of  $^{26}\text{Al}/^{27}\text{Al}$  (radioactive/stable) is  $3 \times 10^{-6}$  while the deduced ratio in the CAI gives  $(1.5-5) \times 10^{-5}$ .

The young solar-like stars emit copious amount of x-rays indicating intense magnetic activity. The most spectacular present day heliospheric abundance enhancement involves the energetic (MeV)  $^3\text{He}$  isotope and selective heavy elements in impulsive solar flares. The process of  $^3\text{He}$  energization due to resonant interaction with waves observed at a similar terrestrial auroral environment as flaring solar corona will be described. Therefore, at the early epoch of the young Sun a large number of impulsive flares have occurred and the heliosphere was filled with a significant amount of energetic MeV  $^3\text{He}$ , as is observed in the present epoch. The abundance of  $^{26}\text{Al}$  isotopes was increased significantly before solidification through  $^{24}\text{Mg}(^3\text{He},p)^{26}\text{Al}$ ,  $^{28}\text{Si}(^3\text{He},\alpha)^{26}\text{Al}$ ,  $^{25}\text{Mg}(^3\text{He},pn)^{26}\text{Al}$ ,  $^{27}\text{Al}(^3\text{He},\alpha)^{26}\text{Al}$  reactions, which require these energetic  $^3\text{He}$  ions. Therefore, solar acceleration of rare isotopes in the early solar system contributes to a selective formation of radioactive elements which are observed as fossil elements in the meteorites.

# DYNAMICS AND EVOLUTION OF RINGS AROUND CENTAURS CHARIKLO AND CHIRON

**B.P. Kondratyev**

*1Sternberg Astronomical Institute, M.V. Lomonosov Moscow State University, 13 Universi-tetskij prospect, 119992, Russia*

From the observations, the asteroid Chariklo (and possibly Chiron) have outer rings. The purpose of this paper consists in constructing the equilibrium models of these asteroids and developing the kinetic mechanism of evolution of their rings. We have specified for Chariklo the density  $\rho_0 \approx 2.71 \text{ g/cm}^3$ , the mass  $M_0 \approx 8.817 \cdot 10^{21} \text{ g}$  and the average radius  $R_0 \approx 128.16 \text{ km}$ . Consistent estimation of the parameters of Chiron with the average radius  $R_0 \approx 109 \text{ km}$  gives the density  $\rho_0 \approx 1.2 \text{ g/cm}^3$  and the mass  $M_0 \approx 6.5 \cdot 10^{21} \text{ g}$ . The rings are modeled by circular gravitating toruses consisting of the small rock-ice particles that orbit the asteroid. The method does not imply the presence of hidden satellites near to asteroid, and the equilibrium of rings is determined by small velocity dispersion and gravity of particles. The problem of calculating the gravitational energy of the torus is solved. By using the energy, it is possible to express the mass of the ring through the mass of asteroid  $M_0$ . For the

Chariklo's inner (outer) ring the mass ratio is equal to  $\frac{M_{r1}}{M_0} \approx 10^{-3} \left( \frac{M_{r2}}{M_0} \approx 10^{-4} \right)$ ;

and for Chiron  $\frac{M_{r1}}{M_0} \approx 3.66 \cdot 10^{-4} \left( \frac{M_{r2}}{M_0} \approx 1.66 \cdot 10^{-3} \right)$  respectively. The ratio of

mass of the rings is equal to  $\frac{M_{r1}}{M_{r2}} \approx 10$  (Chariklo) and  $\frac{M_{r2}}{M_{r1}} \approx 4.54$  (Chiron).

The rings of both asteroids are located out of the Roche limit. We studied in detail the kinetics of particle motion in the rings. The dissipation rate equation for the rings is derived. From this equation a surprising result follows: the time of energy dissipation (the time of evolution of rings) is only  $T_{d1} \approx 10^3 \div 10^4$  years that to astronomical measures is very short time scale. We present the arguments supporting the idea that these rings in the future can become satellites of the asteroids.



# THE SURFACE TENSION OF SMALL BODIES UNDER SELF-GRAVITY, ROTATION AND TIDAL FORCES

S.A. Voropaev <sup>1</sup>

<sup>1</sup>Institute for Geochemistry and Analytical Chemistry (GEOKHI) RAS  
119991 Moscow, Kosygina 19, Russia, voropaev@geokhi.ru

## KEYWORDS:

Asteroids, small bodies, tidal, gravity, rotation, deformation, tension.

## INTRODUCTION:

The formation of the solar system passed through the stage of interacting planetesimals and small bodies [1]. Currently, the result is asteroid belt, satellite systems of the giant planets and, in particular, the Earth-Moon system [2]. Accurate accounting of the stresses and strains caused by planetary processes that accompanied the growth planetesimals allow us to better understand the peculiarities of their migration, decay and merging.

## ANALYTICAL PROCEDURE:

Together with geological/geophysical studies and laboratory-scale experiments [3], analytical and numerical consideration of surface stress is a great deal to our knowledge of the large-scale deep structure of planetary interiors. So, the material is an elastic solid for shear stress  $\tau$ , less than a critical value  $\tau_p$ . Once the critical shear stress (or "yield stress") is exceeded, the material flows.

To calculate elastic deformations and stresses of small bodies, one can use well developed theory of gravitational and tidal potential [4]. The force field strength  $\mathbf{F}$  is determined by the gradient of the total potential

$$\mathbf{F} = \rho_0 \text{grad}[V(\mathbf{r})], \quad V(\mathbf{r}) = V_g(\mathbf{r}) + V_\omega(\mathbf{r}) + V_t(\mathbf{r}) \quad (1)$$

$\rho_0$  is the rock's density,  $V_g$  is gravitational,  $V_\omega$  is centrifugal and  $V_t$  is tidal potential. If the small body has an axis of symmetry, the problem simplifies to the exact solution. In the cylindrical coordinate system (the  $z$  is an axis of symmetry), the displacement vector  $\mathbf{u}$  will be presented as the expansion

$$\mathbf{u} = \mathbf{e}_\rho u_\rho + \mathbf{e}_z u_z, \quad (2)$$

where  $u_\rho(\rho, z)$ ,  $u_z(\rho, z)$  and  $u_\phi = 0$  are the radial, vertical, and azimuth components of the displacement, respectively. Then, the equilibrium equation of an isotropic body in the general (gravitational, tidal etc.) force field takes the form

$$\mu \Delta \mathbf{u} + (\lambda + \mu) \text{grad}(\text{div} \mathbf{u}) = -\mathbf{F}, \quad (3)$$

where  $\mu$ ,  $\lambda$  are the Lamé constants and

$$\mu = E/2(1+\nu); \quad \lambda = \nu E/(1+\nu)(1-2\nu) \quad (4)$$

where  $\nu$  is the Poisson ratio, and  $E$  is the Young modulus of the bodies rock.

Important to evaluate the deformation of a planetary body have the boundary conditions: magnitude and distribution of load on the surface. In general, it is three equations like

$$2\mu [e_{11} \text{Cos}(\mathbf{n}, \mathbf{k}_1) + \frac{1}{2} e_{12} \text{Cos}(\mathbf{n}, \mathbf{k}_2) + \frac{1}{2} e_{13} \text{Cos}(\mathbf{n}, \mathbf{k}_3)] + \lambda e \text{Cos}(\mathbf{n}, \mathbf{k}_1) = f_1, \quad (5)$$

where  $e_{ij}$  are the components of the strain tensor,  $e = e_{11} + e_{22} + e_{33}$  – the unit volume change,  $\mathbf{n}$  – the normal vector to the surface,  $\mathbf{k}_i$  – unit vectors of the Cartesian coordinate system and  $f_i$  – the corresponding projection of the surface forces. If the surface is free of load, as is usually the case for small bodies and asteroids,  $f_i = 0$ .

To analyze the surface deformation of a small body, tension and the maximum stress deviator  $\tau_{\max}$  are of the most interest. The latter it is determined by the difference between the maximum  $\sigma_1$  and minimum  $\sigma_3$  main stresses:

$$\tau_{\max} = (\sigma_1 - \sigma_3)/2 \quad (6)$$

Tension is the composition of stretching (rotation and tidal) and pressure (gravity) forces. It is final value will be determined by the ratio of the intensities of the involved potentials:

$$\begin{aligned}
 V_g &= \rho_0^2 a^2 G 2\pi/3, \quad G - \text{gravitational constant}; \\
 V_\omega &= \rho_0 a^2 \omega^2, \quad \omega = 2\pi/T, \quad T - \text{the period of rotation}; \\
 V_t &= \rho_0 a^2 G M/d^3, \quad M \text{ is the central body mass, } d - \text{distance the distance to the} \\
 &\text{satellite and } a - \text{the largest semi-axis of the small body.}
 \end{aligned}
 \tag{7}$$

**RESULTS AND DISCUSSION:**

Unfortunately, none of the elegant spherical theory can be applied to an arbitrary asteroid or small body because of its huge eccentricity. For instance, Saturnian satellite, Hyperion has eccentricity  $\epsilon = 0.812$ . On the other hand, small body in first approximation is tolerably well presented by a two-axial prolate ellipsoid of principal semiaxes  $a$  and  $c$ ,  $a > c$ . For instance, the gravitational potential  $V_g$  of a two-axial elongated ellipsoid is rather simple in the interior and, if the density  $\rho_0$  is assumed constant, can be written as

$$V_g(x,y,z) = V_g [ A(\epsilon) - x^2 B(\epsilon) - (y^2 + z^2) C(\epsilon) ],
 \tag{8}$$

where  $(x, y, z)$  are Cartesian coordinates directed along the  $(a, c, c)$  axes respectively;  $A, B, C$  are functions of eccentricity  $\epsilon = (a^2 - c^2)/a^2$  have been found analytically.

Similarly, will be presented the components of the stress tensor, which occur as functions of Poisson's ratio  $(\nu)$ , and eccentricity,  $t = c^2/a^2$  or  $\epsilon = 1 - t$ . For instance, in the equatorial plane ( $z = 0$ ,  $z$ -axis coincide with the axis of rotation) stress component  $s_{11}$  caused by gravity ( $s_{11}G_e$ ) is

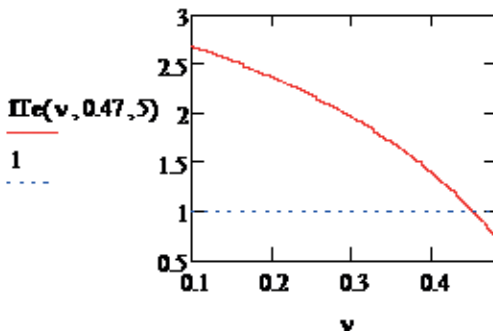
$$s_{11}G_e(\nu, t) := 2 \cdot \frac{(t \cdot \nu^2 + 4 \cdot \nu^2 + 3 \cdot t \cdot \nu - 4) \cdot \nu_1(t) + t \cdot (4 \cdot \nu - 3 \cdot t + t \cdot \nu^2 + 4 \cdot \nu^2 + 2 \cdot t \cdot \nu) \cdot \nu_2(t)}{(1 - \nu) \cdot [ (t^2 + 8 \cdot t + 16) \cdot \nu + 11 \cdot t^2 + 8 \cdot t + 16 ]},$$

where  $\nu_1(t)$  and  $\nu_2(t)$  are determined by  $B(\epsilon)$  and  $C(\epsilon)$ . Also, we can determine the  $s_{11}$  component of the stress tensor caused by rotation ( $s_{11}R_e$ ) and tidal ( $s_{11}T_e$ ) forces. In fact, this component is most important when considering the resulting tensile stresses in the plane  $x = 0$  which is critical for the breakup of the small body. It can be shown that when the tensile forces overcome body's self-gravity, the gap starts at the equatorial point ( $z=0, x=0, y=c$ ) on the surface and goes through along this plane. So, the beginning of the gap can be started when the ratio

$$ITe(\nu, t, p) = \frac{|s_{11}G_e(\nu, t)| \cdot p}{s_{11}R_e(\nu, t) + s_{11}T_e(\nu, t)};
 \tag{9}$$

will be less than 1, where  $p$  is the ratio of the intensities  $V_g/V_\omega$ .

We can illustrate this approach on the example of the Martian satellite -Phobos. It is small body with size  $27 \times 22 \times 18$  km and synchronous rotation with period 7 h 39.2 min. Phobos exceeded the Roche limit for a "fluid" satellite, and is held only by the strength of its rocks. Because of its mean density,  $1.876 \text{ g/cm}^3$ , Phobos composition similar to carbonaceous chondrite material, with Poisson's ratio about 0.3. Of course, the exact elastic characteristics of the rocks is unknown, but we can analyze by (9) its stability as a whole for any value of the Poisson's ratio



where  $t = c^2/a^2$  is 0.47 and  $p = V_g/V_\omega$  is about 5. As we can see from the above picture, Phobos is stable with respect to the breakup by almost all reasonable values of Poisson's ratio. Instability could occur by  $\nu > 0.45$ , when a rocks behaves as an incompressible fluid. Obviously, this is not happening and Phobos is stable at the moment as the graph shows.

In general, an asteroid should be modeled as homogeneous, elastic three-axial ellipsoid ( $a > b > c$ ) subject to self-gravitational stress, rotational and tidal forces. An exact analytical treatment then gives the stress and strain fields throughout its interior and surface. Now, we obtained exact expressions for the stress and strain tensors of a prolate ellipsoid only and estimates main and shear stress value on its surface. Applications of the new formulation to the number of non spherical small bodies and comets in the solar system will be discussed.

### **ACKNOWLEDGMENT:**

The study was performed by a grant of the Russian Science Foundation (project No. 17-17-01279).

### **REFERENCES:**

- [1] Marov M.J., Kolesnichenko A.V. Turbulence and Self-Organisation. Problems of Space and Environments Modeling. Springer, 2012, 632 p.
- [2] Galimov E.M., Krivtsov A.M. Origin of the Moon. New concept. De Gruyter, 2012, 168 p.
- [3] Voropaev S.A. et al. Constructing passport strength of extraterrestrial matter on the example of the Chelyabinsk meteorite // Doklady Astronomy & Mechanics, 2017 (in print).
- [4] Melchior P. Physics and Dynamics of Planets. Vander, 1971, v. 2, 556 p.

# UPDATE OF SHAPE PARAMETERS AND LIBRATION AMPLITUDE FOR SATURNIAN SATELLITES DIONE AND RHEA

**A.B. Dubovitskaia, A.E. Zubarev, E.S. Brusnikin**

*Moscow State University of Geodesy and Cartography (MIIGAiK), MIIGAiK  
Extraterrestrial Laboratory (MExLab), 105064, Gorokhovskiy per., 4, Moscow,  
Russia*

## KEYWORDS:

Control point network, Saturnian satellites, Dione, Rhea, planetary mapping  
Control point networks have been created based on the latest Cassini data (06/2016) for Saturnian satellites Dione and Rhea [1,2]. This allowed us to check the libration amplitude of the satellites, as well as to prepare new cartographic products.

The results of the subsequent photogrammetric processing will be also used for online mapping of these bodies.

## ACKNOWLEDGMENT

The cartography of Dione and Rhea was partly supported by Russian Foundation for Basic Research (RFBR), grant No. 16-37-00316.

## REFERENCES:

- [1] Roatsch T., Oberst J., Giese B., Wählisch M., Winkler V., Matz K.-D., Jaumann R., Neukum G. Cartography of the icy saturnian satellites // ISPRS 2004. <http://www.isprs.org/proceedings/XXXV/congress/comm4/papers/467.pdf>.
- [2] Roatsch Th., Jaumann R., Stephan K., Thomas P.C. Cartographic Mapping of the Icy Satellites Using ISS and VIMS Data // Saturn from Cassini-Huygens. Springer, 2009, P. 763-781.

# DIFFUSE INTERSTELLAR BANDS CARRIERS AND COMETARY ORGANIC MATERIAL

R. Lallement<sup>1</sup>, J.L. Bertaux<sup>2</sup>

<sup>1</sup>GEPI, CNRS UMR8111, Observatoire de Paris, 5 place Jules Janssen, 92195 Meudon, France; rosine.lallement@obspm.fr

<sup>2</sup>LATMOS/IPSL, 11, Bd d'Alembert, 78280 Guyancourt, France

## KEYWORDS:

Comets, Interstellar matter, Solar System formation

## INTRODUCTION:

We suggest that the large organic molecules found in dust of comet 67P/CG were formed in the interstellar medium (ISM), many of them being at the origin of Diffuse Interstellar Bands (DIBs) imprinted as absorptions in stellar spectra. This conservation of organic molecules during the formation of comets in the solar nebula is indeed possible with the scenario of a gentle, hierarchical process of accretion emerging from many lines of evidences from Rosetta *ren-dez-vous* mission (Davidsson et al., 2016). Within this scenario, large organic molecules found now in the comet were formed in the ISM before the existence of the pre-solar nebula. In contrast H<sub>2</sub>O ice sublimated, according to diverse comet D/H values. While the organic to mineral mass ratios  $R_C$  for comet Halley and 67P/CG was measured in the range  $\sim 0.32-1.0$ , we estimated crudely that the DIB carriers alone provide  $R_{ISM}=0.32$ , but clearly some other organic molecules of the ISM (in unknown quantity) do not show up in absorption and could increase this  $R_{ISM}$  ratio. The DIB decrease for lines-of-sight crossing the dense cores of interstellar clouds and simultaneous steepening of the Far UV part of the reddening curve suggest that DIB carriers coagulate and are part of the very small grains finally preserved in comets. Such a conclusion implies that a future sample-return mission from a comet nucleus would return information not only on comets, but also on the exact nature of the interstellar species producing the hundreds of DIBs, whose carriers have been unsuccessfully searched for since seven decades.

## REFERENCES:

[1] Davidsson, B.J.R. et al., 2016, A&A 592, A63

# COLOR-SLOPE INTERPRETATION OF COMET C/2013 UQ4 (CATALINA) USING THE MODEL OF AGGLOMERATED DEBRIS PARTICLES

O. Shubina<sup>1</sup>, O. Ivanova<sup>1,2</sup>, E. Zubko<sup>3</sup>, G. Videen<sup>4</sup>, M. Mommert<sup>5</sup>, J. L. Hora<sup>6</sup>, Z. Seman Křišandová<sup>2</sup>, J. Svoreň<sup>2</sup>, A. Novichonok<sup>7</sup>, S. Borysenko<sup>1</sup>

<sup>1</sup>Main Astronomical Observatory of National Academy of Sciences, Kyiv, Ukraine

<sup>2</sup>Astronomical Institute of the Slovak Academy of Sciences, SK-05960 Tatranská Lomnica, Slovak Republic

<sup>3</sup>School of Natural Sciences, Far Eastern Federal University, 8 Sukhanova Street, Vladivostok 690950, Russia

<sup>4</sup>Space Science Institute, 4750 Walnut Street, Suite 205, Boulder, CO80301, USA

<sup>5</sup>Northern Arizona University, Department of Physics and Astronomy, PO Box 6010, Flagstaff, AZ, 86011, USA

<sup>6</sup>Harvard-Smithsonian Center for Astrophysics, 60 Garden Street, MS65, Cambridge, MA02138-1516, USA

<sup>7</sup>Petrozavodsk State University, 33 Lenina Street, Petrozavodsk, Russia

## KEYWORDS:

Comet C/2013 UQ4 (Catalina); Color Slope; Modeling; Discrete Dipole Approximation; Agglomerated Debris Particles

## INTRODUCTION:

The spectral properties of sunlight scattered from a comet differ significantly from those of unscattered light. The change is the result of the specific wavelength-dependent light-scattering properties of dust particles and gases forming the coma. Therefore, colorimetric measurements may be used to constrain physical and chemical properties of cometary species. What emerges from the photometric measurements of numerous comets is that their color significantly differs from one comet to another [e.g., 1]. The red color is often considered to be a distinctive feature of cometary dust [2]. However, other studies demonstrate that comets may also have blue color [e.g., 3–5]. For example, all four comets whose coma was investigated in [3] displayed blue photometric color. Other examples of blue color of cometary dust can be found in [4, 5]. Finally, it is worth noting the recent Rosetta measurements of the color of dust in Comet 67P/Churyumov–Gerasimenko [6], in which 16 out of 70 individual dust grains detected in the vicinity of the nucleus have blue photometric color. Thus, the blue photometric color also can be a feature of some comets or, at least, some part of their dust. Systematic, long-term studies of the color are still rarely reported in the literature and, therefore, it is difficult to draw statistically reliable conclusions. We report our observations of Comet C/2013 UQ4 (Catalina) that further enriches the knowledge of the variation of cometary color.

## COLOR SLOPE:

It is convenient to characterize the cometary color in terms of the so-called color slope [7]. This characteristic also is referred to as the reflectivity gradient. The color slope can be measured in per cent per 0.1  $\mu\text{m}$  and is defined as follows:

$$S' = \frac{10^{0.4\Delta m} - 1}{10^{0.4\Delta m} + 1} \times \frac{20}{\lambda_2 - \lambda_1}, \quad (1)$$

where  $\Delta m$  stands for the true color index of the comet, i.e., the observed color reduced for the initial solar color. We adapt the color index of the Sun  $B - R = 0.996$  from [8]. In eq. (1),  $\lambda_1$  and  $\lambda_2$  correspond with the effective wavelengths of the filters used. In the present work,  $\lambda_1 = 0.4353 \mu\text{m}$  in the case of the B filter ( $\Delta\lambda = 0.0781 \mu\text{m}$ ) and  $\lambda_2 = 0.6349 \mu\text{m}$  in the case of the R filter ( $\Delta\lambda = 0.1066 \mu\text{m}$ ). Although the filters are broadband, their bandwidths are well isolated one from another.

We note that the geocentric distance of the comet varied by a factor of three over the run of observations. However, we measure nearly the same part

of the coma, adjusting the angular aperture of the signal integration. In the vast majority of cases, the projected radius of the measured area is squeezed between 3133.2 km and 3694.8 km with only one exception, 2091.1 km corresponding to August 1, 2014. The results of computations of the color slope with eq. (1) are shown in Fig. 1 as a function of the phase angle of Comet Catalina.

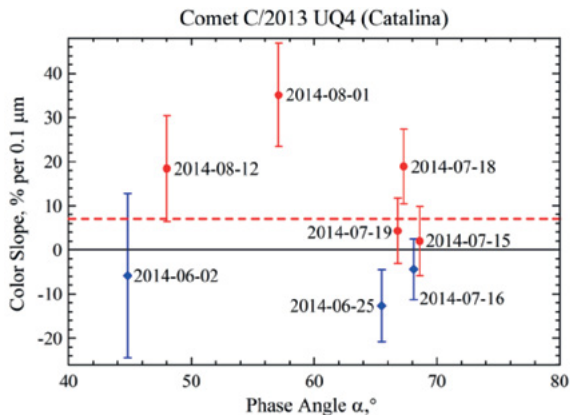


**Fig. 1.** The color slope as a function of phase angle in Comet C/2013 UQ4 (Catalina). Red dots and blue diamonds show positive and negative values of the color slope, respectively. Every data point is labeled with the corresponding date of observation. The red dashed line shows the average color slope for eight available observations.

As one can see in Fig. 1, the color slope  $S'$  in Comet Catalina ranges from  $(-12.67 \pm 8.16)\%$  per  $0.1 \mu\text{m}$  up to  $(35.09 \pm 11.70)\%$  per  $0.1 \mu\text{m}$ . We note that the observations were conducted at different phase angles, which can cause some variation of the color [4]. However, seven out of eight observations of Comet Catalina fall quite well into the two squeezed ranges of phase angle,  $\alpha \approx 44.8^\circ - 48^\circ$  and  $\alpha \approx 65.5^\circ - 68.6^\circ$ . It is significant that within each of those, the observed variation of the color slope cannot be attributed to the change in the geometry of observations and, therefore, they have to be considered in terms of change of the coma constituents.

What also emerges from Fig. 1 is that the coma population may experience dramatic short-term variations. For instance, during a single day spanning July 18-19, the color slope decreases from  $(18.88 \pm 8.44)\%$  per  $0.1 \mu\text{m}$  to  $(4.34 \pm 7.36)\%$  per  $0.1 \mu\text{m}$ , and over a two-day period spanning July 16-18, the color slope increases from  $(-4.43 \pm 6.90)\%$  per  $0.1 \mu\text{m}$  to  $(18.88 \pm 8.44)\%$  per  $0.1 \mu\text{m}$ . Note, the latter case could also suggest qualitative changes in the Catalina color, from blue to red.

These findings have an important practical implication as they reveal that a sole observation hardly characterizes the color of a comet. Indeed, when characterizing the color of Comet Catalina, we meet a fundamental difficulty due to the large dispersion of the observational results. Namely, in three out of eight observations the coma appears blue and in the remaining five, it appears red. During two epochs, June 2 and July 16, the blue color was detected with high uncertainty that also might suggest a slightly red color of the coma. A similar high uncertainty accompanies the measurements of the red color on July 15 and 19. Overall, with confidence we detect blue color on one night and red color on three other nights. Thus, we face the question: what is the color of Comet Catalina?

The average color slope of Comet Catalina is equal to  $6.98\%$  per  $0.1 \mu\text{m}$  that is consistent with other comets [2]. However, this is misleading, since this average color slope does not match any specific observation shown in Fig. 1. While four observations appear consistent with the average color slope within the error bars, the other four observations differ from it considerably. Therefore, in our analysis we do not consider the average color slope in Comet Catalina; instead, we analyze the whole range of the observed color slopes observed.

## MODEL INTERPRETATION:

Using the model of irregularly shaped agglomerated debris particles [4], we retrieve physical and chemical properties of dust in Comet Catalina on the epochs when it revealed its reddest and bluest colors. What emerges from this

study is that the corresponding extreme values of the color slope are unlikely to be reproduced with the same material. This leads us to an important conclusion on chemical heterogeneity of the Catalina coma that there are at least two components in the coma contributing significantly to the optical response. The first component producing the bluest color is consistent with Mg-rich silicates. There are three different options for the second component producing the reddest color. It could be either Mg-Fe silicates, kerogen type II, or organic matter processed with a low dose of UV radiation, as well as a combination of those three species. However, all intermediate values of the color slope in Comet Catalina can be explained in terms of different volume ratios of these two principle components. Our modeling also suggests that the dust particles in both components obey a power-law size distribution  $r^{-n}$  with the index  $n$  being consistent with the *in situ* findings in comets. For more details on this study we refer the Reader to [9].

## REFERENCES:

- [1] Jewitt D., Meech K. J. Cometary grain scattering versus wavelength, or 'What color is comet dust' // *Astrophys. J.* 1986. V. 310. P. 937-952
- [2] Hanner M. S. The scattering properties of cometary dust // *J. Quant. Spectrosc. Radiat. Transfer.* 2003. V. 79. P. 695-705.
- [3] Lamy P. L., Toth I., Weaver H. A. Properties of the nuclei and comae of 10 ecliptic comets from Hubble Space Telescope multi-orbit observations // *Mon. Not. R. Astron. Soc.* 2011. V. 412. P. 1573-1590.
- [4] Zubko E., Muinonen K., Videen G., Kiselev N. N. Dust in comet C/1975 V1 (West) // *Mon. Not. R. Astron. Soc.* 2014. V. 440. P. 2928-2943.
- [5] Ivanova A. V., Korsun P. P., Borisenko S. A., Ivashchenko Y. N. Spectral studies of comet C/2001 Q4 (NEAT) // *Sol. Sys. Res.* 2013. V. 47. P. 71-79.
- [6] Cremonese G., Simioni E., Ragazzoni R., et al. Photometry of dust grains of comet 67P and connection with nucleus regions // *A&A.* 2016. V. 588. A59.
- [7] A'Hearn M. F., Schleicher D. G., Millis R. L., et al. Comet Bowell 1980b // *Astron. J.* 1984. V. 89. P. 579-591.
- [8] Holmberg J., Flynn C., Portinari L. The colours of the Sun // *Mon. Not. R. Astron. Soc.* 2006. V. 367. No. 2. P. 449-453.
- [9] Ivanova O., Zubko E., Videen G., et al. Colour variations of Comet C/2013 UQ4 (Catalina) // *Mon. Not. R. Astron. Soc.* 2017. V. 469. P. 2695-2703.



# NONGRAVITATIONAL EFFECTS IN THE MOTION OF NEAR-SUN COMETS

V.V. Emel'yanenko

*Institute of Astronomy, Russian Academy of Sciences, Moscow,  
Russia, vvemel@inasan.ru*

## KEYWORDS:

Comets, small perihelion distances, many apparitions, nongravitational forces.

## INTRODUCTION:

There is a class of near-Sun comets with perihelion distances  $\sim 0.05$  au (sun-skirting comets). Many of them have been observed in several apparitions [1]. In particular, comets 321P, 322P, 323P have been observed in five apparitions, and 342P has been observed in four apparitions. This allows us to study their orbits and to estimate nongravitational effects in their motions.

## METHODS:

We determined the orbits of 321P, 322P, 323P and 342P using observations in all the apparitions. The gravitational attractions of all the planets were taken into account, and relativistic terms were included in the equations of motion. From consecutive pairs of the apparitions, we obtained four representations of the observations for 321P, 322P, 323P and three representations of the observations for 342P

## NONGRAVITATIONAL EFFECTS:

From a comparison of the different values for the times of perihelion passage in orbits calculated from different pairs of apparitions, we can detect nongravitational effects in the motion. Nongravitational changes were estimated in 2001, 2004 and 2008 for 321P, in 2003, 2007 and 2011 for 322P, in 2004, 2008 and 2012 for 323P, in 2005 and 2011 for 342P. These computations show that there are nongravitational forces acting on the sunskirting comets. The nongravitational forces are very variable. Differences in the values of orientational elements provide evidence that nongravitational components perpendicular to the orbital planes are substantial. Table 1 shows an example of nongravitational changes for 342P near the perihelion passage in 2005.

**Table 1.** Changes of the orbital elements (the semimajor axis  $a$ , the eccentricity  $e$ , the inclination  $i$ , the argument of perihelion  $\omega$ , the longitude of the ascending node  $\Omega$ , the mean anomaly  $M$ ) for 342P near the perihelion passage in 2005

$\Delta a$ , au	-0.000522±0.000011
$\Delta e$	-0.000192±0.000033
$\Delta i$ , deg	0.0960±0.0197
$\Delta \omega$ , deg	0.7293±0.1196
$\Delta \Omega$ , deg	-0.4108±0.1789
$\Delta M$ , deg	-0.0024±0.0004

Potential interpretations of detected nongravitational variations are discussed. In particular, comparisons are made with the results obtained in [2] for the Kreutz sungrazing system's dwarf comets.

## ACKNOWLEDGEMENTS:

This work was supported by the Russian Foundation for Basic Research (Grant 16-02-00805).

## REFERENCES:

- [1] Battams K., Knight M.M. SOHO comets: 20-years and 3,000 objects later // *Philosophical Transactions of the Royal Society A*. 2017. V. 375. Issue 2097. Id. 20160257.  
 [2] Sekanina Z., Kracht R. Strong erosion-driven nongravitational effects in orbital motions of the Kreutz sungrazing system's dwarf comets // *Astrophysical Journal*. 2015. V. 801. Id. 135.

# THE MODELS OF COMETARY GAS PRODUCTION: ANALYSIS FOR 67P/CHURYUMOV-GERASIMENKO

Yu. Skorov<sup>1,2</sup>

<sup>1</sup>Max-Planck-Institut für Sonnensystemforschung, Justus-von-Liebig-Weg 3, 37077 Göttingen, Germany e-mail: skorov@mps.mpg.de

<sup>2</sup>Institute for Geophysics and Extraterrestrial Physics, TU Braunschweig, 38106 Braunschweig, Germany

## KEYWORDS:

comet, 67P/Churyumov-Gerasimenko, numerical models

We consider the old question of the change in the cometary gas production rate with a heliocentric distance. In the simplest case (the Wipple's approach) the absorbed solar energy is spent completely on the sublimation of ice. In this model, the energy loss for thermal re-radiation and for the change in the internal energy of the nucleus is ignored. The production rate grows as an inverse square of the distance. In the more realistic model we assume that the nucleus surface is covered with a porous layer of dust. The layer is characterized in general by thickness, size of dust particles (or pores), layer permeability (a function of porosity and dimensionless thickness), and effective thermal conductivity (a function of pore size). In the presented two-layer heterogeneous model the energy balance equations must be satisfied at the boundaries of the dust layer (that is, at the nucleus surface and at the boundary of the subliming ice): the absorbed solar energy is expanded on the thermal re-radiation, the ice sublimation and the nucleus heating. Our goal is to find out whether the presence of the dust layer can qualitatively change the classical dependence of production rate on the heliocentric distance. We investigate the case when the characteristics of the dust layer do not change with time. The proportionality between the radiative heat conductivity and the particle size may provoke an unreasonable conclusion that a steeper growth in production rate can be caused by the increase in particle size. We revise this hypothesis as well.

The qualitative analysis shows that under the fixed irradiation it is impossible to speed up gas production from under the layer of the fixed dimensionless thickness due to grain size increase leading to the increase of thermal conductivity. The existence of a porous surface layer having the fixed characteristics does not change the production rate as well.

In order to further support our findings, we present the results of massive numerical simulation for a wide range of layer parameters. We use the two-layer model where the heat flux through the overlaying dust layer is determined by the grain size, the layer thickness, and the effective dust conductivity. The last one is simulated considering the hierarchic structure of the medium (porous layer consisting of porous aggregates). A total of 400 options of layer structure were considered. The results of calculations are well approximated by a quadratic dependence and in agreement with the qualitative analysis.

# COMETS 1P/HALLEY AND 67P/CHURYUMOV-GERASIMENKO: COMPARISON OF SOME THEIR PROPERTIES

L.V. Ksanfomality

Space Research Institute of RAS 117997 Moscow Profsojuznaya str. 84/32  
leksanf@gmail.com

## KEYWORDS:

comets, cometary physics, space investigations.

In historical documents, the appearance of comets has always been attributed to major events[1]. Halley's comet was mentioned for the first time in ancient Greek chronicles in 468-466 BC and at the same time was noted in Chinese records. Only in 1531 and 1607 did the appearance of Halley's comet start to be recorded in the Julian and Gregorian calendars, respectively. On March 6 and 9, 1986, for the first time in the history of science, the Russian spacecraft Vega-1 and Vega-2 approached [2] and closely passed by the nucleus of Halley's comet (1P/Halley). A few days later, on March 14, 1986, the same was done by the European Space Agency's (ESA) Giotto spacecraft [3]. These missions, together with the Japanese Suisei [4] (JAXA), marked a successful start to spacecraft exploration of cometary nuclei. Subsequent missions to other comets have been aimed at directly studying cometary bodies carrying signs of the formation of the Solar System. The Rosetta spacecraft [5], inserted into a low orbit around the nucleus of the 67P/Churyumov-Gerasimenko comet, performed its complex measurements August 2014 to September 2016. In this report, some of the data from these missions are compared. Direct studies of cometary nuclei launched 30 years ago by the Vega mission suggest the diverse nature of cometary bodies, their atmospheres, and their formation regions. Comparisons of the most thoroughly studied comets, such as 1P/Halley and 67P/CG, indicate significant differences in their physico-chemical properties, origin, dynamics, and evolution. It can even be noted that the widespread assertion that the study of the physics and the evolution of comets will speed up resolving cardinal issues on the origin of our Solar System is somewhat naive. On the contrary, new processes [6] are being revealed, complicating hypotheses on the Solar System formation.

## REFERENCES:

- [1] Hughes D Wet al. Philos. Trans. R. Soc. A 323 349 (1987)
- [2] Sagdeev R Z et al. Nature 321 259 (1986)
- [3] Reinhard R Nature 321 313 (1986)
- [4] Hirao K, Itoh T Nature 321 294 (1986)
- [5] Ksanfomality L V, Churyumov K I Astron. Vestn. 49 224 (2015)
- [6] Peter Gruber Memorial Lecture, Honolulu, Hawaii. August 4,

# EXPLORING OBVIOUS LUNAR IONOSPHERE BASED ON THE SERVICE MODULE OF CIRCUMLUNAR RETURN AND REENTRY SPACECRAFT

M-Y. Wang<sup>1</sup>, J. Ping<sup>1</sup>, M. Wang<sup>2</sup>, S. Han<sup>2</sup>

<sup>1</sup>National Astronomical Observatories, Chinese Academy of Sciences, Beijing, China, wangmy@nao.cas.cn;

<sup>2</sup>Key Laboratory of Science and Technology on Aerospace Flight Dynamics

## KEYWORDS:

Lunar Ionosphere; the service module of Chinese circumlunar return and reentry spacecraft; electron column content

Since 1960s, radio occultation has been used in planet exploration to detect vertical changing of temperature, pressure and electron density of atmosphere and ionosphere. In 1966, the radio occultation experiment of Pioneer-7 proved the existence of Lunar ionosphere which is very thin (electron density is about  $4 \times 10^4$  el/cm<sup>3</sup>)<sup>[4]</sup>. In Apollo 14 mission, the electron density detected by the Charged Particle Lunar Environment Experiment (CPLLE) was  $10^4$  el/cm<sup>3</sup> at several hundred meters high during lunar day time<sup>[7]</sup>. In Luna-19 & 22 mission, the electron density profiles were detected and the peak densities were about  $10^3$  el/cm<sup>3</sup><sup>[6]</sup>. In the last decade, European mission SMART-1 and Japanese mission SELENE also performed radio occultation experiment for Lunar ionosphere<sup>[1,2,3,5]</sup>.

The circumlunar return and reentry spacecraft is a Chinese precursor mission for the Chinese lunar sample return mission. It was launched into type lunar free-return orbit and loop behind the Moon once to test the high speed atmospheric reentry of a capsule returning from the moon. The circumlunar return and reentry spacecraft was launched on 23 October 2014 and nine days later the return vehicle landed at Inner Mongolia successfully. The service module performed a divert maneuver to avoid re-entry and to go to the Earth-Moon L2 (EML2) point. The service module stayed at EML2 until 4 January 2015 and then conducted a departure maneuver to leave EML2 and begin a transition into a Lunar Orbit. It arrived on 11 January 2015 in a  $200 \times 5300$  km lunar orbit. Finally its orbit would be lower to  $\sim 100$  km to image the target landing zone for the Chinese lunar sample return mission which has not yet been disclosed. During this period, we performed the radio occultation experiment to detect the Lunar ionosphere.

The service module provides a stable and reliable frequency source, whose short-term stability is  $n \times 10^{-9}$ , for both X-band and S-band signal. The signals transmitted from the spacecraft in S and X band passed through lunar ionosphere, interplanetary plasma, Earth ionosphere and atmosphere, finally received by the ground tracking stations. According to the coherent ratio of the S/X signal, we convert the phase information of S-band signal to the frequency of X-band signal and calculate the difference of these two signals. Then, the extrapolation algorithm was used here to deduct the interference error of the earth ionosphere and the interplanetary plasma. Based on the above work, the electron column concentrations of lunar ionosphere were explored preliminarily. The maximums of electron column concentrations are between  $0.4 \sim 0.5 \times 10^{16}$  el/m<sup>2</sup>, are two times of the maximum result from Luna 19/22, are 1~2 orders higher than the SELENE result, but well-matched with the result from CPLLE. These results show that the lunar ionosphere clearly exists and is much stronger than we expected. The result here gives a positive support and some dynamical constraints for the scientific objective of the very low frequency radio astronomical payload onboard the Chang'E-4 lander mission. But it also raises a new question that the characteristics and formation mechanism of a stronger lunar ionosphere remains unknown. More observations will be performed for further scientific targets.

## REFERENCES:

Y. Goto, T. Fujimoto, Y. Kasahara, A. Kumamoto, T. Ono, "Lunar ionosphere exploration method using auroral kilometric radiation," *Earth Planets & Space*, vol 63, pp. 47-56, 2011.

T. Imamura, K.I. Oyama, T. Iwata, Y. Kono, K. Matsumoto, Q. Liu, et al., "The possibility of studying the lunar ionosphere with the SELENE radio science experiment," *Earth*

Planets Space, vol. 60, pp. 387-390, 2008.

- [1] T. Imamura, T. Iwata, Z.I. Yamamoto, N. Mochizuki, Y. Kono, K. Matsumoto, et al., "Studying the lunar ionosphere with selene radio science experiment," *Space Science Reviews*, vol. 154, pp. 305-316, 2010.
- [2] S. Pluchino, F. Schillirò, E. Salerno, G. Pupillo, G. Maccaferri, P. Cassaro, "Radio occultation measurements of the lunar ionosphere," *Memorie Della Società Astronomica Italiana Supplement*, vol. 12, pp. 53, 2008.
- [3] W. Zhen, W. Na, J. Ping, "Electronic content near lunar surface using dual-frequency VLBI tracking data in single lunar orbiter mission," *Research in Astronomy and Astrophysics*, vol. 15, pp. 753-763, 2015.
- [4] A.S. Vyshlov, "Preliminary results of circumlunar plasma research by the Luna 22 spacecraft," *Space Res*, vol. 01, pp. 945-949, 1976.
- [5] D.L. Reasoner, W.J. Burke, "Measurement of the Lunar Photoelectron Layer in the Geomagnetic Tail: Photon and Particle Interactions with Surfaces in Space," Springer Netherlands, pp. 369-387, 1973.

# BEHAVIOR OF HYDROGEN DURING IMPACT EVENTS ON THE MOON

A.A. Berezhnoy<sup>1</sup>, G.V. Belov<sup>2</sup>

<sup>1</sup>Sternberg Astronomical Institute, Moscow State University, Universitetskij pr., 13, 119234 Moscow, Russia

<sup>2</sup>Department of Chemistry, Moscow State University, Leninskie Gory 1/3, 119991 Moscow, Russia

## KEYWORDS:

Impacts, the Moon, impacts, meteoroids, OH, exosphere, adiabatic expansion, equilibrium, quenching, elemental composition.

## INTRODUCTION:

Collisions of meteoroids with the Moon are considered as an important source of metals and hydrogen-containing species in the lunar exosphere. Recently enriched content of Na and K atoms in the lunar exosphere soon after maximum of Quadrantid meteor shower was detected by LADEE space-craft [1]. In our previous papers quenching model of the chemical composition of impact-produced clouds formed after collisions of meteoroids with the Moon was already developed (see, for example, [2]). However, calculations of the equilibrium chemical composition were performed in these papers with usage of CHET program and outdated database of thermodynamical properties of considered species [3]. Now we perform studies of the chemistry of impact events on the Moon with usage of modern thermochemical program IVTANTHERMO [4].

## USED MODEL:

The elemental composition of the target is assumed to be that of the bulk Moon [5]. The elemental composition of impactors is assumed to be that of CI chondrites in accordance with [6]. Based on work [7], chosen target-to-impactor mass ratio in the gas phase of the impact-produced cloud of 5 corresponds to impact velocity of meteoroids equal to 14 km/s. The initial temperature in the impact-produced cloud is taken as  $10^4$  K. The initial pressure is taken as  $10^3$ ,  $10^4$ , and  $10^5$  bar. The adiabatic constant  $\gamma$  was calculated at each step of expansion of the cloud. About 450 gas-phase and solid-state species of 12 elements (O, Si, Mg, Al, Ca, Na, S, Fe, H, C, Ti, and Ni) were considered during calculation of the equilibrium chemical composition of the impact-produced cloud.

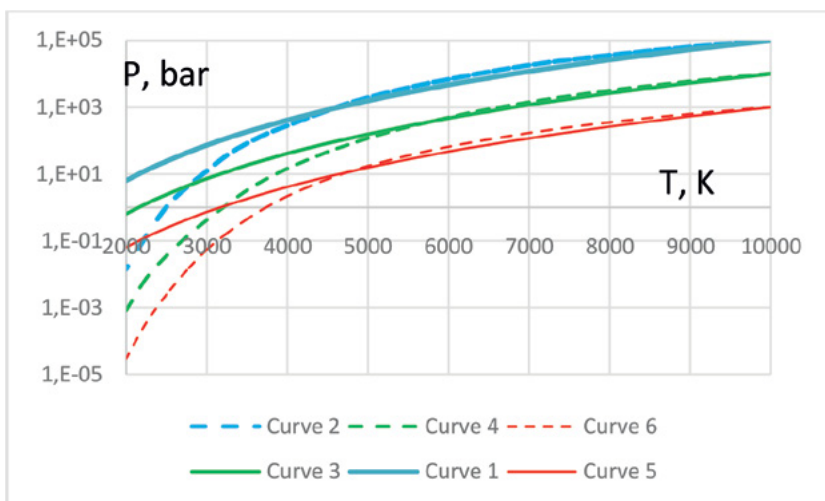


**Fig. 1.** Dependence of pressure on temperature during expansion of the impact-produced cloud. For all curves the initial temperature  $T_0 = 10^4$  K. The initial pressure  $P_0$  is equal to  $10^5$ ,  $10^5$ ,  $10^4$ ,  $10^4$ ,  $10^3$ , and  $10^3$  bar for curves 1, 2, 3, 4, 5, and 6, respectively. The adiabatic constant is 1.2 for curves 1, 3, and 5. Adiabatic constant is calculated with usage of IVTANTHERMO program for curves 2, 4, and 6.

At the beginning of cloud's expansion the chemical composition of impact-produced cloud is in thermodynamic equilibrium. Quenching of the chemical composition occurs when hydrodynamic and chemical time scales became comparable. After quenching during further expansion of the impact-produced cloud the chemical composition remains unchanged.

### ADIABATIC EXPANSION OF IMPACT-PRODUCED CLOUD:

In previous papers (for example, in [2]) it was assumed that the adiabatic constant is constant during expansion and equal to 1.2. This assumption is suitable for temperatures higher than 4500 K. However, this assumption leads to significant overestimation of pressure during quenching of chemical reactions at typical temperatures 2500 – 3500 K (see Fig. 1).

### HYDROGEN BEHAVIOR IN IMPACT-PRODUCED CLOUDS:

For the case of  $T_0 = 10^4$  K,  $P_0 = 10^4$  bar at typical quenching conditions  $T_q = 3300$  K and  $P_q = 1$  bar (see estimation of typical chemical and hydrodynamic time scales in [2]) in clouds, produced during collisions of meteoroids from strongest annual meteor showers with the Moon, main H-containing species are  $H_2$ ,  $H_2O$ , and OH (see Fig. 2).

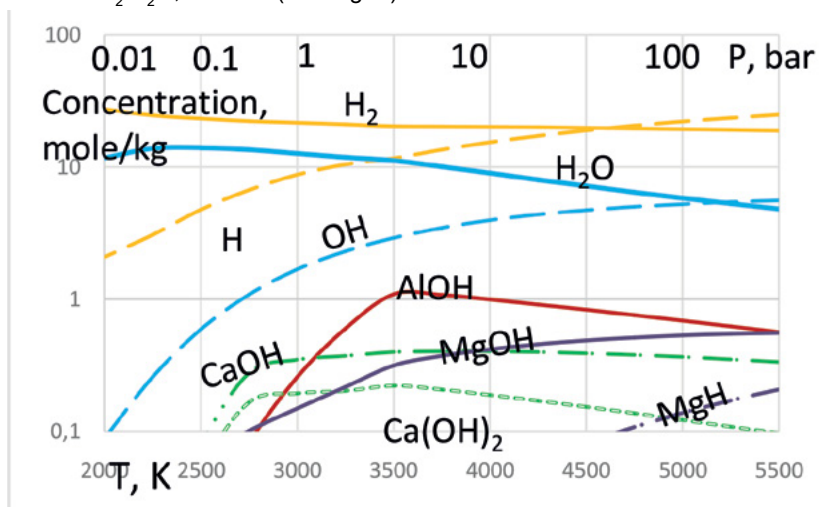


**Fig. 2.** Equilibrium content of H-containing species (in units of mole/kg) in the impact-produced cloud formed during collision of CI chondrite impactor with the Moon. Target-to-impactor mass ratio in the gas phase at the beginning of adiabatic expansion of the impact-produced cloud is 5.

Among OH-containing species water is the main compound at the reasonable range of quenching temperatures. Due to lower quenching pressure at the same quenching temperature and updated thermodynamic database the content of metal hydroxides is significantly lower than that obtained with the usage of CHET program and assumption of constant  $\gamma$  value [8].

### CONCLUSIONS:

Behavior of hydrogen-containing species during impact events on the Moon is considered. It is shown that previously used assumption of constant  $\gamma$  value leads to overestimation of quenching pressure and underestimation of quenching temperature in the impact-produced clouds. Obtained results can be used for modeling of the OH exosphere of the Moon.

### ACKNOWLEDGEMENTS:

A.A.B. was supported by RFBR-DFG grant No. 15-52-12369.

### REFERENCES:

- [1] Colaprete A. et al. How surface composition and meteoroid impacts mediate sodium and potassium in the lunar exosphere // *Science*. 2016. V. 351. Is. 6270. P. 249-252.
- [2] Berezhnoy A. A. Chemistry of impact events on the Moon // *Icarus*. 2013. V. 226. P. 205-211.

- [3] Gurvich L.V. et al. Thermodynamic Properties of Individual Substances. V. 5, fourth ed. Hemisphere Pub Co., New York. 1989.
- [4] Belov G. V., Iorish V. S., Yungman V. S. IVTANTHERMO for Windows — database on thermodynamic properties and related software // Calphad. 1999. V. 23. Is. 2. P. 173-180.
- [5] Anders E. Chemical compositions of the moon, earth, and eucrite parent body// Phil. Trans. R. Soc. Lond. Ser. A. 1977. V. 285. P. 23–40.
- [6] Lodders K. Solar system abundances and condensation temperatures of the elements // ApJ. 2003. V. 591. P. 1220-1247.
- [7] Ahrens T. J., O'Keefe J. D. Impact on the Earth, ocean and atmosphere // Int. J. Impact Eng. 1987. V. 5. P. 13–32.
- [8] Berezhnoy A.A. Behavior of volatile elements during impact events on the Moon // 5th European Lunar Symposium, May 2-3, 2017, Muenster, Germany, Abstract booklet, p. 45.



# ANALYSIS OF SOLAR WIND-MARS INTERACTION REGION AND PICK-UP IONS FROM MAVEN MEASUREMENTS

S.D. Shuvalov <sup>1</sup>, O. L. Vaisberg <sup>2</sup>, V. N. Ermakov <sup>3</sup>

<sup>1</sup> Space Research Institute of the Russian Academy of Sciences, 84/32 Profsoyuznaya str, Moscow, Russia, 117997, shuvalovsergei@gmail.com;

<sup>2</sup> Space Research Institute of the Russian Academy of Sciences 84/32 Profsoyuznaya str, Moscow, Russia, 117997, olegv@iki.rssi.ru;

<sup>3</sup> Space Research Institute of the Russian Academy of Sciences, 84/32 Profsoyuznaya str, Moscow, Russia, 117997, vl.n.ermakov@gmail.com

## KEYWORDS:

Plume, mass-loading, cometary-like shock, solar wind-Mars interaction, MAVEN.

We analyze the plasma and magnetic structure and properties of MM at strong mass-loading conditions as observed on MAVEN at Mars at the solar-zenith angle of  $\sim 80^\circ$  on January 4, 2015 using measurements of STATIC and MAG instruments. This strong mass loading of upstream flow was apparently associated with plume ions ejected from Mars by the solar wind motional electric field. Main parameters of crossing are indicated on the figure 1.

The mass loading ratio  $\rho/\rho_{sw}$  of pick-up ion density  $\rho l$  to solar wind mass density  $\rho_{sw}$  reached about 30%. As a result the jump of the solar wind flow velocity at the shock transition  $V_2/V_1$  constitutes 0.54, and magnetic field magnitude

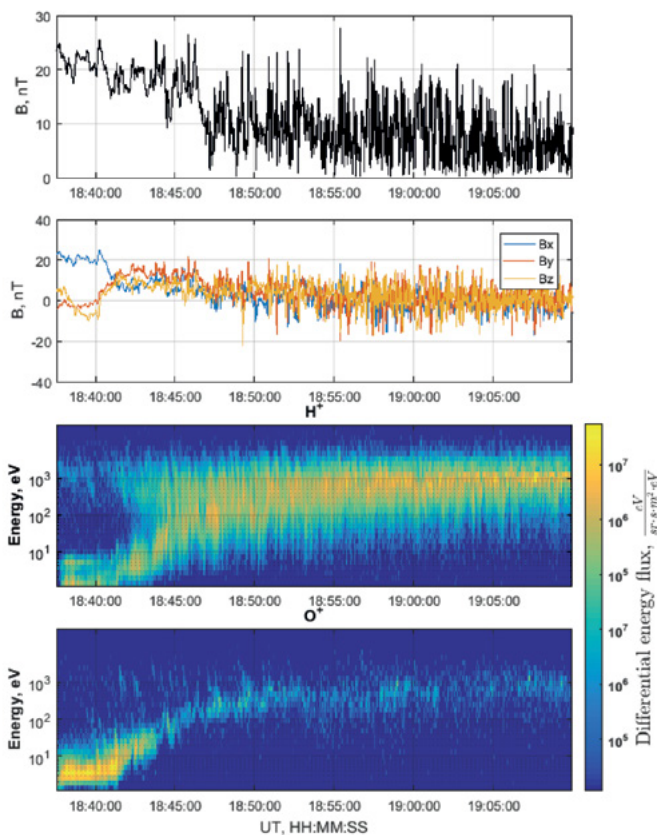


Fig. 1. From up to bottom: magnetic field magnitude, magnetic field components in MSO coordinate system, energy spectra of protons and atomic oxygen.

jump reaches 2.42. Normalizing by velocity ratio of upstream value of 280 km/s to downstream value of 150 km/s we arrive at the 1.3 for magnetic field jump across the tentative shock. This characterizes the shock as cometary-like shock.

Authors are grateful to J. McFadden for possibility to use STATIC data and to J. E. P. Connerney for use MG data.

This work was supported by Russian Science Foundation (Grant Nr.16-42-01103).

# DAYSIDE MAGNETOSPHERE OF MARS

O. Vaisberg, L. Zelenyi, V. Ermakov, S. Shuvalov, E. Dubinin, A. Znobishev

Space Research Institute of the Russian Academy of Sciences,  
84/32 Profsoyuznaya str, Moscow, Russia, 117997, olegv@iki.rssi.ru;

## KEYWORDS:

Mars, mass-loading, solar wind-Mars interaction, magnetosphere, MAVEN.

Magnetosphere of Mars forms from the solar wind magnetic flux tubes mass-loaded by planetary ions. These flux tubes pile-up above dayside ionosphere and then drift around the planet to the night side forming the tail of magnetosphere. This process was understood from analysis in papers [1], [2], and [3] and from experimental evidence [4]. Most frequent name "induced magnetosphere" came from initial assumption that magnetosphere originate from ionospheric current induced by motional electric field  $\mathbf{E}$  by the solar wind,  $\mathbf{E} = -1/c \mathbf{V} \times \mathbf{B}$  where  $\mathbf{V}$  is the solar wind velocity and  $\mathbf{B}$  is interplanetary magnetic field. Misleading name "induced magnetosphere" would be better replaced by "accretion magnetosphere" or "mass-loaded magnetosphere".

Measurements of plasma and magnetic field on Martian satellites Mars-2, -3, -5, Phobos-2, and Mars-Express did not provide sufficiently detailed description of dayside magnetosphere of Mars. Comprehensive measurements on MAVEN spacecraft give the possibility of more detailed analysis of dayside magnetosphere of Mars and its variation with the solar wind conditions. In this presentation we will present analysis of magnetospheric crossings by MAVEN with preliminary description of the flank magnetosphere structure and its dependence on the solar wind conditions.

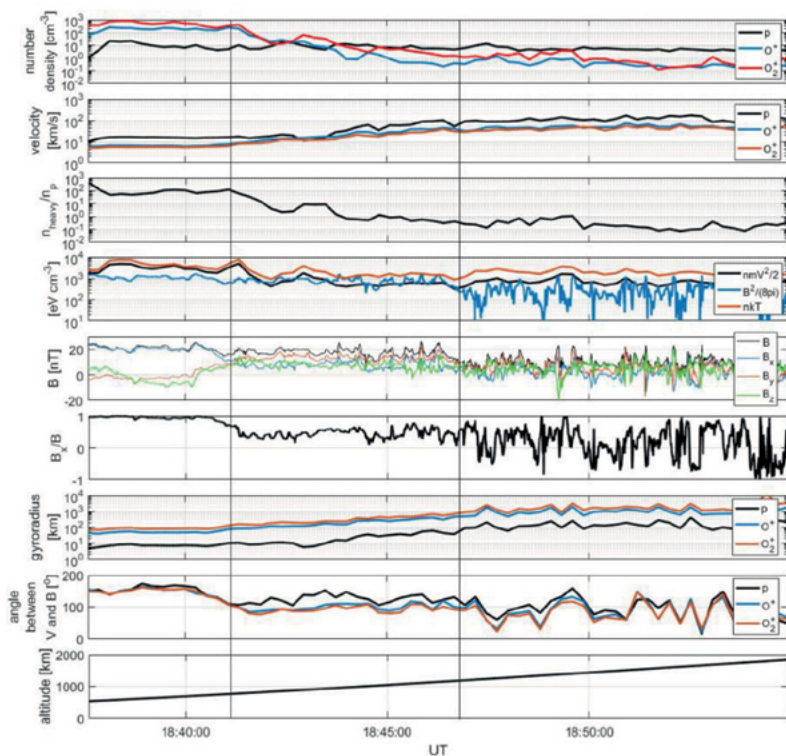


**Fig. 1.** Parameters of plasma and magnetic field. From top to bottom: number densities of protons and heavy ions; convection velocities of these ions; the ratio of number density of protons to the sum of  $O^+$ ,  $O_2^+$  ions; ion kinetic, magnetic, and ion thermal energies; magnetic field components and magnitude; the draping parameter ( $B_x/B$  ratio); protons,  $O^+$ ,  $O_2^+$  gyroradii; angles between velocities of protons,  $O^+$ ,  $O_2^+$  and magnetic field; altitude. Three regions are marked by vertical lines (from left to right): ionosphere, magnetosphere, and ionosheath flow.

Authors are grateful to J. McFadden for possibility to use STATIC data and to J. E. P. Connerney for use MG data.

This work was supported by Russian Science Foundation (grant Nr.16-42-01103).

## REFERENCES:

- [1] Alfven, H., 1957. On the theory of comet tails. *Tellus* 9, 92–96.
- [2] Zwan, B.J., Wolfe, R.A., 1976. Depletion of solar-wind plasma near a planetary boundary. *J. Geophys. Res.* 81, 1636–1648.
- [3] Vaisberg O.L. and Zelenyi L.M., Formation of the Plasma Mantle in the Venusian Magnetosphere, *ICARUS*, Vol. 58, Issue 3, 412-430, 1984. ISSN: 10902643, ISBN: 0019-1035
- [4] Vaisberg, O.L., Mars-Plasma Environment, In: *Physics of Solar Planetary Environment*, Ed. by D.J. Williams, AGU, Boulder, 1976, p.854-871. DOI: 10.1016/0019-1035(84)90087-3

# INITIAL ANALYSIS OF ION FLUXES IN MAGNETOTAIL OF MARS BASED ON SIMULTANEOUS MEASUREMENTS ON MARS EXPRESS AND MAVEN

V.N. Ermakov<sup>1</sup>, L.M. Zelenyi<sup>2</sup>, O.L. Vaisberg<sup>3</sup>, E.A. Sementsov<sup>4</sup>, E.M. Dubinin<sup>5</sup>, S.D. Shuvalov<sup>6</sup>

<sup>1</sup>Space Research Institute of RAS; National Research Nuclear University MEPhI, Moscow, Russia [vl.n.ermakov@gmail.com](mailto:vl.n.ermakov@gmail.com);

<sup>2</sup>Space Research Institute of RAS, Moscow, Russia;

<sup>3</sup>Space Research Institute of RAS, Moscow, Russia;

<sup>4</sup>Space Research Institute of RAS, Moscow, Russia;

<sup>5</sup>Max Planck Institute for Solar System Research, Göttingen, Germany;

<sup>6</sup>Space Research Institute of RAS, Moscow, Russia

## KEYWORDS:

Mars Express, MAVEN, Mars, atmospheric losses, solar wind, simultaneous measurements

Studies of solar wind induced atmospheric losses were started in earlier 1970<sup>th</sup>. Several loss channels have been identified including pick-up of exospheric photo-ions, ionospheric ions, plasma sheet ions, plume ionsescape. Measurements performed during several solar cycles showed variation of these losses by a factor of 10, being largest at maximum solar activity.

Simultaneous observations at Mars by the Mars Expressand MAVENspacecraft open the new perspective to study Martian environment. We carried out an analysis of interplanetary environment influence on the structure of planetary ion fluxes in Martian magnetotail. We used solar wind and interplanetary magnetic field measurements on MAVEN and heavy ions measurements in Martian magnetosphere on Mars Express. These joint observations allowed us to reveal two high latitudes maxima of escape flux (fig. 1). It was also possible to estimate the influence of the disturbed solar wind conditions on the escape rate by a factor of about 1.5.

This work was supported by Russian Science Foundation (grant Nr.16-42-01103).

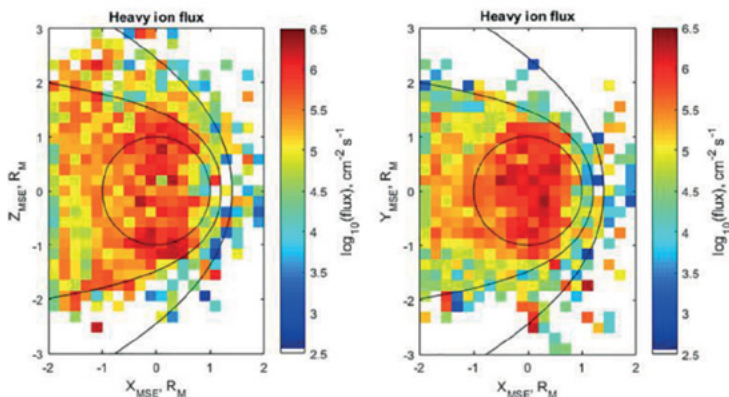


**Fig. 1.** Distribution of heavy ions( $O^+$  and  $O_2^+$ )average fluxes in MSE coordinate system (Mars-Sun-Electric field). X axis is directed to the Sun, Z axis is directed along the electric field  $\mathbf{E} = -[\mathbf{v}_{sw} \times \mathbf{B}]$  and Y axis completes the right-handed coordinate system. The black lines show the average positions of the shock (external curve) and the boundary of Martian magnetosphere.

# HOW TO DESCRIBE THE MARTIAN SPACE ENVIRONMENT AND HOW SOLAR WIND AND EUV CONTROL ION ESCAPE. MAVEN OBSERVATIONS

E.Dubinin<sup>1</sup>, M.Fraenz<sup>1</sup>, M.Pätzold<sup>2</sup>, O.Vaisberg<sup>3</sup>, L.Zelenyi<sup>3</sup>, J. McFadden<sup>4</sup>, J.Halekas<sup>5</sup>, F.Epavier<sup>6</sup>, J.Connerney<sup>7</sup>, G.DiBraccio<sup>7</sup>, D.Brain<sup>6</sup> and Jakosky<sup>6</sup>

<sup>1</sup>Max-Planck-Institute for Solar System Research, Göttingen, Germany, dubinin@mps.mpg.de,

<sup>2</sup>Rheinisches Institut für Umweltforschung, Abteilung Planetenforschung, Cologne, Germany,

<sup>3</sup>Institute of Space Research, Moscow, Russia,

<sup>4</sup>Space Sciences Laboratory, U.C. Berkeley, Berkeley, CA, USA,

<sup>5</sup>Department of Physics and Astronomy, University of Iowa, Iowa City, Iowa, USA,

<sup>6</sup>Laboratory for Atmospheric and Space Physics, Univ. of Colorado, Boulder, CO, USA,

<sup>7</sup>NASA Goddard Space Flight Center, Maryland, USA.

## KEYWORDS:

Mars, MAVEN, Solar wind, Ion escape, Magnetosphere.

We present multi-instrument observations of the influence of the solar wind and solar irradiance on the Martian ionosphere and escape fluxes made by the MAVEN spacecraft. The measurements provide us for the first time the opportunity to study these processes with simultaneous monitoring of the solar wind and ionospheric variations, planetary ion fluxes and solar irradiance. Although solar wind interacts directly with the Martian ionosphere/atmosphere creating the induced (draping) magnetosphere, the existence of the crustal magnetic field essentially influences the magnetic field and plasma environment near Mars. As a result, a combined magnetosphere can arise with elements of the intrinsic and induced magnetospheres. This strongly modifies the geometry of escape channels.

It will be shown that fluxes of planetary ions extracted at different ionospheric altitudes and escaping through different channels (the trans-terminator region, the ion plume, the tail lobes, the plasma sheet) respond differently on variations of the different drivers. Solar irradiance controls the fluxes of low-energy ions in the tail lobes. Ion losses through the plasma sheet and boundary layer vary with solar wind variations. As a result, total escape losses critically depend on the external conditions.

# ESCAPE OF VOLATILES FROM MARS-SIZED PLANETARY EMBRYOS

P. Odert<sup>1</sup>, H. Lammer<sup>1</sup>, N.V. Erkaev<sup>2</sup>, A. Nikolaou<sup>3</sup>,  
H.I.M. Lichtenegger<sup>1</sup>, C.P. Johnstone<sup>4</sup>, K.G. Kislyakova<sup>4,1</sup>,  
M. Leitzinger<sup>5</sup>, N. Tosi<sup>3</sup>, M. Güdel<sup>4</sup>

<sup>1</sup>Space Research Institute, Austrian Academy of Sciences, Schmiedlstr. 6, 8042 Graz, Austria, [petra.odert@oeaw.ac.at](mailto:petra.odert@oeaw.ac.at);

<sup>2</sup>Institute of Computational Modelling of the Siberian Branch of the Russian Academy of Sciences, 660036 Krasnoyarsk, and Siberian Federal University, 660041 Krasnoyarsk, Russian Federation;

<sup>3</sup>Institute for Planetary Research, German Aerospace Center (DLR), Rutherfordstr. 2, 12489 Berlin, and Technical University Berlin, Strasse des 17. Juni 135, 10623 Berlin, Germany;

<sup>4</sup>University of Vienna, Department of Astrophysics, Türkenschanzstr. 17, 1180 Vienna, Austria;

<sup>5</sup>Institute of Physics, IGAM, University of Graz, Universitätsplatz 5, 8010 Graz, Austria

## KEYWORDS:

Planetary embryos, protoplanets, hydrodynamic escape, magma oceans, steam atmospheres

## INTRODUCTION:

Planetary embryos form protoplanets via mutual collisions. This can lead to the development of magma oceans. During their solidification, significant amounts of the mantles' volatile contents may be outgassed. The resulting H<sub>2</sub>O/CO<sub>2</sub> dominated steam atmospheres may be lost efficiently via hydrodynamic escape due to the low gravity of these Moon- to Mars-sized objects and the high stellar extreme ultraviolet (EUV) luminosities of the young host stars. Protoplanets forming from such degassed building blocks after nebula dissipation could therefore be drier than previously expected. We model the outgassing and subsequent hydrodynamic escape of steam atmospheres from such embryos. The efficient outflow of H atoms drags along heavier species like O, CO<sub>2</sub>, and its dissociation products. The full range of possible EUV evolution tracks of a young solar-mass star [1] is taken into account. We consider the atmospheric escape from Mars-sized planetary embryos at the orbital distances of Venus, Earth, and Mars, bracketing the habitable zone. The degassed envelopes may have surface pressures of a few bar to >1kbar, depending on the depth of the magma ocean and its volatile content. Typical atmospheres of a few tens to 100 bar are lost within a few to a few tens of Myr. The most massive atmospheres can only be removed if the young star is a strong EUV emitter and if the embryos spend sufficient time at the closest orbital distances [2].

## REFERENCES:

- [1] Tu L., Johnstone C. P., Güdel M., Lammer, H. The extreme ultraviolet and X-ray Sun in Time: High-energy evolutionary tracks of a solar-like star // *A&A*. 2015. V. 577. L3.  
[2] Odert P., Lammer H., Erkaev N. V., Nikolaou A., Lichtenegger H. I. M., Johnstone C. P., Kislyakova K. G., Leitzinger M., Tosi N. Escape and fractionation of volatiles and noble gases from Mars-sized planetary embryos and growing protoplanets // *Icarus*. 2017. submitted.

# WHO TWISTS VENUSIAN MAGNETOTAIL?

M. I. Verigin, G. A. Kotova

Space Research Institute of Russian Academy of Sciences, Moscow 117997, Profsoyuznaya 84/32, Russia. Contact: verigin@iki.rssi.ru

## KEYWORDS:

Venus, nighttime ionosphere, precipitating electrons, magnetotail twist, magnetotail outward current

## INTRODUCTION:

Fig. 1 presents one of initial illustrations of the magnetic field and ion structures originating during solar wind – Venus interaction [1]. Quite similar schematics with minor modifications were repeated in a number of publications (see e. g. [2]). Though reflecting general features of the solar wind interaction with Venus, these diagrams do not depict important details of the magnetic field and plasma properties in the planetary magnetotail. Really, the reconnection type magnetic field geometry was observed behind the Venus by Venera 9,10 ( $(\mathbf{B}_{sw} \cdot \mathbf{B}_{tail}) < 0$ , [3]), Pioneer Venus (PVO) [4] and Venus Express (VEX) orbiters [5]. Additionally VEX observed flapping waves which are ultimately driven by the magnetic reconnection [6].

The most unusual feature of the Venesian tail – the twisting of its magnetic field lines was originally revealed in PVO magnetic field measurements [7] and later confirmed by VEX observations [8]. Both set of observations will be presented in the talk and optional origins of the planetary magnetotail twisting will be discussed furthermore.

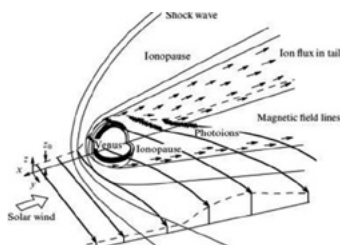


Fig. 1. Customary schematics of the solar wind interaction with Venus.

## VENUSIAN MAGNETOTAIL TWISTING OBSERVATIONS:

Fig 2 presents first PVO observations of the magnetic field lines twisting behind Venus [7]. Orange circles were added to the original figure in order to clarify that in all cases the clock vice field lines twisting was observed from sunward direction. Qualitative view of the magnetotail twisted field lines is depicted in Fig. 3 [7].

Summary plot of PVO measurements of azimuthal magnetic field component along a large number of orbits is presented in Fig. 4a [8]. Yellow-red circle in this figure correspond to systematic presence of the clock vice directed (as viewed from Sun) azimuthal magnetic field in the Venesian magnetotail, thus confirming and detailing earlier analysis of PVO magnetic field measurements [7].

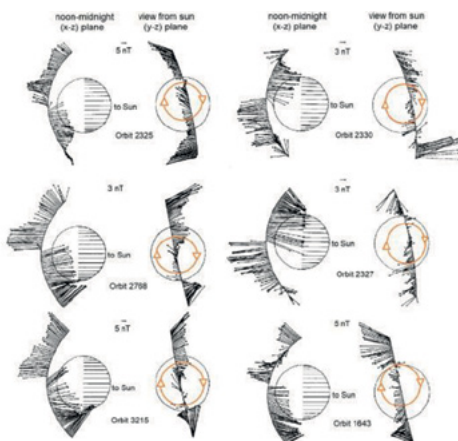
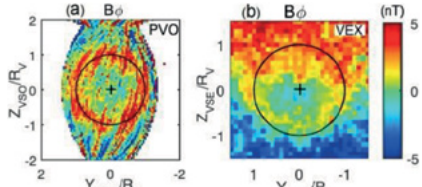


Fig. 2. Magnetic field vectors as measured along PVO orbits. Note clock vice magnetic field lines rotation behind the Venus in all cases [7].





**Fig. 3.** Schematics of Venus' magnetotail field lines twisting after PVO observations [7].



**Fig. 4.** Summary plot of PVO (a) and VEX (b) magnetic field measurements behind Venus [8].

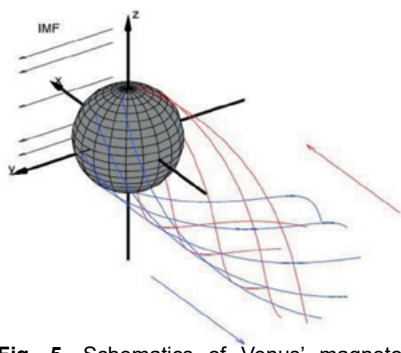


**Fig. 5.** Schematics of Venus' magnetotail field lines twisting after VEX and PVO observations [8].

planet. The above value of  $F$  can easily be supported by the loss of Hydrogen ( $\sim 7.1 \cdot 10^{24} \text{ s}^{-1}$ ), Helium ( $\sim 7.9 \cdot 10^{22} \text{ s}^{-1}$ ) and Oxygen ( $\sim 2.7 \cdot 10^{24} \text{ s}^{-1}$ ) ions by Venus even in the period of low solar activity [9]. The above loss rates provide possibility to estimate upper limit of  $I_{\text{tot}}$  only, because, scavenging associated with magnetotail draping would be expected to pick up both ion and electrons. It is worth mentioning that contribution to the total downstream electric current can be provided also by electrons precipitating to the nightside Venusian atmosphere and creating main maximum ionization in the nighttime ionosphere [10]. Specific omnidirectional flux of these electrons is  $\sim 2 \cdot 10^8 \text{ cm}^{-2} \text{ s}^{-1}$  that corresponds to moving toward planet electron flux  $\sim 5 \cdot 10^7 \text{ cm}^{-2} \text{ s}^{-1}$ , i.e. to downstream current  $I_{\text{tot}} < 10^7 \text{ A}$ . Minor part of this upper limit current can be sufficient for providing Venusian magnetotail field twisting.

An example of Venusian magnetotail current system that can provide proper  $B_{\phi}$  ( $B_{\text{loop}}$ ) is presented in Fig. 6 [8]. In order to confine the azimuthal field in a shell-shaped region, authors [8] used two currents  $I_{\text{outer}}$  and  $I_{\text{inner}}$  (green arrows in Fig. 6) at the outer and inner shells with sunward and antisunward directions, respectively. The average magnitude of  $B_{\phi} \sim 4 \text{ nT}$  is achieved when  $I_{\text{outer}}$  and  $I_{\text{inner}}$  are about  $1.2 \times 10^5 \text{ A}$  [8].

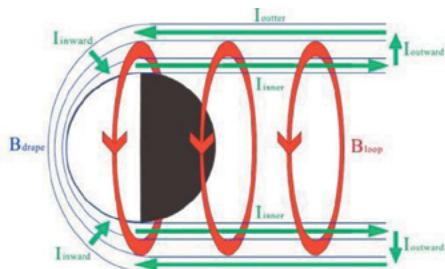


**Fig. 6.** Schematic illustration of the current system (green arrows) of azimuthal magnetic field  $B_{\phi}$  ( $B_{\text{loop}}$ , red cycles) at Venus. [8].

Later VEX magnetic field measurements (Fig 4b, [8]) confirmed the presence and direction of azimuthal magnetic field component in the magnetotail of Venus. Note that plots in Figs. 4 a,b are in different reference frames – VSO and VSE, respectively. This difference explains apparent dissimilarity between figures – complete plate coverage and systematic color variation from blue to red with increase of  $Z_{VSE}$  in Fig. 4b. Both effects are due to alignment of  $Z_{VSE}$  axis with rotating IMF electric field direction. Schematics of Venus' magnetotail field lines twisting after VEX and PVO observations [8] is depicted in Fig. 5.

## DISCUSSION:

Specific value of azimuthal magnetotail field  $B_{\phi}$  is about 2-4 nT (see Figs. 2,4). Estimation of the value of total downstream electric current  $I_{\text{tot}}$  depends on the distribution of downstream current across the planetary magnetotail which to some extent can be evaluated from  $B_{\phi}$  measurements across the tail (see, e.g., Fig. 4a).

For  $B_{\phi} = 2-4 \text{ nT}$  the total downstream electric current was evaluated in the paper [7] as  $I_{\text{tot}} = (1-2) \cdot 10^5 \text{ A}$ . This current corresponds to a flux  $F = (0.6-1.2) \cdot 10^{24} \text{ s}^{-1}$  of singly charged ions per second moving from the

The investigation of the magnetic field at Mars and Titan show that the azimuthal magnetotail field is most likely a universal phenomenon for unmagnetized/weakly magnetized planetary bodies with developed atmospheres [8].

## CONCLUSIONS:

The specific feature of the Venusian tail – the twisting of its magnetic field lines that was originally revealed in PVO mag-

netic field measurements [7], is confirmed by PVO measurement reanalysis and by later VEX observations [8]. Possible reasons for magnetotail magnetic field twisting are the planetary ions escaping from Venus and the magnetotail electrons precipitating into planetary nighttime atmosphere, and responsible for support of Venusian nightside ionosphere. A lot of questions still opened for investigation, such as how does the twisting field form, what is the main agent responsible for it, etc.

## ACKNOWLEDGMENTS:

The paper is partially supported by the program P7 of RAS.

## REFERENCES:

- [1] Vaisberg O.L., Zelenyi L.M. Formation of the plasma mantle in the Venus magnetosphere // *Kosm. Issled.* 1982. V. 20, No. 4. P. 604-619.
- [2] Saunders M.A., Russell C.T. Average Dimension and Magnetic Structure of the Distant Venus Magnetotail // *JGR.* 1986. V. 91. No. A5. P. 5589-5604.
- [3] Verigin M.I., Gringauz K.I., Ness N.F. Comparison of Induced Magnetospheres at Venus and Titan // *JGR.* 1984. V. 89. No. A7. P. 5461-5470.
- [4] Kivelson M.G., Russell C.T. The Interaction of Flowing Plasmas with Planetary Ionospheres: A Titan-Venus Comparison // *JGR.* 1983. V. 88. No. A1. P. 49-57.
- [5] Zhang T.L., et al. Magnetic Reconnection in the Near Venusian Magnetotail. *Science.* 2012., V. 336. No.6081. P. 567-570. doi:10.1126/science.1217013.
- [6] Ron, Z.J., et al. The flapping motion of the Venusian magnetotail: Venus Express observations // *JGR.* 2015. V. 120. P. 5593-5602. doi:10.1002/2015JA021317.
- [7] Verigin M., Luhmann J.G., Russell C.T. On the Venus Ion Magnetotail Structure // in *COSPAR Colloquia Vol. 4. Plasma Environments of Non-magnetic Planets.* ed by T.I. Gombosi. Pergamon Press, 1993. P. 259-263.
- [8] Chai L., et al. (2016) An Induced Global Magnetic Field Looping Around the Magnetotail of Venus // *JGR.* V. 121. P. 688-698. doi:10.1002/2015JA021904.
- [9] Fedorov A., et al. Measurements of the Ion Escape Rates from Venus for Solar Minimum // *JGR.* 2011. V. 116, A07220, doi:10.1029/2011JA016427.
- [10] Verigin M.I. et al. On the Possible Source of the Ionization in the Nighttime Martian Ionosphere. 1. Phobos-2/HARP Electron Spectrometer Measurements // *JGR.* 1991. V. 96. No. A11. P. 19307-19313.

# RADIO-OCCULTATION AND IN-SITU MEASUREMENTS OF PLASMA DENSITY IN HALLEY'S COMET PLASMA

O.L. Vaisberg<sup>1</sup>, A.L. Gavrik<sup>2</sup>

<sup>1</sup>Space Research Institute, Russian Academy of Sciences, olegv@iki.rssi.ru

<sup>2</sup>Kotel'nikov Institute of Radio Engineering and Electronics, Fryazino branch, V.A.Vvedensky sq.1, Fryazino, alg248@hotmail.com;

## KEYWORDS:

Comet, Halley's comet, plasma, cometary plasma, occultation.

## INTRODUCTION:

First direct investigation of the Halley's comet plasma mantle was performed during the VEGA-1 and VEGA-2 flybys in 1986 at the dayside with closed approaches of 8890 km and 8030 km, respectively. Onboard transmitters Radio-occultation experiment was performed with onboard transmitters in 32 cm and 5 cm ranges and ground receivers complex that recorded phase, frequency and power of radio waves [1]. Comparison of radio-physics effects of radio-waves propagation through Halley's comet plasma envelope on March 6 and 9, 1986 with calibration measurements performed in time interval from February 14 till March 1986 allowed one to determine the profiles of electrons number densities. Direct measurements of ion ULF fluctuations, planetary heavy ion velocity, number density and mass were made along VEGA-1 and VEGA-2 trajectories by Faraday cups and planar electrostatic analyzers were performed by BD-3 sensor [2] of APVN instrument [3]. Results of these experiments and their comparison are presented in this talk.

## RADIO-OCCULTATION EXPERIMENT:

Increase of integral electrons number density on the radio link was observed during two fly-bys at the approach to the comet nucleolus as well as during ~90 s afterwards. This unexpected delay required detailed analysis. The method of reverse problem solution of radial electron number density distribution was developed, analysis of limited method was made and the uncertainty of number density was obtained [4].

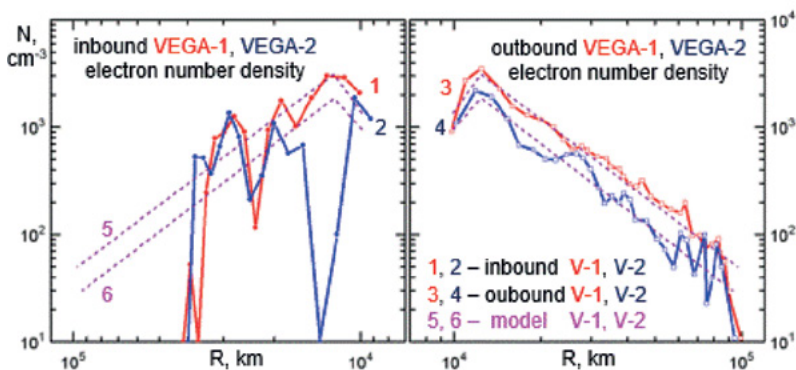


Fig. 1. Electron number density  $N(R)$  profiles obtained from radio-occultation data of VEGA-1 and VEGA-2 at inbound trajectories (left) and at outbound trajectories (right). Straight lines are the approximations of calculated distributions.

Calculated profiles of electrons number densities  $N(R)$  are shown in Fig. 1. Accuracy of  $N(R)$  determination differs for approach and for retreat are different. Steady  $N(R)$  decrease for curves 3, 4 is monotonic as the distance  $R$  increases from  $\sim 1.2 \cdot 10^4$  km to  $\sim 8 \cdot 10^4$  km, but curves 1, 2 show fluctuating number density relative to average  $N(R)$  trend up to  $\sim 10^3$   $\text{cm}^{-3}$  for  $R > 1.2 \cdot 10^4$  km due to higher measurements error. All  $N(R)$  profiles have similar common features: no sharp cometary plasma boundary is seen, the number density is changes as  $R^{-2}$  at the distances from 11,700 km to 80,000 km, maximum of profiles is located at the distance of 11,700 km, and number density decreases at the approach to the nucleus. It is shown that the electron number density depends

of the comet activity: the maximum electron number density was  $\sim 3600 \text{ cm}^{-3}$ , during first fly-by, and was by factor of 1.7 smaller, though the location of the number density remains unchanged.

## DIRECT MEASUREMENTS:

BD-3 measurements were performed during all pass of VEGA-1 near comet. Due to low cometary ions convection velocity these ions entered the instrument nearly along the normal to the entrance window. The measured energy of comet ions approximately corresponds to the water ion group, having a small convective velocity. Calculated ion number density profile is shown in Fig. 2.

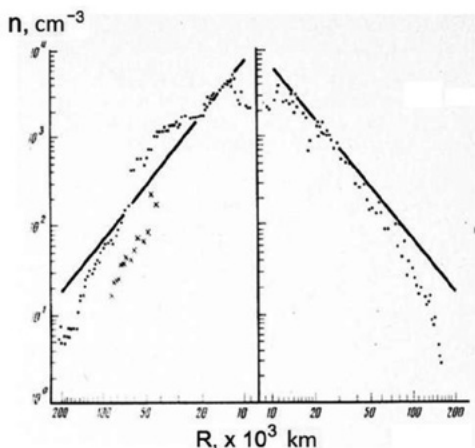


**Fig. 2.** Heavy ions number density profiles measured by BD-3 ion sensor on VAGA-1 (dots) and VEGA-2 (crosses). Straight lines show  $R^{-2}$  profiles drawn through number density maximum at  $R \sim 12,000 \text{ km}$  at inbound trajectory. The heavy ions mantle boundary (cometopause) was determined by sharp ion density gradient at  $R \sim 150,000 \text{ km}$  [5].

Sharp increases of the number density to  $\sim 15 \text{ cm}^{-3}$  at  $(150-155) \times 10^3 \text{ km}$ , were observed at the entrance and exit of plasma mantle. This boundary is analogue of Venus magnetosphere boundary (magnetopause or ionopause) formed due to the mass-loading of the solar wind flow by the planetary ions [6]. It is seen that the ion number density varies with distance till  $R \sim 12,000 \text{ km}$  as  $R^{-2}$  or slightly steeper. Deviations from this law are the large-scale number density increase at inbound trajectory between  $\sim 66,000 \text{ km}$  and  $\sim 25,000 \text{ km}$  and more steep decreases at the outer plasma mantle boundaries. Maximum number density of  $\sim 5 \times 10^3 \text{ cm}^{-3}$  was measured at  $\sim 12,000 \text{ km}$  with subsequent decrease to  $\sim 2 \times 10^3 \text{ cm}^{-3}$  at the distance of  $\sim 9,000 \text{ km}$  from cometary nucleus. Similar ion number density profile was observed at the exit trajectory of VEGA-1 with exceptions of lower number density values and the absence of inhomogeneity. BD-3 on VEGA-2 measurements were obtained at inbound trajectory only at the distances from  $90,000 \text{ km}$  to  $40,000 \text{ km}$ . Malfunction of instrument was apparently due to large projectile impact. It could be seen that the measured number density was about 3 times smaller at VEGA-2 compared to ones at VEGA-1 at similar cometocentric distances

## COMPARISON OF RADIO-OCCULTATION AND ION MEASUREMENTS:

It is not straightforward procedure to compare the results of two experiments. Of three numbers density profiles only one crossing was considered appropriate. BD-3 measurements were obtained along spacecraft trajectory while radio-occultation profile corresponds to the cut along spacecraft-Earth line. As a result, these two profiles do not need to be similar. Fig. 3 shows comparison of two number density profiles along outbound trajectory of VEGA-1. Very strong similarity of two profiles is very encouraging and confirms validity of two experiment results.

## CONCLUSION:

The properties of electrons number densities do not contradict to the main results of the direct measurements of the ions number densities obtained on VEGA-1, VEGA-2 and GIOTTO while some differences can be explained by the fact that radio-occultation data analysis is smoothing the local plasma variations due to averaging the data more than  $1000 \text{ km}$  along radio waves propagation line.

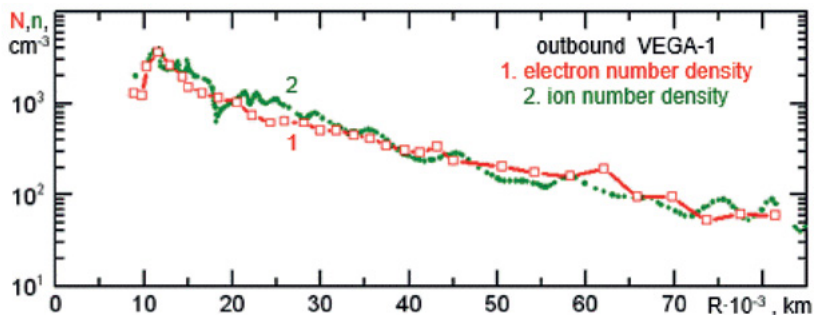


Fig. 3. Comparison of radial distribution of electron content obtained from radio-occultation data (solid line) and ion number density distribution from direct measurements of BD-3 sensor (dotted line). Both are for outbound trajectory of VEGA-1.

## ACKNOWLEDGEMENT:

The work is partially supported by the RAS Presidium Program № 1.7P.

## REFERENCES:

- [1] N.A.Savich et al. Dual-frequency Vega radio sounding of Comet Halley // *Sov. Astronomy Letters*. 1986. V. 12. No. 5. P. 283-286
- [2] D.S.Zakharov et al. Instrumentation for Measurements of Number Density of Cometary Plasma and its Convection // In: *Problems of Atomic Science and Techniques, Nuclear Instrumentation Series*. 1987. No. 3. P. 119-123. (In Russian).
- [3] S.I.Klimov et al. Extremely Low Frequency (ELF) plasma waves near Halle's comet // *Astronomy Letters*. 1986. V. 1. T. 12. No. 9. P. 688-694. (In Russian).
- [4] Andreev V.E. and Gavrik A.L. Plasma envelope of comet Halley from radio science data // *Astronomy Letters*. 1993. V. 19. No. 6. P. 437-440.
- [5] O.Vaisberg et al. Spatial Distribution of Heavy Ions in Comet P/Halley's Coma // *Astron. Astrophys.* 1987. V. 187. P. 183-190,
- [6] L.M.Zelenyi and O.L.Vaisberg. Venusian Interaction with the Solar Wind Plasma Flow as a Limiting Case of the Cometary Type Interaction // In: *Advances of Space Plasma Physics*, ed. Buti. World Scientific. 1985. P. 59-76.



(EDR) monochromatic image files were extracted from a NASA Space Science Data Coordinated Archive CD-ROM [6], [7] using PC-based software [8] and saved as digital BitMap Picture (BMP) files. The CD-ROM archive was created by S. LaVoie, JPL, for the Science Digital Data Preservation Task (SDDPT), which was separate from the PDS. A five-layer image cube was produced for each image where: Band 1 was the original EDR monochromatic image; Band 2 had EDR missing lines filled and noise spikes, blemishes and reseaux removed; Band 3 was a high pass filtered version of Band 2 with latitude / longitude / limb / terminator / sub-spacecraft / sub-solar / Phobos / Deimos / star overlays; Band 4 was a simulated Mars image produced by illuminating the Mars Global Surveyor Mars (MGS) Orbiter Laser Altimeter (MOLA) global digital terrain model (DTM) [9], [10]; and Band 5 was Band 4 with Mars quadrangle and lander location information as overlays (Figure 1). For Phase I of the restoration effort, 5-band cubes have been produced for each image in the Mariner 6 and 7 Far Encounter mission phases and archived as PDS4 formatted images having detached XML label records.

## THE NAIF SPICE ARCHIVE COLLECTION:

The Navigation Ancillary Information Facility (NAIF) [11] did not exist at the time of the 1969 Mariner Mars mission; therefore there were no SPICE kernels for these images. Image timetags, spacecraft positions and camera pointing data were extracted from [12]. The spacecraft positions were fit by a trajectory numerical integrator to produce SPICE trajectory .bsp kernels. The .bsp kernels combined with the pointing data were used as initial guesses to produce frames .tf and attitude / pointing .ck kernels. The MOLA digital image models (DIMs) were registered to the actual images to produce precision pointing data. The reseaux in each image were located and used to produce geometric camera models captured in tables and in instrument .ti kernels. Fictitious spacecraft clock .tsc were created.

## ACKNOWLEDGEMENT:

This effort is being supported by the National Aeronautics and Space Administration, Science Missions Directorate, Planetary Science Division Planetary Data Restoration, Archive and Tools (PDART) Program.

## REFERENCES:

- [1] Leighton, R. B., and B. C. Murray, One year's processing and interpretation--an overview. *J. Geophys. Res.*, **76**, 2, 1971.
- [2] Danielson, G. E., and D. R. Montgomery, Calibration of the Mariner Mars 1969 television cameras. *J. Geophys. Res.*, **76**, 2, 1971.
- [3] Dunne, J. A., W. D. Stromberg, R. M. Ruiz, S. A. Collins, and T. E. Thorpe, Maximum discriminability versions of the near-encounter Mariner pictures. *J. Geophys. Res.*, **76**, 2, 1971.
- [4] Rindfleisch, T. C., J. A. Dunne, H. J. Frieden, W. D. Stromberg, and R. M. Ruiz, Digital Processing of the Mariner6 and 7 Pictures. *J. Geophys. Res.*, **76**, 2, 1971
- [5] Collins, S. A., The Mariner 6 and 7 Pictures of Mars, NASA SP-263, Washington, D.C., 1971.
- [6] <http://nssdc.gsfc.nasa.gov/nmc/spacecraftDisplay.do?id=1969-014A>
- [7] <http://nssdc.gsfc.nasa.gov/nmc/datasetDisplay.do?id=PSPG-00046>
- [8] <http://members.tripod.com/petermasek/mariner67.html>
- [9] Neumann, G., F. Lemoine, D. Rowlands, D.E. Smith, and M.T. Zuber, (2001), Crossover analysis in MOLA data processing, *J. Geophys. Res.*, 106, No. E10, pp. 23753-23768.
- [10] Smith, D. E., M. T. Zuber, H. V. Frey, J. B. Garvin, J. W. Head, D. O. Muhleman, G. H. Pettengill, R. J. Phillips, S. C. Solomon, H. J. Zwally, B. Banerdt, T. C. Duxbury, M. P. Golombek, F. G. Lemoine, G. A. Neumann, D. D. Rowlands, O. Aharonson, P. G. Ford, A. B. Ivanov, C. L. Johnson, P. J. McGovern, J. B. Abshire, R. S. Afzal, and X. Sun (2001), Mars orbiter laser altimeter: experiment summary after the first year of global mapping of Mars, *J. Geophys. Res.*, 106, E10, 23,689-23,722.
- [11] C. Acton, N. Bachman, B. Semenov, E. Wright; A look toward the future in the handling of space science mission geometry; *Planetary and Space Science* (2017); DOI 10.1016/j.pss.2017.02.013
- [12] Campbell, J. K., Mariner Mars 1969 Simulated TV Pictures, JPL Document 605-237, 15 June 1970.

# THE INTERNATIONAL PHOBOS / DEIMOS SURFACE CHARACTERIZATION AND SITE SELECTION WORKING GROUP

T. Duxbury<sup>1</sup>, J-P. Bibring<sup>2</sup>, M. Fujimoto<sup>3</sup>, R. Jaumann<sup>4</sup>, A. Zaharov<sup>5</sup>

<sup>1</sup>Physics and Astronomy Department, George Mason University, Fairfax, VA, USA, [tduxbury@gmu.edu](mailto:tduxbury@gmu.edu);

<sup>2</sup>Institute of Space Astrophysics, Paris University, Orsay, FR;

<sup>3</sup>Institute of Space and Aeronautical Sciences, Japan Aerospace Exploration Agency, Tokyo, JP;

<sup>4</sup>Institute for Planetary Research, German Aerospace Center, Berlin, DE;

<sup>5</sup>Space Research Institute, Russian Academy of Sciences, Moscow, RU

## KEYWORDS:

Phobos, Deimos, Mars, MMX, Sample Return

## WORKING GROUP FORMATION:

The International Phobos / Deimos Surface Characterization and Site Selection Working Group (PDWG) was formed by members and scientists of the European Space Agency (ESA), the National Aeronautics and Space Agency (NASA), the Japanese Aerospace Exploration Agency (JAXA) and the Russian Space Agency (Roscosmos) during the Seventh Moscow Solar System Symposium (7M-S3) in October 2016. The 7M-S3 participants covered a wide range of science disciplines that included space agency members and scientists who had or were operating past and current missions and instruments, implementing new exploratory missions and studying future missions to the Martian moons. Past mission included Viking and Phobos 88. Current missions include Mars Express, MAVEN, MRO, and Odyssey. New missions include MMX with potential future missions such as Boomerang and Phootprint. The group is open to all past, present and future explorers of Phobos and Deimos, both robotic and human exploration missions that could be stepping-stones to Mars.

## WORKING GROUP OBJECTIVES:

The objectives of the PDWG developed during the 7M-S3 include: encourage current missions to continually obtain observations of the two moons to improve global surface spatial and spectral resolutions and improve knowledge of their topographies, orbits, interiors and environments; encourage / participate with the science community to produce higher-level, derived global multi-spectral datasets from past and current missions to support surface characterizations and future landing / sample site selections; recommend data interchange / archive standards for the higher-level, registered and map projected datasets to insure ease of use by GIS-type tools; continually involve the planetary science community through focused meetings and presentations at international science conferences as well as at active mission science team meetings.

## DATA PRIORITIES:

The PDWG identified the existing and continuing Mars Express High Resolution Stereo Camera and OMEGA observations as the highest priority to produce global, multispectral registered and map projected datasets for surface characterization and for improving digital terrain models (DTMs) and orbits. Of similar priority was the development of a searchable catalog of the Mars Express HRSC / OMEGA, Viking Orbiter and Phobos 88 multispectral images to enable the international science community to study selected surface areas and produce desired datasets. The observations from the other instruments in the Mars Express science payload and unique observations from MAVEN IUVS and THEMIS IR were identified as very desirable. The Viking Orbiter and Phobos 88 image data were identified as high priority existing datasets.

## FOCUS:

The JAXA Mars Moon Exploration Mission (MMX) was identified as the mission to focus the development of new, derived data products to keep the PDWG continued activities relevant. Evolving missions under study would also provide focus as they mature and their surface / environment data requirements become defined.



# DEPHINE – THE DEIMOS AND PHOBOS INTERIOR EXPLORER – A MISSION PROPOSAL TO ESA’S COSMIC VISION PROGRAM

J. Oberst<sup>1,2</sup>, K. Wickhusen<sup>1</sup>, K. Willner<sup>1</sup> and the DePhine Proposal Team\*

<sup>1</sup>German Aerospace Center, Institute of Planetary Research,

Juergen.Oberst@dlr.de

<sup>2</sup>Technical University Berlin, Institute of Geodesy and Geoinformation Sciences

## KEYWORDS:

Deimos, Phobos, DePhine, ESA M-class mission

## INTRODUCTION:

DePhine – Deimos and Phobos Interior Explorer – is proposed as an M-class mission in the context of ESA’s Cosmic Vision program, projected for launch in 2030. The mission will explore the origin and the evolution of the Martian satellite system, by focusing on the interior structures and the diversities of the two moons.

## THE MISSION:

The DePhine spacecraft will be inserted into Mars transfer (the baseline mission assumes a launch on a Soyuz Fregat) and will initially enter a quasi-satellite orbit of Deimos to carry out a comprehensive global mapping with various remote-sensing instruments. We aim at a global stereo and multispectral imaging with 5 m/pixel minimum and local high-resolution imaging with 1 m/pixel and better. Close flybys (1-2 km at speeds of 3-4 m/s) will be performed, during which radio tracking, stereo imaging, radar sounding, observations of the magnetic field and recordings of the Gamma-Ray/Neutron flux will be carried out. A steerable antenna will allow simultaneous radio tracking and remote sensing observations (which, e.g., is technically not possible for Mars Express during Phobos flybys). The close flybys at low velocities offer longer data integration times as well as higher signal strength and data resolution. 10 – 20 flyby sequences, including polar passes, will result in a dense global grid of observation tracks, where data from grid intersection points will be used for cross-over analysis. The spacecraft will then transfer into a 2:1 Phobos resonance orbit to carry out multiple close flybys and to perform similar remote sensing experiments as in the case of Deimos, for comparative studies. Additional instrumentation, e.g. a dust detector or a solar wind sensor, will study the space environment of the Martian satellites.

## FUTURE PROSPECTS:

If Ariane 6-2 and significantly greater lift performance are available for launch, we expect to carry and deploy a small lander on Deimos. DePhine will be launched approximately 6 years after the MMX (Mars Moon Exploration) mission, currently being prepared by JAXA, which is to return a sample from Phobos. DePhine will build upon the experience of this mission and address follow-on science issues pertaining to the Martian satellite system that may not be resolved by this early mission to Phobos alone.

\*) The DePhine Proposal team:

Jürgen Oberst, Kai Wickhusen, Konrad Willner, and Klaus Gwinner, German Aerospace Center Berlin, Germany; Sofya Spiridonova and Ralph Kahle, German Aerospace Center Oberpfaffenhofen, Germany; Alain Herique, IPAG Grenoble, France; Dirk Plettmeier, TU Dresden, Germany; Andrew Coates, University College London, MSSL, UK; Marina Diaz Michelena, Instituto Nacional de Tecnica Aeroespacial, Spain; Alexander Zakharov, Space Research Institute Moscow, Russia; Yoshifumi Futaana, Swedish Institute of Space Physics, Sweden; Martin Pätzold, Universität zu Köln, Germany; Pascal Rosenblatt, Royal Observatory of Belgium, Belgium; David J. Lawrence, Johns Hopkins University, APL, USA; Valery Lainey IMCCE Paris, France; Alison Gibbings and Ingo Gerth, OHB System AG, Bremen, Germany.



# MARS EXPRESS SCIENCE HIGHLIGHTS AND FUTURE PLANS

D.V. Titov<sup>1</sup>, J.-P. Bibring<sup>2</sup>, A. Cardesin<sup>3</sup>, T. Duxbury<sup>4</sup>, F. Forget<sup>5</sup>, M. Giuranna<sup>6</sup>, F. González-Galindo<sup>7</sup>, M. Holmström<sup>8</sup>, R. Jaumann<sup>9</sup>, A. Määttänen<sup>10</sup>, P. Martin<sup>3</sup>, F. Montmessin<sup>10</sup>, R. Orosei<sup>11</sup>, M. Pätzold<sup>12</sup>, J. Plaut<sup>13</sup>, and MEX SGS Team<sup>3</sup>.

<sup>1</sup>ESA-ESTEC, 2200 AG Noordwijk, The Netherlands, [dmitri.titov@esa.int](mailto:dmitri.titov@esa.int);

<sup>2</sup>IAS-CNRS, Orsay, France;

<sup>3</sup>ESA-ESAC, Madrid, Spain;

<sup>4</sup>George Mason University, Fairfax, VA, USA;

<sup>5</sup>LMD, Paris, France;

<sup>6</sup>APS-INAF, Rome, Italy;

<sup>7</sup>IAA, Granada, Spain;

<sup>8</sup>IRF, Kiruna, Sweden;

<sup>9</sup>IPF-DLR, Berlin, Germany;

<sup>10</sup>LATMOS/IPSL, CNRS, Guyancourt, France;

<sup>11</sup>IRA-INAF, Bologna, Italy;

<sup>12</sup>RIU-Uni Cologne, Cologne, Germany;

<sup>13</sup>JPL, Pasadena, CA, USA.

Mars Express remains one of ESA's most scientifically productive missions whose publication record now exceeds 1000 papers. Characterization of the geological processes on a local-to-regional scale by HRSC, OMEGA and partner experiments on NASA spacecraft has allowed constraining land-forming processes in space and time. Recent results suggest episodic geological activity as well as the presence of large bodies of liquid water in several provinces (e.g. Eridania Planum, Terra Chimeria) in the early and middle Amazonian epoch and formation of vast sedimentary plains north of the Hellas basin. Mars Express observations and experimental teams provided essential contribution to the selection of the Mars-2020 landing sites. More than a decade-long record of the atmospheric parameters such as temperature, dust loading, water vapor and ozone abundance, water ice and CO<sub>2</sub> clouds distribution, collected by SPICAM, PFS and OMEGA spectrometers as well as subsequent modeling have provided key contributions to our understanding of the martian climate. ASPERA-3 observations of the ion escape covering complete solar cycle have revealed important dependencies of the atmospheric erosion rate on parameters of the solar wind and EUV flux. The structure of the ionosphere sounded by the MARSIS radar and the MaRS radio science experiment was found to be significantly affected by the solar activity, the crustal magnetic field, as well as by the influx of meteorite and cometary dust. MARSIS and ASPERA-3 observations suggest that the sunlit ionosphere over the regions with strong crustal fields is denser and extends to higher altitudes as compared to the regions with no crustal anomalies. Reconnection of solar magnetic field lines carried by the solar wind with field lines of crustal origin opens channels through which the ionospheric plasma escapes to space, producing strong and narrow cavities in the density. The situation is very different on the night side where the ionosphere has patchy structure. Such patchy ionizations are observed in the regions where field lines have a dominant vertical component. Through these patches the ionospheric plasma from the dayside penetrates and supplies the nightside ionosphere.

Mars Express has fully accomplished its objectives set for 2015-2016. The mission provides unique observation capabilities amongst the flotilla of spacecraft investigating Mars. The mission has been confirmed till the end of 2018. The science case for the mission extension until the end of 2020 has been submitted to the ESA Science Program Committee. The observation program proposed for 2019-2020 includes both augmenting the coverage and extending long-time series, as well as new elements and potentially new opportunities for discoveries. It will be boosted by collaboration and synergies with NASA's MAVEN, ESA-Roscosmos Trace Gas Orbiter (TGO) and other missions. The talk will give the mission status, review the recent science highlights, and outline future plans focusing on synergistic science with TGO.

# **WATER CONTENT IN THE MARTIAN SUBSURFACE ALONG THE NASA/MSL “CURIOSITY” ROVER TRAVERSE: DATA OF THE DAN INSTRUMENT IN PASSIVE MODE**

**S.Y. Nikiforov<sup>1</sup>, I.G. Mitrofanov<sup>1</sup>, M.L. Litvak<sup>1</sup>, D.I. Lisov<sup>1</sup>, A.B. Sanin<sup>1</sup>**  
*<sup>1</sup>Space Research Institute of the Russian Academy of Sciences (IKI)*

## **KEYWORDS:**

Mars exploration, Surface, Neutron Spectroscopy, Water

## **INTRODUCTION:**

This overview presents physical principles, the latest results and summary of operations of the Dynamic Albedo of Neutrons (DAN) instrument on the surface of Mars. Scientific instruments of the DAN experiment were set onboard NASA Mars Scientific Laboratory interplanetary mission. It will be presented latest science products which were measured in the passive mode. In this mode the instrument detects reflected flux from Martian subsurface. Flux is induced by galactic cosmic rays as a source of neutrons that are reflected by subsurface hydrogen.

# CHARGED PARTICLES RADIATION QUANTITIES ONBOARD EXOMARS TRACE GAS ORBITER DURING THE TRANSIT AND IN HIGH ELLIPTIC MARS ORBIT

J. Semkova<sup>1</sup>, R. Koleva<sup>1</sup>, T. Dachev<sup>1</sup>, St. Maltchev<sup>1</sup>, B. Tomov<sup>1</sup>, Yu. Matviichuk<sup>1</sup>, P. Dimitrov<sup>1</sup>, K. Krastev<sup>1</sup>, I. Mitrofanov<sup>2</sup>, A. Malahov<sup>2</sup>, M. Mokrousov<sup>2</sup>, A. Sanin<sup>2</sup>, M. Litvak<sup>2</sup>, A. Kozyrev<sup>2</sup>, V. Tretyakov<sup>2</sup>, D. Golovin<sup>2</sup>, S. Nikiforov<sup>2</sup>, A. Vostrukhin<sup>2</sup>, F. Fedosov<sup>2</sup>, N. Grebennikova<sup>2</sup>, V. Benghin<sup>3</sup>, V. Shurshakov<sup>3</sup>, S. Drobyshhev<sup>3</sup>

<sup>1</sup>Space Research and Technology Institute, Bulgarian Academy of Sciences, Sofia, Bulgaria, jsemkova@stil.bas.bg

<sup>2</sup>Space Research Institute, Russian Academy of Sciences, Moscow, Russia, mitrofanov@np.cosmos.ru

<sup>3</sup>State Scientific Center of Russian Federation, Institute of Biomedical Problems, Russian Academy of Sciences, Moscow, Russia, v\_benghin@mail.ru

## KEYWORDS:

ExoMars TGO, FRIEND, dosimeter, charged particles, radiation dose, particle flux, manned flight to Mars.

## ABSTRACT:

Since April 2016 the dosimeter Liulin-MO has been conducting radiation environment investigations aboard the Trace Gas Orbiter (TGO) of the joint ESA-Roscosmos mission ExoMars. Liulin-MO is a module of the Fine Resolution Epithermal Neutron Detector (FRIEND) aboard TGO. Presented are data for the radiation dose rates, particle fluxes and dose equivalent rates of the ionizing charged particles measured in the interplanetary space and in high elliptic Mars orbit from 22.04.2016 to 07.03.2017 in the phase of declining solar activity of 24-th solar cycle. Data obtained are compared to the data of other radiation measurements in the interplanetary space.

The obtained results indicate that during the cruise to Mars and back (6 months in each direction), taken during the declining of solar activity, the crewmembers of future manned flights to Mars will accumulate at least 60% of the total dose limit for the cosmonaut's, astronaut's career.

A similar to Liulin-MO module, called Liulin-ML for investigation of the radiation environment on Mars' surface as a part of the active detector of neutrons and gamma rays ADRON-EM on the Surface Platform is under preparation for ExoMars 2020 mission.

# FINE RESOLUTION NEUTRON DETECTOR (FREND) INSTRUMENT ONBOARD EXOMARS 2016 TGO ORBITER. FIRST RESULTS

A.V. Malakhov<sup>1</sup>, I. G. Mitrofanov<sup>1</sup>, M.L. Litvak<sup>1</sup>, A.S. Sanin<sup>1</sup>,  
D.V. Golovin<sup>1</sup>, A.S. Kozyrev<sup>1</sup>, M.I. Mokrousov<sup>1</sup>, A.A. Vostrukhin<sup>1</sup>,  
J. Semkova<sup>2</sup>, T. Dachev<sup>2</sup>, V.N. Shvetsov<sup>3</sup>, G.N. Timoshenko<sup>3</sup>,  
V.V. Benghin<sup>4</sup>

<sup>1</sup> Space Research Institute, Profsoyuznaya st 84/32, Moscow, Russia.

<sup>2</sup>Space Research and Technology Institute, Sofia, Bulgaria

<sup>3</sup>Joint Institute for Nuclear Research, Dubna, Russia

<sup>4</sup> Institute of Medico-biological Problems, Moscow, Russia.

## KEYWORDS:

Neutron telescope, Mars, water, Exomars, first results, dosimetry, exploration, instrument

## INTRODUCTION:

ExoMars is a two-launch mission undertaken by Roscosmos and European Space Agency. Trace Gas Orbiter, a satellite part of the 2016 launch carries the Fine Resolution Neutron Detector instrument as part of its payload. The instrument aims at mapping hydrogen content in the upper meter of Martian soil with spatial resolution of up to 40 km. This resolution is achieved by a collimation module that limits the field of view of the instruments detectors. A dosimetry module that surveys the radiation environment in cruise to Mars and on orbit around it is another part of the instrument.

This paper describes briefly the mission and the instrument, its measurement principles and technical characteristics. We then focus on the first data accumulated during cruise to Mars and the commissioning elliptical orbits where the instrument could operate before the aerobraking maneuvers started. These data give an estimation of what the instrument mapping capabilities during the nominal science phase could be and are of particular use.

# NEUTRON COMPONENT OF RADIATION ENVIRONMENT FOR INTERPLANETARY MISSIONS

A.A. Vostrukhin <sup>1</sup>, D.V. Golovin <sup>1</sup>, M.L. Litvak <sup>1</sup>, A.V. Malakhov <sup>1</sup>,  
A.B. Sanin

<sup>1</sup> Space Research Institute, Profsoyuznaya 84/32, 117997, Russia

## KEYWORDS:

Neutrons, radiation, interplanetary missions, Mars, Moon.

## INTRODUCTION:

Radiation environment and its influence on the astronaut's health and electronic equipment reliability is one of the fundamental challenges in interplanetary space flights. Radiation environment in space mostly consist of galactic cosmic rays (GCR) and Solar proton events (SPE). In the estimation of total equivalent dose, secondary radiation shall be accounted as well, mostly caused by neutron component of the radiation environment. Amount of neutron component depends on spacecraft structure and radiation shield properties. This is vital to study radiation environment neutron component for far missions preparation and planing. In the last 15 years with participation of the authors of this presentation four neutron detectors were built: HEND, LEND, DAN and FRENDA as a payload for NASA and ESA spacecrafts Mars Odyssey, Lunar Reconnaissance Orbiter, Mars Science Laboratory and ExoMars missions respectively with primary goal to estimate elemental composition and hydrogen-rich materials on the planets. In this presentation data from these instruments will be used to estimate neutron component of the equivalent dose in interplanetary space.

# VENERA-D - CONCEPT MISSION TO VENUS: SCIENTIFIC GOALS AND ARCHITECTURE

L. Zasova<sup>1</sup>, D. Senske<sup>2</sup>, T. Economou<sup>3</sup>, N. Eismont<sup>1</sup>, L. Esposito<sup>4</sup>, M. Gerasimov<sup>1</sup>, D. Gorinov<sup>1</sup>, N. Ignatiev<sup>1</sup>, M. Ivanov<sup>5</sup>, K. Lea Jessup<sup>6</sup>, I. Khatuntsev<sup>1</sup>, O. Korablev<sup>1</sup>, T. Kremic<sup>7</sup>, S. Limaye<sup>8</sup>, I. Lomakin<sup>9</sup>, A. Martynov<sup>9</sup>, A. Ocampo<sup>10</sup>, O. Vaisberg<sup>1</sup>, A. Burdanov<sup>11</sup>

<sup>1</sup>Space Research Institute, Moscow, Russia,

<sup>2</sup>Jet Propulsion Laboratory, Pasadena, California Institute of Technology, USA,

<sup>3</sup>Enrico Fermi Institute, Chicago, USA,

<sup>4</sup>University of Colorado, Boulder, USA,

<sup>5</sup>Vernadsky Institute, Moscow, Russia,

<sup>6</sup>Southwest Research Institute Boulder, USA,

<sup>7</sup>Glenn Research Center, Cleveland, USA,

<sup>8</sup>Univ. of Wisconsin, USA,

<sup>9</sup>Lavochkin Assoc., Khimki, Russia,

<sup>10</sup>NASA Headquarters, Washington, USA,

<sup>11</sup>TSNIIMASH, Korolev, Russia.

lzasova@gmail.com

NASA and IKI/Roscosmos established in 2015 a Joint Science Definition Team (JSDT), a key task of which was to codify the synergy between the goals of Venera-D [1] with those of NASA [2,3]. In addition, the JSDT studied potential NASA provided mission augmentations (experiments /elements) that could to fill identified science gaps. The first report to NASA - IKI/Roscosmos was provided in January 2017. The baseline Venera-D concept includes two elements, and orbiter and a lander, with potential contributions consisting of an aerial platform/balloon, small long-lived surface stations or a sub-satellite.

## INTRODUCTION:

The Venera-D mission concept is devoted to the detailed study of the atmosphere, surface, and plasma environment of Venus [1]. Envisioned as launching in the post-2025 timeframe and consisting of an orbiter and lander with advanced, modern instrumentation, this mission would build upon the Venera, VEGA, Pioneer Venus, and Magellan missions carried out in the 1970's and 1990's [4,5,6] along with the more recent Venus Express [7].

Our knowledge of Venus' basic atmospheric properties (composition, thermal structure, clouds, winds, etc.), and how different this planet is from Earth has come through the success of the Soviet, US, ESA and now, JAXA missions to Venus as well the Earth-based observations of last decades. Venus was formed in the inner solar system out of the same proto-planetary material as Earth, and is considered Earth's twin. Although these siblings have nearly the same size, mass, and density, unlike Earth, which has a comfortable condition for the life, Venus' climate presents a "hellish" condition, fueled by a massive (90 atm) CO<sub>2</sub> atmosphere which is responsible for an enormous greenhouse effect and a near-surface temperature of 470°C, sulfuric acid clouds, lack of water. Its young surface is sculpted by volcanism and is deformed by folding and faulting resulting in belts of mountains and rifts. The lack of an intrinsic magnetic field suggests the planet's interior structure may also be different than that of the Earth. Why did Venus take an evolutionary path so different from that of the Earth, why and when did the evolutionary paths of these twin planets diverge? Were there ever favorable conditions for starting life on Venus?

## THE GOALS OF VENERA-D MISSION COMPONENTS:

Specific areas of scientific investigation would focus on the dynamics of the atmosphere with emphasis on atmospheric superrotation, the origin and evolution of the atmosphere, and the geological processes that have formed and modified the surface with emphasis on the mineralogical and elemental composition of surface materials, the chemical processes related to the interaction of the surface and atmosphere, solar wind interaction and atmospheric losses.

*Orbiter Goals* consist of the following: study of the dynamics and nature of superrotation, radiative balance and greenhouse effect; investigation of the thermal structure of the atmosphere, winds, thermal tides and solar locked structures; measurement of the composition of the atmosphere; study of the clouds, their structure, composition, and chemistry; evaluation of the nature of

the 'unknown' UV-absorber; and investigation of the upper atmosphere, ionosphere, electrical activity, magnetosphere, and the escape rate.

*Lander Goals* focus on the detailed chemical analysis of the surface material; study of the elemental and mineralogical composition of the surface, including radiogenic elements; characterize of the geology of local landforms at different scales; study of the interaction between the surface and the atmosphere; investigation of the structure and chemical composition of the atmosphere down to the surface, including abundances and isotopic ratios of the trace and noble gases; and direct chemical analysis of the cloud aerosols.

To fill the "science gaps," where important VEXAG science may not be addressed by the baseline Venera-D concept, the JSDT generated a list of possible contributed options: from specific instruments such as a Raman Spectrometer and an Alpha-Particle X-Ray Spectrometer (APXS) to possible flight elements such as a maneuverable aerial platform, small long-lived surface stations, a balloon, and a small sub-satellite.

In situ measurements, both in the atmosphere and on the surface have not been carried out for more than 30 years. The Venera-D mission is proposed to correct this gap. Long-duration measurements in the atmosphere (from several weeks to several months) would aid in understanding the processes that drive the atmosphere. A well instrumented mobile platform or balloon that could maneuver to different altitudes in the clouds could help understand the 'puzzles' of the UV-absorber, its nature, composition, vertical and horizontal distribution as well as providing a platform to measure key trace and noble gases and their isotopes, meteorology and cloud properties, composition, etc., depending on scientific payload. Another high priority augmentations that are considered are small long-lived surface station (possibly 1-5 stations with an operation life time from 60 days to up to one year) and subsatellite.

## **JSDT RECOMMENDATIONS:**

The JSDT identified priorities for the science goals and objectives for the comprehensive scientific exploration of Venus. Based on these priorities, a baseline Venera-D mission would consist of a single highly capable orbiter and a single highly capable lander. In addition to the baseline mission, the JSDT identified potential "contributed" augmentations that would enhance the science return. In formulating a strategy for the development of Venera-D, the JSDT identified areas where investments would need to be made to bring the mission concept to fruition.

## **FUTURE WORK:**

The next phase of development of the Venera-D concept would focus on a more detailed examination of the science measurements and potential instrumentation along with the specifications of the spacecraft requirements.

In its ongoing work, the JSDT will incorporate into its deliberations information from a set of science community modeling workshops (in May at GRC, Cleveland, USA and in October at IKI, Moscow) to identify additional key measurements (and corresponding instruments) that could be achieved by the planned Venera-D mission. In addition these workshops will identify needed high-value data that could be obtained by Venera-D that would advance future modeling work, specifically the development of new GCMs.

## **ACKNOWLEDGEMENTS:**

The members of the JSDT acknowledge NASA and Roscosmos for support of our current activities and future work

## **REFERENCES:**

- [1] Venera-D feasibility study. <http://venera-d.cosmos.ru>.
- [2] Space Studies Board (2011). The National Academies Press, Washington, DC.
- [3] Herrick, R. et al. VEXAG (2014), 1-15.
- [4] Sagdeev, R. V., et. al. (1986). Science. 231, 1407-1408.
- [5] Colin, L., et al. (1980), JGR, 85, A13.
- [6] Saunders, R. S. et al. (1992) JGR, 97, 13067.
- [7] Svedhem et al. (2009), JGR, 114, E00B33..



# ACTIVE GAMMA RAY SPECTROMETER PROPOSED FOR FUTURE VENUS SURFACE MISSIONS

M.L. Litvak<sup>1</sup>, A.B. Sanin<sup>1</sup>, D.V. Golovin<sup>1</sup>, I.G. Mitrofanov<sup>1</sup>,  
A.A. Vostrukhin<sup>1</sup>

<sup>1</sup>Space Research Institute, Russia, Moscow, 117997, Profsoznaya street,  
84/32, litvak@mx.iki.rssi.ru

## KEYWORDS:

Gamma-ray spectroscopy, Venus, elemental composition.

## INTRODUCTION:

Nuclear instrumentation based on neutron and gamma-ray spectroscopy methods were often used by different planetary missions to derive the bulk elemental abundances of surface materials. Usually these nuclear instruments were implemented on orbital missions to produce global elemental maps [1,2,3,4]. For surface operations, active gamma-ray spectrometers could be accommodated onboard landing missions. For such instrumentation, a pulsed neutron generator that can generate short and very intense pulses of high energy neutrons (14 MeV) is used to irradiate subsurface under the lander and produce secondary gamma emission. The use of active gamma and neutron spectrometers commonly occurs in various Earth applications related to geology, security applications, transportation, medicine, etc. Active gamma ray and neutron spectrometers have been proposed for space missions to the planets and satellites of the solar system, including Moon, Mars and Venus. [5-11].

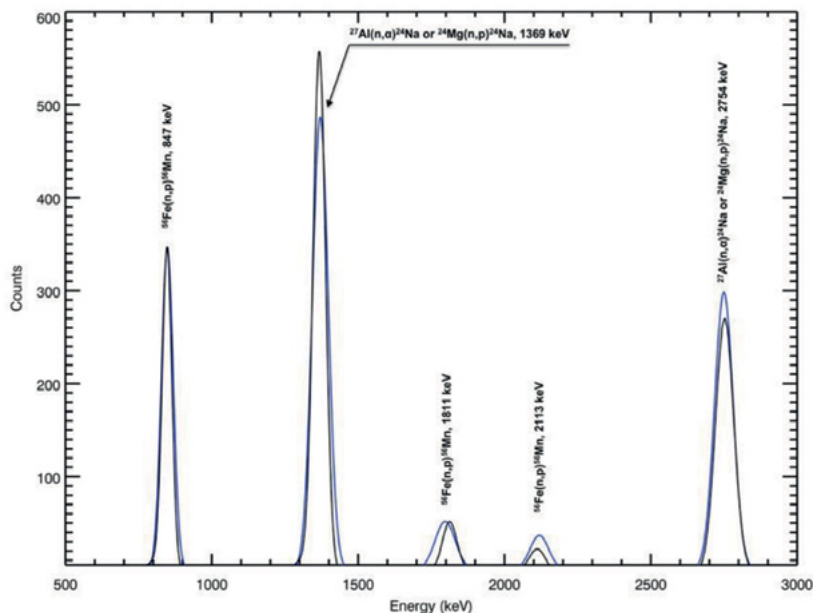


**Fig. 1.** The example of comparison between measured by gamma spectrometer (blue color) and numerically modeled (black color) gamma ray lines for radioisotopes produced in the reactions with Al, Mg, Fe with fast neutrons.

In our study, we presented the results of a series of ground tests with a prototype of an active gamma-ray spectrometer based on a new generation of scintillation crystal ( $\text{CeBr}_3$ ). These tests have been conducted with a consideration to its applicability to future Venus landing missions. We evaluated the instrument's capability to distinguish the subsurface elemental composition of primary rock forming elements such as O, Na, Mg, Al, Si, K and Fe. We have estimated that the expected accuracies achieved in this approach could be as high as 1-10% for the particular chemical element being studied.

**REFERENCES:**

- [1] Boynton W.V. et al., (2004), *Space Sci., Rev.* 110:37-83.
- [2] Boynton W.V. et al., (2006), *JGR*, 112, doi:10.1029/2007JE002887
- [3] Prettyman T.H. et al., (2006), *JGR*, 111, CiteID E12007.
- [4] Prettyman T.H. et al., (2011), *Space Sci. Rev.*, 163, 371-459.
- [5] Bruckner J. et al., (1987), *JGR*, 92, E603-E616
- [6] Jun I. et al., *Nuclear Instruments and Methods A*, 629, 140.
- [7] Litvak M. L. et al., (2008), *ASTROBIOLOGY*, 8, 3, 605-612.
- [8] Litvak M.L. et al., (2016), *Nuclear Instruments and Methods*, A822, 112–124.
- [9] Litvak M.L. et al., (2016), *Nuclear Instruments and Methods*, A822, 112–124. *Nuclear Inst. and Methods*, A 848, 9-18.
- [10] Mitrofanov I.G., et al., (2011), *European Planetary Congress 2010*, p.264.
- [11] Parsons, A., et al., (2011), *Nucl. Instr. and Meth. A*, 652, 674.

# EXOMARS-2020 SURFACE PLATFORM SCIENTIFIC PAYLOAD

D. Rodionov <sup>1</sup>, O. Korablev <sup>1</sup>, J. Vago <sup>2</sup>

<sup>1</sup>*Space Research Institute, Moscow, Russia, rodionov@iki.rssi.ru;*

<sup>2</sup>*European Space Research and Technology Centre (ESTEC),  
Noordwijk, Netherlands*

## KEYWORDS:

Mars, ExoMars, surface, platform, payload, atmosphere, climate

## INTRODUCTION:

ESA and Roscosmos have signed a cooperation agreement to work in partnership to develop and launch two ExoMars missions—in 2016 and 2020. The first mission is currently in progress, aiming to study Mars' atmospheric composition in unprecedented detail. The second mission will deliver the ExoMars Rover and a Surface Platform to the surface of Mars.

The ExoMars Rover will carry a comprehensive suite of instruments dedicated to exobiology and geology research named after Louis Pasteur. After the rover egress the Surface Platform will serve as long-lived stationary platform (expected lifetime is 1 Earth year) to study surface environment with suite of scientific instruments. The scientific objectives of the Surface Platform are:

- Context imaging;
- Long-term climate monitoring and atmospheric investigations.
- Studies of subsurface water distribution at the landing site;
- Atmosphere/surface volatile exchange;
- Monitoring of the radiation environment;
- Geophysical investigations of Mars' internal structure.

To address these objectives scientific payload has been selected and is currently in development. Payload consists of 13 instruments with total mass of 45 kg.

# CHARACTERISATION OF DUST SUSPENDED IN THE ATMOSPHERE OF MARS: THE DUST SUITE - MICROMED SENSOR FOR THE EXOMARS 2020 MISSION

F. Esposito<sup>1</sup>, C. Molfese<sup>1</sup>, F. Cozzolino<sup>1</sup>, F. Cortecchia<sup>2</sup>, B. Saggin<sup>3</sup>, D. Scaccabarozzi<sup>3</sup>, I. Arruego Rodriguez<sup>4</sup>, A. Martín Ortega Rico<sup>4</sup>, Ismael Traseira Rodriguez<sup>4</sup>, P. Schipani<sup>1</sup>, S. Silvestro<sup>1</sup>, C.I. Popa<sup>1</sup>, A. Zakharov<sup>5</sup>, G. Dolnikov<sup>5</sup>, A. Lyash<sup>5</sup>, I. Kuznetsov<sup>5</sup>

<sup>1</sup>INAF – Osservatorio Astronomico di Capodimonte, Salita Moiarillo 16, 80131 Napoli, Italy;

<sup>2</sup>INAF – Osservatorio Astronomico di Bologna, Via Ranzani 1, 40127 Bologna, Italy;

<sup>3</sup>Politecnico di Milano, 1/c via Previati, 23900, Lecco, Italy;

<sup>4</sup>INTA, Ctra. Ajalvir km 4, Torrejón de Ardoz, Madrid, Spain;

<sup>5</sup>IKI, 84/32 Profsoyuznaya Str, Moscow, Russia, 11799.

francesca.esposito@na.astro.it

## KEYWORDS:

Martian suspended dust, dust detector, Mars, dust, dust devils, dust storms, saltation

## INTRODUCTION:

Nowadays, dust is a relevant agent that affects environmental conditions in the lower Martian atmosphere and, thus, may interact / interfere with any instrumentation delivered to Mars surface for in situ analyses.

MicroMED is an Optical Particle Counter, proposed as a European contribution to the Russian-led Instrument "Dust Suite". It is a novel experiment, never developed for space applications. It has been designed to measure, for the first time directly and in situ, the size distribution and number density vs size of dust particles suspended into the atmosphere of Mars, close to the surface. This information represents a key input in different areas of interest: 1) to improve knowledge on airborne mineral dust in terms of physical properties and lifting mechanism, 2) to improve climate models and 3) to address potential hazards for future landed Martian exploration missions.

Indeed, Martian atmosphere contains a significant amount of suspended dust. It varies with seasons and with the presence of local and global dust storms, but never drops entirely to zero. Aerosol dust has always played a fundamental role on the Martian climate. Dust interaction with solar and thermal radiation and the related condensation and evaporation processes influence the thermal structure and balance, and the dynamics (in terms of circulation) of the atmosphere.

Main dust parameters influencing the atmosphere heating are size distribution, abundance, albedo, single scattering phase function, imaginary part of the index of refraction. Moreover, major improvements of Mars climate models require, in addition to the standard meteorological parameters, quantitative information about dust lifting, transport and removal mechanisms. In this context, two major quantities need to be measured for the dust source to be understood: surface flux and granulometry. While many observations have constrained the size distribution of the dust haze seen from the orbit, it is still not known what the primary airborne dust (e.g. the recently lifted dust) is made of, size-wise.

MicroMED has been designed to fill this gap. It will measure the abundance and size distribution of dust, not in the atmospheric column, but close to the surface, where dust is lifted, so to be able to monitor dust injection into the atmosphere. This has never been performed in Mars and other planets exploration.

MicroMED is a miniaturized/optimized version of the MEDUSA [1], [2] instrument, which was selected by ESA for the Humboldt Payload, on board the lander of the previous configuration of the ESA ExoMars, before the mission changes approved in 2009.

MicroMED (Figure 1) is able to measure the size of single dust grains entering into the instrument from 0.2 to 10 mm radius, giving as products the dust size distribution and abundance. It analyses light scattered from single dust particles. A pump is used to sample the Martian atmosphere, generating a flux of gas and

dust across the instrument trough the inlet. When the dust grains reach the Optical Sensor, they cross a collimated IR laser beam emitted by a laser diode. The light scattered by the grains is detected by a photodiode, which is amplified by the Electronics. The detected signal is related to the size of sampled dust particle.

An Elegant Breadboard of MicroMED has been realized and fully tested by the proposing team. Tests performed in relevant environment (in a Martian simulation chamber) have demonstrated the fully functionality and performances of the instrument.

We will present the progress in the development of the instrument.

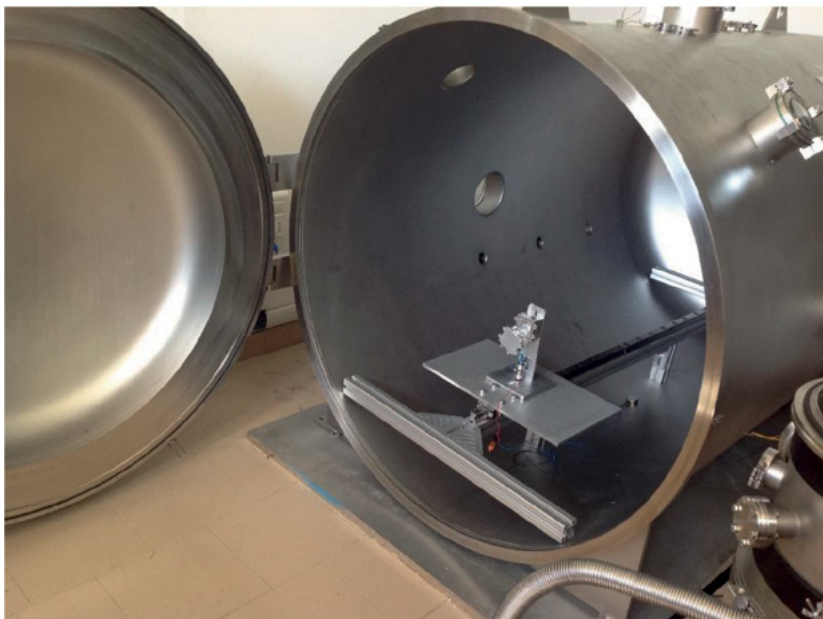


**Fig. 1.** MicroMED Breadboard in the Martian Simulation Chamber at INAF Naples (Italy).

## REFERENCES:

- [1] F. Esposito, L. Colangeli, V. Della Corte, C. Molfese, P. Palumbo, S. Ventura, J. Merrison, P. Nørnberg, J.F. Rodriguez-Gomez, J.J. Lopez Moreno, E. Battistelli, S. Gueli, R. Paolinetti, and The International MEDUSA Team: MEDUSA: Observation of atmospheric dust and water vapor close to the surface of Mars, *Mars - The International Journal of Mars Science and Exploration*, 6, 1-12, 2011. Doi: 10.1555/mars.2011.0001.
- [2] L. Colangeli, J.J. Lopez-Moreno, P. Nørnberg, V. Della Corte, F. Esposito, E. Mazzotta Epifani, J. Merrison, C. Molfese, P. Palumbo, J.F. Rodriguez-Gomez, A. Rotundi, G. Visconti, J.C. Zarnecki, The International MEDUSA Team: MEDUSA: the ExoMars experiment for in-situ monitoring of dust and water vapour, *Planetary and Space Science*, 57, pp. 1043-1049, 2009. doi:10.1016/j.pss.2008.07.013

# AMR INSTRUMENT FOR STATIONARY MAGNETIC MEASUREMENTS ON MARS

D. R. Díaz<sup>1</sup>, J. V. López<sup>1</sup>, J. García-Martínez<sup>1</sup>, R. Sanz<sup>1</sup>, A. A. Ordóñez<sup>1</sup>, V. González<sup>1</sup>, J. Pazos<sup>1</sup>, R. Kilian<sup>2</sup>, M. A. Rivero<sup>1</sup>, J. de Frutos<sup>1</sup>, M. C. Parrondo<sup>1</sup>, A. Aguilar<sup>1</sup>, M. Díaz Michelena<sup>1</sup>

<sup>1</sup>INTA Crta. Torrejón-Ajalvir km 4, 28850 Torrejón de Ardoz, Madrid, Spain;

<sup>2</sup>Geology Department, University of Trier, Behringstrasse, 54286 Trier, Germany;

## KEYWORDS:

ExoMars 2020, Surface Platform, METEO, Anisotropic Magnetoresistance-AMR, 3-axis vector magnetometer, magnetic cleanliness, terrestrial analogues of Mars, crustal magnetic anomalies.

## INTRODUCTION:

The primary objective of the ExoMars 2020 mission is to land at a site on Mars with high potential for scientific exploration. After that purpose is accomplished, and in order to achieve the scientific objectives for the mission, the rover will leave the Lander and travel across the surface of Mars. The Surface Platform (SP) will remain stationary for the duration of the mission and will use its scientific payload to obtain data regarding the context imaging on the landing site, long-term climate monitoring, and atmospheric and surface investigation.

An Anisotropic MagnetoResistive (AMR) instrument is part of the scientific payload on the SP within METEO (METEOrological instrumentation module), that will travel onboard the ExoMars mission, with the objective of performing local magnetic field measurements at the landing site on Mars.

This work describes the instrument and summarizes the scientific objectives. Additionally, we give an insight in the measurements which will be accomplished in terrestrial analogues of Mars prior to the exploration of the Red Planet.

The scientific goals of AMR instrument are the determination of local crustal magnetic signatures at the landing site and the measurement of the variations of the magnetic field on the surface: the latter comprise short term daily variations and superimposed anomalies due to the interaction with the solar wind along the duration of the mission (Fig. 1). This part of the investigation will include the comparison with MAVEN data to improve the interpretation and extent of the events.

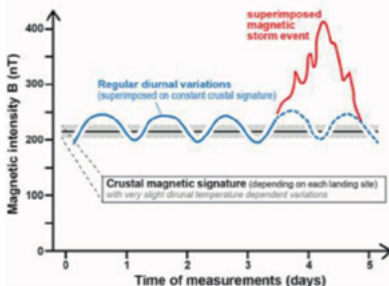


Fig. 1. Time varying magnetic superimposed events.

The AMR instrument consists of two main units, the E-BOX, whose main tasks are the power distribution, control and data processing, and serves as physical interface for communications with METEO; and the S-BOX, which is the deploying sensor head of the instrument. It comprises a 3-axis vector magnetometer based on AMR technology, a tilt angle sensor and a temperature sensor (PT-1000).

The S-BOX is linked to the E-BOX through an SPI communications I/F that will operate as a slave unit in charge of collecting the scientific data (Fig. 2).

The AMR instrument has been designed as a balance between compactness, mass reduction and magnetic cleanliness at the head (S-BOX). Its final location is a solar panel of the SP, from which the S-BOX will be further ejected to a distance of 2 m lying on the Martian surface.

The rocks exposed at the pre-selected ExoMars 2020 landing sites have been formed during the Noachian period (>3.7 Ma) by fluvial, deltaic or lagoon-like sedimentation processes under oxygen-poor and highly acid hydrous condi-

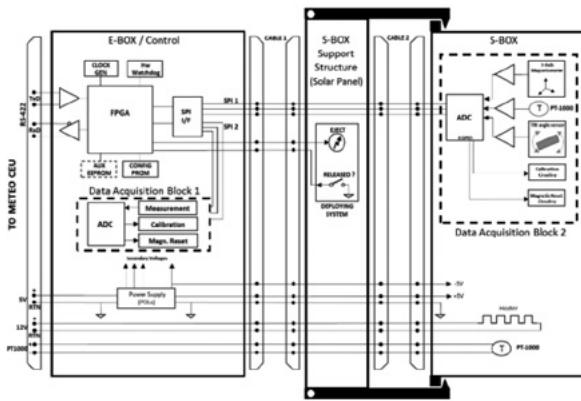


Fig. 2. Block diagram of AMR instrument.

tions. This is documented by the occurrence of different phyllosilicates and hydroxide minerals (e.g. Ehlmann et al. 2011).

In particular, minerals like jarosite and lepidocrocite, which have been detected on Mars and were also formed along terrace systems of the Río Tinto in Huelva, Spain, indicate formation under similar highly acidic conditions and thus have been considered as a Martian analogue on Earth (Amils et al. 2014). These aqueous mineral formations have also been associated with a microbial-related iron enrichment (Oggerin et al. 2016). The type and amount, as well as the regional distribution and vertical extension of the distinct precipitated iron-ore minerals (including goethite and maghemite), should be traced and mapped with our AMR instrument to prove its capacity to determine the magnetic signatures of different ore minerals.

Like on Mars, the early geological history of the Earth was characterized by oxygen-poor and hydrous conditions. But after the great oxidation event on Earth at around 2.3 Myr (Canfield et al. 2013), most aquatic systems became more or less completely oxygenated. Only ocean basins with strong density gradients which inhibit vertical mixing, like that of the Black Sea which has been the place of many groundbreaking new discoveries, still provide anoxic conditions.

Recently the discovery of a stratified anoxic basin at the Golfo Almirante Montt in southern Chile (Silva & Vargas, 2014) offers a unique opportunity to understand the natural effects of deep water anoxia as well as related mineral precipitation and transformation under these conditions. Due to the smaller dimensions of this basin (35 x 40 km), mineral sources and regional variations of the magnetic signatures can be better traced than in the Black Sea. Magnetic mapping of the Golfo Almirante Montt basin combined with representative piston sediment core drilling of RV Sonne Cruise in 2018 along transects of this basin will provide unique information concerning the differences in the (magnetic) mineralogy between oxygenated and anoxic basins.

## REFERENCES:

- [1] M. Díaz Michelena, R. Kilian, R. Sanz, F. Ríos, O. Baeza. Mars MOURA magnetometer demonstration for high-resolution mapping on terrestrial analogues. *Geosci. Instrum. Method. Data Syst.*, 5.P. 127–142. 2016.
- [2] M. Díaz Michelena, R. Sanz, A.B. Fernández, V. de Manuel, M.F. Cerdán, V. Apéstigue, I. Arruego, J. Azcue, J.A. Domínguez, M. González, H. Guerrero, M.D. Sabau, R. Kilian, O. Baeza, F. Ríos, M. Herráiz, L. Vázquez, J.M. Tordesillas, P. Covisa, J. Aguado. MOURA magnetometer for Mars MetNet Precursor Mission. Its potential for an in situ magnetic environment and surface characterization. *Física de la Tierra Vol. 28* (2016). P. 65-82.
- [3] B.L. Ehlmann, J.F. Mustard, S.L. Murchie, J.-P. Bibring, A. Meunier, A. Abigail, A.A. Fraeman, Y. Langevin. Subsurface water and clay mineral formation during the early history of Mars. (2011). *Nature* 479. P. 53-60.
- [4] R. Amils, D. Fernández-Remolar and the IPBLS Team. Río Tinto: A Geochemical and Mineralogical Terrestrial Analogue of Mars. *Life* 2014, Vol. 4 (2014). P. 511-534.
- [5] M. Oggerin, F. Tornos, N. Rodríguez, L. Pascual, and R. Amils. Fungal Iron Biomineralization in Río Tinto. (2016). *Minerals*, P. 6-37.
- [6] D.E. Canfield, L. Ngombi-Pemba, E.U. Hammarlund, S. Bengtson, M. Chaussidon, F. Gauthier-Lafaye, A. Meunier, A. Riboulleau, C. Roillion-Bard, O. Rouxel, D. Asael, A.-C. Pierson Wickmann, A. El Albani. Oxygen dynamics in the aftermath of the Great Oxidation of Earth's atmosphere. *Proc. Nat. Acad. Sci.* (2013). USA 110. P. 16736-16741.
- [7] N. Silva, C.A. Vargas. Hypoxia in Chilean Patagonian Fjords. (2014). *Prog. Oceanogr.* 129. P. 62-74.

# NEWTON PROJECT: NEW OPPORTUNITIES FOR MAGNETIC SURVEYS IN THE PLANETARY EXPLORATION

M. Díaz-Michelena<sup>1</sup>, P. Cobos<sup>2</sup>, J. de Frutos<sup>1</sup>, M. Maicas<sup>2</sup>, J.L. Mesa<sup>1</sup>, M. Pérez<sup>1</sup>, M.A. Rivero<sup>3</sup>, M.M. Sanz-Lluch<sup>2</sup>, C. Aroca<sup>2</sup>

<sup>1</sup>INTA Crta. Torrejón-Ajalvir km 4, 28850 Torrejón de Ardoz, Madrid, Spain;

<sup>2</sup>ISOM-UPM, Madrid, Madrid, Spain

<sup>3</sup>ISDEFE-INTA External Consultant, Madrid, Spain

## KEYWORDS:

Planetary Magnetic surveys, Rovers, Magnetic Payload, Stray Field, Susceptometer, Magnetic Amplifiers

NEWTON project aims to develop a new multisensory instrument to measure the real and imaginary susceptibility of rocks and soils at different frequencies in contrast to other commercial devices [1].

In order to achieve this, the head of the sensor is a resonant circuit with an open autoinductance "L". The susceptibility is measured by the change in the L due to the closure of the gap when a rock approaches the head. A first prototype has been conceived to be part of a surveying system (Fig. 1) in which the head is approached to the rocks during the tracks and therefore there is no need to load the samples, which simplifies the prospectations. A latter prototype will be developed for near future planetary rovers as part of the geological suites.



Fig.1. Surveying system where NEWTON first prototype will be integrated.

Since in both cases the power of the systems is limited, the circuit is based on a modified tank circuit (Fig. 2), which has a resonance frequency that minimises the power consumption from the power supply achieving intense currents in resonance in the autoinductance.

One of the concerns of the circuit is to achieve a sufficiently intense and extensive stray field in the L to penetrate the samples and magnetize them avoiding the effect of their surface roughness. In relation with this respect, a discussion is made regarding the different topologies of autoinductance used (H, C, and 8 shapes) paying attention to the intensity of the flux lines and the produced stray field.

The other question is how to vary the resonance frequency avoiding the switching among different branches of tuning capacitors. In this device, this goal has been achieved by means of magnetic amplifiers [2]. At his point, different architectures are shown, and their characteristics described.

The degree of consecution of the objectives and the miniaturisation levels reached [3] together with the potential to include such capability in the geological modules of planetary rovers present a very attractive scenario for missions such as Martian Moons eXploration (MMX) or Mars sample return missions.



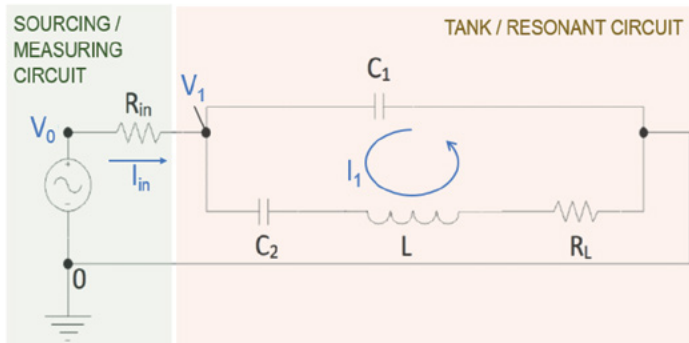


Fig. 2. Modified tank circuit scheme.

## ACKNOWLEDGEMENTS:

This work has been funded by European Union's Horizon 2020 research and innovation programme under grant agreement No 730041.

## REFERENCES:

- [1] S. Geuna, L. Escoteguy, B. Díaz Apella, F. D'Eramo and L. Pinotti; Stud. Geophys. Geod., 61. 2017.
- [2] US Navy, Magnetic amplifiers, another lost technology (1951)". G. B. Trinkaus, High Voltage Press. 2000.
- [3] L. Austrina et al., Journal of Magnetism and Magnetic Materials 272–276 e1709–e1710. 2004.

# LOW FREQUENCY RADIO ASTRONOMICAL MISSIONS ON THE FARSIDE SPACE OF THE MOON

J. Ping<sup>1</sup>, Y. Ji<sup>2</sup>, M. Huang<sup>1</sup>, Y. Yan<sup>1</sup>, G. Fang<sup>1</sup>, M. Zhang<sup>1</sup>, M. Wang<sup>1</sup>, L. Chen<sup>1</sup>, H. Zhang<sup>1</sup>, C. Li<sup>1</sup>, and X. Chen<sup>1</sup>

<sup>1</sup>National Astronomical Observatories of CAS, No.20A Datun Rd. Beijing, China, 100012, Contact: jsping@bao.ac.cn;

<sup>2</sup>Institute of Electrics, Chinese Academy of Sciences, No.7 Beisihuan West Rd. Hadian District, Beijing, China, 100190;

## KEYWORDS:

Radio astronomy, Low frequency, Moon, Farside.

## INTRODUCTION:

Following the development of the Chinese lunar exploration program, astronomical facilities have been planned to set on the surface of the Moon so as to obtain new sciences from the Moon. The Chang'E 4 explorer (including a relay satellite, a lander and a rover, etc.) is a mission to the lunar far side, designed, assembled, and tested by CNSA. In Chang'E-4 lunar lander mission, a low frequency radio astronomical detector will be firstly settled on the far side surface of the Moon to detect the solar burst, and to investigate the lunar ionosphere. Additionally, it will be tested technically as a pathfinder mission for the future lunar surface low frequency radio observatory.

## LOW FREQUENCY DETECTOR OF CHANG'E-4 LANDER:

After ~10 years preparation of a radio astronomical team from National Astronomical Observatory of Chinese Academy of Science, a very low frequency radio astronomical detector will be settled on the far side surface of the Moon [1], in Chinese Chang'E-4 lunar lander mission. The 3 monopole detector of 5 meter long each will mainly investigate the type II and type III solar burst, and will also to investigate the possible lunar ionosphere above the landing site [2], by means of taking the advantage of radio quiet environment of lunar far side. Figure 1 shows the concept of the lander with radio astronomical payload.

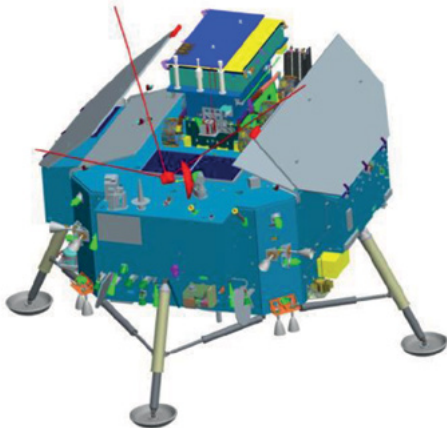


Fig.1. Three monopole HF antenna onboard lander.

After the successful Chang'E-3 lunar nearside landing mission, the backup mission of Chang'E-4 with an identified lander platform and the same designed rover as YUTU has been planned to launch and land to the lunar far side in a couple of years by CNSA. A relay communication satellite will operate in the orbit around the Earth-Moon Lagrange point L2.

Due to the geometric limitation and the data link limitation from the lunar far side to the Earth, two ultra-violet optical payloads have been removed from the lander. The saved installing space, launch mass, and power consuming of the lander makes a unique chance for testing some advanced payload techniques of the science from the Moon. Very low frequency

(of 100KHz~40MHz) radio astronomical payload becomes one of the leading choices.

However, due to the absorption by the Earth's ionosphere and hampered by the man-made low frequency signals (RFI), the radio sky below ~15 MHz cannot be viewed from earth-based facilities. In fact, up to date the range from several kHz to 15-30 MHz remains the least explored electromagnetic frequency range and is expected to conceal many scientific discoveries. Hence, the future advent in radio astronomy is expected by the realization of low-frequency radio space-based facilities to open up this frequency domain for astronomical exploration.

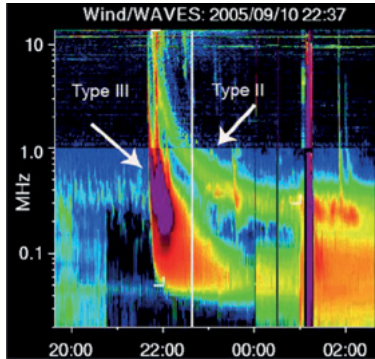


Fig.2. Type II and III solar burst measured by the Wind/WAVES instrument (credit: NASA)

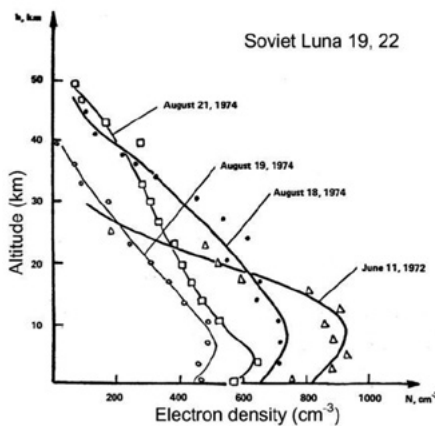


Fig.3. Ionospheric profile of the Moon by Luna 19, 22 (credit: Vyshlov, 1976)

In Chang'E-4 mission, considering EMC control not being carefully designed for the lander platform, and considering that a long-time working low frequency GPR on board the rover will give serious effect to HF band, the mission team has less chance of using the radio payload to detect the sky background for cosmological observation. During the 6 months nominal mission of the lander, the low frequency payload will focus on the solar burst so as to follow CMEs out to 1 AU, and will study the possible lunar ionosphere simultaneously with the solar activity [2]. The lunar ionosphere was 1<sup>st</sup> reported by Luna missions [3]. Also below 2MHz, the payload will monitor the possible Jupiter burst, which may be used to explain the planetary radio burst in other solar planetary system.

## EARTH-MOON VLBI

Many limitations of nature or artificial are blocking the interferometric observation between the lander and the Earth ground, as well as between the lander and the relay satellite, where a joint Dutch and Chinese low frequency receiver installed. The nature limitations include: (1) not easy to find a compact HF radio source in the space; (2) HF signal from radio source to the receiver(s) may be totally scattered or blown away by the interplanetary plasma or by the solar wind [4]. The artificial limitations include: (1) range and range rate link between lander-relay satellite-ground station has not been required and designed from very beginning; (2) only the optical image match method will be

applied to find the position of lander in the lunar coordinate frame with large systematic biases; (3) OCXO of payload with enough stability and perfect time synchronization to UT1 has least chance; (4) only up to ~90Kbps low data rate link downlink to the Earth.

Mission team are trying the best to solve above limitations, so as to find a route to test the interferometric observatory between the lander and other possible low frequency unites. Among them, the most important ones are developing a time synchronization method among the lander, a relay satellite and the Earth ground UT1, and a 4-way range & range rate link between lander-relay satellite and the ground tracking station. Also, several kinds of OCXO of space qualified or military qualified have been selected. The Allen deviation analysis of a best stability USO is shown in Figure 4. Mission team are still working on the choice of OCXO now.

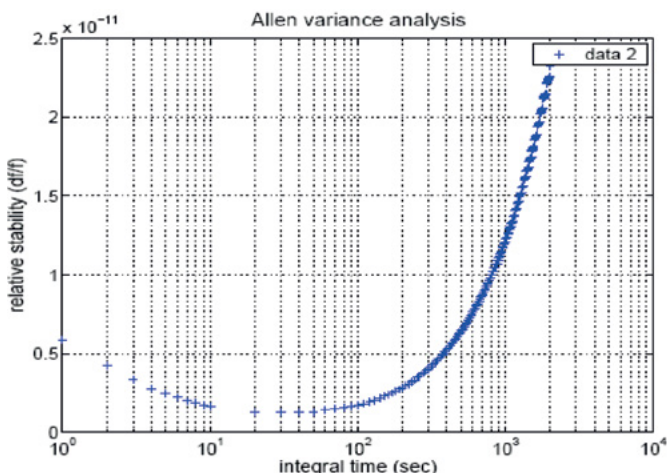


**Fig.4** The Allen variance analysis for a selected space qualified ultra-stable oscillator.

Additionally, with the possible 4-way link, lander positioning and POD of relay satellite can be done at the same time. After that, with the relay communication link, a reasonable time synchronization can be carried out.

The payload may using the lander bus information and tag two layers time signal on the recording data, one from the lander and another from the payload OCXO time counter. A short period linear model of time drift between them will be retrieved for correlation analysis.

Jupiter may be a reasonable candidate compact radio source at HF band. However, even after above solutions being applied in the mission development, there will still be some large blocks for space VLBI. We will use the payload as a pathfinder radio observatory, to test and to find the new techniques for the future special designed lunar far side low frequency mission.

## ACKNOWLEDGEMENT

This study is supported by a NSFC grant (No. 41590851), by the National Key Basic Research and Development Plan (Grant No. 2015CB857101), and by the State Key Laboratory of Astronautic Dynamics and by Chinese Chang'E-4 exploration lunar project.

## REFERENCES:

- [1]Zhang M..(2014) Ph.D. Thesis,
- [2]Wang M. et al., (2017) this meeting.
- [3]Vyshlov A. S.(1976) Spacecraft, Space Res., 16, 945-949.
- [4 Barrow C.H. et al. (1999) A&Ap. 344, 1001-1013.

# COMPILING THE NAVIGATIONAL 3D MODEL FOR PROSPECTIVE LUNAR BASE AREA

M.A. Zakharova<sup>1</sup>, E.N. Slyuta<sup>1</sup>

<sup>1</sup>*Vernadsky Institute, Kosygin str., 19, 119991, Moscow, Russia, mari.al.zakharova@gmail.com*

## KEYWORDS:

Moon, Lunar Base, 3D modelling, DEM, LOLA, LROC

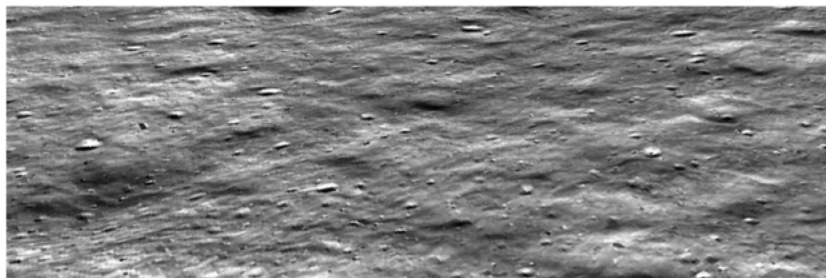
## INTRODUCTION:

The colonization of the Moon remains one of the primary targets of Space Agencies all over the world. We have chosen the area located at the South Pole of the Moon for prospective placement of Russian Lunar Base. We analyzed several base placement factors including solar radiation intensity, elevations and relief, temperature differences and the possibility of having direct radio communication with the Earth. Then we have created a 3-dimensional multiscale navigation model which is supposed to be used while landing to the site.

## 3D NAVIGATIONAL MODEL:

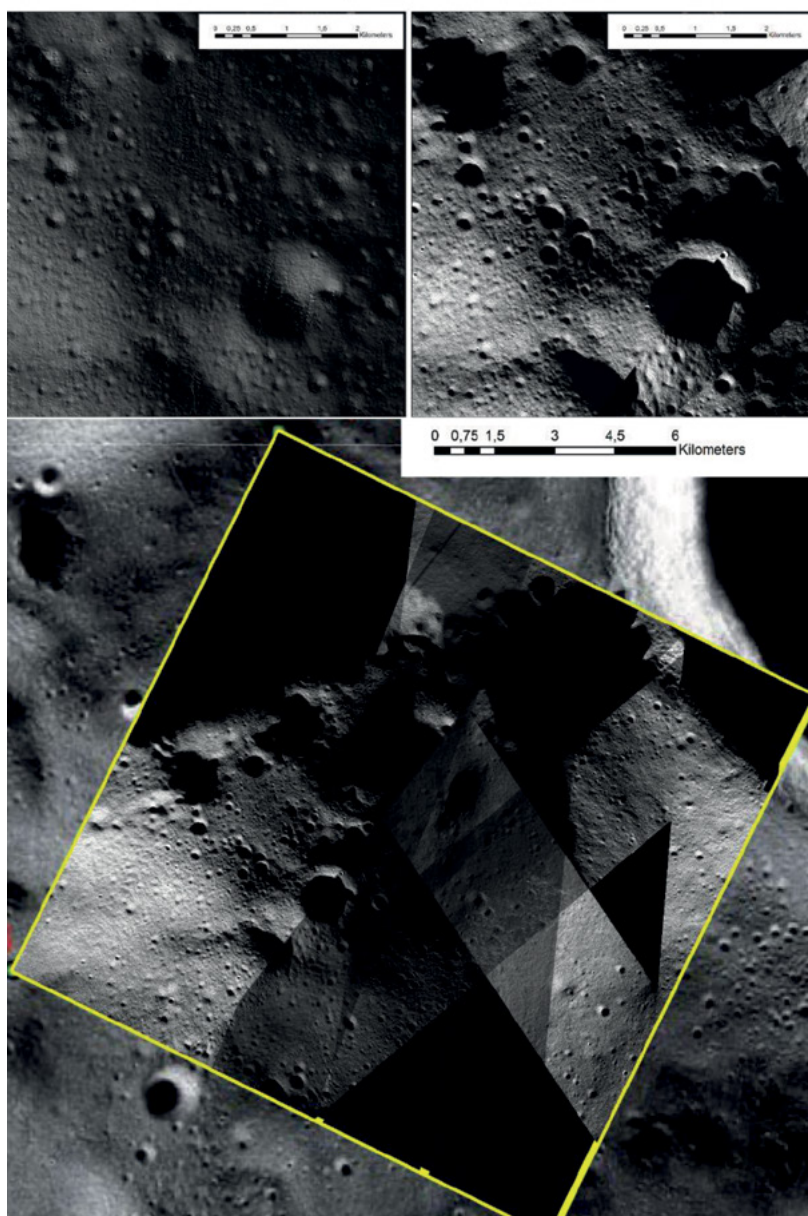
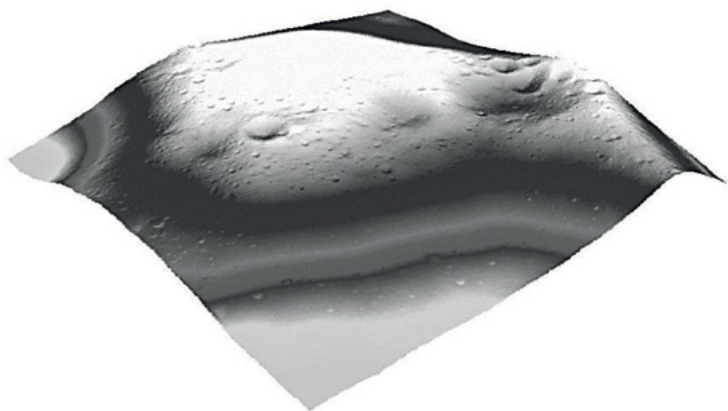
The navigational model consists of two scale levels. The first one includes LRO LOLA Elevation Model with resolution 118m [1] and LRO LROC-WAC Global Mosaic with resolution 100m [2]. It's designed to simulate approach to the Moon. The second scale level has the 1-meter resolution and was designed to simulate the landing process and rover routes at the lunar base area. At the beginning, we planned to obtain the high-resolution model using stereophotogrammetric processing NAC images at ISIS and ASP. Then we figured out that it was impossible with our processing method because of inappropriate convergence angles of NAC images, which were too small for good resulting DEMs. Afterward, we decided to use the DEM obtained by Rosiek M.R. et al [5] and to combine it with LOLA measurements. This kind of decision helped us to reduce the LOLA and NAC DEMs local distortions caused by qualities of the NAC LROC and LOLA shooting. Also, we have designed the mosaics of 14 NAC images using ISIS processing. All Images were selected so that the maximum possible area was illuminated by sunlight. The final DEM and NAC mosaics with 1-meter spatial resolution combined together allow us to simulate the real lunar surface at the prospective lunar base area. We also made the comparison of the final DEM hillshade and NAC images to check the quality of processed DEM.

## RESULTS:



## REFERENCES:

- [1] LRO LOLA Elevation Model 118m (LDEM GDR) [https://astrogeology.usgs.gov/search/details/Moon/LRO/LOLA/Lunar\\_LRO\\_LOLA\\_Global\\_LDEM\\_118m\\_Mar2014/cub](https://astrogeology.usgs.gov/search/details/Moon/LRO/LOLA/Lunar_LRO_LOLA_Global_LDEM_118m_Mar2014/cub) // LOLA Science Team 11 March 2014 Goddard Space Flight Center USGS
- [2] LRO LROC-WAC Global Mosaic 100m June2013 [https://astrogeology.usgs.gov/search/details/Moon/LRO/LROC\\_WAC/Lunar\\_LRO\\_LROC-WAC\\_Mosaic\\_global\\_100m\\_June2013/cub](https://astrogeology.usgs.gov/search/details/Moon/LRO/LROC_WAC/Lunar_LRO_LROC-WAC_Mosaic_global_100m_June2013/cub) // Arizona State University LROC Team Arizona State University USGS
- [3] USGS ISIS – Integrated Software for Imagers and Spectrometers, 2009. <http://isis.astrogeology.usgs.gov>



- [4] Moratto, Z. M., M. J. Broxton, R. A. Beyer, M. Lundy, and K. Husmann. 2010. Ames Stereo Pipeline, NASA's Open Source Automated Stereogrammetry Software. // Lunar and Planetary Science Conference 41, abstract #2364. [ADS Abstract].
- [5] Broxton, M. J. and L. J. Edwards. 2008. The Ames Stereo Pipeline: Automated 3D Surface Reconstruction from Orbital Imagery. // Lunar and Planetary Science Conference 39, abstract #2419. [ADS Abstract].
- [6] Rosiek M.R. USGS Verification and Validation Report Lunar South Pole Digital Elevation Model // Program-NNH08ZDA008C Scientific and Exploration Potential of the Lunar Poles, 2013.

# RADIO SCIENCE EXPERIMENTS FOR MARTIAN AND LUNAR MISSIONS

A.S. Kosov<sup>1</sup>, V.D. Gromov<sup>1</sup>, D.P. Skulachev<sup>1</sup>, V.N. Nazarov<sup>1</sup>,  
V.V. Korogod<sup>1</sup>, J. Ping<sup>2</sup>, V. Dehant<sup>3</sup>, S. Le Maistre<sup>3</sup>, O. Karatekin<sup>3</sup>,  
D. Firre<sup>4</sup>, A.V. Gusev<sup>5</sup>, V.G. Grachev<sup>6</sup>

<sup>1</sup>IKI RAS, 84/32 Profsovnaya, Moscow, Russia, 117997.  
akosov@iki.rssi.ru;

<sup>2</sup>National Astronomical Observatories, Chinese Academy of Sciences, 20A Datun Road, Chaoyang District, Beijing 100012, China;

<sup>3</sup>Royal Observatory of Belgium, Avenue Circulaire 3, B-1180 Brussels, Belgium;

<sup>4</sup>European Space Agency, European Space Operations Centre, ESA/ESOC, Robert-Bosch-Str.5, 64293 DARMSTADT, Germany;

<sup>5</sup>Kazan University, Kazan, Russia;

<sup>6</sup>OKB MEI, 14, Krasnokazarmenaya, Moscow, Russia, 111250

## KEYWORDS:

Radio science, Doppler, Moon, Mars, Interior structure, Atmosphere, Core properties.

## INTRODUCTION:

The radio-science (RS) experiments are widely used for most space missions. They exploit existing telecommunication systems of space vehicles and ground-based space communication networks for extremely high accuracy ranging and Doppler measurements. These data have applications for exact orbit parameter determinations and for investigations of gravitational field, interior and atmosphere of solar system planets and their satellites.

A progress in precision of RS-measurements is possible by use of coherent transponders in on-board telecommunication systems, an by simultaneous involvement of maximum number of space vehicles (orbiters and landers) and ground-based stations. The radio beacon instrument [1-3] manufactured in IKI for Luna-Resource and Luna-Glob space missions includes the coherent transponder for Lunar landers. An extension of number of RS-active landers on the Moon is planned by cooperation with Chang'E – 6/7/8 missions [4-5].

3D RS-ranging accuracy is tied with number and distance between ground-based antennas. It needs therefore a global cooperation. For Lunar [4-5] and Martian [6-8] RS-investigations the signals will be generated and received by Earth-based giant antennas belonging either to the NASA deep space network (DSN), the ESA tracking network (at low Earth-Mars distances), and the Russian ground stations network.

## MOON:

RS-experiments with Luna's Radio Beacons, for L-R-1 and future Chang'E – 6/7/8 missions for a lunar geophysical and dynamical exploration. Chinese Academy of Sciences suggest a mission with 1-2 landers at the near side or rim area of the Moon, of >2000km separated away from each other and from Luna-Glob/Resource mission. The experiment will uncover how a rocky body forms and evolves to become a planet by studying the size, thickness, density

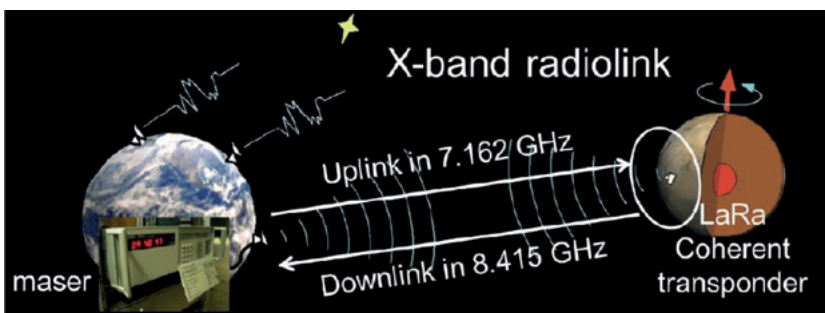


Fig. 2.



and overall structure of the Moon's core, mantle and crust, as well as the rate at which heat escapes from the lunar interior.

- The mission will conduct five investigations on and below the surface of the Moon to uncover the evolution history for solid bodies of the solar system:
- Determine the size, composition, physical state (liquid/solid) of the lunar core;
- Determine the thickness and structure of the lunar crust;
- Determine the composition and structure of the lunar mantle;
- Determine the thermal state of lunar interior;
- Measure the magnitude, rate and geographical distribution of lunar internal seismic activity.

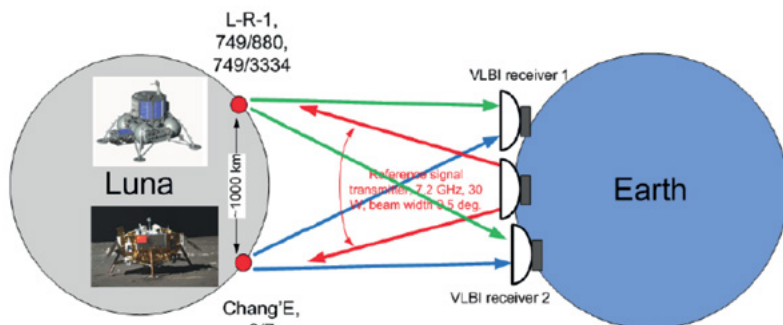


Fig. 1.

## MARS:

The ExoMars Lander RS-experiment (LaRa) is designed to obtain coherent two-way Doppler measurements from the radio link between the lander and the Earth over at least one Martian year. The instrument lifetime is thus almost twice the one Earth year of nominal mission duration. The LaRa instrument consists of a coherent transponder with up- and downlinks at X-band radio frequencies. The Doppler measurements will be used to observe the orientation and rotation of Mars in space (precession, nutations, and length-of-day variations), as well as polar motion. The ultimate objective is to obtain information/constraints on the Martian interior, and on the sublimation/condensation cycle of atmospheric CO<sub>2</sub>. Rotational variations will allow us to constrain the moment of inertia of the entire planet, including its mantle and core, the moment of inertia of the core, and seasonal mass transfer between the atmosphere and the ice caps.

## GROUND SEGMENT:

Ground Segment (GS) is extremely important part of RS measurements. Figure 1 shows GS for Luna RS experiments. Russian antennas (VLBI network Quasar) and Chinese antennas would be used as GS for Luna RS experiments. Mars investigation needs larger antennas because of additional 60 dB attenuation due to larger distance. Figure 2 shows RS experiments planned in "ExoMars" international project with LaRa instrument.

GS would use big Russian antennas: "Bear Lakes" – 64 m; "Kalyazin" – 64 m; "Ussuriysk" – 70 m, "Evpatoria" – 70 m. Also the Russian Complex for Receiving Scientific Information (RKPNI) would be used for RS experiments with LaRa. The RKPNI includes two antennas: "Bear Lakes" and "Kalyazin"; and has the needed infrastructure: Up-link and Down-link facilities, processors for signal treatment to support RS experiments with LaRa.

## REFERENCES:

- [1] Kosov A. S. New features of radio science experiments in Russian "Luna-Glob" and "Luna-Resource" programs // The Sixth Moscow Solar System Symposium 6M-S<sup>3</sup>. Moscow. Russia. 2015. P. 201-203 (6MS3-PS-15).
- [2] Gromov V. D., Kosov A. S. The objectives of the radioscience experiment in Luna-Resource and Luna-Glob space projects // The Sixth Moscow Solar System Symposium 6M-S<sup>3</sup>. Moscow. Russia. 2015. P. 43-44 (6MS3-MN-20).
- [3] Gromov V. D., Kosov A. S. The ranging accuracy of the radioscience experiment with the radio-beacon transponder in comparison with laser ranging // The Seventh Moscow Solar System Symposium 7M-S<sup>3</sup>. Moscow. Russia. 2016. P. 278 (7MS3PS65).
- [4] Gusev A., Hanada H., Kosov A., Ping J., Titov O. Dynamics of the inner solid and outer liquid cores of the moon for ChangE-4/5, Luna-25/26, ILOM projects // The Sixth

Moscow Solar System Symposium 6M-S<sup>3</sup>. Moscow, Russia. 2015. P. 35 (6MS3MN17).

[5] Gusev A., Hanada H., Kosov A., Meng Z., Ping J., Titov O., Vasilyev M.

Tidal-librational dissipative dynamics of the Moon and radio/laser beacons

VLBI/LRR/LLR technologies for ChangE-5/6, Luna-25/26/27, ILOM missions // The Seventh Moscow Solar System Symposium 7M-S<sup>3</sup>. Moscow, Russia. 2016. P. 61 (7MS3-MN-18).

[6] Dehant V. et al. Future Mars geophysical observatories for understanding its internal structure, rotation, and evolution // Planetary and Space Science. 2012. V. 68. P. 123-145.

[7] Rivoldini A., Van Hoolst T., Verhoeven O., Mocquet A., Dehant V. Geodesy constraints on the interior structure and composition of Mars // Icarus. 2011. V. 213. P. 451-472.

[8] Le Maistre S., Rosenblatt P., Rivoldini A., Dehant V., Marty J.C., and Karatekin Ö. Lander Radio science experiment with a direct link between Mars and the Earth // Planet. Space Sci. 2012. V. 68(1), P. 105-122, DOI: 10.1016/j.pss.2011.12.020.

# FUNCTIONAL TESTS OF ARIES-L INSTRUMENT

D.A. Moiseenko<sup>1</sup>, O.L. Vaisberg<sup>1</sup>, R.N. Zhuravlev<sup>1</sup>, S.D. Shuvalov<sup>1</sup>,  
A.Yu. Shestakov<sup>1</sup>, P.P. Moiseev<sup>2</sup>, M.V. Mitjurin<sup>2</sup>, E.I. Rodkin<sup>2</sup>,  
V.V. Letunovsky<sup>2</sup>, I.I. Nichushkin<sup>2</sup>, A.D. Vasiliev<sup>2</sup>

<sup>1</sup>Space Research Institute of the Russian Academy of Sciences (IKI),  
modaldi@iki.rssi.ru;

<sup>2</sup>Astron Electronics, Orel, Russia, info@astronel.ru

## KEYWORDS:

Plasma instrument, space plasma diagnostics, energy-mass analyzer, mass-spectrometry, Moon, Secondary Ion Mass Spectrometry .

## INTRODUCTION:

Study of lunar regolith is an important part of investigation of origin, evolution, and properties of the Moon. The purpose of experiment is investigation of solar wind interaction with the surface of the Moon, desorption of surface layer, and composition of surface layer. Secondary Ion Mass Spectrometry is common methods of analysis solid bodies. Experiment on the Moon allows one to use the solar wind flux as primary ion beam.

Panoramic ions and neutrals analyzer ARIES-L is an energy-mass spectrometer with field-of-view  $\sim 2\pi$ . Scheme of the ARIES-L electronic optics and ARIES-L qualification model is presented in Figure 1. Wide viewing angle allows this instrument to measure simultaneously the solar wind flux and characteristics of secondary ion flux sputtered from lunar regolith. Instrument also includes converter of neutral atoms located within the field of view of instrument. Secondary neutrals sputtered by the solar wind are ionized on the surface of converter and are measured by the same ion energy-mass analyzer. Secondary goal of experiment is the study of solar wind interaction with Earth's magnetosphere and magnetotail.

We are presenting results of functional tests and calibrations of qualification model ARIES-L instrument for LUNA-Glob mission. Functional tests of the instrument includes energy range and energy resolution tests, estimations of angular resolution and field of view, mass resolution test for time-of-flight scheme.

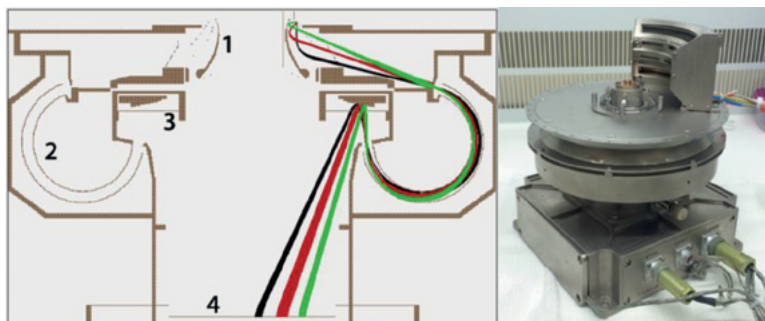


Fig. 1. Scheme of the ARIES-L electronic optics: 1 – mirror M1 with gate; 2 – electrostatic analyzer; 3 – mirror M2; 4 – position-sensitive MCP-detector.

# MARS 2020 RADIATION AND DUST SENSOR TECHNICAL OVERVIEW

V. Apéstigue<sup>1,5</sup>, I. Arruego<sup>2</sup>, J. Martínez<sup>1</sup>, J.J. Jiménez<sup>2</sup>, J. Rivas<sup>2</sup>, M. González-Guerrero<sup>1</sup>, F.J. Álvarez<sup>2</sup>, J. Azcue<sup>2</sup>, A. Martín-Ortega<sup>1</sup>, J.R. de Mingo<sup>2</sup>, A. Gonzalo<sup>2</sup>, B. Martín<sup>2</sup>, N. Andrés<sup>1</sup>, L. Bastide<sup>1</sup>, A. Carretero<sup>2</sup>, I. Martín<sup>2</sup>, M.A. Alcacera<sup>2</sup>, J. Manzano<sup>2</sup>, S. Aparicio<sup>2</sup>, R. López Heredero<sup>2</sup>, M. T. Álvarez<sup>2</sup>, P. Manzano<sup>2</sup>, J. Boland<sup>4</sup>, R. Urqui<sup>1</sup>, J.A. Rodríguez Manfredi<sup>2,3</sup>

<sup>1</sup>ISDEFE, as external contractor at INTA

<sup>2</sup>INTA

<sup>3</sup>CAB

<sup>4</sup>JPL

<sup>5</sup>Universidad Politécnica de Madrid

## KEYWORDS:

Mars 2020. MEDA. Mars. Dust. Atmosphere.

## INTRODUCTION:

MEDA (Mars Environmental Dynamics Analyzer) is a Spanish scientific contribution to the MARS2020 rover. The Radiation and Dust Sensor, here and after RDS [6], is one of the instruments included in this payload and it will provide the characterization of the Mars dust: opacity, size and morphology, as well as other interesting atmospheric data.

## BACKGROUND:

The RDS includes two different sensors that share the same structure but have totally independent electrical interfaces:

## RDS DISCRETE PHOTO-DETECTORS (RDS-DP).

This sensor is based on a set of photo-detectors, with different wavelength and oriented to different angles, to be used as a radiometer. This design takes its heritage from previous designs as MetSiS [2], DREAMS-SIS [1] and REMS-UV [3]

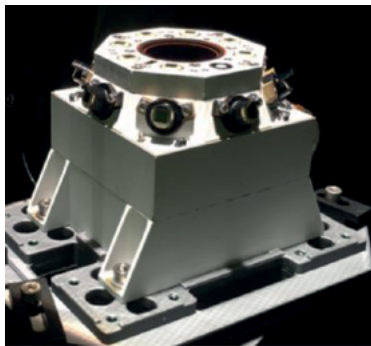


Fig. 1. MEDA RDS Qualification Model

## RDS SKYCAM.

It is based on the MERs [4] and MSL [5] engineering cameras that use the same hardware with a new lens set, designed to perform observations of the Sun and the brightness of the sky as a function of the observation angle and dust load in the atmosphere.

## TECHNOLOGICAL VALIDATION CAMPAIGN:

To manufacture a payload to be able to survive to a long-duration mission on the Martian surface environment, special tests have to be carried-out. The most critical parameter in the design is the extreme thermal cycling to which the hardware will be exposed during the mission life [-130°C to +40°C]. Therefore, a long time validation test was performed to all the technologies, materials and integration processes previously selected, to design the RDS.

## RDS TECHNICAL DESIGN:

Once the building blocks have been validated and tested, a complex phase of design of the instrument started. The major problems were the weight and size of the instrument taking into account the camera was a sensor to use "as is", at least the major internal parts. Hence, the RDS-DP was grown all around the camera optimizing the use of the available volume and its functionality.

This optimization process has permitted to design two independent sensors, in one hand a 1024x1024 camera with fish-eye lens and in the other hand, a 17 photo-detector radiometer sensor that contains a 16-bits ADC, memory and a FPGA that permits to operate it digitally (RS-422 interface with master-slave protocol).

## RDS QUALIFICATION CAMPAIGN:

The model philosophy of the RDS is the classical one, with several models manufactured with different aims: Structural Model (SM) to ensure in an early stage that the mechanical design was compatible with the qualification campaign, a Thermal Model (TM) to correlate the thermal analysis with a representative model, the Electrical Model (EM) to test electrical I/F, Qualification Model (QM) to validate the design under extreme mission conditions and the Flight Model and Spare for the final rover assembly.

## CONCLUSION:

RDS is a complex instrument to be part of the MEDA payload of Mars2020 rover. The design key-points, development status and qualification issues will be presented.

## REFERENCES:

- I. Arruego, V. Apéstigue, J. Jiménez-Martín, J. Martínez-Oter, F.J. Álvarez- Ríos, M. González-Guerrero, J. Rivas, J. Azcue, I. Martín, D. Toledo, L. Gómez, M. Jiménez-Michavila, M. Yela. DREAMS-SIS: The solar Irradiance Sensor on-board the ExoMars 2016 lander // *Advances in Space Research*. 2017. V. 60. No.1, P. 03-120.
- H. Guerrero. Development of miniaturized instrumentation for Planetary Exploration and its application to the Mars MetNet Precursor Mission // *European Geosciences Union General Assembly*, 2010.
- María-Paz Zorzano, Francisco Javier Martín-Torres, Rafael Navarro-Gonzalez, Javier Martín-Soler, Javier Gómez-Elvira, REMS Ultraviolet Sensor: First UV measurements from the Martian Surface. // *European Geosciences Union General Assembly*, 2013.
- J. N. Maki , J. F. Bell III, K. E. Herkenhoff, S. W. Squyres, A. Kiely, M. Klimesh, M. Schwochert, T. Litwin, R. Willson, A. Johnson, M. Maimone, E. Baumgartner, A. Collins, M. Wadsworth, S. T. Elliot, A. Dingizian, D. Brown, E. C. Hagerott, L. Scherr, R. Deen, D. Alexander, and J. Lorre, Mars Exploration Rover Engineering Cameras // *Journal of Geophysical Research*. 2003. V. 108, No. E12, 807.
- J. Maki, D. Thiessen, A. Pourangi, P. Kobzeff, T. Litwin, L. Scherr, S. Elliott A. Dingizian, M. Maimone. The Mars Science Laboratory Engineering Cameras // *Space Science Review*. 2012. No 170. P. 77-93.
- V. Apéstigue, I. Arruego, J. Martínez, J.J. Jiménez, J. Rivas, M. González, J. Álvarez, J. Azcue, A. Martín-Ortega, J.R. de Mingo, M. T. Álvarez, L. Bastide, A. Carretero, A. Santiago, I. Martín, B. Martín, M.A. Alcacera, J. Manzano, T. Belenger, R. López, D. Escribano, P. Manzano, J. Boland, E. Cordoba, A. Sánchez-Lavega, S. Pérez, A. Sainz López, M. Lemmon, M. Smith, C. E. Newman, J. Gómez Elvira, N. Bridges, P. Conrad, M. de la Torre Juárez, R. Urqui, J.A. Rodríguez Manfredi. Radiation and Dust Sensor for MARS2020: technical design and development status overview // *EPSC2015*.

# LUNAR CAVING: USAGE AND EXPLORATION

R.R. Chau<sup>1</sup>, A.A. Mardon<sup>2</sup>

<sup>1</sup>*Antarctic Institution of Canada, 12y4jv@gmail.com;*

<sup>2</sup>*Antarctic Institution of Canada, aamardon@yahoo.ca*

## KEYWORDS:

Rilles, lunar caves, habitation

## INTRODUCTION:

With what little information we have about the surface of the moon, there is very little documentation detailing much about the surface of the moon apart from images we obtain from satellites. Lunar caves are more of a prediction than actual knowledge not because of how much we know but how little we know. However, there have been few predictions of the existence of lunar lava tubes and caves stemming from pictures taken by various satellites. This includes rilles on the surface as well as what is predicted to be a lava tube skylight. One major prediction of the formation of rilles is the flowing of a liquid, most likely lava from a volcano or other source since there is no evidence of other liquids. Flowing liquid erosion also accounts for the fact that many rilles have walls that run parallel as opposed to a more erratic shape [1]. Another piece of evidence for lunar caves is the picture taken by SELENE Terrain Camera. It shows a hole on the surface of the moon that is unlike many of the craters that dot the surface of the moon [2]. Whereas many craters on the moon show definite illumination on both sides of the depression, the photograph of the skylight only has half of the circumference illuminated suggesting that there is a possibility that this depression has more depth.

These caves could be used as places for human habitation, supply storage, emergency shelters, as any infrastructure that is capable of withstanding radiation damage from the sun or physical bombardment is worth investigating. These structures can aid in the safety and preservation of future inhabitants if utilized properly.

## REFERENCES:

- [1] Masursky H., Colton G.W., El-baz F. Apollo over the moon: A View From Orbit // NASA SP-362. 1978. [Retrieved July 9, 2017] <https://history.nasa.gov/SP-362/contents.htm>
- [2] Haruyama J., Hioki K., Shirao M., Morota T., Hiesinger H., Bogert C.H., Miyamoto H., Iwasaki A., Yokota Y., Ohtake M., Matsunaga T., Hara S., Nakanotani S., Pieters C.M. Possible lunar lava tube skylight observed by SELENE cameras // *Geophysical Research Letters*. 2009. V. 36. DOI: 10.1029/2009GL040635

# METHOD AND LASER ABLATION MASS-SPECTROMETER FOR THE SEARCH OF EVIDENCE OF LIFE FROM THE EUROPA LANDER

K.A. Luchnikov<sup>1</sup>, G.G. Managadze<sup>1</sup>, W.B. Brinckerhoff<sup>2</sup>, P. Wurz<sup>3</sup>,  
M. Tulej<sup>3</sup>, A.E. Chumikov<sup>1</sup>, V.S. Cheptsov<sup>1,4</sup>

<sup>1</sup>Space Research Institute of the Russian Academy of Sciences (IKI),  
84/32 Profsoyuznaya Str, Moscow, Russian Federation, 117997;

<sup>2</sup>NASA Goddard Space Flight Center, Greenbelt, MD 20771, USA;

<sup>3</sup>University of Bern, Sidlerstrasse 5, CH-3012, Bern, Switzerland;

<sup>4</sup>Lomonosov Moscow State University, Leninskie Gory, 1, Moscow, Russian Federation, 119991.

## KEYWORDS:

Astrobiology; Europa; Biomarkers; Elemental Analysis; Mass Spectrometry.

The main scientific goal of the Europa Lander is to search for evidence of life. The abundances of some inorganic compounds, and their combinations in certain ratios, could serve as a powerful biosignature, particularly if found in association with biogenic organic compounds [1]. We propose a new technique for the detection and identification of terrestrial type microorganisms by elemental composition analyses of Europa subsurface samples. We also describe the design of a laser ablation time-of-flight mass-spectrometer (LA-TOF-MS) accompanied by a simple sample preparation unit (SPU) to conduct these analyses.

This next-generation instrument is based on the heritage of the LASMA instrument developed for Phobos-Grunt, Luna-25 and Luna-27 missions – a LA-TOF-MS [2, 3]. It is able to perform various tasks in the study of sample elemental and isotopic composition, and structure. Combining both a method of laser ablation and of soft ionization, the device allows for study of both elemental and isotopic composition of samples as well as the mineralogical composition of the sample indirectly with the detection of oxides, salts and other compounds.

A laboratory prototype of the instrument based on the LASMA TOF-MS was used to detect the microbial biomass in ice samples and their solid residues via analysis of the elemental composition. Our method is based on the fact that the matrix structure of any terrestrial microorganisms contains about the same amount of elements H, N, C, O [4]. It was essential that the ratios of these elements in living organisms could be accurately reproduced. Of all the matrix elements, the content of N and C can be the most reliably reconstructed. The content of H and O heavily depends on the water content in the biomass, while the content of N and C is not affected. Moreover, due to the high concentration of these elements in terrestrial type organisms, they can be easily detected. In addition to the abundances of N and C we also chose as biomarkers the ratios P/S and Ca/K. It is very important to remember that these ratios do not change dramatically over time, and even fossils can exhibit certain stable values. Our approach is based on the selectivity of nutrient absorption by microbial cells from the environment. Previously, it was found that the ratios P/S and Ca/K inside microorganisms change over the life cycle and depend on the physiological state of the cells. Also, fossilized microorganisms can be distinguished from living microorganisms. The elemental microanalysis makes the detection of cells in a native mineral environment possible due to the selective accumulation of these elements by cells.

We have conducted numerous laboratory studies on cultures of microorganisms and polar permafrost samples as terrestrial analogs for martian polar soils while working on the proposal for ExoMars lander to confirm experimentally the possibility of biomass identification via the following biomarkers: P/S and Ca/K ratios, and C and N abundances. We emphasize that only the combination of these measurements will allow to discriminate microbial from purely geological samples [5, 6, 7]. This technique, currently aimed at the search and identification of microorganisms in icy samples from Europa subsurface, can also be applied to other samples like sediments and dust.

One of the advantages of the LA-TOF-MS is that it also enables assessment of sample compositional heterogeneity on a per-spot basis rather than measurements of the bulk sample. It is possible to perform both mapping across the

sample surface and depth profiling. Expected spatial resolution of mapping is  $30 \times 30 \mu\text{m}^2$  across the surface and  $1 \mu\text{m}$  in depth.

The huge experience in this field gained during last decades of joint work in our common team will allow us to solve this challenging task.

## REFERENCES:

- [1] Managadze, G.G., Managadze, N.G., Saralidze, G.Z., Chumikov, A.E., and Wurz P. Mass spectrometric measuring complex for the detection of the signs of life in the ice surface of Europa. // In Europa Lander workshop: science goals and experiments. 2009. Institute of Space Research, Moscow, pp. 51–53.
- [2] Managadze G.G. TOF mass-spectrometer. // Patent 1732396 (RF). Priority of invention: 1988. Registered: 1992. Published in: Russ. Bull. Inventions No. 17.
- [3] Managadze, G.G., Managadze, N.G. TOF mass spectrometer. // Patent 2096861 (RF). Priority of invention: 1994. Registered: 1997. Published in Russ. Bull. Inventions No. 32.
- [4] Managadze G.G. Plasma of meteorite impact and prehistory of life. // NY. Nova Science Publishers, Inc., 2013.
- [5] Managadze, G.G., Vorobyova E.A., Luchnikov K.A., Safronova A.A., Chumikov A.E., Managadze N.G. Method of detecting presence of microbial biomass of terrestrial type on space bodies. // Patent RU 2586778 C1. Priority of invention: 2015. Registered: 2016.
- [6] Luchnikov, K.; Managadze, G.; Chumikov, A.; Managadze, N.; Vorobyova, E.; Safronova, A. Mass-spectrometric method for signs of life search via analysis of the element composition of the supposed biomass extracted from regolith of Mars. // 40th COSPAR Scientific Assembly. 2014. Abstract B0.6-14-14.
- [7] Managadze G.G., Safronova A.A., Luchnikov K.A., Vorobyova E.A., Duxbury N.S., Wurz P., Managadze N.G., Chumikov A.E., and Khamizov R.Kh. (2017) A New Method and Mass-Spectrometric Instrument for Extraterrestrial Microbial Life Detection Using the Elemental Composition Analyses of Martian Regolith and Permafrost/Ice. // *Astrobiology*, 2017, 17(5): 448-458.



# MESOSCALE VORTEX CIRCULATIONS ON VENUS OBSERVED IN AKATSUKI IR2 IMAGES

S.S. Limaye<sup>1</sup>, T. Satoh<sup>2</sup>, J. Peralta<sup>2</sup>, T. Horinouch<sup>3</sup>, T. Imamura<sup>4</sup>

<sup>1</sup>University of Wisconsin, Madison, Wisconsin, USA;

<sup>2</sup>ISAS/JAXA, Sagamihara, Kanagawa, JAPAN

<sup>3</sup>Hokkaido University, Sapporo, Hokkaido, JAPAN

<sup>4</sup>University of Tokyo, Tokyo, JAPAN

## KEYWORDS:

Venus cyclone, anticyclone, mesoscale, circulation

## INTRODUCTION:

A vortex pair (“mushroom” feature) consisting of a cyclone and anti-cyclone, was first observed in nightside images from the IR2 camera [1] on Akatsuki orbiter [2] on April 15, 2016 at 1.74, 2.26 and 2.32  $\mu$  wavelengths in the northern hemisphere (Figure 1). Such vortex pairs were first detected on Earth when water vapor images became available from geosynchronous weather satellites[3]. A sequence of three images about two hours apart reveals the vortex circulation. The detection of such pairs on Venus raises questions about the forcing mechanisms for the formation on the slowly rotating planet with only the fast zonal winds providing vorticity generation.

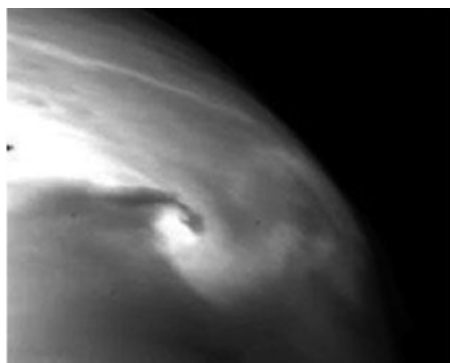


**Fig. 1.** The “mushroom” feature seen in this IR2 image on the night side of Venus is interpreted as a pair of cyclone and anticyclone circulations in the mid to lower cloud layer of Venus. Similar formations have been seen at other times and also were found in VIRTIS images of Venus from Venus Express.

## WHAT CAUSES THESE CIRCULATIONS ON A SLOWLY ROTATING PLANET?

The Coriolis force on Venus is low due to the very slow rotation rate of the planet, and the only vortex circulations observed so far on Venus are the global circulation vortices over each pole [4]. Surface topography and vertical shear of the zonal flow may be two contributing factors that lead to the development of the observed mesoscale circulations. However, what makes the circulations visible through opacity variations of the upper cloud are still unknown.

## REFERENCES:

1. Satoh, T., et al., Development and in-flight calibration of IR2: 2- $\mu$ m camera onboard Japan's Venus orbiter, Akatsuki. *Earth, Planets and Space*, 2016. **68**(1): p. 74.
2. Nakamura, M., et al., AKATSUKI returns to Venus. *Earth, Planets, and Space*, 2016. **68**.
3. Houghton, D.D. and V.E. Suomi, Information content of satellite images. *Bulletin of the American Meteorological Society*, 1978. **59**(12): p. 1614-1617.
4. Suomi, V.E. and S.S. Limaye, Venus: further evidence of vortex circulation. *Science*, 1978. **201**(4360): p. 1009-11.

# VENUS CLOUD PARAMETERS MODULATING THE 1.28- $\mu\text{m}$ NIGHTSIDE WINDOW EMISSION OBSERVED BY SPICAV IR

D.G. Evdokimova<sup>1</sup>, A.A. Fedorova<sup>1</sup>, D.A. Belyaev<sup>1</sup>, O.I. Korablev<sup>1</sup>, E. Marcq<sup>2</sup>

<sup>1</sup>Space Research Institute of the RAS (IKI), 84/32 Profsoyuznaya Str., Moscow 117997, Russia. evd.dar@yandex.ru

<sup>2</sup>LATMOS, CNRS/UVSQ/IPSL, Guyancourt, France

## KEYWORDS:

Venus, clouds, transparency windows, SPICAV IR, cloud model.

## INTRODUCTION:

Optically thick Venus clouds are consisted of concentrated sulfur acid aerosol and located at altitudes of 50-70 km. Three layers can be specified within the clouds according to sizes of prevailed aerosol particles [1]. The upper haze at altitudes above 70 km is consisted of sub-micron particles of mode 1 with radius of less than 0.4  $\mu\text{m}$ . The upper cloud layer (50-70 km) contains particles of mode 1 and 2. The mode 2 size is about 1  $\mu\text{m}$ . The biggest particles relating to mode 3 have radius value of 3-4  $\mu\text{m}$ . Modes 3 and 2 are prevailed in the middle (50-57 km) and lower (47-50 km) clouds. Mode 3 particles determine the opacity and bulk of the Venus cloud layer [1]. Clouds are the reason for the strong greenhouse effect and form the current Venus climate. Thus, cloud characteristic variations may cause changes in the entire atmospheric dynamic and composition. Moreover, there is a probability of both short and long term variations in the cloud layer [2, 3, 4].

## THE 1.28- $\mu\text{m}$ TRANSPARENCY WINDOW OBSERVED BY SPICAV IR:

Remote observations of clouds lower layer parameters are almost impossible due to its opacity. However, there are narrow IR spectral windows named "transparency windows" where IR emission formed in lower atmosphere is able to escape to space [5]. These windows are located between strong absorption bands of  $\text{CO}_2$ . The weak emission can be observed in the night atmosphere of Venus. The dataset of measurements of 1.28- $\mu\text{m}$  window emission forming at altitudes of 15-30 km is used in this work. Emission of the 1.28- $\mu\text{m}$  window is not sensitive to minor species composition in atmosphere but determined by scattering within the cloud layer. The major influence is exerted by the biggest particles of mode 3 concentrated in the deep clouds. However, oxygen airglow at 1.27  $\mu\text{m}$  producing in night atmosphere at 100 km is registered within 1.28- $\mu\text{m}$  window [6] as well. Thus, the spectral interval near maximum of window intensity is chosen in the way to eliminate the airglow emission line from consideration.

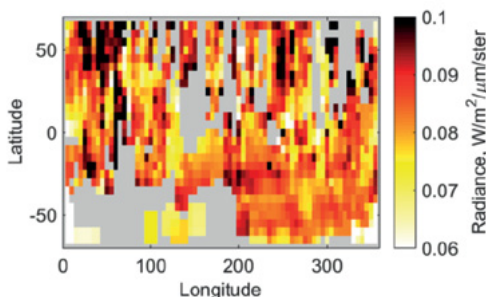


**Fig. 1.** Geographical distribution of maximum value of 1.28- $\mu\text{m}$  window intensity. Data is averaged within latitude-longitude cells of 5 degrees width each. Gray areas mean the lack of data.

The whole dataset of nadir observations performed by SPICAV IR instrument onboard Venus Express covered time range of 2006-2015. The maximum emission intensity value varied from 0.05 to 0.1  $\text{W}/\text{m}^2/\mu\text{m}/\text{ster}$  in this period. Moreover, the geographical distribution of values was not uniform: northern hemisphere values appeared to be higher than southern ones (Fig. 1).

## CLOUDS PARAMETERS VARYING THE 1.28- $\mu\text{m}$ TRANSPARENCY WINDOW EMISSION:

Direct modeling of the window aimed to distinguish the cloud parameters that were responsible for the strongest fluctuations of the emission. The synthetic spectrum is built according to multiply scattering radiative transfer model calculated by the SHDOMPP program realizing the spherical discrete ordinate [7] method for plane parallel atmospheres [8, 9, 11]. Atmospheric characters are from the VIRA database and the surface emissivity is equal to 95% here. The 75% solution of sulfur acid is taken for the aerosol composition. The optical depth, single scattering albedo, asymmetry parameter are calculated using Mi theory for the two models described in Bezaud et al., 2009 and 2011 [8, 9] and Haus et al., 2016 [10]. Sensitivity of the emission intensity to low extinction change within each 1-km wide layer was computed. The first model gave the most influential layer at the altitude of  $\sim 65$  km. The second one showed the emission might be more sensitive for layer of 50-55 km. The current difference between results prevents us from the certain conclusion which cloud layer plays the major role in modulation of 1.28- $\mu\text{m}$  window emission. The future improvement of cloud model should clarify more precisely the changes that occur in the lower clouds.

## ACKNOWLEDGEMENTS:

D.G. Evdokimova, A.A. Fedorova, D.A. Belyaev and O.I. Korablev acknowledge support from the RFFI #16-52-16011.

## REFERENCES:

- [1] Esposito L.W. et al. Chemistry of lower atmosphere and clouds. Venus II, The University of Arizona Press. 1997. P. 415–458.
- [2] McGouldrick K. et al. Quantification of middle and lower cloud variability and meso-scale dynamics from Venus Express/VIRTIS observations at 1.74  $\mu\text{m}$ . // *Icarus*. 2011. V. 217. P. 615-628.
- [3] McGouldrick K., Toon O.B. Investigation of possible causes of the holes in the condensational Venus cloud using a microphysical cloud model with a radiative dynamical feedback. // *Icarus*. 2007. V. 191. P. 1–24.
- [4] McGouldrick K., Toon O.B., 2008. Modeling the effects of shear on the evolution of the holes in the condensational clouds of Venus. *Icarus*, 196. 35–48.
- [5] Pollack J.B., et al. Near-infrared light from Venus' nightside: a spectroscopic analysis. // *Icarus*. 1993. V. 103. P. 1–42.
- [6] Crisp, D. et al. Ground-based near-infrared observations of the Venus nightside: 1.27- $\mu\text{m}$  O<sub>2</sub> (a $\Delta$ g) airglow from the upper atmosphere. // *J. Geophys. Res.* 1996. V. 101, E2. P. 4577-4594.
- [7] Evans, K. F. The spherical harmonic discrete ordinate method for three-dimensional atmospheric radiative transfer. // *J. Atmos. Sci.* 1998. V. 55. P. 429-446.
- [8] Bezaud B. et al. Water vapor abundance near the surface of Venus from Venus Express/VIRTIS observations. // *J. Geophys. Res.* 2009. V. 114. P. E00B39.
- [9] Bezaud B. et al. The 1.10- and 1.18- $\mu\text{m}$  nightside windows of Venus observed by SPICAV-IR aboard Venus Express. // *Icarus*. 2011. V. 216. P. 173-183.
- [10] Haus R. et al. Radiative energy balance of Venus based on improved models of the middle and lower atmosphere. // *Icarus*. 2016. V. 272. P. 178–205.
- [11] Fedorova et al. The CO<sub>2</sub> continuum absorption in the 1.10- and 1.18- $\mu\text{m}$  windows on Venus from Maxwell Montes transits by SPICAV IR onboard Venus Express. // *Planetary and Space Science*. 2014. V. 113-114. P. 66–77.

# GLORY ON THE UPPER CLOUD DECK OF VENUS AND IDENTIFICATION OF THE UNKNOWN UV ABSORBER

E.V. Petrova

Space Research Institute RAS, Profsoyuznaya 84/32, Moscow, 117997  
Russia; e-mail: [epetrova@iki.rssi.ru](mailto:epetrova@iki.rssi.ru)

## KEYWORDS:

Venus atmosphere, glory, UV absorber

## INTRODUCTION:

Photometric and polarimetric observations of Venus show that particles in the upper clouds of Venus form such an optical phenomenon near opposition as glory. The presence of glory itself poses stringent constraints on the properties of cloud particles: they are to be spherical, and the dominant size strongly governs the glory feature position. The VMC/VEx measurements at small phase angles allowed the radius  $R_{\text{eff}}$  and the refractive index  $m$  of cloud particles in the observed regions to be estimated [1,2]. In most cases, the obtained values of the refractive index turned out to be somewhat higher than those expected for the  $\text{H}_2\text{SO}_4$  solution. Such an effect can be produced by an admixture with a high refractive index, which seems quite natural, since small submicron particles that are ubiquitous in the Venus clouds and hazes can serve as condensation nuclei for  $\text{H}_2\text{SO}_4$  droplets. The radiative-transfer modeling showed that, to fit the VMC UV phase profiles, one should take into account the presence of small submicron particles in the clouds, some of which are absorbing in UV.

The nature of these submicron particles is not clear yet, and it likely varies with altitude. Among probable candidates with a high refractive index, ferric chloride and sulfur are worth mentioning. Since sulfur cannot be wetted by sulfuric acid [3], the microphysical models consider the sulfuric acid condensation on a surface fraction of a polysulfur particle, so that the actual particles would be made up of a polysulfur particle stuck to the side of the  $\text{H}_2\text{SO}_4$  droplet [4]. From the point of microphysics, such a scenario may successfully work; however, from the point of interpretation of observations of glory, it poses a problem, since the irregular surface of complex particles may break the conditions for producing glory [5]. At the same time, it has been recently shown that sulfur aerosol cannot be the unknown UV absorber, because its abundance is too low at the cloud tops, while the delivery of  $\text{FeCl}_3$  into the upper cloud layer and the production of  $\text{H}_2\text{SO}_4$  are just in proportion that is required to fit the observed UV albedo of Venus, and the small submicron and 1- $\mu\text{m}$  modes of particles fit this proportion as well [6,7]. The ferric chloride particles may serve as condensation nuclei for sulfuric acid, and the 1% concentration is close to that required to explain the blue absorption [8]. Moreover, the 1- $\mu\text{m}$  complex particles may be produced in coagulation of smaller droplets with cores and have several very small  $\text{FeCl}_3$  inclusions.

The purpose of this study is to check how small submicron particles (with a relatively high refractive index) stuck to  $\text{H}_2\text{SO}_4$  droplets or included into them may influence the phase profiles of such complex cloud particles at small phase angle characteristic to a glory feature.

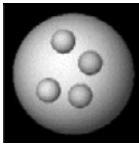
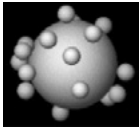
## MODELING:

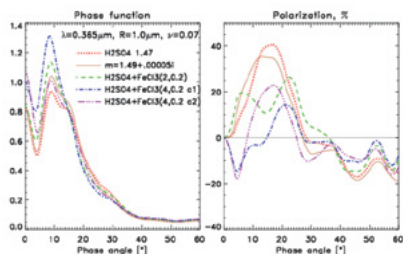
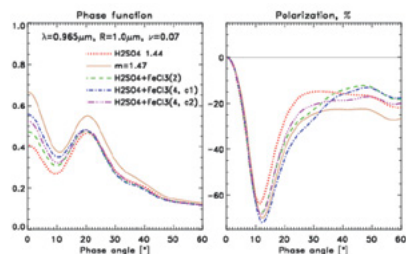
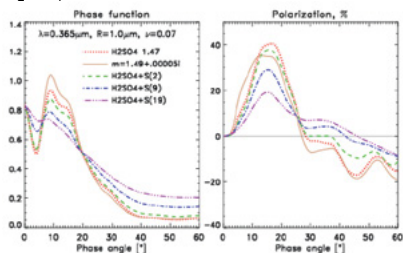
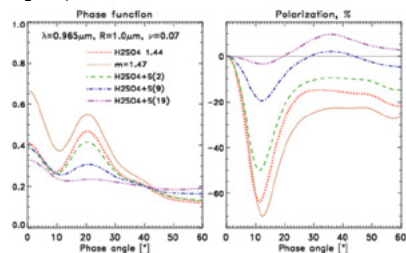
Though the Venus atmosphere is optically thick, the glory feature produced by single scattering of cloud particles survives in diffuse multiple scattering. Consequently, the influence of particles' heterogeneity on the glory feature can be studied by the single-scattering models. They were calculated with a multiple-sphere T-matrix code [9] for several cases of randomly oriented particles (see Table, where the examples of particles are also shown) at two VMC wavelengths  $\lambda$  (the effective variance of the size distribution is 0.07).

## RESULTS:

Below there are the phase dependences of intensity and polarization of light scattered once by  $\text{H}_2\text{SO}_4$  droplets with  $\text{FeCl}_3$  particles included (Fig.1) and sulfur particles stuck (Fig. 2). Only the backscattering domain is shown.

Table. Parameters of the complex particles tested

particle	$R_{\text{eff}}$ (number) $\lambda=0.365 \mu\text{m}$	Refractive index	
		$\lambda=0.965 \mu\text{m}$	
$\text{H}_2\text{SO}_4$ (host)	$1 \mu\text{m}$	$1.47 + 0.0i$	$1.44 + 0.0i$
$\text{FeCl}_3$ (inside)	 $0.2 \mu\text{m}$ (2, 4) $0.1 \mu\text{m}$ (4, 9)	$1.65 + 0.01i$	$1.60 + 0.0i$
Sulfur (stuck)	 $0.2 \mu\text{m}$ (2, 4, 9, 19)	$2.339 + 0.025i$	$1.95 + 0.0i$

Fig. 1a.  $\text{FeCl}_3$  particles are added into  $\text{H}_2\text{SO}_4$  droplets,  $\lambda=0.365 \mu\text{m}$ .Fig. 1b.  $\text{FeCl}_3$  particles are added into  $\text{H}_2\text{SO}_4$  droplets,  $\lambda=0.965 \mu\text{m}$ .Fig. 2a. Sulfur particles are stuck to  $\text{H}_2\text{SO}_4$  droplets,  $\lambda=0.365 \mu\text{m}$ .Fig. 2b. Sulfur particles are stuck to  $\text{H}_2\text{SO}_4$  droplets,  $\lambda=0.965 \mu\text{m}$ .

The phase functions for  $\text{H}_2\text{SO}_4$  droplets with  $0.1\text{-}\mu\text{m}$   $\text{FeCl}_3$  inclusions are not displayed here, since their effect has turned out to be very weak.

According to the recently developed ideas on the glory formation, glory is caused by interference of two surface waves, which are generated by rays entering the droplets at almost diametrically opposite points and suffering one internal reflection [5]. In this view, the more additional particles on the spherical surface of droplets, the less favorable conditions for interference of the surface waves; and this makes the glory feature less prominent down to smoothing. The presence of additional particles inside the droplets changes the propagation conditions for differently polarized components of light inside the particles, which destroys the glory pattern in polarization, if the inclusions are comparable to the wavelength in size; and the glory feature in intensity remains well developed. Note that the angular position of the glory maximum in intensity is not sensitive to the presence of admixtures (at least in the considered size range), while the glory minimum moves, as if the refractive index of the droplets increases.

## CONCLUSIONS:

The light-scattering simulations for complex spherical particles of sulfuric acid containing admixtures with a high refractive index help us to make a choice between the candidates to the so-called UV absorber in the Venus clouds. Now we may conclude that sulfur cannot be responsible for the contrasts

observed at  $\lambda=0.365 \mu\text{m}$ , since submicron sulfur particles, if stuck to  $\text{H}_2\text{SO}_4$  droplets, would smooth the glory feature, while this feature is practically always seen in the images of the upper clouds of Venus taken at small phase angles. At the same time, the presence of the other widely discussed UV absorber,  $\text{FeCl}_3$ , in  $\text{H}_2\text{SO}_4$  droplets poses no problem from the point of interpretation of observations of glory.

## REFERENCES:

- [1] Markiewicz W.J., Petrova E., Shalygina O., Almeida M., Titov D.V., Limaye S.S., Ignatiev N., Roatsch T., Matz K.D. Glory on Venus cloud tops and the unknown UV absorber // *Icarus*. 2014. V. 234. P. 200-203.
- [2] Petrova E.V., Shalygina O.S., Markiewicz W.J. The VMC/VEx photometry at small phase angles: Glory and the physical properties of particles in the upper cloud layer of Venus // *Planet. Space Sci.* 2015. V. 113-114. P. 120-134.
- [3] Young A.T. Venus cloud microphysics // *Icarus*. 1983. V. 56. P. 568-577.
- [4] Gao P., Zhang X., Crisp D., Bardeen C.G., Yung Y.L. Bimodal distribution of sulphuric acid aerosols in the upper haze of Venus // *Icarus*. 2014. V. 231. P. 83-98.
- [5] Laven P. How are glories formed? // *Appl. Opt.* 2005. V. 44. N. 27. P. 5675-5683.
- [6] Krasnopolsky V.A. Sulfur aerosol in the clouds of Venus // *Icarus*. 2016. V. 274. P. 33-36.
- [7] Krasnopolsky V.A. On the iron chloride aerosol in the clouds of Venus // *Icarus*. 2017. V. 286. P. 134-137.
- [8] Zasova L.V., Krasnopolsky V.A., Moroz V.I. Vertical distribution of  $\text{SO}_2$  in the upper cloud layer of Venus and origin of UV absorption // *Adv. Space Res.* 1981. V. 1. P. 13-16.
- [9] Mackowski D.W., Mishchenko M.I. A multiplesphere T-matrix Fortran code for use on parallel computer clusters // *JQSRT*. 2011. V. 112. N. 3. P. 2182-2192.

# RADIO OCCULTATION RETRIEVALS OF ZONAL WIND SPEED AT THE HIGH-LATITUDE ATMOSPHERE OF THE VENUS

V.N. Gubenko<sup>1</sup>, I.A. Kirillovich<sup>1</sup>, A.G. Pavelyev<sup>1</sup>

<sup>1</sup>*Kotel'nikov Institute of Radio Engineering and Electronics of the RAS, Vvedensky square 1, 141190 Fryazino, Moscow region, Russia, vngubenko@gmail.com*

## KEYWORDS:

Radio occultation, atmosphere of Venus, temperature profile, zonal wind speed, cyclostrophic balance.

## INTRODUCTION:

The available data indicate a zonal wind rotation of the Venus's atmosphere from East to West. The wind speed changes almost monotonically with altitude, reaching about 100 m/s at the level of the upper cloud layer. The cyclostrophic balance approximation and the results of temperature and pressure determination from the radio occultation (RO) data of the Pioneer Venus Orbiter were also used to determine the zonal wind profiles by [1, 2]. The zonal wind speed at altitudes from 40 to 80 km in the latitude range from 15° to 85° under the assumption of the Northern and Southern hemispheres symmetry was determined by [1]. The authors of this work indicated that the radio occultations used in their study had been carried out, in general, in the Southern hemisphere at low latitudes and in the Northern hemisphere at high latitudes. Nevertheless, they did not exclude the possibility of hemispheric asymmetry at high latitudes. In this connection, it is interesting to determine the zonal wind speeds for the Northern and Southern hemispheres, separately.

## PROCESSING AND ANALYSIS OF EXPERIMENTAL DATA:

For determining the zonal wind speed we used the cyclostrophic approximation balance and RO measurements at latitudes from 60° to 87° in 17 regions of the Southern hemisphere, and in 27 regions of the Northern hemisphere of Venus. These measurements were made during the period from October 1983 to September 1984. Orbits of the Venera-15 and -16 spacecraft were such that the entries into occultation took place in the Northern hemisphere and exits in the Southern one. Some details about the Venera-15 and -16 spacecraft investigations, the dates and location of RO measurements in latitude, longitude, solar zenith angle can be found in [3–6]. The aim of this work is to determine the zonal wind speed in the polar and near-polar regions of Venus at altitudes from 50 to 80 km from RO data of the Venera-15 and -16 spacecraft. To find the zonal wind speed, we used the altitude profiles of temperature and pressure obtained from the processing of RO data at a decimeter radio wavelength ( $\lambda = 32$  cm). The characteristic properties of the radio occultation technique and of the experimental data processing are described in [3, 6]. The result of the RO data processing are temperature  $T$  and pressure  $P$  altitude profiles, which give the values of these parameters at various altitudes in the interval from 40 to 90 km [3]. In the range of pressure variations corresponding to this altitude interval we marked 28 fixed "standard" pressure levels from 1098 to 5 mb.

The temperatures at these pressure levels were found by linear interpolation of temperatures nearest to the chosen fixed levels. The number of chosen levels allowed the retention of individual characteristics of the temperature profiles. Fig. 1 shows the temperature dependence on the latitude at four pressure levels (602, 181, 122 and 55 mb) in the Southern hemisphere. The temperature values obtained from RO data at the corresponding latitudes and pressures are shown by circles and squares in Fig. 1. The circles apply to the curves 1 and 3, the squares – to the curves 2 and 4. The curves describing the latitude-temperature dependence are the cubic polynomials fitted by the least squares technique to the experimental data. These least squares fits were used by us to obtain the latitude-temperature gradients. The quality of fitting is defined by the root mean square variance  $\sigma$  on every "standard" pressure level (representative values of  $\sigma$  are drawn as error bars for each curve in Fig. 1 and 2).

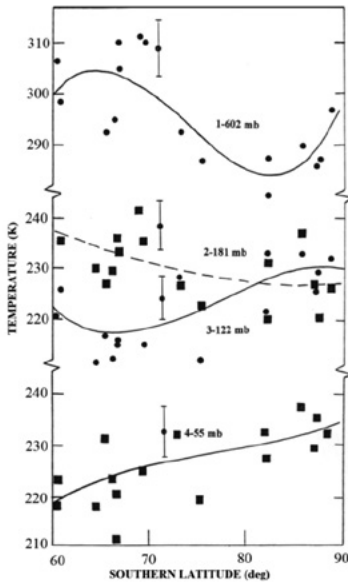


**Fig. 1.** Profiles of temperature on latitude at four pressure levels in the Southern hemisphere of Venus: 1–602 mb; 2–181 mb; 3–122 mb; 4–55 mb.

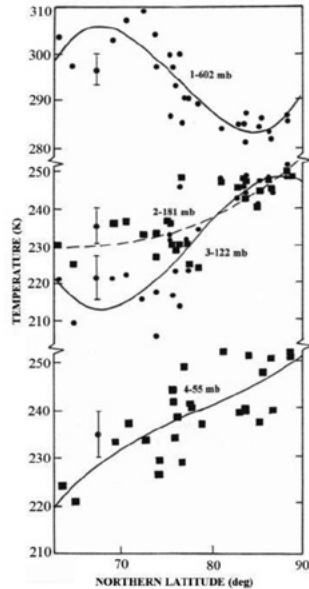


**Fig. 2.** Profiles of temperature on latitude at four pressure levels in the Northern hemisphere of Venus.

The fitted curves in Fig. 1 show the latitudinal dependence of the temperature at different pressure levels. The temperature decreases with increasing latitude at a pressure level 602 mb in the latitude interval from 66° to 82°. This trend is characteristic also for temperature-latitude dependence at lower pressure levels down to 180 mb. The transitional region lies within the pressure range of 180 to 120 mb, corresponding to the altitude interval from 61 to 63 km, where a change of the sign of temperature-latitude gradient occurs in the latitude interval from 66° to 82° as shown in Fig. 1 (curves 2 and 3). Small temperature contrasts between the polar and near-polar atmosphere are characteristic of the transitional region [3]. In the Southern hemisphere the temperature increases with increasing latitude at fixed pressure levels from 120 to 30 mb, which correspond to altitudes from 63 to 70 km. For determining the zonal wind speed in the Northern hemisphere, we use the temperature and pressure data obtained from radio occultations in 27 regions at latitudes greater than 60° [3]. The circles refer to curves 1 and 3, and squares to curves 2 and 4 in Fig. 2. The temperature decreases with increasing latitude at the level of 602 mb in the latitude interval from 69° to 84°. This trend continues at lower levels down to 220 mb. A change of sign of the latitude-temperature gradient at latitudes from 69° to 84° occurs in the pressure range from 220 to 180 mb. A transitional atmospheric region for which small values of the latitude-temperature gradient are characteristic, exists in this pressure range corresponding to the altitude interval from 60 to 61 km. Curve 2, corresponding to the upper boundary of this transitional region, illustrates this tendency. A temperature rise with increasing latitude (curves 3 and 4) is observed at pressure levels lower than 180 mb. By comparing the latitude profiles of the temperature in the Northern and Southern hemispheres, one notices that the latitude-temperature gradients are negative at pressures from 1100 to 220 mb at latitudes from 70° to 80°, and that their values are almost the same at corresponding latitudes and pressure levels in the Northern and Southern hemispheres of Venus. This indicates symmetry of the atmospheric thermal structure of both hemispheres in this pressure range. However, indicated symmetry no longer exists at pressures lower than 220 mb, i.e. at altitudes higher than 60 km.

## CONCLUSION:

Temperature and pressure data in the Venus's atmosphere obtained by the radio occultation method using the Venera-15 and -16 spacecraft from October 1983 to September 1984 are used for a wind speed analysis. The altitude and latitude profiles of zonal wind speed in the middle atmosphere of Northern and Southern hemispheres of Venus at alti-



tudes from 50 to 80 km in the latitude interval from 60° to 85° have been found. Wind speeds were determined assuming cyclostrophic balance of the planetary atmosphere. A jet with a maximum speed 100–115 m/s located at altitude of approximately 60 km at 73°–75° N is shown to exist in the Northern near-polar atmosphere. Above 65 km, the wind speed usually decreases with altitude, as the polar atmosphere in the Northern hemisphere is warmer than the near-polar one at these altitude levels. The speed of zonal wind increases with altitude at high latitudes of the Southern hemisphere above 70 km, showing a possibility of the existence of a jet at altitudes greater than 70 km. *Acknowledgments:* This work was partially supported by the Program 1.7 of the RAS Presidium.

## REFERENCES:

- [1] Newman M., Schubert G., Kliore A.J., Patel I.R. Zonal winds in the middle atmosphere of Venus from Pioneer Venus radio occultation data // *J. Atmos. Sci.* 1984. V. 41. P. 1901-1913.
- [2] Limaye S.S. Venus atmospheric circulation: observations and implications of the thermal structure // *Adv. Space Res.* 1985. V. 5. P. 51-62.
- [3] Yakovlev O.I., Matyugov S.S., Gubenko V.N. Venera-15 and -16 middle atmosphere profiles from radio occultations: Polar and near-polar atmosphere of Venus // *Icarus*. 1991. V. 94. P. 493–510, doi: 10.1016/0019-1035(91)90243-M.
- [4] Gubenko V.N., Yakovlev O.I., Matyugov S.S. Radio occultation measurements of the radio wave absorption and the sulfuric acid vapor content in the atmosphere of Venus // *Cosmic Res.* 2001. V. 39. No. 5. P. 439–445, doi: 10.1023/A:1012336911928.
- [5] Gubenko V.N., Andreev V.E. Radio wave fluctuations and layered structure of the upper region of Venusian clouds from radio occultation data // *Cosmic Res.* 2003. V. 41, P. 135–140, doi: 10.1023/A:1023378829327.
- [6] Gubenko V.N., Andreev V.E., Pavelyev A.G. Detection of layering in the upper cloud layer of Venus northern polar atmosphere observed from radio occultation data // *J. Geophys. Res.* 2008. V. 113. No. E03001, doi: 10.1029/2007JE002940.

# SPACE BISTATIC RADIO-HOLOGRAPHY AS APPLIED TO STUDY ATMOSPHERE AND SURFACE OF VENUS AND EARTH

A.G. Pavelyev<sup>1</sup>, A.A. Pavelyev<sup>1</sup>, S.S. Matyugov<sup>1</sup>, V.N. Gubenko<sup>1</sup>

<sup>1</sup>*Kotelnikov Institute of Radio Engineering and Electronics RAS, Space Radio Physics Department, Vvedenskogo sq. 1, Fryazino, Moscow region, 141190, Russian Federation. alxndr38@mail.ru*

## KEYWORDS:

Satellite radio-holography, Venus, Earth, atmosphere, surface, bending angle, refractivity, attenuation, radio wave

## INTRODUCTION:

The presence of powerful atmosphere of Venus leads to a significant refraction of radio signals during propagation at low elevation angles [1-4]. Periodically repeated radar experiments and radio occultation investigations using orbital spacecraft do not give details on the magnitude of refraction in the lower layers of the Venus atmosphere. High stability of radio signals emitted by ground-based transmitters and appropriate onboard data handling can enable high precision radioholographic investigation of the atmosphere and ionosphere of Venus by use of bistatic and radio occultation methods to obtain vertical profiles of the physical characteristics of the atmosphere and ionosphere. Refined experimental data on the magnitude of refraction in the atmosphere of Venus obtained by use of analysis of the "Venera-10 and 15" bistatic radar experiments are presented and future directions developed in sounding the Earth using signals of navigational systems are described.

## SPACE RADIO-HOLOGRAPHY:

Highly stable radio signals emitted by Earth-based transmitter after propagation through the ionosphere and atmosphere along the direct (1) and reflected path arrived to receiver aboard an artificial satellite on the near planetary orbit (Fig. 1). The direct signal is used to analyse: (1) the plasma structures and vertical distribution of the electron density in the ionosphere; (2) the layers, wave activity, absorption, bending angle, refractivity, pressure, temperature in the atmosphere above the critical level near the height 34 km. The reflected signal is analysed to reveal: (1) the relief features, subsurface structures, reflectivity, soil parameters; (2) the refractive attenuation, absorption, bending angle, and, possibly, layered or wave structures in the lower atmosphere.

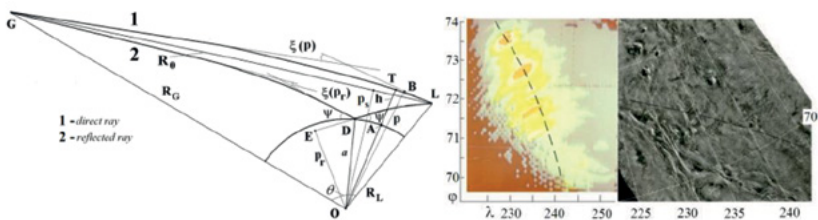


**Fig.1.** Bistatic radio-holographic investigation of the Venus (left) and Earth's atmosphere and surface. The first bistatic (middle) and monostatic (right) radio images of Venus surface obtained in 1983 by Venera-9 satellite.

## BENDING ANGLES IN THE LOWER ATMOSPHERE FROM DATA OF "VENERA-9, 10 AND 15, 16" ORBITAL MISSIONS:

The first bistatic experiments has been provided by "Venera 9 and 10" mission (1975) [3,4]. Bistatic experiments have been repeated in 1983 during existence of the orbital spacecraft "Venera 15 and 16" [4]. The monochromatic mode for radio signals emitted from Venus satellite at wavelength 32 cm has been used for investigation. The reflected signals have been received and analysed by a system on the Earth based station. In Fig. 2 (left) the curves 1-3 described the time frequency story of the reflected signal during three RO events provided in November 1983. The frequency of the direct signal is constant because closed loop mode of receiver. Curve (1) corresponds to immersion in radio shadow, and curves (2), (3) relate to emersion of the satellite "Venera-15".

Because variations in the orbital speed of satellite the inclination of curves 1-3 and observation time of reflections are different.

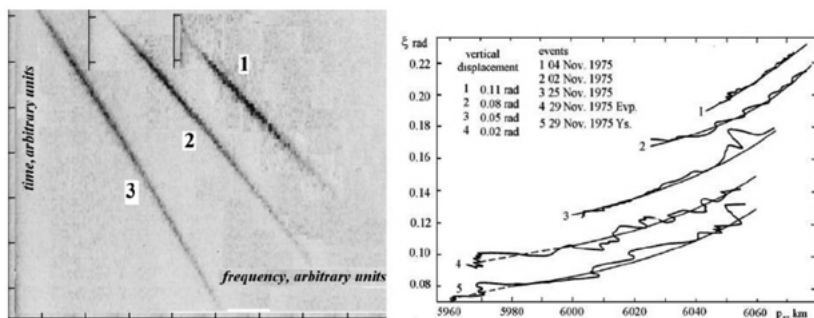


**Fig. 2.** Left. Time-frequency map of the reflected signal observed during radio occultation experiments provided during 1983 November 09, 12, and 11, curves (1)-(3), respectively. Position of the direct signal is shown by vertical lines (in the left, top corner). Right. Results of restoration of the bending angle from bistatic radar data. The impact parameter and bending angle are indicated along the horizontal and vertical axis, respectively.

The curves 1-5 (Fig. 2, right) described results of the bending angle measurements during 1975 November RO events 04, 02, and 25 (curves 1-3) and 29 (curves 4 and 5 correspond to observations of in the Evpatoria and Yssuriisk). The curves 1-4 are displaced for comparison. The displacement values are shown in the upper left corner in Fig. 2 (right). The thin smooth lines in Fig. 2 (right) indicate approximation of the experimental data. The bending angle varies in the interval 0.06-0.13 radian when the impact parameter changes in the range 5060...6075 km.

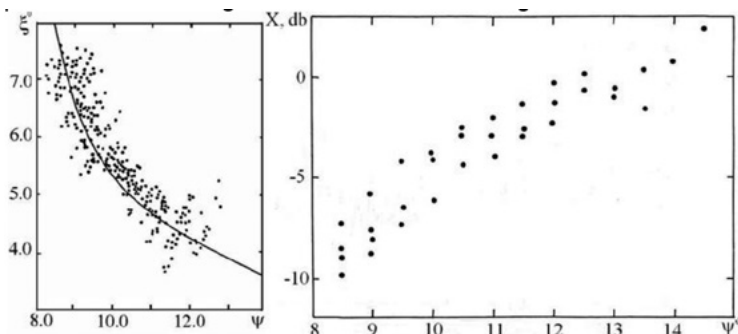


**Fig. 3.** Bending angle (left) and refractive attenuation (right) in the atmosphere of Venus at wavelength 32 cm (data of "Venera - 9 and 10" [4]).

Irregular systematic variations of the bending angle are of order 0.01 rad and have very small correlation in data of measurements from different receiving stations (curves 4,5 in Fig. 2). The noise fluctuations are about 0.002 rad and illustrate an instrumental accuracy. The difference between data of events is about 0.015 rad that can correspond to changes of physical conditions in the investigated regions. In Fig. 3 (left) the smooth line shows functional dependence of the bending and sliding angles. The points correspond to experimental data measured in five equatorial regions of Venus [3]. The data have significant scatter caused by features of bistatic radar measurements: influence of small and large scales of relief, possible effects of horizontal atmospheric inhomogeneity, irregularities, and/or layered structures. The angle of refraction exceeds about 10 - 20 times the same value at the appropriate geometry in the Earth's atmosphere. Refractive attenuation of radio waves (Fig. 3, right) is correspondingly about 5 - 10 times higher than under the same conditions in the Earth atmosphere and varies from 1-2 dB at grazing angle 14°-15° radio waves to 9-10 dB at 8°-9°. It should be noted that the sliding angle of the reflected radio waves bounded below by a value of about 8° because of capture by constantly existing waveguide in the atmosphere of planet. First measurements made by satellite "Venera - 9,10" showed a possibility of determining the refractivity in the lower Venus atmosphere at wavelength 32 cm, and remains unique.

## DIRECTIONS OF FUTURE INVESTIGATIONS:

Highly stable signals synchronized by atomic frequency standards and radiated by GPS satellites at wavelength 19 and 24 cm create at the altitudes from 0 to 20 000 km above the Earth surface radio fields that can be used for the development of the bistatic radiolocation and RO method as a new tool for global monitoring of the planetary ionosphere, neutral atmosphere, and surfaces [5]. During extended experimental and theoretical studies new radio-holographic approaches and principles have been derived that can be directly applied for bistatic radar and RO investigation during future interplanetary missions. There are four important directions: (i) innovative estimating the altitude dependence of the **total absorption** of radio waves using the RO amplitude and phase variations **at a single frequency**; (ii) evaluation of the slope, altitude, and horizontal displacement of the atmospheric and ionospheric layers from the RO signal intensity and phase data using the eikonal acceleration/intensity technique; (iii) **separation of layers and irregularities contributions** in the RO signal, determination of vertical profiles of the turbulent and small-scale structures by joint analysis of the RO signal eikonal and intensity variations **at a single frequency**; and (iv) introduction of the new combined phase-intensity index for the RO study of multilayered structures and wave processes. This regularity is valid for every RO ray in geometrical optics approximation including reflections from the surface [5].

## CONCLUSIONS

During the GPS RO analysis it is shown that the eikonal acceleration has the same importance for bistatic radar and the RO method as the phase path and Doppler shift for radio location [5]. Satellite radio-holography approach derived during multiple satellite missions working in the near Earth space can be directly applied for planetary investigations.

## REFERENCES:

- [1] Mariner Stanford Group. Venus: Ionosphere and atmosphere as measured by dual-frequency radio occultation of Mariner 5 // *Science*. 1967. V.158. P. 1678-1683.
- [2] Eshleman V. R., Fjeldbo G., Anderson J. D., et al. Venus: Lower atmosphere not measured // *Science*. 1968. V.162. P. 661-665.
- [3] Kolosov M.A., et al. Characteristics of the surface and features of the propagation of radio waves in the atmosphere of Venus from data of bistatic radiolocation experiments using "Venera 9, 10" satellites // *Icarus*. 2001 V. 48. P. 188-201.
- [4] Pavelyev A.G., et al. Results of measurement of the refraction angle of radio waves in the atmosphere of Venus from bistatic radar data // *Journal of Commun. Techn. and Electronics*. 1993. V.38. No.8. P.1379-1388 (in Russian).
- [5] Pavelyev A. G., et al. Application of the locality principle to radio occultation studies of the Earth's atmosphere and ionosphere // *Atmos.Meas.Tech*. 2015. V. 8., 2885–2899.

# THE MINERALOGIC ALTERATION HISTORY OF EARLY MARS: THE ROLE OF LARGE CRATERS AND BASINS IN TRANSIENT REGIONAL HIGH-TEMPERATURE ALTERATION

A.M. Palumbo<sup>1</sup>, J.W. Head<sup>1</sup>

<sup>1</sup>Department of Earth, Environmental, and Planetary Sciences, Brown University, Providence, RI 02912 USA (Ashley\_Palumbo@Brown.edu)

## KEYWORDS:

climate, impact cratering, alteration, rainfall, high-temperature

## INTRODUCTION:

The ~1500 km diameter Isidis basin is the third largest impact structure on Mars. Regions surrounding Isidis, including Nili Fossae and NE Syrtis, provide insight into the mineralogical and climatological history of Mars. The formation, alteration, and erosion of features in the circum-Isidis region are well-constrained with time, beginning in the early Noachian after the formation of the Isidis basin, and ending in the Hesperian before the Syrtis Major lava flows embayed the area. Throughout the region, there are distinct stratigraphic layers with correspondingly distinct alteration products, suggesting multiple different aqueous alteration regimes [1]. The stratigraphically lowest layers in the region are (1) the basement unit, characterized by low-Ca pyroxene and rich in Fe/Mg smectites, contains mega breccia blocks, and exhibit patches of kaolinite;

(2) the overlying olivine-rich unit, which is variably altered to Mg-carbonates; and (3) a spectrally flat and crater preserving capping unit [1-3]. Above the sealayers, emplaced later, is a sulfate-rich unit and a capping unit of Syrtis Major lava flows. In the past, it has been assumed that the different aqueous alteration regimes, related to the alteration of the different stratigraphic layers, were temporally separated [e.g.]. Here, we suggest that this is not the case, and that the three lowest units were formed and altered contemporaneously with the Isidis event, following the description of the Impact Cratering Atmospheric and Surface Effects (ICASE) model [4,5,6].

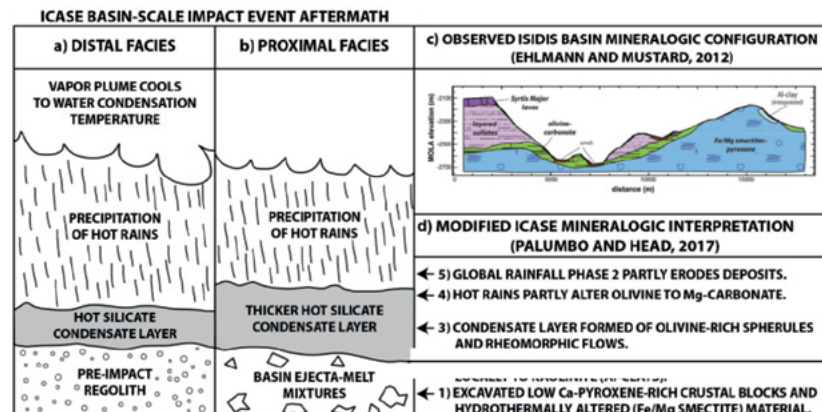


**Fig. 1.** Isidis Basin impact event aftermath. (a) and (b) explore expected variation in observed stratigraphy with varying distance from the basin. (c) shows the observed mineralogic configuration, from [2]. (d) demonstrates our interpretation for the formation of the observed layers, highlighting the corresponding ICASE-related steps [e.g.6].

## PREVIOUS INTERPRETATIONS:

**Basement unit.** The Fe/Mg smectites within the basement unit may represent deep hydrothermal alteration in the martian subsurface [8] that was later exhumed by the Isidis event [9]. Terrestrial analogs suggest that formation of the smectites through this mechanism would take thousands of years and

require temperatures up to ~873 K [1,8]. This interpretation of the basement unit is consistent with the presence of megabreccia blocks within the unit that were likely excavated during the impact event. Following emplacement, the basement unit experienced aqueous alteration (**Fig. 1c**), producing patches of kaolinite-bearing material. The kaolinite-bearing unit is tens of meters thick [1] and does not exhibit bedding, suggesting that the alteration was *in-situ*, and leads to two formation hypotheses [e.g. 1]: (1) top-down leaching of the Fe/Mg smectite-rich basement unit, and (2) hydrothermal alteration in the subsurface and subsequent excavation. Large impact events could have caused regional high-temperature surface alteration, leading us to explore the former hypothesis further in the context of the Isidis basin event.

**Olivine-rich and capping units.** Overlying the basement unit is the olivine-rich unit (**Fig. 1c**). Leading formation hypotheses include (1) post-Isidis lava flows [10,11] and (2) the Isidis impact melt sheet [9,12]. The unit ranges in thickness from 5 [3] to 160 m [2] and conforms to the underlying topography [2]. Aqueous activity has variably altered the unit to Mg-carbonate [1]. The spectral signature of Mg-carbonate is more uniform and pervasive in NE Syrtis than Nili Fossae, suggesting that aqueous alteration was more extensive in NE Syrtis [3], closer to the basin interior. Additionally, the olivine-rich unit has a high thermal inertia when compared to the other stratigraphic units [3], suggesting that it is more coherent. Overlying this layer in NE Syrtis is a ~10 m thick, spectrally flat, silica-rich capping unit [3].

**Summary.** The observed stratigraphy and mineralogy require at least three episodes of aqueous activity [1]: (1) formation of the Fe/Mg smectites, (2) alteration of the basement and olivine-rich units, and (3) an episode involving less water-rock interaction that erodes the units. The episodes are canonically interpreted to be temporally distinct [1], possibly spanning 250 Myr [3].

## APPLYING ICASE TO THE ISIDIS BASIN EVENT AND ASSOCIATED MINERALOGY:

We explore the possibility that the emplacement and alteration of the basement, olivine-rich and capping units are essentially contemporaneous and related to the Isidis event and post-impact effects.

Basin-scale impacts vaporize significant volumes of target and projectile material [e.g. 7]. The vaporized material expands away from the impact site as a vapor plume composed of vaporized silicate material and water. The vapor plume cools through radiation and expansion through the atmosphere. When the plume cools to condensation temperature for the silicate material, the silicate material will condense and fall out as molten spherules. We hypothesize that the global fallout of silicate condensate material [e.g. 4] corresponds to the emplacement of the observed olivine-rich unit. The olivine-rich unit drapes underlying topography [1,3], consistent with a silicate condensate layer (SCL) being emplaced over pre-existing topography. The average thickness of the Isidis SCL is estimated to be ~20 m [12], similar to the thickness of the observed olivine-rich unit. Silicate condensate material preferentially deposits at the impact site, suggesting a thicker layer in the Isidis region, relative to more distal locations (**Fig. 1**). Proximal to the basin, the very high temperatures of the SCL (~1600 K) could encourage rheomorphic flow off topographic highs and ponding in topographic lows, leading to local variations in thickness and exposure of the underlying basement unit. For these reasons, the Isidis SCL is a potential candidate for the observed structure and distribution of the olivine-rich unit (**Fig. 1c,d**).

The olivine-rich unit has a stronger olivine spectral signature than surrounding regions and stratigraphic layers [2,12] and is the strongest olivine signature detected on Mars [2]. Plausible explanations for this observation in the context of the ICASE model [4,5,6] are (1) Noachian volcanic crustal compositions that were richer in olivine than later extrusives [9], (2) an olivine-rich projectile that contributed a significant olivine component to the vapor plume, or (3) early crystallization of olivine and quenching in the cooling plume.

The olivine-rich unit is emplaced on top of the basement unit and thermal interaction and hydrothermal alteration between the units could account for some of the observed alteration products. Following the condensation and fallout of the silicate material, the vapor plume continues cooling and eventually reaches the condensation temperature for water vapor. The water rains out and reaches

the surface at temperatures close to condensation temperature (~373 K). The rainfall (1) acts to cool the SCL, causing the water to cycle through the layer and atmosphere for hundreds of years, a phase characterized by rainfall rates of ~2 m/a [5]; (2) hydrothermally alters the upper portions of all exposed layers; and (3) quenches the upper-most parts of the SCL, producing spectrally flat, silica-rich glass (capping unit).

The high temperatures of both the substrate and aqueous medium (rainfall) suggest that the upper portions of the olivine-rich unit and exposed areas of the basement unit could be altered to clays on timescales of tens of years [13]. Due to differences in parent rock composition, alteration of the olivine-rich unit is predicted to produce Mg-carbonate [2], and alteration of the basement unit is predicted to produce Al-phylosilicates. Spectral analyses of the region show both the variable alteration to carbonate and patchy distributions of kaolinite [1]; the alteration of both units is partial, with both products (alteration) and reactants (initial units) remaining [2]. The ICASE model [4,5,6] could help account for this observation; the aqueous alteration related to impact-induced rainfall is intense (**Fig. 1**) but geologically short-lived, suggesting that the parent rock will undergo only partial alteration.

To summarize, our interpretation of several of the stratigraphic units follows (**Fig. 1**): Low-Ca pyroxene-rich crustal blocks and hydrothermally altered Fe/Mg smectite material are excavated and emplaced during the Isidis event (**Fig. 1 d1**). The vapor plume cools to silicate condensation temperature and precipitates the olivine-rich SCL (**Figs. 1b and d3**); the SCL may aid to play a role in thermally altering the basement unit locally to produce Al-phylosilicates (**Fig. 1d2**). The silicate condensate material with the coolest temperatures will be emplaced last, producing the capping unit. Soon thereafter, the vapor plume cools to the water condensation temperature and precipitates abundant hot rainfall (**Fig. 1b**); the ensuing hot rains (1) partly alter the olivine-rich unit to Mg-carbonates (**Fig. 1d4**), (2) partly alter exposed regions of the basement unit to Al-clays, and (3) quench the capping unit to produce silica-rich, spectrally flat, glass. Last, the final impact-related rainfall partly erodes the deposit (**Fig. 1 d5**). In summary, the emplacement of the lower-most three units and several of the key alteration phases associated with the Isidis basin stratigraphy may be related to the Isidis event and its aftermath (**Fig. 1d**), rather than to separate subsequent environmental phases or events.

## CONCLUSIONS:

Following [4,5,6], we have characterized the mineralogical influence of large cratering events on early Mars. Critical to this analysis is the prediction of a hot SCL tens of meters thick and subsequent intense impact-induced rainfall [4,5] (**Fig. 1**). These impact cratering depositional and alteration effects will clearly influence the pre-existing substrate, a factor that has not been widely considered in the past. We propose that the circum-Isidis region offers an opportunity to explore and assess the different aqueous environments and resulting mineralogical effects that characterize the region (**Fig. 1**) and may have occurred elsewhere throughout martian history in association with other large craters and basins.

The proposed explanation for the observed stratigraphy in the circum-Isidis region suggests that the emplacement of the lower-most three stratigraphic layers and subsequent aqueous alteration occurred over hundreds of years, in contrast to the previous estimate of hundreds of millions of years. Additionally, this explanation does not require a global climate transition, instead it explains the geology and mineralogy through a climatic perturbation related to the Isidis impact event. It is possible that post-impact conditions are responsible for the observed stratigraphic sequence, suggesting that a continuous warm and wet Noachian climate [e.g. 14] was not required for formation of these clays.

## REFERENCES:

- [1] Ehlmann B. et al. Identification of hydrated silicate minerals on Mars using MRO-CRISM: Geologic context near Nilii Fossae and implications for aqueous alteration. *JGR: Planets*. 2009. V. 114 No. E2. E00D08.
- [2] Ehlmann B. and Mustard J. An in-situ record of major environmental transitions on early Mars at Northeast Syrtis Major. *GRL*. 2012. V. 39. No. 11. L11202.
- [3] Bramble M. et al. The geological history of Northeast Syrtis Major, Mars. *Icarus*. 2017. V. 293. P. 66-93.
- [4] Segura T. et al. Modeling the environmental effects of moderate-sized impacts on Mars. *JGR: Planets*. 2008. V. 113. No. E11. E11007.
- [5] Toon O. et al. The Formation of Martian River Valleys by Impacts. *Ann. Rev. Earth*

*Plan. Sci.* 2010. V. 38. P. 303-322.

[6] Palumbo A. and Head J. Impact Cratering as a Cause of Climate Change and the Effects on Dating of Surfaces on Late Noachian Mars. *MAPS*. In Revision.

[7] Melosh H. Impact cratering: A geologic process. *Oxford U. Press*. 1989.

[8] Ehlmann B. et al. Subsurface water and clay mineral formation during the early history of Mars. *Nature*. 2011. V. 479. No. 7371. P. 53-60.

[9] Mustard J. et al. Composition, Morphology, and Stratigraphy of Noachian Crust around the Isidis basin. *JGR: Planets*. 2009. V. 114. No. E2. E00D12.

[10] Hamilton V. and Christensen P. Evidence for extensive, olivine-rich bedrock on Mars. *Geology*. 2005. V. 33. No. 6. P. 433-436.

[11] Tornabene L. et al. Surface and crater-exposed lithologic units of the Isidis Basin as mapped by coanalysis of THEMIS and TES derived data products. *JGR: Planets*. 2008. V. 113. No. E10. E10001.

[12] Mustard J. et al. Mineralogy of the Nili Fossae region with OMEGA/Mars Express data: 1. Ancient impact melt in the Isidis Basin and implications for the transition from the Noachian to Hesperian. *JGR: Planets*. 2007. V. 112. No. E8. E08S03.

[13] Browning L. et al. Minimum times to form clay in martian surface and near-surface environments. *LPSC XXXIV*. 2003. P. 1708.

[14] Craddock R. and Howard A. The case for rainfall on a warm, wet early Mars. *JGR: Planets*. 2002. V. 107. No. E11. P. 5111.



# IMPACT OF THE MARTIAN ATMOSPHERE PROPERTIES ON THE SPATIAL RESOLUTION OF THE FREND/TGO

A. B. Sanin <sup>1</sup>, I. G. Mitrofanov <sup>1</sup>, A. V. Malakhov <sup>1</sup>

<sup>1</sup> Space Research Institute of the Russian Academy of Sciences (IKI), 84/32 Profsoyuznaya Str, Moscow, Russia, 117997

## KEYWORDS:

Mars, atmosphere, neutron, FREND, TGO.

## INTRODUCTION:

Collimated neutron detector FREND [1,2] have been designed to provide information about distribution of the epithermal neutron flux from Martian surface with geometric spatial resolution up to 40 km from the 400 km TGO orbit [3]. However, presence of the Martian atmosphere may influence on the instrument's resolution by blurring out the neutron flux or by absorbing neutrons while they are travel from Mars surface to the FREND detectors. It is well known that Martian atmosphere column density varies significantly along the Martian surface (due to topography). Also, it varies along Martian seasons due to seasonal CO<sub>2</sub> depositions at Polar Regions. We would present results of numerical simulations of neutron transport through the atmosphere and provide estimation of FREND spatial resolution.

## REFERENCES:

- [1] Mitrofanov I.G., et al. FREND experiment on ESA's TGO mission: science tasks, initial space data and expected results // Proceedings of the 19th EGU General Assembly, EGU2017, Vienna, Austria. 2017. P. 14685.
- [2] Mitrofanov I.G., et al. FREND neutron telescope for mapping the Martian water with fine spatial resolution // Proceedings of the EGU General Assembly, EGU2016, Vienna, Austria. 2016. P. 16402.
- [3] Håkan S., Vago, J., de Groot R. The ExoMars 2016 mission // Proceedings of the American Astronomical Society, DPS meeting #47. id.419.19

# INFLUENCE OF SUPRATHERMAL ATOMS ON THE ESCAPE AND EVOLUTION OF THE MARTIAN CO<sub>2</sub> ATMOSPHERE

H. Lichtenegger<sup>1</sup>, U.V. Amerstorfer<sup>1</sup>, H. Gröller<sup>2</sup>, F. Tian<sup>3</sup>, H. Lammer<sup>1</sup>, L. Noack<sup>4</sup>, C. Johnstone<sup>5</sup>, L. Tu<sup>5</sup>

<sup>1</sup>Space Research Institute, Austrian Academy of Sciences, Graz, Austria (*herbert.lichtenegger@oeaw.ac.at*);

<sup>2</sup>Lunar and Planetary Laboratory, University of Arizona, Tucson, AZ, USA;

<sup>3</sup>Ministry of Education Key Laboratory for Earth System Modeling, Center for Earth System Science, Tsinghua University, Beijing, China;

<sup>4</sup>Royal Observatory of Belgium, Brussels, Belgium;

<sup>5</sup>Department of Astrophysics, University of Vienna, Vienna, Austria.

## KEYWORDS:

Particle escape, suprathermal atoms, CO<sub>2</sub> atmosphere, early Mars, young Sun, Monte Carlo modeling.

## INTRODUCTION:

Escape processes in planetary atmospheres are triggered by the stellar wind and radiation of their host star and determine the long term stability of the atmosphere. In the present work the escape of hot oxygen and carbon from the martian atmosphere for 1, 3, 10, and 20 times the present solar EUV flux, corresponding to different epochs in Mars's evolution, is investigated. Based on simulated 1D profiles for neutrals and ions of the upper atmosphere for the various EUV fluxes [1], the stochastic motion of hot O and C produced via different chemical reactions is calculated by means of a 3D Monte Carlo model [2]. From the obtained energy distribution of the suprathermal particles at the exobase, the escape rates of O and C corresponding to the different EUV fluxes can be estimated.

## RESULTS:

We discuss different sources of hot oxygen and carbon atoms in the martian thermosphere and their changing importance with the EUV flux. The increase of the production rates due to higher densities resulting from the higher EUV flux competes against the expansion of the thermosphere and corresponding increase in collisions. We find that the escape due to photodissociation continuously increases with increasing EUV level, while other processes show a different behavior. E.g., the escape of particles due to dissociative recombination of O<sub>2</sub><sup>+</sup> reaches a maximum at the ~10 EUV level and starts to decrease again for higher values.

Depending on the initial rotation rate of the Sun and its rotational evolution, the different EUV fluxes can be related to different times in the past of the martian history by comparing a sample of solar like stars of different age and rotation rate [3]. If we assume that the Sun has been a slow rotator in the past, our findings show that Mars could not have had a dense atmosphere at the end of the Noachian epoch, since such an atmosphere would not have been able to escape until today. In the pre-Noachian era, most of a magma ocean and volcanic activity related outgassed CO<sub>2</sub> atmosphere could have been lost thermally until the Noachian epoch, when non-thermal loss processes such as suprathermal atom escape became dominant. Assuming a 2:1 relation for lost hot O to lost hot C, our results suggest that not more than an equivalent of some hundred millibar of CO<sub>2</sub> could have been removed since the Noachian epoch by suprathermal atom escape.

## REFERENCES:

- [1] Tian, F., Kasting, J. F., Solomon, S. C. Thermal escape of carbon from the early Martian atmosphere // *Geophys. Res. Lett.* 2009. V. 36. No. L02205. P. 1-5.
- [2] Gröller, H., Shematovich, V. I., Lichtenegger, H. I. M., Lammer, H., Pfleger, M., Kulikov, Y. N., Macher, W., Amerstorfer, U. V., Biernat, H. K. Venus' atomic hot oxygen environment // *J. Geophys. Res.* 2010. V. 115. No. E12017. P. 1-9.
- [3] Tu, L., Johnstone, C. P., Güdel, M., Lammer, H. The extreme ultraviolet and X-ray Sun in Time: High-energy evolutionary tracks of a solar-like star. // *Astron. Astrophys.* 2015. V. 577. No. L3. P. 1-4.

# MCMURDO DRY VALLEYS: EXPLORING ANTARCTICA AS A MARS ANALOG

Hunter Quintal, James Head III

*Brown University Department of Earth, Environmental, and Planetary Sciences hunter\_quintal@brown.edu; james\_head@brown.edu*

## KEYWORDS:

McMurdo Station, Onyx River, Wright Lower Glacier, Noachian, Hesperian, Lake Vanda, Lake Brownworth, Dry Valleys, Valley Networks, Antarctica

## INTRODUCTION:

The use of terrestrial analogs to extraterrestrial bodies is well established for understanding the geologic processes required for the formation of observable features today. We have chosen to explore the Dry Valleys of Antarctica in order to understand the likely processes of valley network formation on Mars before and after a period of significant climate change on the Noachian Hesperian boundary. The cold and hyper-arid environment within the Dry Valleys closely simulate the climate of Mars today (Marchant & Head, 2007), and the geomorphology of the Onyx River within the Dry Valleys may prove to be similar to a subset of previously mapped valley networks in a global martian valley network database produced by Hynes et al. 2010. Classification of both the geomorphology and meteorology of the Onyx River will therefore play an important role in characterizing the Antarctic Dry Valleys and may also provide insights into Mars' climate history (Head & Marchant, 2014).



Fig. 1. Glacial meltwater forming Onyx River tributaries from Clarke Glacier to the west (left of photo) and Wright Glacier to the north (top of photo) captured via CAMBOT imagery December 2001. Width of photo is approximately 1 km.

## ONYX RIVER SOURCES AND SINKS:

The Onyx River located in Wright Valley Antarctica is a meltwater stream, and is an example of endorheic dendritic drainage that forms annually from ablation of multiple glacial toes bounding the valley in the austral summer. This drainage network is not well developed; all ~30 tributaries are sourced from cold-based glaciers with stream orders typically of 2 to 3 and up to 5 where both the Wright Lower Glacier and Clarke Glacier tributaries merge. Ablation at the Wright Lower Glacier terminus collects into the spillway glacial Lake Brownworth at 300 m above sea level, which then overflows into the headwaters of the Onyx River. Precipitation (snowfall) does not appear to influence river recharge significantly; precipitation instead feeds the Onyx River via snowfall to glacier accumulation zones sourced from oceanic evaporation. The Onyx River then flows 32 km southwest through abraded and meandering

channels within the glacially carved valley and terminates at the closed-basin Lake Vanda at 160 m above sea level (Shaw et al. 1980).

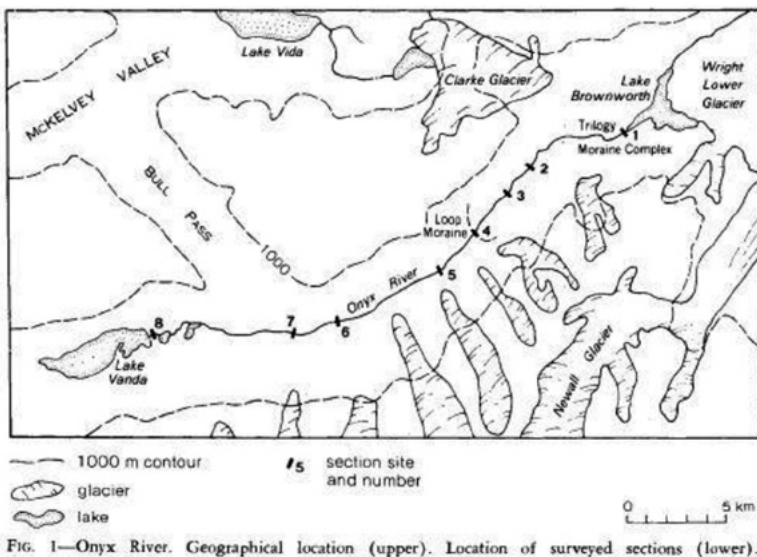


Fig. 1—Onyx River. Geographical location (upper). Location of surveyed sections (lower).

Fig. 2. Schematic map view of Southfork Valley Antarctica with surveyed cross sections depicted as numbers. (Shaw et al. 1980).

## HYDROMETEOROLOGY AND GEOMORPHOLOGY:

Relatively fresh water sourced from glacial melt comes in contact with poorly sorted soils near Lake Brownworth along the Onyx River. This process controls the major ion composition within the river, which is significantly different than that of the terminus of the river in the meromictic Lake Vanda. Keys and Williams (1981) argue that marine aerosols are critical to maintaining the near equal Na and Cl concentrations found within Onyx. From the source to the terminus of the Onyx River, the Gibbs Boomerang demonstrates that the Onyx river transitions from a precipitation dominated river into a rock-dominated river at relatively low salinities (Green et al. 1984). Flow duration within the Onyx River is highly variable between the two extremes of river flooding that causes bank erosion and no flow years when the river fails to reach Lake Vanda. The maximum calculated stream discharge is 20 m<sup>3</sup>/s. Early austral summer discharge appears minimal – water is constrained mainly to inner channels carrying relatively high sediment yields – as glacial meltwater contribution is not continuous. The location of glaciers and the basement geology of Wright Valley including glacial till, moraines, and igneous dikes control the morphology of the Onyx River. The Onyx's characteristic flow path appears to align with low magnitude low flooding associated with -2°C daily surface averages during the summer season. Hoke and Hynek also suggest regional episodic temperature change was sufficient to produce the water required for valley carving observed today (Hynek et al. 2010). The majority of flows are sourced from glacial meltwater because groundwater input is largely contained as permafrost centimeters beneath surface soils that spans 100's of meters thick. However, the capacity of regional hyper-arid soils to wick water from tributaries that do not surificially feed the Onyx River may still act as a recharge source to the river when travelling along the permafrost.

## IMPLICATIONS FOR MARS:

We are assessing meteorological data obtained from the LTER database for the Onyx River and geomorphological classification of the stream order, length, and width of Valley Networks on Mars in order to find candidate analogs on Mars to the Onyx River. We are documenting the climate parameters required for the maintenance of the Onyx River during the austral summer, and are using this analog to understand the likely climate required for the formation and maintenance of similar water-carved features on Mars during a period of climate change on Mars 3.6-3.8 Ga (Hynek et al. 2010). We are also interested

in documenting similarities between the Onyx River and any of the 10 major valley networks on Mars summarized by Som into three different classifications (Som 2009).



**Fig. 3.** Meandering main river travelling southwest (towards the left of the photo) with tributary flow from the north (from the top of the photo) contributing to the Onyx River captured via CAMBOT imagery December 2001. Length of main river in photo is approximately 1 km.

## REFERENCES:

- [1] Marchant, D. R., and J. W. Head, Antarctic dry valleys: Microclimate zonation, variable geomorphic processes, and implications for assessing climate change on Mars, *Icarus*, 192, 187-222 (2007)
- [2] Hynek, Brian M., Michael Beach, and Monica RT Hoke. "Updated global map of Martian valley networks and implications for climate and hydrologic processes." *Journal of Geophysical Research: Planets* 115.E9 (2010).
- [3] Head III, J. W., and D. R. Marchant, The climate history of early Mars: Insights from the Antarctic McMurdo Dry Valleys hydrologic system, *Antarctic Science*, 26, 774-800 (2014)
- [4] Shaw, John, and Terry R. Healy. "Morphology of the Onyx River system, McMurdo sound region, Antarctica." *New Zealand journal of geology and geophysics* 23.2 (1980): 223-238.
- [5] Keys, JR Harry, and Karen Williams. "Origin of crystalline, cold desert salts in the McMurdo region, Antarctica." *Geochimica et Cosmochimica Acta* 45.12 (1981): 2299-2309.
- [6] Green, William J., and Donald E. Canfield. "Geochemistry of the Onyx River (Wright Valley, Antarctica) and its role in the chemical evolution of Lake Vanda." *Geochimica et cosmochimica acta* 48.12 (1984): 2457-2467.
- [5] Som, Sanjoy M., David R. Montgomery, and Harvey M. Greenberg. "Scaling relations for large Martian valleys." *Journal of Geophysical Research: Planets* 114.E2 (2009).

# THE FRETTED TERRAIN, MARS: IMPLICATIONS OF MISSING VOLUME FOR HYPOTHESES OF ORIGIN

C.A. Denton<sup>1</sup>, J. W. Head<sup>1</sup>

<sup>1</sup>*Brown University, Providence, RI 02912, USA, camille\_denton@brown.edu.*

## KEYWORDS:

Mars Noachian geologic history, geomorphology, fretted terrain.

## INTRODUCTION:

The fretted terrain [1], a heavily dissected geologic terrain observed for hundreds of thousands of square kilometers along the martian hemispheric dichotomy boundary, has no overt terrestrial analogues and has eluded complete scientific explanation. Key unanswered questions include: 1) the timing/duration of the fretting process, 2) the mechanisms instigating the breakup, and 3) the processes responsible for the removal of the material and the volumes of material removed. Here we estimate the limits on the amount of material removed during the formation of the fretted terrain and explore implications for existing formation hypotheses.

## GEOLOGIC BACKGROUND:

The most extensive example of the martian fretted terrain occurs as a part of a plateau over a surface area of  $\sim 1.19 \times 10^6$  km<sup>2</sup> at the northern edge of Arabia Terra (Fig. 1a). Here mesas, plateaus, and knobs of Noachian highland plateau material are arranged in irregular configurations and separated by wide, flat-floored channels occupied by sedimentary valley floor fill [1]. Geological observations of this region suggest that the intervening material between highland plateau outcrops has been removed [1,2], although its removal processes and depositional location are unknown. The steep  $\sim 1$ -2 km high scarps surrounding the mesas, as well as their polygonal shape, suggest that erosion was highly effective [1]. Many of the mesas directionally align in pairs or regional groups, suggesting a possible structural cause [2]; these mesas decrease in size and increase in spacing with increasing distance northward across the dichotomy boundary [1]. Examination of high-resolution CTX images (Fig. 1b) shows that cross-sections of the plateaus display three main geologic units: 1) a steep upper slope with outcrops of erosion-resistant bedrock, 2) an intermediate talus unit with a shallower slope, and 3) a highly textured debris apron at the base [3]. The erosion-resistant upper layers are attributed to a series of volcanic flows observed on the surface of Arabia Terra [2], which date to the mid and late Noachian. The thickness of these volcanic units and the nature of older units beneath them are obscured by the multiple sections of eroded material derived from the steep scarps (Fig. 1b).

Previous hypotheses for the origin of the fretted channels and fretted terrain have called on mass wasting [1], groundwater sapping [4], aeolian erosion [5], overland water flow [6], and extensional faulting [7]. Each of these conceptual models is quite different and each has certain implications for surface conditions and major processes operating during the late Noachian. For example, removing the intervening material from the fretted terrain through predominantly overland flow requires large amounts of water to erode and carry the requisite sediment and deposit it in the northern lowlands. Despite the large number of hypotheses, relatively little work has been done to assess them quantitatively in order to more rigorously test each proposed origin, compare it to geologic observations, and match conceptual hypotheses to geologic reality. Through assessing quantitatively the volume of material that was removed from the fretted terrain, we can begin to constrain these hypotheses and assess their plausibility.

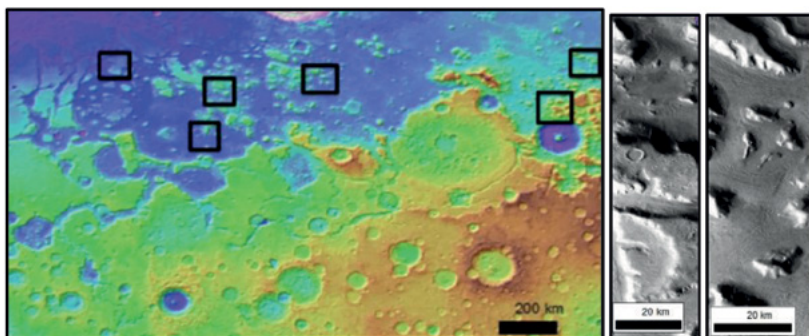


**Fig. 1a:** Regional view of the fretted terrain north of Arabia Terra, with selected regions analyzed for surface area. (MOLA 128 pixel/degree topography). **1b,c:** High resolution CTX image of sections of the fretted terrain observed in northeast Arabia Terra.

## MATERIAL REMOVED AND IMPLICATIONS:

The Late Noachian fretted channels and terrain have been modified by Amazonian glaciation processes [8]. Previous work analyzed the amount of ice and overlying debris in the debris aprons and lineated valley fill associated with these processes [9]; these estimates can be adapted to quantify the total amount of recent debris shed by the scarps of the fretted terrain based on a SHARAD-estimated average debris layer thickness of 5-10 m. Because previous work has suggested that mass wasting is an effective mechanism to remove the entirety of the fretted terrain [1], quantifying the amount of present-day debris in comparison to the full volume of missing material allows us to assess this hypothesis. As such, the amount of debris contained in the lineated valley fill and lobate debris aprons of Arabia Terra is  $\sim 4.72 \times 10^3 \text{ km}^3$  [9]. As we will show, this volume is far less than the range of estimates for material removed from northern Arabia Terra during the fretting process.

To establish basic constraints on the volume of material removed from the fretted terrain, we first set basic assumptions to accommodate the variable nature of the fretted terrain, which varies both latitudinally and longitudinally across the region. Therefore, to estimate the surface area of material removed, we assessed ten  $100 \times 100 \text{ km}^2$  sections within the fretted terrain containing distinct varieties of plateaus, mesas, and knobs (selected boxes shown in Fig. 1a). From these localized studies, we estimate that an average area of fretted terrain has experienced 50-67% dissection/material removal. To assess the missing volume we consider the vertical thickness of material removed from the fretted terrain, and whether this value remained reasonably consistent across the region. The greatest elevation difference between the top of the plateau and the lowland floor is  $\sim 2 \text{ km}$  at the dichotomy boundary scarp, along the mouths of the fretted channels in Arabia Terra. The smallest elevation difference is measured at the northern edge of the fretted terrain, where the mounded deposits are at their minimum height:  $\sim 500\text{-}700 \text{ m}$ . As an approximate upper bound on the amount of material removed from the fretted terrain system over an area of  $1.19 \times 10^6 \text{ km}^2$  (Fig. 1a), we assume that the  $\sim 2 \text{ km}$  scarp at the southern boundary of the fretted terrain once extended to the present northern edge. Such an assumption, along with the calculated dissection range of 50-67%, yields upper estimates for the volume of material removed:  $\sim 1.20 - 1.56 \times 10^6 \text{ km}^3$  of material over an area of  $1.19 \times 10^6 \text{ km}^2$ . However, it is more likely that some iteration of the gentle northward slope of the Arabia Terra plateau ( $\sim 0.1\text{-}0.5^\circ$ ) continued north of the present dichotomy boundary [2], and thus for a more realistic estimate of preexisting topography we assume that the present elevation difference observed at the northern edge ( $500\text{-}700 \text{ m}$ ) is consistent with pre-fretting conditions, yielding a more realistic range in volume estimates:  $7.44 \times 10^5 - 1.07 \times 10^6 \text{ km}^3$ .

To properly assess candidate removal processes, these estimates must also account for the variations in lithology of material removed, which varies down section. The stratigraphy of the highland plateau includes up to several hundred meters of a friable mantling deposit from the late Noachian [10], which overlies multiple Noachian extrusive volcanic episodes whose total thickness is not well constrained due to the presence of debris cover, and thus may be over  $1 \text{ km}$  thick [2]. Beneath these volcanic units lies a heavily fractured basement or megaregolith unit. The variations in porosity between these units does not significantly affect the volume of material removed, but does have ramifications

for the different methods proposed to remove large sections of the plateau. While the overlying mantling unit and the underlying fractured basement may be relatively easily removed through low-intensity erosional processes such as fluvial overland flow [6] and aeolian transport [5], removal of up to 1 km of volcanic flows through such mechanisms requires either longer timescales than estimated [2] or pervasive, preexisting fractures facilitating breakup [e.g., 11]. We suggest that processes such as aeolian and fluvial overland flow are inefficient in producing the fretted terrain without additional modification to the plateau unless higher-magnitude occurrences are invoked, i.e., large-scale flooding [11].

This first-order examination of the amount of material involved in the production of the fretted terrain ( $\sim 7.44 \times 10^5 - 1.07 \times 10^6 \text{ km}^3$ ) suggests that observed mass wasting associated with glacial processes in the region cannot account for the volume removed from the area. Furthermore, hypotheses invoking long-term overland flow of water or aeolian processes to remove the fretted terrain must account for the presence of multiple lithologies in the missing material, which respond to such erosional patterns differently and on varying timescales. Future work examining the origin of the fretted terrain will continue detailed geomorphic and numerical investigation to assess the remaining hypotheses and propose more robust formation mechanisms accounting for the geologic history of the Arabia Terra plateau.

## REFERENCES:

- [1] Sharp R.P. Mars: Fretted and chaotic terrains. // JGR. 1973. V. 7. No. 20. P. 4073-4083.
- [2] McGill G.E. Crustal history of north central Arabia Terra, Mars. // JGR. 2000. Vol. 105. No. E3. P. 6945-6959.
- [3] Carr M.H. Mars Global Surveyor observations of martian fretted terrain. // JGR. 2001. V. 106. No. E10. P. 23571-23593.
- [4] Carr M.H. The martian drainage system and the origin of valley networks and fretted channels. // JGR Planets. 1995. V. 100. No. E4. P. 7479-7507.
- [5] Irwin R.P. et al. Sedimentary resurfacing and fretted terrain development along the crustal dichotomy boundary, Aeolis Mensae, Mars. // JGR. 2004. V. 109.
- [6] Brakenridge G.R. The origin of fluvial valleys and early geologic history, Aeolis Quadrangle, Mars. // JGR. 1990. Vol. 95, No. B11. P. 17289-17308.
- [7] Irwin R.P., Watters T.R. Geology of the Martian crustal dichotomy boundary: Age, modifications, and implications for modeling efforts. // JGR. 2010. Vol. 115.
- [8] Head J.W., et al. Northern mid-latitude glaciation in the Late Amazonian period of Mars: Criteria for the recognition of debris-covered glacier and valley glacier land system deposits. // Earth Planet. Sci. Lett. 2010. Vol. 294. P. 306-320.
- [9] Levy J.S., et al. Enhanced erosion rates on Mars during Amazonian glaciation. // Icarus. 2016. Vol. 264. P. 213-219.
- [10] Fassett C.I., Head J.W. Layered mantling deposits in northeast Arabia Terra, Mars: Noachian-Hesperian sedimentation, erosion, and terrain inversion. // JGR. 2007. Vol. 112.
- [11] Lamb M.P., Dietrich W.E. The persistence of waterfalls in fractured rock. // GSA Bulletin. 2009. Vol. 121. No. 7/8. P. 1123-1134.



# OUTFLOW CHANNELS ON MARS: TESTING THE ORIGIN OF REULL VALLIS IN HESPERIA PLANUM BY LARGE-SCALE LAVA-ICE INTERACTIONS AND TOP-DOWN MELTING

J.P. Cassanelli<sup>1</sup>, J.W. Head<sup>1</sup>

<sup>1</sup>*Department of Earth, Environmental, and Planetary Science, Brown University, Providence, RI 02919, USA;*

## KEYWORDS:

Mars; Ices; Outflow channels; Volcanism; Volcano-ice interactions

## INTRODUCTION:

Much work has been dedicated to understanding the mechanisms responsible for the formation of the martian outflow channels, enormous channels thought to have been carved by episodic outburst floods [1,2]. Outflow channel formation has been canonically interpreted to have occurred by catastrophic eruptions of groundwater from pressurized confined aquifers [e.g. 1,2]. However, these models for outflow channel formation have been challenged by difficulties in generating sufficient hydraulic head [3] and overpressure [4] and by limited recharge sources [5].

In light of climate model results predicting the accumulation of regional ice sheets across the martian highlands [6-8], and the widespread distribution of contemporaneous volcanism on Mars [9], recent work has proposed large-scale lava-ice interactions as a potential alternative mechanism for outflow channel formation [10]. The relationship between Hesperia Planum volcanism and outflow channel development has been explored by previous investigators who proposed heating and melting of ground-ice through extrusive and intrusive volcanism as a possible outflow channel formation mechanism [11]. However, generating sufficient volumes of water and accounting for the complete geomorphology of the system by this previously proposed mechanism is difficult because the ice volume available to melt is constrained by the subsurface pore space.

Here we assess in detail the potential formation of outflow channels by large-scale lava-ice interactions and top-down melting [10] through an applied case study of the Reull Vallis outflow channel system. We first review the geomorphology of Reull Vallis to outline criteria that must be met by the proposed formation mechanism and then evaluate the consistency of ice sheet lava heating and loading formation predictions.

## REULL VALLIS:

The Reull Vallis outflow channel consists of 5 individual segments grouped into the upper and lower systems [12-14]. Distinct morphologic differences between the upper and lower systems have been interpreted [14] to suggest that the upper Reull Vallis served as a tributary to the lower system and that formation of the lower system occurred by other mechanisms, with different sources of water, and predated that of the upper system. Here we focus on the upper Reull Vallis system due to the close spatial and temporal association with the Hesperian Ridged plains unit [14].

The upper Reull Vallis system emanates from the northern trough, a ~140 km long, tens of kilometers wide, ~100-200 m deep linear depression in southern Hesperia Planum (Fig. 1). South of the northern trough, the upper Reull Vallis system emerges abruptly as a large steep-sided canyon within Waikato Vallis (Fig. 1). The Waikato Vallis segment of the upper Reull Vallis system shows an abundance of evidence (Fig. 1) consistent with an origin by fluvial activity and erosion involving undercutting by subsurface flow [13,14]. The abrupt emergence, lack of tributaries, depressed channel head, valley terraces, and collapsed features at the channel head (Fig. 1) have been interpreted to suggest that the water which carved the upper Reull Vallis system originated in multiple flooding events from the subsurface of Hesperia Planum within the northern trough [13,14]. The total volume eroded in the formation of the upper Reull Vallis system is equal to the volume of the downstream valley segments

$\sim 2,200 \text{ km}^3$  [14]. Assuming an average porosity of 0.3 [15] an upper-limit sediment to water ratio of 0.4 (the maximum volumetric sediment load which can be carried before the flood transitions to a debris flow; [16]), this translates to a minimum required water volume of  $\sim 2,310 \text{ km}^3$ . Finally, the flux required to sustain flow within the upper Reull Vallis system is estimated through the implementation of the Darcy-Weisbach equation [e.g. 17]. Peak flux estimates are derived from valley width, depth, and slope measurements from upper Reull Vallis assuming bankfull flow (which overestimates flow discharge, but provides a firm upper bound estimate) yielding a value of  $\sim 10^7 \text{ m}^3/\text{s}$ . Minimum flux estimates are derived by calculating the minimum discharge required for incipient bed sediment motion [e.g. 18], yielding a value of  $\sim 10^4 \text{ m}^3/\text{s}$ .

These geomorphologic characteristics place several constraints on the formation of Reull Vallis: 1) Formation post-dating Hesperian ridged plains emplacement. 2) Episodic release of water. 3) Release of water from the subsurface. 4) Subsidence of  $\sim 100\text{-}200 \text{ m}$  within the northern trough, with retention of the Hesperian ridged plains surface morphology. 5) Production and release of a minimum of  $\sim 2,310 \text{ km}^3$  of water. 6) Supply of a volumetric flux of water of  $\sim 10^4\text{-}10^7 \text{ m}^3/\text{s}$ .

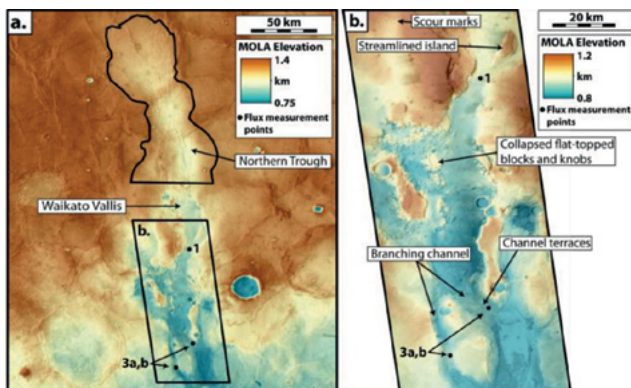


**Fig. 1.** (a.) The head of the upper Reull Vallis fluvial system within Hesperia Planum. The northern trough has been interpreted as the source for the water which carved the upper Reull Vallis system, which emerges abruptly as a fully-sized fluvial valley within Waikato Vallis. (b.) Inset panel from (a.) showing a portion of Waikato Vallis in CTX mosaic data with overlain gridded MOLA topography data. Fluvial and collapse/subsidence related features are indicated.

## FORMATION BY ICE SHEET LAVA HEATING & LOADING:

Having outlined these geomorphic formation constraints, the origin of the upper Reull Vallis system by ice sheet lava heating and loading is assessed. We find that an ice sheet lava heating and loading scenario involving the accumulation of thick lava flows ( $> \sim 100 \text{ m}$ ) atop regional ice sheets generally satisfies the morphologic formation criterion derived from the upper Reull Vallis outflow channel. The most consistent scenario involves sequential phases of melting of thin ice deposits, which re-accumulate under an ambient “icy highlands” climate [6-8] to undergo continual lava-ice interactions.

Meltwater production by this mechanism is predicted to occur after lava emplacement over timescales of  $\sim 1 \text{ kyr}$  [10], consistent with the first criterion. Successive events of lava emplacement would result in successive episodes of heating and melting and could account for the episodic nature of the upper Reull Vallis fluvial system, consistent with the second criterion. Water generated by top-down heating and melting due to supraglacial emplacement of lava flows would be expelled from below the superposed lava flows [10], thereby satisfying the third criterion. Ice sheet lava heating and loading is also predicted to result in subsidence of the superposed lava flows due to melting of the subjacent ice and removal of structural support [10]. This satisfies the fourth morphologic criterion requiring subsidence within the northern trough source area.

The cumulative volume of water which can be produced by the ice sheet lava and loading mechanism is dependent upon the area over which melting occurs and the thickness of ice available to melt. In order for melting confined within the bounds of the northern trough (approximately  $6,100 \text{ km}^2$ ) to supply the minimum  $2,310 \text{ km}^3$  of water, an average of  $\sim 980 \text{ m}$  of ice would need to be melted and removed throughout the depression (which would likely cause significantly more

subsidence than the observed ~100-200 m). If an average of 150 m (the approximate average depth of the trough) to 300 m (the approximate average predicted Late Noachian regional ice sheet thickness; [19]) of ice was removed from the subsurface, melting would have had to occur over an area of ~40,000 km<sup>2</sup> and ~20,000 km<sup>2</sup>, respectively (~1-2% of the total area of Hesperia Planum), though subsidence is not observed over these extended areas. The final morphologic criterion requires supply of a meltwater discharge of ~10<sup>4</sup>-10<sup>7</sup> m<sup>3</sup>/s. Estimates of top-down melting rates induced by ice sheet lava heating and loading [10], applied over the required melting areas (6,100-40,000 km<sup>3</sup>), provide maximum discharges on the order ~10<sup>4</sup> m<sup>3</sup>/s, sufficient to satisfy the final minimum discharge criterion.

## CONCLUSION:

We explored the potential genetic relationship between Hesperia Planum volcanism and the upper Reull Vallis fluvial system and assessed an ice sheet-lava heating and loading model as a potential alternative formation mechanism. We find that a scenario involving successive events of large-scale lava-ice interactions that melt thin ice deposits which then undergo re-deposition due to climatic mechanisms, best meets the upper Reull Vallis geomorphic criteria. This ice sheet lava heating and loading formation mechanism offers advantages over previous models in the ability to account for the wide array of geomorphic characteristics of the upper Reull Vallis system as well as in the ability to more readily supply the requisite volumes of water and discharges.

## REFERENCES:

- [1] Baker et al. (1992) Channels and Valley Networks, *Mars*, 493-522.
- [2] Carr (1996) *Water on Mars*, 1-248.
- [3] Carr (2002) *JGR Planets*, 107, 5131.
- [4] Hanna and Phillips (2005) *JGR Planets*, 110.
- [5] Russell and Head (2007) *PSS*, 55, 315-332.
- [6] Forget et al. (2013) *Icarus*, 222, 81.
- [7] Wordsworth et al. (2013) *Icarus*, 222, 1.
- [8] Wordsworth et al. (2015) *JGR Planets*, 120.
- [9] Head et al. (2002) *JGR Planets*, 107, 3.
- [10] Cassanelli and Head (2016) *Icarus*, 271, 237.
- [11] Squyres et al. (1987) *Icarus*, 70, 385.
- [12] Mest and Crown (2001) *Icarus*, 153, 89.
- [13] Ivanov et al. (2005) *JGR Planets*, 110.
- [14] Kostama et al. (2007) *JGR Planets*, 112.
- [15] Clifford (1993) *JGR Planets*, 98, 10973-11016.
- [16] Andrews-Hanna and Phillips (2007) *JGR Planets*, 112.
- [17] Wilson et al. (2004) *JGR Planets*, 109.
- [18] Lamb and Fonstad (2010) *Nature Geoscience*, 3, 477-481.
- [19] Fastook and Head (2015) *PSS*, 106, 82.

# THE PRINZ-HARBINGER SHIELD VOLCANO: A TRANSITION IN LUNAR VOLCANIC ERUPTION STYLE

E. R. Jawin<sup>1</sup>, J. W. Head<sup>1</sup>, M. A. Kreslavsky<sup>2</sup>, L. Wilson<sup>3</sup>

<sup>1</sup>Brown University, Providence, RI, USA, Erica\_jawin@brown.edu

<sup>2</sup>UC Santa Cruz, Santa Cruz, CA, USA

<sup>3</sup>Lancaster University, Lancaster, UK

## KEYWORDS:

Moon; Volcanism; Pyroclastic; Cooling-Limited; Effusive shield; Sinuous Rille

## INTRODUCTION:

The Aristarchus Plateau and the surrounding region contain some of the highest density of volcanic features on the lunar surface[1]. The Prinz-Harbinger region, ~100 km east of the Aristarchus Plateau, contains multiple sinuous rilles and is bound by Prinz crater to the southwest and Montes Harbinger to the northeast. In this work, we used a combination of visible images and topography data to observe the detailed stratigraphy and morphology of the Prinz-Harbinger region. Detrended topography data<sup>2</sup> reveal a complex volcanic feature spanning the Prinz-Harbinger region containing distinct surface textures that provide insight into the region's past. This feature is analyzed and a geologic history is summarized for the region.

The detrended topography data reveal a circular topographic rise in the central Prinz-Harbinger region ~80 km in diameter and over 500 m in height relative to the surrounding mare, with slopes generally between 0-2°. There is a well-defined boundary between the circular rise and the mare, and there is a textural contrast between the units, as the flanks of the circular rise contains linear grooves hundreds of meters wide extending for several kilometers. The smooth, topographically higher region of the Prinz-Harbinger region contains the highest density of sinuous rille source depressions in the region. The entire region has been mantled by pyroclastic material, as can be seen in Clementine VNIR spectral data.

We interpret this circular rise to have formed from cooling-limited extrusive volcanic flows. The circular rise is ~4600 km<sup>2</sup> in area, much larger than other lunar mare domes. These characteristics suggest that the cooling-limited flows necessary to form it were of higher effusion rates than was typical elsewhere on the Moon for smaller shields.

The grooved terrain appears morphologically similar to ejecta textures typical of crater formation, and was probably formed when a large crater, potentially Prinz crater, formed nearby and scoured the region.

Additional volcanic material was subsequently emplaced on the top portion of the circular rise, embaying the NE rim of Prinz crater and parts of the sculpted terrain. This volcanic material was either erupted from, or contributed to by, the formation of the sinuous rilles which flow directly downhill off the circular rise, and contributed lava to the surrounding plains. The density of sinuous rilles (representing higher-effusion rate eruptions<sup>3</sup> and lava composition on erosion rates during the formation of Rima Prinz", "container-title": "Journal of Geophysical Research: Planets", "page": "E00H14", "volume": "117", "issue": "E12", "source": "Wiley Online Library", "abstract": "Lunar sinuous rilles have long been interpreted as features that formed as the result of surficial lava flow, though the precise mechanism responsible for channel formation (constructed versus eroded origins) on the circular rise represent a shift in eruption conditions through time to higher effusion rates. Pyroclastic materials are expected to have been emplaced as a result of these high-effusion rate eruptions[4].

## REFERENCES:

[1] Zisk et al., *The Moon*, 17 (1977).

[2] Kreslavsky et al., *Icarus*, 283 (2017).

[3] Hurwitz et al., *JGR*, 117 (2012).

[4] Head & Wilson, *Icarus*, 283 (2017).

# SMALL LUNAR CRATER DEGRADATION: TIME SCALE AND MECHANISMS

B.A. Ivanov<sup>1</sup>

<sup>1</sup>Institute for Dynamics of Geospheres, Russian Academy of Science, Leninsky Prospect 38-1, Moscow, Russia, 119334. baivanov@idg.chph.ras.ru

## KEYWORDS:

Crater degradation, bombardment rate, Apollo landing sites, LROC images.

## INTRODUCTION:

New LROC images and DTM [1, 2, 3] allow us to analyze size-frequency distributions of small lunar craters (diameters less than ~100m) in the equilibrium state for craters with the given level of degradation. This analysis gives estimates of absolute time of degradation. The degradation rate varies from site to site, giving better knowledge of the lunar subsurface geology and modern surface processes. Also new demands for mechanical models of the crater degradation might be formulated.

## SMALL CRATER DEGRADATION MEASUREMENTS:

We use published data [2, 3] and additional measurements with LROC DTMs to establish general trends of crater degradation at Apollo landing sites. The state with  $d/D=0.06$  and the corresponding internal crater slope  $\alpha=11^\circ$  is taken the reference state. The number of craters with given  $d/D$  and  $\alpha$ , normalized to the crater number at the reference state gives a proxy for the relative time  $t/T_{0.06} \approx N(d/D)/N(0.06)$ . An example is shown in Fig. 1 for the Apollo 17 site.

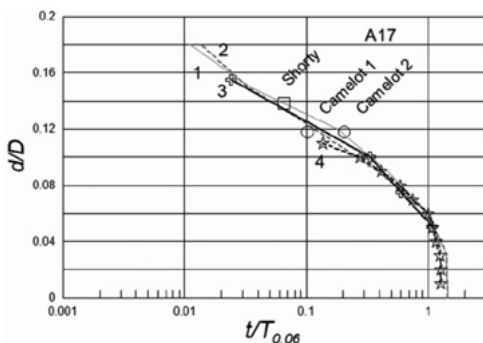


Fig. 1. The general trend of degradations at the Apollo 17 landing site. 1 and 2 – Lunokhod 1 and 2 areas [2], 3 – [3], 4 – this work, open square – crater Shorty, open triangles – two possible positions for Camelot crater.

## ABSOLUTE TIME ESTIMATES:

Absolute times to reach the reference state of degradation are estimated with (1) the standard Neukum's chronology, assuming the equilibrium crater areal density, and (2) by fitting measured  $d/D$  and  $\alpha$  values for a few craters dated with returned Apollo samples to the general local trends (exampled on Fig. 1).

The summary of results is shown in Fig. 2. Some of dated Apollo craters are too young and have  $d/D$  outside the reliable measured local trends. A15 crater at Station 9 may be an anomalous (secondary?), or simply poorly resolved at the available DTM with 2 m/pix resolution. Other craters illustrate factor of 3 dispersion around values, estimated with Neukum's chronology.

The assumption that  $T_{0.06}$  is proportional to the crater diameter  $D$  seems to be valid, in general, with some increase for  $D>100m$ .

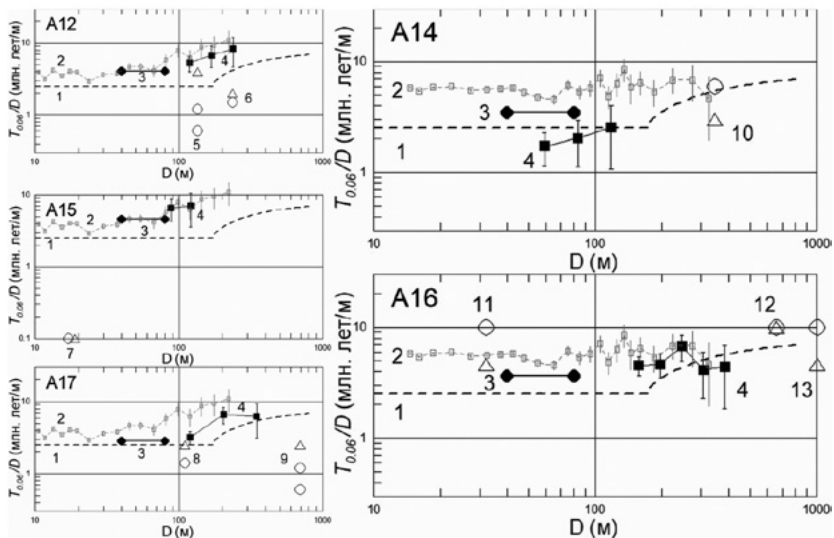


**Fig. 2.** Estimates of the normalized time,  $T_{0.06}/D$  (vertical axis in Myr/m), to reach the degradation state with  $d/D=0.06$  for Apollo landing sites labeled in each plate. Horizontal axis in meters. Estimates based on Neukum's chronology: 1 – [4]; 2 - crater areal densities based on [5] for maria (A12, A15, A17) and on [6] for highlands (A14, A16),  $d/D$  is not defined; 3 – [3], 4 – this work. Dated Apollo craters: 5 - Head, 6 - Surveyor, 7 - (anomaly) Station 9, 8 - Shorty, 9 - Camelot, 10 - Cone, 11 - Plum, 12 - South Ray (preliminary), 13 - North Ray (open circles –  $d/D$  trends, open triangles – slope trends).

## CONCLUSIONS:

1. The comparison of general trends of crater's degradation with dated craters at Apollo landing sites shows a good coincidence with the bombardment flux estimates based on Neukum's chronology.
2. The normalized time,  $T_{0.06}/D$ , to reach the  $d/D=0.06$  degradation state varies from  $\sim 2$  Myr/m to  $\sim 10$  Myr/m for various landing sites. On lunar mare, we see a tentative trend for an increase of  $T_{0.06}/D$  for craters with  $D > 100$  m.
3. "Sandblasting" regolith transport is not the main agent in the late degradation, as bombardment rate is independent of the location.

## ACKNOWLEDGEMENTS:

The project is supported by Russian Academy of science Presidium's Program 7P.

## REFERENCES:

- [1] M. Robinson, et al. Lunar Reconnaissance Orbiter Camera (LROC) instrument overview, (2010) // Space science reviews. 2010. V. 150. No. 1. P. 81-124.
- [2] Basilevsky, A.T. et al. Morphometry of small impact craters in the Lunokhod-1 and Lunokhod-2 study areas. Planetary and Space Science. 2014. V. 92. P. 77-87.
- [3] Mahanti, P. et al. Small crater degradation at the Apollo landing sites - characterizing differences in degradation rates. LPSC 48<sup>th</sup>. Houston, USA. Abs. #2089.
- [4] Basilevsky, A. T. On the evolution rate of small lunar craters // 7<sup>th</sup> Lunar and Planetary Science Conference Proceedings, edited by R. B. Merrill. 1976. P. 1005-1020.
- [5] Gault, D. E. Saturation and equilibrium conditions for impact cratering on the lunar surface: Criteria and implications. // Radio Science. 1970. V. 5. P. 273-291.
- [6] Shirley, K. A. et al. Crater size-frequency distribution measurements and age of the Compton-Belkovich Volcanic Complex. // Icarus. 2016. V. 273. P. 214-223

# MORPHOMETRIC CATALOGUE OF LUNAR CRATERS 1-10 KM IN DIAMETER

N.A.Kozlova, I.Yu. Zavyalov, M.M. Kolenkina  
 MIIGAIK Extraterrestrial Laboratory (MExLab), Moscow State  
 University of Geodesy and Cartography (105064, Moscow,  
 Gorokhovskiy per, 4, natally.ko@gmail.com)

## KEYWORDS:

The Moon, Crater, Crater catalogue, Morphometry, GIS.

## INTRODUCTION:

The goal of the study is to provide global morphometric catalogue of lunar craters for scientific public use and at the same time to automatize the process of morphometric characterization of craters.

## THE STUDY:

We base on global data products with resolution about 100 m/pixel obtained by LRO mission: WAC global mosaics and GLD100 [1]. That explains the smallest size of the considered craters as 1 km (10 pixels). The largest craters in the developing catalogue are 10 km in diameter, because bigger craters already have morphologic description [2].

Identification of craters is carried out manually on image mosaics using ArcGIS *CraterTools* instrument [3]. Then morphometric parameters of the craters are calculated by means of two program modules: *dD Calculation* [4] and *CraMo* [5].

## THE FIRST RESULTS:

We have finished catalogization of craters in polar areas (up to 60 degrees latitude). Because of complicated lunar relief and imposed or half-destroyed craters in some cases automatic morphometric measurements fail. Due to different algorithms used in the two implemented program modules, their results can complement each other (Fig. 1).

Now we are working on equatorial zone.

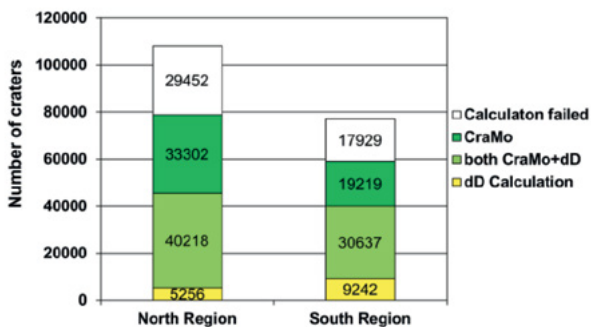


Fig. 1. First results of automatic morphometric measurements of lunar craters in polar areas. The diagram shows how many craters have calculated morphometry using each software module.

## ACKNOWLEDGMENTS:

The work has received funding from Russian Foundation for Basic Research (RFBR), Project No. 16-37-00323 mol\_a.

## REFERENCES:

- [1] [http://wms.lroc.asu.edu/lroc/view\\_rdr/WAC\\_GLOBAL](http://wms.lroc.asu.edu/lroc/view_rdr/WAC_GLOBAL)
- [2] Rodionova Zh.F., Karlov A.A., Skobeleva T.P., Konotopskaya E.V., Shevchenko V.V., Kozubstky K.E., Dekhtyareva K.I., Smolyakova T.F., Tishik L.I., Fedorova E.A. (Edited by Shevchenko V.V.) Morphological catalog of craters of the Moon. - Moscow: Publishing House of Moscow State University, 1987. 173 p.
- [3] Kneissl T., van Gasselt S., Neukum G., Map-projection-independent crater size-re-

quency determination in GIS environments – New software tool for ArcGIS, *Planetary and Space Science*, 59, 1243-1254, DOI: 10.1016/j.pss.2010.03.015, 2011.

[4] Kokhanov A.A., Kreslavsky M.A., Matveev E.V., Kozlova N.A., Karachevtseva I.P. Automatization of morphometrical measurements in GIS for estimation of local characteristics of lunar relief. *Ecology, economics, informatics. Collection of articles: in 3 T.-Rostov-on-Don, Publishing House of Southern Federal University. T. 3: Geoinformation technologies and space monitoring*, 2015, p. 166-171, [http://conf-durso.ru/docs/gis\\_1\\_2015.pdf](http://conf-durso.ru/docs/gis_1_2015.pdf).

[5] Kokhanov A.A., Kreslavsky M.A., Karachevtseva I.P. 2015. Small impact craters in the polar regions of the Moon: peculiarities of morphometric characteristics. *SolarSystem Research*. 49 (5): 295-302. (doi:10.1134/S0038094615050068).



# ORIENTALE SECONDARY CRATERS: INSIGHTS INTO ORIENTALE IMPACT PARAMETERS AND THE LARGEST SECONDARY CRATER SIZE OF THE SOUTH POLE-AITKEN BASIN EVENT

Dijun Guo<sup>1,2,3</sup>, Jianzhong Liu<sup>1</sup>, James W. Head<sup>3</sup>

<sup>1</sup>Center for Lunar and Planetary Science, Institute of Geochemistry, Chinese Academy of Sciences, 99 Lincheng West Road, Guiyang 550051, China, liujianzhong@mail.gyig.ac.cn.

<sup>2</sup>University of Chinese Academy of Sciences, Beijing 100049, China.

<sup>3</sup>Department of Earth, Environmental and Planetary Sciences, Brown University, Providence, RI 02912 USA, james\_head@brown.edu

## KEYWORDS:

Secondary crater, Orientale, South Pole-Aitken, impact angle, impact direction

## INTRODUCTION:

Secondary craters (or secondaries) represent the craters formed by the impact of fragments ejected from the primary impact, generally occurring beyond the continuous ejecta deposit [1-3]. As one of the youngest lunar basins, Orientale basin has the best-preserved secondary craters and other ejecta facies among basins of comparable scale [4, 5]. The characteristics and distribution of its secondaries can form a paradigm for other large basins on the Moon. Because post-basin mare lava flooding to the east of Orientale has buried original ejecta deposits, secondary crater distribution provides an additional approach to recognize the distribution of Orientale ejecta, from which the parent impact parameters, such as projectile approach direction and angle can be speculated.

## DETECTING ORIENTALE SECONDARY CRATERS:

We report on our investigation of Orientale secondary craters carried out in the area as far as 6 R (R = Orientale radius) from the Orientale basin rim, i.e. Monte Cordillera. To display better the spatial distribution of secondaries, the area of investigation is divided into small annular sectors with each annular sector being half of an Orientale radius wide in radial direction and 20 azimuthal degrees wide in the concentric direction (Figure 1).

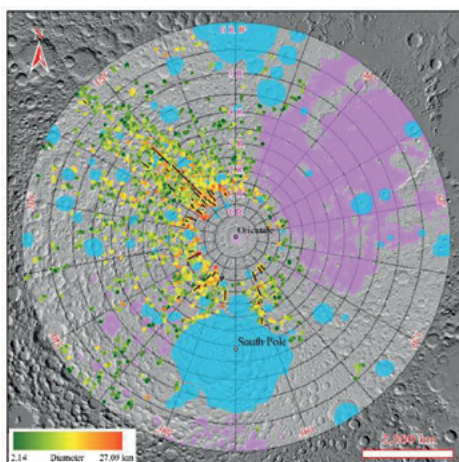


**Fig. 1.** Locations of 2728 identified Orientale secondary craters; red color indicates larger diameter and green color represents smaller diameter. Secondary chains are marked with short black lines radial to Orientale. The purple shaded area designate that mare basalt was emplaced in these regions. Blue shaded areas are interference zones where the secondaries are subdued or the light condition does not support crater identification. Basemap is hill-shade image from LOLA. The map is in stereographic auxiliary projection centering at Orientale center (95° W, 19° S).

We identified 2728 secondary craters with diameters (D) ranging from 2.14 km to 27.09 km in a total area of  $\sim 1.66 \times 10^7$  km<sup>2</sup> (Figure 1). The results suggest that secondaries are concentrated in the northwest and their diameter decreases as distance increases. There are 47 secondary chains identified (Figure 1), whose lengths range from 27 km to 410 km, and are 128.7 km long on average.

## ORIENTALE IMPACT SCENARIO:

The diameter and density of secondaries are inhomogeneous with azimuth angle, indicating the heterogeneities of ejecta deposits with respect to azimuth (Figure 1, Figure 2). It is obvious that mean diameter does not closely relate to azimuth, while the density dramatically varies in different sectors.

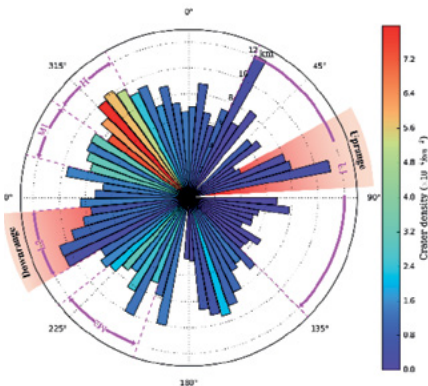


**Fig. 2.** Density and average diameter of secondaries located in different azimuthal bins. Each bar represents a sector of 5 azimuthal degrees wide in a concentric sense. The color of the bar represents density, and the length represents average diameter. H-high density, M1 and M2-medium density, L1 and L2-low density. The azimuth range of the estimated uprange and downrange of Orientale basin impact directions are shown.

## IMPACT DIRECTION

As show in Figure 2, the density of secondaries can be subdivided into five regions: the northwest high-density region (H) and medium-density region (M1), the southwest medium-density region (M2), the wide low-density area (L1) in the east side and the other narrow low-density area (L2) in the west. H region (305° to 330°) and M2 region (200° to 230°) show an approximately bilateral symmetry, indicating the downrange of Orientale impact direction was about the azimuth of 265°. Considering that the density of M1, next to H, is apparently higher than most of the other regions, and that the existence of the very low density area around 240°, the downrange direction of impact could be south to azimuthal 240°. In conclusion, the Orientale impact downrange direction could be 240° to 265°, therefore the uprange could be 60° to 85° (Figure 2)

## IMPACT ANGLE

The secondary crater density discrepancy at different azimuthal angles implies that the pattern of Orientale ejecta is between the planform characteristics of (1) offset and concentrated cross-range and (2) forbidden zone [6, 7]. On the Moon, the transition angles of offset, forbidden zone and butterfly are 45°, 25° and 10° respectively, but the transition angle of offset and concentrated cross-range is unknown [6], therefore the incidence angle of Orientale impact is in the range of 25 to 45 degree. Considering the incidence angle for offset and concentrated cross-range ejecta planform is lower than the gentle offset planform, the upper limit of incidence angle could be smaller than 45°.

## ESTIMATE THE LARGEST SECONDARY CRATERS OF SOUTH POLE-AITKEN:

Several previous studies of secondary craters [1, 4, 8, 9] make it possible to obtain the scaling relationship of the largest secondary craters and their parent craters on the Moon, as shown in

Figure 3 (A). Because the ratio of largest secondary crater diameter ( $d_s$ ) to parent transient cavity diameter ( $d_p$ ) decreases with increasing in primary diameter, the largest secondary diameter versus parent diameter is separated into two groups (Figure 3). The relationship of  $d_s$  and  $d_p$  for large craters is (Figure 3, B), which can be used to estimate  $d_s$  of the heavily degraded South Pole-Aitken (SPA) basin. Estimates of the transient cavity diameter of the SPA basin ranges from 840 km to 2500 km according to different estimations, corresponding to a diameter range of the largest secondary crater of 29.7 km to 49.5 km. The study of Garrick-Bethell and Zuber [10] reveals that the major axis of SPA outer ring is 2400 km, therefore we infer that the largest secondary crater of South Pole-Aitken basin is not greater than 40 km in diameter.

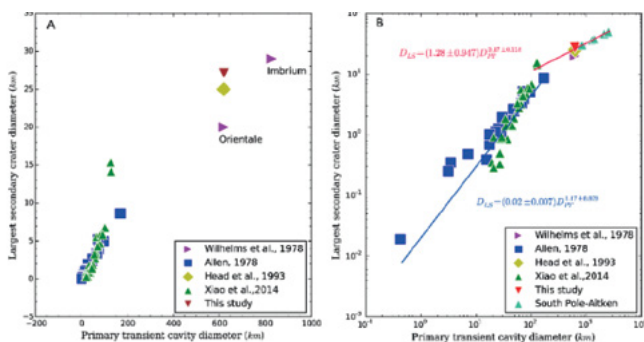


Fig. 3. The largest secondary crater diameter versus transient cavity diameter of parent crater (A) and power law fits (B). Power law fits are separately made for small primary craters (equation in blue) and large primary craters (equation in pink).

## REFERENCES:

- [1] Xiao, Z.Y., et al., Comparisons of fresh complex impact craters on Mercury and the Moon: Implications for controlling factors in impact excavation processes // *Icarus*. 2014. V. 228. No. P. 260-275.
- [2] Schultz, P.H. and J. Singer. A comparison of secondary craters on the Moon, Mercury, and Mars // 11th Lunar and Planetary Science Conference. 1980. P. 2243-2259.
- [3] Xiao, Z.Y., Size-frequency distribution of different secondary crater populations: 1. Equilibrium caused by secondary impacts // *Journal of Geophysical Research-Planets*. 2016. V. 121. No. 12. P. 2404-2425.
- [4] Head, J.W., et al., Lunar Impact Basins: New Data for the Western Limb and Far Side (Orientale and South-Pole Aitken-Basins) from the 1st Galileo Flyby // *Journal of Geophysical Research-Planets*. 1993. V. 98. No. E9. P. 17149-17181.
- [5] Fassett, C.I., et al., Thickness of proximal ejecta from the Orientale Basin from Lunar Orbiter Laser Altimeter (LOLA) data: Implications for multi-ring basin formation // *Geophysical Research Letters*. 2011. V. 38. No. L17201.
- [6] Herrick, R.R. and N.K. Forsberg-Taylor, The shape and appearance of craters formed by oblique impact on the Moon and Venus // *Meteoritics & Planetary Science*. 2003. V. 38. No. 11. P. 1551-1578.
- [7] Herrick, R.R. and K.K. Hessen, The planforms of low-angle impact craters in the northern hemisphere of Mars // *Meteoritics & Planetary Science*. 2006. V. 41. No. 10. P. 1483-1495.
- [8] Wilhelms, D.E., V.R. Oberbeck, and H.R. Aggarwal. Size-frequency distributions of primary and secondary lunar impact craters // 9th Lunar and Planetary Science Conference. 1978. P. 3735-3762.
- [9] Allen, C.C., Large lunar secondary craters: Size-range relationships // *Geophysical Research Letters*. 1979. V. 6. No. 1. P. 51-54.
- [10] Garrick-Bethell, I. and M.T. Zuber, Elliptical structure of the lunar South Pole-Aitken basin // *Icarus*. 2009. V. 204. No. 2. P. 399-408.

# GLOBAL DEGASSING PRODUCING FORMATION IN CRUST OF HYDROCARBON CONCENTRATIONS, KIMBERLITES, AND ALKALINE ROCKS

G.G. Kochemasov

*IGEM of the Russian Academy of Sciences, 35 Staromonetny, 119017 Moscow, RF, kochem.36@mail.ru*

## KEYWORDS:

asthenosphere, degassing, crust, basalts, hydrocarbons, diamonds, kimberlites, alkaline rocks, Earth rotation rates

“Orbits make structures” – a main point of the new wave planetology based on one important property of the keplerian elliptical planetary orbits. The ellipticity implies periodical changes of accelerations and, thus, orbital forces structuring cosmic bodies. The Earth and the Moon sharing the same circumsolar orbit have similar main structural features. among them there are terrestrial Oceans and lunar Basins. The most obvious are two tectonic triads: Pacific Ocean – Malay Archipelago – Indian Ocean on Earth and Procellarum Basin – Mare Orientale – SPA Basin on the Moon. Basalts cover the planetary depressions of both bodies, but basaltic effusions are drastically different in age: the AR on Moon and Mz-Cz on Earth. These ages well correlate with the body masses. The more massive and inert Earth has heated and melted mantle much later (the Newton’s law of inertia). Energy of movement transfers to the heat energy.

The Earth and Moon’s subsided hemispheres, for keeping angular momenta of hemispheres equal, are filled with dense basaltic material. However, times of the fillings are significantly different. The Earth-Moon system expands with time. This means increasing its angular momentum. A natural response to it is in slowing down rotation of both bodies diminishing their angular momentum (action - opposite action). Diminishing momenta are compensated by melting and uplifting to surfaces dense basaltic material [1]. However, on the Moon it happened much earlier (4.5-3 billion years ago) because of diminished inertia of the small mass satellite. At Earth - much larger and massive body than Moon – 81 times – it happened much later. (3-4.5 billions):  $81 = 37-55$  million years. According to this calculation, a “peak” of the basaltic reaction of Earth, filling in by basalts of oceanic depressions is in the boundary of Mesozoic and Cenozoic.

Enormous heating of terrestrial lithosphere documented by thick planetary wide asthenosphere (stable and thick in oceanic tectonic blocks) leads to massive liberation (release) of volatiles, among them H<sub>2</sub>, CH<sub>4</sub>, N<sub>2</sub>. They penetrate in the upper solid geosphere making large concentrations of hydrocarbons in form of conventional deposits in “voids” and occurrences in slates and oceanic bottom ices. ages of hydrocarbon deposits are mainly Mesozoic (70% Mesozoic in age, 20% Cenozoic, 10% Paleozoic) and well agree with the episode of global heating and effusions of oceanic basalts [1]. These events are not occasional but tied causatively. This means that origin of hydrocarbon deposits is mainly inorganic though some decomposition of organic matter in sedimentary rocks also exists. Flux of volatiles could accelerate the organic decay.

Another unexpected coincidence of the global heating, basalt “explosion”, hydrocarbon concentrations and kimberlite magmatism is evident and impressive. thick “roots” of Archean cratons, massive lithosphere help to keep certain volumes of volatiles strongly pressed. Overcoming enormous pressure of the upper lithosphere strongly squeezed fluids (“fluidizites”, according to prof. A. M. Portnov) find way up using narrow cracks. Reaching upper predominantly sedimentary layers with small pressure the fluids explode making kimberlite “cones”, pipes. methane, meeting oxygen, burns to CO<sub>2</sub> and H<sub>2</sub>O producing usual in kimberlites serpentines. In some very rare cases (3 to 5 % of kimberlite pipes) carbon is not burned totally and precipitates as crystalline substance – diamond. Normally it keeps ideal angular shapes proving that it do not suffered long hard way out of the mantle –asthenosphere (other hard minerals often are rounded). Diamond age normally judged by seized inclusions is much older than kimberlites, but actually it is comparable to the host kimberlites. Now the low pressure and very transparent diamonds were obtained from vapor in experiments [3]. Many years ago prof. A.M. Portnov proposed and substantiated this way to origin of natural kimberlites and diamonds [4].

A very important fact concerns the global distribution of alkali magmatism. It starts about 2.5-2.7 billion y. ago [2, fig. 3] and covers all periods up to Present but with very pronounced maximum in the Phanerozoic (0-600 mln. y. ago). within this period the last 200 mln. y. (Mz-Cz) are the most productive. one could note that the especially rich in alkalis (Na, K) and volatiles apgaitic syenites tend to be relatively old (large devonian Lovozero and Khibina massifs of Kola peninsula, permian Oslo rift, Norway intrusions, mesoproterozoic-1100 mln.y. lilimaussaq complex in south Greenland) (5). It means that easily melted apgaitic melts were produced at the very beginning of the asthenosphere formation when temperatures were not relatively high. At the later stages with the higher temperatures the asthenosphere produced enormous masses of less alkaline melts.

Not random coincidence of the global basalt "explosion", degassing and hydrocarbon concentrations in the crust, alkaline and kimberlite magmatism means that these terrestrial global geologic processes are closely tied. the asthenosphere formation due to transition of the mechanical orbital energy to the heat energy is in a basis of these geologic processes. It is interesting that the "age of dinosaurs", "age of conifers", appearance of birds and first mammals coincide with mentioned above Mesozoic "maxima".

Transition of large masses of materials to the crust from mantle with increasing angular momentum of Earth naturally requires slowing planet's rotation to keep existing angular momentum. One observes a sharp slowing of rotation in the Phanerozoic eon (fig.4).

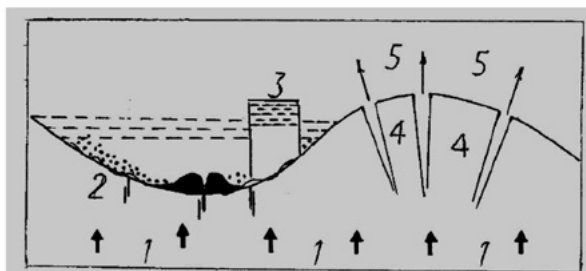


**Fig. 1.** Scheme of hydrocarbon degassing of Earth (1) with a principal difference between uplifted and subsided tectonic blocks (for the fundamental wave these are two hemispheres-segments). 2- crumpling and faulting, "squeezing" basalts in middle-ocean ridges, gas hydrate formation (points). 3- uplifted continents of the subsided hemisphere with "slate barriers" on continents impregnated with slate gases and light oil. 4- broken by cracks-rifts uplifted block enriched with less movable liquid hydrocarbons as a result of intensive degassing (5).

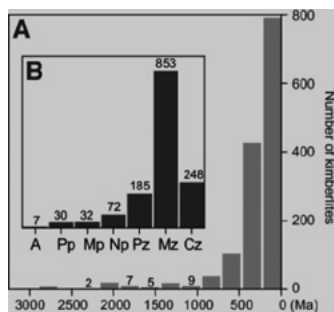


**Fig 2.** Histogram of kimberlite ages based on the compilation of Faure, 2006-a-ages.

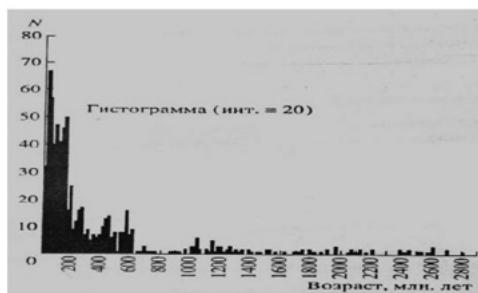


**Fig. 3.** Distribution of alkaline rocks with time. n-number of massifs [2]

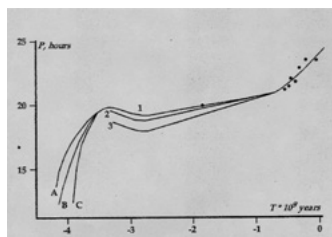


**Fig. 4.** Change of the Earth's rotation with time according to various scenarios



**Fig. 5.** Recent methane explosion on Yamal Pen. Degassing goes on.

## REFERENCES

- [1] Kochemasov G.G. New planetology and geology: tectonic identity and principal difference of terrestrial oceans and lunar basins // *New Concepts in Global Tectonics (NCGT) Journal*, 2017, V. 5, # 1, p 131-133.
- [2] Kogarko L.N. and Khain V.E. Alkaline magmatism in the Earth's history: geodynamical interpretation // *Doklady of the Academy of Sciences*, 2001, Tome 377, # 5, p. 677-679 (In Russian).
- [3] Meng Yu-fei, Yan Chih-shine, Krasnicki S.....Hemley R.J. High optical quality multi-carat single crystal diamond produced by chemical vapor deposition // *Physica status solidi (a)*, v. 209, Issue 1, p. 101-104, January 2012. DOI: 10.1002/pssa.201127417.
- [4] Portnov A.M. . Secrets of origin of diamond and gold deposits // *Industrial registers*, # 7-8, July-August 2012 (In Russian).
- [5] Sorensen H. The agpaitic rocks; an overview // *Mineralogical Magazine*, 1997, v. 61, # 4, 485-498.

# ORBITAL ENERGY AS A MAIN SOURCE FOR SHAPING AND STRUCTURING COSMIC BODIES

To the 60th anniversary  
of the First satellite launch  
and the Start of Space era.  
To the 80th anniversary  
of the Chkalov flight  
over North Pole from  
the USSR to USA.

**G. G. Kochemasov**

*IGEM of the Russian Academy of Sciences, 35  
Staromonetny, 119017 Moscow, RF, kochem.36@mail.ru*

## KEYWORDS:

Orbital energy, Cosmic bodies, tectonics, structures, waves, impacts.

The classical planetology considers impacts as a main source of energy reworking surfaces and partly the deeper spheres of celestial bodies. However a region or regions of origin of impacting objects affecting all without exception planetary bodies in all parts of the Solar system is poorly understood. At the same time, planetologists now have several tens of images of full discs of these bodies. Distribution patterns of "impact traces" – craters in many of them are surprisingly regular. They show alignments, regular grids not related to random hits expected from impacts but rather require more regular and ubiquitous structuring force. Moreover, such regular patterns appear in the outer gaseous spheres of some bodies including the Sun's photosphere (Fig. 1).

It was shown earlier (Kochemasov, 1995-2013) [1, 2] that such regular patterns appear due to warping action of inertia-gravity waves affecting all bodies moving in keplerian elliptical orbits (Fig. 2). Periodically changing accelerations of celestial bodies cause their wave warping having in rotating bodies (but all bodies rotate!) four ortho- and diagonal directions. An interference of 4 directions of standing waves brings about a regular net of uprising, subsiding and neutral tectonic blocks. Naturally polygonal in details they appear as rings in cosmic images. This is one of reasons why they often are confused with round impact craters and essentially disfigure their statistics.

A fundamental nature of the wave woven nets of even sized round "craters" (granules) is dependence of the "crater" sizes on orbital frequencies of bodies. The lower frequency the larger size, the higher frequency the smaller granule sizes. One could compare 5 bodies with widely differing orbital frequencies, sizes and compositions: Titan (1/15.94days), Callisto (1/16.69), Moon (1/27.32), Mercury (1/87.97), Earth (1/365.3). Moon (1/27.32), Mercury (1/87.97), Earth (1/365.3). Images of their discs "peppered" with round features diameters of which precisely correspond to their orbital frequencies witness that such tectonic patterns can originate due to orbital energies. "Orbits make structures" – this short notion adequately reflects the expressed above observations (Fig. 1).

The existing correspondence between orbital frequencies and tectonic granulations proving the structuring role of orbital energy was earlier noted in comparative planetology of the terrestrial planets. The row of Mercury, Venus, Earth, Mars, and asteroids with decreasing orbital frequencies is remarkable by increasing relative sizes of tectonic granules, relief ranges, iron content in lowland basalts and decreasing atmospheric masses from Venus to Mars.

In summary, firmly established tectonically identical structural features observed in cosmic bodies of various classes, sizes, compositions (Fig. 1) underline important role of external structuring energy. It presents itself as the orbital mechanical energy. In full consent with the classical physics, the mechanical energy transfers into heat energy of cosmic bodies influencing their tectonics. That is why extremely frozen and small body as Pluto has comparable tectonic structures with large full of inner energy planets as Earth. Recently appeared paper [3] shows comparable tectonic structures in Earth and Moon, Earth and Mercury.

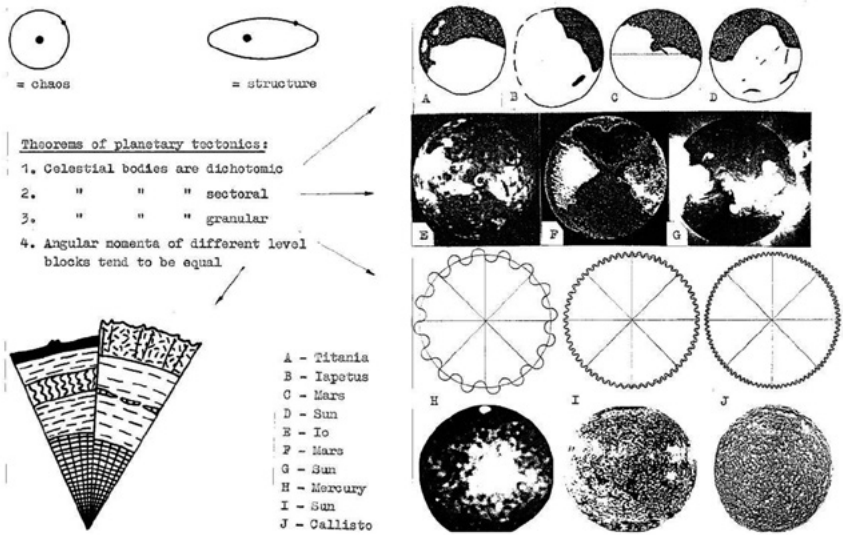


**Fig. 1.** Wave woven tectonic segments, sectors, and granules in cosmic bodies of various sizes, states, and compositions [1]

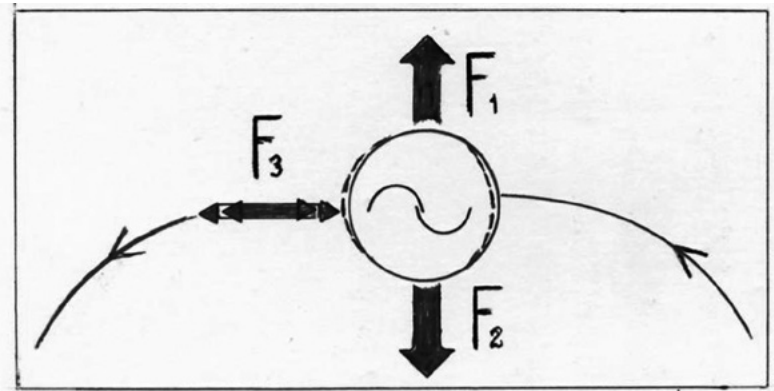


**Fig. 2.** Forces acting upon a celestial body moving in an elliptical keplerian orbit. F1-centrifugal, F2-gravity, F3- varying orbital force making a body to oscillate and produce structures (Fig. 1).

## REFERENCES

- [1] Kochemasov, G.G. Tectonic dichotomy, sectoring and granulation of Earth and other celestial bodies // Proceedings of the International Symposium on New Concepts in Global Tectonics, "NCGT-98 TSUKUBA", Geological Survey of Japan, Tsukuba, Nov 20-23, 1998, 144-147.
- [2] Kochemasov, G.G. Theorems of wave planetary tectonics.// Geophys. Res. Abstr., v.1, no. 3, p. 700.
- [3] Kochemasov G.G. New planetology and geology: tectonic identity and principal difference of terrestrial oceans and lunar basins // New Concepts in Global Tectonics (NCGT) Journal, 2017, V. 5, # 1, p 131-133.



# ON ATTENUATION OF TORSIONAL OSCILLATIONS ON MARS

T.V. Gudkova<sup>1</sup>, V.N. Zharkov<sup>1</sup>, A.V. Batov<sup>2</sup>

<sup>1</sup>Schmidt Institute Physics of the Earth RAS, B.Gruzinskaya, 10, Russia, gudkova@ifz.ru

<sup>2</sup>Institute of Control Sciences of RAS, 65 Profsoyuznaya street, Moscow, Russia

## KEYWORDS:

dissipative factor, attenuation, free oscillations, interior structure, Mars

## INTRODUCTION:

At present the scientists who study Mars are looking forward to the seismic study of Mars. As a result of preparing for the experiment, the papers in which seismic fields in the Martian interiors due to marsquakes are modeled [1-4]. In studies [5, 6] an attempt to model the distribution of the dissipative factor of Mars  $Q(l)$  has been made. The periods of free oscillations of a planet are its important physical characteristics. If during the seismic experiment of mission InSight [4] an event with low enough number of oscillation is recorded, the problem of interior structure of the planet and the distribution of the dissipative factor could be significantly moved forward.

## INTERIOR STRUCTURE MODEL:

For numerical modeling we take two interior structure models M\_50 and M\_100 with the crust thickness of 50 and 100 km, respectively [5, 6]. The mean density ( $\rho_{\text{crust}}$ ), the crust thickness ( $l_{\text{crust}}$ ), mantle ferric number Fe# ( $\text{Fe\#} = \text{Fe}^{2+} / (\text{Fe}^{2+} + \text{Mg}) \times 100$ ), the hydrogen content in the core ( $H_{\text{core}}$ ), the core radius ( $r_{\text{core}}$ ), the pressure at the core-mantle boundary ( $P_{\text{core}}$ ), weight Fe/Si ratio, the content of Fe in the planet, normalized moment of inertia ( $I/MR^2$ ), and elastic Love number  $k_2^S$  for these models are given in the table.

**Table.** Parameters of trial interior structure models of Mars

Model	$\rho_{\text{crust}}$ kg/m <sup>3</sup>	$l_{\text{crust}}$ km	Fe# mantle	$H_{\text{core}}$ mol. %	$r_{\text{core}}$ km	$P_{\text{core}}$ (GPa)	Fe/ Si	Fe total, wt. %	$I/MR^2$	$k_2^S$
M_50	2900	50	20	70	1821	19.0	1.8	27.8	0.3639	0.162
M_100	2900	100	22	80	1870	18.4	1.9	29.5	0.3639	0.170

## CALCULATION OF TORSIONAL AND SPHEROIDAL OSCILLATIONS SPECTRA:

The method of free oscillations calculations is described in detail in [7, 8]. Functions proportional to vertical displacements of spheroidal oscillations  ${}_0U(r)$  and horizontal displacements of torsional oscillations  ${}_0W_l(r)$  for M\_50 model are shown in fig. 1. Qualitatively free oscillations sound the depth of a planet where the displacements  $\leq 0.3$ .

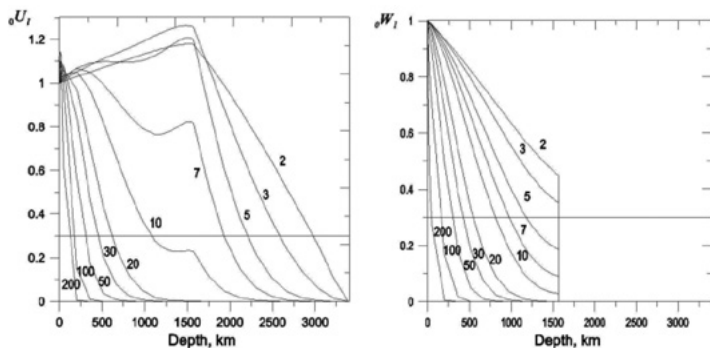


**Fig. 1.** Functions  ${}_0U_l(r)$ , proportional to vertical displacements of spheroidal oscillations (on the left) and horizontal displacements of torsional oscillations  ${}_0W_l(r)$  (on the right) for fundamental tones,  $n=2-200$  along the depth. At the surface  ${}_0U_p$  and  ${}_0W_l$  are normalized to unity.

## ATTENUATION OF TORSIONAL OSCILLATIONS:

Let  $k_0$  be the dimensionless eigenfrequency of torsional oscillations for a model with the dimensionless density  $\rho_0(x)$  and the dimensionless shear modulus  $\mu_0(x)$ . Introducing some corrections to these values  $\rho(x)=\rho_0(x)+\Delta\rho(x)$ ,  $\mu(x)=\mu_0(x)+\Delta\mu(x)$ , we obtain new values of the  $k=k_0+\Delta k$ . When  $\Delta\rho \ll \rho_0$ ,  $\Delta\mu \ll \mu_0$ , we have [9]

$$\Delta k = \sum_{i=1}^S [k_{\rho_i} \Delta\rho_i + k_{\mu_i} \Delta\mu_i], \quad (1)$$

where  $i$  is the layer number,  $S$  is the total number of solid layers in the model,

$$k_{\rho_i} = \left( \frac{\partial \Delta k}{\partial \Delta \rho_i} \right) = - \frac{k_0}{2} \frac{\int_{x_{i-1}}^{x_i} x^2 z_{10}^2 dx}{\int_0^{x_{i-1}} x^2 \rho_0 z_{10}^2 dx}, \quad (2)$$

$$k_{\mu_i} = \left( \frac{\partial \Delta k}{\partial \Delta \mu_i} \right) = - \frac{1}{2k_0} \frac{\int_{x_{i-1}}^{x_i} [x^2 z_{20}^2 / \mu_0^2 + (\ell^2 + \ell - 2) z_{10}^2] dx}{\int_0^{x_{i-1}} x^2 \rho_0 z_{10}^2 dx}. \quad (3)$$

Here  $\Delta\rho_i$  and  $\Delta\mu_i$  are the constant increments to  $\rho_0$  and  $\mu_0$  at the  $i$ th ( $x_{i-1}$ ,  $x_i$ ) layer of the considered model,  $z_{10}$  and  $z_{20}$  are dimensionless functions  $W/r$  and  $\mu(dW/dr-W/r)$ , respectively. According to the seismic waves profiles of model M 50, we consider the planetary model consisting of seven zones along the radius: 0-1821, 1821-1934, 1934-2215, 2215-2725, 2725-3185, 3185-3339.5 and 3339.5-3389.5 km ( $i=1-7$ ). Coefficients  $k_{\rho_i}$  and  $k_{\mu_i}$  are numerically calculated.

For the model of Mars with piecewise-constant distributions of  $\rho$  and  $\mu$ , the dissipative factors  $Q_{Tj}$  for torsional modes can be calculated as [10]

$$Q_T^{-1} = \frac{2}{k_0} \sum_{i=1}^S \frac{k_{\mu_i} \mu_{0i}}{Q_{\mu_i}}, \quad (4)$$

where the indices  $j$  and  $l$  are omitted for all the quantities;  $\mu_{0i}$  is the value of the dimensionless shear modulus in the  $i$ -th layer,  $k_{\mu_i}$  is a derivative of  $k_0$  with respect to  $\mu_{0i}$  [see Eq.(3)], which can be calculated and use in eq. (4),  $Q_{\mu_i}$  is the value of  $Q_{\mu}(l)$  in the  $i$ -th layer.

The wave amplitude  $A$  is decreasing with time as an exponent:

$$A = A_0 \exp(-\pi t / Q_T \tau) = A_0 \exp(-\sigma t / 2Q), \quad (5)$$

where  $t$  is the time,  $\tau$  is the period of a wave or an oscillation,  $f = \sigma / 2\pi$  is the frequency.

Attenuation of oscillations because of unelastic dissipation can be characterized by the values:  $Q_T$ ,  $\alpha$ ,  $\Delta E/E$ , which for  $Q_T \gg 1$  are related by ratio

$2\pi Q_T^{-1} = 2\alpha / f = 2\pi \Delta f / f = \Delta E / E$  where  $\alpha$  is the amplitude coefficient of the attenuation of free oscillation:  $\exp(-\alpha t) \sin(2\pi f t)$ ;  $f$  is the frequency,  $\Delta f$  is a half-width of a resonant line of the considered free oscillation,  $\Delta E/E$  is the portion of elastic energy lost during the cycle.

For calculations, the values of  $Q_{\mu_i}$  from model M\_QML9 [5,6] are taken. The dissipation function  $Q_T$  for torsional modes is shown in fig. 2 for a fundamental tone and two first overtones. If overtones are recorded on Mars, this means that the thickness of the Martian lithosphere is rather large, 300 km or more, and the focuses of marsquakes are quite deep.

Displacements of the overtones penetrate noticeably deeper in the interiors than in the case of fundamental tones. As seen from fig. 2, the attenuation of overtones for a trial dissipative profile is larger (the function  $Q_T$  is lower), than for a fundamental tone. That is why overtones of torsional oscillations attenuate faster than a fundamental tone.

Let us list some values of time, during which the amplitude of a torsional mode e-times decreases: for a fundamental tone  $n=2$   $t \sim 24$  ч;  $n=5$   $t \sim 9$  ч;  $n=10$   $t \sim 5$  ч;  $n=100$   $t \sim 2.5$  ч.

This work is partly financially supported by RFFR (project 15-02-00840) and the Programme of Presidium RAS 7.

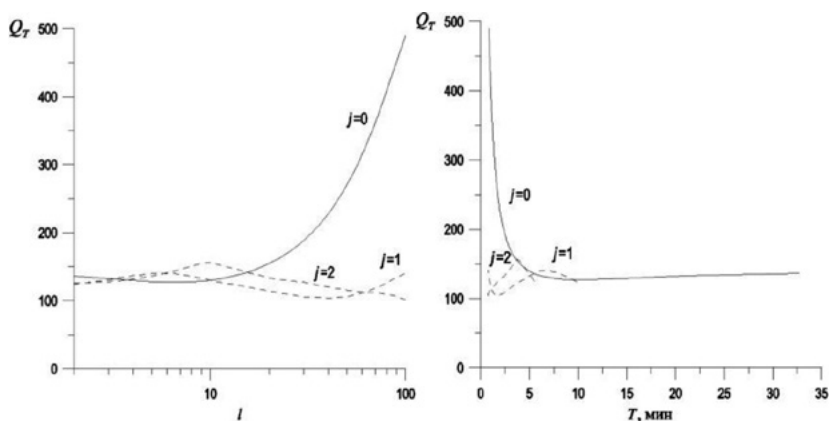


**Fig. 2.** Attenuation of fundamental tones of torsional oscillations  $Q_T$  (solid line  $j=0$ ) and two first overtones (dashed lines  $j=1$  and  $j=2$ ) as function of the oscillation number  $l$  (on the left) and the period of the oscillation (on the right).

## REFERENCES:

- [1] Lognonné Ph., Johnson C. Planetary seismology // Treatise on Geophysics (section 10.03). 2015. P.65-120.
- [2] Zheng Y., Nimmo F., Lay T. Seismological implications of a lithospheric low seismic velocity zone in Mars // Phys. Earth Planet. Int. 2015. V.240. P. 132 – 141.
- [3] Khan A., van Driel M., Böse M., Giardini D., Ceylan S., Yan J., Clinton J., Euchner F., Lognonne P., Murdoch N., Mimoun D., Panning M., Knapmeyer M., Banerdt W.B. Single-station and single-event marsquake location and inversion for structure using synthetic Martian waveforms // Phys. Earth Planet. Int. 2016. V.258. P.28 – 42.
- [4] Panning M.P., Lognonne Ph., Banerdt W.B., et al. Planned products of the Mars structure service for the InSight mission to Mars, Space Science Rev. 2017. DOI 10.1007/s11214-016-0317-5
- [5] Zharkov V.N., Gudkova T. V., Batov A. V. On the estimate of dissipative factor of martian interiors, Sol. Syst. Res. 2017, in press.
- [6] Zharkov V.N., Gudkova T. V., Batov A. V. On the estimate of dissipative factor of martian interiors, Abstract The eighth Moscow Solar System Symposium, IKI, 2017.
- [7] Gudkova, T.V., Zharkov, V.N. The exploration of Martian interiors using the spheroidal oscillation method // Planet. Space Sci. 1996a. V.44. P.1223-1230.
- [8] Gudkova, T.V., Zharkov, V.N. On investigation of Martian crust structure using the free oscillation method. // Planet. Space Sci. 1996b. V.44. P. 1231-1236.
- [9] Zharkov V.N., Pan'kov V.A., Kalachnikov A.A., Osnach A.L. Vvedenie v fiziku Luny (Introduction to Lunar Physics), Moscow: Naukam 1969.
- [10] Zharkov V.N., Lyubimov V.M., Movchan A.A., Movchan A.I. Influence of physical parameters on the periods of torsional oscillations of the Earth // Fizika Zemli. 1967.V.2. P.3-12 (in Russian).

# ON THE ESTIMATE OF THE DISSIPATIVE FACTOR OF MARTIAN INTERIORS

Zharkov V.N.<sup>1</sup>, Gudkova T. V.<sup>1</sup>, Batov A. V.<sup>2</sup>

<sup>1</sup>*Schmidt Institute Physics of the Earth RAS, B.Gruzinskaya, 10, Russia, zharkov@ifz.ru*

<sup>2</sup>*Institute of Control Sciences of RAS, 65 Profsoyuznaya street, Moscow, Russia*

## KEYWORDS:

dissipative factor, attenuation, seismic waves, interior structure, Mars

## INTRODUCTION:

For Mars there is the only constraint on the distribution of the dissipative factor of the interiors  $Q_{ii}(l)$  obtained from observations, this is the secular deceleration of its satellite Phobos [1, 2]. In the interiors of Mars, which is dissipative medium, the physical parameters of the problem under consideration:  $Q_{ii}(l)$ , the shear modulus  $\mu(l)$  and tidal Love number of the planet  $k_2$  depend on frequency (the period of Phobos rotation around Mars,  $T_{2Ph} = 5.55 \text{ h} = 2 \times 10^4 \text{ s}$ , the period of the solar semidiurnal tidal wave  $T_{2S} = 12 \text{ h } 19 \text{ min} \approx 4.434 \times 10^4 \text{ s}$ ). This problem was considered in detail in [3]. The values of the dissipative factor of Martian interiors are discussed from physical point of view in [4], where the distribution  $Q_{ii}$  in PREM was taken as a trial one. In this study, in order to better understand this problem, we take some distribution  $Q_{ii}(l)$  in the interiors of the Earth up to the depth of  $l \leq 670 \text{ km}$  as a trial zero approximation, which is adapted to the conditions of Martian interiors. Making selections of a trial distribution of  $Q_{ii}(l)$  in Martian interiors, we try to take into account both the data of laboratory experiments and the experience in study of the Earth.

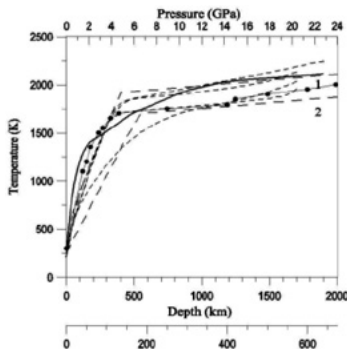


**Fig. 1.** Model distributions of temperature in the interiors of Mars and the Earth as a function of pressure (or depth for Mars and the Earth, respectively): black points present a geotherm [5]; an areotherm: solid line [6]; dashed lines: 1-hot and 2 – cold profiles [7]; dotted lines [8].

Trial areotherms [6-8] (fig. 1) and a geotherm [5] are shown on the  $P - T$  plane. It is seen, that the areotherms and the geotherm are similar and rather close. Hence, it is assumed that the structure of  $Q_{ii}(l)$  in Martian interiors should topologically look like as such for the Earth.

## INTERIOR STRUCTURE MODEL:

At constructing a trial model of interior structure of Mars we base on the cosmochemical WD – model [9] and the laboratory high pressure-temperature experiments along a trial areotherm and WD composition [10,11] (solid line, fig.1). The moment of inertia and Love numbers of models M\_50 (crust 50 km) and M\_100 (crust 100 km) are in agreement with the recent data [12, 13]. Model M\_50 (chemical composition, the radius and the pressure at the boundaries) is shown in fig.2 (on the right).

In the present study the four-layers piecewise constant distribution  $Q_{ii}(l)$  from QLM9 model [14] is taken as a zero approximation, which overlaps the pressure range in the silicate envelope of Mars (fig. 2a). This distribution is based on short period seismic data in the range of 5-55 s of waves phases ScS and S. The values of  $Q_{ii}$  in the first three layers coincide with values in the PREM model, in the fourth layer of QLM9 model the values of  $Q_{ii}$  are somewhat higher than it was

taken for PREM. The task is to clear up a question, how much  $Q_{\mu}(f)$ , shown in fig. 2, is in agreement with the data on the tidal deceleration of Phobos, if the index in the power dependence of  $Q_{\mu}(f)$  is in the range of  $\sim 0.1-0.3$ .

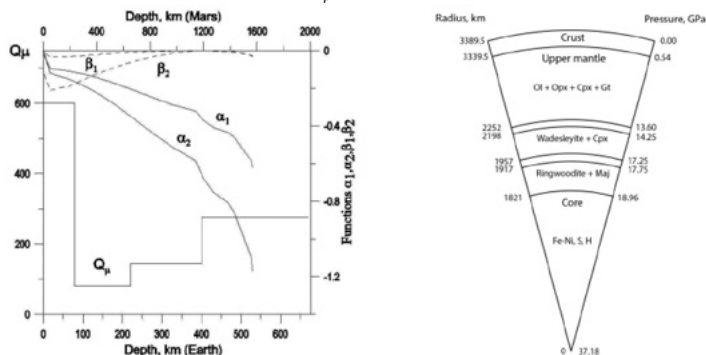


**Fig. 2.** The distribution of the dissipative factor  $Q_{\mu}(f)$  in the crust and the upper mantle of the Earth in the QLM9 model (solid line) and functions  $\alpha_1$ ,  $\alpha_2$ ,  $\beta_1$ ,  $\beta_2$  for the second order tide for M\_50 model as a function of depth (on the left) and a scheme of trial interior model M\_50 (chemical composition and the values of radius and pressure at the boundaries) (on the right).

Love numbers are functional of the shear modulus  $\mu_0(r)$ , the bulk modulus  $K_0(r)$  and the density  $\rho_0(r)$ . The variation of tidal Love numbers  $k$  and  $h$ , and the tidal lag from Phobos  $\varepsilon_2$  [3]

$$\delta h = \int_0^1 \left\{ \frac{h_{\mu} \mu_0}{Q_{\mu}} + \frac{h_K K_0}{Q_K} \right\} dx, \quad \delta k = \int_0^1 \left\{ \frac{k_{\mu} \mu_0}{Q_{\mu}} + \frac{k_K K_0}{Q_K} \right\} dx,$$

$$\varepsilon_2 = \frac{1}{2Q_{t_2}} = \frac{1}{k_2} \int_{x_c}^1 k_{\mu}(x) \frac{\mu_0(x)}{Q_{\mu}(x, \sigma_t)} dx$$

where  $x=r/R$ ,  $x_c$  is the core radius,  $h_{\mu}$ ,  $h_K$ ,  $k_{\mu}$  и  $k_K$  - functional derivatives of  $k$  and  $h$  over  $\mu$  and  $K$ . Let us denote  $\alpha_1 = k_{\mu} \mu_0$ ,  $\beta_1 = k_K K_0$ ,  $\alpha_2 = h_{\mu} \mu_0$ ,  $\beta_2 = h_K K_0$ . These functions for the second order tide are calculated for M\_50 model and drawn in fig. 2. They show fraction of  $Q_{\mu}$  and  $Q_K$  of the  $i$ -th layer to  $Q_{t_2}$ .

## TRIAL DISTRIBUTION OF THE DISSIPATIVE FACTOR IN THE INTERIORS OF MARS:

For trial models we take  $k_2=0.17$  and  $\bar{Q}_{t_2} \sim 92.5$  (table 1). In the standart PREM model for the Earth  $Q$  is constant in the (1s-1h) frequency interval. The logarithmic creep function (Lomnitz model) suits this case [5]. In the long-period domain (tides, Chandler wobble)  $Q_{\mu}$  weakly depends on frequency, and it can be described by a phenomenological power creep function, which relates to a transitional creep stage [15, 16]. Let  $\sigma_1$  and  $\sigma_2$  be the frequencies corresponding to the period of  $1h=3.6 \times 10^3$  s and the basic Phobos tidal wave of period  $\sim 2 \times 10^4$  s, respectively.

**Table 1.** Parameters  $k_2$  and  $\bar{Q}_{t_2}$ .

$k_2$	$\bar{Q}_{t_2}$	$\bar{Q}_{t_2} / k_2$	Ref.
0.152±0.009	82.8±0.2	545	[17]
0.183±0.009	99.5±4.9	544	[18]
0.169±0.006	91.9±3.3	544	[12]

**Table 2.** The values of the dissipative factor  $\bar{Q}_{t_2}$  for trial models  $Q_{\mu}(f)$  in Mars at transformation from 1 h to 5.5 h,  $n=0.1$  and 0.3.

n	0.1				0.3			
	$Q(\sigma_1)$	600	80	143	276	600	80	143
$Q(\sigma_2)$	505	67.4	120.5	232.5	359	47.8	85.5	165
$\mu(\sigma_2) / \mu(\sigma_1)$	0.998	0.998	0.985	0.984	0.992	0.991	0.996	0.995
$\bar{Q}_{t_2}$ (M_50)	96.2				68.3			
$\bar{Q}_{t_2}$ (M_100)	89.9				63.8			

The results of calculations at the transformation of a primary distribution of  $Q_{\mu}(l)$  in the seismic range of periods to the Phobos period of 5.55 h are given in table 2 for two values of index  $n=0.1$  and 0.3.

The values of  $\bar{Q}_{1/2}$  for interior structure models of Mars M\_50 and M\_100 - 96.2 and 89.9 - are rather close to the observed value  $91.9 \pm 3.3$  in table 1 for  $n=0.1$ . For  $n=0.3$  the disagreement with the observed value is significant. Taking into account all uncertainties in the considered problem, the distribution  $Q_{\mu}(l)$  for the seismic range of periods on Mars, given in the upper line in table 2 at  $n=0.1$ , can be considered as a first step. Let us call this model of a trial distribution of  $Q_{\mu}(l)$  for Mars M\_QML9. The authors hope, that after the successful seismic experiment some corrections (perhaps significant) could be inserted in this distribution.

This work is partially financially supported by RFFR (project 15-02-00840) and the Programme of Presidium RAS 7.

## REFERENCES:

- [1] Zharkov V.N., Gudkova T.V. Dissipative factor of the interiors of Mars // Sol. System. Res. 1993.V. 27. P. 3-15.
- [2] Zharkov V.N., Gudkova T.V. On the dissipative factor of the Martian interiors // Planet. Space Sci. 1997. V. 45. P. 401 – 407.
- [3] Zharkov V.N., Gudkova T.V. Construction of Martian Interior Model // Sol. Syst. Res. 2005. V.39. № 5. P.343-373.
- [4] Lognonné Ph., Mosser B. Planetary seismology // Surv. Geophys. 1993. V.14. P. 239-302.
- [5] Zharkov V.N. Fizika zemnux nedr. OOO Nauka i Obrazovanie. 2012. 386c. (in Russian)
- [6] Zharkov V.N., Gudkova T.V., Molodensky S.M. On models of Mars' interior and amplitudes of forced nutations. 1. The effects of deviation of Mars from its equilibrium state on the flattening of the core-mantle boundary // PEPI. 2009. V.172. P. 324-334.
- [7] Verhoeven, O., Rivoldini, A., Vacher, P., et al. 2005. Interior structure of terrestrial planets: Modelling Mars' mantle and its electromagnetic, geodetic and seismic properties. J.Geophys. Res., 110: E04009.
- [8] Plesa A.C., Grott M., Tosi N., Breuer D., Spohn T., Wieczorek M. How large are present-day heat flux variations across the surface of Mars? // J.Geophys.Res.Planets. 2016. doi:10.1002/2016JE005126.
- [9] Wänke H., Dreibus G. Chemistry and accretion history of Mars // Phil. Trans. Roy. Soc. Lond. 1994. V.349. P.285-293.
- [10] Bertka C.M., Fei Y. Mineralogy of the Martian interior up to core-mantle boundary pressures// J. Geophys. Res., 1997. V. 102. № 3. P. 5251-5264.
- [11] Bertka C.M., Fei Y. Density profile of an SNC model Martian interior and the moment-of-inertia factor of Mars // Earth Planet. Sci. Lett. 1998. V.157. P. 79-88.
- [12] Konopliv A.S., Park R.S., Folkner W.M. An improved JPL Mars gravity field and orientation from Mars orbiter and lander tracking data // Icarus. 2016. V. 274. P. 253-260.
- [13] Genova A., Goossens S., Lemoine F.G., et al. Seasonal and static gravity field of Mars from MGS, Mars Odyssey and MRO radio science // Icarus. 2016. V.272. P. 228-245.
- [14] Lawrence J.F., Wyession M.E. QLM9: A new radial quality factor ( $Q_{\mu}$ ) model for the lower mantle // Earth Planet. Sci. Lett. 2006. V. 241. P. 962-971.
- [15] Akopyan S.Ts., Zharkov V.N., Lubimov V.M. Theory of attenuation of torsional oscillations of the Earth// Phys. Solid Earth. 1977. V.8. P.3-11).
- [16] Molodensky S.M., Zharkov V.N. On Chandler wobble and frequency dependence  $Q_{\mu}$  of Earth' mantle // Izv. AN SSS. Fizika Zemli. 1982. № 4. C. 3-16.(in Russian).
- [17] Jacobson R.A. The orbits and masses of the Martian satellites and the libration of Phobos // Astron. J. 2010. V. 139. P. 668-679.
- [18] Jacobson R.A., Lainey V. Martian satellite and ephemerides//Planet.Space Sci.2014.V.102.P.35-44.

# MODEL STRESSES IN MARTIAN INTERIORS FOR TWO-LEVEL LOADING

A.V. Batov<sup>1</sup>, T. V. Gudkova<sup>2</sup>, V.N. Zharkov<sup>2</sup>

<sup>1</sup>Institute of Control Sciences of RAS, 65 Profsoyuznaya street, Moscow, Russia, batov@ipu.ru

<sup>2</sup>Schmidt Institute Physics of the Earth RAS, B.Gruzinskaya, 10, Russia

## KEYWORDS:

Mars, tension-compression stresses, shear stresses, gravity, topography

## INTRODUCTION:

Studying of stress field in the Martian interiors is of interest to understand the level of seismic activity of the planet and to localize zones of possible marsquakes' sources for forthcoming seismic experiments on Mars. Joint analysis of gravity and topography data in a frame of the static method let us some knowledge on stress field in the crust and in the lithosphere of Mars [1, 2]. At present detailed data on topography [3] and gravity field [4, 5] are available. In present study numerical calculations of tension-compression stresses and maximum shear stresses are carried out for two trial interior structure models of Mars, with a 1x1 arc-deg spherical grid and up to 1000 km depth.

## INTERIOR STRUCTURE MODEL:

Trial models of Mars have 50 km (M\_50) and 100 km (M\_100) thick crust [6]. The mean density ( $\rho_{\text{crust}}$ ), the crust thickness ( $l_{\text{crust}}$ ), the core radius ( $r_{\text{core}}$ ), moment of inertia ( $I/MR^2$ ), elastic Love number  $k_2^S$  and the density drop at crust-mantle boundary for these models are given in the table. An outer surface of a hydrostatic model is taken as reference surface for topography and gravity field of Mars [7, 8]. Parameters of the equilibrium spheroid  $s_2, s_4$ ; gravitational moments  $J_2, J_4$  are listed in the table.

## STRESSES CALCULATIONS:

We use loading factors technique, which was developed in [9-11]. Two types of models: 1) an elastic model and 2) a model with the elastic lithosphere (150-500 km thick), and a weakened layer, which partly lost elastic properties (shear modulus is ten times lower), under the lithosphere, are considered (fig.1). The source of gravity anomalies is assumed to be the topographic loading and density anomalies at crust-mantle boundary.

**Table 1.** Parameters of trial interior structure models

Model	$\rho_{\text{crust}}$ kg/m <sup>3</sup>	$l_{\text{crust}}$ km	$r_{\text{core}}$ km	$I/MR^2$	$k_2^S$	$\rho_{\text{crust}}/\rho_{\text{mantle}}$	$-s_2,$ $10^{-3}$	$s_4,$ $10^{-6}$	$J_2^0,$ $10^{-3}$	$-J_4^0,$ $10^{-6}$
M_50	2900	50	1821	0.3639	0.162	3.00/3.36	3.338	9.374	1.800	7.634
M_100	2900	100	1870	0.3639	0.170	3.12/3.39	3.338	9.338	1.800	7.598

Figure 2 shows the maps of tension-compression and maximum shear stresses for M\_50 with 300 km thick lithosphere (on the surface, under the crust, and at the lower boundary of the lithosphere). On the surface and in the crust, there is concentration of stresses in the zones of Olympus Mont, the volca-

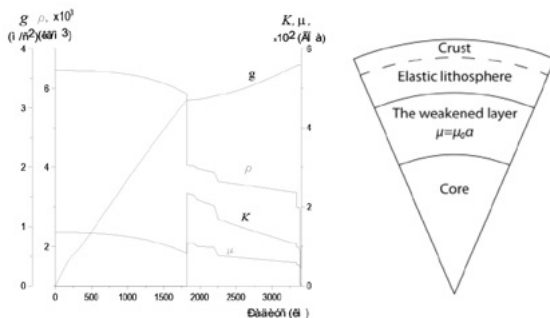


**Fig.1.** Density  $\rho$ , gravity  $g$ , the bulk modulus  $K$  and shear modulus  $\mu$  along the radius for model M\_50.

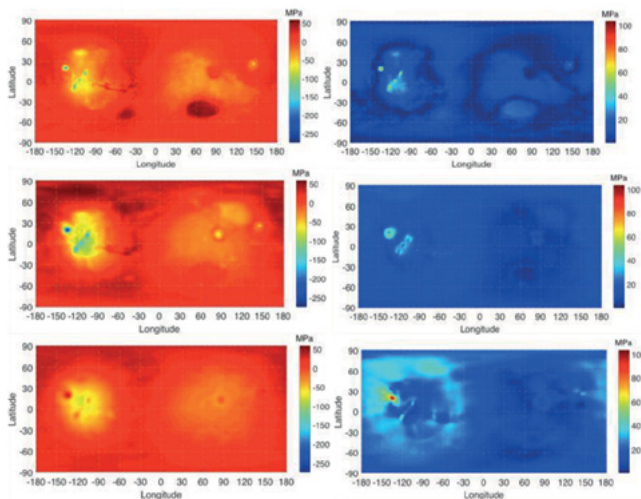


**Fig. 2.** Tension-compression stresses (on the left) and maximum shear stresses (on the right) on the surface, at the depth of 50 km (under the crust) and 300 km (at lower boundary of the lithosphere) for model  $M_{50}$  with the lithosphere of 300 km.

noes: Ascræus, Pavonis and Arsia; Valles Marineris, Utopia Planitia, Hellas and Isidis. Under the crust the pattern is smoothed, the absence of intense stresses under many topographic structures, except for Tharsis. At lower boundary of the lithosphere there is a transition from compression stresses to tension stresses under Olympus and Elysium, while compression stresses being around them; the values of maximum shear stresses are 1.5-2 times higher than on the surface. On the whole, the values of stresses for the model with a 300 km thick lithosphere are 2-3 times larger than stresses at the same depths for an elastic model. The difference of stresses for  $M_{50}$  and  $M_{100}$  models are about 10 percents.

Let us consider stresses under different structures for all types of models. Under Olympus maximum shear stresses in the crust reach 20-30 GPa, decreasing up to 5 GPa under the crust, while the values of compression stresses reaching very large values - 50-130 GPa, depending on the lithosphere thickness. Under such structures as Hellas and Argyre, Acidalia Planitia, Arcadia Planitia and Valleys Marineris, both the maximum shear stresses and the tension stresses are quite large, up to 20-30 GPa for tension in the lithosphere (fig.3). The large values of shear stresses in the zones of large tension stresses are the most likely areas for focuses of marsquakes.

This work is partly financially supported by RFFFR (project 15-02-00840) and the Programme of Presidium RAS 7.

## REFERENCES:

- [1] Zharkov V.N., Koshlyakov E.M., Marchenkov K.I. Composition, structure and gravitational field of Mars // Sol. Syst. Res.1991. V.25. P.515-547).
- [2] Koshlyakov E.M., Zharkov V.N. On gravity field of Mars // Sol. Syst.Res.1993. V.27. № 2. P.12-21).
- [3] Smith D.E., Zuber M.T., Frey H.V. и др. Mars Orbiter Laser Altimeter: Experimental summary after the first year of global mapping of Mars // J.Geophys.Res. 2001. V.106 (E10). P. 23689-23722.
- [4] Konopliv A.S., Park R.S., Folkner W.M. An improved JPL Mars gravity field and orientation from Mars orbiter and lander tracking data // Icarus. 2016. V. 274. P. 253-260.
- [5] Genova A., Goossens S., Lemoine F.G., et al. Seasonal and static gravity field of Mars from MGS, Mars Odyssey and MRO radio science // Icarus. 2016. V.272. P. 228-245.
- [6] Zharkov V.N., Gudkova T. V., Batov A. V. On the estimate of dissipative factor of marian interiors, Sol. Syst. Res. 2017, in press.
- [7] Zharkov V.N., Gudkova T.V., Molodensky S.M. On models of Mars' interior and amplitudes of forced nutations. 1. The effects of deviation of Mars from its equilibrium state on the flattening of the core-mantle boundary // PEPI. 2009. V.172. P. 324-334.
- [8] Zharkov V.N., Gudkova T.V. On model structure of gravity field of Mars // Sol. Syst. Res. 2016. V.50. P.250-267.
- [9] Marchenkov K.I., Lyubimov V.M., Zharkov V.N. Calculation of load factors for deeply buried density anomalies // Doklady Earth Science Sections. V.279.1984. P.14-16.
- [10] Zharkov V.N. Marchenkov K.I., Lyubimov V.M. On long-waves shear stresses in the lithosphere and the mantle of Venus // Sol. Syst. Res. 1986. V.20. P.202-211.
- [11] Marchenkov K.I., Zharkov V.N. Stresses in the Venus crust and the topography of the mantle boundary // Sol. Astron. Lett. 1989. T.16. № 1. P.77-81.



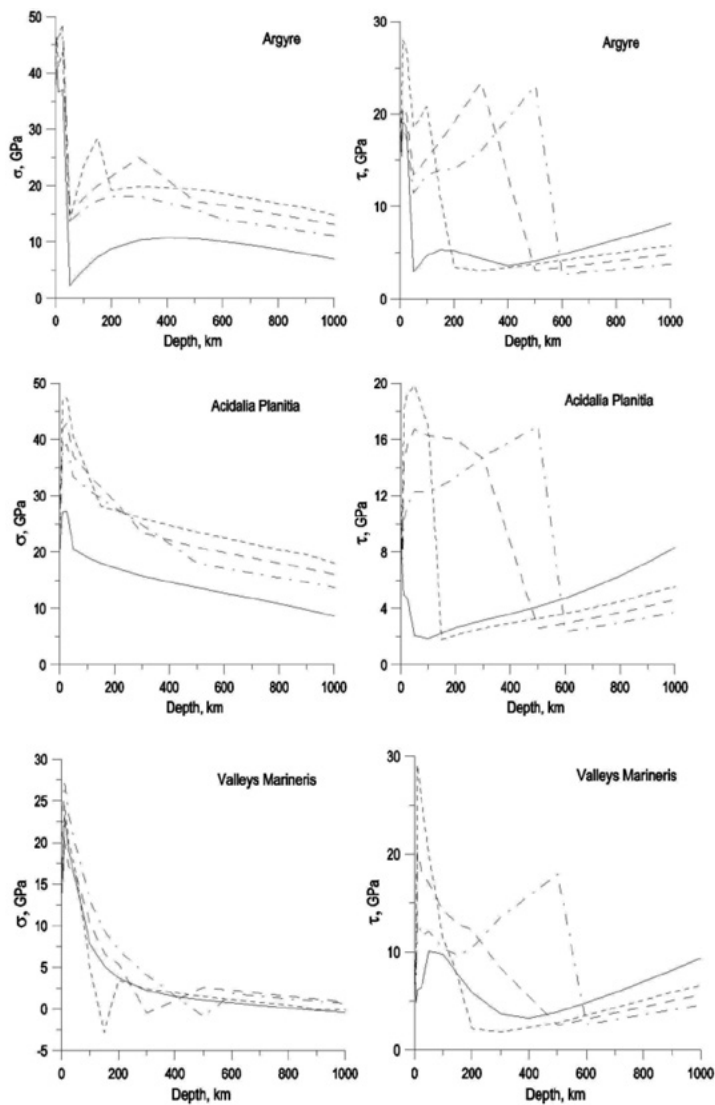


**Fig. 3.** Tension-compression (on the left) and maximum shear stresses (on the right) along the depth for model **M\_50** under Argyre, Acidalia Planitia, and Valleys Marineris for an elastic case (solid line) and the model with the lithosphere of different thickness: 150 km (points), 300 km (dashed) and 500 km (dot-dashed lines).

# THE SCIENTIFIC TASKS OF THE LUNA-GRUNT PROJECT (LUNA-28)

E.N. Slyuta

*Vernadsky Institute of Geochemistry and Analytical Chemistry,  
Moscow, Kosygina str. 19, Russia, slyuta@mail.ru;*

## KEYWORDS:

Moon, Luna-Grunt, Luna-28, regolith, drilling rig, logging probe, stratified core, implanted volatile, weakly bound volatile, frozen volatile.

## INTRODUCTION:

The Federal Space Program 2016-2025 includes the development and creation of the spacecraft "Luna-Grunt" (project "Luna-28") for landing on the lunar surface, drilling and sampling lunar soil, and delivering lunar soil to Earth. Delivering lunar rock samples to Earth is a necessary and key element in the exploration of the Moon. Only under laboratory conditions it is possible to study the texture, structure and microstructure of rocks and minerals in detail, to determine and study the main, accessory and rare minerals and inclusions, to analyze with any degree of chemical composition accuracy, including basic, subordinate and rare elements, the analysis of the ratios of any stable and radiogenic isotopes, determination of the absolute age of minerals, rocks, and, accordingly, geological structures and the processes accompanying their formation. These data form the basis of knowledge about the origin, the conditions for the formation and evolution of local and regional structures, the cortex and the entire planetary body as a whole. An important element of the information content of the delivered samples is also the way and place of sampling.

## LUNAR ROCKS:

The lunar regolith has a complex stratified structure and its own stratigraphic and geochemical history, which can be traced over several billion years from the time of the formation of the underlying rocks (bedrocks) (Fig. 1). Layers are a stratified sequence of ejection deposits from neighboring impact craters located at distances from the first meters to several hundred kilometers, depending on the size of these craters. The larger the crater, the farther the ejection. The stratified core of regolith carries information on the composition and age of regolith and bedrocks not only at the site of drilling, but also on a fairly large adjoining area. If there are rare lunar rocks in the vicinity of the borehole, these rocks are also likely to be represented in the form of one of the layers in the selected core of the regolith.

## LUNAR VOLATILES:

Volatile components, depending on the mechanism of confinement and the form of being in the lunar regolith, are divided into three main types: implanted, weakly bound and frozen volatiles [1-3]. The composition of the implanted gases is determined not only by the noble gases of the solar wind, but also by the gases of the Earth's wind, i.e. gases of the Earth's upper atmosphere, which under the action of the solar wind ionized and implanted into the particles of the lunar regolith. According to the age of exposure of regolith layers in the delivered stratified column of regolith and the appearance in the layers of regolith of the component of terrestrial biogenic oxygen depleted of  $^{16}\text{O}$ , the time of appearance and spread of life on Earth can be determined [4]. The change in the concentration of isotopes N (the main component of the early atmosphere of the Earth) and light elements (He, Ne, Ar, etc.) in regolith layers, makes it possible to estimate the time of the formation of the Geomagnetic Field (Magnetosphere) of the Earth [5]. The study of the composition of implanted gases of terrestrial origin in the regolith particles before the formation of the Earth's magnetosphere allows us to estimate the composition of the primary terrestrial atmosphere. In the presence of soil from the far side of the Moon, the time of synchronization of the rotation of the Moon relative to the Earth can be estimated from the change in the composition of the implanted gases (to the absence of gases of terrestrial origin) [5]. The stratified column of regolith will also

allow studying changes in the activity and composition of the solar wind and galactic cosmic rays for the period from the moment of the formation of the underlying rocks, i.e. 3.5-4 billion years or more.

Implanted gases are resistant to mechanical and thermal influences within a few hundred degrees. The method of thermodesorption mass spectrometry is one of the few methods that allow studying the chemical and isotope composition of implanted volatiles and their concentration depending on the depth of implantation and activation energy [2].

Weakly bound gases are gases that saturate the porous space of the lunar regolith. The content and composition of weakly bound gases in the lunar regolith is determined by the following parameters: diffusion, which depends on the surface temperature and the saturation concentration of the regolith at a given temperature, the sublimation temperature and the composition of frozen volatiles, the composition of gases from the Moon interior (volcanic origin), and the density of the solar wind flux, which depends on the geographical longitude and latitude. This is one of the least investigated types of lunar volatiles.

Frozen volatile components are in the open pore space in the form of particles of micron size (hoarfrost) on the surface of regolith particles. The presence of massive deposits of water ice in the form of lenses in the regolith is estimated as unlikely. Unlike implanted components, weakly bound and frozen volatiles are extremely unstable, and evaporate readily under temperature and mechanical influences on the lunar regolith. Investigation of concentration and distribution by depth, chemical and isotopic composition of weakly bound and frozen volatiles is possible only *in situ*.

## TOOLS:

In the Vernadsky Institute for this project, the concept of a drilling rig, combining two scientific tasks, is being developed. The first is drilling to a depth of 1.5 to 6 meters (length of the drill rod is 1.5 m, set of up to 4 drill rods) and selection of the core in the elastic sampler in the receiver cassette (Fig. 2). In one cassette includes a sampler length of 1.5 m and a diameter of 20 mm (internal diameter of the drill rod). The weight of the core of 1.5, 3.0, 4.5, 6.0 m long is 840, 1680, 2520 and 3360 grams, respectively. At the base of the rig is a bell, which is lowered before drilling to the surface of the ground (Fig. 3). During the drilling and selection of the regolith column, with the help of an auger from the outside of the drill rod, regolith slurry, together with weakly bound and frozen volatiles, is fed under a sealed bell. Weakly bound and frozen volatiles when submitting slurry upward sublimate (evaporate) and fall under the bell, and from there they enter a gas analyzer (mass spectrometer). Measurements of chemical and isotopic composition, and gas concentrations are carried out continuously during drilling to the full depth of the well.

The second device under development at Vernadsky Institute for this project is a self-penetrating up to 3 meters logging thermal probe (Fig. 4), which is currently being developed for the Luna-27 (Luna-Resurs-1). The logging tool serves to measure the temperature distribution to a depth and measure the internal heat flux (flexible tape with temperature sensors), as well as to measure the dielectric and magnetic properties of the regolith and the depth density distribution (IK probe, Fig. 4). The total weight of the logging probe is about 3 kg.

## SUMMARY:

Expected scientific results of the automatic landing mission with the examined set of scientific equipment:

1. The stratified column of regolith to a depth of 1.5 to 6 m, delivered to Earth for the study of lunar rocks, minerals and implanted volatiles.
2. Chemical and isotopic composition and distribution in the regolith to a depth of 1.5 to 6 m of loosely bound and frozen volatiles.
3. Electromagnetic properties of the regolith and their distribution to a depth of 3 m.
4. Thermophysical properties of regolith and internal heat flow.

For the first time geological, geochemical and geophysical sections will be obtained, tied to the reference borehole, which will provide the maximum possible scientific performance of the landing spacecraft according to the results of the scenario considered.

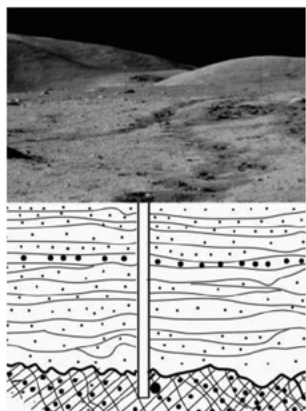


Fig. 1.



Fig. 3



Fig. 4

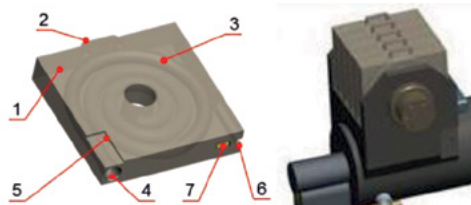


Fig. 2. A cassette for receiving and storing a core in an elastic sampler (on the left) and a drilling rig with a core storage (right). 1 - housing; 2 - the handle; 3 - spiral channel for placing the sampler; 4 - receiving window; 5, 6 - guide grooves; 7 - electrical connector

## REFERENCES:

- [1] Slyuta E.N. et. al. He implantation and concentration in minerals and lunar regolith particles // *Geochemistry Int.* 2013. V. 51. No. 12. P. 959-967.
- [2] Slyuta E.N. et. al. Application of thermodesorption mass spectrometry for studying proton water formation in the lunar regolith // *Geochemistry Int.* 2017. V. 55. No. 1. P. 27-37.
- [3] Slyuta E.N. Basic types of Moon's resources and their mining and processing // *Gornyi Zhurnal.* 2017. No. 4. P. 13-18.
- [4] Terada K. et al. Biogenic oxygen from Earth transported to the Moon by a wind of magnetospheric ions // *Nature Astronomy.* 2017. V. 1, #0026, P. 1-5.
- [5] Ozima M. et al. Toward understanding early Earth evolution: Prescription for approach from terrestrial noble gas and light element records in lunar soils // *PNAS.* 2008. V. 105, No. 46, P. 17654-17658.

# ESTIMATION OF PROBABILITY OF DANGEROUS SLOPES IN THE LANDING SITES OF LUNA-GLOB SPACECRAFT THROUGH ANALYSIS OF SHADOW AREA ON THE LROC NAC IMAGES

S.S. Krasilnikov<sup>1</sup>, M.A. Ivanov<sup>1</sup>, A.T. Basilevsky<sup>1</sup>, A.M. Abdrakhimov<sup>1</sup>, A.A. Kokhanov<sup>2</sup>

<sup>1</sup>Vernadsky Institute of geochemistry and analytical chemistry of RAS, Moscow, Russia; krasilnikovruss@gmail.com

<sup>2</sup>Moscow State University of Geodesy and Cartography, Moscow, Russia.

## KEYWORDS:

Moon, Luna-Glob, Luna-25, landing site, LROC NAC, slopes.

## ABSTRACT:

Was estimated the probability of encountering of dangerous slopes ( $>7^\circ$  on a 3.5-m-baseline) in five landing ellipses of the Luna-Glob (Luna-25) mission. In order to make these estimations, we analyzed dependence between a fraction of a shadowed area on the LROC NAC images and the Sun angle over horizon. We used a high-resolution DTM and the NAC images for the Apollo 16 landing site to calibrate our results and estimate the probabilities of encountering of the slopes in five classes:  $<7^\circ$ ,  $7^\circ-10^\circ$ ,  $10^\circ-15^\circ$ ,  $15^\circ-20^\circ$  and  $>20^\circ$ .

## INTRODUCTION:

During selection of the landing sites, determination of the short baseline slopes is one of the most important tasks. In [1], several high-priority landing sites were selected mostly on the basis of the frequency distribution of slopes on a 60-m-baseline provided by the LOLA instrument [4]. This spatial resolution of the LOLA DTM is rather coarse for a confidential selection of the safe surfaces. In our approach, we first analyzed a dependence between a fraction of a shadowed area on the LROC NAC images and the Sun angle over horizon and then calibrated the results using a high-resolution DTM and the NAC images for the Apollo 16 landing site. Such a procedure allowed estimates of the frequency distribution of the slopes on much shorter baselines, specifically 3.5 m, in five categories:  $<7^\circ$ ,  $7^\circ-10^\circ$ ,  $10^\circ-15^\circ$ ,  $15^\circ-20^\circ$  and  $>20^\circ$ .

The landing ellipses are in a region between  $65-75^\circ\text{S}$  and  $0-60^\circ\text{E}$  (fig. 1): ellipse 1 is at  $68.77^\circ\text{S}$ ;  $21.21^\circ\text{E}$ , ellipse 4 is at  $68.64^\circ\text{S}$ ;  $11.55^\circ\text{E}$ , and ellipse 6 is at  $69.54^\circ\text{S}$ ;  $43.54^\circ\text{E}$  [1]. Two additional ellipses are in Boguslavsky crate: Boguslavsky-1 ( $73.9^\circ\text{S}$ ;  $43.9^\circ\text{E}$ ) and Boguslavsky-2 ( $72.9^\circ\text{S}$ ;  $41.3^\circ\text{E}$ ) [1].

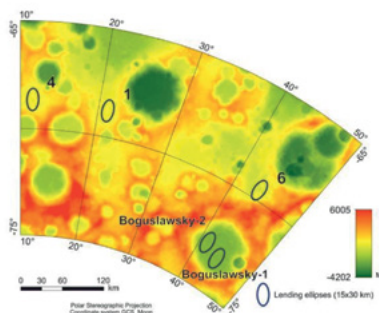
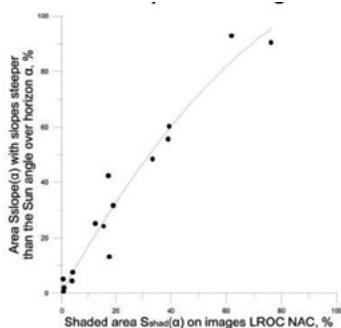


Fig. 1. Several preliminary selected landing ellipses of the Luna-Glob mission.

## DEPENDENCE BETWEEN THE SHADOWED AREAS IN THE NAC IMAGES AND REAL AREA WITHIN SPECIFIC RANGE OF SLOPES

Landing site of Apollo 16 was selected for our analysis because this area shows similar morphology and elevation range as the preliminary selected landing sites of the Luna-Glob mission. The analysis of the Apollo 16 landing site was



**Fig. 2.** Dependence of real slopes area more than angle ( $\alpha$ ) and shadow area on LROC images with the same Sun angle ( $\alpha$ ).

conducted in two steps. First: we estimated a fraction of the shadowed area on the LROC NAC images as a function of the Sun angle over the horizon. Second: using the high-resolution DTM for the same region, we determined a real area of slopes within specific intervals and compared it with the fraction of the shadowed area estimated at the first step. The least square root approximation of the measured relationship between the area of real slopes steeper than a specific angle ( $\alpha$ ) and the shadowed area in the image with the same Sun angle ( $\alpha$ ), defines a calibration curve (fig.2).

## ESTIMATION OF SLOPES IN THE POTENTIAL LANDING ELLIPSES OF THE LUNA-GLOB MISSION.

The calibration curve allows estimation of slopes to be made within the Luna-Glob ellipses (fig.3).

Depending upon the local morphologic characteristics of the surface, coefficient of determination ( $R^2$ ) and mean square error ( $\sigma^2$ ) of the calibration curve approximation can vary. Results for the ellipses 1, 4, and Boguslawsky-1, 2 have the higher  $R^2$  and the lower  $\sigma^2$  (tab.1).

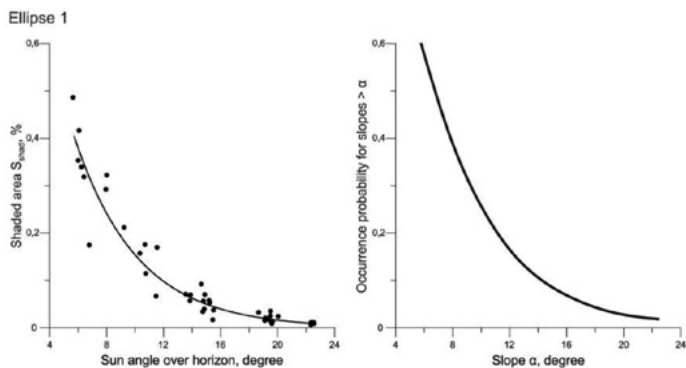


**Fig. 3.** Ellipse 1. Left – dependence of shadow area on the LROC images and Sun angle. Right – probability of slopes, produced after calibration of left graph.

These values indicate a tight dependence between the shadowed area and the Sun angle; they can be used for more confidential determination of the probability of encounter of the slopes within specific intervals. The low  $R^2$  value

**Table 1.**

Ellipses	Probability to find the slopes in the classes Вероятность встречи уклонов по классам					$R^2$	$\sigma^2$
	<7°	7°–10°	10°–15°	15°–20°	>20°		
1	0.52	0.22	0.17	0.07	0.02	0.92	0.12
4	0.58	0.19	0.15	0.06	0.02	0.94	0.11
6	0.68	0.15	0.10	0.05	0.02	0.66	0.65
Boguslawsky-1	0.62	0.23	0.11	0.03	0.01	0.97	0.04
Boguslawsky-2	0.62	0.20	0.13	0.04	0.01	0.85	0.24

(0.66) and high of  $\sigma^2$  value (0.65) characterize ellipse 6 (tab. 1). Low, flattop hills are the most common small-scale topographic features within ellipse 6 [2]. Because of these hills, the areal fraction of shadows varies significantly (tab. 1) but mostly for slopes that are less than  $7^\circ$ . These values, however, are within the safety restrictions of the mission and, thus, ellipse 6 does not appear as a potentially dangerous place to land.

## CONCLUSIONS:

Among the five analyzed ellipses, the smallest probability of encountering of slopes higher than  $10^\circ$ , characterizes ellipses number 6, Boguslawsky-1 and Boguslawsky-2 (tab.1). Thus, considering the other criteria for the selection of the landing sites, such as visibility of Earth and the Sun, ellipse 6 appears as the most attractive landing site for the Luna-Glob mission.

It should be emphasized that for ellipse 6, the probability to find the slopes steeper than  $10^\circ$  is relatively high (0.17). To minimize the risk of landing, one can recommend either to re-locate the ellipse or to install an automatic pre-land navigation system in order to avoid dangerous features on the surface (as it realized on Chang'e-3 [3]).

## ACKNOWLEDGMENTS:

Sergey Krasilnikov, Mikhail Ivanov and Alexander Basilevsky worked on this project in Vernadsky institute and were financially supported by Russian Science Foundation, grant no. 17-17-01149 "Reconstruction of the geologic history of the lunar sub-polar regions on the base of new high-precision data for establishing sources, distribution, and accumulation of volatiles (water) on the Moon".

## REFERENCES:

- [1] Djachkova M.V., Litvak M.L., Mitrofanov I.G., Sanin A.B. Selection of Luna-25 Landing Sites in the South Polar Region of the Moon // *Solar System Research*. 2017. V. 51. No. 3. pp. 185-195.
- [2] Ivanov M.A., Abdrakhimov A.M., Basilevsky A.T., Demidov N.E., Djachkova M.V., Guseva E.N., Head J.W., Hiesinger H., Kohanov A.A., Krasilnikov S.S., Mitrofanov I.G. Geological characterization of the three high-priority landing sites for the Luna-Glob mission // *Planet. Space Sci.* 2017 (in press)
- [3] Li S., Jiang X. and Tao T. Guidance Summary and Assessment of the Chang'e-3 Powered Descent and Landing // *Journ. of Spacecraft and Rockets*. 2016. Vol. 53. № 2. p. 258-277.
- [4] Smith, D.E., Zuber, M.T., Jackson, G.B. et al (29 others), The Lunar Orbiter Laser Altimeter investigation on the Lunar Reconnaissance Orbiter Mission // *Space Sci. Rev.* 2010. V. 150. p. 209-241.

# SAP “LUNA” SYSTEM FOR AUTOMATED SCIENTIFIC PLANNING OF FUTURE LUNAR MISSIONS

A.V. Malakhov<sup>1</sup>, I. G. Mitrofanov<sup>1</sup>, A.B. Sanin<sup>1</sup>, M.V. Djachkova<sup>1</sup>,  
D.I. Lisov<sup>1</sup>, A.S. Kozyrev<sup>1</sup>, S.Yu. Nikiforov<sup>1</sup>, N.E. Karpushkina<sup>1</sup>  
<sup>1</sup>*Space Research Institute, Profsoyuznaya st 84/32, Moscow, Russia.*

## KEYWORDS:

Moon, future missions, planning, analysis, cartography, landing sites, operations.

## INTRODUCTION:

The Russian Federal Space Program for 2016-2025 provides for an extensive program of space exploration of the Moon. It is planned within the Program to launch one orbital (Luna-26) and four landing robotic spacecrafts (Luna-25, Luna-27 - Luna-29) into the polar regions of the Earth's natural satellite.

Successful implementation of tasks assigned to the robotic spacecraft will create conditions for preparation of Russian manned expedition to the polar region of the Moon. In addition, Russia, together with the European Space Agency, prepares ExoMars and BepiColombo missions to Mars and Mercury respectively. The success of these missions will largely depend on the quality of scientific results obtained. It is obvious that these cannot be achieved without proper preparation of scientific instruments, organization, planning and data support of scientific research. Unfortunately, these objectives are paid insufficient attention to currently. It seems necessary to us to develop in 2017-2020 the System for Analysis and Planning of scientific research (SAP-Luna) for the Russian Lunar Program Projects which are planned in 2019-2025. This system can be expanded in the medium and long term both to prepare manned missions to the Moon and to prepare projects for studying Mars and other celestial bodies of the Solar system. In our opinion, the proposed information system will allow the scientific community, on one hand, and space industry on the other, to most effectively implement the objectives of the missions planned and thus acquire the best possible scientific results.



# SOURCES OF MATERIALS AT THE THREE HIGH-PRIORITY LANDING SITES OF THE LUNA-GLOB MISSION

M.A. Ivanov<sup>1</sup>, A.M. Abdrakhimov<sup>1</sup>, A.T. Basilevsky<sup>1</sup>, N.E. Demidov<sup>1</sup>,  
E.N. Guseva<sup>1</sup>, J.W. Head<sup>2</sup>, H. Hiesinger<sup>3</sup>, A.A. Kohanov<sup>4</sup>,  
S.S. Krasilnikov<sup>1</sup>

<sup>1</sup>*Vernadsky Institute of Geochemistry and Analytical Chemistry  
Russian Academy of Sciences, 19, Kosygin st., 119991 Moscow, Russia;  
mikhail\_ivanov@brown.edu;*

<sup>2</sup>*Department of Geological Sciences, Brown University, Providence, RI 02912  
USA;*

<sup>3</sup>*Institut für Planetologie, Westfälische Wilhelms-Universität Münster, Wilhelm-  
Klemm-Str. 10, 48149 Münster, Germany;*

<sup>4</sup>*Moscow State University of Geodesy and Cartography (MiiGAIK), Moscow,  
Russia*

## KEYWORDS:

Moon, Luna-Glob, ejecta emplacement, material sources, absolute model ages

## INTRODUCTION:

The Luna-Glob landing zone is in the southern sub-polar region within the heavily cratered highlands, near the southern portion of the rim of the South Pole-Aitken (SPA) basin [1], [2]. In the landing zone, numerous large craters (up to 100-120 km in diameter and a few kilometers deep) form a very rough surface at tens of kilometers scale. During their formation, these craters have redistributed materials emplaced within the Luna-Glob landing zone by the lunar basins. Which sources are the most important at the top-three landing sites? Determination of the sources will help to facilitate the final selection of a landing site and the following interpretation of the in-situ analyses.

## THE HIGH-PRIORITY LANDING SITES:

Three major criteria were applied for selection of the landing sites. (1) The surface within the landing ellipses should be relatively smooth. (2) The sites must have optimal illumination and communication conditions for the 2019 launch windows. (3) The sites must be characterized by as high content of hydrogen as possible. Application of these criteria resulted in the selection of twelve potential sites [3], [4]. The combination of the 60-m-baseline roughness of the surface, the Sun and Earth visibility, and the specific WEH values were used to collectively define landing ellipses 1 (68.77°S, 21.21°E), 4 (68.65°S, 11.55°E), and 6 (69.55°S, 43.54°E) as the higher priority sites [3], [4].

## SOURCES OF MATERIALS IN THE LANDING ELLIPSES:

Although the ejecta from the SPA basin should strongly dominate the Luna-Glob landing zone, most of the younger lunar basins also have contributed materials to this region but at much smaller proportions. The mean model thickness of the post-SPA basin ejecta in the Luna-Glob area is ~3.2 km, which is ~96% of the total thickness of ejecta of all lunar basins in the Luna-Glob landing zone [5]. Assuming a no-mixing scenario for the ejecta emplacement, which represents an extreme case [6], a layer of the post-SPA basin ejecta will overlay the SPA ejecta. Constant impact gardening will eventually redistribute material of this layer and mix it with the SPA ejecta. In the Luna-Glob landing zone, there are 72 craters larger than 20 km in diameter [7], [8]. Their diameters vary from 20 km to 128 km, and the mean diameter is ~68 km. The total area of these craters comprises ~50% of the landing region and the mean nearest neighbor distance for these craters is  $\sim 36.3 \pm 15.5$  km, which is close to the mean radius of the larger craters. Thus, even under a conservative assumption of no mixing during the basin ejecta emplacement, the larger craters alone appear to be able to remix ejecta from the lunar basins in the landing zone.

## MAJOR TERRAIN TYPES AT LANDING SITES:

The proportions of the basin-related ejecta estimated for the Luna-Glob landing zone as a whole could be different at the specific landing sites. For example, flat, light-toned plains make up either the majority or significant portions of landing ellipses 1 and 4. The other occurrences of flat plains are scattered

throughout the southern sub-polar area [1] and likely belong to a class of the lunar smooth plains known as Cayley Formation [9], [10]. These plains originally were interpreted as having a volcanic origin [9] but samples collected by the Apollo 16 mission imply that an impact-related origin of the plains is more plausible [11]. This interpretation is often applied to all occurrences of light plains [12], [13], [14], [15], although a volcanic origin of some light plains [17], [18], [19] cannot be ruled out [20], [21].

## MODELS OF THE LIGHT PLAINS FORMATION:

The volcanic hypothesis for the formation of light plains in the Luna-Glob landing zone faces the difficulty of the absence of volcanic sources and volcanic features (flow fronts, domes, edifices, lava channels, or vents) in association with the occurrences of the plains. In contrast, the impact-related hypotheses do not have this problem and are strongly supported by the observations made at the Apollo 16 landing site [22] and by the samples delivered to the Earth [23]. Three types of models for the impact related origin of light plains were proposed: (1) emplacement of ejecta of the Imbrium and Orientale basins [11], (2) emplacement of ejecta of large craters in the vicinity of the light plains occurrences [13], and (3) formation of light plains due to the emplacement of impact melt [14].

Neither landing ellipse 1 nor ellipse 4 show any evidence for the presence of volcanic activity in their surroundings. The topographic analysis of the light plains occurrences around crater Manzinus suggests that these plains likely have a non-volcanic nature [24]. Thus, we favor an impact-related origin of light plains in the Luna-Glob landing sites. In [20] and [21] it was shown that light plains have a rather broad range of absolute model ages ranging from  $\sim 4.1$  to  $\sim 3.7$  Ga [21]. Such a wide variation of the model ages disfavors the hypothesis of the preferential relation of light plains to either Imbrium or Orientale events [21], although a large number of light plains patches are associated with Orientale and occur as far as about 2000 km from the basin rim or  $\sim 4$  basin radii [16]. The photogeologic analysis of the light plains occurrences shows that they typically lack characteristic features of impact melt pools such as cooling cracks, flow-like features, and lower albedo of the pools [21]. These observations disfavor the impact melt hypothesis for the light plains formation. Thus, the emplacement of the finer-grained facies of ejecta from a variety of sources appears as the most plausible explanation of the nature of light plains [13].

## SOURCES OF MATERIALS AT THE LUNA-GLOB SITES:

**Ellipse 1.** What is the possible source of light plains in landing ellipse 1? CSFD measurements for these plains suggest their age of emplacement to be  $\sim 3.82 \pm 0.02 / -0.02$  Ga (Fig. 1). Some of the chains of secondary craters on the surface of the flat plains point toward Schomberger crater and the CSFD measurements on the floor of this crater indicate its age to be  $\sim 3.82 \pm 0.03 / -0.03$  Ga (Fig. 2). The identical absolute model ages of the flat plains in the ellipse 1 and the Schomberger floor suggest that the plains represent a distal portion of ejecta of this crater. The excavation depth of the Schomberger event exceeds the total thickness of the basin ejecta in the Luna-Glob landing zone. In this case, the flat plains within ellipse 1 would represent materials that underlie the SPA ejecta blanket and represent the oldest periods of the geologic history of the Moon.

The hilly unit within the landing ellipse 1 corresponds to the contiguous ejecta of pre-Nectarian crater Manzinus. The size of this crater ( $\sim 100$  km in diameter) suggests that its impact was also able to penetrate through the SPA ejecta blanket and excavate material from beneath of it. The continuous ejecta of an impact crater represent the lowermost portions of the target stratigraphy [25] and, thus, hilly unit in ellipse 1 likely consists of materials pre-dating the SPA event.

**Ellipse 4.** At the landing ellipse 4, two units make up the surface in about equal proportions. The hilly unit obviously represents rough ejecta of Moretus crater. The chains of secondary craters and the floor of Moretus have identical absolute model ages of  $\sim 3.81 \pm 0.02 / -0.03$  Ga (Moretus, Fig. 2) and  $\sim 3.82 \pm 0.06 / -0.09$  Ga (hilly unit, Fig. 1). Because of its diameter, it is very likely that the Moretus impact has penetrated through the entire layer of basin ejecta in the Luna-Glob landing zone. This means that the Moretus ejecta (unit 1) in landing ellipse 4 may consist of materials predating the SPA event.

The absolute model age for the flat plains in the ellipse 4 is  $\sim 3.69 \pm 0.03 / -0.03$  Ga (Fig. 1), which corresponds to the Upper Imbrian period [26]. Large craters

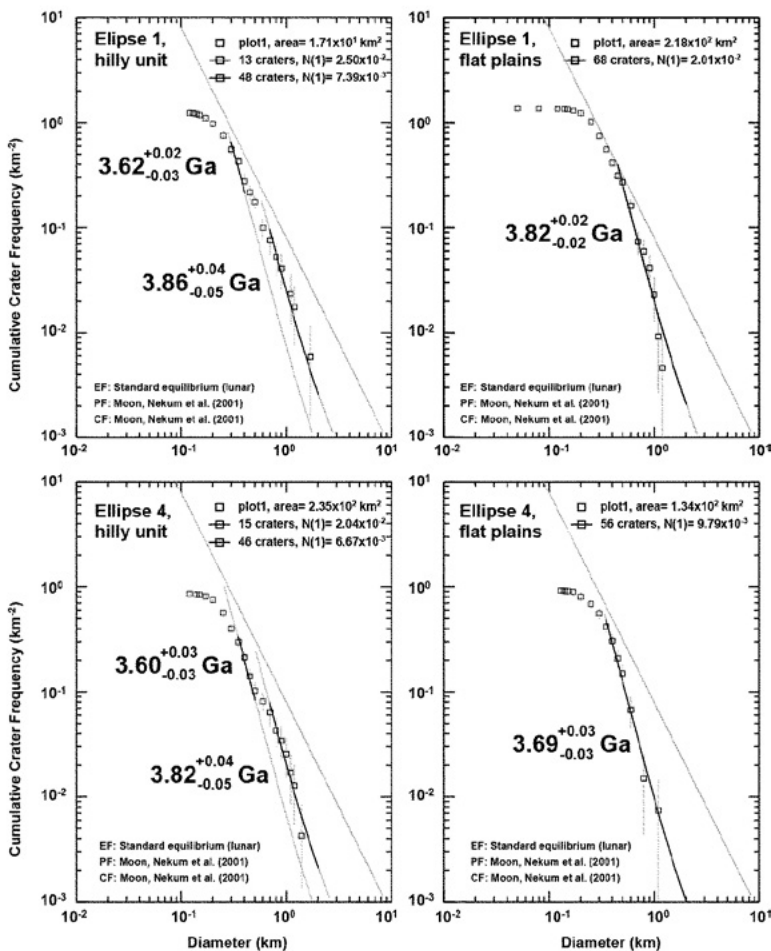
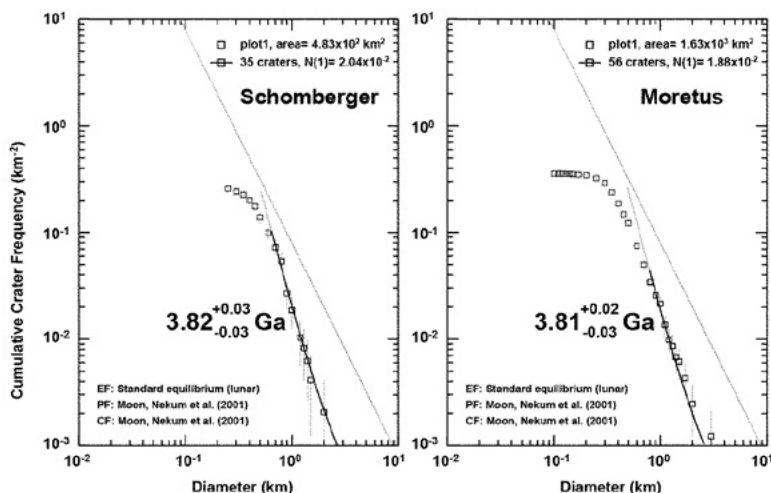


Fig. 1. Absolute model ages of units within ellipses 1 and 4



of this age are absent in the broad surroundings of landing ellipse 4 [1]. Thus, the Schrödinger basin is the best candidate for the source of the flat plains material in the ellipse. If this is the case, the flat plains also represent materials that predated the SPA event, have been excavated from a depth of

tens of kilometers [27], and characterize the lower crustal (or upper mantle) material of the early Moon.

**Ellipse 6.** Landing ellipse 6 appears to have the simplest geology among the top three landing sites. The bulk of materials in ellipse 6 (unit 1) consists of superposed and mixed contiguous ejecta of the craters Boguslawsky, Boussingault, and an unnamed crater at 66.9oS, 46.7oE. All these craters are large (100-120 km in diameter) and potentially could excavate materials from beneath the entire layer of basin ejecta. Because the contiguous ejecta are samples of the lowermost layers of the target, unit 1 would largely consist of materials predating the SPA basin with a minor fraction of ejecta of this basin. Unit 2 in ellipse 6 likely represents mass-wasted materials derived from the surrounding hills of unit 1. Thus, the composition of both units in the ellipse 6 is expected to be identical to each other.

## ACKNOWLEDGEMENTS:

The work is supported by the Russian Science Foundation grant № 17-17-01149: «Reconstruction of geologic history of polar areas of the Moon using new high-accuracy data to understand sources, distribution and accumulation of volatiles (water) on the Moon.

## REFERENCES:

- [1] Wilhelms, D.E., Howard, K.A., Wilshire, H.G., Geologic map of the South Side of the Moon // 1979. US Geological Survey Map I-1192.
- [2] Garrick-Bethell, I., Zuber, M.T. Elliptical structure of the lunar South Pole-Aitken basin // *Icarus* 2009. V. 204, P. 399-408.
- [3] Mitrofanov, I., Djachkova, M., Litvak, M., Sanin, A., The method of landing sites selection for Russian lunar lander missions // EGU 2016, 2016. V. 18, abstr. 10018.
- [4] Djachkova, M.V., Litvak, M.L., Mitrovanov, I.G., Sanin, A.B. Selection of landing sites of the Luna-25 lander in the vicinity of lunar South Pole // *Solar System Res.*, 2017. in press.
- [5] Ivanov, M.A., Abdrakhimov, A.M., Basilevsky, A.T., et al. Geological characterization of the three high-priority landing sites for the Luna-Glob mission // *Planetary and Space Sci.* 2017., in press.
- [6] Petro, N. Pieters, C.M., Modeling the provenance of the Apollo 16 regolith // *J. Geophys. Res.*, 2006. V. 111, E09005.
- [7] Head, J.W., Fassett, C.I., Kadish, S.J., et al. Global Distribution of Large Lunar Craters: Implications for Resurfacing and Impactor Populations // *Science*, 2010. V. 329, P. 1504-1507.
- [8] Kadish, S.J., Fassett, C.I., Head, J.W., et al. A global catalog of large lunar craters ( $\geq 20$  km) from the Lunar Orbiter Laser Altimeter // 42nd Lunar and Planetary Sci. Conf., 2011. Abstract 1006.
- [9] Wilhelms, D.E. Summary of Lunar stratigraphy-telescopic observations // USGS Prof. Paper, 599-F 1970.
- [10] Wilhelms, D.E., McCauley, J.F. Geologic map of the near side of the Moon // US Geological Survey Map I-703, 1971.
- [11] Eggleton, R.E., Schaber, G.G. Cayley Formation interpreted as basin ejecta // NASA Apollo 16 Preliminary Scientific Report 1972. P. 29-7 - 29-16.
- [12] Chao, E.C.T., Soderblom, L.A., Boyce, J.M., Wilhelms, D.E., Hodges, C.A., Lunar light plains deposits (Cayley Formation) - A reinterpretation // 4th Lunar and Planetary Sci. Conf. 1973. P. 127-128.
- [13] Oberbeck, V.R., Morrison, R.H., Hertz, F., Quaide, W.L., Gault, D.E., Smooth plains and continuous deposits of craters and basins // *Proc. Lunar and Planetary Sci. Conf.*, 5, 1974. P. 111-136.
- [14] Head, J.W. Orientale multi-ringed basin interior and implications for the petrogenesis of lunar highland samples // *The Moon*, 1974. V. 11, P. 327-356.
- [15] Meyer, H.M., Denevi, B.W., Boyd, A.K., Robinson, M.S. The distribution and origin of Lunar light plains around Orientale basin // 44th Lunar and Planetary Science Conference, 2013. Abstract 1539.
- [16] Meyer, H.M., Denevi, B.W., Boyd, A.K., Robinson, M.S. The distribution and origin of lunar light plains around Orientale basin // *Icarus*, 2016. V. 273, P. 135-145.
- [17] Schultz, P.H. Spudis, P.D. Evidence for ancient mare volcanism // *Proceedings of 10th Lunar and Planetary Sci. Conf.*, 1979. P. 2899-2918.
- [18] Neukum, G. Different ages of lunar light plains // *The Moon*, 1977. V. 17, P. 383-393
- [19] Hawke, B.R., Head, J.W. Lunar KREEP volcanism: geologic evidence for history and mode of emplacement // *Proc. Lunar and Planetary Sci. Conf.*, 9, 1978. P. 3285-3309.
- [20] Thiessen, F., Hiesinger, H., van der Bogert, C.H., et al. Surface ages and mineralogy of lunar light plains in the South-Pole Aitken basin // 43rd Lunar and Planetary Sci. Conf., 2012. Abstract 2060.
- [21] Hiesinger, H., van der Bogert, C.H., Thiessen, F., Robinson, M.S. Absolute model ages of light plains in the southern lunar hemisphere // 44th Lunar and Planetary Sci. Conf., 2013. Abstract 2827.
- [22] Young, J.W., Mattingly, T.K., Duke, C.M. Crew observations // *Apollo 16 Prelim. Sci. Rep.*, 1972. P. 5-1.
- [23] Apollo 16 Preliminary Examination Team The Apollo 16 lunar samples: Petrographic

and chemical description // *Science*, 1973. V. 179, P. 23-34.

[24] Ivanov, M.A., Hiesinger, H., Abdrakhimov, A.M. et al. Landing site selection for Luna-Glob mission in crater Boguslawsky // *Planet. Space Sci.*, 2015. V. 117, P. 45-63.

[25] Oberbeck, V.R. The role of ballistic erosion and sedimentation in lunar stratigraphy // *Rev. Geophys. Space Phys.*, 1975. V. 13, P. 337-363.

[26] Stöffler, D., Ryder, G., Ivanov, B.A., et al., Cratering history and lunar chronology // *Rev. Mineral. Geochem.*, 2006. V. 60, P. 519-596.

[27] Wieczorek, M.A., Phillips, R.J. Lunar multiring basins and the cratering process // *Icarus*, 1999. V. 139, P. 246-259.

# LUNA-25 LANDING SITES CANDIDATES: DETAILED ANALYSIS

M.V. Djachkova<sup>1</sup>, I.G. Mitrofanov<sup>1</sup>, A.B. Sanin<sup>1</sup>,

<sup>1</sup>*Space Research Institute of the Russian Academy of Sciences (IKI), 84/32  
Profsoyuznaya Str, Moscow, Russia, 117997*

## KEYWORDS:

Moon, Luna-25, landing site.

## INTRODUCTION:

The landing site selection method developed by our team allowed us to identify eleven candidates, from which the main landing site and preliminary reserved landing site for Luna-25 mission were selected. Detailed analysis of these two candidates based on data of a large scale (such as LRO/LOLA measurements and LRO/LROC images) is presented in this work.

# CONTRIBUTION OF THE LUNAR BASIN EJECTA TO MATERIALS WITHIN THE LUNA-GLOB LANDING ZONE

M.A. Ivanov<sup>1</sup>, A.M. Abdrakhimov<sup>1</sup>, A.T. Basilevsky<sup>1</sup>, N.E. Demidov<sup>1</sup>, E.N. Guseva<sup>1</sup>, J.W. Head<sup>2</sup>, H. Hiesinger<sup>3</sup>, A.A. Kohanov<sup>4</sup>, S.S. Krasilnikov<sup>1</sup>

<sup>1</sup>Vernadsky Institute of Geochemistry and Analytical Chemistry, Russian Academy of Sciences, 19, Kosygin st., 119991 Moscow, Russia; mikhail\_ivanov@brown.edu;

<sup>2</sup>Department of Geological Sciences, Brown University, Providence, RI 02912 USA;

<sup>3</sup>Institut für Planetologie, Westfälische Wilhelms-Universität Münster, Wilhelm-Klemm-Str. 10, 48149 Münster, Germany;

<sup>4</sup>Moscow State University of Geodesy and Cartography (MiiGAIK), Moscow, Russia;

## KEYWORDS:

Moon, Luna-Glob, lunar basins, ejecta emplacement

## INTRODUCTION:

The Luna-Glob landing zone is in the southern sub-polar region within the heavily cratered highlands. The main feature of this area is the southern portion of the rim of the South Pole-Aitken (SPA) basin [1, 2]. The major impact structures, basins, are the main sources of materials that form the megaregolith of the Moon [3], [4] and in the landing zone as well. In this region, numerous large craters (up to 100-120 km in diameter and a few kilometers deep) and high-standing massifs (several tens of kilometers across, 3-6 km high) form a very rough surface at tens of kilometers scale. The ancient terrains of pre-Nectarian and Nectarian ages prevail in the landing zone [1]. The units that compose the pre-Nectarian terrains are mostly related to the emplacement of ejecta of impact basins, especially SPA. However, during formation of the post-SPA basins, their ejecta that also were transported to large distances [5], [6], [7], [8] could be deposited within the Luna-Glob landing zone. In order to facilitate interpretation of the results of the Luna-Glob in-situ analyses, it is important to assess the potential contribution of ejecta of the lunar impact basins to the materials that may be encountered in the landing zone.

## MODELS OF THE EJECTA THICKNESS RADIAL VARIATIONS:

A range of models of the material transport and ejecta emplacement have been developed [9], [10], [11], [12], [13], [14], [15], [16] (Fig. 1). Among these, only the model by [15] is supported by the observations of topography associated with the best preserved lunar basin, Orientale. The application of this model, however, is limited by the estimated ejecta thickness at the Cordillera rim. For the other basins, this thickness can be different and, thus, the estimates of the ejecta radial thickness can be biased. Because of this limitation, in our study we used the theoretical model by [13], which relates the ejecta thickness,  $T$ , and the distance from the impact point,  $r$ , by the following formula:  $T=0.0078 \cdot R \cdot (r/R)^{-2.61}$ , where  $R$  is the radius of the crater transient cavity. It must be emphasized that all models of the ejecta emplacement do not account for the separation of the ejecta curtain into individual rays and consider the emplaced ejecta as a contiguous blanket. This obviously erroneous assumption shifts the model thickness values up and tends to overestimate the thickness of the ejecta.

## MODEL THICKNESS OF LUNAR BASIN EJECTA IN THE LUNA-GLOB LANDING ZONE:

In order to assess the possible amount of materials from different major remote sources within the landing zone, we used the approach developed in [17]. Specifically, we constructed a  $1 \times 10$  grid for the southern sub-polar region (southward of 60oS) and in each point of the grid we calculated the thickness of materials ejected by each lunar basin [18]. In order to estimate the basin ejecta thickness, we implemented the model developed in [13].

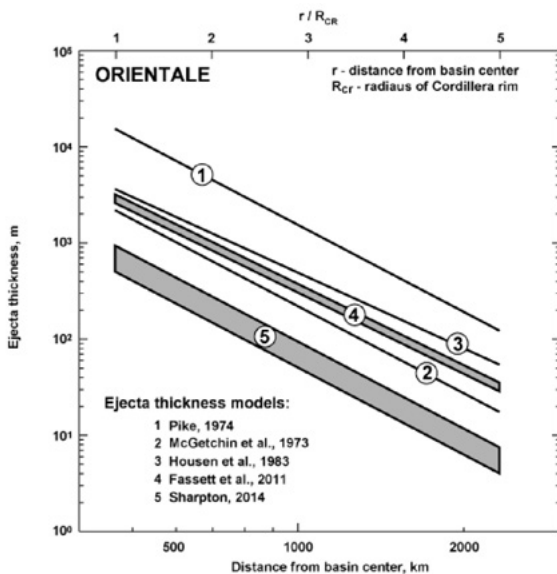


**Fig. 1.** Comparison of the radial ejecta thickness of the Orientale basin estimated with the help of different models.

An important part of the investigations of the variation of the basin ejecta thickness [17], [19], [20] was an assessment of the mixing ratio [12] of local and remote materials brought by large impacts. This parameter helps to estimate the depth to which the ejecta affect the original material upon their emplacement. Unfortunately, the mixing ratio is poorly constrained and its usage sometimes gives unrealistic results. For example, attempts to estimate the depth of mixing in the case of the SPA basin yield values of the mixing depth as large as ~50 km. Such a depth is about six times larger than the estimated thickness of the basin ejecta. Thus, in our work, we did not employ the mixing ratio to determine the depth of mixing and simply calculate the fraction of the brought materials based on their model thicknesses. We also grouped the basins by their stratigraphic position [4] and estimate fractions of materials delivered to the Luna-Glob landing zone by the SPA basin and by the pre-Nectarian, Nectarian, and Imbrian basins separately.

## RESULTS AND DISCUSSION:

The results of our model show the following. As expected, the major contributor of materials to the Luna-Glob landing zone is the SPA basin (Fig. 2). Near the rim of the basin transient cavity, the thickness of the ejecta is estimated to be ~8.1 km.

However, because the model thickness follows a power law, it rapidly decreases away from the basin rim. For example, the model thickness of the SPA ejecta at the southeast corner of the Luna-Glob landing zone (the closest to the SPA) is ~5.5 km. For the most distant, northwest, corner of the Luna-Glob landing zone the model thickness is ~1.8 km. The mean model thickness of the SPA ejecta within the Luna-Glob area is ~3.2 km, which is ~96% of the total thickness of ejecta of all lunar basins in this region. We assume that the SPA basin is the oldest lunar basin and, thus, its ejecta form the base of the stratigraphy of the basin ejecta in the study area.

All the pre-Nectarian basins have added a small fraction, ~3.6%, to the total thickness of the basin ejecta within the Luna-Glob landing zone. Among these basins, Australe (Fig. 2) appears as the most important source of materials. The model ejecta blanket of Australe overlays the eastern side of the landing zone where its thickness can be ~130-150 m. Within the landing zone, the mean model thickness of the Australe ejecta is ~70 m. The mean model thickness of the ejecta of the other pre-Nectarian basins in the landing zone is a few meters or less.

Both the Nectarian and Imbrian basins (Fig. 2) have delivered a negligible amount (a few tens of meters) of materials to the Luna-Glob landing region compared with the thickness of the SPA ejecta (several kilometers). Among the Nectarian basins, the most important sources of the remote materials in the



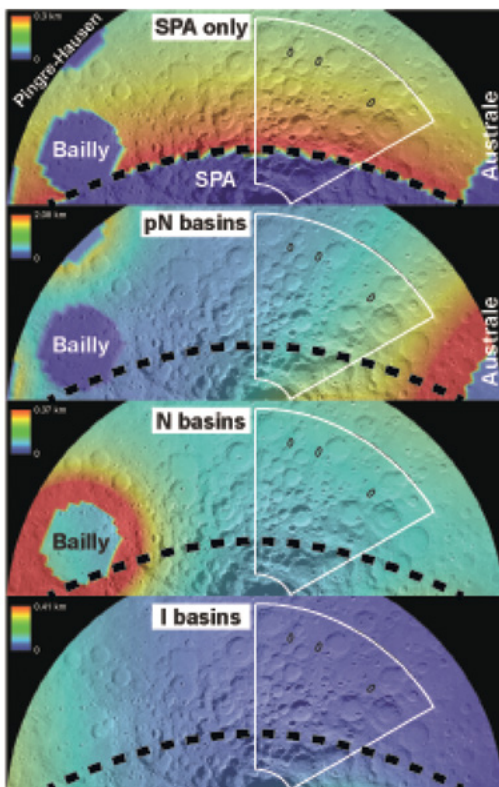


**Fig. 2.** The model estimates of the thickness of lunar basin ejecta in the Luna-Glob landing zone (white outline).

Luna-Glob zone are Serenitatis and Nectaris. Despite the fact that the Imbrian Schrödinger basin is the closest to the landing zone, the mean model thickness of its ejecta is estimated to be less than one meter and the main Imbrian source of foreign material in the landing zone is the Imbrium basin itself.

In the framework of the no-mixing model, ejecta of the post-SPA basins form the upper portion of the composite layer of ejecta of the basins in the landing zone. The crater gardening, however, locally would tend to change the regional stratigraphy of the basin ejecta and an analysis of local geology is needed in order to estimate the most probable sources of material at each specific landing site [21].

## ACKNOWLEDGEMENTS:

The work is supported by the Russian Science Foundation grant № 17-17-01149: «Reconstruction of geologic history of polar areas of the Moon using new high-accuracy data to understand sources, distribution and accumulation of volatiles (water) on the Moon.

## REFERENCES:

- [1] Wilhelms, D.E., Howard, K.A., Wilshire, H.G. Geologic map of the South Side of the Moon // US Geological Survey Map I-1192, 1979.
- [2] Garrick-Bethell, I., Zuber, M.T. Elliptical structure of the lunar South Pole-Aitken basin // *Icarus* 2009. V. 204, P. 399-408.
- [3] Moore, H.J., Hodges, C.A., Scott, D.H. Multiringed basins - illustrated by Orientale and associated features // *Proc. Lunar and Planetary Sci. Conf.* 1974. V. 5, P. 71-100.
- [4] Wilhelms, D.E. The geologic history of the Moon. US Geological Survey Special Paper 1348, 1987. 302 p.
- [5] Arvidson, R., Drozd, C.M., Hohenberg, C.M., et al. Horizontal transport of the regolith, modification of features, and erosion rate on the lunar surface // *The Moon* 1975, V. 13, P. 67-79.
- [6] Head, J.W. Processes of Lunar crater degradation: Changes in style with geologic time // *The Moon*, 1975. V. 12., P. 299-329.
- [7] Haskin, L.A., Korotev, R.L., Rockow, K.M., Jolliff, B.L. The case for an Imbrium origin of the Apollo thorium-rich impact-melt breccias // *Meteoritics and Planetary Sci.*, 1998.

V. 33, p. 959-975.

- [8] Wieczorek, M.A., Zuber, M.T. A Serenitatis origin for the Imbrian grooves and South Pole-Aitken thorium anomaly // *J. Geophys. Res.*, 2001. V. 106, P. 27853-27864.
- [9] McGetchin, T.R., Settle, M., Head, J.W. Radial thickness variation in impact crater ejecta: Implications for lunar basin deposits // *Earth Planet. Sci. Lett.*, 1973. V. 20, P. 226-236.
- [10] Pike, R.J. Ejecta from large craters on the Moon: Comments on the geometric model of McGetchin et al. // *Earth and Planetary Science Letters*, 1974. V. 23, P. 265-274.
- [11] Oberbeck, V.R., Morrison, R.H., Hertz, F., Quaide, W.L., Gault, D.E. Smooth plains and continuous deposits of craters and basins // *Proc. Lunar and Planetary Sci. Conf.*, 1974. V. 5, P. 111-136.
- [12] Oberbeck, V.R. The role of ballistic erosion and sedimentation in lunar stratigraphy // *Review of Geophysics and Space Physics*, 1975. V. 13, P. 337-363.
- [13] Housen, K.R., Schmidt, R.M., Holsapple, K.A. Crater ejecta scaling laws' fundamental forms based on dimensional analysis // *J. Geophys. Res.*, 1983. V. 88, P. 2485-2499.
- [14] Haskin, L.A., Moss, B.E., McKinnon, W.B. On estimating contributions of basin ejecta to regolith deposits at lunar sites // *Meteoritics and Planetary Sci.*, 2003. V. 38, P. 13-33.
- [15] Fassett, C.I., Head, J.W., Smith, D.E., Zuber, M.T., Neumann, G.A. Thickness of proximal ejecta from the Orientale Basin from Lunar Orbiter Laser Altimeter (LOLA) data: Implications for multi-ring basin formation // *Geophys. Res. Lett.*, 2011. V. 38, L17201.
- [16] Sharpton, V.L. Outcrops on lunar crater rims: Implications for rim construction mechanisms, ejecta volumes and excavation depths // *J. Geophys. Res.*, 2014. V. 119, P. 154-168.
- [17] Petro, N. Pieters, C.M. The lunar-wide effects of basin ejecta distribution on the early megaregolith // *Meteoritics and Planetary Sci.*, 2008. V. 43, P. 1517-1529.
- [18] Spudis P.D. *The Geology of Multi-ring Basins: The Moon and Other Planets*. Cambridge University Press, New York and Cambridge, 1993. 263 p.
- [19] Petro, N.E. Pieters, C.M. Surviving the heavy bombardment: Ancient material at the surface of South Pole-Aitken Basin // *J. Geophys. Res.*, 2004. V. 109, E06004.
- [20] Petro, N. Pieters, C.M. Modeling the provenance of the Apollo 16 regolith // *J. Geophys. Res.*, 2006. V. 111, E09005.
- [21] Ivanov, M.A., Abdrakhimov, A.M., Basilevsky, A.T., et al. Sources of materials three high-priority landing sites of the Luna-Glob mission // *MSSS-8*, 2017. (this volume).

# GEOLOGY OF THE CHANG'E-5 CANDIDATE LANDING REGION IN NORTHERN PROCCELLARUM

Y.Q. Qian<sup>1</sup>, L. Xiao<sup>1</sup>, J.N. Zhao<sup>1</sup>, G.X. Wang<sup>2</sup>, Z. Zhao<sup>2</sup>, S. Ying<sup>2</sup>, J.W. Head<sup>3</sup>

<sup>1</sup>Planetary Science Institute, China University of Geosciences (Wuhan), Wuhan, Hubei, 430070, China, yuqi\_qian@cug.edu.cn;

<sup>2</sup>Beijing Spacecrafts, Beijing, 100089, China;

<sup>3</sup>Brown University, Providence, RI, 02912, USA

## KEYWORDS:

Moon; Chang'E-5; Geology; Regolith; Procellarum

## INTRODUCTION:

Chang'E-5, China's first sample return mission, is targeted to land within the Northern Oceanus Procellarum region (41-45°N, 49-69°W; an area of ~55 000 km<sup>2</sup>), named as the Rümker region (Fig. 1, 2). Early geologic mapping [1] showed that the region was characterized by a volcanic complex (Rümker Hills), large expanses of volcanic plains, and a few kipukas of highland materials. Subsequently, more detailed analysis using multispectral data and crater counts [2] subdivided the mare plains into two major units with significantly different model ages; P10 (western; ~3.44 Ga) and P58 (eastern; ~1.33 Ga). More recently, multiple data sets were used to assess the geology, mineralogy and age of the Rümker Hills [3], the northern part of which extends into the target area. The purpose of the current study is 1) to describe the characteristics of the main geologic units in the area, 2) to assess their importance in the context of major outstanding scientific problems in lunar science, 3) to suggest broad geologic units that most directly address these outstanding problems, and 4) to provide broad guidelines for optimizing landing and surface operations success.

## KEY QUESTIONS IN LUNAR AND PLANETARY SCIENCE:

Among the key questions in lunar science related to the target region [4] are: 1) What is the absolute age of the youngest phase of lunar volcanism? 2) What does its mineralogy and petrology tell us about conditions in the lunar mantle at that time?, and 3) What is the flux of impactors at this time and how can we use the absolute age of these youngest units to improve calibration of the impact flux and lunar and planetary chronology?

## GEOLOGY:

Detailed study of the Rümker Hills [3] showed that it was a center of volcanism during the Imbrian Period, when three main low-Ti basalt units were emplaced (~3.71, 3.58, and 3.51 Ga); the broad rise contains small shield volcanoes and local evidence of emplacement of Fra Mauro Formation, interpreted as Imbrium basin ejecta. Local domes may be as young as Eratosthenian [3].

Important in distinguishing and characterizing mare basalt units are their FeO and TiO<sub>2</sub> abundances; we derived these for the study region from Kaguya Multi-band data using the method described by Lucey [5] and further developed by Otake [6]. We used the FeO and TiO<sub>2</sub> abundances together with OMAT values [7, 8] and crater density to analyze the geology of the candidate landing region to address our four broad goals and address the three fundamental scientific questions. According to the TiO<sub>2</sub> and FeO abundances (Fig. 1), the candidate landing region can be divided into at least four mare geologic units. Region 1 (northwest) has relatively low TiO<sub>2</sub> (1-2.5%) and FeO (14-17%) abundances and contains many more craters than Region 3. Region 3 (east) has high TiO<sub>2</sub> (3.5-7%) and FeO (16-17.5%) abundances. Region 2 represents a transition zone between 1 and 3. Region 4, on the western edge of the Rümker Hills, is low TiO<sub>2</sub> but high FeO, with a smaller number of impact craters. A few kipukas of possible highlands occur in the mare units (Fig. 2) and the Rümker Region and Dome Region can also be mapped. We used CFSD methods [9] in four mare regions to acquire their model ages (Table 1). On the basis of our analysis, supplemented by the detailed Rümker Hills analysis [3], we have reconstructed the geologic history of the Chang'E-5 candidate landing site region: Volcanic activity in the Rümker Hills was active between ~3.71-3.51 Ga [3]. Subsequently, the late-Imbrian low-Ti and Fe magmas erupted

at  $\sim 3.46$  Ga and formed the Region 1  $I_2$  unit. At a much later time,  $\sim 1.48$ – $1.59$  Ga, the Region 2, late-Eratosthenian high Ti and Felavas erupted, spread across the surface, and buried the  $I_2$  unit. In Region 3,  $E_2$  covered the highland material directly and perhaps the  $I_2$  also covered the highland material in Region 3 beneath  $E_2$ . This initial geologic map is the basis for the 1:250 000 geologic map already in progress.

## DISCUSSION:

### LUNAR REGOLITH.

The properties of lunar regolith are closely related to the bedrock and impact-gardening history. Crater morphology methods were used to assess the depth of regolith [10, 11] (Table 1). Compared with Apollo landing site regolith depths, the relationship between model ages and mare basalt regolith depths (Table 1) are consistent with the regolith growth history.

### LANDING SITE SUGGESTION.

On the basis of the importance of analysis of samples of very young mare basalts for the understanding of lunar thermal and petrogenetic evolution and impact flux [4], we propose Region 3 as the most interesting region for sample drilling and return. Additional analyses are underway to assess more specific optimal sites for landing and drilling, guided in part by previous successful Luna sample return missions [12].

**Table 1.** Model ages and regolith thicknesses of mare basalt regions in the candidate landing region. Model age are acquired from CFSD methods [9] and regolith thickness are acquired from crater morphology methods [10-11].

Unit	Model Age (Ga)	Era	Regolith Depth(m)	
			Median	Mean
Region1	3.46	$I_2$	2.9	4.0
Region2	1.48	$E_2$	2.6	3.1
Region3	1.59	$E_2$	2.4	2.9
Region4	1.78	$E_2$	1.9	2.3

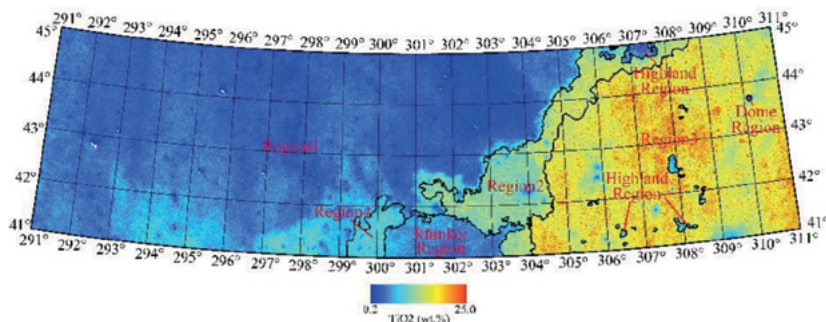


**Fig. 1.**  $TiO_2$  Abundances Map of the Chang'E-5 Candidate Landing Region.

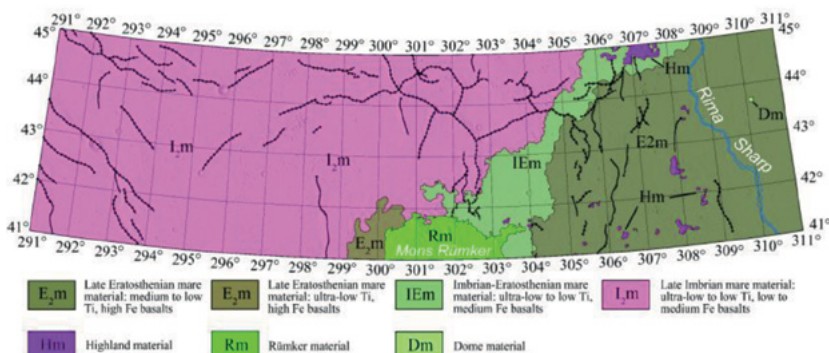


**Fig. 2.** Regional Geologic Map of the Chang'E-5 Candidate Landing Site Region.

**REFERENCES:**

- [1] Scott D.H., Eggleton R.E. USGS. 1973. Map I-805.
- [2] Hiesinger H., Head J.W., Wolf, U. JGR. 2003. 108. E7, 1-27.
- [3] Zhao J.N., Xiao L., Qiao L. et al. JGR. 2017. 122, 1-24.
- [4] Paulikas, G. A., Pieters, C. M. et al. 2007. The Scientific Context for Exploration of the Moon, COMPLEX/NRC, National Academies Press.
- [5] Lucey P.G., Blewett D.T. JGR. 2000. V. 105. No. E8. P. 297-305 .
- [6] Otake H., Ohtake M., Hirata N. LPSCXLIII. 2012. 1905.
- [7] Lucey P.G., Blewett D.T. JGR. 2000. V. 105. No. E8. P. 377-386.
- [8] Lemelin M., Lucey P.G., Gaddis L.R. LPSC XLVII. 2016. 2994.
- [9] Neukum G., Ivanov B.A., Hartmann W.K. Space Science Reviews. 2001. V. 96. No. 4. P. 55-86.
- [10] Quaide W.L., Oberbeck V.R. JGR. 1967. V. 73. No. 16. P. 5247-5270.
- [11] Bart G.D., Nickerson R.D., Lawder M.T. Icarus. 2011. V. 215. No. 2. P. 485-490.
- [12] Basilevsky A.T., and Head J.W. Planet. Space Sci., 2012, 73, 302-309.

# CRATER VON KARMAN: CHANG'E-4 FARSIDE LANDING MISSION

Yangxiaoyi Lu<sup>1</sup>, V.V. Shevchenko<sup>2</sup>

<sup>1</sup>Beijing Planetarium, Beijing, China, luyangxiaoyi@gmail.com;

<sup>2</sup>Sternberg State Astronomical Institute, Moscow state University, Moscow, Russia.

## KEYWORDS:

Chang'E-4 soft landing mission, Lunarfar-side, Von Karman, South Pole-Aitken basin.

## INTRODUCTION:

Chang'E-4 will be the first soft landing mission on the lunar far-side in 2018 year. Chang'E-4 landing area is initially selected as the Von Karman crater inside the South Pole-Aitken basin on the lunar far-side. A relay satellite is used to realize the lander and rover to the ground communication, and a Halo orbit around the L2 point is chosen as its mission orbit. The lander, rover and relay satellite containing six domestic scientific payloads and three international scientific payloads, have carried out scientific exploration focusing on VLF radio astronomical observation, roving area topography survey, mineral composition and shallow structure investigation. As we know, that area Von Karman (~3.97 Ga) is more like the Imbrian aged smooth mare. It include volcanic and impact categories. Volcanic products are primarily discrete, noncontiguous mare deposits occurring exclusively within, or breaching the rims of, craters or basins.

## REFERENCES:

- [1] J. Ziglaret. al. (2007), Technologies toward Lunar Crater exploration, Carnegie Mellon University – Robotics Institute
- [2] Scholten, F. et al. (2012), J. Geophys. Res., 117, E00H17
- [3] Zuber, M. et al. (2010) Space Sci. Rev., 150, 63–80
- [4] National Science Foundation of China, China Academy of Sciences. Space Science, Chinese disciplinary development strategy in the next 10 years [M]. Beijing, Science Press, 2012
- [5] Yu D Y. Wu X Y. Wu W R. Review of technology development for Chinese Lunar Exploration Program [J]. Journal of Deep Space Exploration. 2016.3.4..307-314.



Fig.1 . Von Karman basin(LRO data)

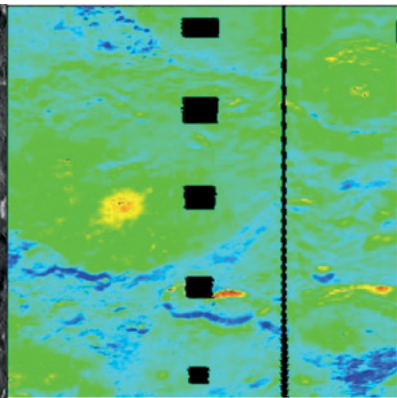


Fig.2. Iron distribution(Clementine )

# SPIN-ORBITAL EVOLUTION AND INTERIOR OF THE MOON: PAST, MODERN, FUTURE

A. Gusev<sup>1</sup>, H. Hanada<sup>2</sup>, A. Kosov<sup>3</sup>, J. Ping<sup>4</sup>, M. Vasilev<sup>5</sup>

<sup>1</sup>Kazan Federal University, Kazan, Russia;

<sup>2</sup>National Astronomical observatory of Japan, Oshu, Japan;

<sup>3</sup>IKI RAS, Moscow, Russia;

<sup>4</sup>NAOC CAS, Beijing, China;

<sup>5</sup>IAA RAS, S-Petersburg, Russia. agusev33@gmail.com

## KEYWORDS:

The Moon, physical libration, interior, Lunar Radio Exploration, Phase Radio Ranging.

## INTRODUCTION:

The problem of rotation, physical librations and inner structure of the multi-layer Moon remain a central problem for selenodesy, selenodynamics and selenophysics [1]. Its actuality increases with an increase of accuracy of different kind observations of the Moon. Now the laser ranging measurements of distances to the lunar reflectors achieves a few centimeters level of accuracy. The LRO, GRAIL, ChangE-3/4, ILOM [2] projects are focused on even more precision description of a topography, gravitational field, physical librations, spin-orbital evolution and interior structure of the Moon.

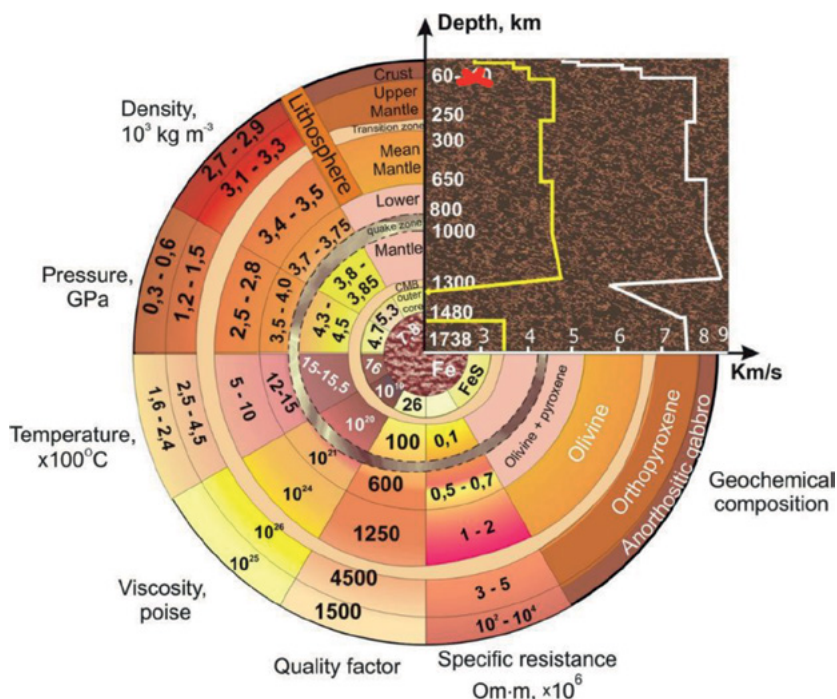


Fig.1. Interior structure of the Moon.

## MODERN METHODS:

We will show how the milliarsecond precision observations of lunar physical librations and lunar tides in the project ChangE-3/4/5/6, Luna-25/26/27: the radio beacons on the Moon [3], or the long-term observations of the lunar satellite with high-precision camera and laser altimetry by Differential, Inverse and Same Beam Interference (SBI) of VLBI/VGOS /GNSS astrometry may be used for determining the parameters of liquid and rigid cores of the Moon.

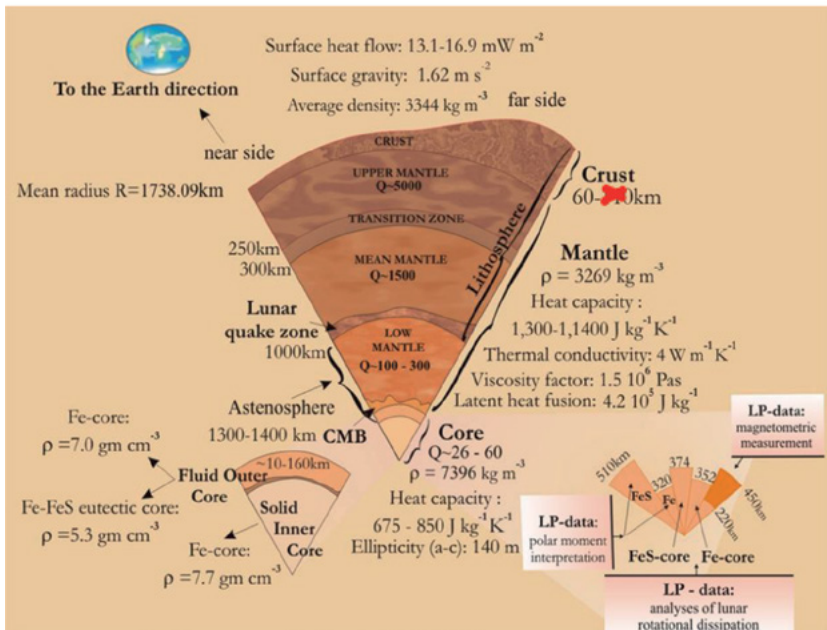


Fig.2. Two-layer Lunar Core

## RESULTS:

It will be shown also, that the analytical and numerical theories of physical librations of the Moon can be used as the convenient tool for carrying out of modeling of the future observation from a lunar surface, for understanding of distinctions in lunar coordinate systems and carrying out of the approached estimations of changes in Lunar dynamic characteristics and Lunar Navigation Almanac (LNA).

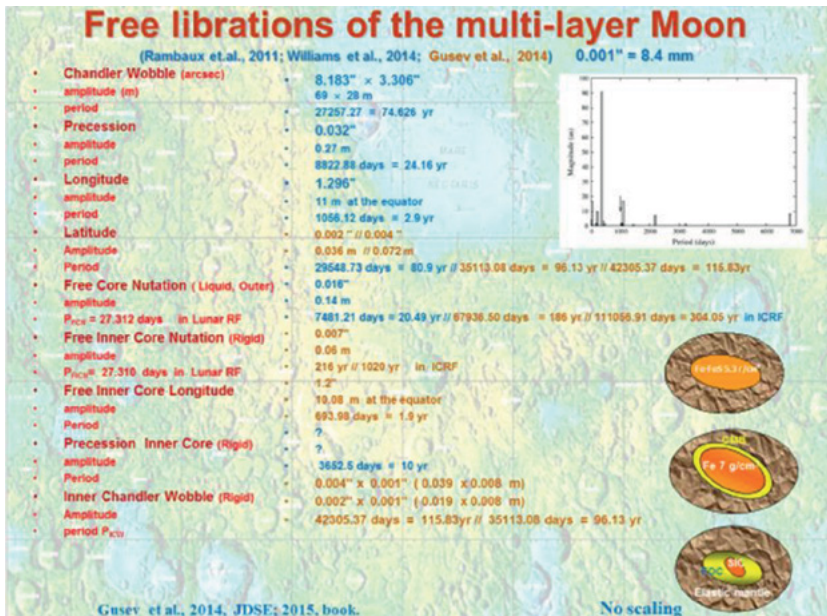


Fig.3. Free Librations of the multi-layer Moon

The LNA, which is based on the high-precision theory of the orbital-rotational motion of the Moon, is intended for the accurate navigation of space vehicles in the vicinity of the Moon, for coordinate - time and navigation support for the precise landing of space vehicles on the Moon, for remote comparison of time



scales and frequencies for lunar scientific equipment. A new stage of exploration and development of the Moon requires detailed measurements of the position and speed of instruments on the lunar surface, selenographic coordinate systems, lunar mapping, navigation on the lunar surface and near-moon space, time-temporal correlation and the transfer of a huge amount of data from scientific experiments such as a stable long-lived beacons, an effective laser angular reflectors of big dimensions (bCCR), lunar seismological instruments.

## DISCUSSIONS:

The new prospects for establishment of a liquid/rigid core existence and for studying its contribution in physical librations and spin-orbital evolution of the Moon, and also for direct studies of tidal and non-tidal “breath” of the Moon: variations of its shape, gravitational field and selenopotential coefficients will be opened.

## FUTURE PLANS:

Radio Ranging and VLBI/VLBI 2010/VLBI Global Observing System (VGOS, formerly VLBI2010) techniques are considered now as important part of the programs using for both space probes navigation and the study of orbital and rotational motion of the Moon. China and Russia have the potential to support Lunar and Martian explorations by means of existing and planned VLBI/VLBI 2010/VGOS networks, by rapidly developing technology of phase radio ranging and using advanced methods of analysis of VLBI and ranging observations. Adding here their good geographical locations and distribution, the joint solve and develop the key techniques which are limiting the Chinese and Russian Lunar exploration and navigations in deep space could be very productive.

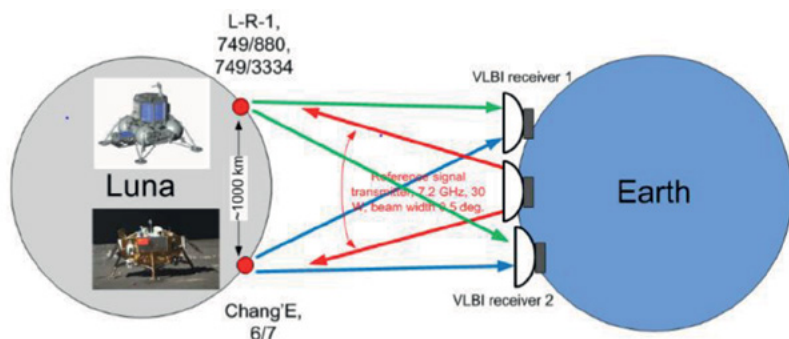


Fig.4. China-Russia Lunar Radio Science Experiment [4]

Differential radio and optical technologies have been proposed for measurements of Lunar physical librations and lunar tides. A new big size corner cubes reflectors (CCR) and a stable long-lived radio beacons would be desirable experiments on future lunar landers. Sensitivities to physical libration and tidal displacements would be enhanced by a broad geographical spread of the CCR, radio beacons, seismometers at ChangE - 4/5/6, Luna - 25, 26, 27 projects.

## REFERENCES:

- [1] Gusev A., Hanada H., Petrova N., Kosov A., Kuskov O., Kronrod V., Kronrod E., Rotation, physical librations and interior structure of the active and multi-layer Moon, Monograph, Kazan University Publishing Co., 2015, Kazan. 328pp. (Russian+English)
- [2] Hanada H., Gusev A. et al., Development of Small Telescope like PZT and Results of Experiments on the Ground. // Gyroscopy and Navigation, v.8, 27p. (2017, in press)
- [3] Gromov V., Kosov A., Abstract of 7M-S3 Int. symposium, Oct. 10-14, 2016, IKI RAS, Moscow, p. 278 (7MS3PS65).
- [4] Kosov A., Report on Russia-China workshop, Jan. 26, 2017, IKI RAS, Moscow.

# LUNAR INTERNAL STRUCTURE MODELS CONSISTENT WITH SEISMIC AND SELENODETTIC (GRAIL AND LLR) DATA AND THERMODYNAMIC CONSTRAINTS

E. Kronrod<sup>1</sup>, K. Matsumoto<sup>2</sup>, R. Yamada<sup>3</sup>, O. Kuskov<sup>1</sup>, V. Kronrod<sup>1</sup>

<sup>1</sup>Vernadsky Institute of Geochemistry and Analytical Chemistry (GEOKHI RAS), e.kronrod@gmail.com

<sup>2</sup>RISE Project, National Astronomical Observatory of Japan,

<sup>3</sup>The University of Aizu, Research Center for Advanced Information

## KEYWORDS:

Moon, internal structure, thermodynamics, numerical modeling

## INTRODUCTION:

In the recent paper [1] lunar interior models by complementing Apollo seismic travel time data with selenodetic data which have recently been improved by Gravity Recovery and Interior Laboratory (GRAIL) and Lunar Laser Ranging (LLR) were explored. Important information on the thickness of the crust, Low-velocity/viscosity zone (LVZ), core structure and seismic velocities was obtained. But this problem statement retains lunar mantle composition to be uncertain. In [2, 3] mantle composition can be simulated based on thermodynamic approach and petrological evidence from seismic data, moment of inertia (MOI) and mass.

The goal of our investigation is to obtain geochemically and geophysically consistent information on the internal structure of the Moon. The first step was to use thermodynamic approach to calculate elastic properties in the Moon's layers (shear modulus  $\mu$ , bulk modulus  $\kappa$ ) and density  $\rho$ . But it lead to increasing number of model parameters, and it was impossible to obtain reasonable result. Here we modified problem statement and included geochemical data (bulk Al and Fe composition) as observed data and used more constraints on the model (such as magma ocean condition and fixed some model parameters).

We apply spherically symmetric viscoelastic hydrostatic model of the Moon [1]. The Moon consists of nine layers: megaregolith, crust, four-layers mantle, low viscosity zone (LVZ), liquid outer core and fluid inner core. In each zone physical properties are assumed to be constant. We employed same data as [1]: four selenodetically observed data of mean radius, mass, MOI, and tidal Love number  $k_2$ . Seismic travel time data was selected by [4].

## GEOCHEMICAL MODELS OF BULK AL AND FE COMPOSITION:

Currently there are two main groups of geochemical models of the Moon [5]: 1. Moon's composition with Al content similar to models with Earth's  $Al_2O_3$  content; 2. The Moon is enriched in Al against Earth. The analysis of majority of current Moon's composition models [5] revealed that  $Al_2O_3 = 4,05 \pm 0,36$  wt.% for group 1 and  $Al_2O_3 = 5,91 \pm 0,39$  wt.% for group 2,  $FeO = 12,25 \pm 1,33$  wt.% for both groups. Division mantle into 4 layers was performed according to [6] model. Concentrations of main oxides were equal in first 3 upper mantle layers and we applied the model of magma ocean to calculate oxide concentrations in fourth lower mantle layer (which implies that concentrations of main oxides in the lower mantle is equal to average concentrations in the upper mantle and in the crust and equal to bulk concentrations). The models of the magma ocean in such a formulation were considered in our previous study [3]. Temperature in the lunar mantle is defined by equation from [7].

## THERMODYNAMIC APPROACH:

Our general methodology is to combine geophysical and geochemical constraints and thermodynamic approach, and to develop, on this joint basis, the self-consistent models of the Moon. The crustal composition of Taylor [8] was taken as representative of the crust material. Thermodynamic modeling of phase relations and physical properties in the multicomponent mineral system CFMAS was used to develop a method for solving the inverse problem [3].

## INVERSION:

A Bayesian inversion approach is an effective method to solve for a nonlinear problem such as planetary internal structure modeling. The solutions of the parameters and their uncertainties are obtained from the posterior distribution which is sampled by the MCMC algorithm. This method is described in detail in [1]. In the present model bulk Al content and bulk Fe content are included into likelihood function (LHF).

## RESULTS:

The main results are shown in Fig. 1. Probable concentration of  $Al_2O_3$  is 2,7-2,9 wt.% in the upper mantle and 4,1-4,3 wt.% in the lower mantle. Bulk FeO is within 11,5-12,5 wt.%. Seismic P-wave velocity ( $\sim 7,92$  km/s) in the lower mantle is close to lower bound of velocity range from [6]. From these results it can be concluded that the models of the Moon with Earth's bulk Al content is in a good agreement with geophysical data.

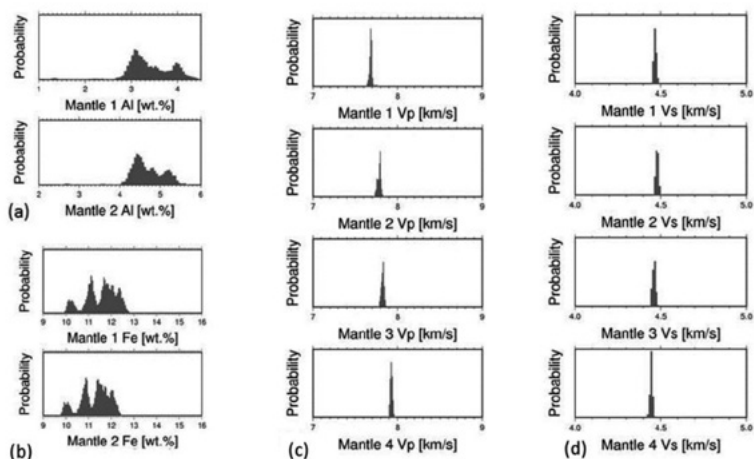


**Fig. 1.** Posterior probability density functions in layers 1-4 of the lunar mantle for (a)  $Al_2O_3$  concentration, (b) FeO concentration, (c) P-wave seismic velocity distribution, (d) S-wave seismic velocity distribution.

## CONCLUSIONS:

We investigated lunar internal structure models which are consistent with the seismic data, the selenodetic (GRAIL and LLR) data, and thermodynamic constraints. This study revealed that additional constraints on model parameters (constraints on bulk composition, magma ocean condition, fixed crustal parameters, etc.) are necessary to obtain reasonable results, otherwise the solution appears to be out of feasible range of oxide concentrations and temperatures. Probably this result substantially stems from paucity of observation data used or the problem is overspecified (too much model parameters). In our future study, we will include more geophysical observation such as electromagnetic data into our inversion process, and will investigate the optimal resolution of the model (number of model parameters).

## ACKNOWLEDGMENTS:

This work was supported by JSPS KAKENHI grant 17K05643, the RFBR grant 15-05-01161 and Russian Academy of Sciences under Programs 7 and 22.

## REFERENCES:

- [1] Matsumoto, K., Yamada, R., Kikuchi, F., Kamata, S., Ishihara, Y., Iwata, T., ... Sasaki, S. Internal structure of the Moon inferred from Apollo seismic data and selenodetic data from GRAIL and LLR // *Geophysical Research Letters*. 2015. V. 42, No 18. P. 7351-7358.
- [2] Khan, A., Connolly, J. A. D., MacLennan, J. & Mosegaard, K. Joint inversion of seismic and gravity data for lunar composition and thermal state // *Geophys. J. Int.* 2007. V. 168. P. 243-258.
- [3] Kronrod V.A., Kuskov O.L. Inversion of seismic and gravity data for the composition and core sizes of the Moon // *Izv. Phys. Solid Earth*. 2011. 47. P. 711-730.

- [4] Lognonne, P., Gagnepain-Beyneix J., and H. Chenet., H. A new seismic model of the Moon: Implications for structure, thermal evolution and formation of the Moon // *Earth Planet. Sci. Lett.*, V. 211, P. 27-44.
- [5] Kuskov, O. L., Kronrod, V. A., Kronrod, E. V. Thermo-chemical constraints on the interior structure and composition of the lunar mantle // *Phys. Earth Planet. Inter.* 2014. V. 235. P. 84-95.
- [6] Gagnepain-Beyneix J., Lognonné P., Chenet H., Lombardi D., Spohn T. A seismic model of the lunar mantle and constraints on temperature and mineralogy // *Phys. Earth and Planet Int.* 2006. V. 159, P. 140-166.
- [7] E. V. Kronrod et al. // *Proceedings of The Fourth Moscow Solar System Symposium (4M-S3)*, Space Research Institute Moscow, Russia October 14-18. 2013. P. 94-104
- [8] Taylor S.R. *Planetary Science: A Lunar Perspective* // Houston, TX. LPI. 1982. P. 481.

# PROBLEM OF MASCONS ORIGIN

A.A. Barenbaum<sup>1</sup>, M.I. Shpekin<sup>2</sup>

<sup>1</sup>Oil and Gas Research Institute of RAS, Moscow, azary@mail.ru

<sup>2</sup>Kazan Federal University, Kazan, michaels1@yandex.ru

## KEYWORDS:

*Gravitational anomalies Bouguer, mascons, craters, seas, galactic comets, Galactocentric paradigm*

## INTRODUCTION:

Mascons are large concentrations of rocks of increased density in the lunar crust, causing specific positive Bouguer gravitational anomalies in the gravitational field of the Moon. For the first time such anomalies were noticed in 1966 by the Soviet automatic station "Luna-10" [1], and in 1968 the mascons were discovered by the automatic stations "Lunar Orbiter" [2]. In recent years, important new information about the mascons has been obtained [3] in the study of the Moon by the mission of GRAIL and on according data of laser altimetry LOLA. At present time, mascons are also found on the Mars and the Mercury.

The origin of the mascons is associated with the falls of massive space bodies, which create a giant craters flooded with basalts – the lunar sea basins, under which the lenses of substance of high density are located. A model is proposed [4], according to which the mascons are formed by cosmic bodies falling on the Moon from 4.1 to 3.8 billion years ago during the "late heavy meteorite bombardment" [5], which caused melting and rising to the surface of large masses of heavy matter lunar mantle. However, the formation of mascons cannot be explained [3] by the falls of bodies with the same diameter distribution as for the bodies of modern asteroids belt. The same conclusion was made earlier for craters of the Moon [6].

## AN ALTERNATIVE APPROACH TO THE PROBLEM:

We discuss the problem of mascons origin on the base of the representations of the Galactocentric paradigm [7], according to which the main factor in the formation of the surface relief of the Moon, the Earth, and the other terrestrial planets are the falls of galactic comets during periods when the Solar system moves through jet streams and spiral arms of the Galaxy [8].

The falls of galactic comets have character of "comet showers" lasting ~1–5 million years, which are repeated in 20–37 million years. During one shower, ~10<sup>4</sup>–10<sup>7</sup> galactic comets can fall to the surface of the Earth. At the same time, every ~150 million years the comets alternately bombard mainly or the southern or northern hemisphere of the Earth, the Moon and other planets.

The last cometary bombardment, which in many respects determined the modern appearance of the planets of the solar system, took place from 5 to 0.7 million years ago. The comets moved relative to the Sun at a speed of ~450 km/s, consisted mainly of water ice with a density of ~1 g/cm<sup>3</sup>, had a diameter of ~0.1 ÷ 3.5 km, a mass of ~10<sup>12</sup> ÷ 10<sup>17</sup> g and energy of ~10<sup>20</sup> ÷ 10<sup>25</sup> J. Their size distribution was exponential character, the density of falls was 3 – 5 comets of all sizes on the area of 100x100 km<sup>2</sup>, and the comets themselves bombarded mainly the southern hemisphere of the planets. The last circumstance lets explain the asymmetry of the relief of the southern and northern hemispheres which is similar for different planets [9, 10, 11]

## TWO PHYSICAL MECHANISMS INTERACTION OF GALACTIC COMETS WITH PLANETS:

At a speed of 450 km/s, galactic comets interact with planets in another way [12,13] than interplanetary bodies [14], dropping out onto planets with velocities on order of magnitude smaller. The main factors of interaction with planets are: 1) the density of the planet's gas shell, 2) the thickness of the lithosphere, 3) the composition and degree of heating rocks of lithospheric, 4) the frequency of falls of galactic comets, and 5) the situation at the fall region.

Depending on the combination of these factors, the impact process can occur by the mechanisms of "elastic" and "inelastic" impact [13]. On planets without an atmosphere (the Moon, Mercury, and also Mars), the first mechanism is realized, when the cometary energy is mainly used for making mechanical

work and is spent on crater formation. Planets with an atmosphere (Earth and Venus) interact with galactic comets according the second mechanism. In this case, most of the comet's energy and momentum are transmitted to a narrowly-directed supersonic shock wave of stresses, which penetrates deeply into the lithosphere of the planet, causing heating and melting of rocks down to depths of  $\sim 300$  km.

At the same time, a large lenses (a magmatic chambers) of heated and partially melted rocks of the asthenosphere appear in the base of the lithosphere [15], which play the role of "geodynamic foci" [16], whose energy is later released in different tectonic and magmatic processes. The formation of asthenospheric lenses on the Earth in conditions of the "thick" lithosphere (a continents) causes a significant rising in the surface of the continents, and in the conditions of the "thin" lithosphere (an oceans), large quantities of basaltic magmas are poured out onto the ocean bottom. In the intervals between cometary bombardments, the rocks of asthenosphere are cool down and the relaxation processes in lithosphere flatten out the resulting irregularities of surface.

## MAIN RESULTS:

The processes caused by the fall of galactic comets occur on the Moon today [8, 13]. In this paper, we reinforce this conclusion with the results of studies of the mascons [3, 17]. The main conclusions of this work are as follows:

1. The mascons, as well as large craters and basalt sea basins on the Moon, arose not as a result of meteoric bombardment  $4.1 \div 3.8$  billion years ago, as now believe [4], but formed by galactic comets during the last ( $5 \div 1$  million years ago) and two – three previous ( $\sim 22 \pm 2$ ,  $\sim 43 \pm 2$  and  $\sim 65 \pm 2$  million years ago) cometary bombardments.
2. Unlike continental craters with diameters from 10 to 160 km, caused by the fall of single comets, magmatic chambers are involved in the creation of seas and mascons, which are formed in "complex" craters of a larger size. Such craters are formed under conditions of high density of cometary falls, when the crater funnel is created by the falls of several comets, and the summation of thermal effects produces magmatic chambers. With increasing number of overlaps, the diameter of "complex" craters, as well as the volume of chambers and the depth of their formation, are increasing.
3. The amount of magma necessary for the formation of the sea basin is formed in complex craters with a diameter of more than 160 km, while mascons form in pools whose diameter exceeds  $218 \pm 17$  km [17]. In the latter case, the area of heating and melting extends to the denser rocks of the lunar mantle under the crust of the Moon, which raise to the surface in form a diapir. Such diapirs create Bouguer positive gravitational anomalies of over large craters and lunar seas, whereby detect themselves at measuring the gravitational field of the Moon from board of artificial satellites.
4. Sea basins with mascons evolve quite quickly. In Fig. 1 shows the latitude distributions of marine basins on Moon of the two main morphological types: 29 mascons with one topographic ring without internal structure that are "young", and 71 mascons of unclassified structure, which we consider "old". We constructed these graphs on the basis of the data of [3]. We see that the youngest basins dominate in the southern hemisphere of the Moon, whereas in the northern hemisphere there are more old structures. Continental craters behave similarly.

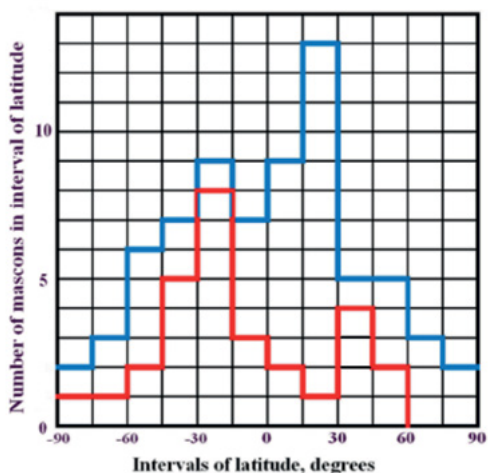


**Fig. 1.** Distribution of the mascons of the Moon along latitude belts, constructed by us according to [3]. Legend: red line – “young” basins, blue line – “old” basins.

## REFERENCES:

- [1] Akim E.L. The definition of the gravitational field of the Moon on the motion of the artificial lunar satellite “Luna-10” // *Doklady Akademii Nauk SSSR*.1966.170(4).P.799-802.
- [2] Paul M., Sjogren W. Mascons: lunar mass concentrations // *Science*.1968.V. 161.P. 680–684.
- [3] Neumann G.A. et al Lunar impact basins revealed by Gravity Recovery and Interior Laboratory measurements // *Science Advances*.1. 2015. e1500852.
- [4] Melosh H.J. et al. The origin of lunar mascon basins // *Science*.2013.V. 340. Issue 6140. P. 1552–1555.
- [5] Gomes R. et al. Origin of the cataclysmic Late Heavy Bombardment period of the terrestrial planets // *Nature*.2005.V.435. Issue 7041. P. 466–469.
- [6] Woronova. Crater saturation and equilibrium: A Monte Carlo simulation // *J. Geophys. Res.*1977. V.82. P. 2447–2456.
- [7] Barenbaum A.A. Galactocentric Paradigm in Geology and Astronomy. Moscow: LIBROKOM. 2010. 546 p.
- [8] Barenbaum A.A., Shpekin M.I. About age of the lunar surface // *Vestnik Otd. nauk Zemle*. 2011. 3. NZ6011.
- [9] Kazimirov D.A. Dessimetry of the terrestrial planets and satellites and the main phases of their development // *Questions of planetary tectonogenesis. Transactions of GIN*. Issue 1. Moscow. 1977.P. 23-66.
- [10] Rodionova Zh.F., Dekhtyaryova K.I. Hypsometric features of the Moon and the terrestrial planets // *Problems of complex study of the Moon*. Moscow.MSU Publ., 1986.P. 56-71.
- [11] Barenbaum A.A. On the asymmetry of the surface terrestrial planets, caused by the falls of galactic comets // *Vestnik. Otd. nauk o Zemle*. 2012. 4. NZ9001.
- [12] Barenbaum A.A. On the mechanism of energy dissipation of galactic comets bombarding terrestrial planets // *J. of Physics: Conf. Ser.* 2015. 653 012073
- [13] Barenbaum A.A., Shpekin M.I. To the development of the mechanism of interaction of galactic comets with the terrestrial planets // *J. of Physics: Conf. Ser.* 2016 774 012096.
- [14] Melosh H.J. *Impact Cratering: A Geological Process*. Oxford monographs on Geology and Geophysics. No. II. 1989. Oxford University Press Inc., New York.
- [15] Barenbaum A.A. The formation of asthenosphere by galactic comets as a new trend in tectonophysics // *Tectonophysics and topical issues of Earth sciences. Conference proceedings*. Moscow: IPE RAS. 2016. V.2. Section 5.P. 430-438.
- [16] Barenbaum A.A., Khain V.E., Yasamanov N.A. Large-scale tectonic cycles: analysis from the standpoint of the galactic concept // *Bulletin of the Moscow State University*. 2004. Ser.4. Geology.No.3.P.3-16.
- [17] Soderblom J.M. et al. The fractured Moon: Production and saturation of porosity in the lunar highlands from impact cratering // *Geophys. Res. Lett.* 2015. 42. 6939–6944.

# THE ANALYSIS OF MAGNETIC AND GRAVITY FIELD OF THE MOON FROM SATELLITE DATA FOR THE GEOLOGICAL ANALYSIS OF LUNAR ROCKS

A.L. Kharitonov

*Pushkov Institute of Terrestrial Magnetism, Ionosphere and Radio Wave Propagation of the Russian Academy of Sciences (IZMIRAN), 108840, Moscow, Troitsk reg., Kaluzhskoe Hwy, 4, IZMIRAN, ahariton@izmiran.ru*

## KEYWORDS:

the Moon, magnetic, gravity fields, satellite data, lunar geology.

## INTRODUCTION:

The magnetic field [1] and the gravity field of the Moon [2] at different altitudes from the data of satellites Apollo-15 and Apollo-16 are analysed. The spectral method and autocorrelation method [2] was applied for the analysis of these fields. The outcomes of the analysis have allowed to determine optimum altitude integrated gravity – magnetic surveys of the Moon, as well as to state some suppositions about the history of the system the Moon – Earth [3] on early period of its development.

## EXPERIMENTAL DATA AND MATHEMATICAL METHODS:

Experimental studies of the magnetic and gravity field of the Moon over its equatorial region [1] provide the opportunity to draw a number of conclusions about the nature of this field. The radial component of the Moon's magnetic field and gravity field are presented. The results of a lunar magnetic field survey at a height of 100 km according to the data of the Apollo-15 sub-satellite [1] are presented. As is well known, the most convenient way to explain the general properties of the magnetic field of the Moon are statistical estimates of the field characteristics. The autocorrelation function and the power spectrum were calculated for the lunar magnetic and gravity field data. A step of the reading of the initial data was taken as 28 km. Since anomaly in the region of the crater Van de Graaff significantly disturbs the steadiness of the field under investigation, that part of the curve on which this anomaly is apparent was not included in the statistical analysis. From statistical analysis it therefore follows that harmonic with a period length of around 720 km determines the basic energy of the lunar magnetic field in the considered range of wavelengths. A statistical estimate of the autocorrelation function of the Moon's magnetic field appeared quite reliable since the length of the magnetic profile exceeded, by a factor of 10, the length of the fundamental period of the field, while the mean square error in the determination of the normalized autocorrelation function was about 0.22 [3]. The frequency properties of the fundamental magnetic field harmonic with long wave (T) is characterized by a correlation radius (r), which if we estimate it as (T/5) turns out to be 144 km. The spatial spectrum lunar magnetic anomalies is presented. Here the 100 km altitude data of the Apollo-15 and Apollo-16 magnetic surveys were used. In order to estimate the intensity of the magnetic field at the lunar surface we have used the usual method of transferring the field from one level to another.

## CONCLUSIONS:

If the lower intensity of the lunar magnetic field is apparently connected with a lower concentration of ferromagnetic material, then the greater rate of damping of lunar magnetic anomalies with altitude is connected with the absence in lunar rocks of an inductive magnetization. The same horizontal dimensions of long period magnetic anomalies on the Moon an increasing intensity of magnetic anomalies in both spectra with decreasing linear size, the essentially identical law of summation of separate magnetic sources in a large effective magnetic active bodies indicate a similarity in magnetic field formation on the Moon.

## REFERENCES:

[1] Russell C.T., Coleman P.J., Fleming B.K., Hilburn L., Ianidis G., Lichtenstein B.R. et al., Radial, East and North components, respectively of the fine scale lunar magnetic field as observed at the Apollo 16 subsatellite during the first pass through the geomag-



netic tail over the lunar longitude band from 80 to 200 dgr // Proc. Lunar Sci. Conf. 6-th. 1975. 2955 p.

[2] Kharitonov A.L., Hassan G.S., Kharitonova G.P. Spectral and autocorrelation analysis of gravity and magnetic fields of the Moon and Earth from satellite data // Issledovanie Zemli iz Kosmosa. 2009. No. 4. P. 17-23.

[3] Vanyan L.L., Yeroshenko Ye.G., Lugovenko V.N., Okuleskii B.A., Kharitonov A.L. A comparison of the magnetic field anomalies for the Moon and Earth // The Moon. 1997. No. 16. P. 289-294.

# A SPHERICAL HARMONIC AND STATISTICAL ANALYSIS OF THE SURFACE TOPOGRAPHY OF THE MOON AND THE CONNECTION OF THE RELIEF WITH GRAVITATIONAL FIELD

N.A. Chujkova<sup>1</sup>, Zh.F. Rodionova<sup>1</sup>, S.A. Kazaryan<sup>1</sup>, E.A. Grishakina<sup>2</sup>

<sup>1</sup>Moscow State University, Sternberg Astronomical Institute, Universitetsky pr., 13, Moscow 119234, Russia. chujkova@sai.msu.ru, marss8@mail.ru

<sup>2</sup>Moscow State University, Faculty of Geology, GSP-1, Leninskie Gory, Moscow, 119991, Russia, orskatya@mail.ru

## KEYWORDS:

Moon, gravity field, relief, correlation, harmonic analysis, statistical characteristics, mascons distribution

To study the global structure of the deep interior of the Moon based on the developed by us method of solving the inverse problem of gravimetry [1,2], it is necessary to remove from the gravity field influence of surface layers. The initial data for this task was the array of the relief height [3], averaged on 5x5° grid. The averaging was made on the basis of hypsometric map of the Moon, compiled by Sternberg astronomical Institute and Geographical faculty of Moscow State University in 2014.

The topography of the lunar surface in details is displayed on the Hypsometric map [3] using contour lines, color layers, elevation and a hillshade. We used digital elevation model based on the data of laser altimeter (LOLA) spacecraft Lunar Reconnaissance Orbiter (LRO) with an accuracy of 64 pixels per degree (0.5 km per pixel) [4]. Cartographer - Grishakina E. A., editors, Lazarev E. N. and Rodionova Zh. F., scientific supervisor - Shevchenko V. V.

Names of major formations of the Moon are given on the map in addition to the relief. The centers of craters with names are marked by points. The names on the map are given in Latin language, adopted by IAU. Conventional signs marked the places of the landings of spacecrafts and manned space vehicle exploring the surface. The main map is compiled in equal-area azimuthal projection for the visible and the opposite hemispheres of the Moon. The meridians and parallels are drawn through 30°. Longitude is measured East and West from the Central Meridian 0° to ±180°. In addition, it shows the polar region to ±60° of latitude built in polar stereographic projection.

Height is measured from the sphere the average radius of which is 1737,4 km. This level is taken as zero. Altitude scale comprises 17 stages: seven stages of elevation are located above the zero mark 0, 1, 2, 3, 4, 6, 8 and more than 8 km, and for portions of the surface are located below zero level were used for more detailed scale 0, -1; -1,5; -2; -2,5; -3; -4; -5; -6, -7 and below -7 km away. Thus, on the seas, occupying a large area, the relief surface is transferred in more details. Contours on the map are given in accordance with the scale heights. Fig. 1 shows the profiles of lunar surface along equator, meridians 0° and 180° based on [3].

The average of relief heights on 5x5° grid allows to receive the expansion of the heights  $h_i$  in terms of a spherical function system up to the degree  $N_k = 180°/5° = 36$ . We developed a methodology and created a theory [5], that allows to receive for each degree  $N = 1 + N_k$  the most well-conditioned solution, which does not give, with a large degree of  $N$ , accumulation of computational errors. Since the system of spherical functions is orthogonal on the sphere, the coefficients of each successive degree of  $N$  is determined independently by successively solving  $N_k$  systems of conditional equations of the form

$$\sqrt{\cos \varphi_i} \sum_{m=0}^N S_{nm}^i = \sqrt{\cos \varphi_i} (h_i - \sum_{n=0}^{N-1} \sum_{m=0}^n S_{nm}^i),$$

where  $\cos \varphi_i$  – weights of 5° cells,

$$S_{nm}^i = (\bar{A}_{nm} \cos m\lambda_i + \bar{B}_{nm} \sin m\lambda_i) \cdot \bar{P}_{nm}(\sin \varphi_i),$$

$\bar{P}_{nm}$  – normalized adjoined Legendre polynomials.

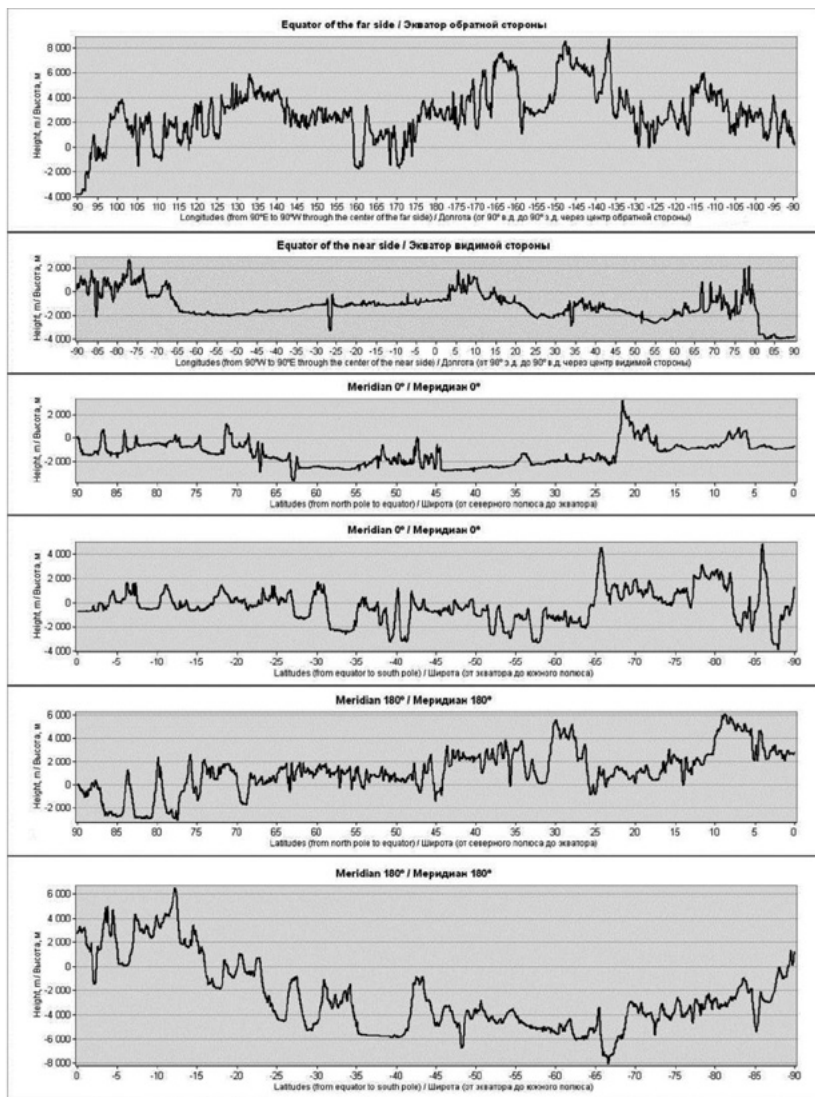
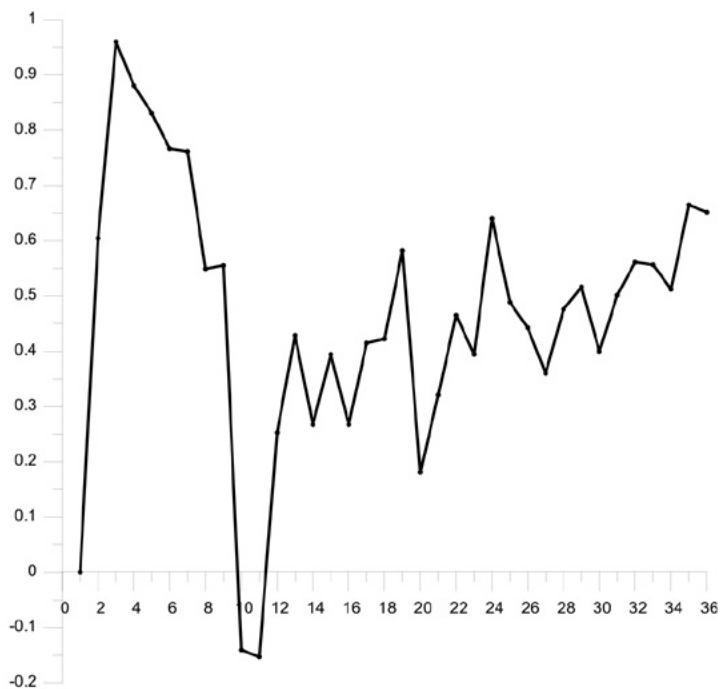


Fig. 1. Profiles of the Moon based [3] along equator, meridians  $0^{\circ}$  and  $180^{\circ}$

The coefficients of the expansion allowed to determine the average radius of the relief surface, the displacement of the center of the figure relative to the center of mass, the equatorial and polar compression, some statistical features (power dispersion and autocorrelation function), and correlation between topography and gravitational field.

## REFERENCES:

- [1] Chujkova N.A., Nasonova L.P., Maximova T.G. Density, stress and gravity anomalies in the interiors of the Earth and Mars and the probable geodynamical implications: comparative analysis // *Izvestia, Physics of the Solid Earth*, 2014, V.50, No.3, P. 427-443.
- [2] Chujkova N.A., Nasonova L.P., Maximova T.G. The new method to find the anomalous internal structure of terrestrial planets and its test on the Earth // *IAG Symposia Series*, 2016, V.144, chapter 195, P.1-11.
- [3] Hypsometric Map of the Moon 1:13 000 000, 2014. Cartographer: Grishakina E.A., Editors: Lazarev E.N., RodionovaZh. F. Editor in chief: Shevchenko V.V. Sternberg Astronomical Institute(SAI MSU), MGU Geographical Department.
- [4] Smith, D.E., Zuber, M.T., Jackson, G.B., et al. The lunar orbiter laser altimeter investigation on the lunar reconnaissance orbiter mission // *Space Sci. Rev.*, 2010, v.150, P. 209-241. doi: 10.1007/s11214-009-9512-y
- [5] Chujkova N.A, Maximova T.G. A spherical harmonic and statistical analysis of the Moho surface depths // *Trudy GAISH*, 1996, V.LXV, P. 33-50, in Russian



**Fig.2.** shows a plot of the correlation between the coefficients of topography and gravity field for different degrees of expansion. The negative correlation of harmonics of degree  $n=9-11$ , which corresponds to the horizontal size of mascons  $\Delta=20^\circ \pm 16^\circ$ , a maximum at  $\Delta=18^\circ$  is visible in the plot. Comparative analysis of the heights of selenoid and the relief allows to allocate space for negative correlation, i.e., a possible distribution of mascon. Our subsequent analysis of the internal structure will allow to find connection of mascons with anomalies of the internal structure of the Moon.

# RESULTS OF MODELING THE ROTATION OF THE MOON ON THE BASIS OF MODERN THEORIES OF ITS PHYSICAL LIBRATION

A.A. Zagidullin<sup>1</sup>, N.K. Petrova<sup>2</sup>, Yu.A. Nefediev<sup>3</sup>

<sup>1</sup> Kazan Federal University, arthur.zagidullin@ya.ru

<sup>2</sup> Kazan Federal University, Kazan Power Engineering University, nk\_petrova@mail.ru

<sup>3</sup> Kazan Federal University, star1955@yandex.ru

## KEYWORDS:

lunar physical libration, selenodesy, analytical and numerical theories of the lunar rotation.

## INTRODUCTION:

Observing physical libration of celestial bodies and the Moon represents one of astronomical methods of remote assessing the internal structure of a celestial body without conducting expensive space experiments. The work contains a review of recent advances in studying the Moon's structure using various methods of obtaining and applying the lunar physical libration (LPhL) data.

In this studying, LPhL simulation methods of assessing viscoelastic and dissipative properties of the lunar body, lunar core parameters, whose existence has been recently confirmed during the seismic data reprocessing of "Apollo" space mission, are described. Much attention is paid to physical interpretation of the free libration phenomenon and the methods for its determination.

In the work, the practical application of the most accurate analytical LPhL tables Rambaux N. and Williams J. G [1] is discussed. The tables were built on the basis of complex analytical processing of the residual differences obtained when comparing long-term series of laser observations with the numerical ephemeris DE421.

In the work, an efficiency analysis of two approaches to LPhL theory is conducted: the numerical and the analytical ones. It has been shown that in lunar investigation both approaches complement each other in various aspects: the numerical approach provides high accuracy of the theory, which is required for the proper processing of modern observations, the analytical approach allows to comprehend the essence of the phenomena in the lunar rotation, predict and interpret new effects in the observations of planets' physical libration.

## ANALYTICAL AND NUMERICAL APPROACHES IN THE LIBRATION THEORY

In selenology the theory of the lunar rotation remains one of the key fronts of studying the Moon. On the one hand, closeness of the Moon to the Earth provides a wide range of various experimental data. The new geophysical data, the modern high-precision models of the lunar gravitational field provide opportunities to improve both numerical and analytical LPhL theories in terms of including parameters characterizing the complex structure of the lunar body. On the other hand, the more precise a theory of physical libration is, the more subtle effects may be obtained from the analysis of residual differences, when compared with high-precision observations. The modern mathematical methods and computer technologies expand opportunities of large amount of new observations processing, allow effectively interpreting new types of phenomena, simulating processes, and pre-calculating the effects of the lunar internal structure on the behavior of measured values. The work is focusing on the review of new data, new capabilities, and new results in theory and observation of physical libration.

Today, one has to admit, although there are significant improvements in lunar laser ranging and high-precision satellite studies of the Moon's gravitational field, it has not been managed to reveal the free core nutations (FCN) with sufficient certainty, which means the question of the lunar core size remains open. One also lacks of the gravimetric data precision in order to unambiguously estimate characteristics of the inner core. These are the tasks of future researches.

Nevertheless, one can safely say the modern lunar rotation theory considers forced librations of not only the solid Moon, but a number of effects of its complex internal structure as well: tidal viscoelastic deformations, the presence

of the liquid core, dissipative processes of various origins. Thus, the reliable discovery of the free librations gave rise to new investigations of a source for their excitation and maintenance, which led to the necessity to consider effects of the viscoelastic mantle and liquid core interaction.

Developed in the presented study, the numerical approach in the theory of LPhL allowed constructing the parameters of physical libration - the angles of libration and the impulses conjugated to them - over an interval of the one year. These results showed that on the backdrop of limited periodic changes in all parameters, the impulse of one of the variables demonstrates an apparent secular trend: it increases from 27 arc seconds per day in the beginning of the simulating, reaching 47 arc seconds per day for the year. It was impossible to find any physical justification for this phenomenon [2].

Analyzing the analytical solution on the basis of Petrov's theory [3], we have found out that in the analytical description of this impulse there is a term with a period of 6 years and an amplitude of 13.8 seconds. Recalculating the numerical results for a period of 10 years, we saw that the "mysterious" impulse also has a periodic behavior, but this requires a longer observation period. In the work we give a physical interpretation of such a long-period change.

At the moment, our numerical theory gives results on the interval of 800 years.

## CONCLUSIONS

Currently, the theory of libration by Rambaux, Williams represents the most accurate semi-analytical theory of libration, whose parameters are reconciled with the laser ranging observations in the period of 38 years using the most powerful tools of computer mathematics.

The results achieved by the libration theories and their practical application have been obtained by the efficient use of the numerical as well as the analytical theory. This means the both approaches should be developed for the lunar rotational motion theory.

This work was funded by the subsidy allocated to Kazan Federal University for the state assignment in the sphere of scientific activities and it was supported by grants RFBR 16-02-00496-a and 15-02-01638-a.

## REFERENCES:

- [1] Rambaux N., Williams J. G. The Moon's physical librations and determination of their free modes. // *Celest Mech Dyn Astr* 2011. V. 109. P. 85–100.
- [2] Petrova N., Zagidullin A., Nefediev Yu. Analysis of long-periodic variations of lunar libration parameters on the basis of analytical theory // *The Russian-Japanese Workshop*, 20-25 October, Tokyo (Mitaka) - Mizusawa, Japan. – 2014.
- [3] Petrova N., Analytical extension of Lunar libration tables // *Earth, Moon and Planets* 1996. V. 73. No 1. P. 71-99.

# ANALYSIS OF PLANETOPHYSICAL PARAMETERS ON THE BASIS OF HARMONIC AND FRACTAL METHODS AND SPACE MISSIONS DATA

A.O. Andreev<sup>1</sup>, Y. A. Nefedyev<sup>2</sup>, N.Y. Demina<sup>3</sup>

<sup>1</sup>Kazan Federal University, 18 Kremlyovskayastreet, Kazan 420008, Russian Federation, alexey-andreev93@mail.ru;

<sup>2</sup>Kazan Federal University, 18 Kremlyovskaya street, Kazan 420008, Russian Federation, star1955@mail.ru;

<sup>3</sup>Kazan Federal University, 18 Kremlyovskayastreet, Kazan 420008, Russian Federation, vnu\_357@mail.ru.

## KEYWORDS:

planetophysicalparameters, space missions data, harmonic and fractal analysis

## INTRODUCTION:

The new programs used for space investigations apply techniques of multi-parameter analysis of internal structure of celestial bodies showing features and benefits of multidisciplinary approach: astronomical observations and computer simulation are combined with geophysical methods. The first objective of these studies is to determine the position of a planet's core and its basic characteristics including the position of center of mass relative to symmetry center. Considering the Earth, we may solve this task using large amount of cosmic and land-based observations but for other celestial objects this is rather complicated. In this study, the method of obtaining lunar center of mass position relative to its symmetry center is considered, for there is much observational data on the Moon.

At the present time, one of the promising directions of heterogeneous natural objects' structure, materials and their properties investigation is fractal geometry [1]. For instance, the fractal analysis of the Solar system bodies' parameters has been carried out in the work [2]. The fundamental property of fractal objects is similarity or scaling when zooming. The quantitative measure characterizing distribution of structure in space is the fractal dimension  $D$ . Investigation of fractal dimension enables us to study not only the structure but the connection between the structure and its formation processes as well. The fractal structures have been found in the dynamical systems, too. The methods for the fractal structure recognition are used for heterogeneous surfaces' properties investigations to find the similarity in certain parameters. In particular, the methods of fractal analysis allow to describe quantitatively the models of celestial bodies' surfaces.

## THE DETERMINING THE POSITION OF THE LUNAR CENTER OF MASS ON THE BASIS OF HARMONIC ANALYSIS

In this study, when estimating the selenocentric models the method of regression simulation as an alternative to the traditional approach involving in the tasks of estimation the regression analysis, checking the conditions, adaptation in case of their violation, and providing the presence of a special software to automatize processes of computation and analysis are used. Regression simulation is a systematic approach at which correctness of the system's any element application (sampling, model, method of parameters estimation, method of structures estimation, quality measure, a set of conditions) may be questioned and checked with a corresponding adaptation application in case of the given conditions violation. The digital models of relief for the full lunar sphere are obtained from «Clementine» and «KAGUYA» space missions, «ULCN 2005» and KSC (Kazan selenocentric catalogue) data systems. The model describing the Moon's surface relief the expansion of altitude function in a series of spherical function in the form of regression is used:

$$h(\varphi, \lambda) = \sum_{n=0}^N \sum_{m=0}^n (\overline{C_{nm}} \cos m\lambda + \overline{S_{nm}} \sin m\lambda) \cdot \overline{P_{nm}}(\cos \varphi) + \varepsilon, \quad (1)$$

where:

is altitude function;

$\varphi, \lambda$  are latitude, longitude – known parameters of the lunar objects;

$C_{nm}, S_{nm}$  are normalized harmonic amplitudes;

$\overline{P}_{nm}$  are normalized associated Legendre functions;

$\varepsilon$  is random regression error.

First order coefficients determine the displacement of lunar symmetry center relative to center of mass Chukova, N., *et al.* 13:

$$\Delta\xi = \sqrt{3C_{11}}, \Delta\eta = \sqrt{3S_{11}}, \Delta\zeta = \sqrt{3C_{10}} \quad (2)$$

Table 1 contains values  $\Delta\xi, \Delta\eta, \Delta\zeta$ ; these are differences in position of the lunar center of mass relative to its center of figure in orthogonal selenographic reference system.

**Table 1.** Coordinates of the lunar center of mars relative to its center of figure from four sources of hypsometrical information

	Clementine (km)	ULCN 2005 (km)	KAGUYA (km)	KSC (km)
$\Delta\xi$	-1,80	-1,71	-1,77	-1,75
$\Delta\eta$	-0,74	-0,73	-0,78	-0,75
$\Delta\zeta$	-0,64	0,26	0,24	0,11

Analysis of this data allows concluding that selenocentric dynamical model KSC with its system reduced to the lunar center of mass and main axes of inertia is in conformity with the results of modern studies. Within this project, the new method of direct use of harmonic analysis of the selenocentric catalogue of lunar objects is used for the purpose of determining the position of the lunar center of mass relative to its figure. Thus, this method could be applied in order to analyze other celestial bodies.

## THE FRACTAL ANALYSIS THE GRAVIMETRIC AND TOPOGRAPHIC PLANETARY MODELS

For the analysis of gravimetric and topographic parameters of planetary bodies, the following observational data were used: for the Earth the most accurate measurements taken via Japanese ASTER (Advanced Spaceborne Thermal Emission and Reflection Radiometer) [3] set on the board of Terra (NASA) [4] spacecraft are used; in order to analyze Martian structures the data received from the boards of the spaceships, particularly «Mars Global Surveyor» [5], has been used; for the Moon the model built on the basis of harmonic analysis by the catalogue [6] were taken.

The fractal dimension was defined which is sufficient to conduct a comparative analysis:

$$D = \lim_{\delta \rightarrow 0} \frac{\ln N(\delta)}{\ln(1/\delta)}, \quad (3)$$

where:

$D$  – fractal dimension;

$\delta$  – small segments dimension;

$N$  – number of small segments.

As resultswereobtained:

**Table 2.** Averagefractaldimensions

N	An object	D average
1	Mars in latitudes (gravity)	1.02
2	Mars by longitude (gravity)	1.92
3	Mars in latitudes (topography)	0,865
4	Mars by longitude (topography)	0,878
5	Earth by geographical latitude	1,178
6	Moon	1,36



## CONCLUSIONS

Conducting the present study, the data on mutual positions of the Moon's center of mass and its geometrical center has been obtained. Besides, the new method of direct harmonic analysis of the studied systems based on the analysis of the known reference points' radius vectors has been developed. It has also been found that use of fractal method for planetary structures variations allows assessing them by topological inhomogeneity and drawing conclusion on their structural similarity. Thus, investigation of planetary fractal structures is a very important and interesting direction in the studies of these objects as well as natural systems. The qualitative feature of planetary fractal objects is their inherent invariance when rescaling. Fractal geometry allows to estimate inhomogeneity of complex physical systems quantitatively.

## ACKNOWLEDGEMENTS

The work is performed according to the Russian Government Program of Competitive Growth of Kazan Federal University. This work was partially supported by the Russian Foundation for Basic Research, grant nos. 15-02-01638-a, 16-32-60071-mol\_a\_dk (N.D.).

## REFERENCES:

- [1] Peter R. Massopust. Fractal Functions, Fractal Surfaces, and Wavelets. Academic Press. Inc. San Diego. California, 1994. 379 p.
- [2] Turcotte D.L. A fractal interpretation of topography and geoid spectra on the earth, moon, Venus, and Mars// Journal of Geophysical Research. 1987. V. 92. Issue B4, P. 597-601.
- [3] Abrams M. The Advanced Spaceborne Thermal Emission and Reflection Radiometer (ASTER): data products for the high spatial resolution imager on NASA's Terra platform, International Journal of Remote Sensing. 2000. V. 21. issue 5, P. 847-859.
- [4] Yue L.W., Shen H.F., Zhang L.P., Zheng X.W., Zhang F., Yuan Q.Q. High-quality seamless DEM generation blending SRTM-1, ASTER GDEM v2 and ICESat/GLAS observations// Journal of Photogrammetry and Remote Sensing. 2017. Vol. 123, P. 20-34.
- [5] Genova A., Goossens S., Lemoine F.G., Mazarico E., Neumann G.A., Smith D.E. and Zuber M.T. Seasonal and static gravity field of Mars from MGS, Mars Odyssey and MRO radio science // Icarus. 2016. N 272. P. 228-245.
- [6] Varaksina N.Y., Valeev S.G., Nefedyev Y.A. Catalogue of selenocentric reference objects (CSRO). KFU. 1-5253 [http://libweb.ksu.ru/ebooks/06-IPh/06\\_dc000002.pdf](http://libweb.ksu.ru/ebooks/06-IPh/06_dc000002.pdf) (2014).

# FORMATION AND GROWTH OF EMBRYOS OF THE EARTH-MOON SYSTEM

S.I. Ipatov<sup>1,2</sup>

<sup>1</sup>*Vernadsky Institute of Geochemistry and Analytical Chemistry, Kosyginast., 19, Moscow 119991, Russia, siipatov@hotmail.com;*

<sup>2</sup>*Space Research Institute, Moscow, Russia*

## KEYWORDS:

The Earth-Moon system, a rarefied condensation, angular momentum, growth of solid embryos, planetesimals

## INTRODUCTION:

Galimov and Krivtsov [1] presented arguments that the giant impact concept [2] of the formation of the Moon has several weaknesses. They suggested that embryos of the Earth and the Moon have been formed from the same rarefied dust condensation. Below we discuss this model of formation of the Moon. Formation of massive (up to  $0.1M_E-0.6M_E$ , where  $M_E$  is the mass of the Earth) condensations was considered by several scientists (e.g. [3]). Ipatov [4-7] and Nesvorniy et al. [8] studied formation of trans-Neptunian satellite systems formed by contraction of rarefied condensations. In my opinion, models of formation of trans-Neptunian satellite systems and the Earth-Moon system can be similar.

## FORMATION OF SOLID EMBRYOS OF THE EARTH AND THE MOON AT THE STAGE OF RAREFIED CONDENSATIONS:

My studies showed [9] that the angular momentum  $K_s$  used by Galimov and Krivtsov [1] in their computer simulations of the formation of the embryos of the Earth and the Moon as a result of contraction of a rarefied condensation could not be acquired during formation of the condensation from a protoplanetary disk. I obtained that the angular momentum  $K_{SEM}$  of the present Earth-Moon system could be acquired at a collision of two rarefied condensations with a total mass not smaller than  $0.1M_E$ . In principle, the angular momentum of the condensation needed for formation of the Earth-Moon system could be acquired by accumulation only of small objects. In this case, there could be  $K_s=K_{SEM}$  for a parental condensation with mass  $m>0.2M_E$ . However, for such accumulation other terrestrial planets would have large satellites. Probably, the condensations that contracted and formed the embryos of the terrestrial planets other than the Earth did not collide with massive condensations, and therefore they did not get a large enough angular momentum needed for formation of massive satellites. The mass of the rarefied condensation that was a parent for the embryos of the Earth and the Moon could be relatively small ( $0.02M_E$  or even less), if we take into account the growth of the angular momentum of the embryos at the time when they accumulated planetesimals.

In our estimates of  $K_s$  discussed above, the radius of the parental condensation with the angular momentum needed for the formation of the embryos of the Earth-Moon system was comparable with the Hill radius  $r_H$  of the system and was greater than the radius of the parental gas-dust condensation equal to  $0.023r_H$  considered in [1]. At such small radius of the condensation, Galimov and Krivtsov [1] obtained evaporation of FeO from dust particles and the formation of embryos of the Earth and the Moon depleted in iron. In order to get the angular momentum needed for formation of a satellite system, the condensation considered by Galimov and Krivtsov had to be a result of a compression of the condensation with a larger size than that considered in [1]. After the compression of the condensation to radius of  $0.023r_H$ , it could contain objects greater than dust. Some scientists (e.g., [10]) consider that condensations in the feeding zone of the terrestrial planets could consist of objects of decimeter size, which were greater than dust. Could the above evaporation of FeO take place for such objects, e.g. if they had fractal structure?

There could be also the second main collision of the parental condensation with another condensation, at which the radius of the Earth embryo condensation was smaller than the semi-major axis of the orbit of the Moon embryo. The second main collision (or a series of similar collisions) of condensations or solid bodies could change the tilt of the Earth.

## GROWTH OF SOLID EMBRYOS OF THE EARTH AND THE MOON:

The solid embryos formed from the parental condensation grew by accumulation of smaller objects, e.g., planetesimals. For the case of small relative velocities of planetesimals, effective radii  $r_{ef}$  of the embryos are proportional to  $r^2$ , where  $r$  is the radius of a considered embryo. In this case,  $m_{Mo}^{-1/3} = m_M^{-1/3} + k_d m_{Eo}^{-1/3} - k_2 m_E^{-1/3}$ , where  $k_2 = k_d^{4/3}$ ,  $k_d$  is the ratio of the density of the growing Earth of mass  $m_E$  to that of the growing Moon of mass  $m_M$  ( $k_d \approx 1.65$  for the present Earth and Moon),  $m_{Mo}$  and  $m_{Eo}$  are initial values of  $m_M$  and  $m_E$ . For  $m_M = 0.0123 m_E$ ,  $m_{Eo} = 0.1 m_E$ ,  $m_E = M_E$ , the above equation is true at  $k_2 = 1$  and  $m_{Mo} = 0.00605 M_E$ , and also at  $k_2 = 1.65$  and  $m_{Mo} = 0.0035 M_E$ . For such data, the mass of the Moon embryo grew by a factor of 2 – 3.5 while the Earth embryo grew by a factor of 10. At  $r_{ef}$  proportional to  $r^2$ , the embryo of the Earth grew faster than that of the Moon. For large enough eccentricities of planetesimals, the effective radii of proto-Earth and proto-Moon were proportional to  $r$ . In this case  $m_{Mo}^{1/3} = m_M^{1/3} + k_1 m_{Eo}^{1/3} - k_1 m_E^{1/3}$  (where  $k_1 = k_d^{2/3}$ ) and the increase of  $m_M / m_{Mo}$  is greater than that of  $m_E / m_{Eo}$ .

According to Galimov and Krivtsov [1], initial embryos of the Earth and the Moon were depleted in iron, and the Earth got a larger fraction of iron than the Moon because it grew faster by accumulation of dust. To estimate the maximum growth of  $m_M$ , let us consider the following simple model: The initial embryos didn't contain iron, and the incoming material contained 33% of iron. For a considerable growth of the mass of the Earth embryo, the final fraction of iron in the embryo can be close to the present 32%. The fraction of iron in the Moon would be  $0.33(1 - m_{rMo})$ , where  $m_{rMo}$  is the ratio of the initial mass of the Moon embryo to the present mass of the Moon. Taking the present fraction of iron in the Moon to be equal to 8% and solving  $0.33(1 - m_{rMo}) = 0.08$ , we get  $m_{rMo} = 0.76$  and the growth of the Moon embryo mass by a factor of 1.3. This estimate is in accordance with the estimates by Galimov and Krivtsov [1] of the growth of the Moon embryo mass by a factor of 1.31 at the growth of the mass of the Earth embryo by a factor of 26.2. For the above formula, the fraction of iron in the Earth is  $0.33(1 - 1/26.2) = 0.317$ . In [1] the increment  $dm$  of the embryo mass  $m$  was proportional to  $m^2$ , i.e. to  $r^6$ . At  $r_{ef}$  proportional to  $r^2$  or to  $r$  (i.e., at  $dm$  proportional to  $r^4$  or  $r^2$ ), the growth of the Moon embryo mass is greater than it is needed to obtain the present fraction of iron in the Moon for growth of the Earth embryo mass  $m_E$  by a factor of 26. May be at the gas/dust stage the relative growth of  $m_E$  was faster than at  $r_{ef}$  proportional to  $r^2$ ? For growth of the embryos only by direct accretion of solid planetesimals, the initial mass of the Earth embryo could not differ by an order of magnitude or more from the present mass of the Earth if we try to explain the differences in the fractions of iron in the Earth and the Moon.

Besides direct collisions with planetesimals, the Moon embryo could also grow by accumulation of almost iron-free material ejected from the Earth embryo at impacts of planetesimals with the Earth embryo. It allows one to consider smaller (than in the above estimates) initial masses of the embryos. In the case of such accumulation, the fraction of iron in the initial embryos could be close to that in the present Earth. This model differs from the known multiple impact models (e.g., [11]) by that the embryo of the Moon in my model was formed from the same rarefied condensation, as the Earth embryo, but not from a disk of material ejected from the Earth embryo. The model of the formation of a solid planet with a large satellite can also work for some exoplanet.

## CONCLUSIONS:

The embryos of the Earth and the Moon could form as a result of contraction of the same parental rarefied condensation. A considerable fraction of the angular momentum of such condensation could be acquired at a collision of two rarefied condensations. The present angular momentum of the Earth-Moon system could be acquired at the collision of two identical rarefied condensations with sizes of their Hill spheres, which total mass was about 0.1 of the mass  $M_E$  of the Earth and which heliocentric orbits were circular. The initial mass of the rarefied condensation that was a parent for the embryos of the Earth and the Moon could be relatively small ( $0.02 M_E$  or even less) if we take into account the growth of the angular momentum of the embryos at the time when they accumulated planetesimals. The angular momenta of the condensations that were parents for the embryos of the terrestrial planets other than the Earth were not large enough for formation of large satellites as the Moon, because these condensations did not collide with such large condensations as

the parental condensation for the Earth-Moon system did. The Moon embryo could get more material ejected from the Earth embryo than that fell directly on the Moon embryo.

The work was supported by the grant of Russian Science Foundation N 17-17-01279.

## REFERENCES:

- [1] Galimov E.M., Krivtsov A.M. Origin of the Moon. New concept. De Gruyter. Berlin, 2012. 168 p.
- [2] Canup R.M., Barr A.C., Crawford D.A. Lunar-forming impacts: High-resolution SPH and AMR-CTH simulations // *Icarus*. 2013. V. 222. P. 200-219.
- [3] Lyra W., Johansen A., Klahr H., Piskunov N. Embryos grown in the dead zone. Assembling the first protoplanetary cores in low mass self-gravitating circumstellar disks of gas and solids // *Astron. Astrophys.* 2008. V. 491. P. L41-L44.
- [4] Ipatov S.I. The angular momentum of two collided rarefied preplanetsimals and the formation of binaries // *Mon. Not. R. Astron. Soc.* 2010. V. 403. P. 405-414.
- [5] Ipatov S.I. Angular momenta of collided rarefied preplanetsimals // *Proc. IAU Symp.* No. 293 "Formation, detection, and characterization of extrasolar habitable planets", ed. by Nader Haghighipour. Proc. of the IAU. V. 8. Symposium S293, Cambridge University Press. 2014. P. 285-288. <http://arxiv.org/abs/1412.8445>.
- [6] Ipatov S.I. Formation of trans-Neptunian satellite systems at the stage of condensations // *Solar System Research*. 2017. V. 51. N 4. P. 321-343.
- [7] Ipatov S.I. Formation of orbits of smaller components in discovered trans-Neptunian binaries // *Solar System Research*. 2017. V. 51. N 5, in press.
- [8] Nesvorný D., Youdin A.N., Richardson D.C. Formation of Kuiper belt binaries by gravitational collapse // *Astron. J.* 2010. V. 140. P. 785-793.
- [9] Ipatov S.I. The Earth-Moon system as a typical binary in the Solar System // *Proceedings of "SPACEKAZAN-IAPS-2015"*, ed. by M.Ya. Marov, Kazan, Publishing house of Kazan University. 2015. P. 97-105. <http://arxiv.org/abs/1607.07037>.
- [10] Johansen A., Oishi J.S., Mac Low M.-M., Klahr H., Henning T., Youdin A. Rapid planetesimal formation in turbulent circumstellar disks // *Nature*. 2007. V. 448. P. 1022-1025.
- [11] Ruffo R., Aharonson O., Peters H.B. A multiple-impact origin for the Moon // *Nature Geoscience*. 2017. V. 10. P. 89-94.

# VALIDATION OF DIVINER ROCK ABUNDANCE DATA WITH DIRECT ROCK COUNTING ON LROC IMAGES

N.E. Demidov<sup>1</sup>, M.A. Ivanov<sup>1</sup>

<sup>1</sup>Vernadsky Institute of Geochemistry and Analytical Chemistry, RAN, Kosygin Str., 19, Moscow, 119991, Russia, [nikdemidov@mail.ru](mailto:nikdemidov@mail.ru)

## KEYWORDS:

Diviner, LROC, rock abundance, Boguslavsky crater, Oppenheimer crater

## INTRODUCTION

The influence of rocks on nighttime surface temperatures is a well known phenomenon used to characterize rock abundance (RA) of planetary surface. LRO Diviner Radiometer measurements of surface temperatures, sensitive to the thermal conductivity of the surface layer to the depth from several cm up to meter, were used to construct rock abundance maps of Moon available now through PDS [1]. Taking in to account importance of such data for models of surface evolution and especially for developing engineering models for safe spacecrafts landing we conducted comparison of this data with direct rock count on LRO LROC images.

## DATA

RA Diviner map with resolution 128 pixels per degree and latitude cover  $\pm 80^\circ$  was taken from PDS ([http://pds-geosciences.wustl.edu/lro/lro-l-dire-4-rdr-v1/lroldr\\_1001/data/gdr\\_l3/cylindrical/jp2/](http://pds-geosciences.wustl.edu/lro/lro-l-dire-4-rdr-v1/lroldr_1001/data/gdr_l3/cylindrical/jp2/)). This map was derived from Diviner data collected from July 5, 2009 through September 2, 2012. Pixels values corresponds to the areal fraction of the surface covered by rock fragments as estimated using the technique described in [1].

We performed visual rock counting using LROC NAC images with spatial resolution  $\sim 0.5$  mpp for several areas in Boguslavsky and Oppenheimer crater. Because of the resolution limits, in our study we considered only those rock fragments that are larger than 1 m. The total number of boulders in the 1-13 m range counted at the Boguslavsky site is 21815; for the Oppenheimer area boulders were measured in the 1-14 m range, their total number is 19051. The LROC NAC rocks count were converted to RA map with the same resolution as Diviner RA map.

## METHOD

Correlation between Diviner RA map and LROC RA map was performed using several methods: visual comparison of maps and profiles, calculation of correlation coefficients and plotting histograms. Visualization of maps, rock counting on LROC images and statistical analysis of data were performed with the use of ArcGis software.

## RESULTS

Qualitative agreement between data are seen on the Diviner RA maps of Boguslavsky and Oppenheimer craters with overlaid points of rock location according to LROC images. This conclusion is supported by corresponding profiles through this maps. At the same time Diviner RA maps show higher concentrations of rocks than seen on LROC images. Correlation coefficients between Diviner RA and LROC RA is near to 0.7 for massif of data from Oppenheimer and Boguslavsky craters taken together or independently. Level of correlation significantly decrease in case of correlation on local region represented by  $n10$  pixels with low variance of RA.

## DISCUSSION

On a qualitative level Diviner and LROC RA data are in good agreement. RA are correlated with factor near to 0.7, but absolute values of LROC RA are  $n10\%$  smaller because they are significantly underestimated due to resolution limit of LROC images. This may be also due to Diviner instrument sensitivity to partially buried rocks and near surface buried rocks which could not be analyzed via LROC data. This statement must be taken in to account while constructing rock abundance models of landing sites on the basis of Diviner

data. Decreasing of correlation level at local scale may be interpreted as 128 pixels per degree resolution of Diviner RA map to be overestimated. To fully validate Diviner RA data it is necessary to input in to analyses additional data which may be represented by MiniRF radar data and MOLA roughness data at the scale of laser footprint.

## **ACKNOWLEDGEMENTS**

The work is supported by the Russian Science Foundation grant № 17-17-01149: «Reconstruction of geologic history of polar areas of the Moon using new high-accuracy data to understand sources, distribution and accumulation of volatiles (water) on the Moon.

## **REFERENCES:**

[1] Banfield J.L., Ghent R.R., Vasavada A.R. et al. Lunar surface rock abundance and fines temperatures derived from LRO Diviner Radiometer data // *Journal of Geophysical Research*. 2011. V. 116. P. 1-18.

# MERCURY TOPOGRAPHIC ROUGHNESS: CALCULATION, ANALYSIS, MAPPING

A.Yu. Zharkova<sup>1,2</sup>, E.V. Matveev<sup>1</sup>, A.A. Kokhanov<sup>1</sup>

<sup>1</sup>MExLab, Moscow State University of Geodesy and Cartography, Gorokhovskiy per.4, Moscow, Russia, 105064.a\_zharkova@miigaik.ru;

<sup>2</sup>Moscow State University Sternberg Astronomical Institute  
Universitetskiiy pr.13, Moscow, Russia, 119234.

## KEYWORDS:

Mercury, Morphological studies, Topographic roughness, Relative topographic position, Planetary mapping

Roughness is one of important surface characteristics, which shows relative height variation. It can be defined differently depending on which calculation method is used. In previous studies [1] we calculated global Mercury topographic roughness as interquartile range of the Laplacian second derivative by means of specially developed GIS toolkit [2]. This method was developed and tested earlier on the example of the Moon [3] and Mars [4].

In this study we have used another technique – relative topographic position [5]. By this method topographic position of each pixel is identified with respect to its local neighbourhood. Moreover, we have carried out comparative analysis of these two methods. The results are used to develop a morphological classification for a new global Mercury cartography, including interactive web-maps of topographic roughness.

## ACKNOWLEDGMENT:

The work was supported by Russian Foundation for Basic Research (RFBR), grant No. 16-37-00316.

## REFERENCES:

- [1] Zharkova A.Y., Karachevtseva I.P., Zubarev A.E., Brusnikin E.S., Kokhanov A.A., Kreslavsky M.A. The study of Mercury's surface by cartography methods based on the newest topographic data derived from MESSENGER image processing // *Sovremennyye Problemy Distantionnogo Zondirovaniya Zemli iz Kosmosa* (Current problems in remote sensing of the Earth from space), 2016, V. 13, No. 5, P. 265-274, [http://d33.infospace.ru/d33\\_conf/sb2016t5/265-274.pdf](http://d33.infospace.ru/d33_conf/sb2016t5/265-274.pdf).
- [2] Kokhanov A.A., Bystrov A.Y., Kreslavsky M.A., Matveev E.V., Karachevtseva I.P. Automation of morphometric measurements for planetary surface analysis and cartography // *In Int. Arch. Photogramm. Remote Sens. Spatial Inf. Sci.*, 2016, XLI-B4, P. 431-433, doi: 10.5194/isprsarchives-XLI-B4-431-2016.
- [3] Kokhanov A.A., Kreslavskiy M.A., Karachevtseva I.P., Matveev E.N. Mapping of the statistical characteristics of the lunar relief on the basis of the global digital elevation model GLD-100 // *Sovremennyye Problemy Distantionnogo Zondirovaniya Zemli iz Kosmosa* (Current problems in remote sensing of the Earth from space), 2013, V. 10, No. 4, P. 136-153, [http://d33.infospace.ru/d33\\_conf/sb2013t4/136-153.pdf](http://d33.infospace.ru/d33_conf/sb2013t4/136-153.pdf).
- [4] Kreslavsky M.A., Head J.W. Kilometer-scale roughness of Mars: Results from MOLA data analysis // *Journal of Geophysical Research*, 2000, V. 105, P. 26695-26712, doi: 10.1029/2000JE001259.
- [5] Jenness J. Topographic Position Index (TPI) v 1.2. Extension for ArcView 3x // Jenness Enterprises, 2006, <http://www.jennessent.com/arcview/tpi.htm>.

# MAIN CONSTRAINTS ON THE HYDROUS SILICATES CONTENT FOR THE MODELS OF PARTIALLY DIFFERENTIATED TITAN

A.N. Dunaeva, V. A. Kronrod, O.L. Kuskov

*V.I. Vernadsky Institute of Geochemistry and Analytical Chemistry  
RAS, Moscow, dunaeva.an@gmail.com*

## KEYWORDS:

Satellites of gas giant planets, Titan internal structure, water/rock ratio.

## INTRODUCTION:

It is assumed in a number of papers studying Saturn's icy satellite Titan internal structure, that the satellite contains a significant amount of hydrated silicates, since hydration of silicate minerals is a common process in icy space objects, the formation of which is associated with the melting of ice. In academic literature the models are discussed that allow the long-term stability of hydrous silicates in Titan's core [1], as well as the models that take into account the possible dehydration of a portion of the hydrated substance, leading to the formation of a large silicate core in the center of the satellite [2]. In such models, Titan is assumed to consist of an external water-ice shell ( $H_2O$ -ice  $\pm$  internal water ocean) and a lower-lying layer represented by hydrated minerals of the serpentine group (antigorite, chrysotile, lizardite)  $\pm$  innermost iron-silicate core.

Alternative models represent Titan as a partially differentiated body in which the separation of ice and rock components was not complete. In this case, the internal structure of the satellite includes an outer water-ice shell below which there is an extended layer (mantle) consisting of a homogeneous mixture of rock and water ice in the form of corresponding  $H_2O$  polymorphs stable at the satellite's pressures. In the center of Titan, under the rock-ice mantle, an iron-silicate core of uniform density is assumed to be [3, 4].

Both groups of models are in a good agreement with the measured physical characteristics of Titan (mass, density, moment of inertia). However, preliminary calculations [5] showed that the estimates of the total  $H_2O$  content in Titan obtained for each group of models differ significantly. However, the total  $H_2O$  content, as well as the water/rock ratio, could be important criteria when choosing a certain model for studying the internal structure of the satellite.

## METHODS:

In the present paper we continue our earlier studies of this issue [5]. The internal structure of Titan in terms of partially differentiated model was calculated in more detail. In setting the task, the composition of Titan's rock-iron material was estimated by analogy with the ordinary L/LL chondrites. An additional requirement was to determine the possible extent of silicates hydration in the satellite. Since the degree of Titan's chondrites hydration (the amount of hydrous silicates) is not reliably known, in the performed calculations this value was used as a varying parameter with respect to which the whole density profile in the satellite was built. Thus, the task was to calculate the range of possible models of Titan's internal structure, characterized by varying degrees of silicates hydration and satisfying the data on the satellite's mass and moment of inertia.

To solve this problem, a number of procedures have been added to existing software algorithms [4], which allow us to calculate the density of the rock component in the satellite's mantle and inner core more accurately using the equations of state for silicates and hydrous silicates. When calculating the density of the inner core, the processes of hydration/dehydration of silicates which take place at 900 K under the satellite's pressures were also taken into account.

The total water content in Titan was determined as the bulk concentration of  $H_2O$  in the outer water-ice shell (liquid water +  $H_2O$ -ice) and in the rock-ice mantle ( $H_2O$ -ice + bound water in hydrous silicates). The proportion of bound water in the hydrated minerals was assumed equal to 13 wt%, which corresponds to the average content of  $H_2O$  in the minerals of the serpentine group. The calculations were carried out at various moments of inertia of Titan in the interval of  $0.32 < I/MR^2 < 0.36$ .



## RESULTS:

Research findings show that in chosen interval of moments of inertia the amount of  $H_2O$  in partially differentiated Titan is 38-55% (Fig. 1). For the moment of inertia  $I/MR^2 = 0.342$  [6], the water content in the satellite does not exceed 53.5% (the ratio of  $H_2O$  (liquid, ice)/rock is equal to 1.15). The figure also shows that the minimum values of the water content in Titan correspond to the complete hydration of the satellite's substance. The maximum content of  $H_2O$  is achieved in the complete absence of hydrated phases in Titan. Thus, increase in the substance hydration in Titan leads to decrease in the total water content in it. In this case, there is no essential linkage between the moment of inertia of the satellite and the amount of hydrous silicates in it.

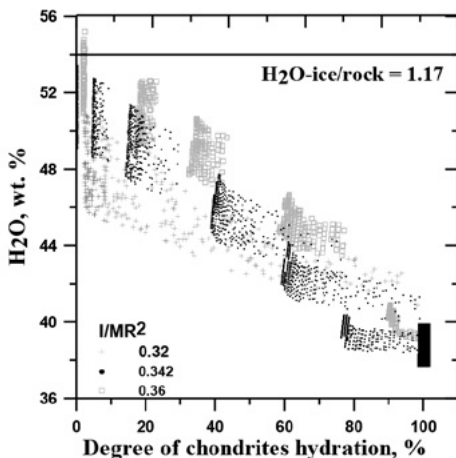


**Fig. 1.** Total  $H_2O$  content in partially differentiated Titan at different degree of chondrites hydration in the moments of inertia interval of 0.32-0.36.

The line indicates the solar ratio of  $H_2O/rock$  [7]. The black rectangle corresponds to the  $H_2O$  content in Titan calculated for models of the fully differentiated satellite with a hydrous silicate mantle.

According to the data on solar water abundance in the Solar system [7], the solar abundance of  $H_2O$  is generally higher than the abundance of the metallosilicate substance: the solar  $H_2O$ -ice/rock ratio is 1.17. The results obtained in the present study show that partially differentiated Titan is slightly depleted of  $H_2O$  ice compared to the ice/rock ratio in the solar composition. Deviations from the solar proportion may indicate ice loss during accretion processes (for example, as a result of the collision and ablation of planetesimals in the gaseous medium of the accretion disk). Another explanation for the low content of  $H_2O$  component in Titan may probably be the initial difference from the solar proportions of the amount of  $H_2O$ -ice in the ice planetesimals accreted by the satellite. Water loss could also be associated with the mechanical removal of surface ice after intensive meteorite bombardment of Titan about 4 billion years ago.

Fig. 1 also shows the water content in Titan, typical for the satellite models with a purely mineral hydrous silicate mantle, implying a complete differentiation of the satellite matter into an ice and rock component [1, 2]. The expected water content in such models does not exceed 38-40%, the water/rock ratio is about 0.6, which is almost two times lower than the solar one [5].

Against the background of the general decrease in the water content in Titan compared with solar abundance, it is nevertheless possible to build the satellite's models that are close to the solar ratio (in Fig. 1 these models are represented by an area of points corresponding to the water content of more than 50%, the ratio of  $H_2O$ -ice/rock is  $\geq 1$ ). As can be seen from the figure, the total degree of silicates hydration obtained in these models does not exceed 30%. Moreover, the calculations show that all the hydrated material is located in the rocky component of the satellite's mantle. The inner iron-silicate core of the satellite contains only a few percents of hydrated silicates and has an average density of 3.4-4.0 g/cm<sup>3</sup>.

In Fig. 2 the structural diagram of Titan as a function of total  $H_2O$  content is shown. It follows from the figure that when the  $H_2O$  content in the satellite exceeds 50%,

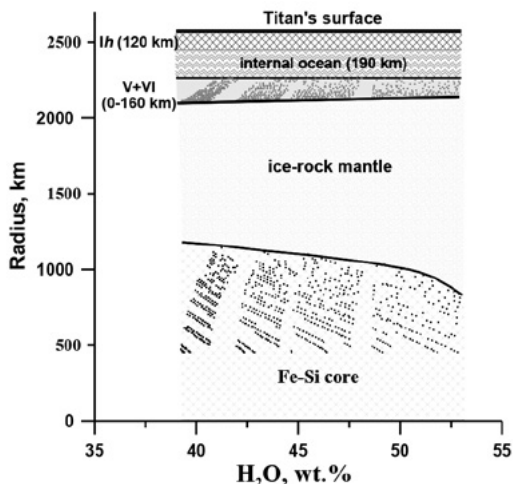


**Fig. 2.** Titan internal structure with internal ocean (the satellite's heat flux value is  $5 \text{ mW/m}^2$ ) as a function of total  $\text{H}_2\text{O}$  content in the satellite.

Titan contains an anhydrous inner core with a radius  $\sim 1000$  km, rock-ice mantle with  $\sim 30\%$  of hydrated silicates and outer water-ice shell  $\sim 440$  km. This model well aligned with the  $\text{H}_2\text{O}$  content in Galilean satellites of Jupiter - Callisto and Ganymede, which makes it more reliable than other discussed models.

## ACKNOWLEDGEMENTS:

This research was supported by the RFBR grant № 15-05-02572.

## REFERENCES:

- [1] Sohl F., et al. Structural and tidal models of Titan [and inferences on cryovolcanism // *J Geophys. Res. Planets*. 2014. V. 119(5). P. 1013-1036.
- [2] Castillo-Rogez J.C., Lunine J.I. Evolution of Titan's rocky core constrained by Cassini observations // *Geophys. Res. Lett.* 2010. V. 37. P. L20205.
- [3] Tobie G., Gautier D., Hersant F. Titan's Bulk Composition Constrained by Cassini-Huygens: Implication for Internal Outgassing // *Astrophys. J.* 2012. V. 752(2). P. 125.
- [4] Dunaeva A.N., Kronrod V.A., Kuskov O.L. Physico-chemical models of the internal structure of partially differentiated Titan // *Geochemistry International*. 2016. V. 54(1). P. 27-47.
- [5] Dunaeva A., Kronrod V., Kuskov O. Models of Titan with rock-ice or hydrous silicate mantle. 2014. Proceedings of the European Planetary Science Congress. Cascais. Portugal. 2014. V. 9. P. 663.
- [6] Iess L., et al. Gravity field, shape, and moment of inertia of Titan // *Science*. 2010. V. 327(5971). P. 1367-1369.
- [7] Lodders K. Solar system abundances and condensation temperatures of the elements // *Astrophys. J.* 2003. V. 591(2). P. 1220.

# MAGNETIC FIELD MEASUREMENTS AROUND GANYMEDE AND AT ITS SURFACE

S.V. Kulikov<sup>1</sup>, A. A. Skalsky<sup>1</sup>

<sup>1</sup>*Space Research Institute of the Russian Academy of Sciences Profsoyuznaya Str 84/32, Moscow, Russia, 117997, kulikov@rx24.ru*

## KEYWORDS:

Ganymede; Jupiter; Magnetic fields; Solar system bodies; Electromagnetic induction; Magnetospheric physics; Plasma waves; Ionosphere.

## INTRODUCTION:

The Ganymede-moon is a very interesting object to investigate. It is known to possess intrinsic magnetic field and, as a consequence, its own magnetosphere embedded into the Jupiter's large magnetosphere. The Jupiter magnetospheric plasma flows around the Ganymede with the subsonic velocity with no bow shock formed around it [1]. Data gathered closely to Ganymede show signatures of induced magnetic field which allows the hypothesized existence of the subsurface ocean in the interior of Ganymede[2,3,4].

The present paper is aimed to overview known and tentatively assumed wave phenomena around the Ganymede and approaches to probe the interior of Ganymede with simultaneous magnetic field observation at its surface and at orbits around it.

## REFERENCES:

- [1] Fatemi S., Poppe A.R., Khurana K.K., Holmstrom M. Jovian plasma interaction with Ganymede's magnetosphere // AGU Fall Meeting Abstracts. 2015.
- [2] Saur, J., Neubauer, F.M., Glassmeier, K.-H. Induced magnetic fields in solar system bodies //Space Sci. 2010. Rev. 152, P. 391 – 421.
- [3] Kivelson, M.G., Khurana, K.K., and Volwerk, M., The permanent and inductive moments of Ganymede //Icarus. 2002. vol. 157. P. 507–522.
- [4] Seufert M., Saur J., Neubauer F. M. Multi-frequency electromagnetic sounding of the Galilean moons //Icarus. 2011. 214. P. 477–494.

# ZONAL-TIME VARIATIONS OF THE AMMONIA ABSORPTION ON JUPITER IN 2005-2015

V. G. Tejfel, V. D. Vdovichenko, A. M. Karimov, P. G. Lysenko,  
G. A. Kirienko, G. A. Kharitonova, V. A. Filippov, A.S. Khozhenetz  
*Fessenkov Astrophysical Institute, Almaty, Kazakhstan, tejf@mail.ru*

## KEYWORDS:

Jupiter, atmosphere, spectrophotometry, ammonia, absorption bands, temporal changes, zonal variations

## INTRODUCTION:

In 2004 on Jupiter we first detected a strange depression in absorption in the 787 nm  $\text{NH}_3$  absorption band, that was observed in the Northern hemisphere at low latitudes [1, 2]. The similar feature was noted with radio observations at the millimeter wave range [3, 4] at enhanced brightness temperature in the NEB. That may be considered as an evidence of decreased ammonia abundance at the lower northern latitudes on Jupiter. Based on our spectral observations of Jupiter in 2005-2015, we carried out a preliminary analysis of the data about the spatial-temporal variations in the 645 and 787 nm  $\text{NH}_3$  absorption bands over this period. These data were derived from the measurements in five main belts of Jupiter: the Southern and Northern Tropical Zones (STZ and NTZ), the Southern and Northern Equatorial Belts (SEB and NEB) and the Equatorial Zone (EZ).

## THE SPECTRAL OBSERVATIONS AND THEIR PROCESSING:

The CCD-spectrograms of the central meridian of Jupiter were selected for processing the spectra of the five measured zones. In general, 600 zonal spectra with a width of 15 pixels or about 3.7 arc sec on the disk of Jupiter were measured. The measurements of the ammonia absorption bands are certainly rather difficult, since they are overlapped with more extended methane bands.

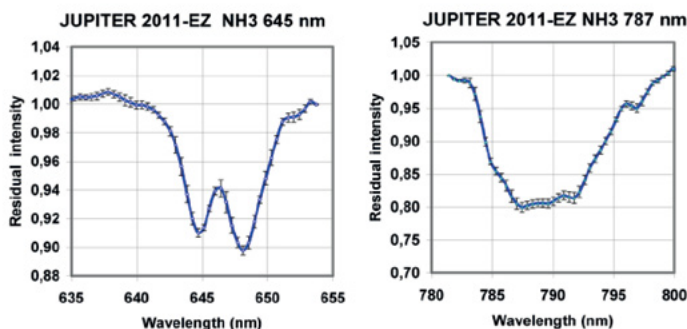


Fig. 1. The examples of the  $\text{NH}_3$  absorption bands profiles

The 787 nm  $\text{NH}_3$  absorption band was extracted with using of ratios of the Jovian spectra to the Saturn's disk spectrum that was taken as a reference. "Clear" profiles of the  $\text{NH}_3$  bands are shown in Figure 1. The result of the measurements consisted in obtaining the estimates of the absorption bands' equivalent widths and variations in their values over zones and years. The average values of the equivalent widths for all measurements are:  $W = 6.24 \pm 0.59 \text{ \AA}$  for the 645 nm  $\text{NH}_3$  band;  $W = 17.98 \pm 1.37 \text{ \AA}$  for the 787 nm  $\text{NH}_3$  band. But over different years and zones the observed variations behave differently.

## MAIN RESULTS AND DISCUSSION:

Figure 2 shows histograms of temporal (annual) changes in ammonia absorption separately in each of the five investigated belts of Jupiter. To compare the zonal behavior of absorption over the years, the data are plotted in Figure 3. One can see that the absorption variations are not the same for these two bands of ammonia. As in our other studies, the latitudinal variations for the two bands

are obviously different. A lowered absorption of ammonia in the 787 nm band in the NEB remains a peculiar feature, repeated every year. Unlike the thermal radio emission, when a cloud layer does not affect its passage, the formation of the  $\text{NH}_3$  bands in the visible spectral range depends noticeably not only on the local content of gaseous ammonia, but also on the properties of the scattering cloud bulk. Perhaps the differences in the behavior of these bands are related to this, although it is strange that a more intense 787 nm band shows a better agreement with the data of radio observations.

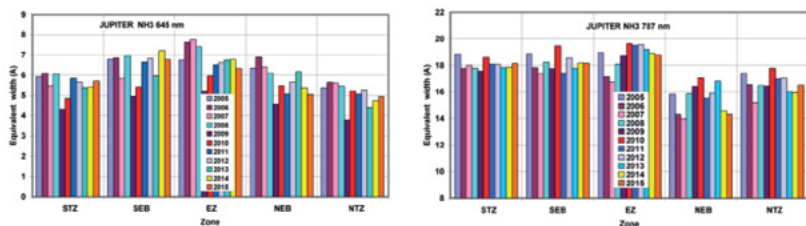


Fig.2. The annual variations of the 645 and 787 nm  $\text{NH}_3$  bands equivalent widths.

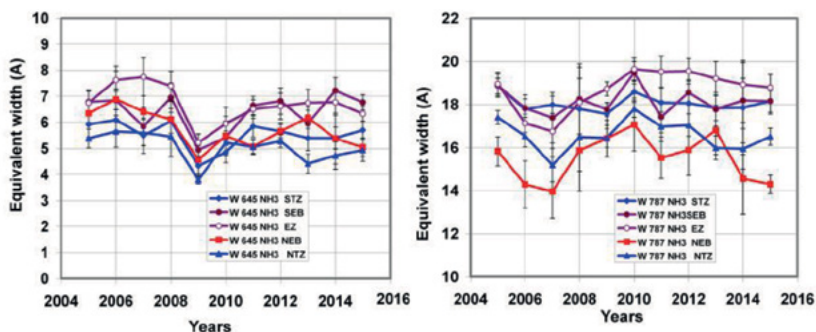


Fig. 3. A comparison of temporal variations in the  $\text{NH}_3$  absorption in the five Jovian latitudinal belts.

Figure 4 shows the relative values for both  $\text{NH}_3$  absorption bands averaged over all years and normalized to EZ. The depression of absorption in the 787 nm band in the NEB manifests itself quite clearly, and on the average it reaches about 20 percent.

This difference may be also seen if one compares the averaged values of equivalent widths of both absorption bands with each other, as shown on the right part of this figure.

## CONCLUSION:

We measured the intensity of the 645 and 787 nm  $\text{NH}_3$  absorption bands in five latitudinal belts of Jupiter (STZ, SEB, EZ, NEB and NTZ) during almost full period of its revolution around the Sun: from 2005 to 2015. The variations in the equivalent widths of the bands were investigated. The permanently lowered intensity of the 787 nm  $\text{NH}_3$  band in NEB is confirmed. There are also some

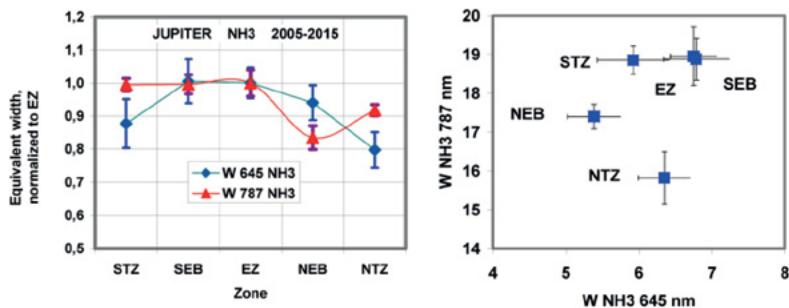


Fig. 4. The ammonia absorption bands' intensities averaged over time and normalized to EZ, and a comparison of the averaged equivalent widths of the two ammonia bands with each other.

systematic differences in latitudinal and temporal variations between the 645 and 787 nm ammonia bands. From the measurements of these bands and from the data on the brightness temperatures in the radio [4] and infrared [5] ranges of thermal radiation, one can see the longitudinal variations are existing. Their study, especially from the standpoint of significant changing. From the measurements of these bands and from the data on the brightness temperatures in the infrared [4] and radio [5] ranges of thermal radiation, one can see the longitudinal variations are existing. the content of gaseous ammonia at different latitudes and longitudes, is very important and interesting. So, all the results obtained, stimulate the continuation of further, more detailed, studies.

### **ACKNOWLEDGEMENTS:**

This work was prepared according the grant 0073/GF4 Ministry of Science and Education of Kazakhstan Republic.

### **REFERENCES:**

- [1] Tejfel V.G ., Karimov A.M., Vdovichenko V.D. Strange latitudinal variations of the ammonia absorption on Jupiter // Bull.AAS, 2005, V. 37, P.682
- [2] Tejfel V., et al. Spatially resolved variation in the methane and ammonia absorption in the atmosphere of Jupiter // Astron. and Astrophys. Transactions , 2005, V. 24, P.359-363.
- [3] Showman A., de Pater, I. Dynamical implications of Jupiter's tropospheric ammonia abundance // Icarus, 2005, V. 174, P. 192-204.
- [4] de Pater I. et al. Peering through Jupiter's clouds with radio spectral imaging // Science 2016, V. 352, P.1290 -1294.
- [5] Fletcher L. et al. Mid-infrared mapping of Jupiter's temperatures, aerosol opacity and chemical distributions with IRTF/TEXES. // Icarus, 2016, V. 278, P.128-161.

## IS SATURN'S MAGNETOSPHERE OPEN TO THE INTERPLANETARY MAGNETIC FIELD?

I.A. Pensionerov<sup>1</sup>, E.S. Belenkaya<sup>1</sup>, S.W.H. Cowley<sup>2</sup>, I.I. Alexeev<sup>1</sup>, V.V. Kalegaev<sup>1</sup>, M.S. Blokhina<sup>1</sup>, and D.A. Parunakian<sup>1</sup>

<sup>1</sup>*Federal State Budget Educational Institution of Higher Education*

*M.V. Lomonosov Moscow State University, Skobeltsyn Institute of Nuclear Physics (SINP MSU), 1(2), Leninskie gory, GSP-1, Moscow 119991, Russian Federation; Contact: pensionerov@gmail.com;*

<sup>2</sup>*Department of Physics & Astronomy, University of Leicester, Leicester LE1 7RH, UK*

Magnetic reconnection is a physical process in which magnetic field changes its topology, converting magnetic energy to the thermal energy and bulk flow energy of the accelerated charged particle flows. This process has a significant impact on the interaction between magnetized planets and the solar wind. It depends on the efficiency of reconnection, whether the interplanetary magnetic field (IMF) can penetrate the magnetosphere. In the present work we consider the case of Saturn. We test two models of the Saturn's magnetosphere. The first one is "open", in which the IMF penetrates the magnetosphere and reconnection is relatively efficient. The second one is the "partially closed" model, in which the IMF does not cross the magnetopause. It is important, that the second model only is partially closed, because magnetospheric magnetic field lines connect with the IMF lines in the distant tail. We use magnetometer data from the Cassini spacecraft, ultraviolet images of Saturn's aurora from the Hubble Space Telescope and the paraboloid model of Saturn's magnetospheric magnetic field to examine which of these cases has been realized in nature. We show, that the efficiency of reconnection at Saturn depends on the orientation of the IMF, with reconnection at the two neutral points in the cusp regions for the case of the strong southward IMF is probably being the mostly efficient.

# PROBABILITY OF NUCLEOTIDE SYNTHESIS IN THE METEORITE-IMPACT PLASMA TORCH

G.G. Managadze<sup>1</sup>, W.B. Brinckerhoff<sup>2</sup>, A.T. Kopylov<sup>3</sup>, A.V. Lisitsa<sup>3</sup>, S.A. Terentyev<sup>4</sup>, L. Kelner<sup>5</sup>, N.G. Managadze<sup>1</sup>, T.A. Abraamyan<sup>1</sup>

<sup>1</sup>Space Research Institute, Profsoyuznaya, 84/32, Moscow 117997, Russia;

<sup>2</sup>NASA Goddard Space Flight Center, Greenbelt, MD 20771, USA;

<sup>3</sup>Institute of Biomedical Chemistry of RAMS Moscow, Russia;

<sup>4</sup>Technological Institute for Superhard and Novel Carbon Materials, Moscow, Russia;

<sup>5</sup>Fenix Technology International, Inc., Leesburg, VA 20176, USA.

The main purpose of this study is to experimentally detect, record, and identify any nucleotides and their oligomers that may be synthesized in impact-produced plasma simulating high-velocity meteorite impact processes with high fidelity under laboratory conditions using both a pulsed laser and a light-gas gun [1].

This empirical study seeks fundamental results that may confirm the feasibility and validity of impact-produced nucleotides under natural conditions. Specifically, Q-switched laser illumination of a solid target produced plasmas that simulated meteorite post-impact plume processes. In addition, in select cases a light gas gun was utilized to conduct more direct impact studies of high-velocity meteoroid impacts on mineral targets.

Results confirmed that, irrespective of the origin of the plasma torch, during adiabatic plume dispersion and cooling, organic compounds crucial for the emergence of life are synthesized with remarkable effectiveness. Furthermore there is evidence of plasma-generated amplification of enantiomeric excesses in chiral compounds, and further complexification, self-assembly, and ordering in these transient, dispersive processes.

To fully investigate this tantalizing process, we developed a technique that makes it possible to study, stepwise, the properties of the impact torch plasma that may contribute to synthesis of amino acids and nucleotides in separate impact experiments. The corresponding target media differed only by the elemental composition of the targets in that the sample used to study amino acids contained no phosphorus.

1. The study of amino acids [2] in impact simulations showed that the following processes occur systematically with targets containing carbon, nitrogen, oxygen, and hydrogen:
  - the synthesis of protein amino acids – glycine, alanine, and serine;
  - the de novo elevation of enantiomeric excess in alanine at the ratio 1.68 in L-alanine over D-alanine (the sign of which coincides with terrestrial biology, despite the lack of any measurable biocontaminating background.) It is proposed that chiral physical fields generated in the plasma torch produce a polarization force yielding enhanced molecular stability consistent with the observed sign (L-excess).
  - self-assembly of organic polymers and some peptides with atomic masses reaching 1300 and 300 AMU, respectively.
2. When studying the possibility of the synthesis of nucleotides in impact-produced plasma we added phosphorus to the sample (in addition to carbon, nitrogen, oxygen, and hydrogen in varying proportions). Impact pressures of 425 GPa generated by 12 high-velocity tungsten impactors ensured complete atomization and ionization in the plasma plume generated from the bulk target.

Initial runs with targets depleted of N and C produced no amino acids or nucleotides. It was shown that the structural unit synthesized in the impact plasma was orthophosphoric acid which was observed as oligomers of degree  $n = 2$  to  $n = 25$  with empirical formula  $(H_3O_4P)_n$ .

The possibility of stochastic synthesis of such a compound is of great interest because it can serve as the skeleton of the reactive center for the synthesis of nucleotide chains (potentially leading to RNA and DNA) with the right conformation to covalently bond with purine or pyridine bases.

Primary nucleic acids could also be represented by poly-orthophosphate chains with sterically axial arrangement of nitrogenous bases.



Following on these studies, new targets additionally containing C and N have been prepared to encourage potential synthesis of nucleotides. These results are pending confirmation.

The results of the studies showed that the plasma torch may create conditions necessary for the formation of the crucial organic compounds for the emergence of life, such as protein amino acids and their derivatives, potentially nucleotides themselves, and important synthetic processes and structures that may enable their polymerization.

## REFERENCES:

- [1] Managadze G.G. Cosmic factors ensuring the conditions for abiogenous emergence of living matter in the plasma torch of a meteorite impact. // Talk at the Scientific coordinating session "Study of non-ideal plasma" (December 7-8, Presidium of the Russian Academy of Sciences, Moscow). 2016.
- [2] Managadze G.G., Engel M.H., Getty S., Wurz P., Brinckerhoff W.B., Shokolov A.G., Sholin G.V., Terent'ev S.A., Chumikov A.E., Skalkin A.S., Blank V.D., Prokhorov V.M., Managadze N.G., Luchnikov K.A. Excess of L-alanine in amino acids synthesized in a plasma torch generated by a hypervelocity meteorite impact reproduced in the laboratory // Planetary and Space Science. 2016. V. 131, P. 70–78.

# ELEMENTAL COMPOSITION MEASUREMENT AS A POWERFUL APPROACH TO SEARCHING AND CHARACTERIZING SAMPLES CONTAINING MICROORGANISMS

A.E. Chumikov<sup>1</sup>, G.G. Managadze<sup>1</sup>, K.A. Luchnikov<sup>1</sup>, V.S. Cheptsov<sup>1,2</sup>, A.I. Kuznetsov<sup>1</sup>, N.G. Managadze<sup>1</sup>, A.L. Bondarenko<sup>1</sup>

<sup>1</sup>Space Research Institute of the Russian Academy of Sciences (IKI), 84/32 Profsoyuznaya Str, Moscow, Russian Federation, 117997;

<sup>2</sup>Lomonosov Moscow State University, Leninskie Gory, 1, Moscow, Russian Federation, 119991.

## KEYWORDS:

Astrobiology; Mass Spectrometry; Laser Desorption; Elemental Composition; Biomarkers.

## INTRODUCTION:

We propose a new technique for the detection of microorganisms by elemental composition analyses of a sample extracted from regolith, permafrost, and ice of extraterrestrial bodies. We also describe the design of the ABIMAS instrument, which consists of the on-board time-of-flight laser mass-spectrometer (TOF LMS) and the sample preparation unit (SPU) for biomass extraction. This instrument was initially approved to fly on-board the ExoMars lander 2020 mission. The instrument can be used to analyze the elemental composition of possible extraterrestrial microbial communities and compare it to that of terrestrial microorganisms.

## TECHNIQUE AND INSTRUMENT:

*Laser ablation mass-spectrometer.*

Laser ablation time-of-flight mass spectrometer LASMA was developed for Phobos-Grunt mission. It is based on the heritage of LIMA-D for PHOBOS mission. LASMA able to solve multiple tasks in the study of regolith composition and structure. [1, 2] A next-generation device ABIMAS based on LASMA has been developed last years. The instrument allows for study of the elemental and isotopic composition of samples in laser ablation mode and molecular ions desorbed from the samples in soft ionization mode.

The spectrometer has an axial symmetry relative to both laser emission and the motion of the plasma ions of the plume. This configuration ensures high reproducibility of the mass spectra and the capability to analyze the sample layers down to a depth of 1-2 mm.

The laser pulse causes ablation, complete dissociation, and ionization of sample material within the focal spot. Its intense heating ensures the emission of the target material in the form of plasma ions. Ions emitted from the target are confined by the ion optics and guided into the drift tube, where they are separated by time of flight proportional to their mass. After reflection in a retarding electrostatic field of the ion reflector, the ions are detected by the secondary electron multiplier – a microchannel plate assembly. The output signal from the electron multiplier is fed through the amplifier to the high-speed analog-to-digital converter and stored in memory as a single spectrum. From the time of flight of the ions and the intensity of their mass peaks, elemental and isotopic composition of the substance under investigation can be accurately determined.

To ensure functioning in the dense atmosphere the instrument must be equipped with a vacuum chamber and appropriate pumping system.

## SAMPLE PREPARATION UNIT

The laboratory prototype of SPU was developed, manufactured, and successfully tested in the Laboratory of Active Diagnostics and Mass Spectrometry, Space Research Institute, Russian Academy of Sciences. This unit serves for partial separation of microorganisms and mineral particles and enrichment of the processed sample in microorganisms along with its desalting using cartridges that contain a mixed layer of ion-exchange anion resin and cation resin.

Their total action achieves a purification factor of  $10^2$ – $10^3$ , given the initial 1500 ppm of dissolved salts. After purification, the suspension, rich in microorganisms, is supplied to the target's substrate. The water evaporation from the surface of the metal substrate ensures the formation of the layer of microorganisms and mineral particles. Subsequently, the target is put for the analysis into the mass spectrometer on the focal plane of the laser beam.

## ANALYSIS TECHNIQUE

A laboratory prototype of the instrument based on LASMA TOF MS after significant improvements was used to detect the microbial biomass in soil and ice/permafrost samples via analysis of the elemental composition. For this analysis, we chose as biomarkers P/S and Ca/K ratios, and abundances of N and C. Our approach is based on the selectivity of nutrient absorption by microbial cells from the environment. Previously, it was found that the ratios P/S and Ca/K inside microorganisms change over the life cycle and depend on the physiological state of the cells. Also, fossilized microorganisms can be distinguished from microorganisms present in the active state. The elemental microanalysis makes the detection of cells in a native mineral environment possible due to the selective accumulation of these elements by cells. [3]

## RESULTS AND CONCLUSION:

We have conducted numerous laboratory studies to confirm the possibility of biomass identification via the following biomarkers: P/S and Ca/K ratios, and C and N abundances. We underline that only the combination of these factors will allow one to discriminate microbial samples from geological ones.

Our technique has been tested experimentally in numerous laboratory trials on cultures of microorganisms and polar permafrost samples as terrestrial analogs for martian polar soils. [4, 5]

The developed technique can be used to search for and identify microorganisms in different martian samples, and in the subsurface of other planets, satellites, comets, and asteroids, in particular, Europa, Ganymede, Enceladus, comets, and asteroids. This approach can also be used to analyze the chemical composition of martian aerosols.

## REFERENCES:

- [1] Managadze G.G. TOF mass-spectrometer. // Patent 1732396 (RF). Priority of invention: 1988. Registered: 1992. Published in: Russ. Bull. Inventions No. 17.
- [2] Managadze, G.G., Managadze, N.G. TOF mass spectrometer. // Patent 2096861 (RF). Priority of invention: 1994. Registered: 1997. Published in Russ. Bull. Inventions No. 32.
- [3] Managadze, G.G., Vorobyova E.A., Luchnikov K.A., Safronova A.A., Chumikov A.E., Managadze N.G. Method of detecting presence of microbial biomass of terrestrial type on space bodies. // Patent RU 2586778 C1. Priority of invention: 2015. Registered: 2016.
- [4] Luchnikov, K.; Managadze, G.; Chumikov, A.; Managadze, N.; Vorobyova, E.; Safronova, A. Mass-spectrometric method for signs of life search via analysis of the element composition of the supposed biomass extracted from regolith of Mars. // Proceedings of 40th COSPAR Scientific Assembly. Moscow. Russia. 2014. Abstract B0.6-14-14.
- [5] Managadze G.G., Safronova A.A., Luchnikov K.A., Vorobyova E.A., Duxbury N.S., Wurz P., Managadze N.G., Chumikov A.E., and Khamizov R.Kh. A New Method and Mass-Spectrometric Instrument for Extraterrestrial Microbial Life Detection Using the Elemental Composition Analyses of Martian Regolith and Permafrost/Ice. // *Astrobiology*, 2017, 17(5): 448-458.

# INORGANIC MARTIAN DUST SIMULANT ENREACHED BY CARBON COMPONENT POSSESS MODULATING EFFECTS ON GLUTAMATE- AND GABA-ERGIC NEUROTRANSMISSION

T. A. Borisova, N.G.Pozdnyakova, A. O. Pastukhov, M.A. Galkin, M.V.Dudarenko, Krisanova N.V.  
*Palladin Institute of Biochemistry NAS of Ukraine; 9 Leontovicha Street, Kiev, 01601, Ukraine; tborisov@biochem.kiev.ua*

## KEYWORDS:

Upgraded Martian dust stimulant; carbon dots; nanodiamonds: neurotoxicity risk assessment; brain nerve terminals

## INTRODUCTION:

Investigation of organic carbon from the Tissint Martian meteorite provided evidence on the past existence of subsurface organic-bearing fluids on Mars [1]. Meteorites containing abundant carbon and carbon-enriched dust particles have reached the Earth daily [2]. During inhalation, nano-/micro-sized particles are efficiently deposited in nasal, tracheobronchial, and alveolar regions and can be transported to the central nervous system [3].

Recently, we have shown that enrichment of inorganic Martian dust stimulant with carbon component, i.e. nanodiamonds, can cause neurotoxicity.

## METHODS:

preparative biochemistry, radiolabeled technique, spectrofluorimetry

## RESULTS:

The aims of this study were to upgrade inorganic Martian dust stimulant derived from volcanic ash (JSC-1a/JSC, ORBITEC Orbital Technologies Corporation, Madison, Wisconsin) by new carbon component – carbon dots and to assess acute effects of upgraded stimulant on the main characteristic of synaptic neurotransmission and to compare its effects with those of inorganic dust and carbon dots per se. Acute administration of carbon dot-containing Martian dust analogue resulted in a significant decrease in Na<sup>+</sup>-dependent uptake of L-[<sup>14</sup>C]glutamate (the major excitatory neurotransmitter in the central nervous system) and [<sup>3</sup>H]- $\gamma$ -aminobutyric acid (GABA) (the major inhibitory neurotransmitter). The ambient level of L-[<sup>14</sup>C]glutamate and [<sup>3</sup>H]GABA in the preparation of isolated rat brain nerve terminals (synaptosomes) increased in the presence of carbon dot-contained Martian dust analogue.

## CONCLUSION:

Our results indicate that carbon dots as a component of native Martian dust can have deleterious effects on glutamate and GABA homeostasis in the central nervous system that can disbalance processes of excitation and inhibition.

## REFERENCES:

- [1] Lin, Y., El Goresy, A., Hu, S., Zhang, J., Gillet, P., Xu, Y., Hao, J., Miyahara, M., Ouyang, Z., Ohtani, E., Xu, L., Yang, W., Feng, L., Zhao, X., Yang, J., Ozawa, S.: NanoSIMS analysis of organic carbon from the Tissint Martian meteorite: Evidence for the past existence of subsurface organic-bearing fluids on Mars. *Meteorit. // Planet Sci.* 2014. 49, 2201–2218
- [2] Pizzarello, S., Shock, E.: The organic composition of carbonaceous meteorites: the evolutionary story ahead of biochemistry. *// Cold Spring Harb. Perspect. Biol.* 2, a002105 2010. doi:10.1101/cshperspect.a002105
- [3] Oberdorster, G., Sharp, Z., Atudorei, V., Elder, A., Gelein, R., " Kreyling, W., Cox, C.: Translocation of inhaled ultrafine particles to the brain. *// Inhal. Toxicol.* 16, 437–445 (2004)

# PLANTS GROWTHS IN SPACE, EFFECTIVE METHODS, AND TECHNIQUES

Ahya Rezaei<sup>1</sup>

<sup>1</sup>*International Occultation Timing Association Middle East Section (IOTA/ME)*

## KEYWORDS:

Life, plant growth, mycorrhiza, Space, water

## INTRODUCTION:

In this paper, first, the conditions for the growth of a plant in space are examined and then the variety of plants that are more compatible with these conditions are studied and examined too.

Due to the vacuum situation and lack of oxygen gas, a suitable solution should be presented in this regard. Accordingly, over the examinations and studies carried out, it seems highly significant that at first find plants, which are capable of germination under conditions of lack of oxygen. Therefore, the shock caused by the effect of changing the amount of oxygen can ultimately lead to mRNA density. It is worth noting that skin thickness is one of the factors that affect this process.

In addition, considering the location constraints in space, it should be possible to reduce the size of the plant to the extent possible in order to preserve plant characteristics. In this case, methods such as root stimulation and reduction of hypocotyl length, which are also effective factors that caused increasing VUE (Volume Utilization Efficiently) should be taken into consideration.

The growing chambers of plants in the space station have environmental conditions such as temperature, humidity, irrigation, etc. and the nutrition system should be designed in order to save energy and ease of use in order to use inactive systems for feeding.

In addition to the factors mentioned regarding the conditions necessary for the growth of plants in space, in order to increase the absorption of nutrients, increase drought resistance and root pathogenic factors and increase plant resistance to water deficit stresses, there is a great deal of evidence that coexistence fungi can cause changes in plant arable relationships and improve drought resistance in the host plant. In this study, the aforementioned points will be discussed and it will be explained why mycorrhiza can have good water absorption efficiency. Generally, mycorrhiza coexistence can provide a clear vision as a suitable strategy for critical situations.

## REFERENCES:

- [1] M.P. K.Hasenstein. (2016) Oxygen dependency of germinating Brassica seeds. Life Sciences in Space Research, 1\_6 .
- [2] T. G, R.W . (2016). Root restriction: A tool for improving volume utilization efficiency in bioregenerative life-support systems. Life Sciences in Space Research 1 .
- [3] M. S, Y. O , Vladimir Sychev d , Natalia Novikova d , Anatoly Grigoriev d.(2016). Gene expression of rice seeds surviving 13- and 20-month exposure to space environment. Life Sciences in Space Research.1,7 .
- [4] L. Poulet a, G.D. Massa b, R.C. Morrowc, C.M. Bourget c, R.M. Wheeler b, C.A.Mitchell a (2014) Significant reduction in energy for plant-growth lighting in space using targeted LED lighting and spectral manipulation. Life Sciences in Space Research.7
- [5] P. Zabel, M. Bamsey, D. Schubert, M. Tajmar (2016) Review and analysis of over 40 years of space plant growth systems. Life Sciences in Space Research. 2\_6

# STUDY OF THE BACTERIAL LIFE ON SIMILAR CONDITIONS OF THE EUROPA, IN THE LABORATORY

M.S.Gheibzadeh <sup>1</sup>

<sup>1</sup>International Occultation Timing Association Middle East Section (IOTA/ME), New.astrobiologist@gmail.com

## KEYWORDS:

Europa (moon), Bacterial life, Desulfotomaculum, Extremophiles, Sulfur compounds

## INTRODUCTION:

Astrophysicists accept that there being life in the universe, elsewhere, on other planets or even on moons and there are many researches that indicate, we are not alone but in a moment, life on Earth is the only known life in the universe.

The life on other planets depends on many parameters. More relevant parameters consist of discovery of water, organic matter, appropriate temperature, pressure and PH. There are some environments in the earth that don't have all conditions, and call extreme environments. But some organisms as extremophiles can live there. The so-called extremophiles belong to a group of microorganisms is said that desire to live in extreme environments[1].

Many moons have acceptable parameters for life. One of the best candidates for possibility of life among the object of the solar system is Jupiter's moons like as Europa. Because of this special properties we can also study the special life on it; microbial life.



Fig. 1. Scanning electron micrograph of *D. gibsoniae*

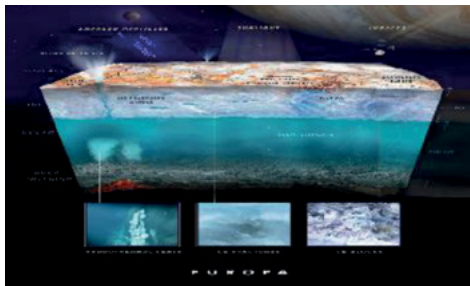


Fig. 2. Europa's surface & subsurface

## 1. EUROPA

Europa, is one of the Galilean satellites of Jupiter. This moon is very important for search about of life in extraterrestrial objects. We need to know about composition of surface, subsurface and temperature of that for create conditionals like Europa.

### 1.1 WATER ICE

Telescopic observation of Galilean satellites by Kuiper suggested the presence of water band confirmed by near-IR obtained [2,3]. Europa's trailing side contains hydrate and H<sub>2</sub>O ice in variable proportion, whereas the leading hemisphere's surface is dominated by water ice. The spacecraft measure magnetic variations across Europa shows that the outer shell is shifting. The surface displacement is anticipated that a subsurface flow like a liquid ocean beneath, on

a planetary scale, is under the icy surface. The structure of Europa is unclear, but most models, show a Silicate mantle and rocky core rich in iron and the outer ice shell, that is thick with liquid water which in total is approximately 170-80 km. Water may be mixed with lime, that results to a chemical transformation, transport of silicate mantle into the ocean as well as transfer them ocean to icy shell.

## 1.2. HYDRATES

Hydrate compounds are any compounds that have chemically attached water molecules or hydrogen and oxygen atoms. Have seen many absorption bands in Europa's surface. Two explanations are given for these bands:

A. Hydrated salts

B. Hydrated sulfuric acid.

Material was taken from the ocean was considered primary salt source of hydrated salts [4]. Primary sulfur source of hydrated sulfuric acid is sulfur ion, sulfide and sulfoxide. At the moment, no definitive evidence for acid and salt with current data. Spectroscopic data show magnesium [5]. Magnesium sulfate accepts easily the water molecule. The ratio of some compounds:

$H_2SO_4 = 25-35\%$

$Na_2SO_4 = 25-40\%$

$MgSO_4 = 24-50\%$  [6]

The main source of these salts is series of hydrogen sulfate, metal oxide and hydroxides [7]. Sulfate and other hydrates is turned to  $SO_2$  with removed of metal atoms. The result of this reaction can be  $MgO$ ,  $Mg(OH)_2$ ,  $Na_2O$ ,  $Na_2O_2$  and  $NaOH$ , that  $Mg(OH)_2$  is stable [8].

## 1.3. $SO_2$

Absorption spectrum in  $0.28\ \mu m$  was observed in leading and trailing side of Europa. Which attributed it to  $SO_2$  [9], this molecule is very reactively and there is gas phase in low temperature ( $<31\ K$ ) [10]. Sulfur trioxide ( $SO_3$ ), reacts with water, rapidly and producing  $H_2SO_4$ . The existence of  $SO_2$  was checked out in the laboratory and it coincided with the trailing side features but,  $SO_2$  features not seen in leading side of Europa.

## 1.4. EUROPA TEMPERATURE

Europa surface temperature is between  $86$  to  $130^\circ$  Kelvin and the temperature is not suitable for life. But beneath the icy surface of Europa Hydrothermal vents have been proposed that could provide the required temperature for life. Temperature hydrothermal vents on the earth between  $350$  and  $400^\circ\ C$ , which by nearing to the Europa icy surface, temperature is gradually reduced and appropriate growth of thermophilic bacteria. In addition, the tidal created as the temperature more than freezing point.

## 2. BACTERIAL SPECIES

After studying environments similar to Europa and extracting bacteria that lives to this environments, *Desulfotomaculum* is selected. This bacteria is Extremophile and it can survive at high temperatures and containing spores that can tolerate freezing conditions. Also this bacteria can using sulfur compounds and producing hydrogen sulfide.

## 3. FUTURE AND FEATURE

As I mentioned, study Europa's life needs some simulation to simulate parameters and situation of this moon in laboratory. In this study, I try to make this condition in laboratory to study Europa's life. By my preliminary study, I understand that Europa has the most likeness with Sari- Soo hot spring in Iran. The survey on the structure of Iran's extreme environment inhabitant extremophiles bacteria are reasons for expecting thermophilic microorganisms [1].

## REFERENCES:

- [1] Gheibzadeh M., Vahedi S. Scrutiny of viability of Iran extremophiles on the extraterrestrial habitable environments similar to Iran extreme environments // Journal Of Occulation And Eclipse. 2016. No. 3 .
- [2] Moroz V. I. (1965) Infrared spectrophotometry of satellites: The Moon and the Galilean satellites of Jupiter. *Astron. Zh.*, 42, 1287, trans. in *Soviet Astron.-AJ*, 9, 999-1006.
- [3] Johnson T. V. and McCord T. B. (1971) Spectral geometric albedo of the Galilean

satellites 0.3–2.5 microns. *Astrophys. J.*, 169, 589–593.

[4] McCord T. B., Hansen G. B., Fanale F. P., Carlson R. W., Matson D. L., Johnson T. V., Smythe W. D., Crowley J. K., Martin P. D., Ocampo A., Hibbitts C. A., and Granahan J. C. (1998b) Salts on Europa's surface detected by Galileo's Near Infrared Mapping Spectrometer. *Science*, 280, 1242–1245.

[5] Carlson R. W., Johnson R. E., and Anderson M. S. (1999b) Sulfuric acid on Europa and the radiolytic sulfur cycle. *Science*, 286, 97–99.

[6] Orlando T. M., McCord T. B., and Grieves G. A. (2005) The chemical nature of Europa surface material and the relation to a subsurface ocean. *Icarus*, 177, 528–533.

[7] Johnson R. E. (2001) Surface chemistry in the jovian magnetospheric radiation environment. In *Chemical Dynamics in Extreme Environments* (R. A. Dressler, ed.), World Scientific, Singapore.

[8] Glagolev V. L., Gordeeva V. A., Zhabrova G. M., and Kadenatsi B. M. (1967) On the radiation decomposition of aluminum and magnesium hydroxides. *High Energy Chem.*, 1, 247–248.

[9] Sack N. J., Johnson R. E., Boring J. W., and Baragiola R. A. (1992) The effect of magnetospheric ion bombardment on the reflectance of Europa's surface. *Icarus*, 100, 534–540.

[10] Hopkins A. G. and Brown C. W. (1975) Infrared spectrum of sulfur monoxide. *J. Chem. Phys.*, 62, 2511–12.



# PUTATIVE MARTIAN MICROBIAL COMPLEXES COULD BE VIABLE CRYOPRESERVED IN REGOLITH DURING TENS OF MILLIONS YEARS

V.S. Cheptsov<sup>1,2</sup>, M.O. Kruchkova<sup>1</sup>, E.A. Vorobyova<sup>1,2</sup>, A.E. Ivanova<sup>1</sup>, A.K. Pavlov<sup>3</sup>, V.N. Lomasov<sup>4</sup>

<sup>1</sup>Lomonosov Moscow State University (119991, Russian Federation, Moscow, Leninskie Gory, 1, cheptcov.vladimir@gmail.com);

<sup>2</sup>Space Research Institute of Russian Academy of Sciences (117997, Russian Federation, Moscow, Profsoyuznaya Street, 84/32);

<sup>3</sup>Ioffe Physical-Technical Institute of the Russian Academy of Sciences (195251, Russian Federation, Saint-Petersburg, Politekhnikeskaya Street, 26);

<sup>4</sup>Peter the Great Saint-Petersburg Polytechnic University (195251, Russian Federation, Saint-Petersburg, Politekhnikeskaya Street, 29).

## KEYWORDS:

Mars, microbial communities, extreme habitats, biodiversity, radioresistance, cryopreservation.

Currently, astrobiology is focused on Mars as one of the most perspective objects in the Solar System to search for microbial life. It is supposed that early Mars was the planet with the fairly mild climate. At this time the biosphere could be formed and preserved to the present day in anabiotic state. The duration of its preservation is limited by the effect of ionizing radiation.

We studied the survivability of the permafrost and desert soil microbial communities (as terrestrial analogs of putative Martian ecosystems) at irradiation by gamma radiation (1 MGy) under simulated conditions (low temperature and pressure) of the surface layer of the Martian regolith. Exposure has not resulted in the death of microbial complexes: they retained a high number of living cells, potential metabolic activity and biodiversity.

Among the cultured bacteria, representatives of the genera *Arthrobacter*, *Microbacterium*, *Bacillus*, *Pseudomonas*, *Sphingomonas*, *Cryobacterium* and *Pseudoxanthomonas* were found. The most resistant species of fungi which dominated after impact of extreme conditions were *Aspergillus fumigatus* and *A. niger*. Moreover, *Emericella nidulans*, *Geomyces pannorum*, *Phialophora fastigiata*, *Rhodotorula mucilaginosa*, and some species of genera *Acremonium*, *Aspergillus*, *Cladosporium*, *Fusarium* and *Penicillium* were observed.

Resistance to 1 MGy dose irradiation in simulated conditions proves that if there was an Earth-like biosphere on the early Mars it could survived in the surface or subsurface layers of the Martian regolith for more than tens of millions years after climate change. The study gives also some new grounds for the approval of transfer of viable microorganisms in space.

# TEMPERATURE DEPENDENCE OF AUTOFLUORESCENCE: DETECTION LIMITS FOR UBIQUITOUS LIFE-SPECIFIC COMPOUNDS

I. Digel, M. Kuhlen

*Institute for Bioengineering, FH Aachen University of Applied Sciences, Heinrich-Mußmann-Str. 1, 52428 Jülich, Germany, digel@fh-aachen.de*

## KEYWORDS:

life search, fluorescence signatures, detection limits, bio-compounds, autofluorescence

Photometric technologies have a potential for fast, simple and reliable identification and characterization of chemical compounds and microorganisms in natural environments via a set of characteristic optical features (signatures). Our study pursued three main goals and primarily focused on fluorescence spectroscopy measurements of selected species of ubiquitous terrestrial bio-compounds as a model for future terrestrial and extraterrestrial applications.

The first aim was to specify the coordinates of maximal fluorescence signal ( $\lambda_{Ex}$ ;  $\lambda_{Em}$ ) and to verify that autofluorescence can be successfully used to differentiate between various biogenic compounds through identification of spectroscopic fingerprints. All measurements were done by using FP 8500 Spectrofluorometer (Jasco Co.). In total, 13 different compounds were tested: FAD, ATP, tryptophan, alanine, arginine, phenylalanine, NADH, riboflavin, chlorophyll, histidine, RNA, pyridoxine, bacteriorhodopsin.

The second aim was to determine the minimal concentrations of the compounds that could be still detectable by the conventional fluorescence spectroscopy. For all 13 substances, 20 mL aliquots of six dilutions ( $10^1$ – $10^6$ ) were prepared from 10-100 mM stock. The signals from the prepared dilutions were measured at fluorescence maxima at room temperature and plotted as a function of the concentration. The lowest still detectable concentrations (0.1-1  $\mu$ M) were found for FAD, NADH, pyridoxine hydrochloride, tryptophan and riboflavin. L-histidine, L-arginine and L-alanine were only detectable starting from 1 mM. L-phenylalanine and ATP could be detected down to 10  $\mu$ M-concentrations. The third goal was to investigate the temperature dependency of intensity. For this, the fluorescence signal of all compounds was measured at peak intensity wavelength at 5°C, 25°C and 45°C (Table 1.).

For tryptophan, L-phenylalanine, L-histidine, L-alanine, NADH, bacteriorhodopsin and pyridoxine hydrochloride, the highest measured sensitivity of the detection was at 5°C, and exceeded the 25°C-sensitivity approximately by factor 2. Interestingly, L-arginine, FAD and ATP demonstrated better detectability at 25°C (labeled yellow).

Table 1:

Substance	5°C	25°C	45°C	I <sub>Ex</sub> /I <sub>Em</sub> [nm]
L-Tryptophan (1mM)	4820	3370	1661	295/354
L-Phenylalanine (10mM)	1618	1091	522	265/281
L-Histidine (100mM)	102	83	66	275/305
L-Arginine (100mM)	16	29	10	290/410
L-Alanine (1M)	51	39	30	275/304
FAD (100mM)	244	348	261	370/528
ATP (10mM)	436	504	446	295/392
NADH (1 mM)	518	308	234	380/460
Pyridoxine (1mM)	3071	1635	1006	330/395
Bacteriorhodopsin	170	149	135	280/317

# HIGH RESISTANCE OF BACTERIA FROM EXTREME HABITATS TO ABIOTIC AND BIOTIC FACTORS

A.A. Belov<sup>1</sup>, V.S. Cheptsov<sup>1,2</sup>, E.A. Vorobyova<sup>1,2</sup>

<sup>1</sup> Lomonosov Moscow State University, 119991, Russian Federation, Moscow, 1 Leninskie Gory Street

<sup>2</sup> Space Research Institute, 117997, Russian Federation, Moscow, 84/32 Profsoyuznaya Street

## KEYWORDS:

Stress tolerance, extreme habitats, astrobiology, antibiotic resistant bacteria, Antarctic, radioresistant bacteria.

## INTRODUCTION:

In spite of large amount of research till now the bounds of life and cell resistance are not elucidated. However, this question is one of the basic in astrobiological investigations and plays the main role in choosing criteria for the search of extraterrestrial life. Special attention to such kind of investigations is drawn to bacteria, which inhabit extreme biotopes and adapted to effect of one or several stress factors [1,2,3].

## OBJECTS:

More than 450 strains of aerobic heterotrophic bacteria which belong to  $\alpha$ -Proteobacteria, Firmicutes, Actinobacteria,  $\gamma$ -Proteobacteria and  $\beta$ -Proteobacteria were isolated from different extreme biotopes: soils, mineral and ice samples taken in Eastern Siberia (Russia), the Sarpinian Basin (Russia), the Gibson desert (Australia), Antarctic, the Sahara desert (Africa), Baskunchak saltlake (Russia), the Negev desert (Israel), Novaya Zemlya archipelago (Russia), the Namib desert (Africa), the Mojave desert (USA) and the Atlas mountains' soil (Morocco). Resistance to wide spectrum of abiotic factors (temperature, pH, presence of salts) and impact of antibiotics (Ampicillin, Kanamycin, Cephalixin, Chloramphenicol, Doxycycline, Rifampicin, Tetracycline) were analyzed. In this research the resistance to the same factors of bacteria, which were isolated from soils and permafrost samples irradiated by ionizing radiation [4,5,6],

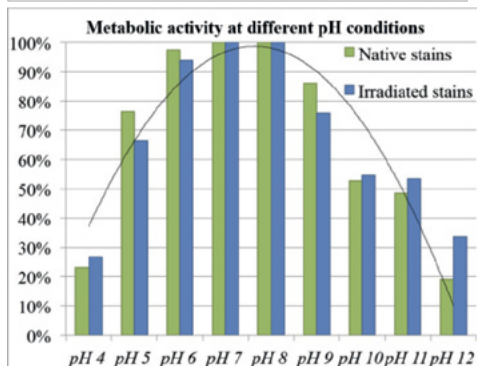
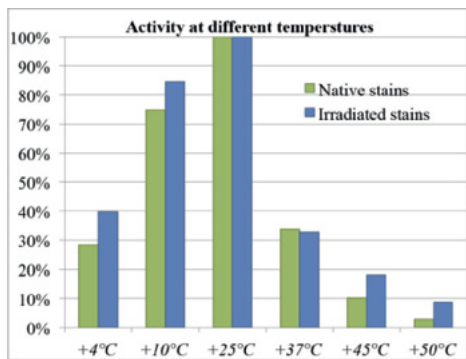
was also estimated. Strains isolated from irradiated samples belong to *Actinobacteria*,  *$\alpha$ -Proteobacteria*, *Firmicutes*, *Bacteroidetes*,  *$\beta$ -Proteobacteria* and  *$\gamma$ -Proteobacteria*.

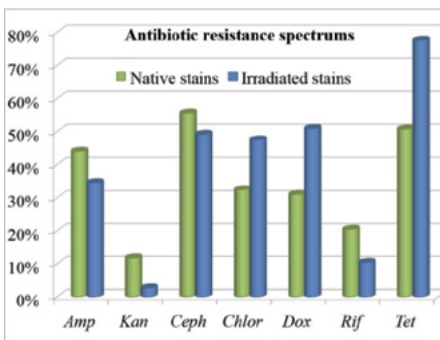
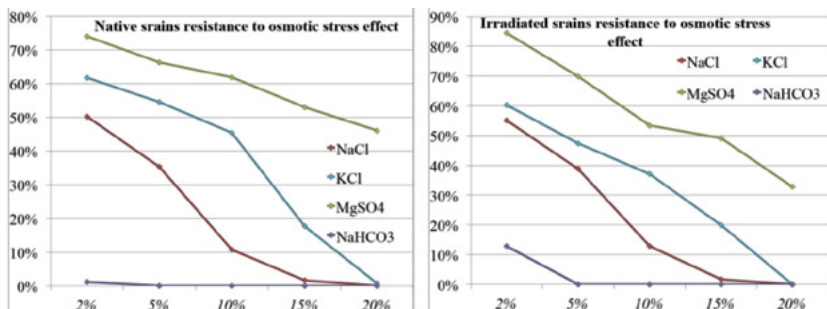
## RESULTS:

Ability of many bacterial strains to active metabolism in a wide range of temperatures from +4 to +50°C was shown. Some strains were able to reproduce at +2°C.

All bacterial strains multiplied at wide diapason of pH values with optimum near 7-8. Strains, which are able to reproduce at pH from 4 to 12, were found. There were revealed no correlations with the temperature or pH conditions in the native biotopes from which bacteria were isolated.

As for the inhibitory effect of salts on the growth of bacteria, they can be arranged in descending order:  $\text{NaHCO}_3$ , NaCl, KCl,  $\text{MgSO}_4$ . High resist-





ance of bacterial strains to high concentrations of  $MgSO_4$  should be noted: bacteria were able to reproduce at concentrations much higher than those which were found in Martian regolith [7].

Apart from high resistance to abiotic impacts, bacterial strains isolated from extreme habitats show high resistance to antibiotics (concentration 100 mg/l) from different classes according to different mechanisms of biological action. Irradiated strains have revealed higher resistance to Chloram-

phenicol, Doxycycline and Tetracycline.

## CONCLUSIONS:

All the above allow us to make the following conclusions:

1. Bacteria isolated from extreme habitats actively metabolize and multiply in wide ranges of temperatures and pH.
2. Resistance to high concentrations of salts indicates active powerful mechanisms of cells' stabilization and adaptation.
3. Bacteria isolated using pretreatment by high doses of ionizing radiation show high resistance to physicochemical and biological stress agents. This attests that radiation leads to activate stress tolerance mechanisms [8].
4. These results extend our knowledge about life bounds and inspire us hope in success in further astrobiological research.

## REFERENCES:

- [1] Gilichinsky D. A. et al. Microbial populations in Antarctic permafrost: biodiversity, state, age, and implication for astrobiology // *Astrobiology*. – 2007. – V. 7. – №. 2. – p. 275-311.
- [2] Rothschild L. J., Mancinelli R. L. Life in extreme environments // *Nature*. – 2001. – T. 409. – №. 6823. – p. 1092-1101.
- [3] Vorobyova E. et al. The deep cold biosphere: facts and hypothesis // *FEMS Microbiology Reviews*. – 1997. – T. Resistance of terrestrial microbial communities to impact of physical conditions of subsurface layers of Martian regolith // *Life and Universe* и *BBM Saint-Petersburg*, 2017. – p. 273-282 (In Russian).
- [5] Cheptsov V.S., Vorobyova E.A., Bulat S.A. Radioreistance of Permafrost Microbial Communities by Culturing and Metabolic Activity Testing // *International Conference «Earth's Cryosphere: Past, Present and Future»* (June 4-8, 2017, Pushchino, Russia). Program and conference materials – 2017, p. 115-116
- [6] Cheptsov V. S. et al. Limits of resistance of soil microbial communities to impact of gamma radiation // *The Seventh Moscow Solar System Symposium (7M-S3)*. – 2016. – P. 265-ab-267-ab.
- [7] Vaniman D. T. et al. Magnesium sulphate salts and the history of water on Mars // *Nature*. – 2004. – V. 431. – №. 7009. – p. 663-665.
- [8] Cheptsov V.S., Vorobyova E.A., Tambiev A.H., Pavlov A.K., Vdovina M.A., Lomasov V.N., Zvyagintsev D.G. Influence of gamma radiation, low pressure and low temperature on catalase activity and reactivity of exometabolites of *Kocuria rosea* and *arthrobacter polychromogenes* // *Modern problems of science and education* – 2016 (In Russian).

# MONITORING OF INTERNAL ENVIRONMENT ON THE BOARD OF SPACE STATION

T.A. Alekhova<sup>1</sup>, E.A. Vorobyova<sup>2,3</sup>, M.V. Gorlenko<sup>2</sup>

<sup>1</sup>*Faculty of Biology, Lomonosov Moscow State University, Moscow, Russia*

<sup>2</sup>*Faculty of Soil Science, Lomonosov Moscow State University, Moscow, Russia*

<sup>3</sup>*Space Research Institute RAS, Moscow, Russia*

## KEYWORDS:

ISS, microbial communities, monitoring

The purpose of this research was to study the functional activity of microbial communities inhabiting living and working areas of the Russian Segment of the International Space Station (ISS RS). The work is carried out in accordance with the "Long-term program of scientific and applied research and experiments planned on the Russian Segment of the ISS", and is designed for the entire period of operation of the station.

The probes were collected in the areas of possible multiplication and accumulation of microorganisms [1-3]. Additionally, microorganisms and biological activity in dust collected by a vacuum cleaner and on air filters have been investigated, since these sites of spore and microbial cell concentration are optimally suited to assess the entire diversity of species. The quantification of bacteria was performed by epifluorescence microscopy. Potential functional activity of bacterial communities was investigated by differential multisubstrate testing (MST "Ecolog", "Taxon"). In the basic version of MCT "ECOLOG" 47 substrates representing different classes of organic substances were tested. The data obtained represent a 47-dimensional array, the processing of which is carried out using multidimensional statistics (component analysis, cluster analysis, etc.) [4]. Statistical software STATISTICA, SPSS, as well as the original software ECOLOG were used for data processing. In the experiment the amount of substrates utilized from the proposed substrate set and the intensity of their consumption was estimated.

Composition of bacterial complexes found on the ISS RS suggests that these organisms were absorbed from air and dust, since many of them, and primarily the dominant species, are known as typical air and pedobionts.

In our research growth of physiological activity of microbial communities occupying the dust in inhabited bays of space station was shown during three years of follow-up. The biodiversity of dust communities has increased, and formation of steady and potentially active heterotrophic ecosystem was established. The data allow to assume increasing concentration of organic substances in the air aerosol of inhabited bays of spacecraft. The amount of substrates (N) to be disposed of increased in the following series of samples: dust filter fragment (sample A) <dust collector (fragment) (B) <dust from the dust collector (C) <mucus from the pipeline (D) (Figure 1).

Bacterial complex in the specimen of the mucus strand (sample D) had a comparatively low total bacterial count ( $8.0 \times 10^7$  cells/cm<sup>2</sup>) (Table 1), and the poor biodiversity of the cultivated forms. It showed low intensity but rather wide range of metabolic activity. Similar signs can manifest a persistent community, formed in flow systems and maintaining a low, but constant level of metabolism. Such systems may have a hidden diversity of oligotrophic forms, which are not detected by cultivation on relatively rich universal nutrient media. Bacterial complex isolated from the dust filter fragment (sample A) had high cell number and the greatest diversity. It actively utilized a narrow spectrum of substrates. These facts indicate the development on the filter potentially very active community with simplified structure. Two other samples (B, C), the dust bag fragment and the dust, have similar characteristics and occupied an intermediate position.

The method of rank distributions provides an opportunity to assess the degree of stability and complexity of the studied living systems. This approach reveals a weak stability and imbalance of the microbial systems under analysis. Apparently, the interaction of microorganisms on the surface of the materials investigated is difficult (there is no common physiological environment), and microbial consortia have not formed stable interpopulation interactions, but maintain the metabolic potential.

The results indicate a difference in the communities formed in different zones

of the ISS, their metabolic potential. The bacterial consortia studied are unbalanced, which implies their development under favorable conditions. A promising task is to identify the parametric limits of environmental factors that keep microbial systems from progressing development.

This work was supported by RSF grant № 14-50-00029

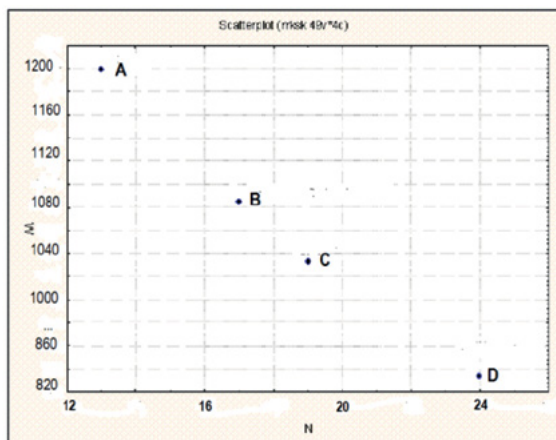


**Fig.1.** Distribution of samples in the space of functional diversity and biochemical activity (M - the average color intensity in the reaction cell, N - the number of utilized substrates).

**Table 1.** The total count of bacteria and the number of culturable bacteria (CFU) in the samples: A- dust filter (fragment), B - dust collector (fragment); C - mucus from the pipeline; C - dust from the dust collector

Образец	N/cm2	KOE/cm2
A	$7,0 \times 10^8 \pm 1,2 \times 10^8$	$5,5 \times 10^6 \pm 0,5 \times 10^6$
B	$1,6 \times 10^8 \pm 0,3 \times 10^8$	$1,2 \times 10^6 \pm 0,6 \times 10^6$
C	$4,1 \times 10^{10} \pm 0,9 \times 10^{10}$	$1,9 \times 10^7 \pm 0,7 \times 10^7$
D	$8,0 \times 10^7 \pm 1,0 \times 10^7$	$6,5 \times 10^5 \pm 1,3 \times 10^5$

## REFERENCES:

- [1]. Alekhova T.A., Novozhilova T.Yu. et al. Isolation of microflora from the surface of construction materials of OS "Mir". Proceedings of 1 Int. Congress "Biotechnology: State and Perspectives". 2002. P.315.
- [2]. Skuratov VM, Zagibalova LB, Pushkin V.P. The generic composition and microbial contamination of the condensate of atmospheric moisture and drinking water of the water supply systems of the Mir orbital complex in the period of EO-4-27 // Aviakosmicheskaya i ekologicheskaya meditsina. 2002. T. 36, No. 2. C. 28-32.
- [3]. Alekhova TA, Alexandrova A.V. et al., "The initial stages of biodegradation and biodegradation in space conditions," Vestnik Moskovskogo Universiteta. Ser. 16. Biology. 2008. № 4. P. 27-33.
- [4]. M.V. Gorlenko, P.A. Kozhevnikov, Multisubstrate testing of natural microbial communities, MAKS Press, Moscow, 2005

# INFLUENCE OF SPACE FLIGHT AND IONIZING RADIATION ON THE PHOTOSYNTHETIC APPARATUS OF CYANOBACTERIA

Konstantin E. Klementiev<sup>1</sup>, Eugene G. Maksimov<sup>1</sup>, Georgy V. Tsoraev<sup>1</sup>, Irina V. Elanskaya<sup>2</sup>, Victor M. Lebedev<sup>3</sup>, Andrew V. Spassky<sup>3</sup>, Vladimir Z. Paschenko<sup>1</sup>

<sup>1</sup> Department of Biophysics, Faculty of Biology, M.V. Lomonosov Moscow State University, 119992, Moscow, Russia, emaksimoff@yandex.ru;

<sup>2</sup> Department of Genetics, Faculty of Biology, M.V. Lomonosov Moscow State University, 119992, Moscow, Russia;

<sup>3</sup> Department of nuclear and space research, Skobeltsyn institute of nuclear physics, M.V. Lomonosov Moscow State, 119992, Moscow, Russia;

## KEYWORDS:

space, cosmic rays, ionizing radiation, cyanobacteria, photosynthesis, phycobilisomes, phycobiliproteins.

## INTRODUCTION:

Modeling the behavior of biological objects in conditions of high radiation and attenuated geomagnetic field is important scientific problem, because modern space missions aim to reach different planets of solar system. The flux of cosmic rays outside the magnetic field of the Earth could be dangerous for space pioneers. It is a well-known fact that exposure to ionizing radiation leads to a decrease of vital activity of biological objects.

In this work, we present a comparative study of the influence of space flight conditions and model experiments on the photosynthetic apparatus of cyanobacterium *Synechocystis* sp. PCC 6803 (*Synechocystis*). The culture of wild type *Synechocystis* was launched into space on the satellite "Foton M4" and it orbited the Earth for 45 days. For modeling conditions of the space flight, we used a cyclotron U-120 SINP MSU, which yields accelerated helium nuclei with energy about 30.3 MeV. Changes in the structural and functional state of the photosynthetic membranes of cyanobacteria was evaluated by variety of optical methods, including fluorescence spectroscopy with picosecond time resolution (Simple-Tau 130, Becker & Hickl).

It was found that the antenna complexes of *Synechocystis* - phycobilisomes are the most sensitive to ionizing radiation and the conditions of space flight,

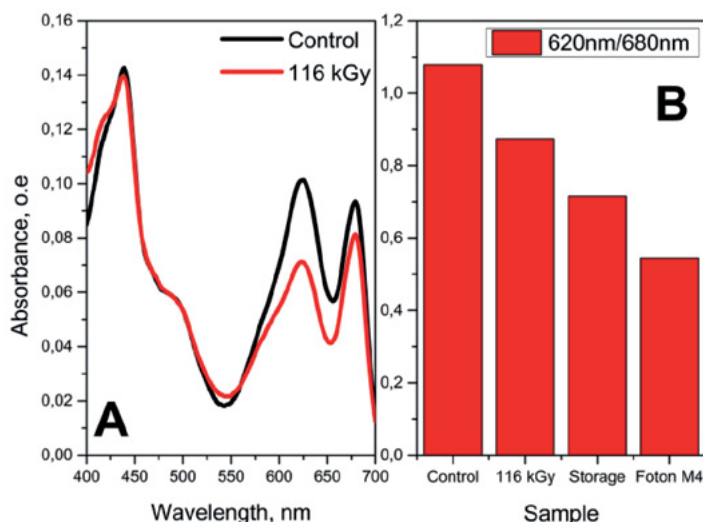


**Fig. 1.** (A) - absorption spectra of the sample after irradiation with alpha particles (116 kGy). (B) - the ratio of optical density at wavelengths of 620 nm and 680 nm for samples after exposure to 116 kGy, long-term storage and cosmic flight (Foton M4).

Figure 1. shows that the presence of cells under these conditions causes a significant decrease of the optical density in the region of phycobilisomes absorption. Simultaneously, we observed an increase in the intensity and fluorescence lifetime in the region of 660 nm (Figure 2), which is probably due to a violation of the integrity of phycobilisomes and decrease in the efficiency of excitation energy transfer within phycobilisomes and from phycobilisomes to the photosynthetic reaction center. The phycobilisomes of the cells exposed to radiation are functionally different due to almost complete absence of non-photochemical quenching (NPQ) [1]. Space flight and high doses of ionizing radiation lead to inactivation of photosystem 2 (PS2). However, even after that some part of the culture remains viable and placing it into normal cultivation conditions leads to full restoration of all monitored parameters. Clarification of the mechanisms of such sustainability of cyanobacterial cells require additional research.

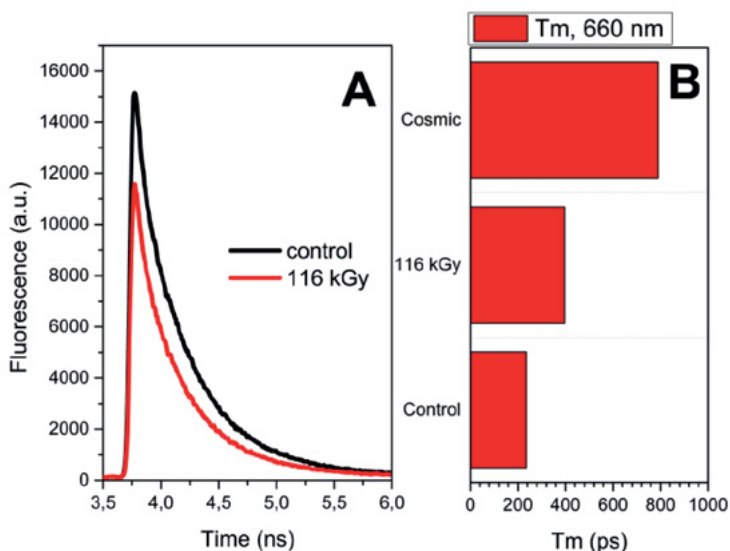


**Fig. 2.** (A) - Fluorescence decay kinetics of phycobilisomes in the control sample and a sample exposed to 116 kGy. The average fluorescence lifetimes of the samples at 660 nm (B).

## ACKNOWLEDGEMENTS

Work was partially supported by the Russian Foundation for Basic Research (project 16-34-00394).

## REFERENCES:

[1] E. G. Maksimov, K. E. Klementiev, E. A. Shirshin, G. V. Tsoraev, I. V. Elanskaya & V. Z. Paschenko. 2015. Features of temporal behavior of fluorescence recovery in *Synechocystis* sp. PCC6803. *Photosynth. Res.* 125:167–178.



# TWO DIFFERENT REGIMES OF INTERACTION OF PLANETARY AND STELLAR WINDS OF THE GLISE 436 B AND TRANSIT ABSORPTION IN LYA LINE

I.F. Shaikhislamov, A.G. Berezutskiy, I.B. Miroschnichenko

*Institute of Laser Physics, Siberian Branch of the Russian Academy of Science, 630090, Novosibirsk, Russia Ac. Lavrentiev Ave, 13 ILP SB RAS, a.berezuckiy@yandex.ru*

In numerical simulations of Gliese 436 b, two regimes of interaction of expanding planetary wind (PW) and stellar wind (SW) were obtained using multi-fluid model [1]. GJ 436 b is a Neptune-sized exoplanet rotating around parent star at the distance of 0.028 au. For GJ 436 b, high value of in-transit absorption  $\sim 50\%$  in Ly $\alpha$  line was observed [2]. We obtained density distributions of planetary protons, atoms and ENAs generated in interaction with SW at different XUV stellar fluxes and in two different regimes: 1- compressed envelope around the planet (Fig.1.); 2- extended day side stream in the direction of the host star.

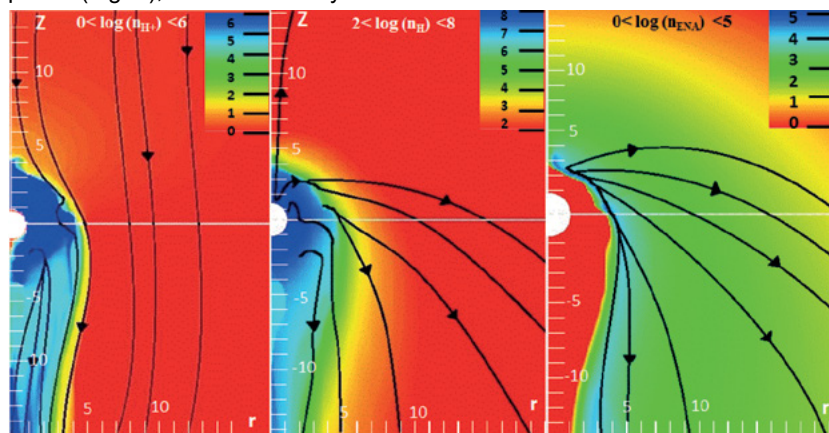


**Fig.1.** From left to right. Density distributions of planetary protons ( $n_{H^+}$ ), atoms ( $n_H$ ) and ENAs ( $n_{ENA}$ ). Plotted values are in log scale. White circle indicates the planet. The streamlines of the corresponding components are shown in black.

The maximum temperature in the stream is about 3000-5000 K. To calculate the transit depth absorption we used the interval of  $[-120; -40]$  km/s in Ly $\alpha$  line profile [3]. Absorption is caused mostly by ENAs, and reaches  $\sim 30\%$  at intense stellar wind ( $V_{SW}=181$  km/s;  $n_{SW}=10^4$  cm $^{-3}$ ;  $T_{SW}=1.5$  MK). At less intense stellar wind ( $V_{SW}=136$  km/s;  $n_{SW}=5 \cdot 10^3$  cm $^{-3}$ ;  $T_{SW}=1.5$  MK) absorption drops to 15%.

## REFERENCES:

- [1] I.F. Shaikhislamov, M. L. Khodachenko, H. Lammer, et al. 2016, ApJ, 832
- [2] D. Ehrenreich, V. Bourrier, P.J. Wheatley, et al. 2015, Nature, 522,459
- [3] V. Bourrier, A. Lecavelier des Etangs, D. Ehrenreich, et al. 2016, A & A

# NUMERICAL SPIS-DUST MODELLING OF PLASMA- “LUNA-GLOB” LANDER INTERACTIONS

I.A. Kuznetsov<sup>1</sup>, A.V. Zakharov<sup>1</sup>, E. Seran<sup>2</sup>, S.L.G. Hess<sup>3</sup>, F. Cipriani<sup>4</sup>, G.G. Dolnikov<sup>1</sup>, A.N. Lyash<sup>1</sup>, I.A. Shashkova<sup>1</sup>

<sup>1</sup>Space Research Institute of the RAS, Moscow, Russia, [kia@iki.rssi.ru](mailto:kia@iki.rssi.ru)

<sup>2</sup>Laboratoire Atmospheres, Milieux, Observations Spatiales, Paris, France

<sup>3</sup>French Aerosp. Lab., ONERA, Toulouse, France

<sup>4</sup>ESTEC/TEC-EES, Noordwijk, The Netherlands

## KEYWORDS:

Lunar Dust, Lunar exosphere, Moon, PiC, Numerical Simulation, Plasma

## INTRODUCTION:

One of the complicating factors of the future robotic and human lunar landing missions is the influence of the dust. Meteorites bombardment has accompanied by shock-explosive phenomena, disintegration and mix of the lunar soil in depth and on area simultaneously. As a consequence, the lunar soil has undergone melting, physical and chemical transformations.

Recently we have the some reemergence for interest of Moon investigation. The prospects in current century declare USA, China, India, and European Union. In Russia also prepare two missions: Luna-Glob and Luna-Resource. Not last part of investigation of Moon surface is reviewing the dust condition near the ground of landers. Studying the properties of lunar dust is important both for scientific purposes to investigation the lunar exosphere component and for the technical safety of lunar robotic and manned missions.

The absence of an atmosphere on the Moon's surface is leading to greater compaction and sintering. Properties of regolith and dust particles (density, temperature, composition, etc.) as well as near-surface lunar exosphere depend on solar activity, lunar local time and position of the Moon relative to the Earth's magnetotail. Upper layers of regolith are an insulator, which is charging as a result of solar UV radiation and the constant bombardment of charged particles, creates a charge distribution on the surface of the moon: positive on the illuminated side and negative on the night side. Charge distribution depends on the local lunar time, latitude and the electrical properties of the regolith (the presence of water in the regolith can influence the local distribution of charge).

On the day side of Moon near surface layer there exists possibility formation dusty plasma system. Altitude of levitation is depending from size of dust particle and Moon latitude. The distribution dust particle by size and altitude has estimated with taking into account photoelectrons, electrons and ions of solar wind, solar emission. Dust analyzer instrument PmL for future Russian lander missions intends for investigation the dynamics of dusty plasma near lunar surface. PmL consists of three parts: Impact Sensor and two Electric Field Sensors.

One of the tools, which allows to simulate the dust emission from the Moon and asteroids, its transport, deposition and its interaction with a lander, is the SPIS-DUST (Spacecraft Plasma Interaction Software) code which based on Particle-in-Cell (PiC) method.

This paper presents first results of SPIS-DUST modelling of the interaction between the lunar plasma environment, regolith and a lander. The model takes into account the geometry of the Luna-Glob lander, the electric properties of materials used on the lander surface, as well as Luna-Glob landing place. Initial conditions were chosen based on the current theoretical models of formation of dusty plasma exosphere and levitating charged dust particles.

## ACKNOWLEDGEMENTS:

The research was carried out using funds of the Russian science foundation (project №17-12-01458).

# THE SPECIFIC FEATURES OF INTERPLANETARY MAGNETIC FIELD AND DUSTY PLASMA FROM “ACE” SATELLITE DATA

A.L. KHARITONOV

*Pushkov Institute of Terrestrial Magnetism, Ionosphere and Radio Wave Propagation of Russian Academy of Sciences, 108840, Russia, Moscow, Troitsk Region, Kaluzhshkoe Hwy, 4, IZMIRAN, ahariton@izmiran.ru*

## KEYWORDS:

interplanetary magnetic field, dusty plasma, “ACE” spacecraft, 2D-spatial electromagnetic IMF cross-sections, the large-scale heterogeneity of IMF spirally-twirled round the basic core

## INTRODUCTION:

Data of changes of amplitude  $B_x$ ,  $B_y$ ,  $B_z$  components of the interplanetary magnetic field (IMF) during the January, 1<sup>st</sup>-11<sup>th</sup>, 2007 measured from “ACE” spacecraft, with 16 second time interval of digitization has been analyzed [10]. “ACE” spacecraft is located in one ( $L_1$ ) from five points of the libration between the Earth and the Sun, on distance about 1.5 million km from the Earth. “ACE” spacecraft allows to give, at least, one hour for possibility of the preliminary prevention about approaching from the Sun to the Earth of streams of the high energy particles resulting at their collision with the magnetosphere of the Earth to raised geomagnetic activity [6]. During the analyzed time period of work of “ACE” spacecraft (January, 1<sup>st</sup>-11<sup>th</sup>, 2007) the independent ground and satellite data («WIND», «GOES» spacecrafts) about parameters of cosmic rays (CR), the data about change of some generalized parameters of plasma of the solar wind ( $Sw\ temp$  – temperatures,  $Nw$  - density the solar wind plasma), and also its speed and the sign in  $B_x$ ,  $B_y$ ,  $B_z$  vector and scalar  $|B|$  components of the interplanetary magnetic field, accessible through the Internet within the limits of the International Program on the solar-terrestrial Physics (ISTP) also has been analyzed [1, 3, 5-10]. The analysis of the decision of the inverse problem of the electromagnetic potential [4] from continuous record in length of 45000 seconds of the part of the data of  $B_z$  – component of the vector of the interplanetary magnetic field measured on January, 8<sup>th</sup>-9<sup>th</sup>, 2007 on “ACE” spacecraft has shown that during the considered temporal period (January, 8<sup>th</sup>-9<sup>th</sup>), in the development phase of heliosphere sub storm in the electromagnetic cross-sections of parameters of the measured interplanetary magnetic field constructed by author, are observed. 2D – temporal and two 2D - the spatial fragment of the electromagnetic structure of IMF depending on the longitude and on latitude GSE-coordinates of the direction of vector of IMF measured in “ACE” spacecraft. 2D-spatial electromagnetic cross-sections are constructed in relative units (rel. un.). Distances ( $r$ ) from “ACE” spacecraft to border of photosphere of the Sun (drawing top -  $r = 140$  rel. un. – values  $B_z$  - component of vector of IMF are closer to border of photosphere of the Sun, the bottom part of drawing -  $r = 1$  rel. un. – values  $B_z$  – component of the vector of the interplanetary magnetic field near to the orbit of “ACE” spacecraft round the libration point ( $L_1$ ), that is are closer to the Earth). In the 2D - temporal electromagnetic cross-section depending on number of the point of visualization ( $N = 900$  points,  $\Delta t = 50$  seconds) are well looked through change of sign  $B_z$  – component of IMF vector, also as well as on usual linear record measurements of IMF. It proves the spent calculations at the decision of the inverse problem of electromagnetic potential [4]. Coordinates of the direction of IMF vector measured in “ACE” spacecraft are resulted in solar-ecliptic system of coordinates (GSE). Besides, on these 2D-spatial electromagnetic cross-sections it is visible that between the orbit of “ACE” spacecraft and border of photosphere of the Sun two absolutely different areas in the sign and structure of isolines of the interplanetary magnetic field are observed. From border of photosphere of the Sun to the middle of distance to “ACE” spacecraft ( $r = 140 - 80$  rel. un.) in 2D-spatial electromagnetic cross-sections the quiet laminar picture of IMF isolines of the negative sign is observed. In the bottom part of 2D-spatial electromagnetic cross-sections ( $r = 1 - 80$  rel. un.) From the libration point ( $L_1$ ) to the middle of distance to

boundary of photosphere of the Sun, that is closer to the orbit of the Earth another is visible absolutely abnormal under the configuration of the electromagnetic heterogeneity and the turbulent structure [6, 7] and the positive sign of the interplanetary magnetic field. In particular, in the bottom part of the 2D-spatial longitudinal electromagnetic cross-section where abnormal structure of IMF is observed, it is possible to see the large-scale heterogeneity of IMF spirally-twirled round the basic core of electromagnetic heterogeneity  $B_z$ -component of vector IMF of the positive sign ( $\lambda = 200^\circ - 340^\circ$ ,  $r = 5 - 75$  rel. un.,  $B_z = 0.3$  nT) ( $\lambda = 280^\circ - 320^\circ$ ,  $r = 10-30$  rel. un.,  $B_z = 0.2$  nT), apparently, connected with so-called heliospheric electro jet – electromagnetic-plasma heterogeneity of the solar wind. Thus, it is possible to tell that the spatial sizes considered spirally-twirled electromagnetic-plasma IMF-structure observed on January, 8<sup>th</sup> -9<sup>th</sup>, 2007 made in the ecliptic plane:  $d\lambda = 140^\circ$  in the GSE-longitude and  $dr = 70$  rel. un. from the distance to the Sun. It is necessary to notice that average electromagnetic field  $B_z$ -components in “core” of this IMF-structure, almost twice is less, than in its twirled “tail” part [2]. It can be connected with more high temperature in rather small “core” on the sizes of this IMF-structure in comparison with its huge “tail” which reduces the electromagnetic field in “core” of this IMF- heterogeneity. As it will be possible to track further from article text, our assumption of lower temperature in the huge “tail”, occupying the most part of volume of this electromagnetic-plasma heterogeneity of IMF, coincides with independent measurements of temperature of plasma according to others spacecrafts. The spent comparison of the data about change of some parameters (intensity) cosmic rays for the period investigated in “ACE” spacecraft has shown that from January, 1<sup>th</sup> to January, 7<sup>th</sup> there was the weak growth of this value, and on January, 8<sup>th</sup> this value has reached some maximum and further to the January, 11<sup>th</sup> changed slightly. At the same time, the generalized parameters of the solar wind (SW temp – temperature and  $Nw$  - density of the solar wind from «WIND» spacecraft, etc.) from January, 8<sup>th</sup> to January, 9<sup>th</sup>, in day on which are constructed temporal and spatial electromagnetic cross-sections of IMF is observed sharp fall of temperature on the order (with 400 to 40 thousand degrees) and sharp increase of density ( $Nw$ ) the solar wind almost on the order (with 2 to 12-20  $\text{sm}^{-3}$ ) that under our assumption is connected with influence on measuring devices of “ACE”, «WIND» spacecraft of the allocated electromagnetic structure of the raised density of plasma and the lowered temperature, different also in the sign (+)  $B_x$ ,  $B_y$ ,  $B_z$  - the vector component and module  $|B|$  of the vector of the induction of the electromagnetic field, and in particular, on falling of speed of the solar wind -  $Sw$  (and even its change on return, in connection with the turbulence, the caused magnetic hydro dynamic processes in “core” of the allocated solar electromagnetic-plasma structures) from other plasma of IMF.

## CONCLUSIONS:

The spatial twirled electromagnetic plasma heterogeneity sharply different in the sign and the spatial helicoid configuration from surrounded interplanetary magnetic field is allocated by results of the decision of the inverse problem of electromagnetic potential, in the measurements executed in the “ACE” spacecraft, on the development phase of the heliospheric substorm in January, 2007.

1. The spatial sizes of observed large-scale heterogeneity of IMF in the libration point ( $L_1$ ) of the Sun-Earth system from “ACE” spacecraft data for January, 8<sup>th</sup> -9<sup>th</sup>, 2007 is more than  $80^\circ$  along GSE-latitude (from  $-80^\circ$  to  $-10^\circ$ ), and  $140^\circ$  along the GSE-longitude at measurement in solar-ecliptic coordinates.
2. In the 2D-electromagnetic longitudinal cross-section of the IMF rather small “core” (1) and big helicoid “tail” (2) - characterizing of the twirled electromagnetic-plasma heterogeneity is observed.
3. The spatial configuration of the electromagnetic plasma heterogeneity fixed in January, 8<sup>th</sup> -9<sup>th</sup>, 2007 from “ACE” spacecraft data more corresponds to the cylinder or to the torus, than to a spheroid in the perpendicular to the ecliptic plane that can be important for the modeling of the MGD-disturbance [1] extending in the stream of the solar wind.

## REFERENCES:

- [1] Barhatov N.A., Queens A.B., Zastenker G.N., et al. MGD dynamics modeling. Sharp indignations of the interplanetary environment in comparison with supervision on the space Devices // *Cosmicheskie issledovania*. 2003. V. 41. No.6. P. 529-538.
- [2] Vysikajlo F.I. Architecture of the cumulation in the dissipative structures. Moscow, MFTI-FGUTISNUM. The Scientifically-educational center «Physics and chemistry of nanostructures», 2009. 192 p.

- [3] Ivanov K.G. Rotary ruptures in a solar wind // *Geomagnetism and Aeronomia*. 1971. No. 11 (5). P. 1032-1040.
- [4] Serkerov S.A. The theory of potential in gravity prospecting and magnetic prospecting. Moscow:Nedra, 2000. 350 p.
- [5] Croocer N.V., Siscoe G.L., Shodhan S. et al. Multiple heliospheric current sheets and coronal streamer belt dynamics // *J. Geophys. Res.* 1993. V. 98(A6). P. 9371-9377.
- [6] Murubashi K. Corotating and transient structures of the interplanetary magnetic field at Venus and Earth // *Solar Wind Eight*. Dana Point (USA), 1996. P. 522-527.
- [7] Wang S., Lee L.G., Wei C.Q. et al. A mechanism for the formation of plasmoids and kink waves in the heliospheric current sheet // *Solar. Phys.* 1988. V. 117(1). P. 157-162.
- [8] Winterhalter D., Smith E.J., Burton M.E. et al. The heliospheric plasma sheet // *J. Geophys. Res.* 1995. V. 99(A9). P. 6667-6674.
- [9] Zhao X., Hoeksema J.T. Effect of coronal mass ejections on the heliospheric current sheet // *J. Geophys. Res.* 1996. V.101(A3). P. 4825-4832.
- [10] Zhoo L., Zurbuchen T.H., Fisk L.A. Global distribution of the solar wind during solar cycle 23: ACE observations // *Geophysical Research Letters*. 2008. V. 36(14), Cite ID L14104.

# DUSTY PLASMA TURBULENCE IN THE REGIONS WHERE THE MOON CROSSES THE EARTH'S MAGNETOTAIL

Yu.N. Izvekova, T. I. Morozova, and S.I. Popel

Space Research Institute of the Russian Academy of Sciences, 84/32

Profsoyuznaya Str, Moscow, Russia, 117997, popel@iki.rssi.ru;

Moscow Institute of Physics and Technology, 9 Institutskiy Pereulok,  
Dolgoprudniy, Moscow Region, 141700, besedina\_yn@mail.ru

## KEYWORDS:

Near-Moon plasma, ion-acoustic waves, dust-acoustic waves, plasma instabilities, magnetic reconnection.

## INTRODUCTION:

About one-fourth of the Moon's orbit lies within the magnetotail. Relative movement of the Moon with the near-Moon plasma and the magnetotail plasma leads to the possibility of the development of plasma instabilities in the regions where the lunar surface interacts with the magnetotail plasma, which underscores the importance of investigation of the wave processes in these regions. Development of plasma instabilities can lead to magnetic reconnection in the regions where magnetic field has oppositely directed components.

## LUNAR DUSTY PLASMA INSTABILITIES:

Let us consider the excitation of ion-acoustic waves due to the dusty plasma motion near the Moon's surface relative to the magnetotail and the development of ion-acoustic turbulence in the corresponding regions. We assume that  $kV_{Td} \ll (kV_{TM}, kV_{TS}) \ll \omega \ll (kV_{Te(ph)}, kV_{TeS}, kV_{TeM})$ . Here,  $k$  is the wave vector,  $k = |\mathbf{k}|$ ,  $\omega$  is the wave frequency,  $V_{Td}$  is the thermal velocity of charged dust grains,  $V_{Te(i)}$  is the thermal velocity of electrons (ions), indices  $S$ ,  $M$ , and  $(ph)$  characterize the quantities related to the solar wind, magnetosphere, and photoelectrons, respectively.

The development of hydrodynamic instability is caused by the relative motion of magnetospheric ions and charged dust grains. Thus, the following scheme of the development of plasma turbulence is suggested. The magnetospheric plasma ions excite oscillations (or waves) due to hydrodynamic instability. As a result, similar to the problem on the anomalous plasma resistance [1], an anomalous loss of the ion momentum takes place (it is transferred to oscillations, i.e., to the collective motion of dust grains). In the saturated state achieved when the growth of the instability becomes limited by nonlinear processes, plasma experiences turbulent heating the nature of which is determined by the turbulence caused by the instability. Turbulent heating is different for the ion and dust components.

The time, during which the dusty plasma interacts with the regions of the magnetic transition and/or boundary layers of the magnetosphere, is sufficient for the generation of waves due to hydrodynamic instability and also efficient nonlinear processes can be expected. The case when ion-acoustic waves are excited due to hydrodynamic instability should be analyzed in terms of strong turbulence.

Under the conditions corresponding to the near-Moon plasma crossing magnetic transition and/or boundary layers of the magnetosphere [2] (the characteristic dust particle size  $a \sim 100$  nm, the relative velocity of the Moon to the magnetotail plasma  $u \sim 1$  km/s, the charge number of a dust grain  $|Z_d| \sim 10$ , the characteristic number density of charged dust grains in the near-surface layer of the illuminated part of the Moon  $n_d \sim 10$  cm<sup>-3</sup>, the number density of magnetospheric ions  $n_{IM} \sim 10$  cm<sup>-3</sup>, the dust grain mass,  $m_d \sim 10^{-14}$  g, magnetospheric ion temperature  $T_{IM} \sim 100$  eV, the photoelectron temperature  $T_{e(ph)} \sim 1$  eV,  $n_{e(ph)} \sim 10^2$  cm<sup>-3</sup>) ion-acoustic turbulence can develop due to hydrodynamic instability. For this case the effects caused by plasma heating prevail over those caused by the interaction of plasma ions with dust grains, and the dissipative properties of the system in the equation for the ion momentum transfer are determined mainly by the effective collision

frequency characterizing the anomalous loss of the ion momentum

$$v_{\text{eff}} \sim \frac{\lambda_{\text{DIM}}}{\lambda_D} \frac{v_{\text{TIM}}}{u} \omega_{\text{pd}} \left( \frac{n_{\text{IM}}}{n_d Z_d} \frac{m_d}{Z_d m_i} \right)^{1/6},$$

where  $\lambda_{\text{De}}$  is the Debye radius,  $\omega_{\text{pd}}$  is the dust plasma frequency, and

$$\frac{1}{\lambda_D^2} = \frac{1}{\lambda_{\text{De}}^2} + \frac{1}{\lambda_{\text{DeS}}^2} + \frac{1}{\lambda_{\text{De(ph)}}^2}.$$

Another kind of turbulence which can be developed in the system lunar dusty plasmas – Earth's magnetosphere is dust-acoustic turbulence. Dust-acoustic waves are excited due to the development of kinetic dust-acoustic instability and can develop when  $kV_{Td} \ll \omega \ll (kV_{\text{TIM}}, kV_{\text{TIS}})$ . The development of kinetic instability is caused by the relative motion of magnetospheric ions and charged dust grains. For typical plasma parameters corresponding to the development of kinetic dust-acoustic instability in the region of interaction of Earth's magnetotail with the Moon we have

$$v_{\text{eff}} \sim \frac{u |Z_d| T_{\text{e(ph)}}^{7/2}}{\lambda_{\text{DIM}} T_{\text{IM}}^{5/2} T_D} \left( \frac{n_{\text{IM}}}{n_{\text{e(ph)}}} \right)^{1/2},$$

where  $T_D$  is the temperature of dust particles.

## TURBULENT MAGNETIC RECONNECTION:

Reconnection in Earth's magnetosphere extends from regions situated at most a few Earth radii ( $R_E$ ) to many tens or hundreds of  $R_E$ . Thus the Moon crosses the region where magnetic reconnection can occur, and plasma turbulence existing in the region of interaction of Earth's magnetotail with the Moon can influence the character of magnetic reconnection. When two magnetic field lines which have opposite directions come close together in a dissipative medium reconnection is possible [3]. The rate of magnetic reconnection depends strongly on the presence of anomalous dissipative processes related to  $v_{\text{eff}}$ , in particular, to the anomalous resistivity. If the resistivity is anomalous then the rate of magnetic reconnection increases by several orders of magnitude in comparison with the classical collision-dominated electrical conductivity.

The typical model for the description of the reconnection is Parker-Sweet diffusion model [4], [5] modified to allow for the anomalous dissipation. In this model, the reconnection is considered as a result of mutual diffusion of magnetic fields in Earth's magnetosphere which are assumed to be opposite directed. The width of the transient layer of the reconnection zone is determined by the following expression

$$d \approx \frac{c}{\omega_{pe}} \left( \frac{L v_{\text{eff}}}{v_A} \right)^{1/2},$$

where  $L$  is the characteristic inhomogeneity scale along the direction of the transient layer and  $v_A$  is the Alfvén velocity. The magnitude of  $L$  is typically from  $5 R_E$  to  $10 R_E$ .

Thus, determination of the effective collision frequency  $v_{\text{eff}}$  is fundamental for the diffusion model and it is natural to associate the dissipative processes in the region of interaction of Earth's magnetotail and the Moon with ion-acoustic and dust-acoustic turbulences. Significant results are obtained when we consider ion-acoustic turbulence. In this case (assuming that  $L = 5 R_E$ , the electron number density  $n_d \sim n_{\text{e(ph)}} \sim 100 \text{ cm}^{-3}$ ,  $|\mathbf{B}| \approx (4 - 5) \cdot 10^{-4} \text{ G}$ ) we find  $d \sim 100 \text{ km}$ . This value is far less than the diameter of the Moon.

We have shown that plasma turbulence existing in the region of interaction of Earth's magnetotail with the Moon can influence the character of magnetic reconnection. The acceleration of plasma away from the reconnection site on recently merged field lines can result in lightning phenomena which occur at the Moon due to the reconnection processes. The wave motions (or any their manifestations) in the region of interaction of the Earth's magnetotail with the dusty plasma near the lunar surface can be detected by means of apparatus that are planned to be installed on the Luna-25 (Luna-Glob) and Luna-27 (Luna-Resurs) lunar modules.

## ACKNOWLEDGMENT

This work was supported in part by the Presidium of the Russian Academy of Sciences (under Fundamental Research Program no. 7 "Experimental and Theoretical Studies of Objects of the Solar System and Planetary System of Stars") and the Russian Foundation for Basic Research (project no. 15-02-05627-a).

## REFERENCES:

- [1] Galeev A.A., Sagdeev R.Z. Nonlinear Plasma Theory // Reviews of Plasma Physics. 1979. V.7. P.1-145.
- [2] Popel S. I., Kopnin S. I., Golub' A. P., Dol'nikov G. G., Zakharov A. V., Zelenyi L. M., and Izvekova Yu. N. Dusty plasma at the surface of the Moon // Solar System Research. 2013. V. 47. No. 6. P. 419-429.
- [3] Tsytovich V. N.. Lectures on Non-linear Plasma Kinetics. Berlin: Springer-Verlag, 1995. 223 p.
- [4] Parker E.N. Sweet's Mechanism for Merging Magnetic Fields in Conducting Fluids // J. Geophys. Res. 1957. V.62. P. 175-178.
- [5] Sweet P.A. The Neutral Point Theory of Solar Flares // Electrostatic Phenomena in Cosmical Physics. 1958. V.6. P.123-134.



# EFFECT OF ELECTROMAGNETIC FIELD ON KORDYLEWSKI CLOUDS FORMATION

T.Salnikova<sup>1</sup>, S.Stepanov<sup>2</sup>

<sup>1</sup> Lomonosov Moscow State University, GSP-1, Leninskie Gory, Moscow 119991, Russia; and Peoples' Friendship University of Russia RUDN University), 6 Miklukho- Maclaya str., Moscow, 117198, Russia, [tatiana.salnikova@gmail.com](mailto:tatina.salnikova@gmail.com)

<sup>2</sup> Dorodnicyn Computing Centre, FRC CSC RAS, 40 Vavilova str., Moscow 119333, Russia; and Lomonosov Moscow State University, GSP-1, Leninskie Gory, Moscow 119991, Russia, [stepsj@ya.ru](mailto:stepsj@ya.ru)

## KEYWORDS:

Lagrange libration points, cosmic dust clouds, gravitational perturbation, light influence, electromagnetic influence.

## INTRODUCTION:

In previous papers the authors suggest a clarification of the phenomenon of appearance-disappearance of Kordylewski clouds - accumulation of cosmic dust mass in the vicinity of the triangle libration points of the Earth-Moon system[1-3]. Under gravitational and light perturbation of the Sun the triangle libration points aren't the points of relative equilibrium. However, there exist the stable periodic motions of the particles, surrounding every of the triangle libration points. Due to this fact we can consider a probabilistic model of the dust clouds formation[4]. These clouds move along periodical orbit in the surrounding of the points shifting on this orbit periodically.

## PROBLEM SETTING:

To continue this research, in this paper we suggest to investigate also the electromagnetic influences, arising under consideration of the charged dust particles in the vicinity of the periodical orbits.

## REFERENCES:

- [1] Salnikova T.V., Stepanov S.Ya. On the Lagrange libration points of the perturbed Earth-Moon system. // Proceeding of the International Astronomical Union, 2014. V. 9. No. 310. P. 192-193.
- [2] Salnikova T.V., Stepanov S.Ya. Mathematical Model of Formation of Kordylewski Cosmic Dust Clouds. // Doklady Physics. Maik Nauka/Interperiodica Publishing, 2015. V.60, No 7, P. 323-326.
- [3] Salnikova T., Stepanov S., Shuvalova A. Periodic trajectories of the particles in the Earth vicinity. // Proceedings of 2016 International Conference «Stability and Oscillations of Nonlinear Control Systems» IEEE Catalog Number CFP16E79-ART RUSSIA, P.1-4.
- [4] Salnikova T.V., Stepanov S.Ya., Shuvalova A.I. Probabilistic Model of Kordylewski Clouds. // Doklady Physics. Maik Nauka/Interperiodica Publishing, 2016. V.61, No 5, P. 243-246.

# GAS OF DUST PARTICLES: A POSSIBLE MECHANISM OF AEOLIAN PROCESSES ON SMALL BODIES

M.A. Kreslavsky <sup>1</sup>

<sup>1</sup>*Earth and Planetary Sciences, University of California – Santa Cruz, Santa Cruz, CA, 95064, USA, mkreslav@ucsc.edu.*

## KEYWORDS:

Small bodies, Microgravity, Aeolian transport, Dune, Brownian motion, Comet 67P/Churyumov-Gerasimenko, Rosetta mission.

## INTRODUCTION:

Images of comet 67P/Churyumov-Gerasimenko nucleus obtained by Rosetta mission show a number of morphological features strongly resembling aeolian features on the Earth and Mars [1,2]. They include wind tails of boulders, longitudinal striations in smooth apparently loose material, and, most conspicuous, a patch of ripples in Hapi region. The major ripples have spacing of ~12 m and height of a few decimeters [1]; smaller ripples have ~5 m spacing; they disappeared and reappeared at a time scale of months [2].

The presence of such features is puzzling, because the comet obviously lacks any "normal" atmosphere and winds. However, the comet nucleus does produce gas due to sublimation of volatile ices: CO<sub>2</sub>, CO, N<sub>2</sub>, etc., and a number of authors attributed aeolian-like features to this gas. Before the ripples on 67P were discovered, A. Cheng et al. [3] had analyzed morphology of three other comets (103P/Hartley 2, 81P/Wild 2, 9P/Tempel 1) and suggested a role of particles lifted by gas flow in formation of morphological features. They had estimated that the outgassing is sufficient for lifting sand-size and larger particles. They had noted that, because of the divergent gas flow geometry, "classic" saltation and, therefore, formation of the "classic" aeolian bedforms is unlikely. Later works [e.g., 4] have argued for saltation or reptation in the comet environment, however, those treatments have caveats. The molecule free path in cometary gas jets is much longer than sand particle size (the Knudsen number  $Kn \gg 1$ ), therefore aerodynamic treatment of gas flow interaction with particles is not applicable; corrections for non-zero  $Kn$  considered in [4] are only valid for weakly rarefied gases ( $Kn \sim 1$ ); the treatment in [4] also ignores the essentially divergent nature of the gas flow on comets.

In [1] it was suggested that the "aeolian" features are produced by fall of relatively large particles lifted with low velocities by gas. I was able to reproduce the observed boulder-related ventifacts with a simple cellular-automata-type model of erosion by falling particles [5], but fail to produce anything resembling ripples with such kind of modeling.

Here I propose a principally different mechanism potentially capable of formation of aeolian features on low-gravity bodies.

## GAS OF DUST PARTICLES IN MICROGRAVITY CONDITIONS:

Free dust particles on a low-gravity body would fly and form a specific dust atmosphere due to their thermal motion also known as Brownian motion. Below I present order of magnitude estimates for such an atmosphere assuming conditions for Hapi region of 67P: gravity  $g = 10^4 \text{ m s}^{-2}$ , and temperature  $T = 200 \text{ K}$ . Dust particles are assumed to have diameter  $d = 0.5 \text{ }\mu\text{m}$  (typical dust in cometary coma) and material density of  $\rho = 1 \text{ g cm}^{-3}$ .

In the thermal equilibrium, dust particle has a thermal energy of  $\frac{1}{2}kT$  per degree of freedom, where  $k$  is the Boltzmann constant. The "atmosphere" of such particles has a scale height  $H = kT / mg \sim 4 \text{ m}$ , where  $m$  is particle mass defined by  $d$  and  $\rho$ . In the terrestrial conditions, such an atmosphere is not forming, because under terrestrial gravity  $H \ll d$  for any  $d$ . The dust atmosphere is forming only when  $H > d$ , that is particles are sufficiently small:  $d < (kT / \rho g)^{1/4} \sim 10 \text{ }\mu\text{m}$ . The typical particle velocity is  $c = (kT / m)^{1/2} \sim 6 \text{ mm/s}$ , and the thermal spin rate is  $\sim 0.5 c / d \sim 6000$  rotations per second.

If the gas of dust particles is rarefied, its density  $\rho_g \ll \rho$ , many properties

of such gas are the same as of an ideal gas. The speed of sound is equal to  $c \sim 6$  mm/s. The adiabatic lapse rate is zero. Specific heat is defined by heat capacity of dust particles (kinetic energy of thermal motion and spin is negligible in comparison to the internal energy of the particles). Diffusivities (kinematic viscosity, thermal diffusivity, self-diffusion coefficient) are extremely low, however, their correct calculation should take the restitution coefficient (non-elastic particle collisions) into account.

If the dust particles at the surface are abundant, the gas density next to the surface is  $\rho_g \sim 0.5\rho \exp(E/kT)$ , where  $E$  is the characteristic bound energy of a dust particle, which is very poorly defined. Even if the particles are "loose" and "free", they are bound to each other with van der Waals forces. Energy of van der Waals interaction of two spheres of diameter  $d$  is usually parameterized following Hamaker's theory as  $E \sim (1/24)A d/l$ , where  $A$  is the Hamaker constant on the order of  $\sim 10^{-21} - 10^{-19}$  J, which depends on particle material, and  $l$  is on the order of a few atomic distances ( $>0.1$  nm) and depends on "clearness" of the particle surface: the presence of adsorbed volatiles, nanoscale surface irregularities, etc. Typical values for freshly grounded rocks, lunar regolith, etc. ( $A \sim 10^{20}$  J,  $l \sim 0.4$  nm, [6]) give  $E/kT \sim 70$ , and no dust atmosphere would exist. Organic material of cometary dust may have a lower  $A$ , and due to adsorbed volatiles  $l$  might be greater; diversity of individual particle properties may lead to a gentler dependence than  $\exp(-E/kT)$ . These factors together may give a way for some dust atmosphere, at least for smaller, submicron particles. On the other hand, particle deformation at the contact is ignored by Hamaker's theory, but might be significant for soft organic particles, which would make them much more cohesive (increase  $E$ ) and thus preclude formation of the dust atmosphere. I assume for a while that  $\rho_g$  is not negligible.

Pressure at the surface is  $P = \rho_g gH$ . The maximum possible pressure (if  $E \ll kT$ ) is  $0.5\rho gH \sim 0.02$  Pa. Geometric optical depth of the atmosphere  $\tau = 1.5(\rho_g/\rho)(H/d)$ . Optical depth is  $\sim 2\tau$  for short wavelength  $\lambda$ , and  $\sim 6\tau(d/\lambda)^4$  for long wavelength. Radiative time scale of a thin dust atmosphere is  $\sim 1$  s and does not depend on  $d$  for micron-scale and smaller particles. Real dust atmosphere would consist of a range of particle sizes, each with its own  $H$ , which would produce strong stratification in the atmosphere. Winds in the dust atmosphere can be generated by thermal tides. Formation of dust atmosphere on tilted surfaces would lead to supersonic downhill flow.

The mean free path in a thin ( $\rho_g/\rho \ll 1$ ) atmosphere is  $\sim 0.1(\rho/\rho_g) d$ . For sand-size particles  $Kn \gg 1$ , and the classic theory of saltation initiation is not applicable. It is obvious, however, that particles slightly larger than the typical atmosphere-forming dust may be mobilized and transported by reptation. The mean free path is always much shorter than the incipient bedform spacing, which is also proportional to  $(\rho/\rho_g)$  according to Claudin & Andreotti [7]. This means that the fluid dynamic-based theory of the incipient bedform spacing is applicable to the dust atmosphere. In a sense, transport by the dust atmosphere is more resembling sub-aqueous rather than sub-aerial transport: the range of saltation particle size between suspension and reptation is narrow, the upper boundary of the atmosphere is close to the surface and may affect bedform formation, similarly to shallow water.

## APPLICATION TO 67P:

Hapi region with the ripple patch coincides with the area of the lowest gravitational potential (corrected for the centrifugal potential) [8] on the nucleus. Its "watershed" comprises over a half of the nucleus area. The region has the highest albedo and the lowest red spectral slope on the nucleus, which is consistent with higher concentration of fine dust in comparison to the other regions. This suggests global transport of fine dust downslope, which would be a straightforward consequence of formation of dust atmosphere. Striations on loose material on slopes and boulder-associated ventifact-looking features might result from (supersonic) flow of dust gas downslope.

The ripple patch is not located at the lowest portion of the Hapi basin: a slope of  $\sim 10^\circ$  is reported in [1], however, the gravity model based on assumption of homogeneous nucleus material might be inaccurate.

If the smallest observed ripples are incipient bedforms following Claudin & Andreotti [7] scaling, and they are formed by  $10 \mu$  (1 mm) particles, the required atmosphere density is  $\rho_g \sim 10^{-4}\rho$  ( $10^{-6}\rho$ ), and corresponding  $\tau \sim 150$  (1.5). This means that such a dust atmosphere, if existed, would be opaque and readily seen in the available images, but it actually is not observed. This might mean that the dust atmosphere has never formed (because of cohesion), and the ripple formation mechanism is different. It is also possible

that the dust atmosphere is optically thin, it forms ripples, but they do not follow the scaling law due to some peculiarities of the diluted gas of dust particles.

### APPLICATION TO OTHER BODIES:

Formation of dust atmosphere and related geomorphic features is possible for bodies in some size range. For bodies smaller than  $\sim 100$  m, the scale height exceeds the body radius, and the extended dust atmosphere would escape. For bodies larger than  $\sim 100$  km,  $H$  is too short, and no real atmosphere is forming, while thermal-induced dust mobility might play some role up to  $\sim 1000$  km bodies. Comets are probably better for dust gas than asteroids because of presumably lower cohesion. Higher surface temperatures favor dust atmospheres.

### REFERENCES:

- [1] Thomas N., et al. Redistribution of particles across the nucleus of comet 67P/Churyumov-Gerasimenko // *Astron. Astrophys.* 2015. V. 583. Id. A17.
- [2] El-Maarry M.R., et al. Surface changes on comet 67P/Churyumov-Gerasimenko suggest a more active past // *Science*. 2017. V. 355. No. 6332. P. 1392-1395.
- [3] Cheng A.F., Lisse C.M., A'Hearn M. Surface geomorphology of Jupiter Family Comets: A geologic process perspective // *Icarus*. 2013. V. 222. No. 2. P. 808-817.
- [4] Jia P., Andreotti B., Claudin P. Giant ripples on comet 67P/Churyumov-Gerasimenko sculpted by sunset thermal wind // *Proc. Nat. Acad. Sci.* 2017. V. 114. No. 14. P. 2509-2514.
- [5] Mottola S., et al. The structure of the regolith on 67P/Churyumov-Gerasimenko from ROLIS descent imaging // *Science*. 2015. V. 349, No. 6247, Id. aab0232.
- [6] Scheeres D.J., Hartzell C.M., Sánchez P., Swift M. Scaling forces to asteroid surfaces: The role of cohesion // *Icarus*. 2010. V. 210. No. 2. P. 968-984.
- [7] Claudin, P., Andreotti B. A scaling law for aeolian dunes on Mars, Venus, Earth, and for subaqueous ripples // *Earth Planet. Sci. Lett.* 2006. V. 252. No. 1-2. P. 30-44.
- [8] Sierks, H., et al. On the nucleus structure and activity of comet 67P/Churyumov-Gerasimenko // *Science*. 2015. V. 347. No. 6220. Id. aaa1044.

# CONFIRMATION OF SUBLIMATION AND DUST ACTIVITY ON 779 NINA AND 704 INTERAMNIA

V. V. Busarev<sup>1,2</sup>, M. P. Scherbina<sup>1,3</sup>, S. I. Barabanov<sup>2</sup>,

<sup>1</sup>Lomonosov Moscow State University, Sternberg Astronomical Institute, University Av., 13, Moscow, 119992, Russian Federation (RF), busarev@sai.msu.ru;

<sup>2</sup>Institute of Astronomy, Russian Academy of Sciences (IA RAS), Pyatnitskaya St. 48, Moscow, 109017, RF;

<sup>3</sup>Lomonosov Moscow State University, Physical Department, Leninskiye Gory, 1, build. 1, Moscow, 199991

## KEYWORDS:

Asteroids, reflectance spectra, sublimation of ices and dust levitation

## INTRODUCTION:

We have discovered spectral signs of simultaneous sublimation and dust activity on four main-belt primitive asteroids (145 Adeona, 704 Interamnia, 779 Nina, and 1474 Beira) connected likely with shortening their heliocentric distances and elevation of the subsolar and average subsurface temperatures [1, 2]. Then, we have undertaken control spectrophotometric observations two of them, namely 779 Nina and 704 Interamnia, at the time of their next passage perihelion, to confirm action of the processes. Here we show that the recent results turned out to be in agreement with our prior conclusions and suggestions.

## OBSERVATIONS AND DATA REDUCTON:

The first and last spectral observations of 779 Nina (in September 2012 and 2016, respectively) and 704 Interamnia (in September 2012 and June 2017, respectively) were performed at Terskol Observatory (Mt. Terskol, 3150 m above sea level, Russia) with 2-m telescope and a low resolution spectrograph of (R=100) in the range of 0.38-0.85  $\mu\text{m}$ . A conventional method of asteroid spectral observations (along with solar analog standard stars) and a standard processing procedures (flat-field correction, bias and dark subtraction, etc.) were used to reduce the CCD-data, to extract asteroid spectra and to calculate asteroid reflectance spectra [1]. Altogether 12 reflectance spectra (on 13 September 2012), 2 and 2 ones (on 26 and 28 September 2016, respectively) of Nina and 5 reflectance spectra (on 13 September 2012) and 21 ones on 24-29 June 2017 of Interamnia were obtained. The spectra were averaged at close relative rotational phases (RRP) on corresponding nights and presented in Figs 1-8. Averaged in ranges of 0.40-0.65  $\mu\text{m}$  and 0.66-0.85  $\mu\text{m}$  relative standard deviations (RSD) in the reflectance spectra are also shown in the insets of figures.

## DISCUSSION OF THE RESULTS:

### 779 Nina.

Average diameter of Nina (X-type) is estimated between 76.62 km [3] and 80.57 km [4]. It rotates with a period of 11.186 h [5] and orbits the Sun for 4.35 yr (<http://ssd.jpl.nasa.gov/sbdb.cgi#top>). As mentioned in our previous publications, despite of detected irregularity of Nina's spectral reflectance with rotation [1, 2], it was classified according to radar data as a primitive asteroid [6]. Nina was observed by us after perihelion passage in September 2012 (Fig. 1, the lower spectrum). The average reflectance spectrum of Nina (of 12 ones) having a strong maximum at  $\sim 0.52 \mu\text{m}$  was explained as an indication of sublimation of subsurface ices (predominately H<sub>2</sub>O ice) on the asteroid [1, 2]. Taking into account results of numeric modeling of light scattering according to Mie theory [7] by spherical H<sub>2</sub>O ice particles, it was interpreted as a sign of coma of ice particles with predominant radius of  $\sim 0.52 \mu\text{m}$  in the vicinity of the body [1, 2]. Detected change of Nina's reflectance spectrum shape with approaching perihelion in September 2016 (Fig. 1, two top spectra with different slopes) agrees likely with a suggestion of graduate growth of density of the coma due to rise of the average temperature [2]. Nina's matter degassing could be accompanied with removal from the

surface fine-dispersed silicate dust and its levitation. It is likely confirmed by a considerable slope change of the spectra in the visible range and a strong growth of short-wavelength reflectance near  $0.4 \mu\text{m}$  by ab. 25% (Fig. 1) at relatively small difference in RRP  $\sim 0.28$  between two consecutive dates.

#### 704 Interamnia.

Average diameter of Interamnia (F-type) is estimated between 307.31 km asteroid [4] and 316.62 km [3]; its rotational and orbiting periods are 8.727 h [5] and 5.35 yr (<http://ssd.jpl.nasa.gov/sbdb.cgi#top>), respectively.

Similarly to Nina, Interamnia was observed by us after perihelion passage in September 2012. Reflectance spectrum of the asteroid had a pronounced maximum at  $\sim 0.52 \mu\text{m}$  as a manifestation of a developed coma  $\text{H}_2\text{O}$  micron-sized particles (Fig. 3(a) in [1]). We have observed the asteroid again, quite ahead perihelion passage in June 2017. For a more primitive nature of Interamnia (and, hence, elevated content of hydrated silicates and/or free water ice into the surface matter) as compared with Nina, more diversity of reflectance spectra at very close RRP's before perihelion passage has been observed (Figs. 2-8). It is important to note that spectral reflectance of other asteroids observed by us closely in time did not show similar changes. Some of Interamnia's reflectance

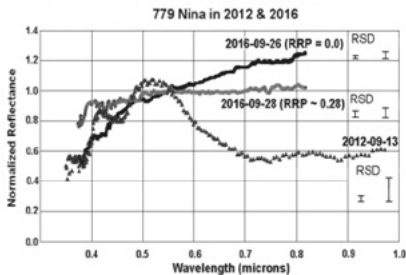


Fig. 1.

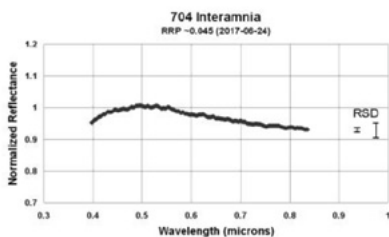


Fig. 2.

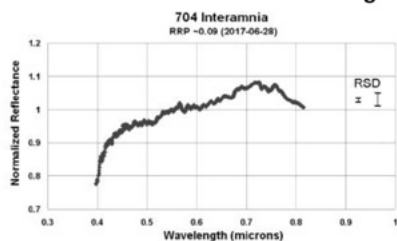


Fig. 3.

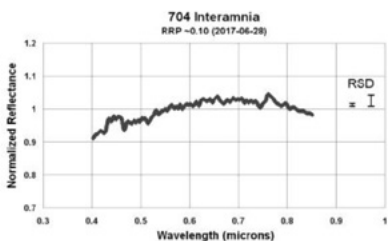


Fig. 4.

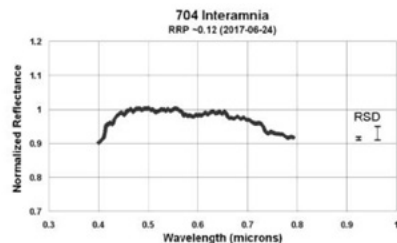


Fig. 5.

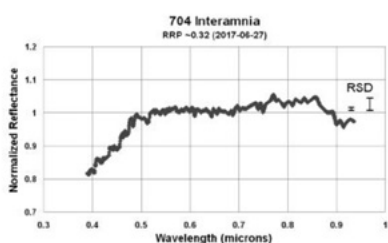


Fig. 6.

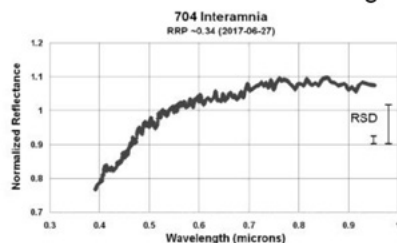


Fig. 7.

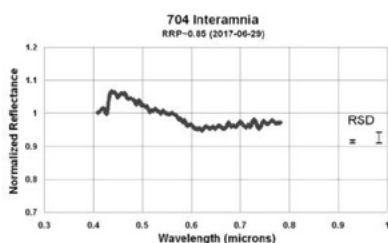


Fig. 8.

tance spectra point undoubtedly to the presence in the coma very small particles (of water ice?) in the range of sizes  $\sim 0.44\text{-}0.55\ \mu\text{m}$  (e. g., Figs. 2, 5, and 8). The rest of them could be conglomerates of ice and silicate ones involved to the coma from the asteroid surface by water vapor streams. It seems ice sublimation process on Interamnia is very irregular in time and space before perihelion passage then after that. On the other hand, it is possible existence on the asteroid of several jets of water vapor connected with near-surface buried ice blocks. Those may be fragments of smaller ice bodies fallen on Interamnia at the period of its formation or over all time of its existence.

## CONCLUSIONS:

Recent discoveries of cometary-like bodies among main-belt asteroids were interpreted in most cases as random events connected with "dynamical" contamination of the asteroid family with atypical icy objects (for instance, extinct comet nucleus) which become active only after sporadic collisions (e. g., [8, 9]). Another point of view based on modeling and observational data is that free water ice is widespread originally in the subsurface interiors of primitive main-belt asteroids themselves (e. g., [10, 11]). Our detection of simultaneous sublimation activity on several main-belt primitive asteroids at shortest heliocentric distances supports the last notions and points likely to similar physical and chemical conditions of the bodies' origin corresponding to the outer edge of the main asteroid belt and beyond.

Monitoring of sublimation and dust activity of 704 Interamnia during 2017 year (it is passing perihelion at the beginning of October 2017) would allow us to study nature of the asteroid and to specify some questions connected with its formation.

## REFERENCES:

- [1] Busarev V.V. et al. Spectrophotometry of (32) Pomona, (145) Adeona, (704) Interamnia, (779) Nina, (330825) 2008 XE3, and 2012 QG42 and laboratory study of possible analog samples // *Icarus*. 2015. V. 262. P. 44-57.
- [2] Busarev V. V., Barabanov S. I., Scherbina M. P., Puzin V. B. Sublimation activity of (145) Adeona, (704) Interamnia, (779) Nina, AND (1474) Beira and some confirmations // 48th Lunar and Planetary Science Conference, 2017. Texas (USA), Abstract #1919.
- [3] Tedesco E.F. 2004. IRAS Minor Planet Survey. IRAS-A-FPA-3-RDR-IMPS-V6.0 NASA Planetary Data System.
- [4] Masiero J.R. et al. 2014. Main-belt asteroids with WISE/NEOWISE: Near-infrared albedos. *Astrophys. J.* 791, 121-131.
- [5] Harris A.W., Warner, B.D., Pravec, P., 2012. Asteroid Lightcurve Derived Data V13.0. NASA Planetary Data System, EAR-A-5-DDR-DERIVED-LIGHTCURVE-V13.0.
- [6] Shepard M.K. and 12 co-authors, 2010. A radar survey of M- and X-class asteroids II. Summary and synthesis. *Icarus* 208, 221-237.
- [7] Hansen, J. E., Travis, L. D., Light scattering in planetary atmosphere. *Space Sci. Rev.* 1974. V. 16. P. 527-610.
- [8] Hsieh, H. H., Jewitt, D., 2006. A Population of Comets in the Main Asteroid Belt. *Science* 312, 561-563.
- [9] Hsieh, H. H., Haghhighipour, N., 2016. Potential Jupiter-Family comet contamination of the main asteroid belt. *Icarus* 277, 19-38.
- [10] Rivkin, A. S., Emery, J. P., 2010. Detection of ice and organics on an asteroidal surface. *Nature* 464, 1322-1323.
- [11] Schorghofer, N., 2008. The lifetime of ice on main belt asteroids. *Astrophys. J.* 682, 697-705.

# ASTEROID REFLECTANCE SPECTRA MODELING WITH LABORATORY DATABASES OF ANALOG SAMPLES

M. P. Scherbina<sup>1,2</sup>, A. A. Rezaeva<sup>1</sup>, V. V. Busarev<sup>2</sup>

<sup>1</sup>Lomonosov Moscow State University, Physical Department, Leninskiye Gory, 1, build. 1, Moscow, 199991, Russian Federation (RF), [morskayaa906@yandex.ru](mailto:morskayaa906@yandex.ru);

<sup>2</sup>Lomonosov Moscow State University, Sternberg Astronomical Institute (SAI MSU), University Av., 13, Moscow, 119992, RF

## KEYWORDS:

Asteroids, reflectance spectra of asteroids, spectral databases of minerals and meteorites, modeling reflectance spectra of asteroids.

## INTRODUCTION:

As is known, asteroids are small solid celestial bodies of predominantly silicate composition. At the same time, they are the oldest planetary bodies in the Solar system, the least altered since formation. Despite their vast amount (only in the Main belt are already more than 500 thousand), a relatively small number (less ~1%) of them are classified taxonomically (spectrally). For the reason, heliocentric distributions of different-type asteroids with their specific mineralogy are studied very approximately.

A standard processing of spectrophotometric data on several tens of Main belt and near-Earth (NEA) asteroids obtained at Crimean Observatory of SAI MSU (1.25-m telescope with a low resolution spectrograph in the range of 0.40-0.95  $\mu\text{m}$ ,  $R \approx 300$  in 2003-2010) and at Terskol Observatory (2-m telescope with a low resolution spectrograph in the range of 0.38-0.85  $\mu\text{m}$ ,  $R \approx 100$  in 2015-2017) was carried out [1, 2]. The aim of the work is modeling reflectance spectra of the observed asteroids with measured reflectance spectra of powdered terrestrial mineral samples and proper meteorite analogs from the most complete spectral databases.

## DISCUSSION OF THE MODELING METHOD AND USING DATABASES:

The ultimate purpose of this simulation is to estimate quantitatively the mineralogical composition of asteroids in the first approximation with a rigid selection of factors influencing the shape of their reflectance spectra. The main of these factors are two strongest absorption bands: "ligand-metal" charge transfer one with a center at 0.2  $\mu\text{m}$  [3] and another common one of electronic transitions in  $\text{Fe}^{2+}$  being in the crystal field of the main rock-forming minerals (predominately pyroxenes and olivine) centered at  $\sim 0.9 - 1.0 \mu\text{m}$  [4]. However, it is not yet possible to solve this problem with a high accuracy, since a general obstacle is incompleteness of our knowledge of the variety of solid matter and the conditions of its origin in space. According to some estimates based on a study of primitive interplanetary dust (e. g., [5]) matter in the meteorite collections is represented only by  $\sim 30\%$ . Nevertheless, our approach could be productive to work out the problem with a certain accuracy using available analogue samples. To implement this, some obtained asteroid reflectance spectra were initially processed, smoothed (or averaged) and normalized with spectral package DECH and ORIGIN program. Additionally, we developed a special code in MATLAB environment allowing selection and adjusting parameters of laboratory reflectance spectra of asteroid analogue samples (powdered terrestrial minerals and meteorites) from accessible international spectral databases. We used reflectance spectra of minerals from the RELAB (KECK / NASA Reflectance Experiment Laboratory) database of Brown University (USA) (<http://www.planetary.brown.edu/rehab/>). The reliability of the obtained results is checked by similar modeling of the asteroid reflectance spectra by the meteorite reflectance spectra from the database of the University of Winnipeg (Canada) (<http://psf.uwinnipeg.ca/index.html>). Fitting reflectance spectra of analog samples with some weighting coefficients, it is achieved a combination (or "model reflectance spectrum") which corresponds to the analyzed asteroid reflectance spectrum (in a number of control points distributed in the used spectral range) with the best accuracy. Actually,



the found weighting coefficients are the proportions characterizing shares of separate minerals on the surface of an asteroid according to a model of "their geographic distribution" corresponding to the asteroid reflectance spectrum and to observed hemisphere of the body.

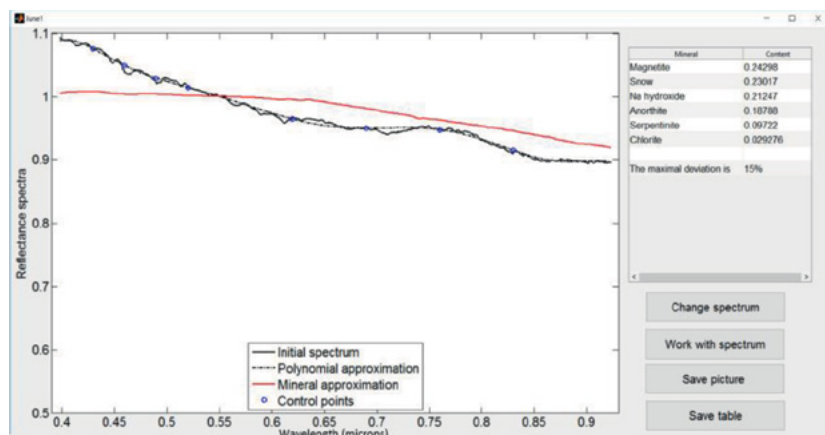


Fig. 1.

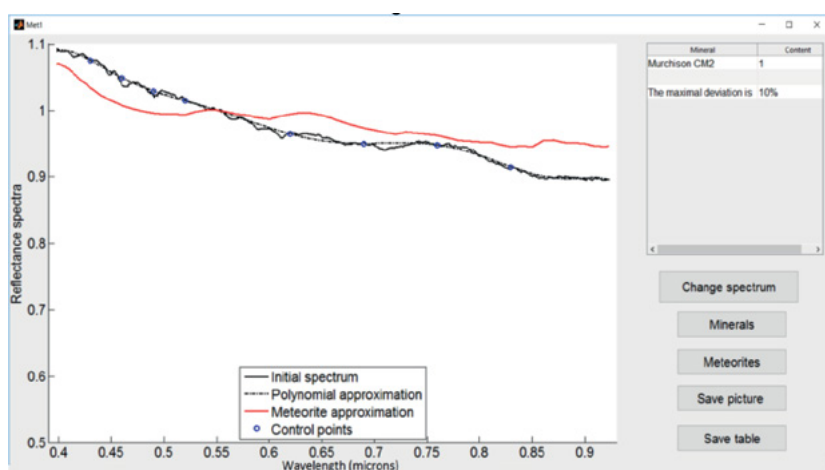


Fig. 2.

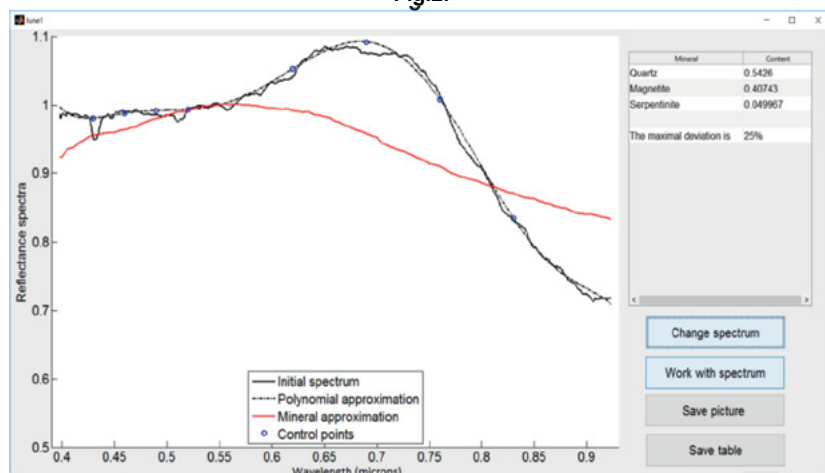


Fig. 3.

## SOME RESULTS:

Some of our modeling examples are shown below. This is a comparison of observed asteroid reflectance spectra of 1 Ceres and 4 Vesta [1] with their model reflectance spectra. Figs. 1 and 2: Reflectance spectrum of Ceres [1] (2009 04 02, 22h27m46s and its mineral and meteorite modeling, respectively). Figs. 3 and 4: Reflectance spectrum of Vesta [1] (2008 10 29, UT 00h06m36s) and its mineral and meteorite modeling, respectively. Suggestions about the surface matter mineral content of the asteroids and their meteorite analogs are made.

## CONCLUSIONS:

Reflectance spectra of 1 Ceres and 4 Vesta and their modeling and interpretation are given in our report. The "maximal deviation" (Figs. 1-4) is a total accuracy of the asteroid reflectance spectrum modeling. It includes spectral features of unknown mineral species, influence of physical-chemical characteristics of surface particles (including space weathering), heterogeneity of asteroid surface, etc. If the value is large it means our inability to find a good spectral match of mineral or meteoritic analog(s) for observed asteroids.

## REFERENCES:

- [1] Busarev V.V. Spectrophotometry of asteroids and its applications / LAP LAMBERT Acad. Publish., ISBN: 978-3-8465-3704-6, 2011, 250 p. [in Russian]
- [2] Scherbina M.P., Rezaeva A.A., Busarev V.V., Barabanov S.I. Spectrophotometric investigations of some asteroids: Qualitative and quantitative interpretation of reflectance spectra // News of Main Astron. Observ. at Pulkovo. 2016. V. 224. P. 123-130. [in Russian]
- [3] Loeffler B.M., Burns R.G., Tossel J.A. et al. Charge transfer in lunar materials: Interpretation of ultraviolet-visible spectral properties of the moon // Proc. of the 5th Lunar Conf. Suppl. 4. Geochim. Cosmochim. Acta. 1974. V. 3. P. 3007-3016.
- [4] Burns R.G. Mineralogical applications of crystal field theory. New York: Cambridge Univ. Press, 1993. 224 p.
- [5] Vernazza P., Marsset M., Beck P. et al. Interplanetary dust particles as samples of icy asteroids // Astrophys. J. 2015. V. 806. P.204-213.

# IMPACT EFFECT CALCULATOR. RADIATION ASSESSMENT FROM ATMOSPHERIC IMPACTS OF COSMIC BODIES

D.O. Glazachev, E. D. Podobnaya, O.P. Popova, V.V. Svetsov,  
V.V. Shuvalov

*Institute for Dynamics of Geospheres RAS, 119334, Leninsky pr.38, Moscow,  
Russia; glazachevd@gmail.com*

## KEYWORDS:

Impacts, asteroid, comets, cosmic bodies, radiation, web-site, online calculator

## INTRODUCTION:

The population of near-Earth objects (NEOs, both asteroids and comets) contains a wide variety of bodies with diverse physical and dynamical properties, and presents a permanent threat to our civilization [1]. The number of undiscovered potentially hazardous asteroids with sizes from 140 meters to 1km is estimated as about 20 000 objects, the number of potentially dangerous bodies with sizes from 50 m to 140 m is estimated to exceed 200 000 objects [2]. The recent Chelyabinsk event demonstrated that even a small object, only 20 m in diameter, has enough energy to cause considerable destruction of property. If the Tunguska-like event occurred not in Siberia but above Moscow or any other megalopolis, the city and its population would be totally demolished.

Detection of new objects proceeds continuously. For any discovered object it is necessary to assess the potential risk and damage resulting from the possible collision of such body with the Earth. Physical processes, which occur during the impact, are complex and their simulations are time consuming. An instrument for quick estimation of the consequences of a comet or asteroid impact on the Earth is needed. Such Web-based calculator was created by Collins et al [3]. We are going to elaborate the next generation version of an impact calculator. Extensive numerical simulations of impacts are carried out using a hydrodynamic model, equations, and a numerical technique described, e.g., in [4].

The radiation produced by the flight and destruction of cosmic bodies, which are decelerated in the Earth's atmosphere, is considered. The scaling relations for the radiation fluxes obtained based on the results of physico-mathematical modeling of the interaction of cosmic bodies different sizes and composition with the Earth's atmosphere and used in the on-line calculator are presented.

## ACKNOWLEDGEMENTS:

This work was supported by the Russian Science Foundation, project no. 16-17-00107

## REFERENCES:

- [1] Harris A. W., Boslough M., Chapman C. R., Drube L., Michel P., and Harris A. W. (2015) Asteroid impacts and modern civilization: Can we prevent a catastrophe? In *Asteroids IV* (P. Michel et al., eds.), pp. 835–854. Univ. of Arizona, Tucson.
- [2] Committee to review near-Earth object surveys and hazard mitigation strategies. *Defending planet Earth: Near-Earth object surveys*. The National Academies Press, 152 p. 2010.
- [3] Collins G.S., Melosh H.J., Marcus R. (2005) Earth Impact Effects Program: A Web-based computer program for calculating the regional environmental consequences of a meteoroid impact on Earth // *Meteorit. Planetary Sci.* V. 40. Nr.6. P.817-840
- [4] Shuvalov, V.V., Svetsov, V.V., Artem'eva, N.A., Trubetskaya, I.A., Popova, O.P., and Glazachev, D.O.: Asteroid Apophis: Evaluating the impact hazards of such bodies, *Sol. Sys. Res.*, Vol. 51, pp. 44-58, 2017.

# POLE OF ROTATION AND SPIN RATE OF DIFFERENT ASTEROIDS

Atila Poro<sup>1</sup>, Fatemeh Montazeri Najafabadi<sup>1</sup>

<sup>1</sup>*International Occultation Timing Association Middle East Section (IOTA/ME)*  
*iotamiddleeast@yahoo.com*

## KEYWORDS:

Asteroid, occultation, light curve, radiation, pole of rotation, spin rate, brightness.

## INTRODUCTION:

Occultations are just one of the tools used to better understand asteroid physiology. They provide timings that equate to an instantaneous measurement of parts of an asteroid between the occulted star and the observer making the observation. If enough observations are compiled a two dimensional silhouette can be constructed at a specific location in the asteroid's rotational light curve.

By investigating the dynamical and physical properties of asteroids, a more accurate picture of the early evolution of our solar system can be envisioned. The rotational states of individual minor planets, along with their shapes and orbits, are indicative of the collisional history of those bodies. The physical properties of minor planets, such as rotational states and shapes, represent a portrait of both history and evolution of these small solar-system objects. Building a three dimensional shape model is possible theoretically from two dimension models; yet this has not been performed effectively with just occultation data. But many such models have been constructed from light curve inversion.

The intensity of the reflected radiation from an asteroid depends on the phase angle, i.e., the angle between the Earth and the Sun, as seen from the asteroid. Because of scattering properties of the surface material and shadowing effects on those same surfaces, more light is reflected at small phase angles than at larger ones. Watching the Moon in its monthly appearance change as it moves about the Earth demonstrates this effect. Especially near opposition (phase angle=0 degrees, equivalent to Full Moon), the intensity increases rapidly.

This is known as the opposition effect. The rotational phase of the asteroid impacts the amount of observed radiation at a certain point in time; since minor planets have irregular shapes, the portion of their surface area which is both visible and illuminated will change as it rotates.

Therefore, the total amount of reflected sunlight seen by a sensor on Earth varies unless we have a pole-on view to the asteroid. A sequence of brightness measurements.

Physical models of minor planets depend on their pole of rotation and spin rate. Observations of occultations provide useful information that can, with additional types of information, assist in determination of physical characteristics of asteroids.

# A STUDY ON OCCULTATION AND TIMING METHODS

Zeinab Sadat Lesani  
zslesani@gmail.com

## KEYWORDS:

Timing, stellar occultation, occultation by solar system, timing methods, accurate timing

## INTRODUCTION:

It has been more than 20 years since the discovery of the first Trans-Neptunian Object (TNO). In the intervening years, too many of TNOs and Centaurs have been discovered, and this is still only a small fraction of the estimated total population.

The study of this population, has provided significant knowledge of the outer solar system. Nevertheless, we are not yet able to translate the conditions in the outer nebula during its various stages (planet formation, subsequent growth and orbital evolution, and physical and chemical changes to surfaces) into a clear picture of the chemical, dynamical, and thermal history of the outer solar system. A crucial missing piece to this puzzle is the size and albedo distribution of small bodies in the outer solar system.

Only a few of TNOs and Centaurs have diameter and albedo determinations, based in most cases on the radiometric technique applied to Spitzer and Herschel observations. These values are typically accurate at best to 10% in diameter and 20% in albedo. The occultation technique is far more powerful because under optimal circumstances it can provide sizes and shapes to an accuracy of about 0.1%.

Historically, occultation observations have also resulted in significant serendipitous discoveries, such as the presence of rings around small bodies, or even the presence of an atmosphere.

For example, occultation observations by Pluto illustrate the power of this observing technique to detect tenuous atmospheres and to monitor seasonal variations in atmospheric structure and surface pressure. The record of the light curve during an occultation enables us to study the vertical profile of the atmosphere, which is key to understanding the equilibrium of the different species of ices on the surface of the body.

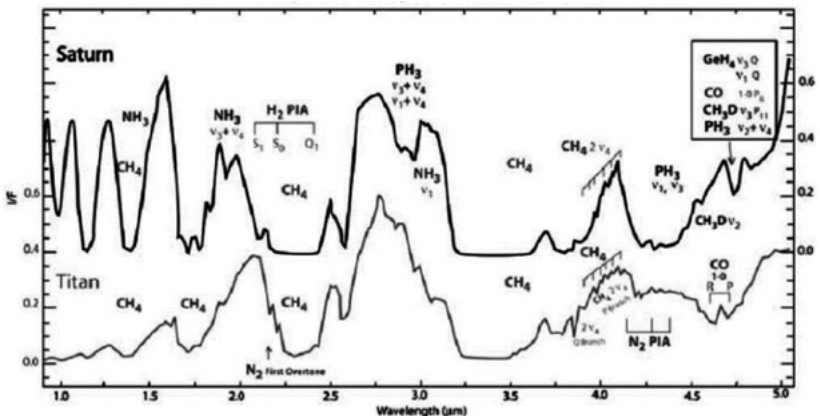


Fig. 1. Saturn's and Titan's atmospheric absorption spectra, from Cassini VIMS. Note the strong CH<sub>4</sub> absorption band above 3.2 μm, which lies just above the NIRCAM F300M filter bandpass.

Stellar occultations are also a powerful tool to explore the outer solar system, where faintness and small angular diameters prevent us from building a complete census of the objects.

The accurate and correct timing is very important in the astronomical researches. Because, it is applied as data for future studies and any minor error lead to incorrect results, and attempts of observer are not effective.

So according to the importance of occultation observations and timing, in this paper tried to study the different methods of timing and its disadvantages and then in order to reduce the problems and increase the accuracy, I going to creating a software "SKYTIMING" for android smart phone ( in next update I develop it for iOS).

"SKYTIMING" is an accurate timing application (at least desired accuracy is 0.01 seconds). It's always available and standalone. So the observer just needs a smart phone and a telescope to have an accurate timing and send a global standard report by it.

Also it Eliminate the problems of other methods, including easy accessing, it's performance will not be affected in Temperature changes, good accuracy because of using GPS for timing and ability to perform all the steps by it "timing in an observation, calculating the exact time by GPS, recording a coded beep sound and the observer sound to determine the start and end of the event, analyzing the recorded sound, reporting and send report for check and using".

## REFERENCES:

- [1] R. G. French and others, JWST observations of stellar occultations by solar system bodies and rings, Cornell University, 2015
- [2] Hoot, J. E., Tools and Techniques for Measuring Asteroid Occultations with DSLR and CCD Cameras, The Society for Astronomical Sciences 31st Annual Symposium on Telescope Science, held May 22-24, 2012 at Big Bear Lake, CA. Edited by Brian D. Warner, Robert K. Buchleim, Jerry L. Foote, and Dale Mais. Published by Society for Astronomical Sciences, 2012, pp.191-199
- [3] P. Clay Sherrod, Thomas L. Koed, A Complete Manual of Amateur Astronomy: Tools and Techniques for Astronomical Observations, Courier Corporation, 2012
- [4] Tony Barry, Dave Gault, Chris Chad, GPS-ABC\_Manual-V10
- [5] <http://www.gps.gov/applications/timing/>

# ESSENCE OF THE WAVE PLANETOLOGY REVEALED IN SHAPE OF ASTEROID 2014J025 AND SOME OTHER SMALL CELESTIAL BODIES

G. G. Kochemasov

*IGEM of the Russian Academy of Sciences, 35 Staromonetny, 119017  
Moscow, RF, kochem.36@mail.ru*

## KEYWORDS:

Asteroid 2014J025, Wave planetology, Eros, Toutatis, Nix, Itokava

The wave warping of celestial bodies due to their movement in non-circular keplerian orbits with periodically changing accelerations is especially notable in shapes of small bodies (asteroids, comet cores, satellites). They are often bent by the fundamental wave 1 and acquire shapes of “dumb-bells”, “bean”, “peanut” and often are disintegrated into two or several peaces moving in an original or slightly different orbits. The disintegration is provoked by nearing deep fissures of the convex hemisphere with diminishing distance of the concave one to the fissures. Thus, a “neck” develops (fig. 1- 9).

The classical planetology considers impacts as a main source of energy reworking celestial bodies. However, a region or regions of impacting objects affecting all planetary bodies everywhere in the solar system is poorly understood. However, now planetologists have several tens of images of full discs of these bodies. Distribution patterns of “impact traces” – craters in many of them are surprisingly regular. They show alignments, regular grids not related to random hits expected from impacts but rather require more regular and ubiquitous structuring force.

It was shown earlier [1-5] that such regular patterns appear due to warping action of inertia-gravity waves affecting all bodies moving in keplerian elliptical orbits. Periodically changing accelerations of celestial bodies cause their wave warping having in rotating bodies (but all bodies rotate!) Four ortho- and diagonal directions. An interference of the four directions of standing waves brings about a regular net of uprising, subsiding and neutral tectonic blocks. Naturally polygonal in details they appear as rings in cosmic images. This is one of reasons why they are often confused with round impact craters and essentially disfigure their statistics.

A fundamental nature of the wave woven nets of evenly sized round “craters” (granules) is dependence of their sizes on orbital frequencies of bodies. The lower frequency the larger sizes, the higher frequency the smaller granule sizes.

The correspondence between orbital frequencies and tectonic granulations proving the structuring role of orbital energy was earlier noted in comparative planetology of the terrestrial planets. The row of Mercury, Venus, Earth, Mars, asteroids with decreasing orbital frequencies is remarkable by increasing relative sizes of tectonic granules, relief ranges, iron content in lowland basalts and decreasing atmospheric masses from Venus to Mars.

In this spectacular row the position of asteroids is especially remarkable. The strongest amplitude fundamental wave1 embraces an asteroid body making it strongly bent. Its extended convex hemisphere is deeply cracked and the concave one from the opposite site approaches the deepest fissures (fig. 4). As a result the body tends to disintegrates and two or several pieces move as binaries, polycomponent asteroids, and asteroids with satellites. Two-lobed dumb-bells shapes often are observed also among comet cores and small satellites (fig. 5, 6, 9). Examples of various stages of this destruction are asteroids Eros, Toutatis, Braille, Castalia, Hector, and recently observed P/2013r3 that shows enormous volumes of gas-dust clouds accompanying the process. The orbiting clouds in the past may have been a media for gravity separation of M-, Ss-, and C-asteroids. The denser M-asteroids enrich the inner main asteroid belt and the less dense S & C asteroids the outer part of the belt fragments.

Several images of small cosmic bodies presented here (fig. 1 to 9) show characteristic bends producing thin parts – “necks” in the middle parts of the bodies and thickenings in their ends (two-lobe forms). Thus, necks are a result of breaking of a whole body [3, 5]. In some rare cases an assemblage of alien fragments also is possible [6]. In future, cosmic robots placed at “neck” regions of various small bodies should resolve this question by measuring

composition and structure of small pieces around. If they are uniform, they are fragments of one body, if not, two different bodies possibly are assembled. Asteroid 2014j025 shows typical forms of a small body deformed (warped, bent and deeply cut) by the inertia-gravity waves (wave1 and shorter ones) due to moving in an elliptical orbit. External orbital energy is a main energetic source structuring cosmic bodies [1-5]. Fig.1 Fig.2

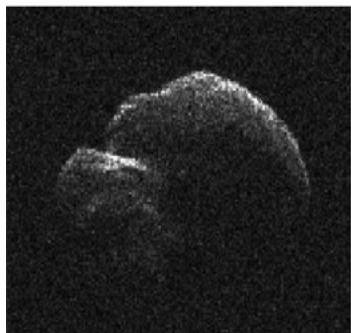


Fig.1

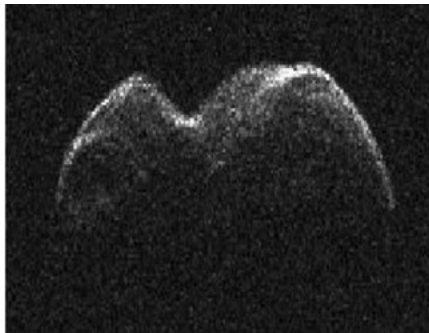


Fig.2

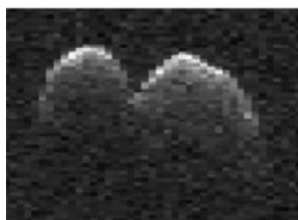


Fig.3

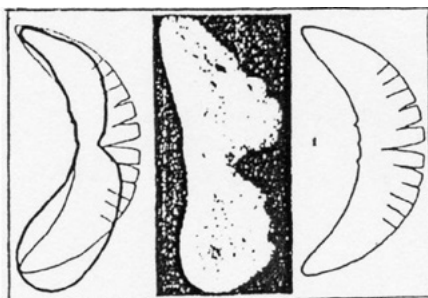


Fig.4

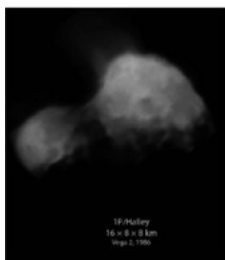


Fig.5

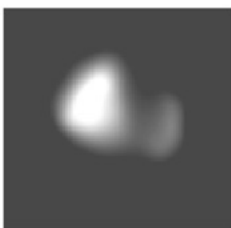


Fig.6



Fig.7



Fig.8



Fig.9

1, 2- Asteroid 2014j025, dimension ~870 m, Arecibo observatory planetary radar system, 17-20 april 2017; 3- Asteroid 1999jd6, 700 400985f8789ec19308d1b-83b5a840ca9, pia19647; 4- Asteroid (433)Eros. 33 km long. Near image & a model of body bending, destruction and two-lobed shape formation; 5- Comet 1p/Hailey, 16 x 8 x 8 km, Vega 2, 1986; 6- Nix-satellites of Pluto; 7- Aster-



oid {25143}Itokawa. 0.5 km long; 8-Asteroid 4179Tutatis. Spectral type S. Chang'e 2 image. 4.75 x 2.4 x 1.95 km. Diameter 5.4 km, two halves 4.6 and 2.4 km; 9- 67p/ Churyumov-Gerasimenko comet core , 4 x 3 km, Rosetta, 2014.

## REFERENCES:

- [1] Kochemasov g.g. tectonic dichotomy, sectoring and granulation of earth and other celestial bodies // proceedings of the international symposium on new concepts in global tectonics, "ncgt-98 tsukuba", geological survey of japan, tsukuba, nov 20-23, 1998, p. 144-147.
- [2] Kochemasov g.g. theorems of wave planetary tectonics // Geophys. res. abstr. 1999. v.1, №3, p. 700.
- [3] kochemasov g.g. "diamond" and "dumb-bells"-like shapes of celestial bodies induced by inertia-gravity waves // the 30th Vernadsky-Brown microsposium on comparative planetology, abstracts, Moscow, geokhi, 1999, 49-50
- [4] kochemasov g.g. celestial bodies: relation between ubiquitous tectonic dichotomy and universal rotation //ncgt journal, v. 3, # 2, june 2015, 155-157.
- [5] kochemasov g.g. characteristic "necks" of small cosmic bodies: formation in process of breaking or smooth impact (sticking together) of two fragments // 48th Ipsc (2017), abstract # 1092;
- [6] Ksanfomality I., Zelenyi I. Does regional surface morphology of comets 67p/cg and 1p/halley carry any traces of their origin in low velocity collisions? // the seventh moscow solar system symposium, 10-14 october 2016, space research institute (iki ras), moscow, p. 135, 7ms3-sb-07.

# INTERLINK BETWEEN PHOTOMETRIC AND POLARIMETRIC PROPERTIES OF ASTEROIDS

D.I. Shestopalov<sup>1</sup>, L. F. Golubeva<sup>1</sup>

<sup>1</sup>*Shemakha Astrophysical Observatory, Shemakha AZ-3243, Azerbaijan*

## KEYWORDS:

Asteroids, albedo, photometry, polarimetry, phase coefficient, surface roughness.

Currently, two ways of determining albedo of asteroids are widely used. One of them is the polarimetric technique that employs empiric correlations between albedo and the characteristics of the negative polarization branch of asteroids. The radiometric method is based on the complementary observations of asteroids in the visible spectral range and in the thermal infrared where the absorbed and reradiated component of the insolation is measured (e.g. [1] and references therein). Though L. Bell was the first who has suggested to use an indirect technique to determine the albedo of asteroids in the early last century [2].

His idea was to apply the phase coefficient,  $b$ , derived from asteroid's photometric functions to evaluate the albedo of asteroids. Recall,  $b$  is the slope of the almost linear portion of photometric function expressed in magnitudes in the range of phase angles of  $\sim 10 - 25^\circ$ . He reasoned that an airless smooth body, which approximately obeys Lambert law, would reveal the phase coefficient independent of its surface reflectivity. In turn, a great surface roughness that provides strong shadowing is likely to produce a large phase coefficient. Therefore, other things being equal, the geometric albedo of an airless body should vary with the phase coefficient, which is an characteristic of the amount of shadowing. The less shadowing, the higher the albedo and the less the phase coefficient.

In those days, however, Bell's method was not widespread because of the low accuracy of photographic measurements. Sixty-five years later, the plot of the geometric albedo–phase coefficient constructed in [3] also revealed a strong data scattering owing to nonuniform and low-precision photometric observations. Only in 1996, V. Shevchenko by specifying the phase coefficient from the precise photometric observations of asteroids established the reasonably accurate correlation between these variables [4].

Subsequently, we confirmed the correlation between  $b$  and the maximum degree of negative polarization  $|P_{min}|$  that was previously found for asteroids in [3] as well as established new relationships between  $b$  and other parameters of the negative polarization branch:  $\alpha_{min}$ ,  $\alpha_{inv}$  and  $h$  [5]. These symbolic names designate the phase angle corresponding to  $P_{min}$ , the inversion angle or the phase angle where polarization degree changes sign from negative to positive, and the slope of polarimetric curve at the inversion angle, respectively.

In 1985, IAU adopted so-called  $H$ ,  $G$  magnitude system developed by K. Lumme, E. Bowell and colleagues [6] to define the apparent magnitudes of asteroids when calculating their ephemerides. This photometric function has two free parameters:  $H$  corresponds to the mean absolute magnitude of asteroid in Johnson V bandpass, and  $G$  parameter describes the shape of the magnitude photometric function. The latter has no physical meaning but correlates with  $b$  and the phase integral  $q$ . So we can estimate Bond albedo  $A_V = p_V q$  as the geometric albedo  $p_V$  is also known at the given  $b$ .

Figure 1 illustrates the above interrelations between the phase coefficient and the brightness-polarization values of asteroids. The proper correlation equations between each pair of variables can be found in the references. Seemingly, the surface roughness and shadowing play important role in the scale of order of particle size to form the optical properties of asteroid surfaces. We argue by analogy with the negative polarization branch, which is observed in cometary envelopes due to cometary dust particles. This effect is believed to arise on the scale compared with the particle size despite the fact if they seat in space or on planetary surfaces [7]. It is noteworthy that the surface roughness is different for asteroids of different optical types [8].

So, the phase coefficient returned from photometric observations can be considered as the key factor in preliminary estimating the albedos and polarimetric

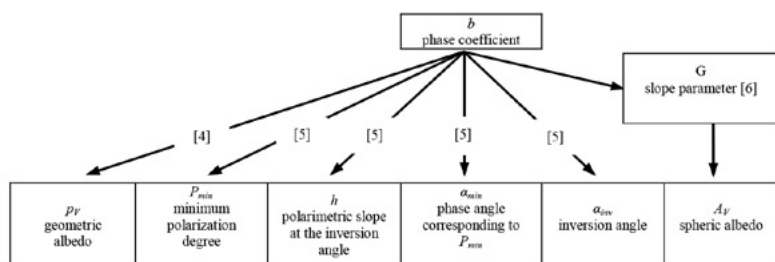


**Fig. 1.** The photometric and polarimetric system of asteroids.

characteristics of asteroids. This property is especially useful for faint main belt asteroids and for a great body of NEAs, the vast majority of which does not pass through optical classification and a cross-section of which remains unknown.

Tens of thousands of asteroids have geometric albedo estimations due to radiometric surveys from WISE and AKARI but have no the optical type. In this situation, it is easy to benefit from the photometric/polarimetric system of asteroids. For these asteroids, we can estimate the phase coefficient from a known albedo and after that the above mention polarimetric characteristics. It is quite enough to exploit the finding for optical classification of such bodies.

## REFERENCES:

- [1] Chapman C.R., Morrison D., Zellner B. Surface properties of asteroids: A synthesis of polarimetry, radiometry and spectrophotometry // *Icarus*. 1975. V. 25. No. 5. P. 104 – 130.
- [2] Bell L. The physical interpretation of albedo // *Ap. J.* 1917. V. 45. No. 1. P. 1–29.
- [3] Golubeva L.F., Shestopalov D.I. Optical properties of asteroid surfaces. A qualitative analysis. *Sov. Astron.* 1983. V.27. No 3. P. 351–357.
- [4] Shevchenko V.G. Analysis of asteroid phase dependences of brightness // *Lunar Planet. Sci. Conf. XXVII. Houston. USA. 1996. Abstract #1086.*
- [5] Shestopalov, D.I., Golubeva, L.F. Polarimetric properties of asteroids // *Adv. Space Res.* 2015. V. 56. No. 10. P. 2254–2274.
- [6] Bowell E.G., Hapke B., Domingue D., Lumme K., Peltoniemi J., Harris, A.W. Application of photometric models to asteroids // *Asteroids II* (Eds.: Gehrels T., Matthews M.T., Binzel R.P.). University of Arizona Press. USA. 1989. P. 524–555.
- [7] Kiselev N., Rosenbush V., Levasseur-Regourd A.-C., Kolokolova L. Comets // *Polarimetry of Stars and Planetary Systems* (Eds.: Kolokolova L., Hough J., Levasseur-Regourd A.-C.). Cambridge University Press. United Kingdom. 2015. P. 379–404.
- [8] Golubeva L.F., Shestopalov D.I., Shustarev P. N. Polarized light scattered from asteroid surfaces. II. Surface photometric roughness // *Lunar Planet. Sci. Conf. XLIV. Houston. USA. 2013. Abstract #1063.*

# A MULTICHANNEL DIODE LASER SPECTROMETER EXPERIMENT ON BOARD OF THE EXOMARS-2020 MISSION LANDING PLATFORM FOR IN SITU STUDY OF ATMOSPHERE NEAR THE MARTIAN SURFACE

I. Vinogradov<sup>1</sup>, A. Klimchuk<sup>2</sup>, V. Barke<sup>1</sup>, A. Fedorova<sup>1</sup>, M. Gerasimov<sup>1</sup>, V. Kazakov<sup>2,1</sup>, T. Kozlova<sup>1</sup>, Yu. Lebedev<sup>1</sup>, M. Patsaeva<sup>1</sup>, A. Rodin<sup>2,1</sup>, O. Roste<sup>1</sup>, V. Semenov<sup>2</sup>, M. Spiridonov<sup>3</sup>, A. Venkstern<sup>1</sup>

<sup>1</sup>Space Research Institute of the Russian Academy of Sciences (IKI RAS), 117997, 84/32 Profsoyuznaya Str., Moscow, Russia, imant@iki.rssi.ru;

<sup>2</sup>Moscow Institute of Physics and Technology (MIPT), Institutskiy Dr. 9, Dolgoprudny, Moscow Region, Russia, art.klimchuk@gmail.com;

<sup>3</sup>Prokhorov General Physics Institute of the Russian Academy of Sciences (GPI RAS), 119991, Vavilov Str., 38, Moscow, Russia

## KEYWORDS:

Tunable diode laser absorption spectroscopy; integrated cavity output spectroscopy; Martian atmosphere; chemical and isotopic composition variations; ExoMars-2020.

## INTRODUCTION:

An application of tunable diode laser absorption spectroscopy (TDLAS) in combination with integrated cavity output spectroscopy (ICOS) has been suggested for Martian atmosphere study as an experiment, named Martian multichannel diode laser spectrometer (M-DLS), by a team of researchers from IKI RAS, MIPT, GPI RAS. M-DLS has been proposed for scientific payload of the ExoMars-2020 mission Landing Platform [1, 2], and further modified into a very compact and lightweight instrument for continuous *in situ* study of chemical and isotopic composition variations of atmosphere near the Martian surface at short-term and seasonal time scales.

## MEASUREMENT METHOD:

In the M-DLS experiment, Martian atmosphere study will be based on regular measurements of molecular absorption spectrum in an optical cell, filled with ambient gas sample, taken at the stationery Landing Platform location. TDLAS flexibility and radical optical path enhancement of ICOS will be combined in the M-DLS instrument for fine measurement of weak absorption values at low pressure of the Martian atmosphere. H<sub>2</sub>O and CO<sub>2</sub> molecular content and isotopic ratio variations will be retrieved from absorption data continuously during one Martian year.

The optical cell with the gas sample will be sounded by highly monochromatic radiation of two tunable distributed feedback diode lasers, emitting at IR range near 2.7 microns. Measurements will be carried out sequentially in series of

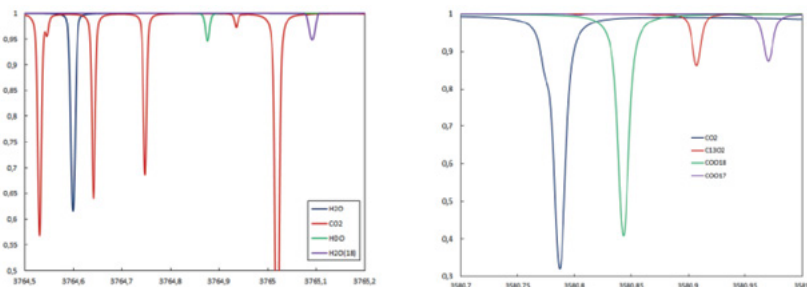


**Fig. 1.** Absorption spectra for CO<sub>2</sub> and H<sub>2</sub>O mixture, modelling atmosphere near the Martian surface: H<sub>2</sub>O isotopologue lines for ~ 1 km effective optical path (left), CO<sub>2</sub> isotopologue lines for 2.5 m effective optical path (right).

1  $\text{cm}^{-1}$  wide intervals at 2.65 microns for  $\text{H}_2\text{O}$  and at 2.79 microns for  $\text{CO}_2$  with spectral resolution of 3 MHz ( $\sim 0.0001 \text{ cm}^{-1}$ ), providing for fine recording of molecular absorption line contours of  $\text{H}_2\text{O}$  and  $\text{CO}_2$  main molecules and isotopologues  $\text{HDO}$ ,  $\text{HO}^{18}\text{O}$ ,  $^{13}\text{CO}_2$ ,  $\text{CO}^{17}\text{O}$ ,  $\text{CO}^{18}\text{O}$ . Examples of simple modelling for Martian atmosphere absorption are shown below.

**Table 1.** Sensitivity estimations for 95%  $\text{CO}_2$  and 200 ppm  $\text{H}_2\text{O}$  gas sample in the ICOS cell.

Isotopologue	Wavelength, $\text{cm}^{-1}$	Precision
$\text{CO}_2$	3580.786	$\sim 0.2\%$
$^{13}\text{CO}_2$	3580.843	$\sim 0.2\%$
$\text{CO}^{18}\text{O}$	3580.907	$\sim 0.2\%$
$\text{CO}^{17}\text{O}$	3580.970	$\sim 0.2\%$
$\text{H}_2\text{O}$	3764.599	$< 0.2\%$
$\text{H}_2^{18}\text{O}$	3765.091	$< 2\%$
$\text{HDO}$	3764.876	$< 2\%$

Modelling of the absorption spectra has shown noticeable temperature dependence of the line amplitudes, which demands for a fraction of a degree precision for the gas sample temperature control in the optical cell (see Figure 2), corresponding to adequate molecular concentration retrieval and isotopic ratio measurement accuracy of:  $\text{D}/\text{H} < 2\%$ ,  $^{18}\text{O}/\text{O} < 2\%$  ( $\text{H}_2\text{O}$ ),  $^{18}\text{O}/^{17}\text{O}/\text{O} < 0.3\%$  ( $\text{CO}_2$ ),  $^{13}\text{C}/\text{C} \sim 0.3\%$ .

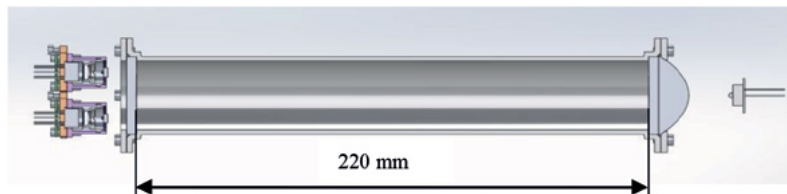


**Fig. 2.** A cross-section model of the optical cell with partially shown input laser and output photodetector interfaces.

Special system of gas sampling for the M-DLS instrument will be shared with Martian Gas Analytic Suite (MGAS), which is another instrument, proposed for the same Landing Platform. Gas sampling inlet will be lifted up by a telescopic tube to a point, 15 cm higher than the Landing Platform top. The sampling system will efficiently refresh ambient Martian atmosphere gas sample in the ICOS cell analytical volume and will optionally enhance measurement accuracy by increasing  $\sim 5$  times up concentration of sampled gas in the ICOS cell.

Following the M-DLS experiment idea, we are carrying out industrial design of a compact and lightweight M-DLS instrument for the ExoMars-2020 mission Landing Platform scientific payload. M-DLS is aimed to continue *in situ* study of atmosphere near the Martian surface after the TLS/SAM/MSL instrument of the NASA Curiosity rover [3].

## SUMMARY AND CONCLUSEION:

The idea of M-DLS experiment, combining TDLAS and ICOS methods, has been proposed for continuous study of atmosphere near the Martian surface during the ExoMars-2020 mission. M-DLS instrument aims for measuring of  $\text{H}_2\text{O}$  and  $\text{CO}_2$  molecule content and of  $\text{D}/\text{H}$ ,  $^{18}\text{O}/^{17}\text{O}/^{16}\text{O}$ ,  $^{13}\text{C}/^{12}\text{C}$  isotopic ratio variations with  $\sim 1\%$  accuracy *in situ* at the stationery Landing Platform location.

## ACKNOWLEDGEMENTS:

Scientific concept in IKI team is supported by the Federal Agency for Scientific Organizations by the Program PLANETA No. 0120.0 602993. Industrial works for the ExoMars-2020 mission are supported by the ROSCOSMOS.

## REFERENCES:

[1] Vinogradov I., Barke V., Klimchuk A., Krasnopolsky V., Rodin A., and the M-DLS team, M-DLS – a multichannel diode laser spectrometer for Martian studies. The 40<sup>th</sup> COSPAR Scientific Assembly, 2-10 August 2014, Moscow, Russia, report #B0.2-0038-14STW-L-118.

- [2] Vinogradov I., Rodin A., Fedorova A., Ignatiev N., Korablev O., Roste O., Benderov O., Churbanov D., Klimchuk A., Krasnopolsky V., Pereslavl'tseva N., Semenov V., Shaposhnikov D., Ushakov A., Kalyuzhnyi A., Nadezhdinskii A., Ponurovskiy Ya., Durry G., Joly L., Cousin J., Amarouche N., Labadie L., Sornig M., Thomson R., Moiseev P., Diode laser spectroscopy for the stationery landing platform of the ExoMars-2018 mission, 10th International Conference on Tunable Diode Laser Spectroscopy (TDLS-2015), July 6-10, 2015, Moscow, Russia, invited report #L10, Book of abstracts, P.14-15.
- [3] Webster C.R., Mahaffy P.R., Flesch G.J., Niles P.B., Jones J.H., Leshin L.A., Atreya S.K., Stern J.C., Christensen L.E., Owen T., Franz H., Pepin R.O., Steele A., the MSL Science Team, Isotope Ratios of H, C, and O in CO<sub>2</sub> and H<sub>2</sub>O of the Martian Atmosphere, *Science*, Vol. 341, 19 July 2013, P.260-263.

# A UNIAXIAL SEISMOMETER IS AN ELEMENT OF A TRIAXIAL SEISMOMETER FOR MEASUREMENTS ON THE SURFACE OF MARS (THE EXOMARS PROGRAM)

A.B. Manukin<sup>1</sup>, I.I. Kalinnikov<sup>2</sup>, A.V. Kalyuzhnyi<sup>1</sup>, O.N. Andreev<sup>1</sup>.

<sup>1</sup>*Institute of Space Research of the Russian Academy of Sciences (IKI RAS), 117997, 84 / 32 Profsoyuznaya st. Moscow, Russia.*

<sup>2</sup>*Institute of Earth Physics of the Russian Academy of Sciences (IPE RAS), 123995, B.Grusinskaya, 10, Moscow, Russia  
amanukin@yandex.ru*

## KEYWORDS:

Uniaxial seismometer, test mass, permanent magnet, magnetic rigidity, natural frequency, temperature dependence.

Earlier, [1] briefly described a three-coordinate highly sensitive seismometer, which includes three uniaxial, mutually orthogonal sensors. A uniaxial seismometer is a cylindrical test mass suspended on three extensions fixed at both ends of the cylinder. Stretch marks - thin wires 0.1 mm in diameter made of beryllium bronze, located at an angle of 120° to each other. Small mechanical vibrations of the test mass are measured with a capacitive converter. Such a scheme provides for the measurement of non-gravitational effects on board a spacecraft where there is no effect of acceleration of free fall and stretching provides the necessary mechanical rigidity. When measuring on the surface of planets, in particular Mars, the gravity projection affects the test mass. The stiffness of the stretch marks is insufficient to hold the test mass and additional stiffness is necessary. This problem was solved with the help of permanent cylindrical magnets mounted in the sensor body and on the trial mass with the same poles facing each other. In this case, the "magnetic" stiffness is determined by the relation:

$$\frac{4mg}{z_0} = k_{mag}$$

where  $m$  is the test mass,  $g$  is the projection of the acceleration of gravity on the sensitivity axis of the sensor, and  $z_0$  is the distance between the magnets, in which the weight of the test mass is completely compensated by the magnetic forces. In Mars conditions at  $m = 20$  g and  $z_0 = 2$  cm, the natural frequency of the oscillation of the test mass is  $\sim 3.3$  Hz. The natural frequency, determined by the rigidity of the mechanical suspensions ( $k = 3\pi ED^4/l^3$ , where  $E$  is the Young's modulus,  $D$  is the diameter of the stretch,  $l$  is the length of the stretch), and the "magnetic" stiffness is  $\sim 5.1$  Hz. Estimates of the magnitude of the temperature dependence of such a sensor have shown that when the temperature changes, the magnetization of permanent magnets changes, which leads to displacement of the test mass. For magnets from SmCo, the relative change in magnetization with a change in temperature by  $1^\circ\text{C}$  is  $\sim 4 \cdot 10^{-4} \text{ 1} / ^\circ\text{C}$ . The majorizing estimate for lifting the trial mass when the instrument temperature is lowered by  $100^\circ\text{C}$  (the surface temperature of Mars) is  $4 \cdot 10^{-3}$  cm. With a gap in the capacitive converter of about  $200 \mu\text{m}$ , the displacement of the rotor plate by  $x = 40 \mu\text{m}$  means that when the sensor is cooled to  $100^\circ\text{C}$ , it will remain in the operating range and will be able to measure at this temperature. Long-term stability of magnetization of permanent magnets (less than 0.1% over 10 years [2]) allows them to be used for a long time and to measure not only seismic, but also long-period processes with the help of these sensors.

## REFERENCES

- [1] A.B. Manukin, I.I. Kalinnikov, A.V. Kalyuzhny, O.N. Andreev. High-sensitivity three-axis seismic accelerometer for measurements at the spacecraft and the planets of the solar system. //The seventh Moscow solar system symposium 7M-S3. Space Research institute Moscow, Russia, October 10-14, 2016, p. 276.
- [2] Mitkevich A.I. Stability of permanent magnets. M.LENAND Publishing House, 2015.

# GALACTIC COSMIC RAYS MODULATION BY SOLAR WIND DISTURBANCES AS OBSERVED ON BOARD OF EXOMARS TGO

R. Koleva<sup>1</sup>, J. Semkova<sup>1</sup>, T. Dachev<sup>1</sup>, Yu. Matviichuk<sup>1</sup>, B. Tomov<sup>1</sup>, K. Krastev<sup>1</sup>, St. Maltchev<sup>1</sup>, P. Dimitrov<sup>1</sup>, V. Bingham<sup>2</sup>, I. Mitrofanov<sup>3</sup>, A. Malahov<sup>3</sup>, D. Golovin<sup>3</sup>, M. Litvak<sup>2</sup>, S. Drobyshev<sup>2</sup>

<sup>1</sup>Space Research and Technology Institute, Bulgarian Academy of Sciences, Sofia, Bulgaria;

<sup>2</sup>Institute of Biomedical Problems of the Russian Academy of Sciences, Moscow, Russia

<sup>3</sup>Space Research Institute, Russian Academy of Sciences, Moscow, Russia

## KEYWORDS:

Galactic cosmic rays, heliosphere, Mars, solar wind, high speed streams.

## INTRODUCTION:

In the quiet heliosphere the galactic cosmic ray (GCR) flux is modulated by interaction with non-homogeneous structures of the solar wind – high speed streams (HSS) and the interplanetary manifestations of coronal mass ejections that could be magnetic clouds (MC) and interplanetary coronal mass ejections (CME) (e.g. [1],[2],[3]). The FRENDD dosimeter Liulin-MO on board ExoMars TGO measured GCR fluxes during TGO transit to Mars and on Mars high ecliptic orbit. Liulin-MO measures the flux of the positively charged particles, it does not resolve the type and the energy spectrum of the incident particles but counts all charged particles that deposit in 300  $\mu\text{m}$  of Si energy greater than 80 keV, which in practice covers a great range of GCR energies.

## DATA:

Liulin-MO GCR fluxes in two perpendicular directions and proton flux  $> 30$  MeV by SIS instrument on ACE satellite (located at L1 libration point at about 1 500 000 km from Earth) obtained from 22.04.2016 to 07.03.2017 are compared in Fig.1. Note that Liulin-MO is not able to measure protons with energies below 30 MeV due to the shielding of its detectors. During the interplanetary transit of TGO a good agreement between the fluxes provided by two instruments is observed. In high elliptic Mars orbit (since 31.10.2016) Liulin-MO data match SIS data “delayed” by 5 days in average.

During the plotted period no CME hit the Earth but multiple HSS were observed according to NOAA Preliminary Reports and Forecasts of Solar Geophysical Data (<http://legacy-www.swpc.noaa.gov/weekly/>). Therefore it were HSS, which modulated SIS and Liulin-MO fluxes. As a first step we used the WSA-Enlil model (<http://iswa.ccmc.gsfc.nasa.gov/>) to look at the propagation of a possible HSS. During April – first half of July the Earth and Mars are located on near-by magnetic field lines and the HSS front reach both planets (and TGO still nearer to Earth than to Mars) roughly simultaneously. During

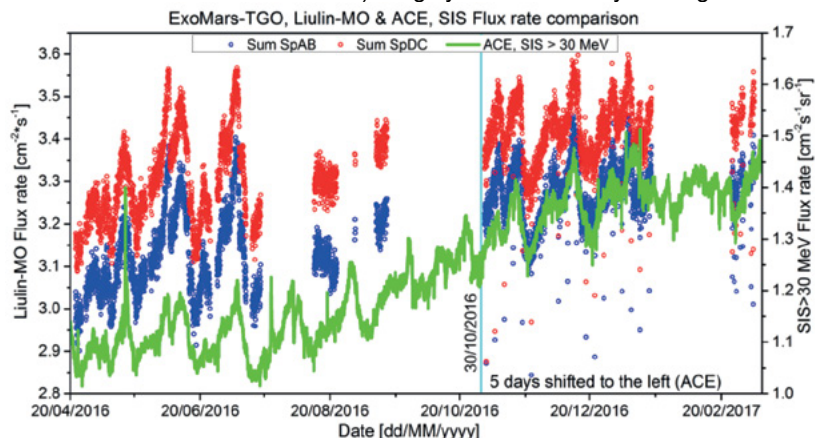


Fig. 1.



2016 a possible HSS reaches Mars first and only after approximately 4 days reaches the Earth. At the end of the period – the beginning of Marc 2017 this delay is already about 6 days. In the scale of Fig. 1. an average delay of 5 days of ACE SIS data gives an admissible agreement with Liulin-MO GCL fluxes. The overall increase of the fluxes in both instruments observed from 22.04.2016 to 07.03.2017 can be attributed to the increase of GCR intensity during the declining phase of the solar activity.

As a second step we investigate the relation of GCR modulations to the observed solar wind parameters to find how the flux depletions are related to the particular HSS. We use ACE solar wind data for the period of TGO cruise phase and MAVEN data for the period of Mars high elliptic orbits.

## ACKNOWLEDGMENTS.

This work is partly supported by: Contracts N 503/2-13 and 63/4-14 between IKI-RAS and SRTI-BAS; Agreement between RAS and BAS on fundamental space research; Contract No. 4000117692/16/NL/NDe Funded by the Government of Bulgaria through an ESA Contract under the PECS (Plan for European Cooperating States). Thanks V.A. Berliand from VNIIFTRI for the support of Liulin-MO calibrations.

## REFERENCES:

- [1] Badruddin, Cosmic ray modulation: effects of high-speed solar wind streams // *Astrophys. and Space Sci.*, 1997, V. 246, P. 171-191.
- [2] Barouch E., Burlaga L.F., Causes of Forbush decreases and other cosmic ray variations, // *J. Geophys. Res.*, 1975, V. 80, P. 449-456
- [3] Cane H. V. 2000, Coronal mass ejections and Forbush decreases, // *Space Sci. Rev.*, 2000, V. 93, P. 55-77.

# ACCESSING ICY MOON'S OCEAN WITH THERMONUCLEAR REACTOR

P.E. Laine<sup>1</sup>

<sup>1</sup>*Departments of Physics and Computer Science and Information Systems, P.O. Box 35, FI-40014 University of Jyväskylä, Finland, pauli.e.laine@jyu.fi;*

## KEYWORDS:

icy moons, subsurface ocean, astrobiology, extraterrestrial life, thermonuclear reactor.

## INTRODUCTION:

The icy moons (e.g. Europa and Enceladus) present some of the promising examples of extended habitable locations in our Solar System. Some of them seem to have potential ocean that could support life.

The primary goal for astrobiology is to find life somewhere else in the Universe. How could we detect biosignatures on icy moons, if we cannot find them on the hostile surface or water plumes? The only solution is to go somehow under the ice and explore the ocean beneath.

## CHALLENGES IN ACCESSING THE OCEAN:

Accessing ocean under ice in remote moon to explore possible biosignatures seems overwhelmingly difficult. We don't even know how thick the icy shells are. It is estimated, that in e.g. Europa the ice is around 15 to 25 km thick [1]. It takes 35 to 52 minutes to send radio signals from Europa to Earth, so any exploration vehicle should be autonomous in all its activities. As these icy moons are in high priority for astrobiology, all vehicles flying-by or landing them should be extremely sterilized in order not to contaminate the target.

## USING THERMONUCLEAR PENETRATOR:

One obvious way to penetrate ice is to melt it. And that would need a lot of energy. On the remote moon, there is only one adequate energy source available today: fission. Thermonuclear reactors are relatively simple nuclear reactors that could be used for providing needed energy to get to ocean. For this purpose, we can do rough estimates about the size of the reactor by using information and estimates about the thickness of the ice cover, diameter of the penetrator (these give us the amount the ice), and the temperature of the ice.

Nuclear reactors have already flown in space. For example, Soviet TOPAZ reactors demonstrated that nuclear reactors could provide steady power for years.

In this presentation, I will present general model of thermonuclear penetrator for accessing oceans beneath icy shells.

## REFERENCES:

[1] NASA (2012) Frequently Asked Questions about Europa. <http://solarsystem.nasa.gov/europa/faq>.

# GEOPHYSICAL SURVEY OF THE SURFACE AND SUBSURFACE PLANETARY GEO-ELECTRICAL MARKERS OF THE SUBSURFACE OCEAN ON THE JUPITER'S AND SATURN'S ICE MOONS: POSSIBILITIES TO ADAPT SPACE TECHNOLOGY FOR RISK ASSESSMENT AND GEOPHYSICAL PRACTICE FOR THE NATURAL ECOSYSTEMS AND SPACE STUDIES

Yu.R.Ozorovich<sup>1</sup>, A. Ivanov<sup>2</sup>, V.Linkin<sup>1</sup>, A.Kosov<sup>1</sup>, S.Klimov<sup>1</sup>, D.Skulachev<sup>1</sup>

<sup>1</sup>Space Research Institute, Moscow, Profsoznaya str., 84/32, [interecos@gmail.com](mailto:interecos@gmail.com)

<sup>2</sup>Scoltech/Swiss Space Center, EPFL

## KEYWORDS:

Ice moons, planetary, geo-electrical markers, geophysical studies, deep space mission

## INTRODUCTION:

New methodology and space instruments for geophysical survey of the surface and subsurface of Jupiter's and Saturn's ice moons should be developed for future space missions. The existing set of instruments should be transformed into a specialized complex for identification of those geoelectric features (markers) on the surface of ice moons that are the evidence of the existence of subsurface oceans under multi-kilometer ice cores of the ice moons.

It is preliminary methodological research that can significantly optimize the planned space missions, as well as identify the most appropriate techniques and instruments for future deep space missions focused on the study of subsurface oceans' characteristics which are currently impossible to measure directly using geophysical techniques.

In this presentation, the basic toolkit for the voluminous composition of geophysical studies is presented, with possible testing and calibration measurements on small satellites and direct measurements on a surface with pronounced of the geoelectrical features of subsurface horizons.

## REFERENCES:

- [1] Yu.Ozorovich., Scientific aspects and opportunities of the "ROBOTIC SPACE MISSION TO EUROPE": Space systems application and technology for space mission to Europa (Enceladus) - Jupiter's and Saturn's ice moons. The Seventh Moscow Solar System Symposium, 2016. [https://www.researchgate.net/publication/304743560\\_Scientific\\_aspects\\_and\\_opportunities\\_of\\_the\\_ROBOTIC\\_SPACE\\_MISSION\\_TO\\_EUROPE\\_Space\\_systems\\_application\\_and\\_technology\\_for\\_space\\_mission\\_to\\_Europa\\_Enceladus\\_-\\_Jupiter%27s\\_and\\_Saturn%27s\\_ice\\_moons](https://www.researchgate.net/publication/304743560_Scientific_aspects_and_opportunities_of_the_ROBOTIC_SPACE_MISSION_TO_EUROPE_Space_systems_application_and_technology_for_space_mission_to_Europa_Enceladus_-_Jupiter%27s_and_Saturn%27s_ice_moons)
- [2] Yu.Ozorovich, et all, Jupiter's and Saturn's ice moons: geophysical aspects and opportunities of geophysical survey of the planetary geoelectrical (dielectric properties) markers and oreols of the subsurface liquid ocean on the surface ice moons. EGU 2016, At Wien, vol.18. [https://www.researchgate.net/publication/292980737\\_Jupiter%27s\\_and\\_Saturn%27s\\_ice\\_moons\\_geophysical\\_aspects\\_and\\_opportunities\\_of\\_geophysical\\_survey\\_of\\_the\\_planetary\\_geoelectrical\\_dielectric\\_properties\\_markers\\_and\\_oreols\\_of\\_the\\_subsurface\\_liquid\\_ocean\\_on\\_t](https://www.researchgate.net/publication/292980737_Jupiter%27s_and_Saturn%27s_ice_moons_geophysical_aspects_and_opportunities_of_geophysical_survey_of_the_planetary_geoelectrical_dielectric_properties_markers_and_oreols_of_the_subsurface_liquid_ocean_on_t)
- [3] Yu.Ozorovich, et all, Space systems application and technology for space mission to Europa (Enceladus) - Jupiter's and Saturn's ice moons. [https://www.researchgate.net/publication/294406932\\_Space\\_systems\\_application\\_and\\_technology\\_for\\_space\\_mission\\_to\\_Europa\\_Enceladus\\_-\\_Jupiter%27s\\_and\\_Saturn%27s\\_ice\\_moons](https://www.researchgate.net/publication/294406932_Space_systems_application_and_technology_for_space_mission_to_Europa_Enceladus_-_Jupiter%27s_and_Saturn%27s_ice_moons)

# THEORY OF STABILITY OF NANOCRAFT EQUIPPED WITH A SAIL ACCELERATED BY A INTENSE LASER BEAM

Popova H.<sup>1,2</sup>,

<sup>1</sup>*Skobeltsyn Institute of Nuclear Physics, Lomonosov Moscow State University, GSP-1, Leninskie Gory, Moscow, 119991, Russian Federation;*

<sup>2</sup>*The Schmidt Institute of Physics of the Earth of the Russian Academy of Sciences (IPE RAS), Bolshaya Gruzinskaya str., 10-1, Moscow 123242, popovaelp@mail.ru*

## KEYWORDS:

Breakthrough Starshot, light sail, light-propelled nanocraft

The light sail concept - harnessing photon pressure to propel a spacecraft - has a long history dating back to some of the earliest pioneers of astronautics. Now this problem has got a new relevance in connection with the advent of the project Breakthrough Starshot.

Breakthrough Starshot is engineering program aiming to demonstrate proof of concept for light-propelled nanocrafts. These could fly at 20 percent of light speed and capture images of possible planets and other scientific data in our nearest star system, Alpha Centauri, just over 20 years after their launch.

In this project nanocrafts are gram-scale robotic spacecrafts comprising two main parts: StarChip and Lightsail. The StarChip is gram-scale wafer, carrying cameras, photon thrusters, power supply, navigation and communication equipment, and constituting a fully functional space probe. The Lightsail is made of increasingly thin (no more than a few hundred atoms thick) and light-weight (gram-scale mass) metamaterial.

To achieve goal of the project it is necessary to solve a lot of complex scientific and engineering problems. One of these tasks is investigation stability nanocraft orientation in intense laser beam which should accelerate it up 60,000 km/s during 2 minutes.

We considered a problem of stability nanocraft orientation while illuminated by intense laser beam. In our model the nanocraft driven by intense laser beam pressure acting on its lightsail is sensitive to the torques and lateral forces reacting on surface of sail. This forces influence the orientation and lateral displacement of spacecraft. We consider stability of its position inside laser illuminated column.

The assumptions in choosing the model: 1. concave (part of the sphere) circular sail; 2. configuration of nanocraft is treated as solid body (applicability of Euler equations); 3. mirror reflection of laser beam from surface of the lightsail; 4. Gaussian profile of the laser beam.

In [1] we discussed how sail shape and profile of the laser beam can affect stability of nanocraft position provided that surface of the sail has a small curvature.

In this work we are developing theory of stability nanocraft orientation taking into account arbitrary curvature of surface of the sail. We obtained conditions for the case of a stable orientation of the sail. We estimated the threshold value of the disturbing force, at which the position of the sail in the beam is still preserved.

## REFERENCES:

[1] Popova E., Efendiev M., Gabitov I. On the stability of a space vehicle riding on an intense laser beam// *Mathematical Methods in the Applied Sciences*. 2017. V. 40. No. 4. P. 1346-1354.

# COMPLEX OF LOW-WEIGHT MINIATURE INSTRUMENTS FOR SOLAR WIND MONITORING

D.A. Moiseenko<sup>1</sup>, A. Yu. Shestakov<sup>1</sup>, R.N. Zhuravlev<sup>1</sup>, I.V. Zimovets<sup>1</sup>, O.L. Vaisberg<sup>1</sup>, S.D. Shuvalov<sup>1</sup>

<sup>1</sup>Space Research Institute of the Russian Academy of Sciences (IKI), 84/32 Profsoyuznaya Str, Moscow, Russia, 117997, modaldi@iki.rssi.ru;

## KEYWORDS:

Solar wind, space plasma, space weather, ion spectrometer, electron analyzer, energetic particles.

## INTRODUCTION:

The problem of reliable forecasting of the space weather and their effects is still far from the solution. This is due both to its fundamental scientific complexity, and to the insufficient amount of observational data available to researchers. It might be a large step forward to create systems for operational control of space weather, in particular, simultaneous measurements of corpuscular solar radiation in different heliosphere locations. For improved forecasts of space weather near the Earth, simultaneous measurements both inside and outside its magnetosphere at different distances from the surface are required.

This goal can be achieved with help of complex scientific diagnostic instruments installed on spacecraft with various orbits. At the same time, it is important that the experimental data obtained will be properly calibrated. This can be more easily achieved with similar complexes of diagnostic equipment installed on different spacecraft after passing a unified system of quality control, calibration and testing. If, in addition, these complexes have small mass and size (i.e., miniaturized), then they can be placed as an additional payload on a wide range of spacecraft (including microsatellites) with different orbit. This extensive network of diagnostic stations of space weather control will be similar to the network of weather stations and multiple and atmospheric probes.

As the space infrastructure develops and the number of spacecraft launches increases the cost of individual elements of space weather network will decrease. We believe that it is now necessary to begin to work out the issue of creating a basic scientific and measurement complex, part of which will be a compact system for the diagnostics of corpuscular radiation, which can be installed onboard different spacecraft, leading to further expansion of the network of monitoring of space weather (space-meteorological network).

We are presenting results of modeling of the instruments being developed in order to solve this problem. The instruments are designed to perform measurements of solar wind ions and electrons within energy range of 0,5-10 keV and 30-10000 eV respectively and  $\Delta E/E$  aimed at 10-15%.

# NEUTRAL GAS MASS SPECTROMETRY IN THE CONTEXT OF THE LUNA-RESURS MISSION

R.G. Fausch<sup>1</sup>, L. Hofer<sup>1\*</sup>, M. Tulej<sup>1</sup>, P. Wurz<sup>1</sup>, D. Lasi<sup>1</sup>, A. Buch<sup>2</sup>,  
M. Cabane<sup>3</sup>, P. Coll<sup>4</sup>, D. Coscia<sup>3</sup>, S. Aseev<sup>5</sup>, M. Zaitsev<sup>5</sup>, M. Gerasimov<sup>5</sup>,  
A. Sapgir<sup>5</sup>, C. Szopa<sup>3</sup>

<sup>1</sup>Physics Institute, University of Bern, Sidlerstrasse 5, 3012 Bern,  
Switzerland (rico.fausch@space.unibe.ch)

<sup>2</sup>LGPM, Ecole Centrale Paris, 92295 Châtenay-Malabry, France

<sup>3</sup>LATMOS, Université Pierre et Marie Curie, 75252 Paris, France

<sup>4</sup>LISA, Université Paris-Est Créteil, Université Denis Diderot & CNRS, 94010  
Créteil, France

<sup>5</sup>Space Research Institute, 117997 Moscow, Russia

\*Present at: CSEM Landquart, 7302 Landquart, Switzerland

## KEYWORDS:

In situ mass spectrometry; Gas chromatography; Neutral gas mass spectrometry; Luna-Resurs; Moon

Chemical composition of solar system bodies is of significant importance to understand their origin and evolution. Investigation of chemical composition of the lunar exosphere and surface is of considerable interest in the Russian Luna-Resurs mission.

Whereas available lunar samples originate from a restricted region near the lunar equator, the instruments selected for investigation enhance our understanding of the composition of the moon and its exosphere, in particular by measuring volatiles and water in the lunar regolith near the poles or examine the composition of the exosphere.

We develop a compact time-of-flight mass analyzer (neutral gas mass spectrometer, NGMS) coupled with a gas chromatograph (GC) to investigate volatile fraction of lunar materials (GC mode) and chemical composition of the tenuous lunar exosphere (exosphere mode). For GC mode, pyrolysis fractionate volatiles in the temperature range up to 1000 °C. The GC-NGMS instrument allows investigating molecular composition of regolith (CHON organics, water) and analysis of noble gas composition [1]. We demonstrate that NGMS is capable to record the continuous GC outflow allowing highly sensitive measurements of chemical compositions (molecules, their structure, elements, isotopes) with high dynamic range up to  $10^6$  within 1 s and mass resolution ( $M/\Delta M$ ) up to 1100 [1,2].

We report on the results of performance studies with standalone NGMS for exosphere mode and investigations conducted by the GC-NGMS instrument [3]. Organic and noble gas mixtures provide reference for measuring retention times and signal to noise ratios resulting in detection limits. In combination with the built-in thermal conductivity detector (TCD) of the GC, the comparison of both the TCD and the NGMS measurements indicate the advantage of the NGMS for analyzing the chemically pre-separated GC sample regarding its capabilities to identify species by their fraction pattern. Since small retention times cause narrow GC-peaks in time, NGMS is capable of varying the integration time of each data point to increase sampling rate.

## REFERENCES:

[1] Wurz P., Abplanalp D., Tulej M., Lammer H. A Neutral Gas Mass Spectrometer for the Investigation of Lunar Volatiles, Planet. Space Sci. 2012. V. 74. 264–269.

[2] Hofer, L., Wurz, P., Buch, A., Cabane M., Coll P., Coscia D., Gerasimov M., Lasi D., Sapgir A., Szopa C., Tulej M. Prototype of the gas chromatograph–mass spectrometer to investigate volatile species in the lunar soil for the Luna-Resurs mission, Planet. Space Sci. 2015. V. 111. 126–133.

[3] Hofer, L., Lasi D., Tulej M., Wurz, P., Cabane M., Coscia D., Gerasimov M., Rodinov D. Prototype of the gas chromatograph–mass spectrometer to investigate volatile species in the lunar soil for the Luna-Resurs mission. Proceedings of EPSC2013-107. 2013. V. 8.

# SPACE GUNS FOR THE MOON AND ON THE MOON

A.V. Staroverov<sup>1</sup>, O.B. Khavroshkin<sup>2</sup>

<sup>1</sup>Moscow State Technical University, Moscow, 107005 Russia

<sup>2</sup>Institute of Physics of the Earth, Russian Academy of Sciences, Moscow, 123810 Russiakhavole@ifz.ru

## KEYWORDS:

moon, ballistic method, space gun, less risk, safety.

## INTRODUCTION:

For carrying out seismological studies of the Moon, the level of development of modern scientific and technical systems and methods is high enough, therefore the solution of any problem is real. For the past 30 - 40 years, old principles and schemes are used, and scientific tasks are slightly updated. The development of electronics and instrumentation allows scientific equipment to occupy minimal space and weight and withstand overloads (deceleration)  $> 10^4$  g. This makes it possible to replace the existing excessively expensive rocket systems with new methods of delivering payload, for example, ballistic (space gun). Thus, the costs of scientific programs are decreasing at times, and many studies are becoming available, less risky and environmentally safer.

Since the 1950s, more than fifty hypervelocity ballistic ranges of different sizes have been built around the world. All of them have done good job in their research fields. However due to limited space, only a few most active ranges are introduced here. They are: AEDC Range G, Hypervelocity Free-Flight Aerodynamic Facility (HFFAF) of NASA Ames, hypervelocity ballistic ranges of the UAH Aero physics Research Center (UAH-ARC), Hypervelocity Impact Test Facilities (HITF) of NASA JSC, Hypervelocity impact ranges of Ernst-Mach Institute (EMI), Hypervelocity Ballistic Range Complex of CARDC [1].

But the most promising and modern project is Quicklaunch, in which its creator, Dr. John Hunter got rid of the piston [2]. In the new system, natural gas burns inside a special heat exchanger chamber, which is surrounded by a second chamber - with hydrogen. Heat is transferred through the walls, resulting in a hydrogen temperature rising to 1000 degrees Celsius. As soon as the pressure reaches the required value, a special sliding valve opens, and hot hydrogen starts to accelerate the projectile along the trunk. After the departure of the device, the end of the barrel immediately closes the diaphragm, minimizing the loss of hydrogen - it is then cooled again for use in the next start. This principle will be considered for designing a space gun for launching equipment to the moon.

The final project of our light-gas gun is capable of delivering a useful cargo of 100kg. And a diameter of 0.4 m, including a stage for accelerating from 5.5 km/s to 11.2 km / s, allowing to reach the surface of the moon with an input speed of 1.5 km / s. The problem of stabilization and leveling of the gun can be solved by placing the system in water and partially supporting it on the mountain, or by forming an ice shell around the gun during the shot, thereby ensuring its buoyancy and eliminating the recoil problem.

Small high-speed penetrator reducing the depth of penetration into the ground by approaching the surface at a large angle and by using beam for cavitation, which has a slanting cut [3]. Total depth of penetration would be around 10 m to provide connection to base station.

## REFERENCES

- [1] S. Liu. Ballistic Range. Springer International Publishing Switzerland. 2016.
- [2] John Hunter. Cannons to the Planets. Google. Tech Talks. 2009.
- [3] V.A. Veldanov, V.E. Smirnov, O.B. Khavroshkin. Lunar Penetrator: Reducing Overload and Penetration Control.//Solar System Research (Official English Translation of *Astronomicheskii Vestnik*), Vol. 33, Number 5, 1999, pp.432-436.

# DEVELOPMENT OF THE EXPERIMENTAL SET-UP FOR LUNAR DUST PARTICLES INVESTIGATION AND INSTRUMENTS CALIBRATIONS

A.N. Lyash<sup>1</sup>, I.A. Kuznetsov<sup>1</sup>, A.V. Zakharov<sup>1</sup>, G.G. Dolnikov<sup>1</sup>, I.A. Shashkova<sup>1</sup>

<sup>1</sup>Space Research Institute of the RAS, Moscow, Russia,  
alyash@iki.rssi.ru

## KEYWORDS:

Lunar Dust, Lunar exosphere, Moon, Plasma, Dust,

## INTRODUCTION:

The complex of scientific instruments of the Lander «Luna-Glob» included device PML. This instrument is designed to study the dust component, its dynamics in the near-surface exosphere of the moon, the registration of micro-meteorites and secondary particles of the lunar regolith, impact by micrometeorites and the measurement of their physical characteristics. The device directly measured momentum, velocity, mass and charge of the particles.

For the purpose of conducting physical experiments on modeling of the dusty environment conditions in the surface layer was created an experimental setup. This unit is designed for carrying out functional tests, adjustments and calibrations of the instrument. The installation is carried out testing of the methodology of space experiment. It is planned to hold correction of the coefficients of relative sensitivity and verification of the scientific data obtained during the mission.

## EXPERIMENTAL SET-UP:

The experimental set-up is realized on the base of the vacuum chamber and includes a system of supply and control of vacuum, the injector (generator) of charged particles. The setup includes the control system for measuring the speed of the charge of particles and the system to measuring and control electrical signals and instrument parameters. Vacuum system provides vacuum with a residual pressure sufficient to operate the injector of the dust particles and simulate the conditions of the dust of the atmosphere. Injector (generator) of dust, charged particles produces a stream of metallic, charged particles with dimensions from units to hundreds of microns with flow rates from units to tens of meters per second with a charge of not less than 1000 electrons per the particle. The measuring system for the control of the speed and charge of particles consists of the induction sensor and charge sensitive amplifiers that allow to display and measure the signal. Method of measuring charge is based on the measurement of the induced mirror charge from the moving particles in the metallic electrode of the induction sensor. The geometry data of the placement of the induction sensors is used to measure the speed of particles by time delays of signals.

The voltage applied to the injector governs the speed and charge of the injected particles. In the experiments are used different in size and mass of particles loaded into the injector.

Since the process of injection and the detection of particles are random, the statistical methods to handle the large volume of accumulated data are used.

## RESULTS:

The set-up made it possible to realize the streams of charged particles with velocities in the range of 2 to 60 m/sec for the metalized particles with sizes from 10  $\mu\text{m}$  to 200  $\mu\text{m}$ .

On the installation was carried out calibration of the engineering sample PML device, had allowed to determine the sensitivity of the sensors of the device. Threshold sensitivity for the charge is amounted to 2 000 the charge of the electron. The threshold sensitivity of the momentum is amounted to the value of  $3 \cdot 10^{-12}$  Newton\*sec.

## ACKNOWLEDGEMENTS:

The research was carried out using funds of the Russian science foundation (project №17-12-01458).



# LUNAR LAVA TUBES AND PRESSURIZED TENTS AS A SUITABLE ALTERNATIVE FOR HUMAN HABITATION

Dr. Austin Mardon<sup>1</sup>, Victoria Throckmorton<sup>2</sup>

<sup>1</sup>*Antarctic Institute of Canada 11919 82 Street, Edmonton, Alberta, T5K-1Z6, Canada.*

<sup>2</sup>*MacEwan University*

## KEYWORDS:

Lunar lava tubes, pressurized tents, habitation, shelter, moon

## INTRODUCTION:

Recently, researchers have proposed building lunar bases for human habitation with 3D printing technology. Robots would be sent to the Moon to survey sites, test terrains, and find any hazards prior to building a base. Once an ideal area for settlement has been selected, astronauts would build the base with the assistance of 3D printing technology [1]. Others have suggested that building a base underground would offer the best protection from solar radiation and the extreme lunar weather conditions [2]. However, another alternative method is the installation of pressurized tents in the already present lunar lava tubes.

## LUNAR LAVA TUBES AS A USEFUL RESOURCE:

Lunar lava tubes are elongated depressions that are formed from channels of molten lava [3]. While they vary in width and depth, a study done by Blair et al. suggests that lava tubes up to five kilometers in width can act as suitable stable structures for shelter [4]. Given the proper size for stability, the tubes can then offer protection from radiation, micrometeorites, and dust [3]. As others have proposed in terms of surveying, robots can be sent to the Moon to explore the lunar tunnels. Through the data collected by the robots, the lava tubes with the most optimal conditions can be selected for human habitation. Since the lava tubes are ready-made structures, building an entirely new infrastructure underground is unnecessary. Inserting pressurized tents within the caverns can offer a less dangerous and an inexpensive alternative for building a lunar base. The intelligent yet simple technology behind inflatable tents will allow for lighter cargo while traveling in a spacecraft, whereas sending the materials for building a completely new shelter on the Moon may require more than one launch [5]. Inflatable tents would also enable astronauts to assemble their shelters with ease while wearing their space suits. Prototypes of pressurized tents have already been made, and they have been and continue to be tested [5]. It would be both resourceful and logical to use the technology that has already been developed to further our goal of making space settlement a reality. Though a suitable lava tube will need to be found and tested,



Fig. 1. Apollo image of lunar lava tubes [6].

the procedure of constructing a pressurized tent within the tube can be relatively less risky, time consuming, and costly than building an entirely new structure.

## CONCLUSION:

Living in the Moon's underground tunnels is a possible and promising method for human habitation. Taking advantage of the natural construction will not only allow for a safe and suitable shelter but, with the addition of pressurized tents, the lava tubes may also serve as relatively a low-cost and low-risk alternative for human settlement on the Moon.

## REFERENCES:

- [1] Gray, Richard. "We could be living on the moon by 2002': Nasa claims a 'cheap' \$10 billion lunar base will be ready for humans in just six years." Mail Online. 24 March 2016.
- [2] Allison, Peter Ray. "This is why lunar colonies will need to live underground." BBC. 18 December 2015.
- [3] Mardon, A. A. Lunar Lava Tubes and Artificial Tunnels: Habitations for the Near Term Future. 28<sup>th</sup> Annual Lunar and Planetary Conference. Huston, Texas. March 1997. P. 869.
- [4] Blair, David M. et al. "The structural stability of lunar lava tubes." Icarus. October 2017. Vol. 285. 52 p.
- [5] National Aeronautics and Space Administration. "Living on the Moon: Inflatable Habitat Research." NASAfacts. 2007. P. 1-2.
- [6] National Aeronautics and Space Administration. "AS15-88-11980." National Aeronautics and Space Administration, Human Space Flight, 11 Jan. 2012, <https://spaceflight.nasa.gov/gallery/images/apollo/apollo15/html/as15-88-11980.html>.

# USING METEOR BURST COMMUNICATIONS ON INHABITED PLANETS

R.R. Chau<sup>1</sup>, A.A. Mardon<sup>2</sup>

<sup>1</sup> *Antarctic Institute of Canada, 12y4jv@gmail.com;*

<sup>2</sup> *Antarctic Institute of Canada, aamardon@yahoo.ca*

## KEYWORDS:

Meteor Burst Communication, short distance emergency communications, human establishment

## INTRODUCTION:

Meteor burst communication is a method of sending information from a station to a single station or multiple stations developed in the 1950's. It uses the ionization trail of a meteor to reflect a signal from one sender to another [2]. It has long been phased out because of the development of other significantly more efficient and reliable methods of communicating. However, during early planet or space body inhabiting, these forms of communication and their extra infrastructure needs may not be readily available for use (such as extra satellites or towers) or in cases of emergencies where infrastructure is not operationally available. Meteor burst communication could fill this need for emergency or low data communication at very low costs.

There are several drawbacks to using meteor burst communication including a lower limited range of transmission and very low data transmission [1]. This form of communication would not be suitable for cross planet or cross body communication but ideally for short range establishment-establishment communication. Additionally, due to the reliance on the ionization trails of meteors and other bodies capable of producing these trails, consistent communication would be difficult at best and would be best used as a "last ditch effort" or in worst case scenarios or as a means to send low amounts of data.

## REFERENCES:

[1] Jernovics J.P. Meteor Burst Communications: An Additional Means of Long-Haul Communications. 1990. [Online Article; retrieved July 2017.] <http://www.globalsecurity.org/space/library/report/1990/JJP.htm>

[2] Meteor Burst Communications: An Ignored Phenomenon?//Cryptoloic Quarterly. 1990. V. 9. No. 3. P. 47-62.

# ANALYSIS OF APPARENT MOTION OF SUN, EARTH AND STARS ON THE LUNAR SKY

B.A. Epishin, M. I. Shpekin

Kazan Federal University, Kazan, epishin.boris@yandex.ru ,  
MichaelS1@yandex.ru,

## KEYWORDS:

Topocentric ephemeris, visible movement, computer program, long-term observatory, observations on the Moon

The report examines the visible motions of the Earth, the Sun and stars on the lunar sky during the year. The analysis is based on the results of calculations on the program developed by us for calculating the topocentric ephemeris of the Earth [1], the Sun [2], and the stars [3] for the lunar surface. Figure 1 shows the interface of our program. The ephemeris calculate (this example) for topocenter with longitude -85 degrees and latitude -15. The topocenter is located near Spring lake in the Mare Orientale region. The example in Fig. 1 shows the input of the coordinates for the Sirius star. The calculations take into account the physical libration [4].

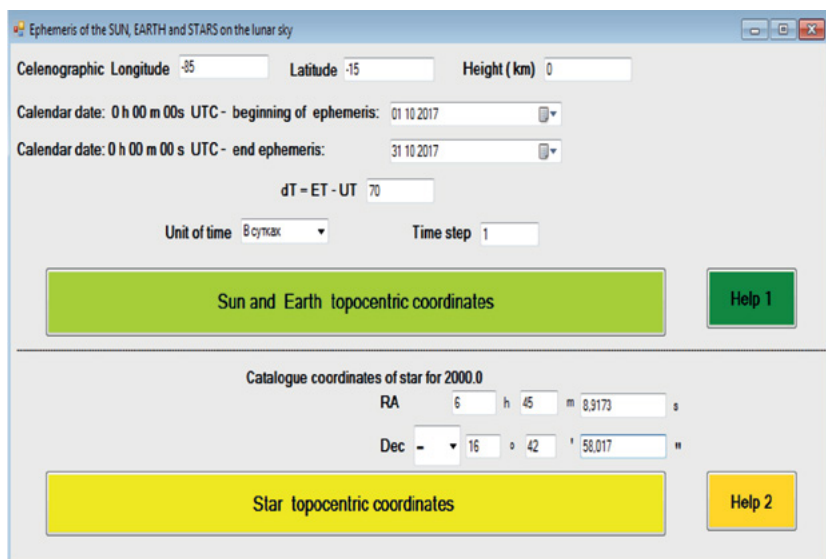


**Fig.1.** View of the calculation program interface of topocentric ephemeris for the observations from the lunar surface. Green and yellow areas of the screen reflect the control elements.

**Table 1.** Earth and Sun Ephemeris (topocenter – Lake of Spring in the Mare Orientale region)

UTC Date	Earth		Sun	
	Azimuth	Altitude	Azimuth	Altitude
0 hours				
13 oct 2017	-93°08' 31"	+0° 09' 33"	+155°06' 51"	+72° 06' 27"
14 oct 2017	-91 30 29	-0 04 11	+128 23 54	+64 38 10

In Table 1, for example, the ephemeris of the Earth and the Sun are given for a topocenter on the surface of the Moon (the Lake of Spring with a longitude of -85 ° and a latitude of -15 °), where the azimuth is measured from the South point (positive azimuth to the west, and a negative value to the east of the South point).

Fig. 2. shows the visible motion of Earth, Sun and star ( $\gamma$  Virginis) at the lunar sky during 2017 for the same topocenter. Here is shown the eastern region of the sky near the horizon. The Earth moves for a year spiraling along ellipses counter-clockwise and makes one revolution for earthly month. But the Sun

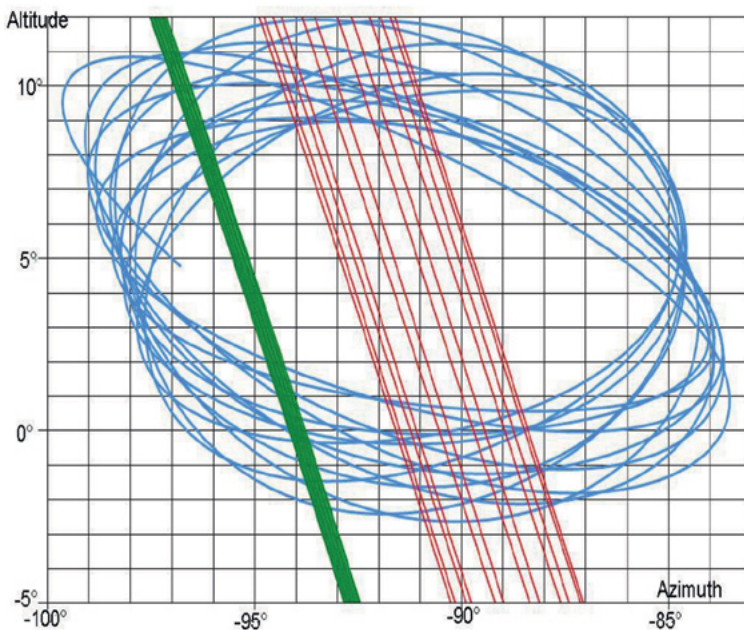


**Fig. 2.** The annual motion of the Earth, Sun and star ( $\gamma$  Virginis) on the Lunar sky at the Lake of Spring. Legend: red line – Sun track, blue line – Earth center track and green line – star track.

enters in this area of the sky for a year about 12 times (every earthly month). The star (declination  $-1.5$  degrees) moves at the lunar sky along celestial equator from east to west not so far from Sun track.

It is important to note that the apparent velocity of sunrise from the horizon and sunset beyond the horizon on the Moon will be about 30 times slower than on the Earth. The star near equator has the same velocity of apparent motion.

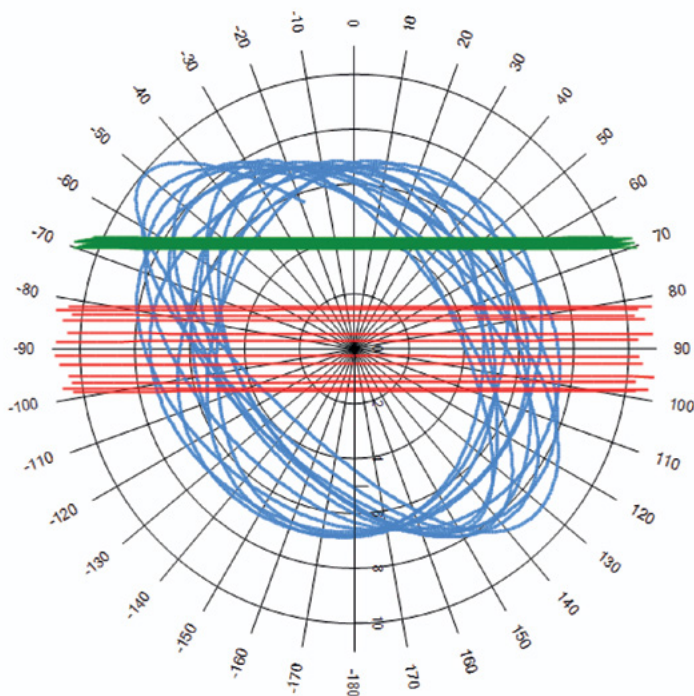


**Fig.3.** The motion of the Earth, Sun and star ( $\gamma$  Virginis) on the lunar sky for the observer in the center of the visible hemisphere.

Fig. 3 shows the motion of the Earth, the Sun and stars near the zenith point for the observer in the region of the "sub-Earth point", that is, in the center of the near side of the Moon. The coordinate system is polar (azimuth and zenith distance), and the Zenith point is located in the center.

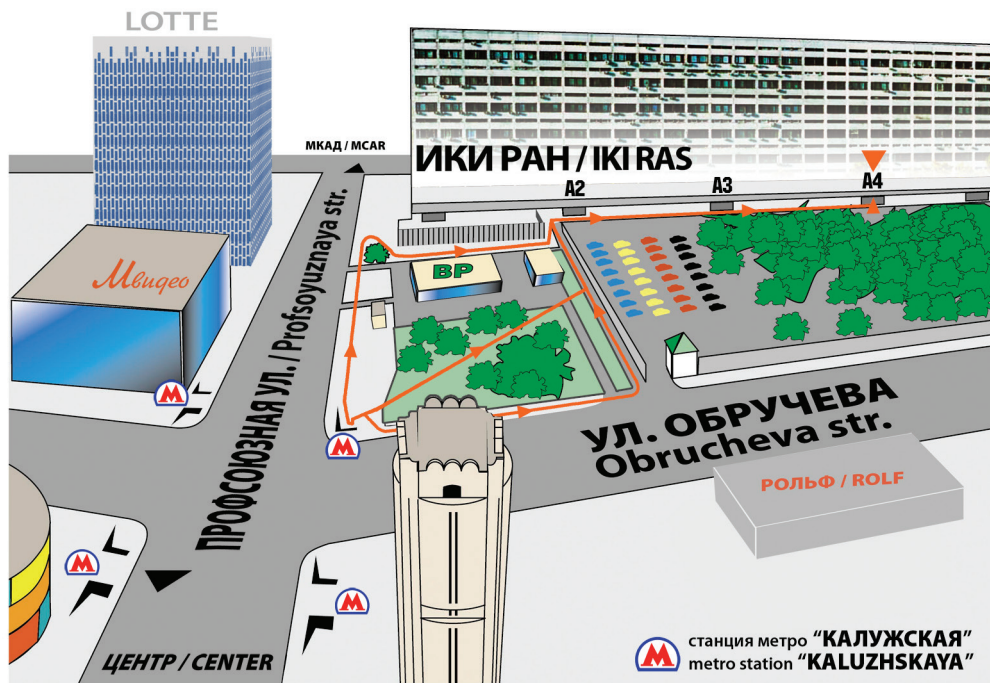
As can be seen from Fig. 3, the center of the Earth (blue line) moves away from Zenith in its movement within a year not more than 5 degrees. The Sun (red line) moves away from Zenith to the north and to the south approximately on 2 degrees moving from East to West. The daily path of the star (the green line) is located somewhat further from Zenith than the solar path. This is due to the declination of the star ( $\gamma$  Virginis). Fig. 3 contains only part of daily path for the Sun and the star within Zenith vicinity limited by radius equals 5 degrees.

It is important to know the location of the Sun during all lunar day to protect the light-receiving devices from solar light. Knowing the concrete movements of objects, you can plan observations in advance. This is especially necessary for long-term observatory on the lunar surface [6].

## REFERENCES:

- [1] Основы лунной астрометрии. Куликов К. А., Гуревич В. Б. Гл. ред. физ-мат.лит. «Наука», 1972, 392стр.
- [2] Jean Meeus *Astronomical algorithms*. Second edition, 1998, 477p.
- [3] Труды ИПА РАН. Вып. 10. В. А. Брумберг, Н. И. Глебова, М. В. Лукашева, А. А. Малков, Е. В. Питьева, Л. И. Румянцева, Л. Л. Свешников, М. А. Фурсенко. Расширенное объяснение к «Астрономическому ежегоднику». - СПб.: ИПА РАН, 2004, 488стр.
- [4] Rambaux N., Williams J. The Moon's physical librations and determination of their free modes. // *Celest Mech Dyn Astr*, 2011a. 109:85–100. Supplementary file. Tables.
- [5] Гусев А.В., Петрова Н.К., Ханада Х. Вращение, физическая либрация, внутреннее строение активной многолоуной Луны. Монография. Изд-во Казанского унив., 323 стр.
- [6] Shpekin M.I. Some principles of creating astrometric observatory on the Moon territory. [http://ms2014.cosmos.ru/sites/ms2014.cosmos.ru/files/5m-s3\\_abstract\\_book.pdf](http://ms2014.cosmos.ru/sites/ms2014.cosmos.ru/files/5m-s3_abstract_book.pdf)





## ИКИ РАН,

площадь академика Келдыша  
Метро "Калужская", первый вагон из центра, по тоннелю — прямо,  
по второму поперечному тоннелю- направо, выход на площадь,  
далее по стрелкам на схеме

## IKI RAS

You should get off at "Kalyzhskaya" metro station using the southern exit.  
After leaving a station lobby through glass doors you should go straight  
to the end of the tunnel, then take right and use the stairs to get to the surface.  
From this point you may follow either arrow on this map



# MOSCOW METRO SCHEME





## **REGISTRATION AND INFORMATION DESK**

location:  
IKI,  
entrance A-4

time:  
**9 october, 8:30–18:00**  
**10 -13 october, 9.00-18.00**

## **SCIENTIFIC SESSIONS**

location:  
IKI conference hall,  
second floor

## **POSTER SESSIONS**

location:  
IKI exhibition hall,  
ground floor

time:  
**9 october, 18.00-19.00**  
**11 october, 18.00-19.00**

# SOCIAL PROGRAM

9 october	10 october	11 october	12 october	13 october
				<b>14:00</b> Visit to <b>RESEARCH,            DEVELOPMENT            &amp; PRODUCTION            ENTERPRISE            "ZVEZDA"</b> Departure from IKI, the entrance № A4
<b>18-00</b> <b>WELCOME            PARTY</b>  Space Research Institute (IKI), Exhibition hall	<b>19-00</b> <b>Ludwig Minkus            "LA BAYADERE"</b> <i>Ballet</i>  Bolshoi theater	<b>19-00</b> <b>IDOL GALA            SHOW</b>  <i>Moscow circus            on Vernadskogo            prospect</i>	<b>18-00</b> <b>CONCERT</b>  Space Research Institute(IKI), Conference hall	
	<b>19-00</b> <b>Paolo Baccianella            "THE BEST"</b> <i>Organ (Italy)</i>  Moscow international performing arts center	<b>19-00</b> <b>MADAMA            BUTTERFLY</b> <i>Opera</i>  Stanislavsky and Nemirovich- Danchenko Mos- cow music theatre	<b>19-00</b> <b>RECEPTION</b>  Space Research Institute(IKI), Exhibition hall	
	<b>20-30</b> <b>ALEKSEY            FETISOV'S            ROCK&amp;ROLL TRIO</b>  Jazz club "Union of composers Club"	<b>19-00</b> <b>CRAZY            DANCES WITH            FABIO            MASTRANGELO</b>  The Russian Philharmonic The State Kremlin Palace		

for additional information and registration for the events please contact  
 Mrs Julia Brekhovskikh  
 E-mail: [yulia.brekhovskikh@yandex.ru](mailto:yulia.brekhovskikh@yandex.ru)

## INTERNET ACCESS AND WIFI

there is Internet access in and near the conference hall

## точки питания вблизи ИКИ / lunch points nearest to IK



1. ИНСТИТУТ КОСМИЧЕСКИХ ИССЛЕДОВАНИЙ РАН, столовая, 1 этаж, секция АЗ  
SPACE RESEARCH INSTITUTE OF THE RAS, Food center, Ground Floor, Section A3
2. ТЦ “КАЛУЖСКИЙ”, ул. Профсоюзная, д. 61А, зона ресторанов, 2 этаж  
“KALUZHSKIY” Market Center, Profsoyuznaya Street, 61A, 2 Floor
3. Ресторан “НИКА” в Бизнес-центре Газпром, ул. Обручева, 23  
“NIKA” restaurant in Bussiness Center Gas Field, Obrucheva street 23
4. Кафе “АндерСон” на ул. Обручева, д. 30/1  
Café “AnderSon”, Obrucheva Street 30/1, Obrucheva street 23

